MATHEMATICAL MODELING OF PHOTOCHEMICAL AIR POLLUTION

Gregory J. McRae
William R. Goodin
John H. Seinfeld

Environmental Quality Laboratory
California Institute of Technology
Pasadena, California 91125

Final Report to the

STATE OF CALIFORNIA AIR RESOURCES BOARD
in

Completion of Research Under

ARB Contract Nos. A5-046-87 and A7-187-30

EQL Report No. 18

27 April 1982

Dum Spiro Sperum

... While I breathe I hope

Hippocrates

ACKNOWLEDGEMENTS

Completion of this research project would not have been possible without the assistance, advice and cooperation of a great number of individuals and organizations. Unfortunately it is not feasible to adequately acknowledge all the unique contributions and so, to those involved, the authors offer their sincere gratitude. There are however, some people who deserve special mention. Dr. John Seinfeld, the project supervisor and faculty advisor to Gregory J. McRae, has been a major source of inspiration. His scientific insights, thoughtful critiques and practical support have been invaluable.

This work was carried out under the auspices of the Environmental Quality Laboratory. The enthusiastic support of its Director, Dr. Norman H. Brooks, and the technical contributions of: Glen Cass, James Tilden, Shohreh Gharib and Pamela McMurry are truly appreciated. The superb secretarial work of Patricia Houseworth and Carol Marr, together with the graphics executed by Philip Dubé, greatly facilitated the preparation of this manuscript. Other staff members, both past and present, who have assisted with the report production include: Theresa Fall, Mary Ann Gray, Jeri Lucas, Dennis Petticoffer and Patricia Rankin.

Some sections of the report are the results of collaborative studies involving other investigators. The objective analysis procedures and numerical analysis techniques were developed jointly with Dr. William Goodin. The formulation, testing and sensitivity analysis

of the photochemical reaction mechanism was a cooperative venture that involved members of the Chemical Engineering Department: Dr. John Seinfeld, Stan Sander, Andrew Falls and Matsato Koda. Many staff members of the South Coast Air Quality Management District (SCAQMD) provided valuable assistance in compiling the needed emissions, air quality and meteorological data.

The California Air Resources Board Research Division, its chief Dr. John Holmes, and the Air Quality Modeling Section: Andrew Ranzieri, Paul Allen, Praveen Amar, Marna Johns, Kit Wagner and Timothy Woody have contributed immeasurably to the success of this venture. Financial support for the work was provided by the California Air Resources Board contracts A5-046-87 and A7-187-30*. Additional funding was met by a Department of Energy Institutional Grant EY-76-G-03-1035. The first author was sustained by Graduate Research Assistantships and Fellowships financed by grants and gifts to the Environmental Quality Laboratory.

---

*A requirement of these contracts is that the following disclaimer be inserted. "The statements and conclusions in this report are those of the Contractor and not necessarily those of the State Air Resources Board. The mention of commercial products, their source, or their use in connection with material reported herein is not to be contrued as either an actual or implied endorsement of such products."

TABLE OF CONTENTS

TABLE OF CONTENTS (Continued)

TABLE OF CONTENTS (Continued)

TABLE OF CONTENTS (Continued)

TABLE OF CONTENTS (Continued)

TABLE OF CONTENTS (Continued)

TABLE OF CONTENTS (Continued)

TABLE OF CONTENTS (Continued)

LIST OF FIGURES

LIST OF FIGURES (Continued)

LIST OF FIGURES (Continued)

LIST OF FIGURES (Continued)

LIST OF FIGURES (Continued)

LIST OF FIGURES (Continued)

LIST OF FIGURES (Continued)

LIST OF FIGURES (Continued)

LIST OF FIGURES (Continued)

LIST OF FIGURES (Continued)

LIST OF FIGURES (Continued)

LIST OF FIGURES (Continued)

LIST OF TABLES

LIST OF TABLES (Continued)

LIST OF TABLES (Continued)

LIST OF TABLES (Continued)

CHAPTER 1

INTRODUCTION

1.1 Objectives

A particularly serious problem facing densely populated areas is the environmental degradation caused by the presence of photochemical air pollution. The problem is both pervasive and difficult to control. An important element of any rational approach directed at attempting to improve the situation is a reliable means for evaluating the air quality impact of alternative control measures. This report presents such a capability in the form of a mathematical description of the production and transport of photochemical oxidants within an urban airshed.

1.2 *Photochemical Air Pollution*

Photochemical oxidant air pollution, or as it is more commonly known--smog, is actually a mixture of chemical compounds. In a typical urban atmosphere there are many oxidants including such species as ozone (O_3), nitrogen dioxide (NO_2), peroxyacetylnitrate (PAN) and hydrogen peroxide (H_2O_2). These, and other pollutants, are produced as a result of the action of sunlight on the emissions of nitrogen oxides (NO_x) and reactive hydrocarbons (RHC). An important characteristic of oxidants is that they are not emitted by the pollutant sources, but rather, are formed as products of chemical reactions in the atmosphere. It is this latter property that makes their control so difficult. When coupled with the fact that the amount of oxidant formed in any given urban area has a complex dependence on time of day, meteorological

conditions and the nature of the pollutant sources, the design of effective abatement programs becomes an even more complex undertaking.

Historically most pollution control measures have been based on the notion that a reduction in precursor emissions leads to a proportionate improvement in air quality. Unfortunately, the inherent non-linear nature of the chemistry of oxidant formation precludes the use of such simple approaches. Indeed, depending on the initial state of the atmosphere, it is possible to produce an increase, decrease or no change in oxidant levels from a simple strategy based on reducing one of the precursor emissions. Figure 1.1, for example, illustrates the effects on ozone concentration arising as a result of lowering the nitrogen oxides. These counter-intuitive results further highlight the need for a formal methodology capable of predicting the air quality impact of changes in emissions.

1.3 Modeling Photochemical Air Quality

At the core of any approach which attempts to relate changes in pollutant emissions to ambient air quality is a reliable prediction method. Whether the prediction scheme is a simple chart, formula or a complex numerical procedure there are three basic elements which must be considered; the meteorology (M), the source emissions (E) and the chemical interactions. Consider the schematic representation shown in Figure 1.2 where the function F, or air quality model, denotes the means of relating changes in contaminant emissions to the resulting air quality AQ. Mathematically F can be an algebraic or differential

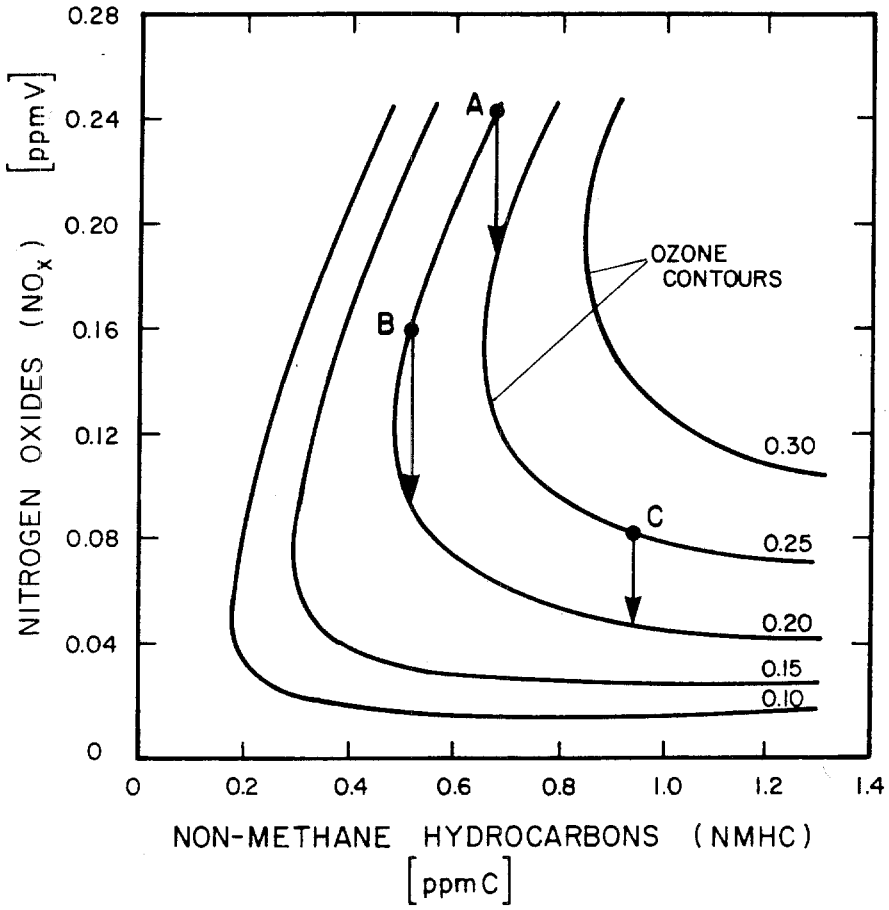

FIGURE 1.1

Ozone Isopleth Plot as a Function of the Precursor Concentration of Nitrogen Oxides (NO_x) and Non-Methane Hydrocarbon (NMHC). The Three Cases A,B, and C Indicate the Effect, On Ozone, of Reducing Nitrogen Oxides. [Graph derived from Whitten and Hogo (1978).]

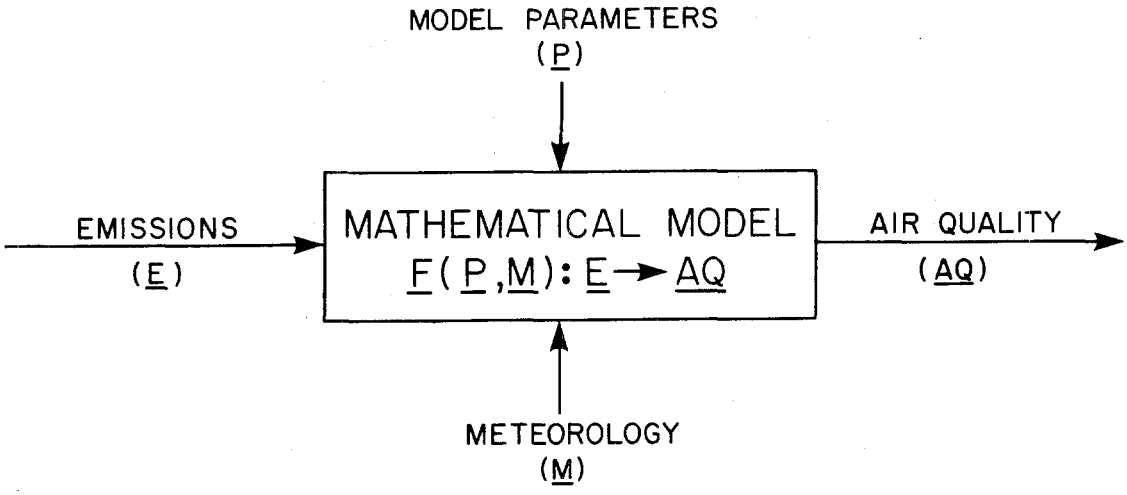

FIGURE 1.2

Schematic Structure of an Air Quality Model

system of arbitrary dimension. Given E, M and a set of additional parameters P, that characterize the atmospheric chemistry, the air quality modeling problem can be represented in a general way by the mapping

$$F(P,M):E \longrightarrow AQ \qquad (1.1)$$

As might be expected there is a considerable literature that describes different functional representations for F, some of which are summarized in the reviews by: Roth et al. (1976), National Academy of Sciences (1977), Dimitriades (1977), Myrabo et al. (1977) and Turner (1979). Despite the diversity of methodologies there two basic types of models. Those which are based on a fundamental description of the physics and chemistry occuring in the atmosphere are classified as a priori approaches. Deterministic models normally incorporate a mathematical treatment of the chemical and meteorological processes and in addition utilize information about emission distributions.

Another class of methods involves the use of a posteriori models in which empirical relationships are deduced from smog chamber or atmospheric measurements. These models are usually very simple and typically bear a close relationship to the actual data upon which they are based. This latter feature is a basic weakness. Because the models do not explicitly quantify the causal phenomena they cannot be reliably extrapolated beyond the bounds of the data from which they were derived. As a result, statistically based models are not ideally suited to the task of predicting the impacts of drastic changes in emissions.

While a detailed evaluation of all the various techniques is beyond the scope of the present study, Tables 1.1 and 1.2 summarize the results of an extensive literature survey conducted to assemble background material for this project. Both a priori and a posteriori methods are useful tools; however as a rule, if data are available to test a model based on scientific fundamentals then that approach is preferable.

1.4 The Atmospheric Diffusion Equation

The various elements which must be linked as part of an a priori methodology for relating emissions to air quality are shown in Figure 1.3 where the mathematical model provides a framework for integrating the following basic components:

A. A kinetic mechanism describing the rates of atmospheric chemical reactions as a function of the concentration of the various species present.

B. A source description, giving the temporal and spatial distribution of emissions from significant pollutant sources within the airshed.

C. A meteorological description, including wind speed and direction at each location in the airshed as a function of time, the vertical temperature structure and radiation intensity.

TABLE 1.1

Empirical Relationships for Predicting the Impact of Photochemical Oxidant Control Strategies

Methodology	Selected References
Smog Chamber Data	Dimitriades (1972, 1976) Hamming, Chass, Dickinson et al. (1973)
Aerometric Data Analysis	Merz, Painter and Ryason (1972) Trijonis (1972, 1974), Trijonis et al. (1978) Paskind and Kinosian (1974) Bailey (1975) Myrabo, Wilson and Trijonis (1977) Tiao, Phadke and Box (1975) Post and Bilger (1978) Trijonis and Hunsaker (1978) Horie, Marians, Trijonis et al. (1979)
U.S. Environmental Protection Agency Recommended Methods	Schuck and Papetti (1973) U.S. Environmental Protection Agency (1971, 1974, 1978)

TABLE 1.2

Physicochemical Models for Predicting the Impact of Photochemical Oxidant Control Strategies

Methodology	Selected References	
Kinetic Mechanisms	Hecht, Seinfeld and Dodge (1974) Dodge (1977) Falls and Seinfeld (1978) Lloyd, Lurmann, Godden et al. (1979) Whitten, Hogo, Meldgin et al. (1979)	
Box Models	Graedel, Farrow and Weber (1976, 1978) Demerjian and Schere (1979) McRae, Goodin and Seinfeld (1981)	
Models Trajectory	Eschenroeder and Martinez (1972) Lloyd, Lurmann, Godden et al. (1979) McRae, Goodin and Seinfeld (1981)	vertically resolved
	Wayne, Kokin and Weisburd (1973) Whitten and Hogo (1978)	single cell
Grid Models	Reynolds, Roth and Seinfeld (1973) Reynolds, Liu, Hecht et al. (1974) Roth, Roberts, Liu et al. (1974) McRae, Goodin and Seinfeld (1979) McRae, Goodin and Seinfeld (1981)	vertically resolved
	MacCracken and Sauter (1975) MacCracken, Walton, Duewer et al. (1978) Duewer, MacCracken and Walton (1978) McRae, Goodin and Seinfeld (1981)	vertically integrated

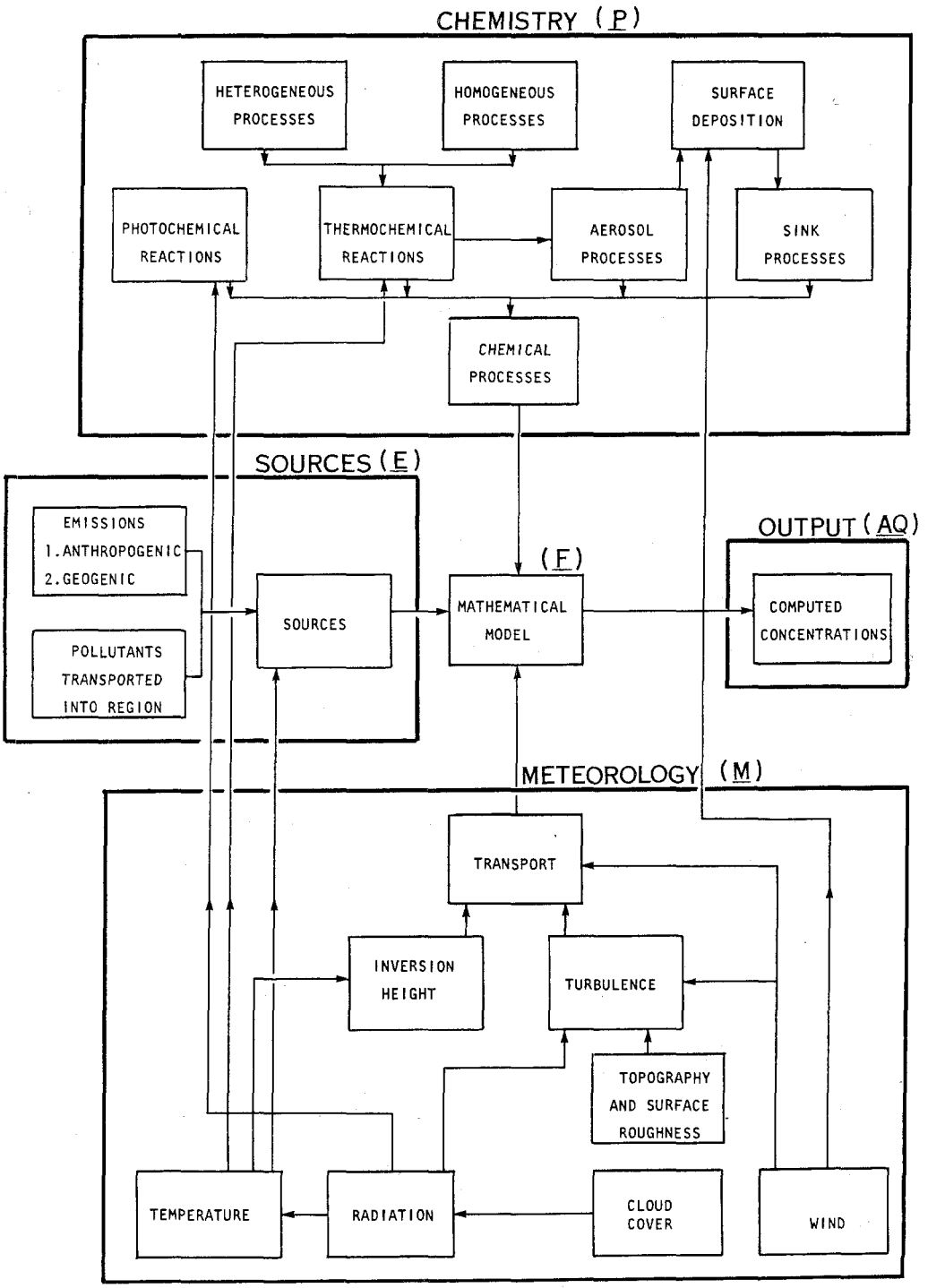

FIGURE 1.3

Elements of a Mathematical Model for Relating Pollutant Emissions to Ambient Air Quality

The detailed formulation of a system which links the components parts, shown in Table 1.3, is a difficult undertaking because it is necessary to maintain a balance between the need for computational economy and the desire for an accurate representation of the underlying physics and chemistry. In this study the formation and transport of chemically-reacting species in the turbulent planetary boundary layer is described by the atmospheric diffusion equation.

$$\frac{\partial c_i}{\partial t} + \nabla\cdot(\underline{u}c_i) = \nabla\cdot(K\nabla c_i) + R_i \qquad (1.2)$$

where c_i is the concentration of the species i, $\underline{u}(\underline{x},t)$ is the prescribed flow field, R the chemical reaction rate and K a parameterization of the turbulent mixing. Various reduced forms of the atmospheric diffusion equation (1.2) provide the basis for less complex models. For example the modeling system developed as part of this study incorporates a vertically integrated, a Lagrangian trajectory and single cell box models. Since each model employs common components and input data they can be used in a unified approach to air quality modeling. The simpler formulations can be used for rapid screening calculations and the more complex models for detailed evaluations. Subsequent chapters of this work discuss the validity and practical implementation of these different representations of atmospheric concentration dynamics.

TABLE 1.3

Summary of Inputs Needed to Solve the
Atmospheric Diffusion Equation

Basic Input	Detailed Components
Meteorology ($\underline{M}$)	Three dimensional wind field Mixing depth Topography and surface roughness Turbulent diffusion coefficients Solar insolation Ultraviolet radiation Temperature Relative humidity
Chemical Kinetics ($\underline{P}^c$)	Reaction mechanism Reaction rate constants Reaction stoichiometry Surface deposition velocities Hydrocarbon lumping procedure
Air Quality Data ($\underline{P}^a$)	Initial and boundary conditions Verification data
Emission Inventory (E)	Mobile sources Stationary sources

1.5 Structure of this Research

A basic goal of this research is the formulation of a practical airshed modeling system that incorporates the the most recent developments in photochemical reaction mechanisms, turbulent diffusion, surface removal processes, numerical solution techniques and objective analysis procedures. The formulation of such a system involves a number of basic steps the first of which is a detailed examination of the validity of the atmospheric diffusion equation as a basis for describing the formation and transport of photochemical air pollution. The second step requires that the form and interaction between the various physical and chemical processes be specified and tested against independent experiments. Once the appropriate mathematical descriptions have been formulated then it is necessary to implement suitable numerical solution procedures. The final step is to assess the ability of the model to predict the actual concentration distributions in an urban airshed.

The following chapters are devoted to these tasks and since this involves a significant amount of material an overall perspective is useful. Table 1.4 presents a summary outline and Figure 1.4 illustrates how each chapter is related to the atmospheric diffusion equation.

TABLE 1.4

Outline of Contents of Chapters

CHAPTER	SUMMARY OUTLINE
2	Model formulation and detailed derivation of the atmospheric diffusion equation
3	Development of objective analysis procedures for specification of wind fields, mixing heights and initial concentration distributions
4,5	Parameterization of the turbulent mixing processes under different meteorological conditions
6	Characterization of the surface removal mechanisms
7	Treatment of point and area source emissions in a grid based model
8,10	Implementation, testing and sensitivity analysis of a photochemical reaction mechanism
9	Numerical solution of the atmospheric diffusion equation using operator splitting and coordinate transformations. Selection of a numerical method for solving the advection-diffusion equation. Solution procedures for the chemical kinetics
12	Evaluation of the model performance in an urban airshed
13,14	Summary and Conclusion

Species Continuity Equation

$$\frac{\partial c_i}{\partial t} + \overset{3}{\downarrow}\nabla\cdot(uc_i) = \overset{4,5}{\downarrow}\nabla\cdot(K\nabla c_i) + \overset{8,10}{\downarrow}R_i \quad ; \; i = 1,2,\ldots,p$$

Initial Conditions

$$\overset{3}{\downarrow}c_i(\underset{\sim}{x},0) = \overset{12}{\downarrow}c_i^0 \quad ; \; t = 0$$

Boundary Conditions (General form of $\underset{\sim}{a},\underset{\sim}{b},f$ depend on application)

$$\left[\overset{6}{\downarrow}\underset{\sim}{a}\,c_i + \overset{4}{\downarrow}\underset{\sim}{b}\,\frac{\partial c_i}{\partial x}\right]\cdot\underset{\sim}{\hat{n}} = \overset{7}{\downarrow}f$$

FIGURE 1.4

Inputs to the Atmospheric Diffusion Equation and Processes Required for Numerical Solution - Numbers Represent Subsequent Chapters.

CHAPTER 2

FORMULATION OF AN URBAN SCALE AIRSHED MODEL

2.1 Introduction

Modeling urban scale air pollution is essentially the problem of describing the formation and transport of chemically reactive species in the turbulent planetary boundary layer. As used in this study, an air quality model will be taken to represent a physiochemical model based on theoretical treatments of atmospheric chemistry and meteorology. This chapter presents the basic model formulation and discusses the key assumptions which must be invoked in order to obtain a tractable set of governing equations.

2.2 Species Continuity Equation

A common starting point for most air quality model derivations is a statement of mass conservation. A differential expression of the mass balance for species c_i, in a p-component mixture, is given by

$$\frac{\partial c_i}{\partial t} + \nabla\cdot(\underline{u}_i c_i) = R_i(c_1,\ldots,c_p,T) \qquad (2.1)$$

where $\underline{u}_i(\underline{x},t)$ is the velocity of species c_i at position $\underline{x}$ at time t and R_i is the chemical generation rate. A more useful form of the mass flux $\underline{u}_i c_i$ can be written in terms of the mass-weighted average velocity $\underline{u}$ of the mixture as a whole. The velocity of species c_i relative to the mean $\underline{\tilde{u}}$ is simply $\underline{u}_i - \underline{\bar{u}}$ and so the diffusive flux of c_i relative to a coordinate system moving with the mean velocity is then $\underline{j}_i\underline{\tilde{u}} = c_i(u_i - \underline{u})$. Equation (2.1) can then be written in the form

$$\frac{\partial c_i}{\partial t} + \nabla\cdot(\underline{u}c_i) = -\nabla\cdot\underset{\sim}{j}_i + R_i \qquad (2.2)$$

The diffusive flux is represented by Fick's law, $\underset{\sim}{j}_i = -D_i \nabla c_i$, where D_i is the molecular diffusion coefficient of c_i with respect to the composite mixture. The molecular diffusion coefficient in general depends upon the temperature and chemical potential gradients of all species in the mixture (Bowen, 1976). If the pollutant species are present in sufficiently dilute amounts, then the conservation of mass for a particular component can be written in the form

$$\frac{\partial c_i}{\partial t} + \nabla\cdot(\underline{u}c_i) = \nabla\cdot(D_i\nabla c_i) + R_i \qquad (2.3)$$

The mixture mass balance consists of two parts; the first is a conservation statement (2.3) for each species and the second is a balance for the mixture as a whole. In order to describe the dynamics of the complete system it is necessary to carry out a simultaneous solution of the coupled equations of mass, momentum and energy conservation. Since the appropriate equations of motion for air are extensively discussed in Dutton and Fichtl (1969), Spiegel and Veronis (1960), Businger (1973), Donaldson (1973) they will not be reiterated here.

2.3 Decoupling Species and Carrier Fluid Equations

Because of the computational difficulties it is useful to attempt a decoupling of the species continuity equations from the equations of motion of the carrier fluid. While this approach simplifies the solution procedure, the temperature and velocity fields must nevertheless

be externally supplied to the airshed model. A key assumption implicit in the separation is that the presence of pollutant gases and particulate aerosols does not significantly affect the meteorology. The objective of this section is to examine the justification for the decoupling, as it has not been extensively discussed in previous photochemical modeling studies.

Two effects could invalidate the assumption. The direct effect on atmospheric temperature structure from heat released in the chemical reactions can be considered to be negligible as most species are present only in trace quantities. A more serious question arises, however, as to the effect of gaseous pollutants and aerosols on the radiative transfer processes. Recently there have been a number of studies on the effects of pollutant material on the microclimates of urban areas. (Ackerman et al., 1976; Ackerman, 1977; Atwater, 1977; Bergstrom and Viskanta, 1973abc; Viskanta and Daniel, 1980; Viskanta et al., 1977; Welch et al., 1978; Zdunkowski and McQuage, 1972; Zdunkowski et al., 1976.) The results of these studies indicate that gaseous pollutants, which interact primarily in the infrared, tend to heat the earth's surface during the day by increasing the downward thermal radiation and conversely enhancing the cooling at night. While there is general agreement on this result, the conclusions regarding the effects of aerosols on the temperature structure are not so straightforward. The reason for this is that the radiation balance depends on both the surface albedo and the aerosol characteristics.

Ackerman (1977) has presented a model which considers the effects of pollutants on both longwave and shortwave radiation and the interaction of the modified radiation field with the surface fluxes. The results are of particular interest because the model was applied to the Los Angeles Basin. An important conclusion of the study was that there is a strong tendency for self stabilizing compensation. This was particularly evident in the relationship between the atmospheric absorption of shortwave radiation and the heat flux. If the radiation is absorbed by a layer near the ground the heat transfer from the surface to the atmosphere is reduced. This in turn tends to keep the surface and the boundary-layer temperatures approximately the same as if no absorption were taking place. Loss of energy due to backscatter may also result in a reduction of the depth of the boundary layer rather than in a reduction in temperature. An additional compensation occurs within the radiative fluxes. The warming of the atmosphere by shortwave radiation is opposed to a lesser degree by an increase in longwave emission, a phenomenon which also tends to maintain the surface temperature.

A number of different studies (Atwater, 1977; Bergstrom and Viskanta, 1973abc; Ackerman, 1977; Viskanta and Daniel, 1980) indicate that the principal effect of aerosols on the urban climate is to increase the daytime temperatures whereas the gaseous pollutants decrease the boundary layer temperature at night. The changes in both cases are quite small; for example, Viskanta and Daniel (1980) predicted that the mean difference in temperature with and without

radiatively interacting pollutants was < 0.5 ^{o}K and the changes in the mixed layer height < 10%. In areas with relatively high background particulate concentrations the aerosol heating tends to retard the growth of the mixed layer. Ackerman (1977) showed, however, that for Los Angeles this tendency could cause a strengthening of the sea breeze circulation which in turn would increase the turbulent mixing and tend to raise the inversion base. An increase in the strength of the sea breeze would bring in more cool air and thus oppose the temperature increase caused by the aerosol absorption. In passing it is important to note that most of the above findings are primarily based on theoretical studies. There is a great need for more experimental data, in particular about the optical properties of aerosols, in order to quantify the feedback mechanisms between pollutants and the thermal structure of the atmosphere.

The major inference to be drawn from the preceding literature survey is that the pollutant gases and aerosols have only a minor influence on the urban climate. In particular, the net impact of particles was to decrease the temperature of the atmosphere-earth system, while the influence of absorption and emission of thermal radiation by gases was to increase the system temperature. The effects of gaseous and particulate pollutants are opposite and to a certain extent partially compensating. Under these conditions decoupling the species continuity equation from the equations of motion is a valid approximation in an urban atmosphere. This conclusion should not, however, be interpreted as a statement that the decoupling can be used in all

situations. There is some evidence to suggest that while on an urban scale the effects are minor, the influence on regional climate may be significant (Atwater, 1977).

2.4 Turbulent Flows

A basic problem with any effort to solve the species continuity equation is that the velocity field $\underline{u}(\underline{x},t)$ is typically not available as a continuous function of space and time. In most urban airsheds the wind field is sampled only at a discrete set of spatial locations. Lamb and Seinfeld (1973) have shown that only the features of the velocity field with spatial scales larger than about twice the average distance between sampling points can be described explicitly. All smaller features cannot be resolved and therefore must be treated as stochastic variables. The conventional representation for $\underline{u}$ is as a sum of a deterministic $\underline{u}$ and a random component $\underline{u}'$, $\underline{u} = \underline{u} + \underline{u}'$. Because of the fluctuating component u', (2.3) is then a stochastic differential equation and c_i is a random variable. Since the probability density function for c_i cannot, in general, be determined only statistical moments are available. In order to make meaningful predictions it is necessary to average the equations in such a manner that model outputs can be identified with experimental measurements in the field. Some information, related to the small scale variations, is lost in the process of taking the mean value. Averaging (2.3) over an infinite ensemble of realizations and neglecting molecular diffusion gives

$$\frac{\partial \langle c_i \rangle}{\partial t} + \nabla \cdot (\underline{\bar{u}} \langle c_i \rangle) + \nabla \cdot \langle \underline{u}' c_i' \rangle = \langle R_i(\langle c_1 \rangle + c_1', \ldots, \langle c_p \rangle + c_p') \rangle \tag{2.4}$$

where $\langle c_i(x,t)\rangle$ is the ensemble mean concentration. This result follows from the linear nature of the ensemble averaging operator defined by (2.5) where $p^i(t)$ is the i-th realization of a particular process p(t). The properties (2.6 - 2.8) are used in the derivation of (2.4).

$$\langle p(t)\rangle = \lim_{N\to\infty} \frac{1}{N} \sum_{i=1}^{N} p^i(t) \tag{2.5}$$

$$\langle Ap(t)\rangle = A\langle p(t)\rangle \quad ; \; A = \text{constant} \tag{2.6}$$

$$\langle p_1(t) + p_2(t)\rangle = \langle p_1(t)\rangle + \langle P_2(t)\rangle \tag{2.7}$$

$$\left\langle \frac{\partial p(t)}{\partial s} \right\rangle = \frac{\partial}{\partial s} \langle p(t)\rangle \tag{2.8}$$

In these expressions s is an independent variable,for example space or time. There is an important difference between the ensemble average, (2.5), and the temporal (or spatial) average implied by the overbar for $\underline{u}$. Mean fluid velocities are normally determined by a process involving temporal and spatial averaging of the form

$$\overline{\underline{u}} = \frac{1}{T} \int_0^T \underline{u}(t)\, dt \tag{2.9}$$

This average itself will fluctuate depending on the starting point and the duration of the averaging process. The use of the temporal average, (2.9), to define $\overline{\underline{u}}$ complicates the process of deriving (2.4) for it is necessary to assume that

$$\langle \underline{\bar{u}} c' \rangle = \underline{\bar{u}} \langle c' \rangle \equiv 0 \qquad (2.10)$$

Strictly speaking, unless $\underline{\bar{u}}$ is a constant, this assumption is not satisfied; however, the averaging interval may be chosen in such a way to approximate the equality with comparatively high accuracy. To do this the averaging interval, T, must be long in comparison with the characteristic periods of the fluctuating quantity $\underline{u}'(t) = \underline{u}(t) - \underline{\bar{u}}(t)$. Sheih (1980) discusses how the averaging time can be selected from a knowledge of the spectral distribution of the wind velocity fluctuations. An investigation of the averaging time needed to approximate ensemble average statistics is presented in Wyngaard (1973). Further, if the ergodic hypothesis can be invoked, i.e., that $\underline{u}(t)$ is independent of starting time, then ensemble and time average are identical. Monin and Yaglom (1971) discuss, in considerable depth, the problem of averaging. Depazo (1977) has considered the more difficult case of intermittent flows.

2.5 The Turbulent Closure Problem

Neglecting molecular diffusion, (2.4) is a rigorously valid equation for the ensemble mean concentration. If the variables $\langle \underline{u}' c_i' \rangle$ and any of those arising from R_i are known functions of space and time, then (2.4) can, in principle, be solved to yield $\langle c_i \rangle$. Unfortunately the $\langle \underline{u}' c_i' \rangle$ cannot be measured at all points in an atmospheric flow and, in addition, cannot be exactly predicted because of the classic closure problem of turbulent flow. A great deal of research effort has been directed at attempts to resolve this problem. The most well-known

method of approximating the fluctuating transport term $\langle \underline{u}' c_i' \rangle$ is the so-called gradient transport approximation proposed originally by Boussinesq (1877). With this approach, the transport is based on an analogy to the simplest molecular models in which the flux is assumed to be proportional to the linear mean gradients. The model for a non-isotropic flow is given by

$$\langle \underline{u}' c_i \rangle = -K \cdot (\nabla \langle c_i \rangle) \tag{2.11}$$

where K is the second rank eddy diffusion tensor. Ignoring, for the moment, the chemical reaction term, (2.11) can be substituted into (2.4) to give

$$\frac{\partial \langle c_i \rangle}{\partial t} + \nabla \cdot (\bar{\underline{u}} \langle c_i \rangle) = \nabla \cdot (K \nabla \langle c_i \rangle) \tag{2.12}$$

Considering the almost universal use of (2.11) as a closure approximation in airshed models it is important to outline some of its limitations. Monin and Yaglom (1971) and, in particular, Corrsin (1974) have identified some conditions which are necessary for the valid use of a gradient transport hypothesis. A basic requirement is that the transport mechanism length scale must be much smaller than the distance over which the curvature of the mean transported field gradient changes appreciably. Similar conditions apply to the temporal scales. A more fundamental difficulty occurs when the flows are buoyancy driven. In this situation, particularly for free convection, the fluxes $\langle \underline{u}' c_i' \rangle$ are no longer described by the local gradient. Under unstable conditions parcels of warm air, displaced from their equilibrium position,

rise to the top of the mixed layer. To compensate for these vertical motions, zones of sinking air occur between the rising air parcels. As a result of this combined motion, positive values of w' are correlated with positive temperature fluctuations θ'. The covariance $\overline{w'\theta'}$ is positive but the mean vertical temperature gradient is zero (Deardorff; 1966, 1970).

In an attempt to circumvent some of these problems, considerable effort has been expended to develop so-called second moment turbulent closure models in which the governing equations are closed by including terms parameterizing various turbulent correlations. See, for example, Lewellen et al. (1974), Wyngaard and Cote (1974), Yamada and Mellor (1975), Lumley and Khajeh-Nouri (1974), Mellor and Yamada (1974), Zeman and Lumley (1976), Zeman and Tennekes (1977), Manton (1979), Binkowski (1979), Freeman (1977), and Yamada (1977). While many of these models are conceptually very appealing, their inclusion in an urban airshed model imposes an unreasonable computational burden. In addition to the problems associated with the solution economy, many of the models have been verified for only limited flow regimes and some require the determination of a large number of empirical constants. In spite of the possible benefits of employing a second-order closure model there remains a need for a simple scheme that produces results consistent with the known behavior of pollutants in the planetary boundary layer. The approach adopted in this work is to retain the use of the eddy diffusion concept and to develop the components of K using modern boundary layer theory.

2.6 Eddy Diffusivities

In most models the second rank tensor K is approximated by the diagonal form

$$K = \begin{bmatrix} K_{xx} & 0 & 0 \\ 0 & K_{yy} & 0 \\ 0 & 0 & K_{zz} \end{bmatrix} \qquad (2.13)$$

The presence of zeros in the off diagonal elements implicitly assumes that the principal axes of K are aligned with the Eulerian co-ordinate system, a situation that seldom occurs in the planetary boundary layer (Monin and Yaglom, 1971; Corrsin, 1974). In general the tensor, K, depends on scalar quantities, such as the turbulent kinetic energy and the magnitude of the vertical shear of the horizontal wind. A major barrier to the inclusion, and parameterization, of the off diagonal elements is the lack of suitable laboratory and field data for a range of stability conditions. Freeman (1977), Yamada (1977) and Manton (1979) have used second-order closure models to calculate the off diagonal components of K for simplified atmospheric flows. The effects on concentration predictions have not as yet been extensively discussed in the literature.

An alternative approach, which retains the simplicity of the K-theory formulation, was introduced by Lamb et al. (1975). The basic idea was to develop vertical K_{zz} profiles which, when used in the atmospheric diffusion equation, reproduced the actual concentration distributions. In their initial work they found expressions for $K_{zz}(z)$

that yielded accurate estimates of ground level concentrations under neutral and slightly unstable conditions. A similar method, which makes use of field measurements, has been developed by Crane et al. (1977). Using these techniques it is possible to obtain solutions of the diffusion equation which closely match observed concentration profiles. A variant of this procedure has been implemented in the present airshed model and further details are discussed in Chapter 4.

2.7 Effect of Turbulence on Chemistry

A major problem in modeling atmospheric concentration dynamics is predicting the species reaction rates in a turbulent fluid. The reason for this is that the true reaction rate R_i is a function of $\langle c \rangle + c'$ but only the mean values $\langle c \rangle$ are available after ensemble averaging. A closure assumption used in most airshed models is that the ensemble mean reaction rate is the same as the rate based on ensemble mean concentrations. There are obvious difficulties with this approach. Consider two elementary mechanism steps and their associated forward reaction rates. Assuming the rate constants k are fixed, the chemical production terms are given by

$$R_i = \begin{cases} -k_1 c_1 & ; \; c_1 \xrightarrow{k_1} \text{products} \\ -k_2 c_1 c_2 & ; \; c_1 + c_2 \xrightarrow{k_2} \text{products} \end{cases} \tag{2.14}$$

Expressing the concentrations as a sum of mean and fluctuating components $c_i = \langle c_i \rangle + c_i'$ and ensemble averaging gives

$$\frac{\partial \langle c_1 \rangle}{\partial t} = k_1 \langle c_1 \rangle \tag{2.15}$$

$$\frac{\partial \langle c_2 \rangle}{\partial t} = -k_2 \langle c_1 \rangle \langle c_2 \rangle - k_2 \langle c_1' c_2' \rangle \qquad (2.16)$$

For the first-order decay it is clear from (2.15) that the turbulence has no effect on the reaction rate. In the multicomponent case, (2.16), there is an interaction between the mean and fluctuating concentration level. The closure assumption $\langle R(c) \rangle = R(\langle c \rangle)$ will not be valid unless

$$\langle c_1 \rangle \langle c_2 \rangle \gg |\langle c_1' c_2' \rangle| \qquad (2.17)$$

An obvious question is: what is the effect of neglecting second order correlations of the form $\langle c_1' c_2' \rangle$ in determining the reaction rates? Despite the importance of understanding reactive mixing in turbulent shear flows relatively little progress has been made in developing valid theories for use in practical situations. The complexity of the problem and approaches for resolving some of the difficulties are outlined in O'Brien (1974), Murthy (1975), Spalding (1975), Hill (1976), Shu et al. (1978). The few closure models that have been developed either require assumptions about the nature of the underlying concentration probability density functions (O'Brien, 1974; Lamb and Shu, 1978; Shu et al., 1978) or introduce additional differential equations (Donaldson, 1975) which in turn impose an unreasonable burden on an already complex computational problem.

Given the difficulties of developing simple closure models, an alternative approach is to attempt a delineation of the conditions

under which terms of the form $\langle c_1' c_2' \rangle$ can be expected to be significant. In the absence of mean gradients, two competing processes influence the magnitude of $\langle c_1' c_2' \rangle$: molecular diffusion and chemical reactions. For example if the dissipative scale of the turbulence is small and the reaction rate is very slow, then molecular diffusion can be expected to keep c_1 and c_2 well mixed and the correlation term $\langle c_1' c_2' \rangle$ can be neglected. A numerical measure of the ratio between the diffusive and reaction time scales is given by the Damkohler number N_D (Hill, 1976). For second-order reactions Shu (1976) evaluated N_D using

$$N_D = \frac{T_D}{T_R} = \frac{\text{Diffusive Time Scale}}{\text{Reaction Time Scale}} = \frac{k[\langle c_1 \rangle + \langle c_2 \rangle]\lambda^2}{2D} \qquad (2.18)$$

where D is the molecular diffusion coefficient, and λ is the dissipation length scale (Corrsin, 1958). When $N_D \gg 1$ the characteristic time for chemical reaction is short compared to that for molecular mixing. In this situation $\langle c_1' c_2' \rangle$ will tend to $- \langle c_1 \rangle \langle c_2 \rangle$ and so the reactions between c_1 and c_2 will be governed not by the kinetics but by the rate at which the reactants can be brought together by molecular diffusion. If the time scale for reaction is longer than that of dissipation ($N_D \ll 1$) then concentration fluctuations are removed before they can affect the chemistry. For this situation the mean reaction rate can be satisfactorily predicted by $-k\langle c_1 \rangle \langle c_2 \rangle$. The Damkohler number has been estimated in Table 2.1 for reactions that often occur in photochemical mechanisms. Further details of rate constants and reaction steps are contained in Chapter 8.

TABLE 2.1

Typical Reaction Rate Damkohler Numbers
for a Smog Chamber Experiment[a]

REACTION $A + B \xrightarrow{k}$	RATE CONSTANT k (ppm^{-1}-min^{-1})	CONCENTRATION (ppm) (A)	(B)	DAMKOHLER NUMBER[b] N_D
$NO + O_3 \rightarrow$	23.9	0.045	0.069	13
$NO_2 + O \rightarrow$	1.34×10^4	0.253	1.94×10^{-8}	15400
$NO_2 + O_3 \rightarrow$	0.05	0.253	0.069	0.08
$NO + HO_2 \rightarrow$	1.20×10^4	0.045	1.56×10^{-6}	2650
$OLE + O_3 \rightarrow$	0.15	0.005	0.069	0.05
$O_3 + HO_2 \rightarrow$	1.5	0.069	1.56×10^{-6}	0.5

(a)

Smog Chamber Experiment SUR-119J at 180 mins (See Chapter 8);

$D = 0.17\ cm^2/sec$, $\lambda = 10$ cm.

(b)

$$N_D = \frac{\text{Diffusion Time}}{\text{Reaction Time}} = \frac{k[(A) + (B)]\lambda^2}{2D} \begin{cases} 0.01 < N_D & \text{kinetically limited} \\ 0.01 \leq N_D \leq 50 & \text{intermediate} \\ N_D > 50 & \text{diffusion controlled} \end{cases}$$

A notable feature of the calculations shown in Table 2.1 is that unless the reactants are well mixed, there exists a possibility that some reaction rates are slower than those inferred directly from the kinetics. The importance of this finding must however be placed in its proper context. A variety of factors are involved: the first of which is that in Table 2.1 only single reaction steps are considered, whereas in the atmosphere, many reactions are occurring simultaneously. In a mixture, some reactions will deplete species and others will generate new material. Those reactions which are diffusion limited are normally so fast that lowering the rate constant to the effective mixing rate does not significantly change the overall kinetics. Another approach is to use sensitivity analysis techniques, like those described in Chapter 12, to examine the mechanism performance when all the diffusion limited kinetic rate constants are reduced.

The degree to which the reactants can be considered to be well mixed has an important practical consequence since steep concentration gradients can often exist in the vicinity of plumes. As an example, emissions from large combustion sources are typically rich in nitric oxide. This material is emitted into a background that typically has a high concentration of ozone and other species. The time required to mix the initially separated reactants (NO and O_3) over the whole plume is longer than that required for reaction between NO and O_3. The macroscopic rate of reaction is controlled by the rate of mixing of the plume with ambient air, rather than by the kinetic rate constant for the reaction. The recent measurements of Hegg et al. (1977) appear to

support this contention. If the closure assumption is to be used for plume modeling then it is necessary to include sufficient computational grid points to resolve the concentration gradients.

In the remainder of this study the approximation $\langle R(c)\rangle = R(\langle c\rangle)$ will be adopted even though there is some doubt about its validity in all situations. The second-order closure models that are available do not represent satisfactory alternatives, either because of computational cost or uncertainties in their formulations. In addition to the theoretical difficulties the lack of good experimental data is a major barrier to further progress.

2.8 The Atmospheric Diffusion Equation

In the previous section, the various assumptions and approximations needed to develop a practical air quality model were presented. For each of the p species present in the atmosphere the governing differential equation is given by

$$\frac{\partial \langle c_i \rangle}{\partial t} + \nabla\cdot(\underset{\sim}{\bar{u}}\langle c_i\rangle) = \nabla\cdot(K\nabla\langle c_i\rangle) + R_i(\langle c_1\rangle,\ldots,\langle c_p\rangle) \qquad (2.19)$$

$$i = 1,2,\ldots,p$$

This equation is the starting point for the derivation of almost all airshed models. Since most practical applications entail numerical solutions of (2.19) the airshed must be subdivided into an array of grid cells, where each cell may have horizontal ($\Delta x,\Delta y$) and vertical (Δz) dimensions on the order of a few kilometers and several tens of meters, respectively. Before (2.19) can be solved, it must be filtered

to remove all small scale variations that cannot be resolved. This averaging process must be applied to both the concentration fields and the input parameters, such as the wind velocities and eddy diffusivities. In addition, (2.19) must be time-averaged over an interval equivalent of that used in each time step of the numerical solution procedure. The necessary spatial averaging can be accomplished with a filter of the form (2.20) that operates on an ensemble average quantity $\langle p \rangle$.

$$\tilde{\langle p(t) \rangle} = \frac{1}{\Delta V} \iiint_{\Delta V} \langle p(t) \rangle \, dxdydz \tag{2.20}$$

where ΔV is the computational cell volume. If it is assumed that $\underset{\sim}{u}$ and K do not possess spatial variations on a scale smaller than the computational grid, then (2.19) can be written in the form

$$\frac{\partial \langle \tilde{c}_i \rangle}{\partial t} + \nabla \cdot (\underset{\sim}{u} \langle \tilde{c}_i \rangle) = \nabla \cdot (K \nabla \langle \tilde{c}_i \rangle) + \tilde{R}_i \tag{2.21}$$

In a manner similar to the turbulence closure problem of the previous section it is necessary to assume that

$$\tilde{R}_i [\langle c_1 \rangle, \ldots, \langle c_p \rangle] \simeq R_i [\langle \tilde{c}_1 \rangle, \ldots, \langle \tilde{c}_p \rangle] \tag{2.22}$$

This approximation assumes that the volume-average reaction rate is the same as the reaction rate based on the volume average cell concentrations. Until the recent work of Lamb (1975) the validity of this assumption had not been discussed in the air pollution literature. Lamb concluded that in computational cells surrounding large point

sources there are circumstances in which errors in the concentration predictions can arise from the use of (2.22). This is to be expected as the spatial scale of a plume near the source is typically much smaller than the cell volume. In contrast the second-order closure model developed by Lamb indicates that for diffuse area sources and commonly encountered line sources, there are negligible subgrid-scale chemistry effects. His comments and examples were directed at the fast nonlinear reactions of the NO - O_3 system; most other reactions are generally slower and as a result are less affected by subgrid-scale variations. A major area for future research is the development of subgrid-scale models which can be used to embed large point sources into urban scale airshed models. Some initial steps in this direction are discussed in Chapter 7.

The form (2.23) which emerges as a result of the averaging operations and closure approximations is the basis of most airshed models.

$$\frac{\partial <\tilde{c}_i>}{\partial t} + \nabla\cdot(\underset{\sim}{u}<\tilde{c}_i>) = \nabla\cdot(K\nabla<\tilde{c}_i>) + R_i(<\tilde{c}_1>,\ldots,<\tilde{c}_p>) \qquad (2.23)$$

The steps in the process used to derive the atmospheric diffusion equation are summarized in Figure 2.1. In order to simplify the notation in subsequent sections, and in the following chapters, symbols indicating the nature of the averaging operation will be omitted.

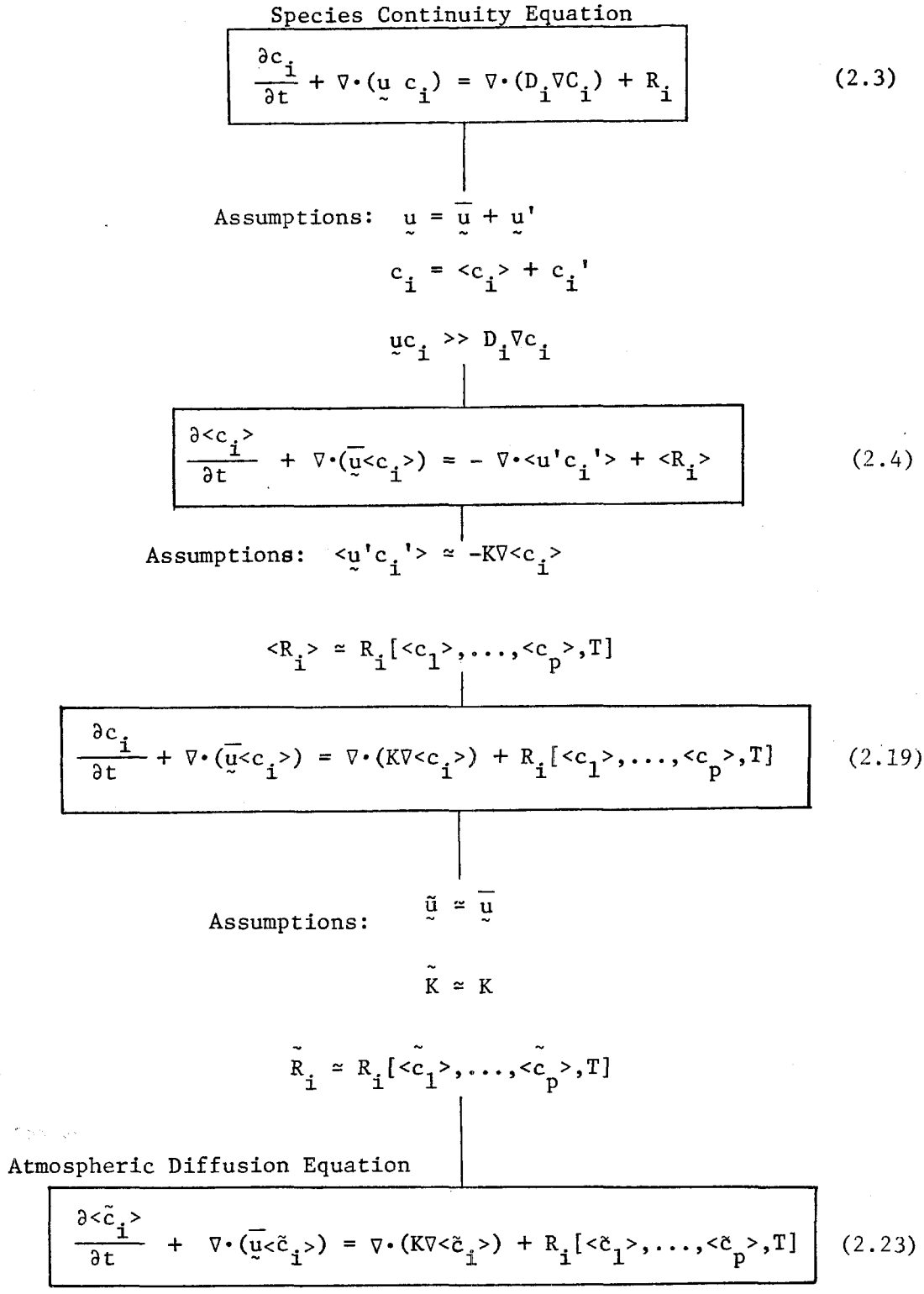

FIGURE 2.1

Summary of the Steps Involved in Deriving the Atmospheric Diffusion Equation

2.9 Vertical Extent of the Airshed Boundaries

In urban areas the definition of the vertical extent of the airshed has a major influence on the choice of the boundary conditions. In most previous studies the top of the airshed has been defined by the base of an elevated inversion. The justification is that, for surface level releases, the extent of vertical mixing is basically controlled by the lower surface of an elevated temperature inversion. In mid-latitudes, over land, this convective boundary layer reaches a height of 1-2 Km by mid-afternoon and exhibits a near-constant distribution of wind speed and potential temperature. The name 'mixed layer' is often used synonymously with the convective boundary layer in much of the literature. Some controversy exists regarding the choice of the height Z_i that defines the thickness of the boundary layer. Tennekes (1970), Zilitinkevich (1972), Clarke and Hess (1973) have suggested that the boundary layer thickness is a function of the Ekman layer depth u_*/f. The modeling studies of Deardorff and Willis (1974) show that the elevation of the lowest inversion base is perhaps a more appropriate measure for unstable conditions.

Use of this height to define the depth of the airshed can, under some conditions, cause great difficulty in establishing appropriate upper level boundary conditions. The calculations by Duewer et al. (1978), using the model described in MacCracken et al. (1978), indicate that ground level predictions for ozone are often quite sensitive to the values chosen for the upper level inflow boundary conditions. Similar findings were noted by Liu et al. (1976). Few concentration

measurements are made above ground level and as a result the upper level boundary conditions are normally set to typical background values. This procedure can severely underestimate the actual concentrations which can exist above the inversion base. Figure 2.2 presents some data measured by Blumenthal et al. (1978) during a special study of the three dimensional structure of concentration distribution over the Los Angeles Basin. The most striking feature, particularly for ozone, is that the concentrations above the inversion base are considerably in excess of normal background levels of 0.04 ppm. These results are similar to the observations made by Edinger (1973) and presented in Figure 2.3. Before discussing how to resolve the difficulties, it is important to understand the origin of the high concentrations and their influence on ground level predictions by the airshed model.

Late in the day the direction of the thermal radiation at the earth's surface changes direction. In particular, after sunset the net heat loss by radiation produces a stable layer close to the ground. With sufficient cooling, the stable layer can extend from the surface to a height of several hundred meters. The stable stratification inhibits vertical mixing and so any ozone trapped aloft is not subject to attack by fresh, ground level, NO_x emissions. In the stable layers dark phase reactions occur which can deplete the ozone. The principal mechanism elements and reaction rate constants from Hampson and Garvin (1977) are:

$$NO + O_3 \rightarrow NO_2 + O_2 \qquad ; k = 23.9 \text{ ppm}^{-1} \text{ min}^{-1} \tag{2.24}$$

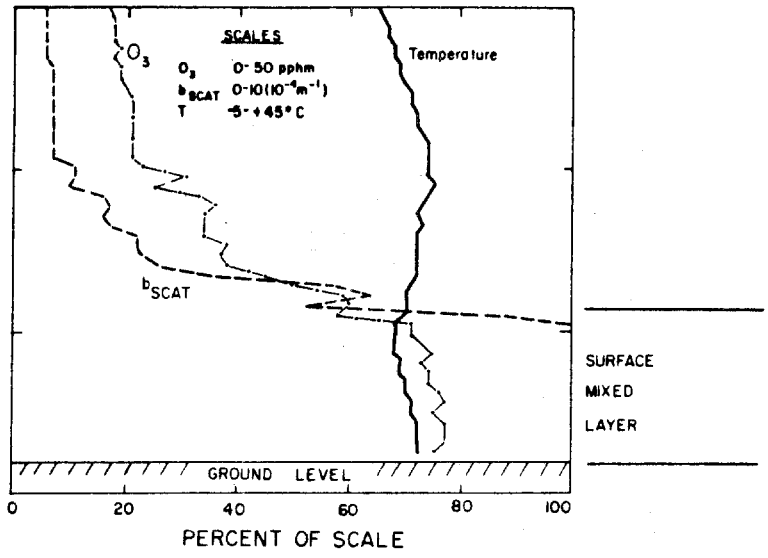

(a)

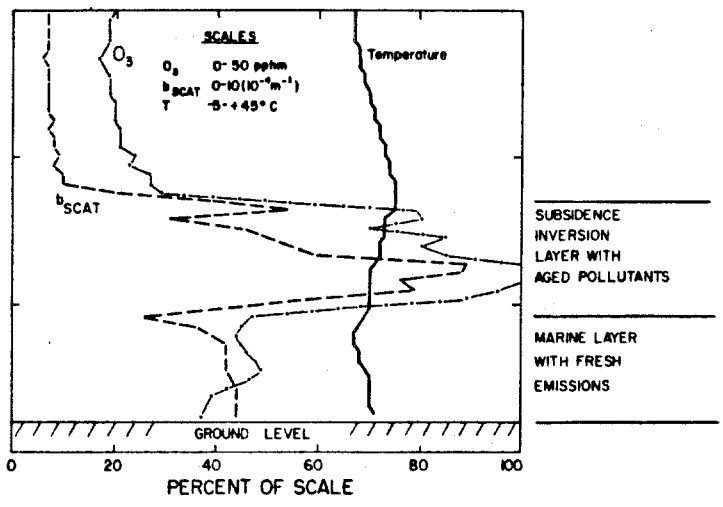

(b)

FIGURE 2.2

Vertical Profiles of Ozone, Temperature and b_{scat} over El Monte Airport (a) 1247 PDT and (b) 1656 PDT. (Blumenthal et al., 1978)

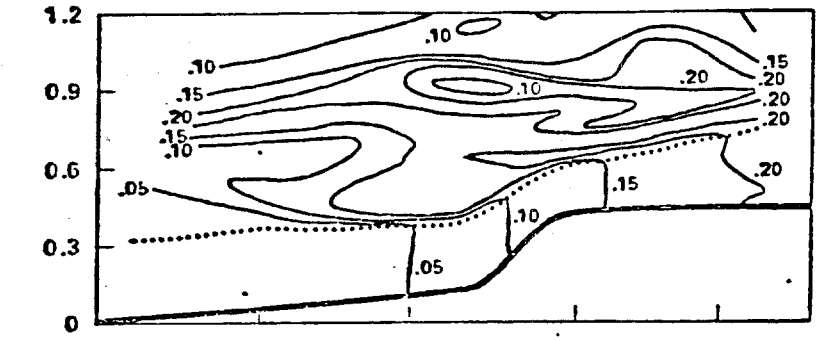

(a)

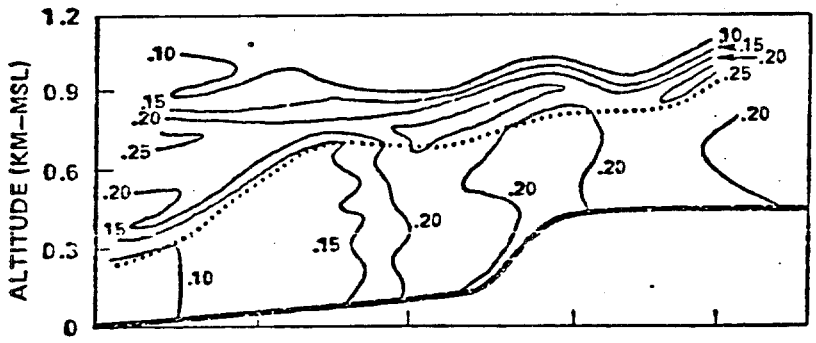

(b)

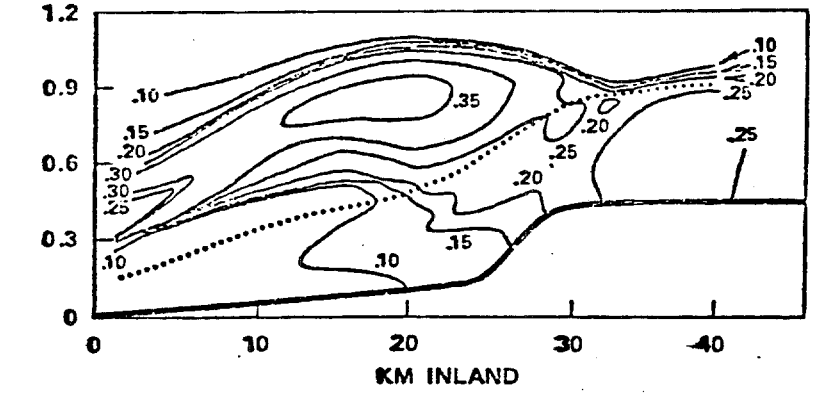

(c)

FIGURE 2.3

Contours of Oxidant Concentrations (ppm) in the Vertical Cross Section from Santa Monica to Rialto-Miro, As Observed by Edinger (1973).
(a) 0900 PDT, (b) 1200 PDT, (c) 1630 PDT 20 June 1970
Dotted Curve Denotes Inversion Base

$$NO_2 + O_3 \rightarrow NO_3 + O_2 \qquad ; k = 0.05 \text{ ppm}^{-1} \text{ min}^{-1}$$

Since by late afternoon the NO concentration levels are already quite small, substantial levels of O_3 can remain aloft. In addition, the little NO_2 that is left can be removed by:

$$NO_3 + NO_2 \underset{\leftarrow}{\overset{\rightarrow}{}} N_2O_5 \qquad ; k = \begin{cases} 2938 \text{ ppm}^{-1} \text{ min}^{-1} \\ 6.85 \text{ min}^{-1} \end{cases} \tag{2.25}$$

$$N_2O_5 + (H_2O) \rightarrow 2HNO_3 \qquad ; k = 0.01 \text{ min}^{-1}$$

The details of the reaction steps are not of major importance; what is of significance is that O_3 produced during one day can be trapped aloft and be fumigated to the ground during the next day. The sequence of events is illustrated in a highly simplified form in Figure 2.4. After sunrise ground heating generates a growing mixed layer which eliminates the stable stratification. As the convective layer grows in depth, material is rapidly entrained and mixed downward. As soon as the layer reaches the height of the high O_3 levels, the ground level concentrations of ozone can be abruptly increased. There is a variety of alternate physical mechanisms which can produce fumigation conditions and they, together with some laboratory experiments, are described in Manins (1977). Zeman and Tennekes (1977) have recently reviewed the literature and presented a parameterized model of the entrainment dynamics at the top of the mixed layer. Zeman and Lumley (1976) have used a second-order closure model to investigate stratified turbulent flows with particular applications to buoyancy driven mixed layers.

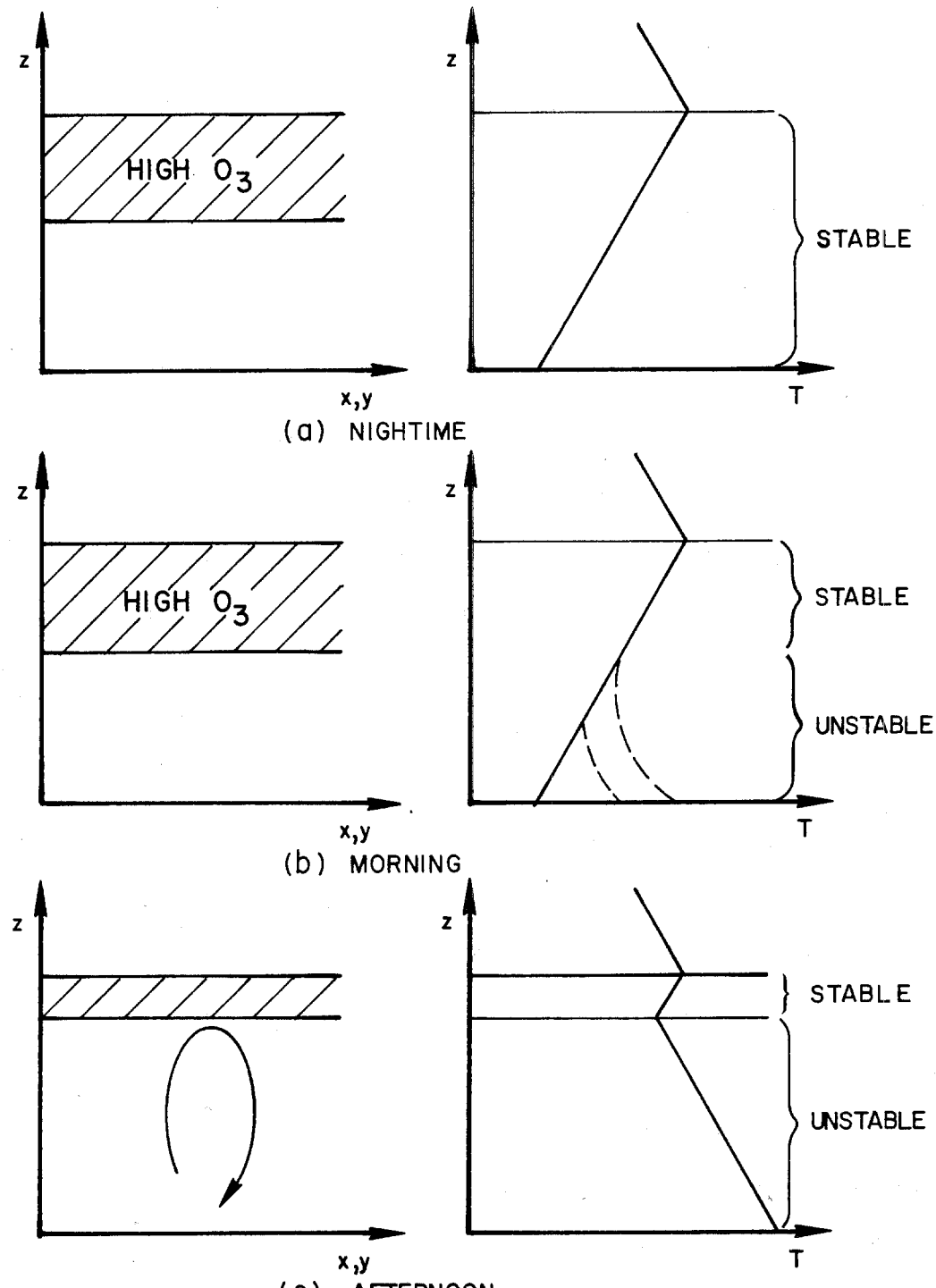

FIGURE 2.4

Sequence of Events Leading to Entrainment of Ozone From Stable Layers Aloft into the Surface Well-Mixed Layer

From the above discussion it is clear that unless upper level concentration data are available, or the airshed is ventilated at night, correct specification of the boundary conditions at the top of the mixed layer is likely to be a difficult problem. An approach which alleviates some of the difficulties is to include computational cells above the mixed layer and to run the airshed model throughout the night. With this method, ozone can be trapped aloft at night and fumigated the next day. Boundary layer growth and entrainment can be modeled by variations in the vertical eddy diffusivity profile. With a combination of time-varying grid spacing and K(z) profiles, considerable flexibility can be attained in practice.

2.10 Initial and Boundary Conditions

To complete the mathematical formulation of the airshed model both the initial and boundary conditions need to be specified. In general the boundary conditions for the model represent statements of mass continuity across the bounding surfaces of the airshed. For parabolic systems like the atmospheric diffusion equation, the inhomogeneous mixed Neumann and Dirichlet boundary condition covers most cases. Normal to the boundary in direction $\hat{\underline{n}}$ this condition can be written in the form

$$[\underline{a}c + \underline{b}\nabla c] \cdot \hat{\underline{n}} = \underline{f} \qquad (2.26)$$

where $\underline{a}$, $\underline{b}$ and $\underline{f}$ are defined for the particular application. Consider, first, the ground level boundary conditions

$$[V_g^i c_i - K_{zz} \frac{\partial c_i}{\partial z}] = E_a(\underset{\sim}{x},t) \qquad (2.27)$$

where E_a is the mass flux per unit area of species c_i, K_{zz} the vertical eddy diffusivity and v_g^i the equivalent pollutant deposition velocity. At the ground the vertical velocity w is zero. The term $v_g^i c_i$, which has been omitted in many previous studies, has been included to parameterize the interaction of the pollutant material with the ground. Chapter 6 presents a model for evaluating the magnitude of the surface removal flux.

The remainder of the boundary conditions are identical to those chosen by Reynolds et al. (1973). At the top of the airshed, z = H(x,y,t), the conditions are given by

$$\begin{aligned} [\underline{V}c_i - K\nabla c_i] \cdot \hat{\underset{\sim}{n}} &= \underline{V}c_i^b \cdot \hat{\underline{n}} \quad ; \underline{V}\cdot\hat{\underline{n}} \leq 0 \\ - K\nabla c_i \cdot \hat{\underline{n}} &= 0 \quad ; \underline{V}\cdot\underline{n} > 0 \end{aligned} \qquad (2.28)$$

where $\underline{V}$, the advective velocity of pollutants relative to the top of the airshed, is given by

$$\underline{v} = u\underline{i} + v\underline{j} + (w - \frac{\partial H}{\partial t})\underline{k} \qquad (2.29)$$

In (2.28) $\hat{\underline{n}}$ is the unit vector normal to the surface defining the top of the airshed and $c_i^b(\underline{x},t)$ is the mean concentration of species i outside the modeling region. The case of a fixed domain corresponds to the condition $\partial H/\partial t = 0$. The two conditions in (2.28) correspond to the case when material is transported into the region, $(\underline{V}.\hat{\underline{n}}) \leq 0$, and

out of the region, $(\underline{V}.\hat{\underline{n}}) > 0$. This second condition must be carefully evaluated in practical applications of the model when H could be below the top of the convective mixed layer. In most circumstances the top of the airshed is in a stable layer in which case the turbulent transport is likely to be quite small and most material is removed by advection. The horizontal boundary conditions are similar to (2.28) and are given by:

$$\begin{aligned} [\underline{U}c_i - K\nabla c_i]\cdot\hat{\underline{n}} &= Uc_i^b\cdot\hat{\underline{n}} \quad ; \ \underline{U}\cdot\hat{\underline{n}} \leq 0 \\ -K\nabla c_i\cdot\hat{\underline{n}} &= 0 \quad ; \ \underline{U}\cdot\hat{\underline{n}} > 0 \end{aligned} \tag{2.30}$$

where $\hat{\underline{n}}$ is the unit vector normal to the horizontal boundary, $c_i^b(x,t)$ is the concentration outside of the airshed and $\underline{U}$ is the advective velocity $\underline{U} = u\underline{i} + v\underline{j}$ in the horizontal plane. The second condition $(\underline{U}.\hat{\underline{n}} > 0)$ states that the turbulent transport is zero, an approximation that is usually satisfied due to the dominance of the horizontal advection. Outflow boundary conditions are a major source of difficulty in implementing numerical solution procedures and for this reason will be discussed further in Chapter 10.

2.11 Validity and Accuracy of the Atmospheric Diffusion Equation

An obvious question after all the preceding simplifications is to ask if the atmospheric diffusion equation is an adequate representation of the ensemble mean concentration $\langle c_i \rangle$. Formally, the validity of (2.23) relates to how closely the predicted mean concentration $\langle c_i \rangle$ corresponds to the true ensemble mean value. If the true ensemble mean

velocities and concentrations are known for a particular flow field, then it is relatively straightforward to assess the model validity for different K, R and S. Unfortunately, in the boundary layer the ensemble mean velocities and concentrations can never be computed because the atmosphere presents only one realization of the flow at any time. Because the true mean velocities, concentrations and source emission rates are not available an unambiguous measure of the validity of (2.23) for any particular flow cannot be obtained.

Using the results of Lamb (1971), Lamb and Seinfeld (1973) and Reynolds et al. (1973) it is possible, however, to establish a set of conditions which must be satisfied if (2.23) is to be a valid representation of atmospheric transport and chemical reaction. The background discussions and data necessary to develop these conditions are extensively discussed in the above references and will not be reiterated here. In summary, however, Reynolds et al. (1973) concluded that the basic model is applicable for resolving those perturbations in the concentration field which have horizontal scales greater than 2 Km, vertical scales greater than 20 m and temporal scales greater than 1000 seconds. These conditions serve as a guide to the choice of grid size and averaging time to be used in the numerical solution procedures.

Table 2.2 summarizes the principal approximations which could be a source of invalidity in an urban scale airshed model. Although the validity cannot be established without question, it is generally accepted that the atmospheric diffusion equation is essentially a correct description of transport, mixing, and chemical reaction

Table 2.2 Sources of Invalidity in Air Quality Models

Source of Error	Comment
A. True form of the turbulent fluxes, $\overline{u'c_i'}$, $\overline{v'c_i'}$, $\overline{w'c_i'}$, is unknown.	Higher order closure models will offer improvement over eddy diffusivities in representing these terms. Such closure methods lead to large computational requirements.
B. Turbulent fluctuating chemical reaction terms are neglected.	Closure models appropriate for turbulent chemistry can be developed but large computational requirements as above may arise.
C. Effect of concentration fluctuations from spatial averaging on chemical reaction rate is neglected.	Introduce "micro-scale model" in regions where strong point and line sources occur.

processes. The major source of invalidity is probably the eddy diffusion representation of the turbulent fluxes. However, as long as the eddy diffusivity functions used in the model have been determined empirically under similar conditions to those to which the equation is applied, then the approximation should be considered valid.

Accepting the validity of the formulation (2.23) the next question which must be addressed is, how accurate are the model predictions? Accuracy-evaluation is an assessment of the errors induced by inaccuracies in the input information. Another term often used in connection with model evaluation is 'verification', referring to the agreement between predictions and observations for the specific case in which the observations used for verification were taken from the same pool of data used to develop the input information for the model. Verification contains elements of both validation and accuracy evaluation.

Accuracy evaluations can be made using estimates of the errors associated with the input information and from numerical sensitivity tests which assess the impact on concentration predictions. The inputs needed to solve the atmospheric diffusion equation together with possible sources of error are shown in Table 2.3. In each instance unless the actual value of the input is known, the level of error in that input can only be estimated. From the standpoint of the effect of errors on the predictions of the atmospheric diffusion equation, joint consideration must be given to the level of uncertainty in each input parameter and the sensitivity of the predicted concentrations to the parameter. Uncertainty relates to the possible error in the parameter

Table 2.3 Sources of Inaccuracy in Air Quality Models

Source of Error	Comment
A. Mean velocities $\bar{u}$, $\bar{v}$, $\bar{w}$ are not true ensemble means (usually $\bar{u}$, $\bar{v}$ and $\bar{w}$ are calculated from data at a finite number of locations).	There is no way to determine the true mean from the data; $\bar{u}$, $\bar{v}$, $\bar{w}$ can be calculated in principle from accurate fluid mechanical turbulence model.
1. Uncertainties in the measurement of wind speed and direction.	
2. Inadequate or non-representative spatial measurements of wind speed and direction.	
3. Uncertainties associated with wind field analysis techniques.	
B. Source emission function E_i is inaccurate.	More detailed emission inventories needed to reduce this source of inaccuracy.
1. Inaccurate or no specification of source location.	
2. Uncertainties in emission factors.	
3. Inaccurate or no temporal resolution of emission.	
4. Inadequate or no verification of emission methodologies.	

Table 2.3 (continued)

Source of Error	Comment
C. Chemical reaction mechanism does not accurately reflect those chemical processes occurring in the atmosphere. 1. Uncertainties in experimental determinations of specific reaction rate constants. 2. Variations of rate constants with temperature either uncertain or unknown. 3. Inadequacies in lumping due to the non-representativeness of lumped class reactions relative to specific species within the class, e.g., reaction rates, products, and stoichiometric coefficients. 4. Inaccuracies in the mechanism due to insufficient verification studies.	Continued study of chemical processes needed to insure that R_1 is accurate. Elimination or quantification of smog chamber related errors: 1. Inadequate or lack of control and measurement of levels of H_2O in the chamber. 2. Impurities in background chamber air. 3. Inadequate or lack of measurements of the spectral distribution and intensity of the chamber irradiation system. 4. Inaccurate or ambiguous analytical methods. 5. Non-homogeneity due to inadequate stirring or poor chamber design. 6. Absorption and desorption of reactants and products on chamber walls. 7. Chemical reactions occurring on chamber surfaces. 8. Inadequate control and measurement of chamber temperature.
D. Boundary conditions inaccurately specified. 1. Concentrations 2. Inversion height	No remedy except for more extensive data.

from its true value, and sensitivity refers to the effect that variation in that parameter has on the solution of the equation. A parameter may have a large uncertainty associated with it but have little influence on the solution. In such a case, effort at reducing the uncertainty may be unwarranted. Conversely small uncertainties in some parameters may have a large impact on the concentration predictions. Thus, both uncertainty and sensitivity must be considered when evaluating the accuracy of the atmospheric diffusion equation. The issues are discussed in detail in Chapters 12 and 13. Finally it must be noted that discrepancies between predicted and measured concentrations may arise because of the basic difference in the nature of the averaging or experimental uncertainties. Field measurements are typical point estimates whereas model predictions are volume averages.

The basic objective of this section has been to explore some of the background questions related to the validity and accuracy of the atmospheric diffusion equation. These considerations are important factors which influence the nature and scope of the air pollution problems which can be addressed with an airshed model.

2.12 Simplified Forms of the Atmospheric Diffusion Equation

The previous discussions were focussed on the development of a single mathematical model which could be used to predict the formation and transport of photochemical air pollution. While the basic objective was to introduce a comprehensive description of atmospheric concentration dynamics there are circumstances where it is desirable to use

less complex forms of the governing equation for screening purposes. This chapter presents a discussion of Lagrangian, vertically integrated and single cell box models, all of which are based on various reduced or averaged forms of the atmospheric diffusion equation. Since these models form subcomponents of the airshed modeling system it is essential to be aware of the limitations imposed by the simplifying assumptions. All of the models to be described incorporate the effects of time dependent emission sources, surface removal phenomena, non-linear chemistry and unsteady meteorology. Unless these processes are included, the contracted formulations are of little use in practical calculations.

While the atmospheric diffusion equation (2.23) is ideally suited for predicting the concentration distribution over extended areas, there are many situations where the air quality impact only needs to be calculated at a particular location. A trajectory model that follows a parcel of air as it traverses the airshed can often be used in these circumstances. Such models are based on a Lagrangian formulation where the co-ordinate system is advected by the horizontal wind field. If the concentration distribution is required over a large area then computational cost associated with multiple trajectories can become comparable to the fixed or Eulerian grid approaches. The most common representation of a trajectory model (Eschenroeder and Martinez, 1972; Lloyd et al., 1979) can be expressed in the form

$$\frac{\partial c}{\partial t} = \frac{\partial}{\partial z} K_{zz} \frac{\partial c}{\partial z} + R(c) \qquad (2.31)$$

Given the widespread use of this formulation it is useful to examine the assumptions which must be adopted to derive the model from the atmospheric diffusion equation (2.23). If a column of air is advected by the wind then the appropriate change of variables from the fixed system [x,y,z,t] to the moving co-ordinate system [ξ,η,z,t] is given by (Aris, 1962)

$$\begin{aligned} \xi &= \xi(x,y,t) \\ \eta &= \eta(x,y,t) \\ z &= z \\ t &= t \end{aligned} \tag{2.32}$$

With this set of transformations the Lagrangian form of the atmospheric diffusion equation, for a divergence-free flow field, is given by

$$\begin{aligned} \frac{\partial c}{\partial t} = {} & \frac{\partial}{\partial \xi} K_{xx} \frac{\partial c}{\partial \xi} \left(\frac{\partial \xi}{\partial x}\right)^2 + \left[\frac{\partial}{\partial \xi} K_{xx} \frac{\partial c}{\partial \eta} + \frac{\partial}{\partial \eta} K_{xx} \frac{\partial c}{\partial \xi}\right] \left(\frac{\partial \xi}{\partial x}\right)\left(\frac{\partial \eta}{\partial x}\right) + \\ & \frac{\partial}{\partial \eta} K_{xx} \frac{\partial c}{\partial \eta} \left(\frac{\partial \eta}{\partial x}\right)^2 + \frac{\partial}{\partial \xi} K_{yy} \frac{\partial c}{\partial \xi} \left(\frac{\partial \xi}{\partial y}\right)^2 + \left[\frac{\partial}{\partial \xi} K_{yy} \frac{\partial c}{\partial \eta} + \frac{\partial}{\partial \eta} K_{yy} \frac{\partial c}{\partial \xi}\right] \left(\frac{\partial \xi}{\partial y}\right)\left(\frac{\partial \eta}{\partial y}\right) + \\ & \frac{\partial}{\partial \eta} K_{yy} \frac{\partial c}{\partial \eta} \left(\frac{\partial \eta}{\partial y}\right)^2 + \frac{\partial}{\partial z} K_{zz} \frac{\partial c}{\partial z} - w \frac{\partial c}{\partial z} + R(c) - \\ & \left[\frac{\partial \xi}{\partial t} + u \frac{\partial \xi}{\partial x} + v \frac{\partial \xi}{\partial y}\right] \left(\frac{\partial c}{\partial \xi}\right) - \left[\frac{\partial \eta}{\partial t} + u \frac{\partial \eta}{\partial x} + v \frac{\partial \eta}{\partial y}\right] \left(\frac{\partial c}{\partial \eta}\right) \end{aligned} \tag{2.33}$$

This is a more general expression of the model presented in Liu and Seinfeld (1975). Clearly, if this equation is to be reduced to the form (2.32) then a number of simplifying assumptions need to be invoked. The first is that the vertical advective transport must be small in comparison to the turbulent diffusion, i.e.

$$\frac{\partial}{\partial z} K_{zz} \frac{\partial c}{\partial z} >> \left| w \frac{\partial c}{\partial z} \right| \tag{2.34}$$

If meteorological conditions are such that the vertical component of the wind field is large then the advective transport term $w \frac{\partial c}{\partial z}$ can be easily retained in the formulation. Another major assumption is that the loss, or gain, of material from horizontal diffusion is neglible. If the horizontal concentration gradients are small then the appropriate terms involving K_{xx} and K_{yy} can be justifiably omitted. Since the co-ordinate system $[\xi,\eta,z,t]$ is advected by the flow field the only way that the column of air can retain its vertical integrity is if the effects of wind shear can be neglected, i.e.

$$u(x,y,z,t) = u(x,y,t) \tag{2.35}$$

$$v(x,y,z,t) = v(x,y,t) \tag{2.36}$$

This is a critical assumption and a major source of error in many trajectory model calculations, especially those which involve long transport times. A quantitative assessment of each of the above simplifications is presented in Liu and Seinfeld (1975).

Another alternative which has been adopted to cut down the computational cost of using the full scale airshed model is to reduce the number of spatial dimensions. For many applications the vertical mixing is sufficiently rapid to enable the atmospheric transport to be considered as a two-dimensional problem. This approach is often used in hydraulic modeling where it is more commonly known as the shallow water analogy (Galloway, 1976; Yotsukura, 1977). Most of the basic concepts were initiated by Taylor (1954) and refined by Aris (1956). Atmospheric

applications of the procedures are described in Saffman (1962), Galloway (1976) and MacCracken et al. (1978).

If the functions h(x,y) and H(x,y,t) define the lower and upper boundaries of the airshed then the equivalent vertical average value of a variable p can be defined as

$$\overline{p(t)} = \frac{1}{H(x,y,t) - h(x,y)} \int_h^H p(x,y,z,t)dz \qquad (2.37)$$

By integrating (2.23) between the limits h(x,y), H(x,y,t) and applying the Liebnitz rule for differentiation under the integral sign (Sokolnikoff and Redheffer, 1958), the equivalent vertically averaged form of the atmospheric diffusion equation is given by

$$\frac{\partial(H-h)\overline{c}}{\partial t} + \frac{\partial(H-h)\overline{uc}}{\partial x} + \frac{\partial(H-h)\overline{vc}}{\partial y} + A$$

$$= \frac{\partial}{\partial x}(H-h)\,\overline{K_{xx}\frac{\partial c}{\partial x}} + \frac{\partial}{\partial y}(H-h)\overline{K_{yy}\frac{\partial c}{\partial y}} + B + (H-h)\overline{R(c)} \qquad (2.38)$$

where

$$A = c(h)\frac{\partial h}{\partial t} - c(H)\frac{\partial H}{\partial t} + u(h)c(h)\frac{\partial h}{\partial x} - u(H)c(H)\frac{\partial H}{\partial x}$$

$$+ v(h)c(h)\frac{\partial h}{\partial y} - v(H)c(H)\frac{\partial H}{\partial y} - w(h)c(h) + w(H)c(H) \qquad (2.39)$$

$$B = K_{xx}(h)\frac{\partial c}{\partial x}\bigg|_h \cdot\frac{\partial h}{\partial x} - K_{xx}(H)\frac{\partial c}{\partial x}\bigg|_H \cdot\frac{\partial H}{\partial x} + K_{zz}(H)\frac{\partial c}{\partial z}\bigg|_H$$

$$+ K_{yy}(h)\frac{\partial c}{\partial y}\bigg|_h \cdot\frac{\partial h}{\partial y} - K_{yy}(H)\frac{\partial c}{\partial y}\bigg|_H \cdot\frac{\partial H}{\partial y} - K_{zz}(h)\frac{\partial c}{\partial z}\bigg|_h \qquad (2.40)$$

The terms A and B in (2.39) can be simplified by utilizing the boundary constraints

$$dz = \frac{\partial h}{\partial t}dt + \frac{\partial h}{\partial x}dx + \frac{\partial h}{\partial y}dy \tag{2.41}$$

$$dz = \frac{\partial H}{\partial t}dt + \frac{\partial H}{\partial x}dx + \frac{\partial H}{\partial y}dy \tag{2.42}$$

At the upper surface there are two cases to consider

$$K\nabla c \cdot \hat{\underset{\sim}{n}} = 0 \quad \text{if} \quad \underline{V} \cdot \hat{\underline{n}} > 0 \tag{2.43}$$

and

$$[\underline{V}c - K\nabla c] \cdot \hat{\underline{n}} = (\underset{\sim}{V}c^b) \cdot \hat{\underline{n}} \quad \underline{V} \cdot \hat{\underline{n}} \leq 0 \tag{2.44}$$

where $\underline{V}$, the relative vertical velocity, is defined by

$$\underset{\sim}{V} = u\underset{\sim}{i} + v\underset{\sim}{j} + (w - \frac{\partial H}{\partial t})\underset{\sim}{k} \tag{2.45}$$

and $\underline{n}$ is the unit normal to the surface H(x,y,t) which is given by

$$\hat{\underset{\sim}{n}} = \frac{-\frac{\partial H}{\partial x}\underset{\sim}{i} - \frac{\partial H}{\partial y}\underset{\sim}{j} + \underset{\sim}{k}}{\sqrt{(\frac{\partial H}{\partial x})^2 + (\frac{\partial H}{\partial y})^2 + 1}} \tag{2.46}$$

Combining (2.39 - 2.46) enables the A term to be reduced to

$$A = \begin{cases} 0 & ; \ \underline{V} \cdot \hat{\underline{n}} > 0 \\ (c - c^b)\left[(w - \frac{\partial H}{\partial t}) + u(H)\frac{\partial H}{\partial x} + v(H)\frac{\partial H}{\partial y}\right] & ; \ \underline{V} \cdot \hat{\underline{n}} \leq 0 \end{cases} \tag{2.47}$$

At the lower level the appropriate boundary condition is given by

$$v_g c - K\nabla c = E_a(\underline{x},t) \tag{2.48}$$

where v_g is the deposition velocity and $E_a(\underline{x},t)$ is the emission flux term. Using the same procedure used to derive (2.47) the B term becomes

$$B = E_a(\underline{x},t) - v_g c \tag{2.49}$$

The final averaged form of the atmospheric diffusion equation is then given by

$$\frac{\partial(H-h)\bar{c}}{\partial t} + \frac{\partial(H-h)\overline{uc}}{\partial x} + \frac{\partial(H-h)\overline{vc}}{\partial y} =$$
$$\frac{\partial}{\partial x}(H-h)\overline{K_{xx}\frac{\partial c}{\partial x}} + \frac{\partial}{\partial y}(H-h)\overline{K_{yy}\frac{\partial c}{\partial y}} + A + E_a - v_g\bar{c} + (H-h)\overline{R(c)} \tag{2.50}$$

From an inspection of (2.50) it is apparent that the presence of terms of the form $\overline{uc}$, $\overline{vc}$ and $\overline{R(c)}$ creates a difficulty similiar to the turbulent closure problem described in Section 2.5. Applying the Reynolds averaging rules and a K-Theory closure hypothesis to the differential advective flux terms results in

$$\overline{uc} = \bar{u}\bar{c} + \overline{u'c'} = \bar{u}\bar{c} - K^a_{xx}\frac{\partial\bar{c}}{\partial x} \tag{2.51}$$

$$\overline{vc} = \bar{v}\bar{c} + \overline{v'c'} = \bar{v}\bar{c} - K^a_{yy}\frac{\partial\bar{c}}{\partial y} \tag{2.52}$$

where the primed quantities represent deviations from the vertical average values. If it is further assumed that

$$\overline{K_{xx} \frac{\partial c}{\partial x}} = \overline{K_{xx}} \frac{\partial \bar{c}}{\partial x} \tag{2.53}$$

$$\overline{K_{yy} \frac{\partial c}{\partial y}} = \overline{K_{yy}} \frac{\partial \bar{c}}{\partial y} \tag{2.54}$$

and

$$\overline{R(c_1,\ldots,c_p)} \simeq R(\bar{c}_1,\ldots,\bar{c}_p) \tag{2.55}$$

The final form of the vertically integrated atmospheric diffusion is then given by

$$\frac{\partial (H-h)\bar{c}}{\partial t} + \frac{\partial (H-h)\overline{u}\,\overline{c}}{\partial x} + \frac{\partial (H-h)\overline{v}\,\overline{c}}{\partial y} =$$
$$\frac{\partial}{\partial x} K^e_{xx} \frac{\partial \bar{c}}{\partial x} + \frac{\partial}{\partial y} K^e_{yy} \frac{\partial \bar{c}}{\partial y} + A + E_a - v_g \bar{c} + (H-h)R(\bar{c}) \tag{2.56}$$

where the effective diffusion coefficients are given by

$$K^e_{xx} = (H-h)[\,\overline{K}_{xx} + K^a_{xx}\,] \tag{2.57}$$

$$K^e_{yy} = (H-h)[\,\overline{K}_{yy} + K^a_{yy}\,] \tag{2.58}$$

One of the most critical assumptions in the above derivation was that the vertical average reaction rate is the same as the rate based on vertical average concentration profiles. For this approximation to be true, the time scale of the reaction must be much slower than the characteristic mixing time. If there are any persistent steep gradients in the vertical concentration profiles then the closure assumption is clearly violated for nonlinear reaction systems.

In an attempt to circumvent the difficulty MacCracken et al. (1978) proposed that the vertical species distribution be described by an expression of the form

$$c_i(z) = a_i + b_i \ln(\frac{z}{z_r}) \tag{2.59}$$

where z_r is a reference height = 1 m and the constants a_i, b_i are determined from the boundary conditions. With an analytic expression for c(z) it is possible to derive the correct forms of the reaction rates. For example, if the product $c_j c_k$ appears in R_i and terms of the order $O(z_r/H)$ are neglected then the vertical average rate is given by

$$\overline{c_j c_k} = \frac{1}{H-z_r} \int_{z_r}^{H} c_j c_k dz = \bar{c}_j \bar{c}_k + b_j b_k \tag{2.60}$$

Unfortunately the validity of the profile assumption, (2.59), has not been established for rapidly reacting species.

Whether or not a a vertically integrated model is appropriate for a particular application or chemical species depends to a large extent on the characteristic mixing time. For unstable conditions Smith et al. (1976) calculated the frequency distribution of the convective mixing time λ from field measurements in the Los Angeles Basin. The characteristic mixing time is given by

$$\lambda = \frac{Z_i}{w_*} \tag{2.61}$$

where Z_i is the depth of the convective mixed layer and w_* is the convective velocity scale defined by

$$w_* = (-\frac{1}{k}\frac{z_i}{L})^{1/3} u_* \qquad (2.62)$$

In this expression k is the von Karman constant, u_* the friction velocity and L is the Monin-Obukhov length. The results of their correlations are shown in Figure 2.5. For unstable conditions Deardorff and Willis (1974) have shown that material released at the surface becomes nearly well mixed within a travel time of 3λ. The mean value of λ is 210 seconds and so within a time step of 0(10 minutes) slowly reacting pollutants can be considered to be well mixed. Thus when the inversion base is low and the mixed layer is unstable (both conditions implicit in the above data) it should be possible to produce acceptable concentration estimates using only a two-dimensional, vertically-integrated model (Smith et al.,1976). This conjecture cannot be satisfactorily generalized until more experimental data becomes available.

There is another approach which can be used to estimate the time after which a surface or elevated pollutant release can be considered to be well mixed. This procedure involves calculating the moments of the concentration distribution, where the (n,m)-moment is defined by

$$c^{n,m} = \int_{-\infty}^{\infty}\int_{-\infty}^{\infty} x^n y^m c \, dxdy \qquad (2.63)$$

Assuming that $c(\underline{x},t) \to 0$ sufficiently rapidly with x,y then the moments can be calculated from the sequence

$$\frac{\partial c^{n,m}}{\partial t} + \frac{\partial w c^{n,m}}{\partial z} = -nuc^{n-1,m} - mvc^{n,m-1} + \frac{\partial}{\partial z} K_{zz} \frac{\partial c^{n,m}}{\partial z} + n(n-1)K_{xx} c^{n-2,m} + m(m-1) K_{yy} c^{n,m-2} \qquad (2.64)$$

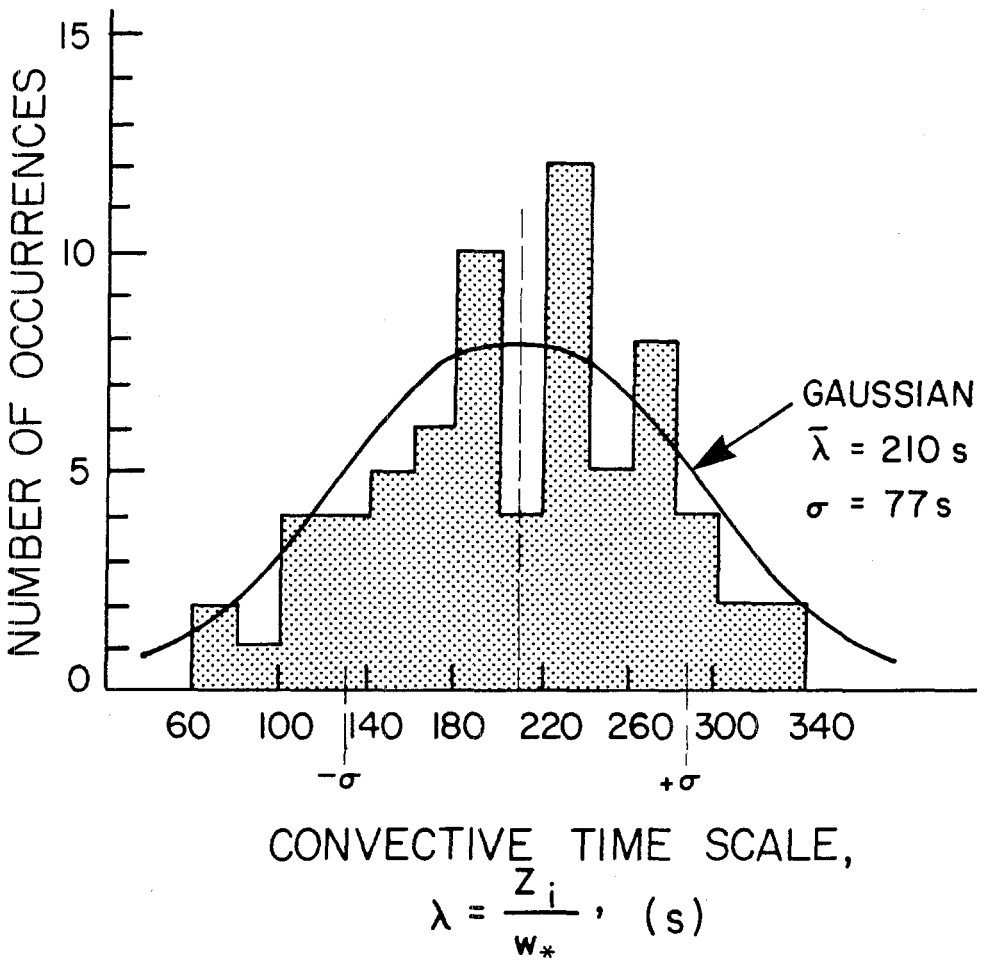

FIGURE 2.5

Frequency Distribution of the Convective Mixing Time Scale λ Observed in the Los Angeles Marine Layer for Different Times (Source: Smith et al. 1976)

Given the moment equations it is possible to solve the Sturm-Liouville problem, formed by (2.64) and its boundary conditions, for the variance of the concentration distribution. The time for the variance to tend to a constant value corresponds to the characteristic mixing time. Saffman (1962) established a bound $\lambda > Z_i'^2/2K_{zz}$ for problems in which the vertical profiles of wind and diffusivities can be described by power laws. Unfortunately, for all but the simplest applications (2.64) must be solved numerically. The fact that it is a one-dimensional problem does, however, considerably simplify the computational task.

An even further reduced photochemical model can be derived if the spatial averaging is carried out over the whole airshed and the resulting formulation is a single or box model. While extensive use has been made of box models (Graedel et al., 1976; Whitten and Hogo, 1976), the set of assumptions which must be invoked to justify their use severely limits the range of valid applications. Unless the meteorological and source distributions are sufficiently simple and uniform, the box approach should not be used for modeling concentration distributions in urban airshed. Further details of these models are presented in Chapter 8.

2.13 Conclusions

In this chapter most of the basic assumptions required to produce a practical airshed modeling system have been discussed. The formulation of such a system is a difficult undertaking because it is necessary to maintain a balance between the need for computational economy

and the desire for an accurate representation of the underlying physics and chemistry. The atmospheric diffusion equation, and its various reduced forms, form the basis of a set of mathematical models which can be used to describe the formation and transport of urban scale photochemical air pollution. Subsequent chapters in this study are devoted to a detailed treatment of the model components and required inputs.

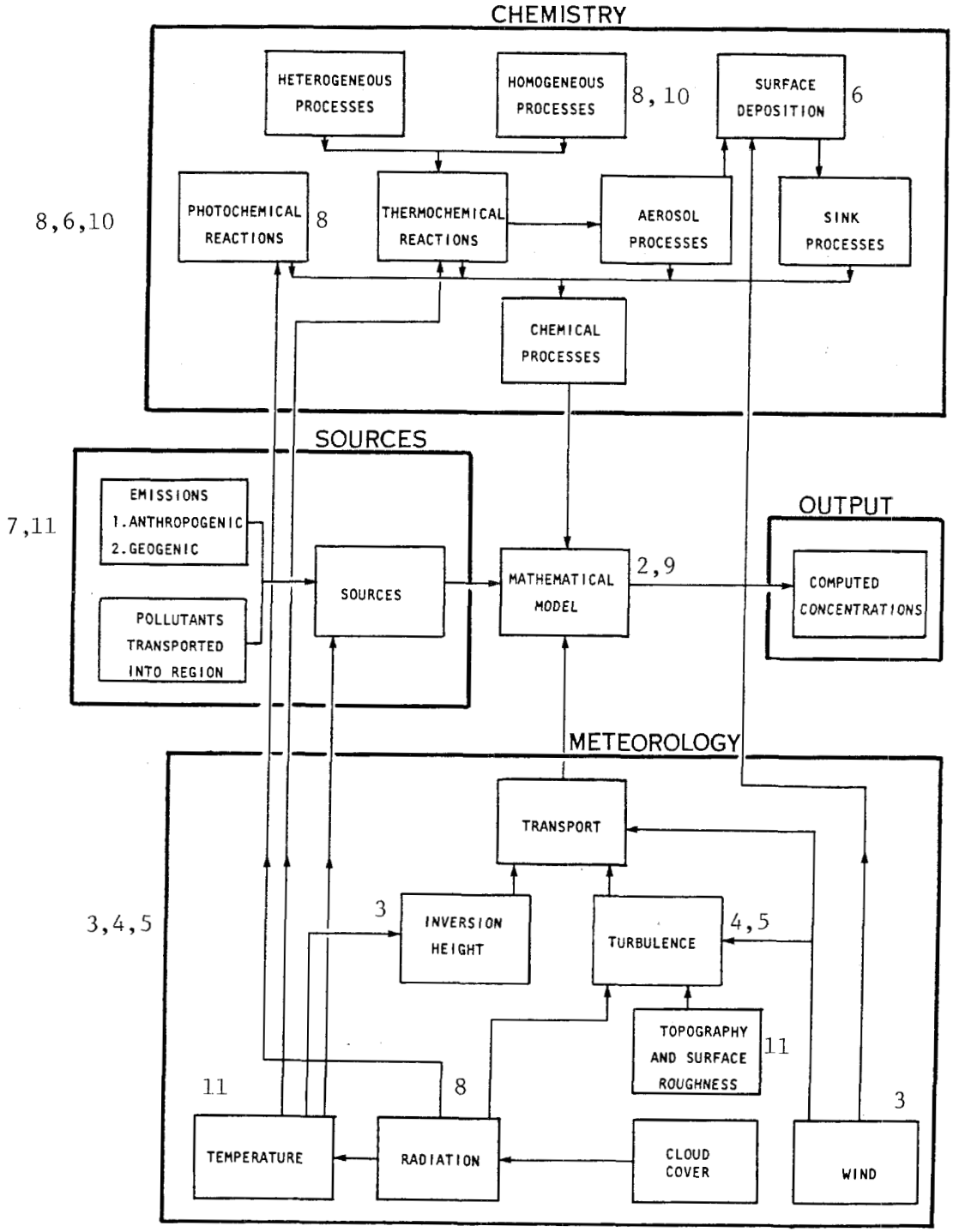

FIGURE 2.6

Simplified View of the Factors Involved in Relating Emissions to Atmospheric Air Quality. Numbers Refer to Subsequent Chapters.

CHAPTER 3

OBJECTIVE ANALYSIS PROCEDURES

3.1 Introduction

A major simplifying assumption adopted in the previous chapter was that the presence of pollutant gases and aerosols does not significantly affect urban scale meteorology. The importance of this approximation is that it allows the concentration dynamics to be decoupled from the equations which describe the flow fields over the airshed. While this approach reduces the complexity of the computational problem it does not remove the need for a priori specification of the velocity and mixing characteristics. In addition the initial concentration distribution is needed as part of the solution procedures. This chapter is devoted to a detailed presentation of the objective analysis techniques which can be used to generate the necessary model inputs.

As with many other aspects of this study the intent is to develop procedures which only employ readily available or routinely measured data. In many cases it is this requirement which limits characterization of the different processes and not the understanding of the physical phenomena. Subsequent sections discuss the interpolation procedures, objective analysis techniques and practical applications of the different methodologies.

3.2 A Comparison of Interpolation Methods for Sparse Data: Application to Wind and Concentration Fields

(Reprinted from J. Applied Meteorology, 18, 761-771.)

Reprinted from JOURNAL OF APPLIED METEOROLOGY, Vol. 18, No. 6, June 1979
American Meteorological Society
Printed in U. S. A.

A Comparison of Interpolation Methods for Sparse Data: Application to Wind and Concentration Fields

WILLIAM R. GOODIN,[1] GREGORY J. MCRAE AND JOHN H. SEINFELD

Environmental Quality Laboratory, California Institute of Technology, Pasadena 91125

(Manuscript received 1 December 1978, in final form 23 February 1979)

ABSTRACT

In order to produce gridded fields of pollutant concentration data and surface wind data for use in an air quality model, a number of techniques for interpolating sparse data values are compared. The techniques are compared using three data sets. One is an idealized concentration distribution to which the exact solution is known, the second is a potential flow field, while the third consists of surface ozone concentrations measured in the Los Angeles Basin on a particular day. The results of the study indicate that fitting a second-degree polynomial to each subregion (triangle) in the plane with each data point weighted according to its distance from the subregion provides a good compromise between accuracy and computational cost.

1. Introduction

A problem common to many disciplines is the development of continuous fields from discrete data sets. For example, in meteorology, wind fields are often generated using a two-step procedure. The first element is the interpolation of the raw station data to a finer mesh. Objective analysis procedures are then employed to adjust the wind vectors at each grid point so that an applied physical constraint, such as minimum field divergence, is satisfied. Much of the literature is devoted to the second step; what is frequently neglected is that the final form of the field is often critically dependent on the results of the initial interpolation. Formally, the objective of this paper is to address the problem: given a bounded region of r-space containing n, error-free data values C_i, at locations $\mathbf{x}^i=[x_1^i, \ldots x_2^i, x_r^i]$, $i=1, 2, \ldots, n$, develop a function, $f(\mathbf{x})$, which will assign a value of C at any arbitrary location $\mathbf{x}$. While simply stated, there is, in general, no unique solution to the interpolation problem. As a result, when alternative techniques are applied to the same discrete data set, different fields are generated. This study was undertaken to identify and test computationally efficient methods for interpolating sparse data measurements onto a regular mesh.

2. A survey of methods for interpolation of sparse data

a. Weighted interpolation methods

A common approach to interpolation of sparse data onto a regular grid is to assume that the grid value is some weighted average of the surrounding data values, i.e.,

$$C_{ij}=\sum_{k=1}^{n} C_k W_k(r)/\sum_{k=1}^{n} W_k(r), \tag{1}$$

where C_k is the measured value at the kth measuring station, $W_k(r)$ the weighting function, and r the distance from the grid point to the station.

In an early study, Cressman (1959) reported on a procedure for use in pressure-surface height analysis which used the weighting factor

$$W(r)=\frac{R^2-r^2}{R^2+r^2}, \tag{2}$$

where R is the distance at which the weighting factor goes to zero, i.e., the "radius of influence." This weighting technique aided the interpolation procedure in areas of sparse data. Decreasing values of R were used on successive scans to analyze a spectrum of scales. The values obtained from each scan were then averaged to produce the final field.

Endlich and Mancuso (1968) combined both polynomial fitting and distance weighting in their interpolation technique. A least-squares fit to a first-order polynomial was performed using five of the nearest station values, according to

$$W(r)=\frac{a}{(r+r^*)^2+a}, \tag{3}$$

where a is a constant, r the distance to the station and r^* a distance factor ($0\leqslant r^*\leqslant r$) that indicates whether the observation is in an upwind–downwind ($r^*=r$) or crosswind ($r^*=0$) direction from the grid point.

[1] Present affiliation: Advanced Technology Group, Dames & Moore, Los Angeles, CA 90024.

0021-8952/79/060761-11$06.75

Shepard (1968) discussed an interpolation technique in which a direction factor was also included which accounted for shadowing of the influence of one data point by a nearer one in the same direction. The method also included the effect of barriers. If a "detour" of length $b(r)$, perpendicular to the line between the point (i,j) and the kth measuring station, was required to travel around the barrier between the two points, then $b(r)$ was considered to be the length of the barrier. An effective distance r' was defined by

$$r'=[r^2+b(r)^2]^{\frac{1}{2}}. \tag{4}$$

If no barrier separated the two points, then $b(r)=0$.

Shenfeld and Boyer (1974) presented a technique for interpolation of a velocity field similar to that proposed by Endlich and Mancuso. The velocity was computed as in Eq. (1). For example, for the x component of the velocity at grid point (i,j),

$$u_{ij}=\sum_{k=1}^{n} u_k W_k(r)/\sum_{k=1}^{n} W_k(r), \tag{5}$$

with the weighting function defined by

$$W_k(r)=\exp\left[-\left(\frac{x_k^2}{S_{xk}}+\frac{y_k^2}{S_y}\right)\right], \tag{6}$$

where $x_k^2+y_k^2=r^2$. The coordinate system was oriented in the direction of the observed wind with the origin at the kth station. S_{xk} was defined by

$$S_{xk}=S_y\left(1+\frac{V_k}{V_s}\right), \tag{7}$$

where V_k was the magnitude of the velocity vector at the kth station and V_s a scaling velocity. S_y was assigned a value between 40 and 70, depending on the density of wind stations. The larger the number of stations, the lower the value of S_y. For low values of S_y, the computed wind velocity at any grid point was more dependent on nearby stations. Also since S_{xk} was always greater than or equal to S_y, the computed wind velocity was more dependent on downwind distance (x_k) than on crosswind distance (y_k).

For interpolation in regions of sparse data, Fritsch (1971) used a cubic spline technique. He first fitted spherical surfaces to the data to obtain an initial field, and then iteratively adjusted these values using the splines until convergence was obtained. He compared his technique with that of Cressman using an idealized data set with a known solution, and the mean error ($\sim 3\%$) was approximately half that of Cressman's.

MacCracken and Sauter (1975) used a Gaussian weighting scheme to eliminate complete dominance of a measuring station near a grid point, i.e.,

$$W(r)=\exp(-0.1r^2). \tag{8}$$

Hovland *et al.* (1977) computed wind and temperature fields using data from the Environmental Protection Agency's Regional Air Pollution Study (RAPS) conducted in St. Louis. An iterative scan procedure was used in which the radius of influence was decreased and the number of stations increased empirically on successive iterations. The advantage to this strategy is that small-scale motions which are only detected in an area of dense station coverage are not transmitted to outlying areas. Moreover, during the initial iterations this procedure places significant weight on outlying stations which may be less reliable than those in the center of the region. The weighting function used was

$$W(r)=\begin{cases}\left(\dfrac{R^2-r^2}{R^2+r^2}\right)^4, & r\leqslant R\\ 0, & r>R.\end{cases} \tag{9}$$

This function decreases rapidly with increasing distance r from a maximum of 1 at $W(0)$.

Recently, Boone and Samuelson (1977) described the application of a distance and directional weighting technique to the display of air pollution data. The weighting factor used in Eq. (1) was

$$W_k(r)=S_k^2(1+T_k), \tag{10}$$

where, based on the work of Shepard (1968), the weighting factor was defined by

$$S_k=\begin{cases}1/r_k, & 0<r_k\leqslant R/3\\ \dfrac{27}{4R}\left(\dfrac{r_k}{R}-1\right)^2, & R/3<r_k\leqslant R\end{cases} \tag{11}$$

where r_k is the distance from the kth station to the (i,j) grid point. The directional weighting factor is computed from

$$T_k=\sum_{l=1}^{m} S_l(1-\cos A)/\sum_{l=1}^{m} S_l, \tag{12}$$

where m is the number of points within the radius R and angle A is defined by the segments $\overline{(x_k,y_k),(i,j)}$ and $\overline{(i,j),(x_l,y_l)}$.

b. Least-squares polynomial interpolation

The second class of methods for producing a continuous surface over a grid is a least-squares fit of a polynomial to the data points. The technique requires minimization of χ^2, the goodness of fit to the data. In a second-degree polynomial, for example,

$$\chi^2\equiv\sum_{k=1}^{n}(\Delta C_k)^2$$

$$=\sum_{k=1}^{n}(C_k-a_1-a_2x_k-a_3y_k-a_4x_ky_k-a_5x_k^2-a_6y_k^2)^2 \tag{13}$$

must be a minimum, where C_k is the measured concentration (or wind speed) at point (x_k,y_k). The minimum value of χ^2 can be determined by setting the derivatives of χ^2 with respect to each of the coefficients a_i equal to zero. For a second-degree polynomial, six simultaneous equations must be solved for the optimum coefficients. The concentration $C(x,y)$ at any grid location (x,y) can then be computed from

$$C(x,y)=a_1+a_2x+a_3y+a_4xy+a_5x^2+a_6y^2. \quad (14)$$

In an early paper, Panofsky (1949) used third-degree polynomials to fit wind and pressure fields for use in weather map construction. The technique was later modified to handle areas with sparse data by Gilchrist and Cressman (1954). These polynomial-fitting procedures were typically applied to the whole grid.

An alternative to applying the polynomial interpolation to the entire grid is to perform the interpolation over areas within the influence of individual stations. Thiessen (1911) defined space-filling polygons over particular areas by assuming that each station measurement is associated with the local region of the area nearer to that station than to any other. Formally, the resultant planar divisions are defined as Dirichlet tessellations although they are sometimes called Voroni or Thiessen polygons. While the recent algorithm of Green and Sibson (1978) simplifies the task of defining the polygons, the attainment of slope continuity in C from one region to another is a difficult problem.

A simpler technique is to triangulate the region using the station locations for the vertex positions. Lawson (1977) described a number of algorithms which perform this task. Given n_b points on the convex boundary of the region, the number of nonoverlapping triangles $n_t=2n-n_b-2$ is unique even though the triangulations may be different. Once the triangle vertices have been established, a variety of interpolation schemes can be used. For example, $C(x,y)$ within each triangle can be determined from the equation of a plane oriented to pass through the three vertex data points.

A natural extension of this idea is to use higher order polynomials to achieve slope continuity between adjacent triangles. Lawson (1977) employed a cubic polynomial based on the finite element method of Clough and Tocher (1965) to obtain

$$C(x,y)=\sum_{i=0}^{M}\sum_{j=0}^{M-i}a_{ij}x^iy^j, \quad (15)$$

where $M=3$. Powell and Sabin (1977) used piecewise quadratic approximation to obtain an interpolation function with continuous first derivatives.

Akima (1975) developed a method of bivariate interpolation and smooth surface fitting for irregularly spaced data based on a fifth-degree polynomial ($M=5$) in x and y defined in each triangular cell. For each polynomial 29 coefficients must be determined. In addition to the values of the function at the data locations, the first- and second-order partial derivatives are also required. Partial derivatives of the function differentiated in the direction perpendicular to each side of the triangle are considered in order that the resulting polynomials intersect smoothly at the triangle edge. Use of higher order polynomials requires more coefficients and accordingly more computer time to solve for the coefficient matrix a_{ij}.

McLain (1974, 1976) has discussed a different polynomial fitting approach, in which the domain is divided into triangular subregions by connecting the data points. A second-degree polynomial is then fitted to each triangle using all data points with each value weighted according to its distance from the given triangle. The weighting scheme r^{-2} was used in the present formulation with the radius of influence effectively set to the dimension of the region. At each edge of the triangle, $C(x,y)$ is required to be the same as that of adjacent polynomials in order that position continuity of the resulting surface is assured.

In each triangle, the final value $C(x,y)$ is found as the weighted average of the three functions [Eq. (14)] corresponding to the vertices, i.e.,

$$C(x,y)=W_1C_1+W_2C_2+W_3C_3. \quad (16)$$

To ensure smooth transition from one triangle to the next, each weight W_i and its leading derivatives must be identically zero along the side of the triangle opposite to the ith vertex. This can be achieved by making W_i proportional to the third power of the distance from that side. The distance d_i from the point (x,y) to the side is a linear function of x and y, i.e.,

$$d_i=l_ix+m_iy+n_i, \quad (17)$$

where l_i, m_i, n_i are the coefficients defining a line through triangle edge opposite vertex i, scaled such that $d_i=1$ at vertex i. The weight W_i, within the triangle, is then

$$W_i=d_i^3/(d_1^3+d_2^3+d_3^3). \quad (18)$$

c. Optimum interpolation

A third general technique, first presented by Gandin (1963), known as optimum interpolation, has proved useful for interpolation of synoptic-scale meteorological data (wind and temperature) for initializing global or synoptic circulation models (Dartt, 1972; Schlatter, 1975; Julian and Thiebaux, 1975; Thiebaux, 1975). The technique produces an interpolated field from data points irregularly spaced in both space and time. The interpolation function can be formulated directly in terms of statistical properties of the wind (temperature) field, i.e., past behavior determines the function's form. This implies, however, that a historical record of data values must be available in

TABLE 1. Summary of interpolation methods and their attributes.

Method	Attributes	Applications
Weighted interpolation (a) $W(r)=\left(\frac{R^2-r^2}{R^2+r^2}\right)^n$ (b) $W(r)=\exp(-ar^n)$ (c) $W(r)=r^{-n}$	1. Easy to implement 2. May be modified if directional influence is important 3. More features of the data are smoothed as n decreases 4. Influence of a station becomes very localized as n (or a) increases 5. Radius of influence R may be fixed or variable	Cressman (1959) Endlich & Mancuso (1968) Shepard (1968) Shenfeld & Boyer (1974) MacCracken & Sauter (1975) Hovland *et al.* (1977) Boone & Samuelson (1977)
Least-squares polynomial interpolation (a) Polynomial of degree n fitted to full grid (b) Polynomials of degree n fitted to subregions of grid	1. Complex to implement 2. Resulting field depends strongly on distribution of data points when using (a) 3. Resulting field is smoothed as n decreases when using (a) 4. (b) fits data almost exactly 5. Execution time increases with n	Panofsky (1949) Akima (1975) McLain (1974, 1976) Lawson (1977)
Optimum interpolation	1. Complex to implement 2. Much historical data may be required 3. Statistics of the data accounted for	Gandin (1963) Dartt (1972) Schlatter (1975)

order to calculate these statistical properties (covariances). Moreover, the variance from the long-term mean of a wind measurement taken at a particular hour may not be useful for a mesoscale flow since the local stability and terrain influences on a particular day may be critically important in determining the flow.

d. Summary

Table 1 summarizes the methods that have been discussed in Section 2.

3. Optimum radius of influence

Theoretically, the choice of weight function and radius of influence for use in a distance-weighted interpolation procedure depends on the field statistics. Since insufficient measured data are available in most practical applications, the choice of an optimum radius must be based on the average station separation. For a two-dimensional domain of area A with N stations randomly distributed over the plane, the average station density ρ and separation d are given by $\rho=N/A$ and $d=(A/N)^{\frac{1}{2}}$. Stephens and Stitt (1970) have shown empirically that the optimum search radius R for large signal-to-noise ratios is $R/d\approx 1.6$. A further finding of their work is that R should be overestimated rather than underestimated. In practice this is important since nonrandom station distributions can lead to situations in which R is commensurate with the dimension of the data separation. In a separate study, Barnes (1964, 1973) came to similar conclusions and was also able to relate R/d to L/d, where L is the half wavelength of a disturbance. As an example, the parameters d and R/d can be calculated for the network of approximately 50 air monitoring stations in the South Coast Air Basin of Southern California (in 1974). Distributed over an area of about 19 400 km^2, the average station separation is calculated to be $\sim$20 km. This implies that a radius of influence between 20 and 40 km would be optimum. In order to calculate air quality distributions over the ocean and desert areas, which have few measurement stations, a larger radius of influence of 30–50 km must sometimes be used.

Careful consideration must be given to the choice of R. If the objective is to produce a set of gridded values, then each point must be within the radius of influence of at least one measurement station. While increasing R reduces the field variance, it does so at an increase of computational cost. For randomly distributed stations the interpolation cost per grid value increases quadratically since the number of data points within each radius of influence is proportional to R^2. Thus, knowledge of an "optimum" radius of influence is important both from the point of view of accuracy of the final interpolated field as well as cost of the calculation. The simple technique discussed in this section for computing an optimum radius of influence, while developed for a random distribution of points, provides a useful range of values even when the measurement points are not randomly located.

4. Comparison of interpolation procedures for scalar fields

The results of interpolating test data sets for which the exact solution is known provide a means to assess the performance of interpolation routines.

A test data set consisting of a hemispherically shaped surface was constructed to compare the various interpolation methods. The hemisphere was arbitrarily centered above the center of a 100×50 grid system overlaying the South Coast Air Basin. Each grid cell was 3.2 km×3.2 km. The height of the surface above

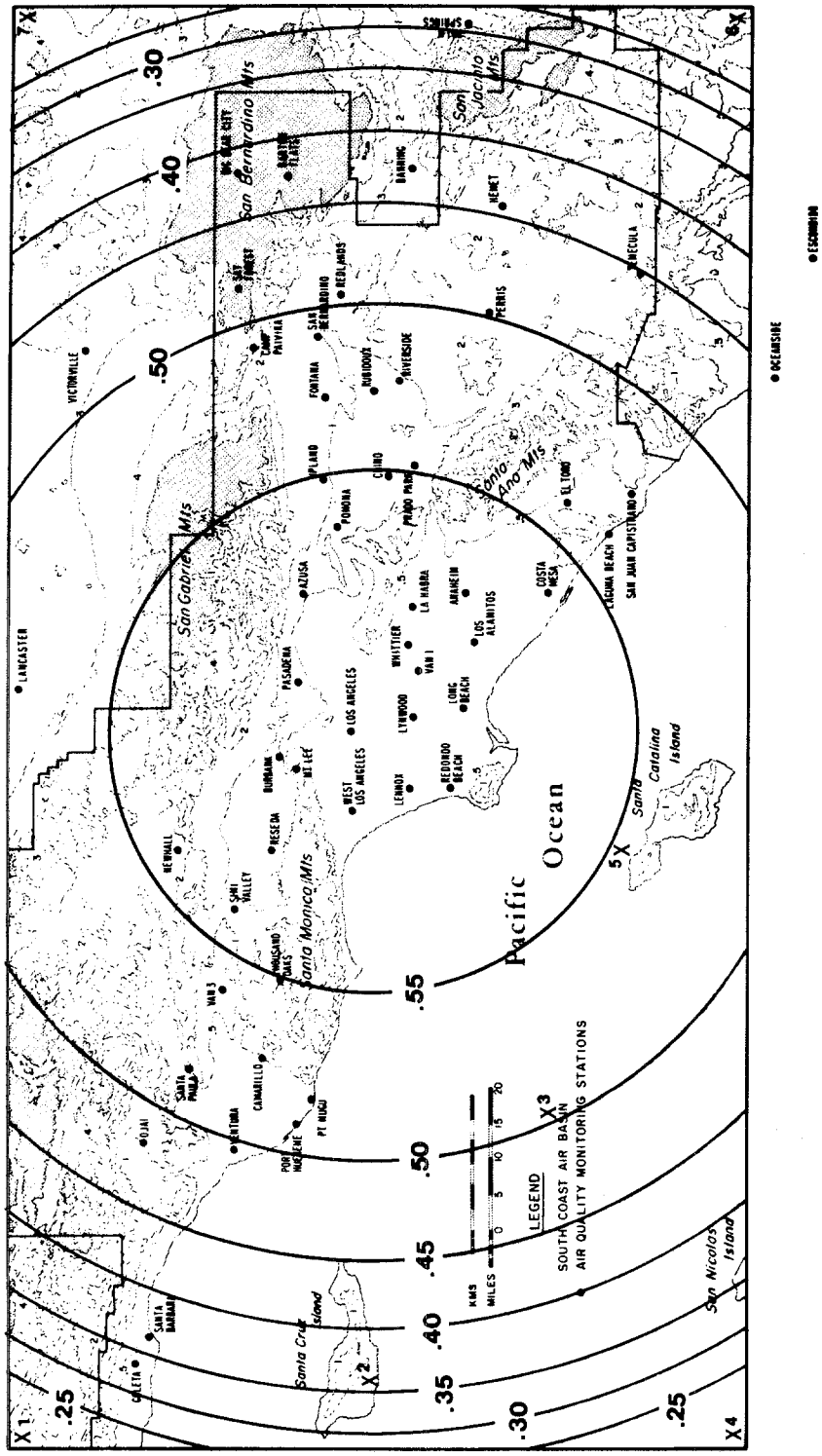

FIG. 1. Distribution of measurement stations and hemispherical test surface.

each grid point corresponded to the field value at that point. The height of the constructed surface was evaluated at each measuring station location (56 points) and these values were used as raw data in the test. Fig. 1 shows the field isopleths and the measuring station locations. The test consisted of attempting to reconstruct the hemispherical surface from these data points (no flow barriers were used).

The methods compared are the second-degree polynomial with r^{-2} weighting and the simple distance-weighting scheme with various weights, the results of which are shown in Table 2. Statistics are given for the station locations as well as for all grid points; in each case the percentage relative residual error E_r is computed from

$$E_r = 100\left[\frac{C_{\text{comp}}}{C_{\text{act}}} - 1\right], \tag{19}$$

where C_{comp} is the computed surface height and C_{act} its actual height. When an interpolation scheme is applied to a set of field data, the residual error at each station is the only measure of the technique's performance. However, for this test data set, the residual error can be computed over the whole grid, indicating the level of accuracy that can be expected away from measuring stations. Such a procedure cannot be expected to resolve sharp gradients which are not reflected in the data.

Contour plots of the reconstructed fields are shown in Fig. 2. Generally, in regions where the number of measuring stations is relatively large, the error is smallest (i.e., toward the center of the region). However, near the boundaries where the data network is less dense the errors can be much larger.

The results indicate that among the simple distance-weighting schemes, the $(R^2-r^2)/(R^2+r^2)$ weighting produces the most hemisphere-like surface. However, the departure from measured values is largest with this scheme. More accuracy is obtained near the data points with the r^{-a} and $\exp(-br^2)$ schemes, but at the expense of accuracy away from measuring stations. The second-degree polynomial fitting procedure provides a compromise. The hemispherical shape is preserved and the accuracy at the measuring station locations is also acceptable. The execution times do not include the square-to-station distance (or formulation of the triangles) calculation times since they need only be calculated once for a given set of stations.

5. Application of selected interpolation procedures to air quality data

On the basis of the simple problem described above as well as a variety of other test cases, three techniques were selected for further examination using actual measured data. These were distance-weighting schemes r^{-2} and $\exp(-0.1r^2)$ and second-degree polynomial fit with r^{-2} weighting. The distance-weighting schemes were chosen based on a compromise between station accuracy, accuracy over the whole grid, and cost. The actual data chosen for testing purposes were ozone measurements on 26 June 1974 taken within the South Coast Air Basin. All data have been corrected for measurement as well as interference errors. The distance-weighting techniques were tested using a fixed radius of influence of 48 km as well as a variable radius of influence. The variable radius of influence was specified to include at least two data points.

The results of the ozone data interpolation tests are displayed in Fig. 3 and Table 3. The r^{-2} weighting scheme produces the smallest residuals in the vicinity of the measuring stations whether a fixed or variable radius of influence is used. While minimizing the station residuals, the overall field variance for the r^{-2} weighting can be much higher than the polynomial fitting procedure as demonstrated in the test problem. Fig. 4 shows a three-dimensional perspective plot of

TABLE 2. Percentage relative residual error tabulated for hemispherical surface, for various weighting functions using 56 stations and a radius of influence (R) of 48 km.

Weighting function* $W(r)$	Residual error E_r (%) at measuring stations				Residual error E_r (%) at all grid points				Relative computation time
	Mean	Minimum	Maximum	Std. Dev.	Mean	Minimum	Maximum	Std. Dev.	
r^{-1}	0.06	−1.27	2.31	0.57	0.52	−52.47	52.12	8.23	2.1
r^{-2}	<0.01	−0.14	0.29	0.06	0.03	−52.47	52.10	8.59	1.4
r^{-3}	<0.01	−0.04	0.11	0.02	−0.38	−52.47	52.08	9.19	3.4
$\frac{R^2-r^2}{R^2+r^2}$	0.93	−9.29	36.64	5.51	−0.06	−52.47	52.08	9.47	1.7
$e^{-0.1r^2}$	0.02	−3.28	3.58	0.72	−1.07	−55.88	54.77	12.42	2.3
$e^{-0.5r^2}$	<0.01	−0.66	0.72	0.16	−1.14	−58.0	58.27	13.15	2.5
Second degree polynomial (r^{-2} weighting)	0.09	−0.75	0.87	0.32	−1.78	−18.92	10.64	4.0	1.0

* r is the distance from grid point to measuring station; for $r>R$, $W(r)$ is set to zero.

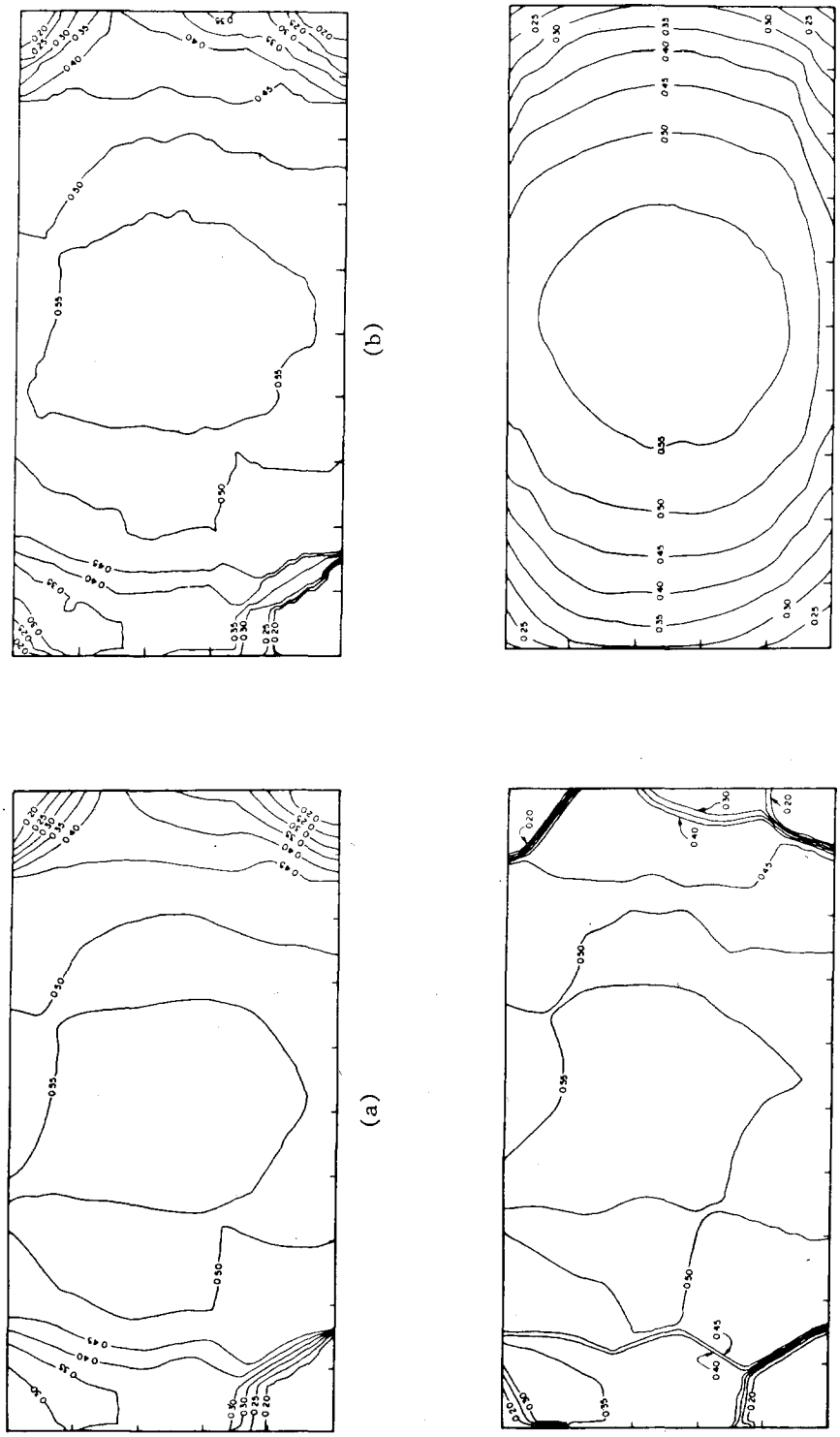

FIG. 2. Surfaces resulting from interpolation of hemispherical data using (a) $(R^2-r^2)/(R^2+r^2)$ weighting of data values, (b) r^{-2} weighting of data values (similar visual results were obtained for the r^{-1} and r^{-3} cases), (c) $\exp(-0.1r^2)$ weighting of data values (similar visual results were obtained for $\exp(-0.5r^2)$, and (d) polynomial fitting procedure.

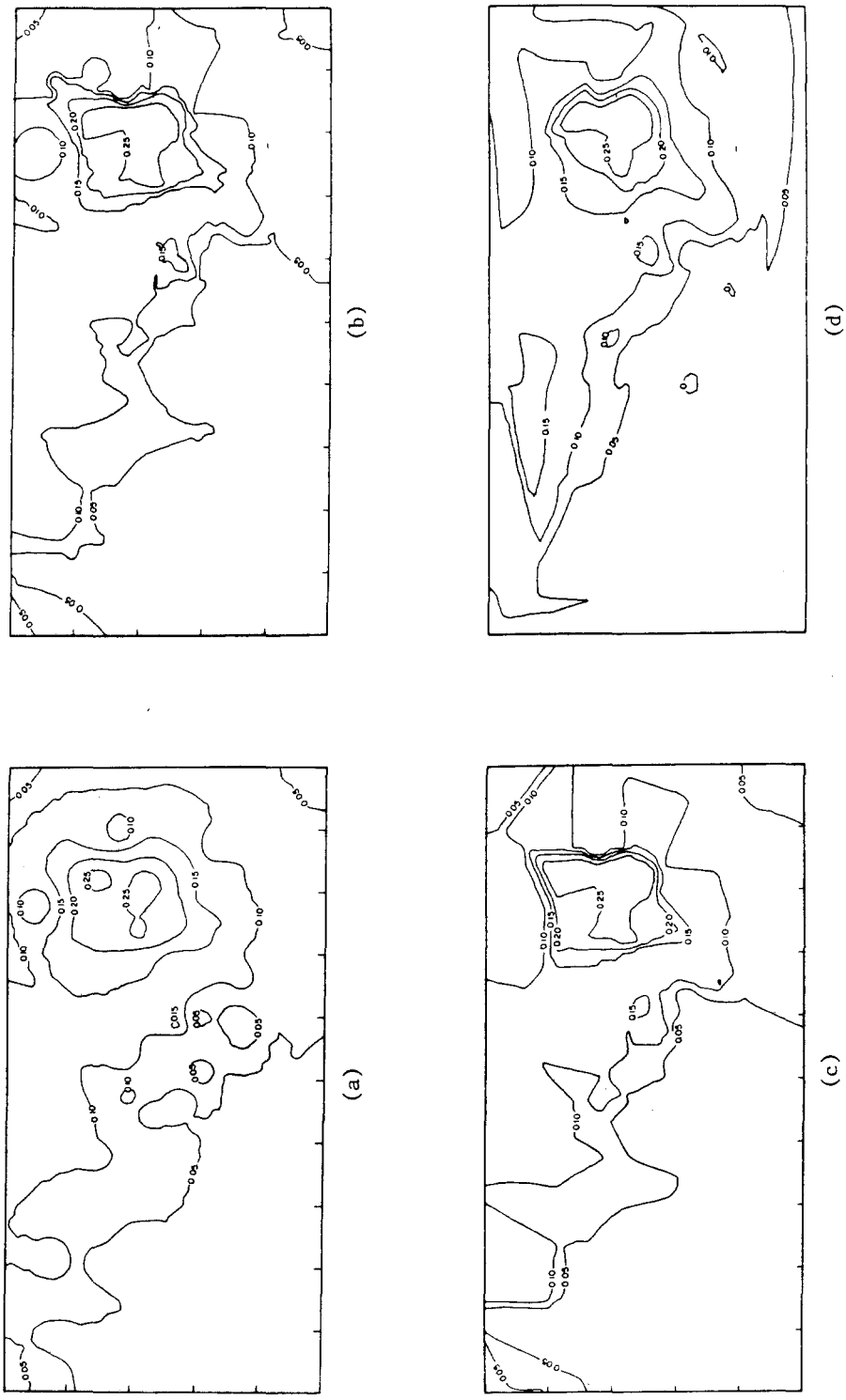

FIG. 3. Surfaces resulting from interpolation of measured ozone values from 1600 PST 26 June 1974 using (a) r^{-2} weighting of data values with a fixed radius of influence R, (b) r^{-2} weighting of data values with a variable R, (c) $\exp(-0.1r^2)$ weighting of data values with a variable R (similar visual results were obtained with a fixed R), and (d) polynomial fitting procedure.

TABLE 3. Percentage relative residual error E_r, tabulated from ozone data analysis for various weighting functions using 56 stations.

Weighting function* $W(r)$	Residual error E_r (%) at stations with radius of influence $R=48$ km				Residual error E_r (%) at stations with variable radius of influence R			
	Mean	Minimum	Maximum	Std. Dev.	Mean	Minimum	Maximum	Std. Dev.
r^{-2}	0.67	− 3.08	10.42	2.04	0.14	−3.22	3.79	1.00
$e^{-0.1r^2}$	5.56	−28.75	85.48	19.62	3.01	−21.59	71.72	15.69
Second degree polynomial (r^{-2} weighting)	4.82	−13.02	49.18	12.60				

* r is the distance from grid point to measuring station, for $r>R$, $W(r)$ is set to zero.

the ozone surface generated by the polynomial fitting procedure.

6. Application of interpolation procedures to vector fields

The procedures outlined in Section 2 can easily be applied to vector as well as scalar fields, for example, by treating the u and v components separately. Based on the results of the hemisphere test data set, the same three techniques used in Section 5 were selected for further detailed examination here. These were distance-weighting schemes r^{-2} and $\exp(-0.1r^2)$ and second-degree polynomial fit with r^{-2} weighting.

The test wind field data set, potential flow over a flat plate inclined at angle α to the flow, free stream velocity v_0, was chosen to illustrate the inclusion of a barrier to flow. The exact solution to the problem can be calculated from potential flow theory. The velocity potential ϕ and streamfunction ψ in an x-y Cartesian coordinate system are given by

$$\phi(x,y)=v_0\left(x+\frac{x\cos2\alpha-y\sin2\alpha}{x^2+y^2}\right), \tag{20}$$

$$\psi(x,y)=v_0\left(y-\frac{x\sin2\alpha+y\cos2\alpha}{x^2+y^2}\right). \tag{21}$$

The velocity components are computed from the velocity potential

$$u(x)=\frac{\partial\phi}{\partial x}=v_0\left(1+\frac{\cos2\alpha(y^2-x^2)+2xy\sin2\alpha}{(x^2+y^2)^2}\right), \tag{22}$$

$$v(y)=\frac{\partial\phi}{\partial y}=v_0\left(\frac{\sin2\alpha(y^2-x^2)-2xy\cos2\alpha}{(x^2-y^2)^2}\right). \tag{23}$$

For the present analysis, the angle of inclination α was chosen to be $\pi/4$. Indicated on Fig. 5 are the

TABLE 4. Percentage relative residual error statistics for interpolation of a potential flow problem.

Weighting function* $W(r)$	Velocity component	Residual error E_r (%) at measuring stations				Residual error E_r (%) at all grid points			
		Mean	Minimum	Maximum	Std. Dev.	Mean	Minimum	Maximum	Std. Dev.
$e^{-0.1r^2}$	u	16.36	−57.23	231.43	49.86	3.49	−80.71	281.16	19.87
$R=8$ squares	v	12.43	−81.38	185.68	54.04	18.20	−787.53	544.39	81.04
r^{-2}	u	0.21	−1.08	2.46	0.63	7.53	−81.26	165.14	14.25
$R=8$ squares	v	−0.10	−1.21	2.86	0.71	−66.27	−989.70	966.45	151.65
Polynomial	u	9.72	−40.85	99.13	24.98	1.62	−76.93	170.49	14.17
	v	−4.85	−55.76	48.25	24.06	−99.93	−192.21	137.29	19.61
$e^{-0.1r^2}$ R variable (includes 2 data points)	u	10.13	−27.64	202.69	39.12	0.70	−81.82	202.69	15.16
	v	2.88	−158.82	151.86	62.89	9.43	−819.73	555.60	87.15
r^{-2} R variable (includes 2 data points)	u	0.10	−0.31	2.24	0.43	0.23	−81.82	198.00	12.76
	v	0.01	−0.59	0.76	0.31	12.47	−702.78	577.71	74.22

* r is the distance from grid point to measuring station; for $r>R$, $W(r)$ is set to zero.
Note: In calculating the error statistics, points on the plate and one grid cell away from the plate were ignored.

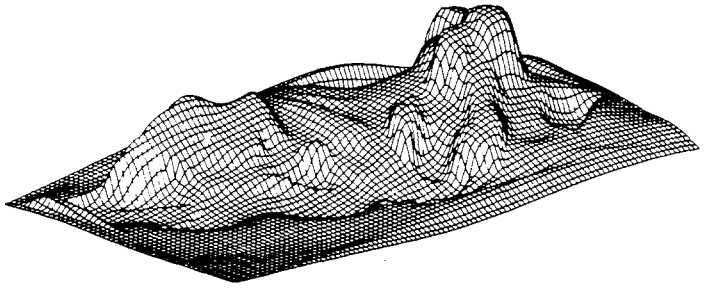

FIG. 4. Perspective plot of ozone distribution generated by polynomial interpolation scheme (a view from the southwest).

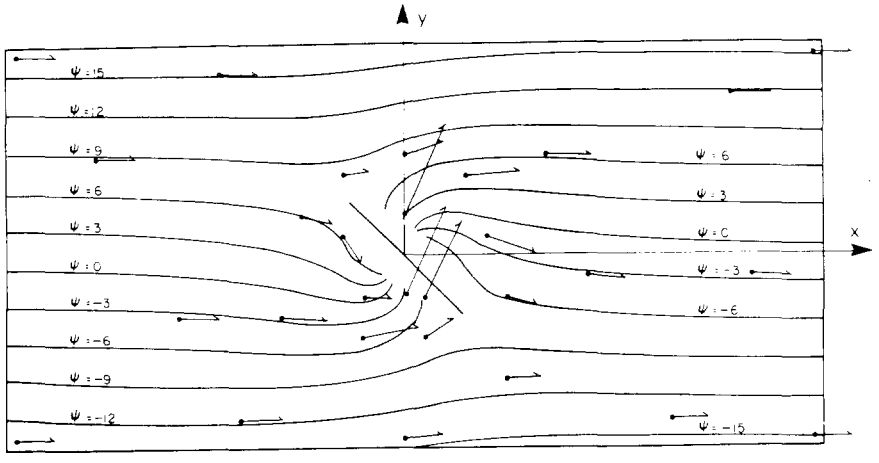

(a)

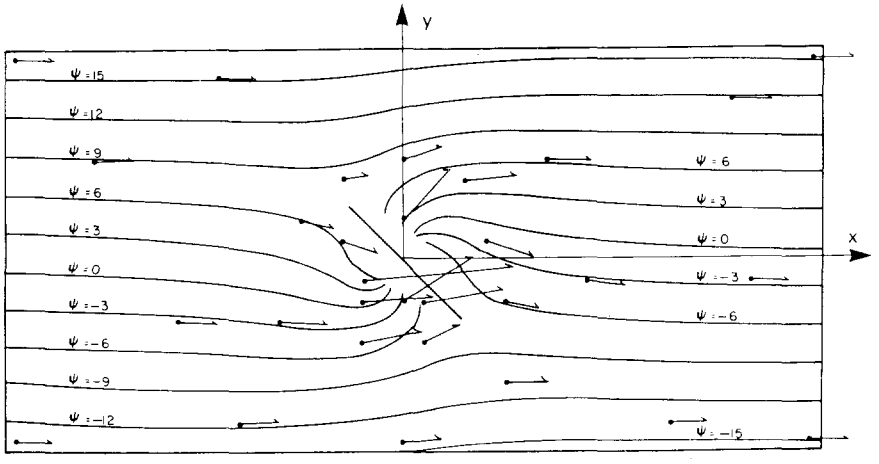

(b)

FIG. 5. Streamfunctions and location of velocity data points (solid circles) for potential flow over a flat plate. Reconstructed velocity field for potential flow over a flat plate for (a) r^{-2} with variable R and (b) polynomial fitting scheme.

streamfunction and velocity data points together with the calculated velocity vectors developed using the interpolation procedures over a 40×20 grid.

In the distance-weighting procedures, a check is made to see whether a line connecting a measuring station to a grid point intersects the barrier. If so, that station's value is not included in the weighting procedure at that grid point. In the polynomial fitting procedure a barrier is treated by requiring that it be an edge of two adjacent triangles. The results of this vector test problem are shown in Table 4 and Fig. 5.

7. Conclusions

Since the interpolation of a set of sparse data does not have a unique solution, it is important that the calculation be done carefully, producing physically realistic resulting surfaces. The interpolated field is critical to calculations such as wind field divergence reduction, contouring of data values, and initialization of pollutant transport calculations. A comparison of a number of procedures for interpolating sparse data indicates that the second-degree polynomial fitting procedure with an r^{-2} distance-weighting scheme provides a good compromise between computational costs and the accuracy of the final surface adjacent to and further away from measurement stations.

Acknowledgments. Portions of this work were supported by the California Air Resources Board under Contract A5-046-87, and by the Department of Energy under Institutional Grant EY-76-G-03-1305.

REFERENCES

Akima, H., 1975: A method of bivariate interpolation and smooth surface fitting for values given at irregularly distributed points. Dept. of Commerce Rep. 75–70, 51 pp. [NTIS COM-75-10812].

Barnes, S. L., 1964: A technique for maximizing details in numerical weather map analysis. *J. Appl. Meteor.*, **3**, 396–409.

——, 1973: Mesoscale objective analysis using weighted time-series analysis. NOAA Tech. Memo. ERL NSSL-62, 60 pp. [NTIS COM-73-10781].

Boone, D. R., and G. S. Samuelson, 1977: Computer mapping of air quality. *J. Environ. Eng. Div. Proc. ASCE*, **103**, **EE6**, 969–979.

Clough, R. W., and J. L. Tocher, 1965: Finite element stiffness matrices for the analysis of plates in bending. *Proc. Conf. Matrix Methods in Structural Mechanics*, Air Force Inst. and Tech., Wright Patterson AFB, Ohio.

Cressman, G. P., 1959: An operational objective analysis system. *Mon. Wea. Rev.*, **87**, 367–374.

Dartt, D. G., 1972: Automated streamline analysis utilizing optimum interpolation. *J. Appl. Meteor.*, **11**, 901–908.

Endlich, R. M., and R. L. Mancuso, 1968: Objective analysis of environmental conditions associated with severe thunderstorms and tornadoes. *Mon. Wea. Rev.*, **96**, 342–350.

Fritsch, J. M., 1971: Objective analysis of a two-dimensional data field by the cubic spline technique. *Mon. Wea. Rev.*, **99**, 379–386.

Gandin, L. S., 1965: *Objective Analysis of Meteorological Fields*. Israel Program for Scientific Translations, Jerusalem, 242 pp.

Gilchrist, B., and G. P. Cressman, 1954: An experiment in objective analysis. *Tellus*, **6**, 309–318.

Green, P. J., and R. Sibson, 1978: Computing Dirichlet tessellations in the plane. *Comput. J.*, **21**, 168–173.

Hovland, D., D. Dartt and K. Gage, 1977: An objective analysis technique for the regional air pollution study, Part I. EPA, Research Triangle Park, N.C., 44 pp. [NTIS PB 266255].

Julian, P. R., and H. J. Thiebaux, 1975: On some properties of correlation functions used in optimum interpolation schemes. *Mon. Wea. Rev.*, **103**, 605–616.

Lawson, C. L., 1977: Software for C^1 surface interpolation. *Mathematical Software*, Vol. 3, J. R. Rice, Ed., Academic Press, 161–194.

MacCracken, M. C., and G. D. Sauter, Eds., 1975: *Development of an Air Pollution Model for the San Francisco Bay Area*, Vol. 2, Appendices. Lawrence Livermore Laboratory, UCRL-51920, 229–230 [NTIS UCRL-51920].

McLain, D. H., 1974: Drawing contours from arbitrary data points. *Comput. J.*, **17**, 318–324.

——, 1976: Two dimensional interpolation from random data. *Comput. J.*, **19**, 178–181.

——, 1976: Errata. *Comput. J.*, **19**, 384.

Panofsky, H. A., 1949: Objective weather-map analysis. *J. Meteor.*, **6**, 386–392.

Powell, M. J. D., and M. A. Sabin, 1977: Piecewise quadratic approximation on triangles. *Mathematical Software*, Vol. 3, J. R. Rice, Ed., Academic Press, 316–325.

Schlatter, T. W., 1975: Some experiments with a multivariate statistical objective analysis scheme. *Mon. Wea. Rev.*, **103**, 246–257.

Shenfeld, L., and A. E. Boyer, 1974: The utilization of an urban air pollution model in air management. Paper presented at Fifth Meeting NATO/CCMS Expert Panel on Air Pollution Modeling, Roskilde, Denmark.

Shepard, D., 1968: A two-dimensional interpolation function for irregularly spaced data. *Proc. 23rd ACM Nat. Conf.*, Las Vegas, 517–524.

Stephens, J. J., and J. M. Stitt, 1970: Optimum influence radii for interpolation with the method of successive corrections. *Mon. Wea. Rev.*, **98**, 680–687.

Thiebaux, H. J., 1975: Experiments with correlation representatives for objective analysis. *Mon. Wea. Rev.*, **103**, 617–627.

Thiessen, A. H., 1911: Precipitation averages for large areas. *Mon. Wea. Rev.*, **39**, 1082–1084.

3.3 Weighted Interpolation Procedures

An important element of the interpolation procedure presented in the previous section was the distance weighting function

$$c(p) = \frac{\sum_{k=1}^{n} c_k W_k(r)}{\sum_{k=1}^{n} W_k(r)} \tag{3.1}$$

where $c(p)$ is the interpolated value of c at the point $p=(x,y)$, c_k; $k=1,2,..,n$ are the data values at the points p_k, $W_k(r)$ the weighting function

$$W(r) = \frac{1}{r^a} \tag{3.2}$$

and r a suitably chosen distance metric of the form

$$r(p,p_i) = [(x-x_i)^2 + (y-y_i)^2]^{\frac{1}{2}} \tag{3.3}$$

Some other functional forms of $W(r)$, which are used in practice, are shown in Figure 3.1. Subsequent to the publication of the paper by Goodin et al. (1979) a discussion was received from Glahn (1981). In the process of preparing a reply, Goodin et al. (1981), it was discovered that (3.1) could be written in the equivalent form

$$c(p) = \sum_{i=1}^{n} F_i c_i \tag{3.4}$$

where

$$F_i = \frac{\prod_{\substack{j=1 \\ j\neq i}}^{n} r_j^a}{\sum_{m=1}^{n} \prod_{\substack{j=1 \\ j\neq m}}^{n} r_j^a} \tag{3.5}$$

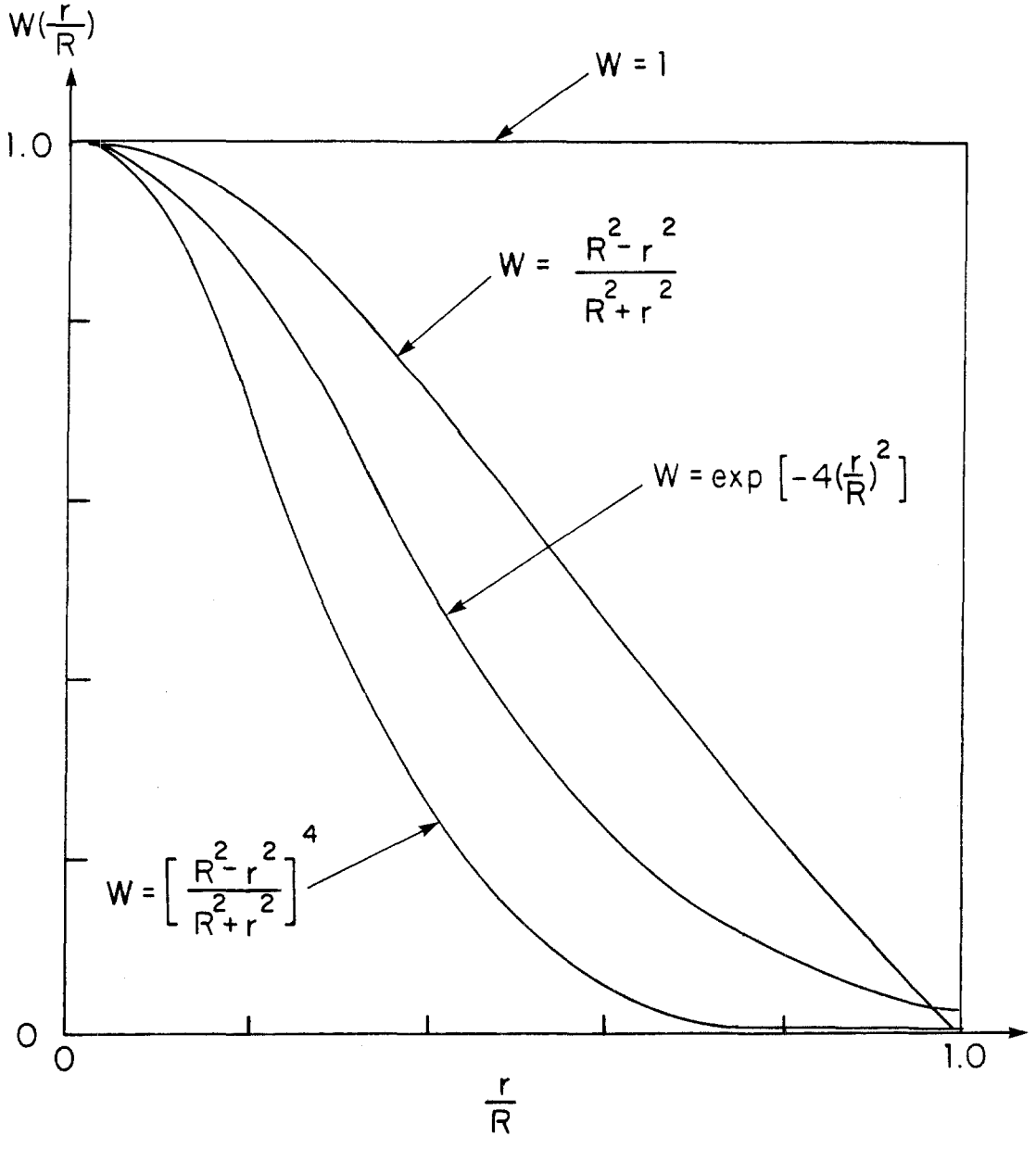

FIGURE 3.1

Some Examples of Different Weighting Functions
of the Form W(r/R) Where R is the Radius of Influence

This section presents some of the results which can be readily derived from the alternate representation of interpolation procedure.

A particular concern of Glahn (1981) was the behaviour of (3.1) in between data points. Using the rearranged form it is a straightforward task to evaluate the partial derivatives of c(p) in the neighborhood of the data points and to show that for a > 1

$$\lim_{p \to p_i} \frac{\partial c}{\partial x} = \lim_{p \to p_i} \frac{\partial c}{\partial y} = 0 \qquad (3.6)$$

and for $0 < a \leq 1$ that the partial derivatives do not exist. These results have important practical consequences because it is evident that for $0 < a \leq 1$ there will be cusps at the data points and when a > 1 the surface slope in the vicinity of each c_k will be zero. These properties are illustrated in Figure 3.2. From a practical point of view it is desirable to avoid the cusps at the data points and so it is customary to choose a > 1. As a is increased the surface tends to become flat near the data points and consequently, quite steep in between. A number of experiments were conducted using different data sets and it was concluded that a = 2 represents a good compromise.

One interesting feature of Figure 3.2 is that as the exponent is increased the interpolated result approximates a piecewise constant function. Since this result will also apply in two dimensions it suggests a simple and direct method for testing if a point is within the tessellation surrounding a particular data point. Gordon and Wixom (1978) and Schumaker (1976) discuss the properties of interpolation

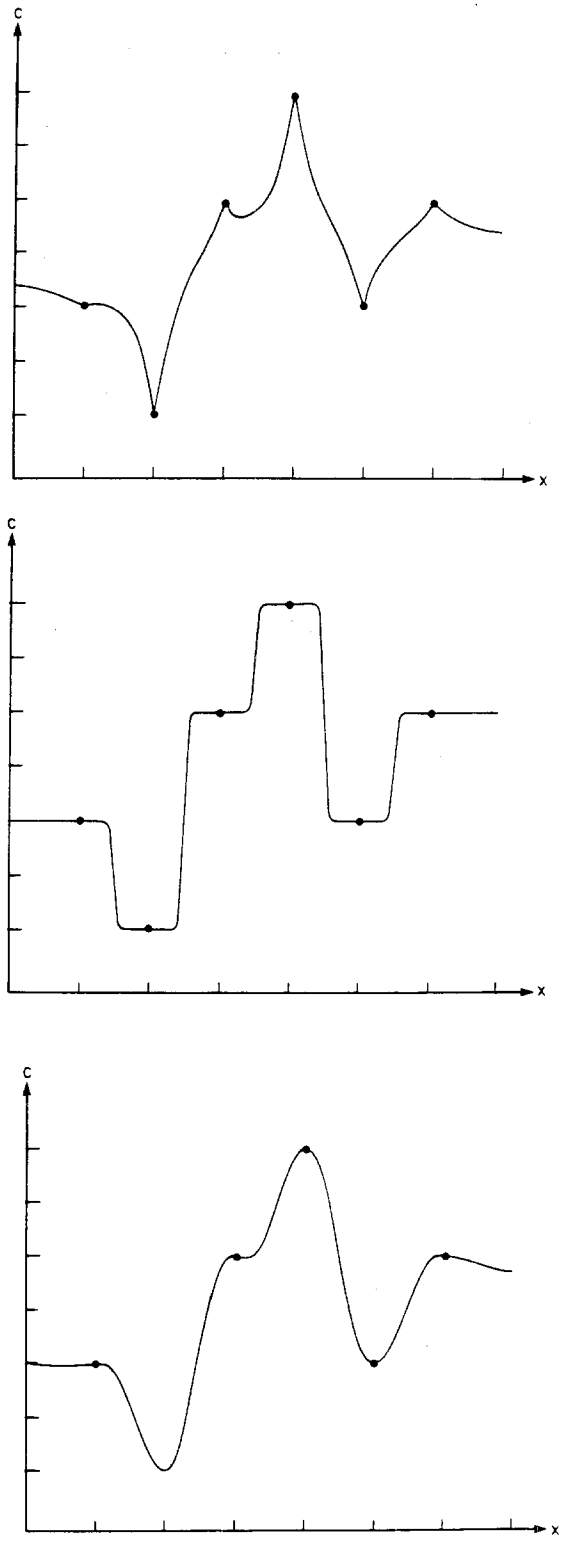

FIGURE 3.2

Results of Using Different Exponents in the Weighting Function $W(r) = 1/r^a$. The three cases correspond to (a) $1/r$, (b) $1/r^{10}$ and (c) $1/r^2$ (After Gordon and Wixom, 1978)

schemes based on (3.1) and in particular show that for the case a = 1

$$\min_i [c_i] < c(p) < \max_i [c_i] \tag{3.7}$$

Further Gordon and Wixom (1978) show that if $c_i \geq 0$ for all i=1,2,...,n then $c(p) \geq 0$ for all p. This is a very desirable result when interpolating concentration fields.

If information about the slope of the surface is available then the procedure developed by Shepard (1968) can be used to overcome the problems associated with flat spots for a > 1. The interpolation formula is given by

$$c(p) = \sum_{i=1}^{n} F_i \, [c_i + (x-x_i)c_x + (y-y_i)c_y] \tag{3.8}$$

where the derivatives in each direction are given by

$$c_x = \left.\frac{\partial c}{\partial x}\right|_{p=p_i}$$

$$c_y = \left.\frac{\partial c}{\partial y}\right|_{p=p_i} \tag{3.9}$$

Franke (1977) and Barnhill (1977) have carried out extensive comparisons of different weighted interpolation schemes and present numerous test cases that have analytic results.

3.4 Generation of Triangulated Computational Domains

One step in the interpolation technique introduced in the previous section involves constructing a mesh of non-overlapping triangles whose vertices correspond to the data point locations. While manual construction of the mesh is straightforward the sheer volume of measurement information which must be processed in typical applications necessitates an automated procedure. This section presents an algorithm which will construct the required triangulation given a set S of n distinct spatial points $P_i(z,y)$; i=1,2,...,n.

While there are many possible triangulations they all contain the same number of triangles. This can be readily deduced, for a bounded polygon, from the Euler-Poincare formula

$$F + V = E + 1 \tag{3.10}$$

In this expression F,V and E are respectively the number of faces, vertices and edges. For the particular problem under consideration F = n_t, the number of triangles, and V = n the number of vertices. Since each internal edge is common to two triangles and the n_b points which define the edges of convex hull of S appear only once then

$$3n_t = 2E - n_b \tag{3.11}$$

Eliminating the number of edges from (3.10-3.11) gives a simple expression for the number of triangles

$$n_t = 2n - n_b - 2 \leq 2n \tag{3.12}$$

There are two basic problems in constructing triangulated meshes: establishing suitable selection criteria for identifying preferred triangulation and avoiding overlap. In general there is no single "best" triangulation although it is clearly desirable to maximize the smallest interior angles in each triangle. The reason for this is to avoid illconditioning the matrices which arise during the polynomial fitting procedures. One procedure that can be used to generate nonoverlapping triangulations that satisfies the minimum angle criterion is due to Green and Sibson (1978). They start by constructing a convex polygon around each data point p_i. Each polygon or tile is defined by

$$T_i = \{(x,y): r(p,p_i) < r(p,p_j) \text{ for all } i \neq j\} \qquad (3.13)$$

$$i = 1,2,\ldots,n$$

where $r(p,p_i)$ is the Euclidean distance (3.3). The resulting pattern is known by a variety of different names: a Dirichlet tessellation, the Thiessen diagram (Thiessen, 1911), or Voronoi polygons (Finney, 1979; Brostow et al. 1978). The diversity of names is a consequence of their independent development in various different applications. Within any polygon each point is closer to the data point than any other in S. In general tiles meet in threes at vertices. The lines joining data points in contiguous polygons define triangles the perpendicular bisectors of which define the tile boundaries and the circumcenters, the polygon vertices. Figure 3.3 illustrates a typical Dirichlet tessellation and its associated dual, the Delaunay triangulation (Rodgers, 1964). This configuration satisfies the local equiangularity property suggested by

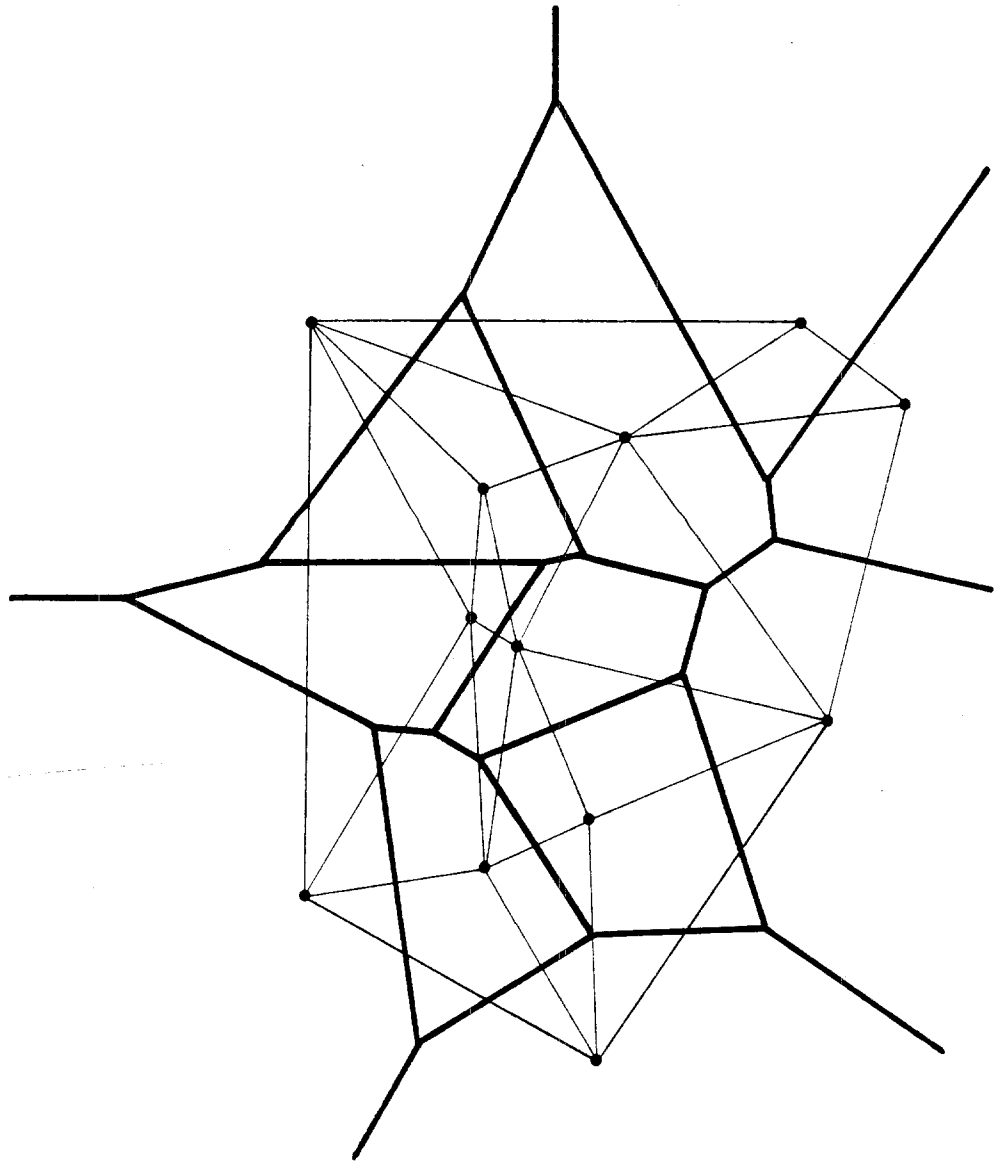

FIGURE 3.3

The Dirichlet Tessellation (bold lines) and
Dalaunay Triangulation (fine lines) for a Small Scale Configuration.
(After Green and Sibson, 1978)

Lawson (1977) which requires that in every convex quadrilateral formed by two adjacent triangles, the minimum of the six angles in the two triangles is not less than it would have been had the alternative diagonal and pair of triangles been chosen. Unfortunately while it is relatively easy to define the tiles, construction of an efficient general purpose algorithm is not straightforward. An alternative, and the procedure adopted in this study is to construct the triangles one at a time using an algorithm due to McLain (1976ab), Nelson (1978) and Thacker(1979). Operationally the technique is easy to implement and Lawson (1977) has shown that it produces the same Delaunay triangulation generated by the Green and Sibson (1978) algorithm.

Consider a triangle T^k formed by the three points ABC in Figure 3.4. Let $\overline{AB}$ be an edge and S_k the subset of S consisting of the points on the opposite side of $\overline{AB}$ from C. McLain (1976a) introduced a simple test for identifying the point in S_k that could be used to construct the next triangle T^{k+1}. The test is as follows. For each point p_i in S_k construct the circumcircle which passes through A,B and p_i and determine the signed distance of the circumcenter from $\overline{AB}$. The signed distance from $\overline{AB}$ is positive on the side of AB opposite to C. The point $\bar{p}_i$ which has the minimum value of $\overline{AB}\bar{p}_i$ is the one to use in extending the triangulation. If any of the points in S_k satisfying this criterion are found to lie on the same circumcircle then they are triangularized in a right hand order. The procedure is terminated when there are no remaining points in S_k and all edges have been tested.

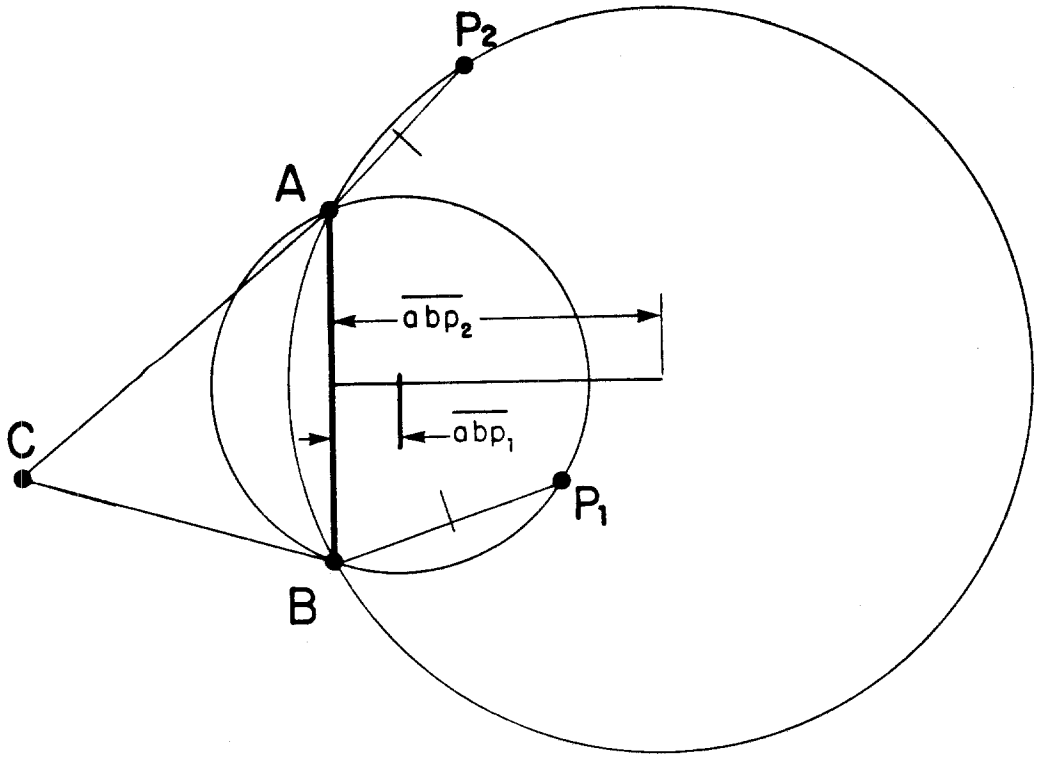

FIGURE 3.4

Procedure for Identifying Triangle Vertices.

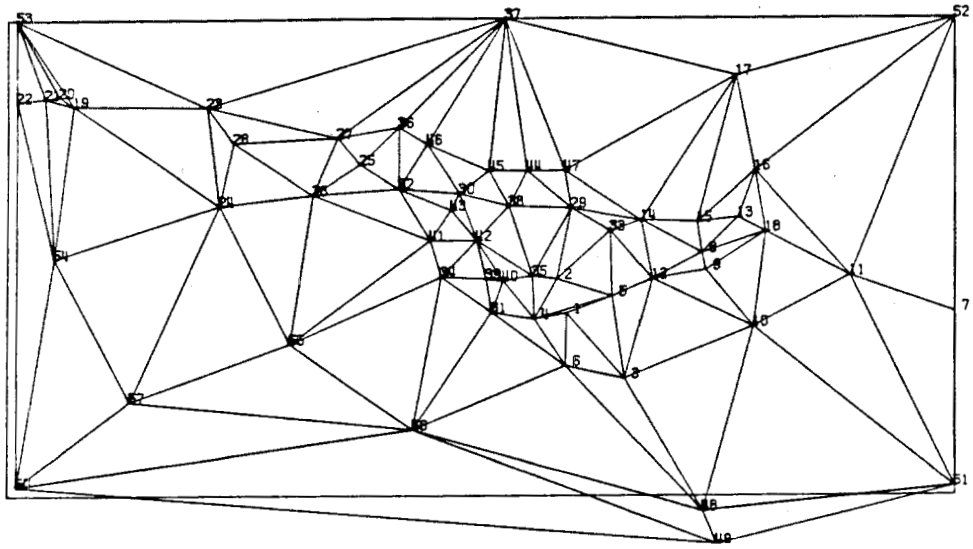

(a)

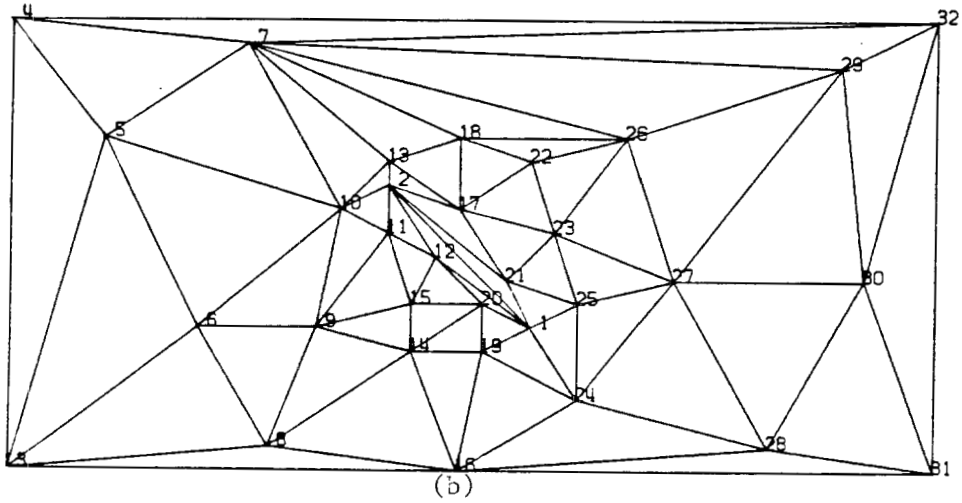

(b)

FIGURE 3.5

Triangulations of the Plane for Examples Presented in Section 3.3

(a) Air Quality Interpolation ($n = 53$, $n_b = 8$, $n_t = 96$)

(b) Flow Over a Flat Plate ($n = 32$, $n_b = 5$, $n_t = 57$)

There are a variety of ways to start the algorithm, the simplest of which is to specify an initial triangle. Another approach is to identify the nodes and edges which form the convex hull of S. The methods of Graham (1972), Jarvis (1973) or Green and Silverman (1979) can be used for this task. Given the boundary edges then the interior triangles can be constructed using the McLain algorithm. A third method is to evaluate the Euclidean distances from the origin or some point outside the convex hull to each data point. A starting triangle can then be formed by using the three points closest to the origin. Figure 3.5 presents some examples of triangulations produced with the above procedure. Once the region has been triangulated the convex hull can be readily determined by identifying those edges which are common to only one triangle.

Given the convex hull then it is possible to easily evaluate moments of the form

$$I^{nm} = \iint x^n y^m dxdy \tag{3.14}$$

using Green's theorem (3.14) can be written in the equivalent form

$$I^{nm} = \frac{1}{2(n+1)} \int x^{n+1} y^m dy - \frac{1}{2(m+1)} \int x^n y^{m+1} \, dx \tag{3.15}$$

Since the boundary of the convex hull is defined by a series of straight line segments (3.15) can be written as

$$I^{nm} = \frac{1}{2(n+1)(m+1)} \sum_{i=1}^{n_b} (x_i^{n+1} y_{i+1}^{m+1} - x_{i+1}^{n+1} y_i^{m+1}) \tag{3.16}$$

For example the area inside the convex hull is given by I^{oo}.

3.5 Polynomial Interpolation over Triangles

Once the plane has been triangulated the next step is to develop the interpolation functions over each triangle. The basic objective is to construct from the nodal values c_i a function $c(p) = c(x,y)$ that interpolates c into the triangle interior. This section has been provided to supplement the necessarily brief discussion of polynomial interpolation procedures presented in Section 3.2.

The simplest surface corresponds to a linear variation over the triangle. For a triangle with vertices at the points (ijm) such a surface is defined by

$$c(x,y) = \frac{1}{D}[(a_0^i + a_1^i x + a_2^i y)c_i + (a_0^j + a_1^j x + a_2^j y)c_j + (a_0^m + a_1^m x + a_2^m y)c_m] \tag{3.17}$$

where

$$a_0^i = x_j y_m - x_m y_j \tag{3.18}$$

$$a_1^i = y_j - y_m \tag{3.19}$$

$$a_2^i = x_m - x_j \tag{3.20}$$

The remaining coefficients in (3.17) can be obtained by cyclic permutation of the subscripts (ijm). The determinant D in (3.17) is given by

$$2D = \det \begin{bmatrix} 1 & x_i & y_i \\ 1 & x_j & y_j \\ 1 & x_m & y_m \end{bmatrix} = 2 \text{ (area ijm)} \tag{3.21}$$

This procedure produces a piecewise linear surface composed of plane facets as shown in Figure 3.6. Because (3.17) reduces to straight lines joining the vertices the surface is globally continuous.

While the construction of interpolating functions which have higher-order smoothness C^1 or C^2 across element boundaries is not straightforward there is an extensive literature which discusses the subject because of its importance in finite element modeling. Some general reviews can be found in Akima (1975), Schumaker (1976), Barnhill (1977), Powell and Sabin (1977) and Lawson (1977). The approach adopted in this study (McLain, 1974; 1976ab) is to construct a local quadratic approximation to $c_i(x,y)$ and then to form the $c(x,y)$ as a weighted average of the functions at the three nodes. There are two reasons for adopting this method, the low computational cost and the general lack of information about the derivatives and function values at points other than the vertices. If these data are available then it is possible to use higher order elements of the type discussed by Barnhill (1977).

In the present work the variation at c_i is of the form

$$c_i(x,y) = a_{00} + a_{10}x + a_{01}y + a_{11}xy + a_{20}x^2 + a_{02}y^2 \qquad (3.22)$$

where the six coefficients are determined from a weighted least squares fit to the surrounding data points. By setting $a_{00} = c_i$ and solving for the remaining five coefficients the interpolating surface passes through the data points. In the surface fitting procedure distant data values are weighted using schemes of the type discussed in Section 3.3.

Once the polynomials have been constructed for each node they can be combined as follows

$$c(x,y) = W_i c_i + W_j c_j + W_m c_m \tag{3.23}$$

where the weighting functions W are chosen to ensure smooth transitions across each of the triangle edges. In the present work the weighting for each polynomial is proportional to the distance d_i of the point from the side of the triangle. The distance from the point (x,y) to the side is a linear function of x and y

$$d_i = a_0 + a_1 x + a_2 y \tag{3.24}$$

where a_0, a_1 and a_2 are the coefficients defining a line through the triangle edge opposite vertex i, scaled such that $d_i = 1$ at the point i. The weight W_i used in the present study is given by

$$W_i = \frac{d_i^3}{(d_i^3 + d_j^3 + d_m^3)} \tag{3.25}$$

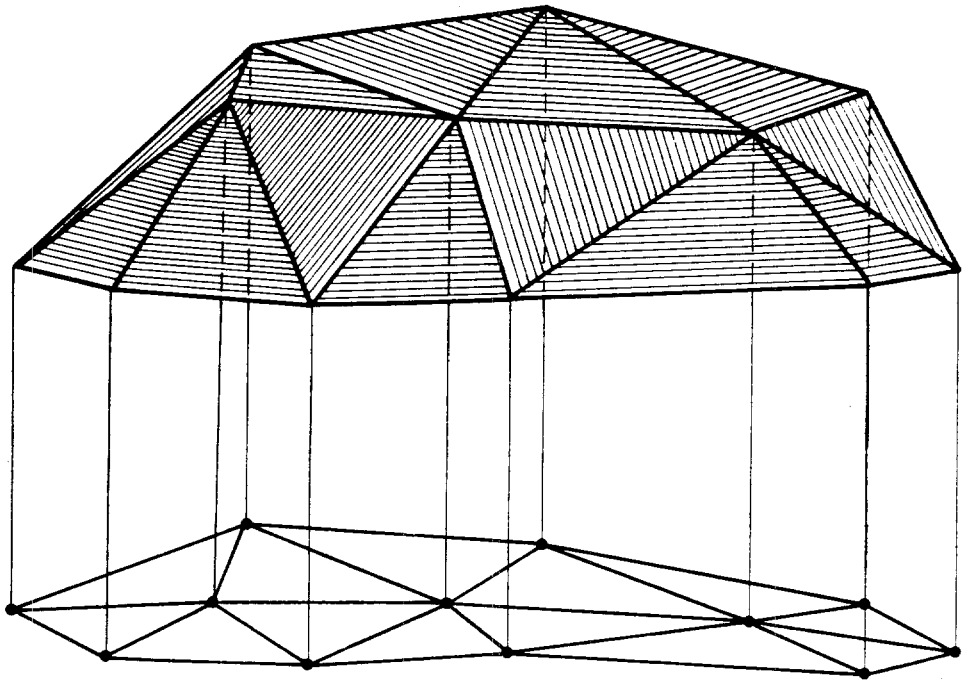

FIGURE 3.6

An Example of a Linear Functional Variation
Over each Triangular Element

3.6 Generation of Three-dimensional Wind Flow Fields

Advective transport and turbulent mixing are two of the physical processes that dominate pollutant dispersion over an urban area. In the airshed model they are characterized by the velocity field $\underline{u}(\underline{x},t)$ and the eddy diffusion tensor K. Considerable research effort has been devoted to developing general procedures for specifying these inputs. Two common approaches for generating the required wind fields are: numerical solution of the governing equations of motion and objective analysis procedures which employ measured data. This section describes some of the different methods for constructing velocity distributions and is intended as an introduction to the material to be presented in the following section.

In the planetary boundary layer the flow dynamics can be described by the conservation equation for mass, momentum, energy and state. Dutton and Fichtl (1969), Busch (1973) and Donaldson (1973) have derived systems for boundary layer flows and in particular have discussed the validity of various simplifying assumptions. Despite the desirability of developing flow fields from solutions of the governing equations, relatively little progress has been made in developing models which can be used on a routine basis for generating three-dimensional mesoscale wind fields. There are two reason for this, severe computational difficulties and practical problems associated with establishing the boundary conditions. For example Nickerson's (1979) model requires a priori specification of all thermodynamic variables at the boundaries. Maher and Pielke (1977) have a more realistic treatment of the heat flux at

the ground but their formulation is only applicable for steady state conditions. Most of the other available models are valid only for two-dimensional flow problems.

An operational constraint on the development of wind field models is the requirement that the input data be either routinely available or readily estimated. In a typical urban area the following data can usually be obtained: synoptic meteorological charts, geostrophic winds, terrain height, surface roughness, cloud cover, solar insolation, temperature, relative humidity, surface winds, and estimates at 850, 700 and 500 mb heights. The availability of this information was an important factor in selecting the objective analysis procedure to be presented in the following section.

There are two basic approaches to objective analysis. One is to use the field data and interpolate them in a manner such that mass conservation or other physical constraints are satisfied directly. This method has been used by Wahba and Wendelberger (1979) to develop 500 mb pressure surfaces. Another scheme, and the focus of Section 3.7, is to interpolate the measurements to a regular grid and then apply variational procedures to minimize the field divergence. The latter procedure has the advantage that any knowledge about measurement errors can be directly incorporated into the formulation. Figure 3.7 summarizes the general approaches that have been adopted to generate three-dimensional wind flow fields.

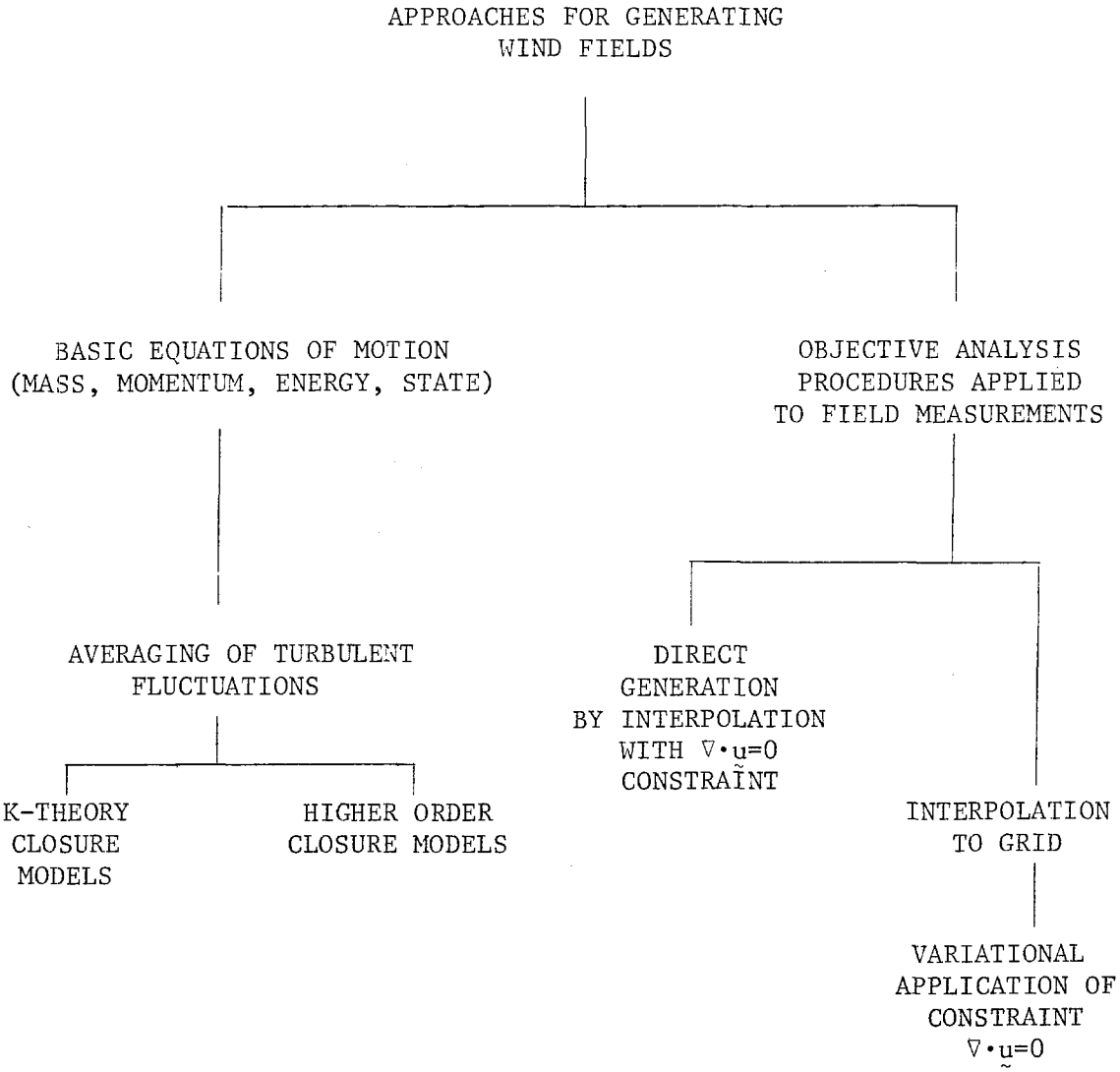

FIGURE 3.7

Summary of Approaches for Generating Wind Fields

3.7 An Objective Analysis Technique for Constructing Three-Dimensional Urban-Scale Wind Fields

(Reprinted from J. Applied Meteorology, 19, 98-108.)

An Objective Analysis Technique for Constructing Three-Dimensional Urban-Scale Wind Fields

WILLIAM R. GOODIN,[1] GREGORY J. MCRAE AND JOHN H. SEINFELD

Environmental Quality Laboratory, California Institute of Technology, Pasadena 91125

(Manuscript received 10 January 1979, in final form 8 September 1979)

ABSTRACT

An objective analysis procedure for generating mass-consistent, urban-scale three-dimensional wind fields is presented together with a comparison against existing techniques. The algorithm employs terrain following coordinates and variable vertical grid spacing. Initial estimates of the velocity field are developed by interpolating surface and upper level wind measurements. A local terrain adjustment technique, involving solution of the Poisson equation, is used to establish the horizontal components of the surface field. Vertical velocities are developed from successive solutions of the continuity equation followed by an iterative procedure which reduces anomalous divergence in the complete field. Major advantages of the procedure are that it is computationally efficient and allows boundary values to adjust in response to changes in the interior flow. The method has been successfully tested using field measurements and problems with known analytic solutions.

1. Introduction

A key input to most urban-scale air pollution models is an accurately specified, mass-consistent wind field. In most practical situations numerical solution of the full Navier-Stokes equations is not feasible as a means of constructing such a field. As a result, simpler objective analysis procedures must be used. The most common approach for generating a gridded wind field consists of a two-step procedure, the first step of which is interpolation of the sparse and discrete measurements within the airshed to a finer mesh (Goodin *et al.*, 1979). Once the initial field has been established, the next step is to employ an objective analysis procedure to adjust the wind vectors at each grid point so that appropriate physical constraints are satisfied. We present here a new technique for constructing three-dimensional velocity fields with a minimum of anomalous divergence.

2. Previous work on wind field divergence reduction

Only a limited number of divergence reduction procedures have appeared in the literature. Endlich (1967) used a point-iterative method to reduce the two-dimensional divergence in a wind field while retaining the vorticity in the original field. Fankhauser (1974) approached the three-dimensional divergence reduction problem from the point of view of accounting for measured data errors; in particular, those which increase with altitude. Liu and Goodin (1976) adapted the technique of Endlich to a two-dimensional mesoscale wind field. The flow field within the mixed layer was assumed to be vertically integrated and divergence was adjusted point by point with the capability of holding wind station values fixed. More recently, Sherman (1978) devised a procedure called MATHEW for constructing three-dimensional mass-consistent wind fields. Based on the variational calculus approach of Sasaki (1958, 1970), the method involves solution of a Lagrange multiplier equation. A two-dimensional vertically integrated version of MATHEW called MASCON (Dickerson, 1978) was incorporated into the LIRAQ model (MacCracken, *et al.*, 1978). The influences on the flow field of topography, surface roughness and temperature gradients were accounted for in a technique developed by Yocke *et al.* (1978) which uses empirically determined coefficients to weight the contributions of the various processes responsible for the flow field divergence.

While each of the above techniques has advantages, several shortcomings are apparent. In a number of cases the final form of the flow field is critically dependent on empirically chosen constants. Little guidance is given in the literature as to how some of these values can be developed for new regions. Another problem with some formulations is the initial estimates of horizontal velocities at region boundaries often force the nature of the interior flow solution. This can be a serious problem because, typically, few measurements are available

[1] Present affiliation: Advanced Technology Group, Dames & Moore, Los Angeles, CA 90024.

0021-8952/80/010098-11$06.75

at boundaries and so there can be large uncertainties associated with specification of the initial velocity field. From an operational point of view, none of the above techniques employ variable vertical grid spacing or terrain-following coordinate systems. The present paper introduces an algorithm which avoids most of the above limitations.

3. The basic algorithm

The present wind field generation algorithm consists of several basic steps. As a starting point, the region boundaries, vertical extent and basic grid cell sizes must be chosen. These are frequently dictated by the nature of the intended application. Once the grid has been established, the surface level velocity measurements and upper level wind and temperature data are interpolated to specify initial values for each computational point. The final step is to adjust the velocity field with the objective of minimizing anomalous divergence.

a. Surface wind field generation

The surface wind field is constructed from the measured data (converted to u and v components) by interpolation to a regular grid using inverse distance-squared weighting (Goodin *et al.*, 1979). A fixed radius of influence R is specified which indicates the distance beyond which the influence of a station's value is no longer felt. The influence of gross terrain features (e.g., mountain ranges) is accounted for by the use of barriers to flow during interpolation of the wind components. This procedure, however, does not incorporate the effects of local terrain features that have scales less than one grid cell length. Following the interpolation procedure, a local terrain-adjustment technique, which is similar to that of Anderson (1971, 1973), is used in the wind field calculation. This adjustment procedure involves solution of Poisson's equation

$$\nabla^2\phi = \psi(x,y), \tag{1}$$

where ϕ is a velocity potential and ψ a forcing function based on layer thickness and terrain gradients. An evaluation of solution techniques for Eq. (1) was made which included a Fourier series method (Dorr, 1970), the successive overrelaxation (SOR) method (Roache, 1972), and the alternating-direction-implicit (ADI) method (Peaceman and Rachford, 1955). Based on efficiency, programming and accuracy considerations, the ADI method was chosen.

As a test of the surface wind field calculation procedure, u and v component data from 63 wind stations in the South Coast Air Basin (SCAB) in California for 1600 PST 26 June 1974 were interpolated to a 100 × 50 square grid. The grid spacing was 3.2 km and the radius of influence used was 25 grid squares (a size large enough to include at least two data points). The measured data together with barriers to flow are shown in Fig. 1. Terrain data were obtained at 200 ft horizontal intervals from the National Cartographic Information Center, U.S. Geological Survey. From these data an average height for each 3.2 km square was then computed. Fig. 2 shows a three-dimensional plot of the terrain, the highest point of which is ~3000 m MSL.

The results of the interpolation and terrain adjustment procedure are displayed in Fig. 3. For most stations, the agreement between computed and measured values, both for magnitude and direction, is quite good. The mean error in magnitude is 0.7 m s^{-1} which is less than a 20% relative error, while the mean direction error is 11.5°; this is within the 22.5° sector to which the wind data are given. Among the stations operated by the South Coast Air Quality Management District (SCAQMD) (from which the most reliable data are obtained), the maximum error in magnitude occurs at Prado Park, a station which may be unduly influenced by localized channeling effects of Santa Ana Canyon. The computed magnitude is 5.1 m s^{-1}, and the measured value is 6.7 m s^{-1}. The largest error in magnitude occurring at any station is at CT33, a station operated by California Department of Transportation (CALTRANS). This station is in the vicinity of a convergence zone behind the Laguna Hills. The computed magnitude is 3.0 m s^{-1} and the measured magnitude is 5.8 m s^{-1}.

The maximum error in direction among the SCAQMD stations occurs at Reseda, where the computed and measured vector differ by 44°. At 1600 PST, Reseda appeared to be near the location of the so-called San Fernando convergence zone, where air from Ventura encounters air from the Los Angeles basin. The measured vector at Reseda probably represents an average of a local fluctuating velocity and is, therefore, less representative of a 3.2 km square for that hour. The largest error in direction occurring at any station is at Station CT35 where the difference in direction is 69°. The location of this station, which is downwind of the pass near Camarillo and adjacent to the Santa Monica Mountains, may not be representative of a larger area.

All the station measurements and calculated results for the sample problem are displayed in Figs. 4a and 4b. Two conclusions are apparent from an inspection of the scatter plots. The first is that there is little or no systematic bias in either the magnitude or direction of the calculated results. The second is that there is a high degree of correlation between observed and predicted, $r = 0.86$ for the wind magnitudes and $r = 0.90$ for direction.

b. Interpolation of the upper level wind and temperature data

Before the transport of urban pollutants can be adequately modeled some knowledge of the vertical

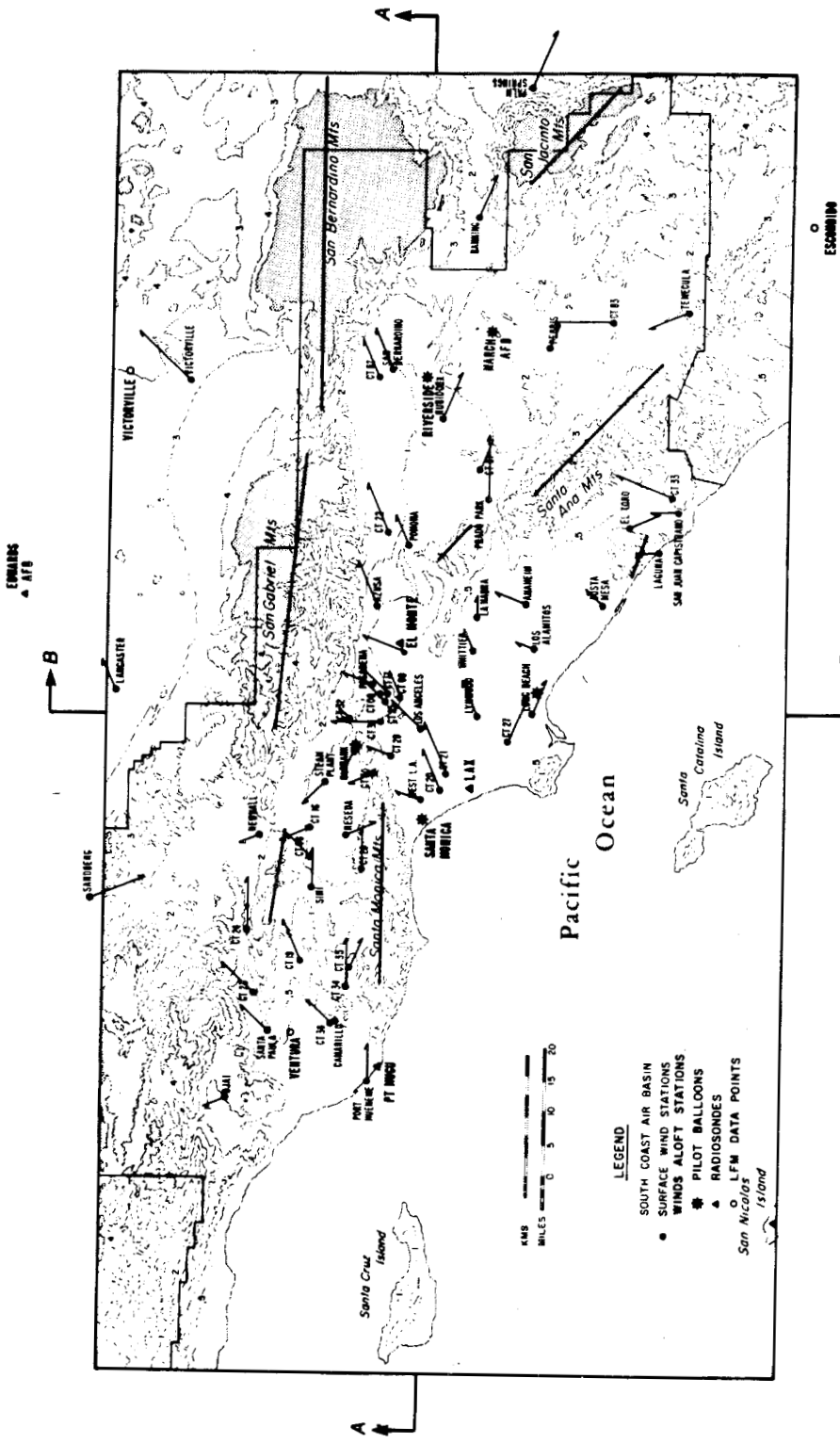

FIG. 1. Measured hourly-averaged wind data for 1600 PST 26 June 1974. Barriers to flow are indicated by solid lines. The largest measured velocity is 7 m s^{-1}.

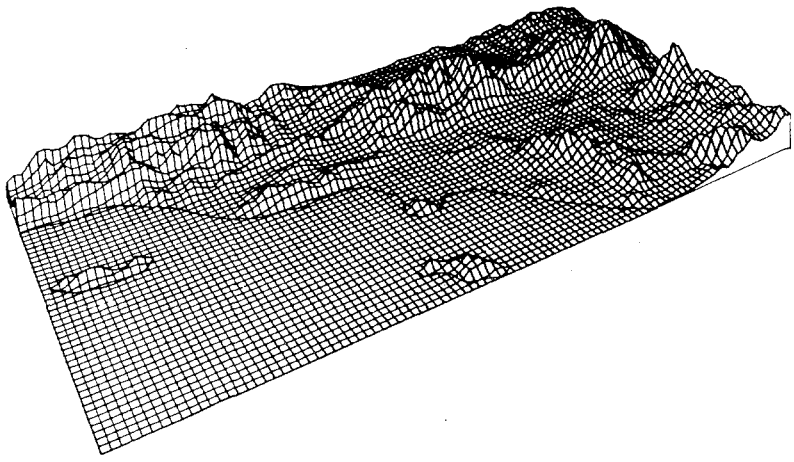

FIG. 2. Topography of Los Angeles basin viewed from the southwest.

temperature structure and the three-dimensional flow field is required. These quantities are known with much less precision than the surface quantities since fewer measurements are customarily available. As an example of available data in the Los Angeles area, Fig. 1 shows the measurement stations for upper level data in the SCAB. This data set includes stations in operation: Los Angeles International Airport (LAX), Pt. Mugu, San Nicolas Island, El Monte, Riverside and Edwards Air Force Base (off grid); sites with data calculated for the days of interest using the Limited-Area Fine Mesh Model (Gerrity, 1976): Victorville, Escondido, Ventura; and stations which have recorded upper level data in the past, providing "typical" data: Long Beach, Burbank, Santa Monica and March Air Force Base. An average of two measurements per day are available at each station except for El Monte where an acoustic sounder records the depth of the mixed layer continuously.

The approach taken for spatial interpolation of mixing depth and upper level wind data is slightly different from that used for the surface quantities. Imprecision in the measured data makes a highly accurate interpolation procedure unnecessary; as a result r^{-1} weighting was chosen since it produces a smoother field than r^{-2} weighting. In performing the interpolation of mixing depth, the height above sea level is first computed at all grid points. The height of the terrain surface is then subtracted to give mixing depth above the surface. This procedure is used because the height of the mixed layer above sea level tends to be a smooth surface while the terrain changes more abruptly. Contours of mixing depth tend to follow the coastline since the degree of heating of air moving inland depends mainly on the distance travelled over land. The mixing depth data for 1600 PST 26 June 1974 were interpolated using the r^{-1} procedure and then smoothed using a simple five-point filter in which the new value at a given point is the average of the value at the point itself and the values at the four adjacent points,

$$h_{ij}^{n+1} = 0.20(h_{ij}^{n} + h_{i-1j}^{n} + h_{i-1j}^{n} + h_{ij+1}^{n} + h_{ij-1}^{n}). \quad (2)$$

The maximum depth was set at 1100 m since a depth greater than this is generally assumed to be unlimited. A three-dimensional plot of mixing depth above sea level is shown in Fig. 5. The mixing depth follows the contours of the terrain at high elevations since negative mixing heights cannot occur.

In order to follow pollutants as they move above the mixed layer, the top of the region was set at a high level (above the mixed layer). The top of the mixed layer was allowed to fluctuate both temporally and spatially within this region. Its only real purpose is a reference height above which vertical diffusion is very small. In addition, to eliminate the difficulty in specifying vertical velocity boundary conditions, a coordinate system which follows the terrain surface was chosen rather than sea level based coordinates. The transformation from sea level to terrain-following coordinates produces a new vertical velocity, W, i.e.,

$$W = w - u\left(\frac{\partial h}{\partial x} + \rho\frac{\partial \Delta H}{\partial x}\right) - v\left(\frac{\partial h}{\partial y} + \rho\frac{\partial \Delta H}{\partial y}\right) - \rho\frac{\partial \Delta H}{\partial t}, \quad (3)$$

where $\Delta H(x,y,t) = H(x,y,t) - h(x,y)$ is the height of the top of the region above the terrain surface, and ρ is the new vertical coordinate ($0 \leq \rho \leq 1$).

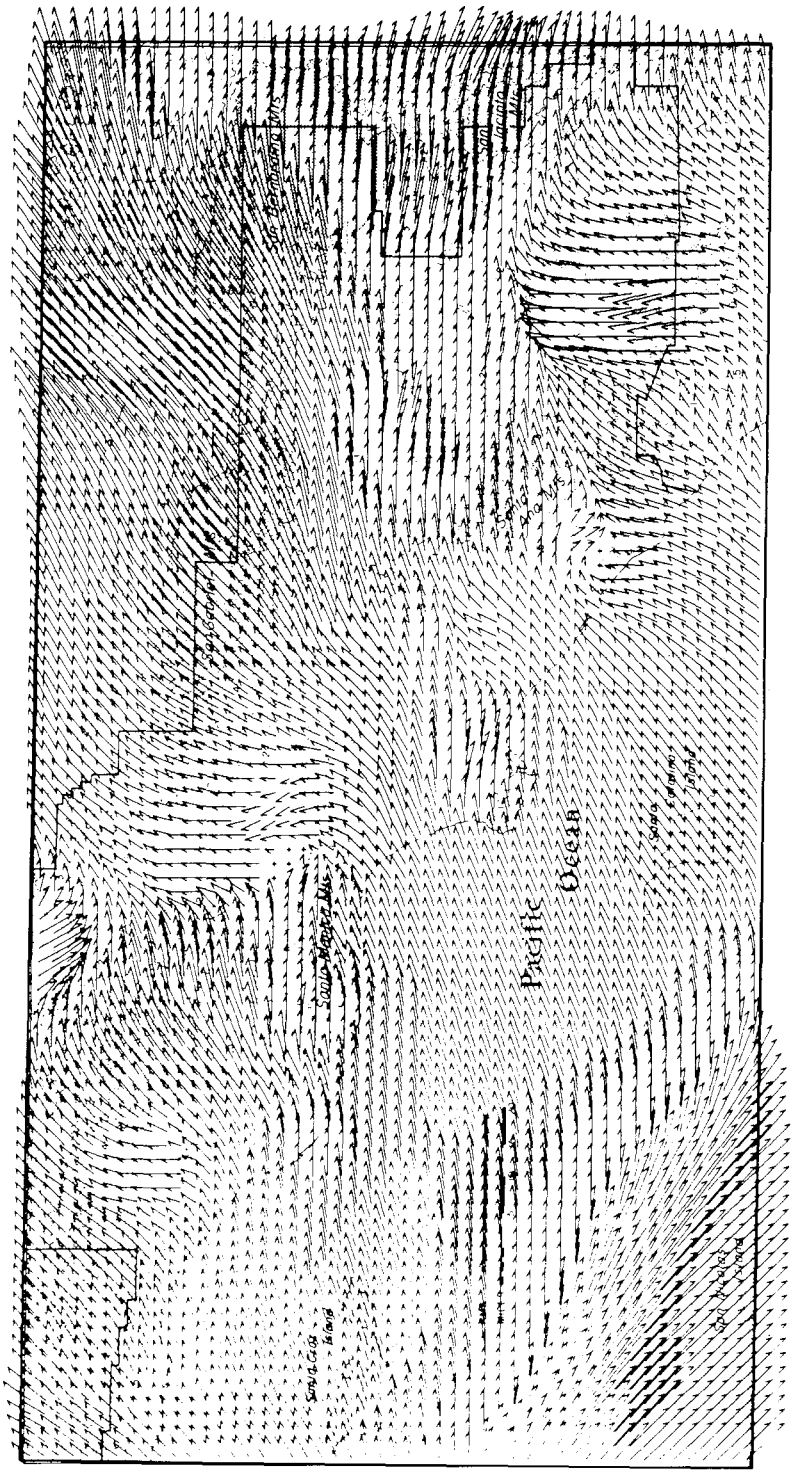

FIG. 3. Flow field in the surface layer following interpolation and adjustment for terrain effects.

Fig. 6a shows the general case where ΔH is a function of space as well as time. In order to eliminate complications introduced into the advection scheme by nonparallelopiped grid volumes in x, y, z space, ΔH is used for normalization. Figs. 6b and 6c show the transformation from the x, y, z space to x, y, ρ space.

In the new coordinate system, the continuity equation is

$$\frac{\partial W}{\partial \rho} + \frac{\partial (u \Delta H)}{\partial x} + \frac{\partial (v \Delta H)}{\partial y} = 0. \quad (4)$$

Given the horizontal velocities at each vertical level from r^{-1} interpolation of the measured data, W can be calculated at each level using Eq. (4). Unfortunately, this simple solution produces unrealistically large values of W at the top of the region since all residual divergence in the field is propagated upward. Therefore, a procedure is required that will reduce the divergence in the flow field to an acceptable level while maintaining small upper level vertical velocities.

c. *New divergence reduction procedure*

Once the surface level flow field has been established and the upper level wind data have been interpolated to the three-dimensional grid, the next step is to reduce the divergence in the total flow field. The proposed procedure involves three steps:

1) The divergence in each of the interpolated u and v fields at each vertical level above the lowest layer is first reduced using a slightly modified version of the simple five-point filter discussed above. The equation for smoothing is

$$u_{ij}^{n+1} = 0.20(u_{ij}^{n} + u_{i-1j}^{n} + u_{i-1j} + u_{ij-1}^{n} + u_{ij-1}^{n})(1 - \alpha_k) + \alpha_k u_{ij}^{n}, \quad (5)$$

where α_k is a parameter which allows the user to keep the measured velocity at station k fixed ($\alpha_k = 1$) or keep only some of its original influence ($\alpha_k < 1$). This parameter is zero at all non-measuring station points. This first step is designed to reduce as much of the anomalous divergence as possible. The number of passes through the smoothing step is related to the relative atmospheric stability at that level and will be determined empirically. A relatively unstable (generally near ground level) layer requires few iterations since less of the divergence present is anomalous, while a more stable upper layer must be smoothed more times. The more smoothing a field of values is subjected to, the more initial anomalous divergence is dissipated horizontally within that layer, i.e., the more the vertical velocity above that layer (which will be computed from the divergence within the layer) will be suppressed.

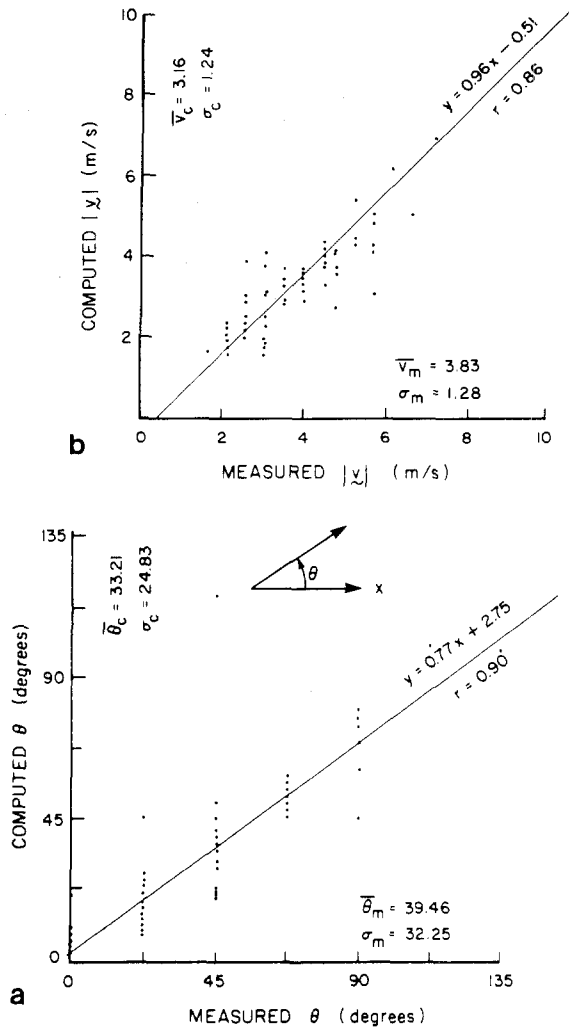

FIG. 4. Comparison of field observations against calculated results: (a) Wind direction, (b) wind magnitude.

2) Following this initial smoothing step, the vertical velocity above each layer is computed from the divergence within that layer. The layers are temporarily disconnected from each other during this calculation so that the calculated vertical velocity above a layer depends only upon the divergence within that layer. This prevents velocities at the top of the region from becoming unrealistically large. These vertical velocities will be held fixed throughout the rest of the divergence reduction procedure.

3) The final refinement reduces the remaining divergence which exists within each layer by application of a two-dimensional technique to each layer similar to that of Liu and Goodin (1976). The equation solved is (with ΔH = constant)

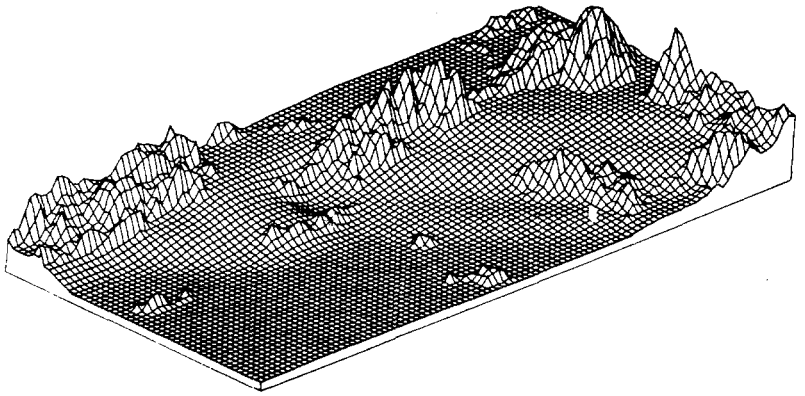

FIG. 5. Mixing heights above sea level computed from measured data for 1600 PST 26 June 1974.

$$\frac{\partial W}{\partial \rho} + \Delta H\left(\frac{\partial u}{\partial x} + \frac{\partial v}{\partial y}\right) = D_R(x,y,\rho), \qquad (6)$$

where $D_R(x,y,\rho)$ is a measure of the remaining divergence. At grid point (i,j,k), Eq. (6) can be written as

$$D^{n+1}_{ijk} = \frac{W_{i,j,k+1/2} - W_{i,j,k-1/2}}{\Delta\rho} + \Delta H\left[\frac{u^{n+1}_{i+1/2,j,k} - u^{n+1}_{i-1/2,j,k}}{\Delta x} + \frac{v^{n+1}_{i,j+1/2,k} - v^{n+1}_{i,j-1/2,k}}{\Delta y}\right], \qquad (7)$$

where the superscript $n + 1$ indicates the values are computed for the $(n + 1)$st iteration, and the subscript R is dropped from D_R for convenience.

To remove the divergence at the point (i,j,k), adjustments are made to the u values at $(i + \frac{1}{2}, j, k)$ and $(i - \frac{1}{2}, j, k)$ and the v values at $(i, j + \frac{1}{2}, k)$ and $(i, j - \frac{1}{2}, k)$ in order that the divergence is exactly zero at (i,j,k). Since this procedure will add additional divergence to surrounding points, the whole grid must be scanned iteratively. The adjustments to the velocity components are

$$\left.\begin{aligned} u^{n+1}_{i-1\,2,j,k} &= u^{n}_{i-1\,2,j,k} + u_T \\ u^{n+1}_{i-1\,2,j,k} &= u^{n}_{i-1\,2,j,k} - u_T \\ v^{n+1}_{i,j+1\,2,k} &= v^{n}_{i,j-1\,2,k} + v_T \\ v^{n+1}_{i,i-1\,2,k} &= v^{n}_{i,j-1\,2,k} - v_T \end{aligned}\right\}, \qquad (8)$$

where u_T and v_T are the adjustment velocities. These velocities are computed by substitution in Eq. (7),

$$0 = D^{n}_{ijk} + \Delta H\left(\frac{2u_T}{\Delta x} + \frac{2v_T}{\Delta y}\right). \qquad (9)$$

Assuming that $\Delta y = \Delta x$ and that the velocity adjustments are equally weighted in each direction, Eq. (9) can be solved to give

$$u_T = \frac{-D^{n}_{ijk}\Delta x}{4\Delta H}. \qquad (10)$$

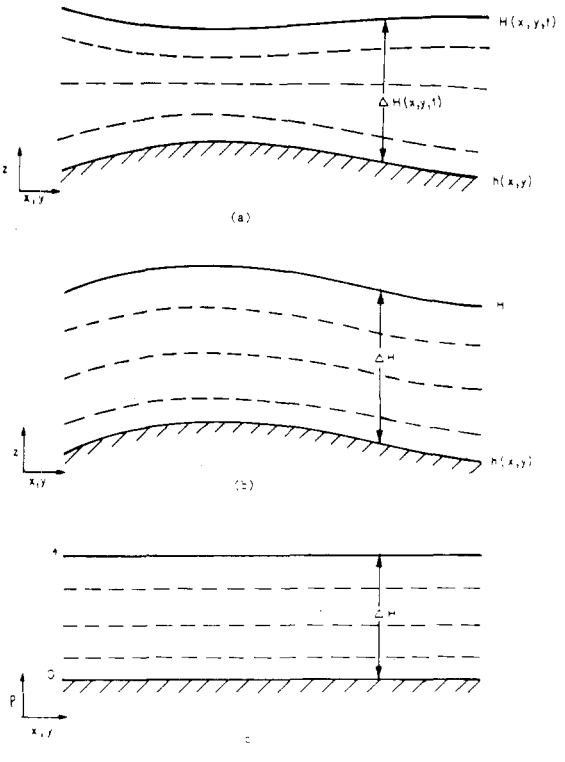

FIG. 6. A terrain-following coordinate system: (a) general case $H = H(x,y,t)$; (b) H is a constant height above the terrain; (c) transformed x, y, ρ coordinate system.

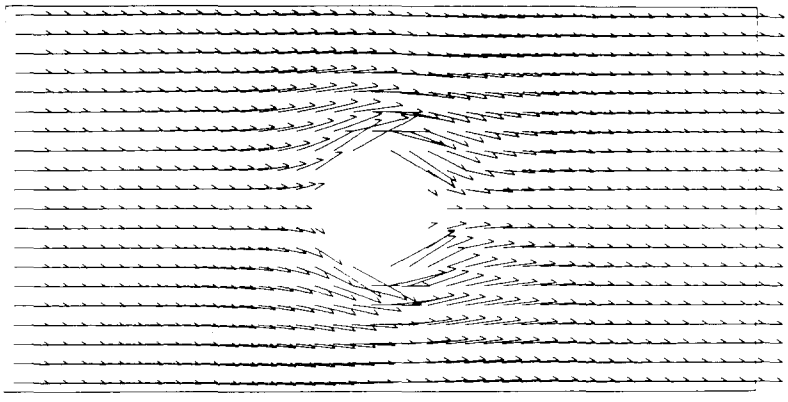

FIG. 7. Idealized three-dimensional flow field—initial state in layer 1.

Thus, the complete three-dimensional divergence reduction procedure consists of 1) smoothing at each level using an empirically determined number of smoothing passes based on local atmospheric stability, 2) followed by solution of Eq. (7) at each level for $W_{i,j,k+1/2}$, temporarily assuming $W_{i,j,k+1/2}$ is zero; and 3) Eqs. (7), (10) and (6) are then solved repeatedly using the calculated values for W until the maximum divergence is reduced to an acceptable level, i.e., the magnitude of the divergence should be less than the local vertical velocity and less than the estimated errors in the horizontal velocity components.

The interaction between the flow field and the change in depth of the mixed layer has not been accounted for in the above procedure because of a lack of upper air data, i.e., mixing depth and vertical velocity are never measured simultaneously, and because attempts to tie the vertical cell heights to the mixing depth resulted in large horizontal wind velocities as the mixing depth approached zero.

4. Test of present divergence reduction procedure

A hypothetical flow field was constructed to test the divergence reduction procedure just discussed and estimate the approximate number of smoothing passes corresponding to each Pasquill stability class. The grid chosen was 40 × 20 × 2 points. The upper layer contained uniform horizontal flow at 5 m s^{-1}. In the lower layer the flow consisted of potential flow around a circular disk located at the center of the grid. Each layer was of equal thickness with a horizontal grid spacing of 2 km. Fig. 7 shows the initial flow pattern in the lower layer.

The test consisted of reducing the divergence in the flow following removal of the disk. First, the smoothing step reduced the gross divergence in the lower layer (the upper layer required no smoothing). The vertical velocity between the layers was then calculated from the divergence in the lower layer using Eq. (10), temporarily assuming zero velocity at the bottom of that layer. (The vertical velocity above layer 2 was identically zero since there was no divergence present initially.) Finally, the refined, iterative divergence-reduction step was performed within each layer as described in Section 3c.

The results for number of smoothing passes ranging from 1 to 40 are shown in Table 1. As expected, the final divergence, as well as maximum W, is a strong function of number of initial smoothing passes. The iterative divergence reduction procedure then reduces the remaining divergence by a factor of 20–40 after 100 iterations. A maximum vertical velocity of 0.28 m s^{-1} approximately corresponds to vertical velocities observed within the mixed layer during the daytime hours in the Los Angeles Basin (Angell *et al.*, 1972), while typical subsidence motion within the inversion is on the order of 0.02 m s^{-1}.

The set of upper air data collected in Los Angeles on 1600 PST 26 June 1974 was then used to test the present procedure. The data measurement locations are indicated in Fig. 1. Five vertical levels were

TABLE 1. Results of the present divergence reduction procedure on an idealized data set.

Number of smoothing passes	Maximum divergence in layer 2: Following initial smoothing ($\times 10^6$ s^{-1})	Maximum divergence in layer 2: Following 100 iterations ($\times 10^6$ s^{-1})	Maximum W above layer 1 (m s^{-1})
1	350.0	8.3	0.28
5	41.7	1.1	0.04
10	16.7	0.3	0.01
20	11.1	0.3	0.01
40	5.5	0.3	0.004

TABLE 2. Results of present divergence reduction procedure on wind data from 1600 PST 26 June 1974.

Layer	Thickness of layer (m)	Number of smoothing passes during first step	rms divergence		
			After initial smoothing ($\times 10^6$ s^{-1})	After 100 iterations ($\times 10^6$ s^{-1})	After 200 iterations ($\times 10^6$ s^{-1})
1	50	0	151	149	148
2	150	5	27	20	20
3	300	10	27	17	14
4	550	20	25	14	11
5	450	20	51	28	20

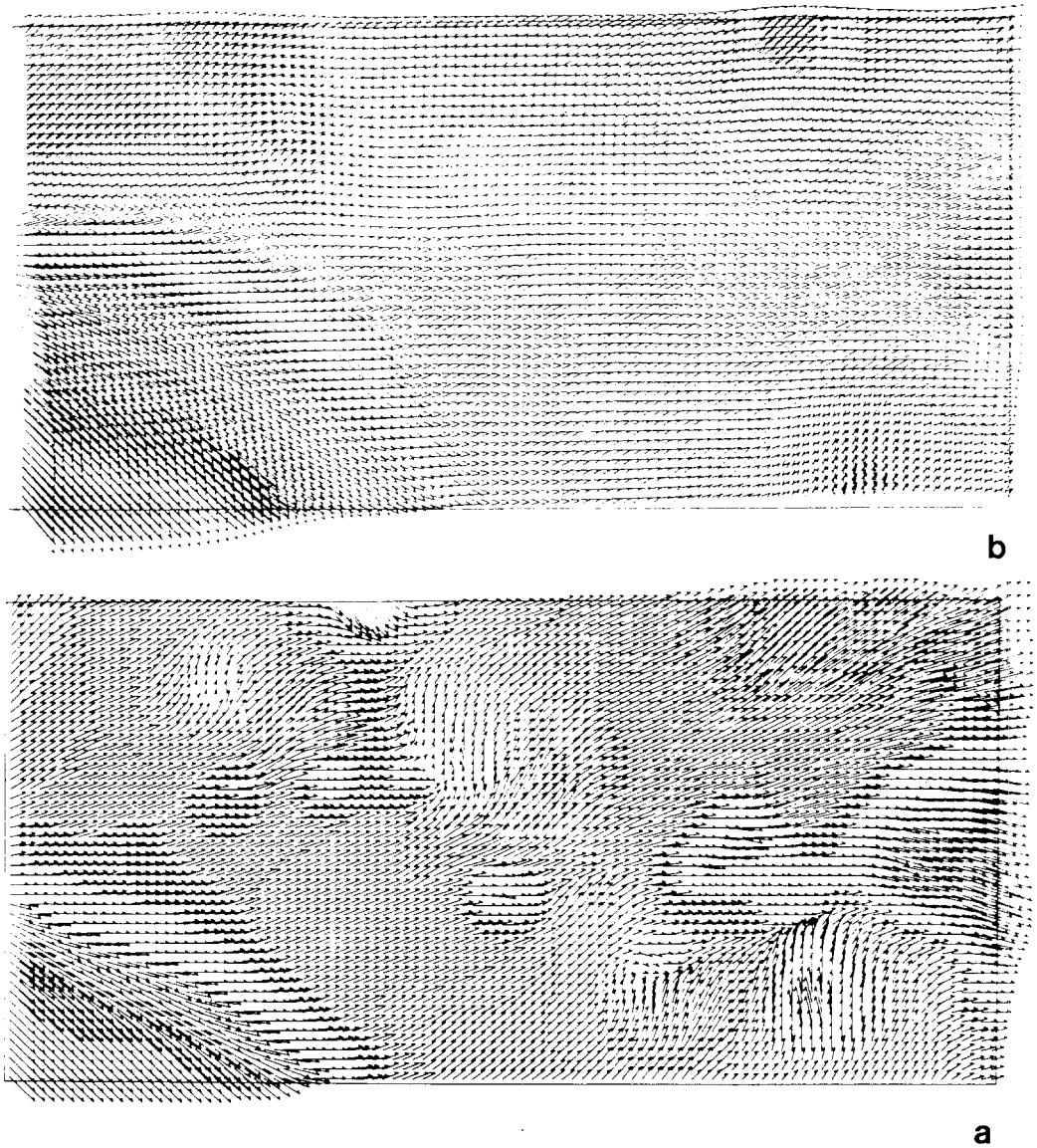

FIG. 8. (a) Horizontal flow field in layer 2 (550 ft above terrain) at 1600 PST 26 June 1974 and (b) horizontal flow field in layer 3 (1200 ft above terrain) at 1600 PST 26 June 1974.

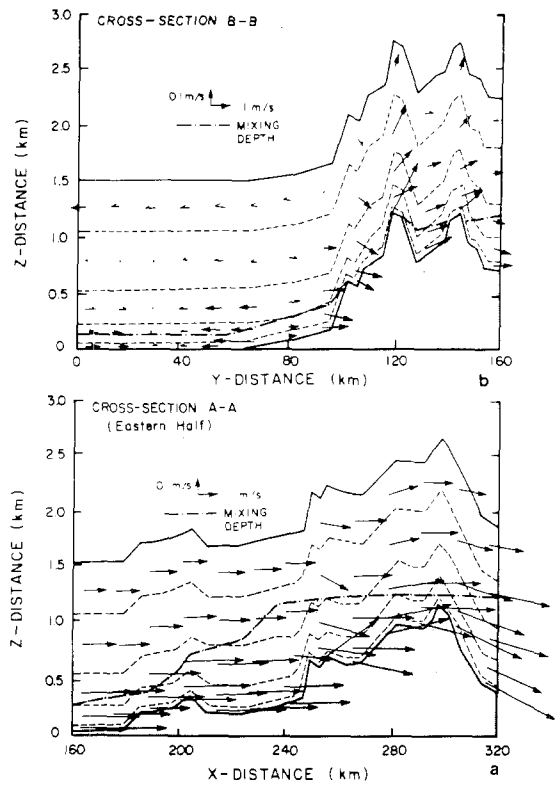

FIG. 9. Vertical velocity cross sections corresponding to locations indicated in Fig. 1. (Note exaggeration of vertical scale.) (a) Eastern half of cross section AA, (b) cross section BB.

chosen with thicknesses of 50, 150, 300, 550 and 450 m, respectively. The lowest layer, of depth 50 m, was the surface layer, the flow pattern of which had been calculated previously from the surface data network. The interpolated u and v fields in layers 2–5 were smoothed 5, 10, 20 and 20 times, respectively. These numbers were obtained empirically from the calculation of the flow around the disk and correspond approximately to Pasquill stability classes B, D and E.

The results of the calculation procedure are displayed in Table 2 and Figs. 8a, 8b, 9a and 9b. The algorithm reduced the divergence to <0.001 s^{-1} in all layers; in the vicinity of downtown Los Angeles, an area of relatively flat terrain, the divergence is of order 10^{-5} s^{-1}. The largest divergence in each layer occurs over mountainous regions, especially the San Jacinto and San Gabriel mountains. In these areas, upper air data are nonexistent, so the interpolation procedure has generated a smoothed flow field which does not accurately reflect the influence of the steep terrain in these regions. Most of the divergence was reduced during the initial smoothing step. The last two columns in Table 2 indicate that 100 iterations were sufficient to refine the divergence reduction during the second step. Very little additional reduction was obtained after 200 iterations. The algorithm has been extensively tested against analytic problems, the results of field releases of SF_6 and has been used to generate 72 different hours of wind fields for use in the modeling study by McRae *et al.* (1980).

TABLE 3. Comparison of attributes of three-dimensional divergence reduction procedures.

Attribute	Present technique	MATHEW
Coordinate system	Terrain-following coordinates	Coordinate system parallel to sea level
Treatment of flow over complex terrain	Barriers to flow are used during interpolation procedure. Surface layer flow is adjusted using $\nabla^2\phi = D$, where D is magnitude of vertical perturbation.	Obstacle cells are used to represent terrain. They are treated as no-flow-through boundaries.
Interpolation procedure	$1/r^2$ weighting of station data at surface. $1/r$ weighting at each level above surface.	$1/r^2$ weighting at surface. Upper level values are obtained from synoptic analysis.
Treatment of horizontal boundary conditions during divergence reduction procedure	Normal component of velocity at boundary is adjusted according to value at adjacent interior point. (Same procedure as at all other interior points.)	Program accepts $\partial\lambda/\partial n = 0$ or $\lambda = 0$ as boundary conditions. Derivative is approximated by three-point difference.
Treatment of atmospheric stability	Number of smoothing passes through interpolated field at each vertical level is related to the stability at that level. Amount of smoothing required for a given stability class is obtained empirically.	Gaussian precision moduli, α_1,α_2, which are functions of measurement errors must be determined empirically.
Variable vertical grid spacing	Yes	No
Computer time required	25 000 points (100 × 50 × 5) Divergence → 10^{-4} s^{-1} 5 min on IBM 370	23 000 points (25 × 33 × 28) Divergence → 10^{-12} s^{-1} 2–5 min on CDC 7600 (20–50 min on IBM 370)

5. Comparison with previous divergence reduction procedures

Table 3 presents a comparison of the proposed method with MATHEW. Each procedure uses an inverse-distance weighting procedure to interpolate the measured values. MATHEW, however, relies on a synoptic analysis to determine the horizontal velocities at the upper boundary. If a vertical profile of wind speed and direction is not available, a linear variation is assumed between the surface layer winds and the upper boundary.

The use of obstacle cells in MATHEW for flow over complex terrain affects the computer time required for solution, since the computer time increases with the complexity of the terrain. The use of terrain-following coordinates in the present technique avoids this difficulty. A major advantage of the present technique is that it allows the boundary values to adjust in response to the interior flow. Each of the techniques requires an empirically determined parameter. Its value is calculated based on atmospheric stability. The choice of the value to be used in each procedure must be determined by the experience of the user.

6. Conclusions

A new technique for constructing a three-dimensional, urban-scale, mass-consistent wind field has been introduced. The interpolation method relies on measured upper air data (when available) for constructing the flow field. If little or no upper air data are available, the user may construct velocity profiles using some assumed profile such as a power law for input to the program. The problem of large vertical velocity at the top of the region has been avoided by reducing divergence significantly at the lower levels rather than allowing it to propagate out of the top of the region. Variable vertical grid spacing is also permitted allowing the user greater flexibility in the concentration calculations. The present technique is easy to implement, computationally efficient, and offers promise as an attractive method for routine meteorological applications.

Acknowledgments. Portions of this work were supported by the California Air Resources Board under Contract A5-046-87, and by Institutional Grant EY-76-G-03-1305 from the Department of Energy.

REFERENCES

Anderson, G. E., 1971: Mesoscale influences on wind fields. *J. Appl. Meteor.*, **10**, 377–386.

——, 1973: A mesoscale windfield analysis of the Los Angeles Basin. EPA-650/4-73-001, The Center for Environment and Man, Inc., Hartford, Conn., 56 pp.

Angell, J. K., D. H. Pack, L. Machta, C. R. Dickson and W. H. Hoecker, 1972: Three-dimensional air trajectories determined from tetroon flights in the planetary boundary layer in the Los Angeles Basin. *J. Appl. Meteor.*, **11**, 451–471.

Dickerson, M. H., 1978: MASCON—A mass consistent atmospheric flux model for regions with complex terrain. *J. Appl. Meteor.*, **17**, 241–253.

Dorr, F. W., 1970: The direct solution of the discrete Poisson equation on a rectangle. *SIAM Rev.*, **12**, 248–263.

Endlich, R. M., 1967: An iterative method for altering the kinematic properties of wind field. *J. Appl. Meteor.*, **6**, 837–844.

Fankhauser, J. C., 1974: The derivation of consistent fields of wind and geopotential height from mesoscale rawinsonde data. *J. Appl. Meteor.*, **13**, 637–646.

Gerrity, J. F., Jr., 1977: The LFM model: A documentation. NOAA Tech. Memo. NWS NMC 60, National Meteorological Center, 66 pp.

Goodin, W. R., G. J. McRae and J. H. Seinfeld, 1979: A comparison of interpolation methods for sparse data: Application to wind and concentration fields. *J. Appl. Meteor.*, **18**, 761–771.

Liu, C. Y., and W. R. Goodin, 1976: An iterative algorithm for objective wind field analysis. *Mon. Wea. Rev.*, **104**, 784–792.

MacCracken, M. C., D. J. Wuebbles, J. J. Walton, W. H. Duewer and K. E. Grant, 1978: The Livermore regional air quality model: I. Concept and development. *J. Appl. Meteor.*, **17**, 254–272.

McRae, G. J., W. R. Goodin and J. H. Seinfeld, 1980. Development of a second generation mathematical model of photochemical air pollution. Final Report to the California Air Resources Board under Contract A5-046-87.

Peaceman, D. W., and H. H. Rachford, Jr., 1955: The numerical solution of parabolic and elliptic differential equations. *J. SIAM*, **3**, 28–41.

Roache, P. J., 1972: *Computational Fluid Dynamics*. Hermosa Publ., 434 pp.

Sasaki, Y., 1958: An objective analysis based on the variational method. *J. Meteor. Soc. Japan*, **36**, 77–88.

——, 1970: Some basic formalisms in numerical variational analysis. *Mon. Wea. Rev.*, **98**, 875–898.

Sherman, C. A., 1978: A mass-consistent model for wind fields over complex terrain. *J. Appl. Meteor.*, **17**, 312–319.

Yocke, M. A., M. K. Liu and J. L. McElroy, 1978: The development of a three-dimensional wind model for complex terrain. *Proc. Joint Conf. Application of Air Pollution Meteorology*, Salt Lake City, Amer. Meteor. Soc., 209–214.

3.8 Extensions of the Wind Field Generation Procedure to Incorporate the Effects of Surface Roughness

In situations where little or no upper air wind data are available it is often necessary to use the surface measurements to estimate vertical velocity profiles. This section summarizes the procedure of Goodin and McRae (1980) which incorporates the influence of local surface roughness and stability in a determination of the vertical variation of the wind speed.

A variety of methods have been used, with varying success, for calculating the wind profile in the lowest layers of the atmosphere ($z < 100$ m). The profiles are either represented by a power-law expression of the form,

$$u(z) = u(z_r) \left(\frac{z}{z_r}\right)^{\alpha} \tag{3.26}$$

or alternatively,

$$u(z) = \frac{u_*}{k(1-\beta)} \left[\left(\frac{z}{z_o}\right)^{1-\beta} - 1\right] \tag{3.27}$$

where the parameters α and β must be determined empirically. Tables of values for these parameters as a function of surface roughness and/or stability have been developed by Deacon (1949), Davenport (1960), Touma (1977), and Irwin (1979). The values for α range from 0.05 to 0.60 increasing with stability and roughness. The parameter β ranges from approximately 0.8 to 1.2 increasing with decreasing stability. The familiar logarithmic profile can be obtained from (3.27) by using a

series expansion and setting $\zeta = 1$ i.e.

$$u(z) = \frac{u_*}{k} \ln \left(\frac{z}{z_o}\right) \tag{3.28}$$

Equation (3.28) is only valid for near neutral conditions. Given the wide variability in α and ζ there is a clear need for a direct approach that incorporates more recent boundary layer measurements. The technique adopted in this study is to use Monin-Obukhov similarity solution in the surface layer. The integral form of the velocity gradient is given by

$$u(z) = u(z_r) + \frac{u_*}{k} \int_{z_r}^{z} \phi\left(\frac{z}{L}\right) \frac{dz}{z} \tag{3.29}$$

where $\phi(z/L)$ is a universal function of atmospheric stability, the Monin-Obukhov length and the height above the ground. The functional form of these expressions is discussed in considerable detail in the following chapter. Given the ϕ functions, (3.29) can be integrated from a reference height z_r to some other elevation $z < 2|L|$.

Above the surface layer ($z>L$) a logarithmic profile is used for stable conditions (Webb, 1970). The procedure involves matching the similarity solution at $z=L$ so that the gradient is continuous. The resulting equation is

$$u(z) = \frac{5.7u_*}{k} \ln\left(\frac{z}{L}\right) + u_L \; ; \; \frac{z}{L} > 0 \tag{3.30}$$

where u_L is the velocity at $z = L$ computed from (3.29). Above the mixed layer the velocity is assumed to be constant with height. Similarly, for unstable conditions a logarithmic profile is matched to the

similarity solution at z = L to give

$$u(z) = \frac{0.5\ u_*}{k}\ \ln(-\frac{z}{L}) + u_L;\ \frac{z}{L} < 0 \qquad (3.31)$$

Under neutral conditions the wind profile appears to follow the logarithmic law to heights greater than the scale height (Panofsky, 1973). Therefore, the simple logarithmic law is used up to the top of the mixed layer here.

In order to evaluate the performance of the proposed algorithm wind profile data obtained from a 1,420 foot (430 m) tower and reported by Thuillier and Lappe (1964) were used. In that study a total of 274 profiles representing four observation times were used in the analysis. Each profile was determined from thirty minute averages of the wind speed at 11 vertical levels. The data were normalized by means of u_* as well as a reference height velocity, $u(z_r)$, computed at the lowest observation level (9.15 m). Profiles for those wind speeds were grouped according to shape characteristics. For each group, an average profile was computed and the vertical variation of mean wind speed was compared to a logarithmic or power law profile form. The surface roughness, z_o, height at the site was estimated to be 3 cm. The reference velocity, reference height and roughness height from three typical profiles presented in the above mentioned work were used to construct wind profiles using the present algorithm.

Figures 3.8 - 3.10 show selected data from Thuillier and Lappe (1964) together with the profiles computed using the present algorithm.

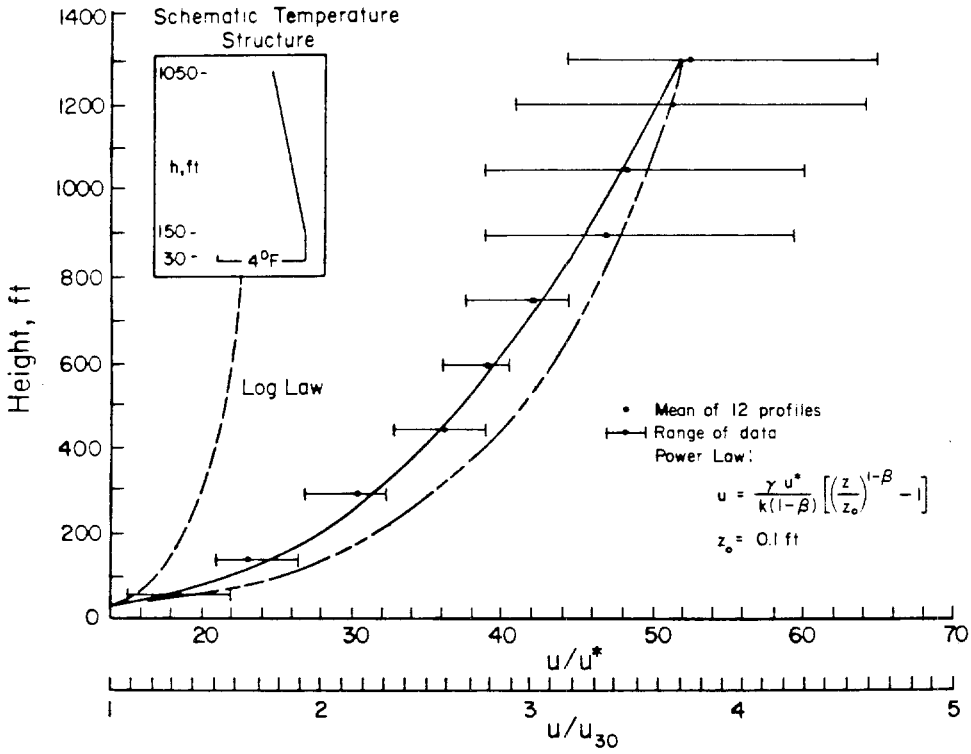

FIGURE 3.8

Plot of Measured Data and Calculated Profiles for E Stability from Thuillier and Lappe (1964) (solid lines) as Well as Results Calculated by Present Algorithm (dashed lines).

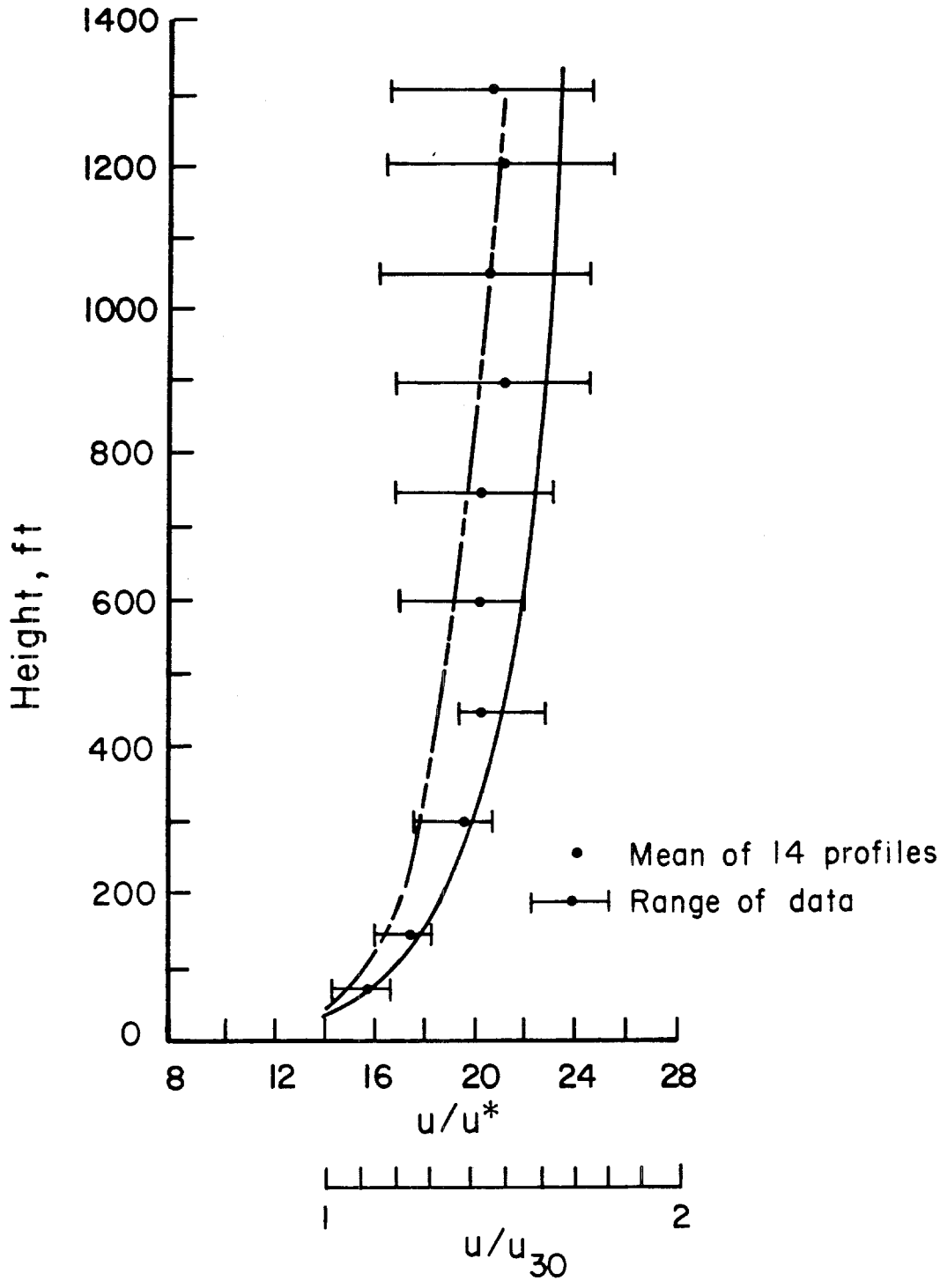

FIGURE 3.9

Plot of Measured Data and Calculated Profiles for C-D Stability from Thuillier and Lappe (1964) as Well as Results Calculated by Present Algorithm (dashed line).

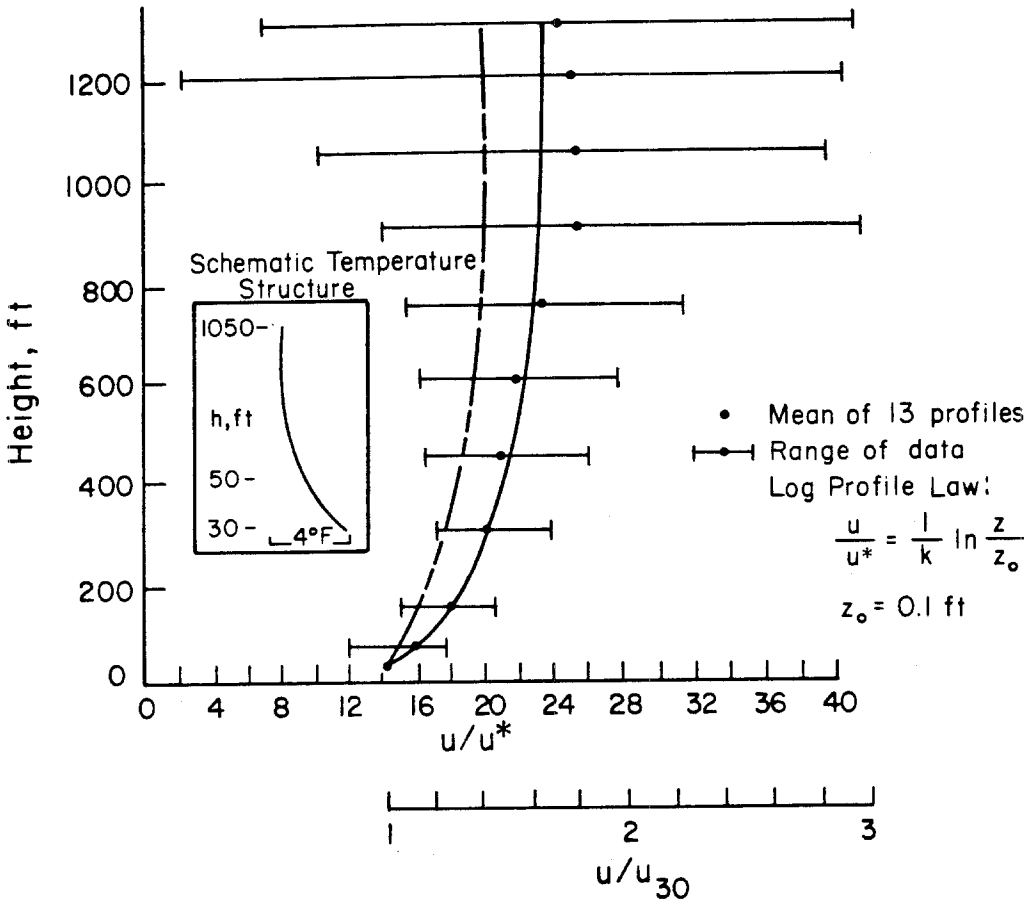

FIGURE 3.10

Plot of Measured Data and Calculated Profiles for B-C Stability from Thuillier and Lappe (1964) (solid lines) as Well as Results Calculated by Present Algorithm (dashed lines).

Generally, the wind profiles computed using the present algorithm fit the data as well as the profiles computed by the authors. A major advantage of the present algorithm is the lack of dependence on parameters such as α or β that were adjusted by Thuillier and Lappe to obtain a good fit. The intent of the present algorithm was to develop procedures for estimating the vertical variation in the absence of any upper air data. Because of the complexity of inversions and wind shear effects aloft, surface data cannot be expected to be indicative of flow aloft at all times.

3.9 Solution of the Poisson Equation

An important element of the wind field generation procedure involves repeated solution of the Poisson equation and its associated Dirichlet boundary conditions over the two-dimensional rectangle R.

$$\nabla^2 f = g \qquad x \varepsilon R \tag{3.32}$$

$$f = 0 \qquad x \varepsilon \partial\Omega \tag{3.33}$$

In (3.32) the function g(x,y) represents the vertical component of the flow field induced by the terrain and f(x,y) is the velocity potential which is used to adjust the initial estimates of the horizontal velocities (u_o, v_o) to account for the topographic effect. Given f(x,y) the variations in the initial field are given by

$$u = u_o + \frac{\partial f}{\partial x} \tag{3.34}$$

$$v = v_o + \frac{\partial f}{\partial x} \tag{3.35}$$

Because solution of the Poisson equation forms part of a procedure, which is repeated many times, it is important to minimize the computational time for an individual step. This section is devoted to a brief evaluation of three different numerical techniques and the selection of one which is suitable for inclusion in the wind field generation program. The methods to be discussed are: successive over relaxation (SOR), Fourier Series and the alternating direction implicit (ADI) methods. These and many other highly efficient techniques are evaluated in the reviews by: Dorr (1970), Buzbee et al. (1970), Roache

(1976), Swarztrauber (1977) and Temperton (1979)

The basis of most approaches to solving the field problem is to approximate the system (3.32) with the second-order finite difference approximation

$$\frac{f_{i-1,j} - 2f_{i,j} + f_{i+1,j}}{(\Delta x)^2} + \frac{f_{i,j-1} - 2f_{i,j} + f_{i,j+1}}{(\Delta y)^2} = g_{i,j} \qquad (3.36)$$

$$2 < i < n-1, \quad 2 < j < m-1$$

and the boundary conditions

$$\begin{aligned} f_{0,j} &= 0 \qquad f_{n,j} = 0 \qquad 1 < j < m \\ f_{i,0} &= 0 \qquad f_{i,m} = 0 \qquad 1 < i < n \end{aligned} \qquad (3.37)$$

If $\Delta x = \Delta y$ these difference expressions can be expressed in the more compact block tridiagonal form

$$[M]\underline{f} = \underline{y} \qquad (3.38)$$

where the matrix M, of dimension (n-2)x(m-2), is given by

$$M = \begin{bmatrix} D & I & & & \\ I & D & \cdot & & \\ & \cdot & \cdot & \cdot & \\ & & \cdot & \cdot & I \\ & & & I & D \end{bmatrix} \qquad (3.39)$$

and is composed of elements of the form

$$D = \begin{bmatrix} -4 & 1 & & & \\ 1 & -4 & . & & \\ & . & . & . & \\ & & . & . & 1 \\ & & & 1 & -4 \end{bmatrix} \tag{3.40}$$

In (3.39) the identity matrices I are of order (n-2). The use of higher order finite difference approximations, as described for example in Roache (1976) and Wurtele and Clark (1965), results in more complex matrix equations. Since the system of equations is usually of high dimension the computational cost of obtaining the solution, without exploiting the special structure, can be prohibitive.

One of the simplest approaches to solving the Poisson problem is to use a point iterative technique called successive over relaxation (Frankel, 1950; Young, 1954). If k is the iteration number then the k+1 iterate can be written in the form

$$f_{ij}^{k+1} = (1-w)f_{ij}^{k} + \frac{w}{2(1+\beta^2)} [f_{i+1j}^{k} + f_{i-ij}^{k} + \beta^2(f_{ij+1}^{k} + f_{ij-1}^{k}) - \Delta x^2 g_{ij}] \tag{3.41}$$

In this equation $\beta = \Delta x/\Delta y$ and w is a relaxation factor used to accelerate convergence ($1 \leq w \leq 2$). The procedure is started with an initial guess f^{o} (usually zero at all interior points) and proceeds through the computational grid until the difference between successive iterates is below a specified error criteria. The optimum value of w depends on the mesh, the shape of the domain, and the type of boundary

conditions. For a rectangular region an estimate of the optimum value can be found from (Roache, 1976)

$$w_o = 2\left(\frac{1-\sqrt{1-a}}{a}\right) \tag{3.42}$$

where

$$a = \left[\frac{\cos(\pi/n) + \beta^2 \cos(\pi/n)}{1 + \beta^2}\right]^2 \tag{3.43}$$

The major advantages of this particular procedure are that it is extremely easy to program and has minimal core storage requirements. Even though the cost per iteration is small there are circumstances where the convergence can be slow especially if a strongly sheared flow is predominantly aligned in one coordinate direction.

Another iterative approach for finding a solution to the Poisson equation is to convert (3.32) to the parabolic problem

$$\frac{\partial f}{\partial t} = \nabla^2 f - g \tag{3.44}$$

and then solve for the steady state solution. This is the basis of the classic alternating direction implicit (ADI) method introduced by Peaceman and Rachford (1955). The procedure makes use of the fact that [M] can be split into two linear operators A and B both of which can be easily decomposed. Starting with an initial guess f^o (3.44) is discretized in time, with a time step Δt, and the system is solved on odd numbered steps (k+1) implicitly in A and explicitly in B,

$$f^{k+1} - f^{k} = \Delta t[\, Af^{k+1} + Bf^{k} - g] \tag{3.45}$$

The process is reversed on even numbered steps (k+2), solving implicitly in B and explicitly in A,

$$f^{k+2} - f^{k+1} = \Delta t[\, Af^{k+1} + Bf^{k+2} - g] \tag{3.46}$$

The combined operations (3.45 - 3.46) make one double sweep of the ADI iteration. The sequence of tridiagonal equations which need to be solved are as follows.

$$[1 \quad -(2+\rho) \quad 1]f^{k+1} = -\beta^2[1 \quad -(2-\rho) \quad 1]f^{k} + \Delta x^2 g \tag{3.47}$$

$$[1 \quad -(2+\rho) \quad 1]f^{k+2} = -\frac{1}{\beta^2}[1 \quad -(2-\rho) \quad 1]f^{k+1} + \Delta y^2 g \tag{3.48}$$

where $\rho = 2\Delta x^2/\Delta t$ and as before $\beta = \Delta x/\Delta y$. If the same Δt is used in both directions then convergence is assured. The procedure is computationally quite efficient because there are fast algorithms available for solving tridiagonal systems of linear equations. Unfortunately there is no general theory for selecting Δt, and in fact a variable sequence is required to take full advantage of the ADI procedure. Roache (1976) discusses different time stepping strategies and Doss and Miller (1979) describe a completely automatic procedure. The ADI algorithm is straightforward to implement, requires little storage and with the appropriate choice of time steps is extremely fast.

In addition to the ADI and SOR iterative procedures there are a number of very efficient direct methods. Most of the direct approaches

for solving the Poisson equation can be divided into two basic categories: those based on Fourier decomposition in one dimension, and those based on cyclic reduction. Dorr (1970) discusses block, cyclic reduction, tensor product and Fourier series methods. The Fourier series methods are based on the fact that an exact solution to the finite difference equation (3.36), in one space dimension (say rows), can be expressed in terms of finite eigenfunction expansions. Consequently the problem is reduced to a set of tridiagonal matrix equations, which couple the variables across the rows, each of which may be solved separately.

The procedure is to Fourier analyse the source function g_{ij} along one dimension to obtain the Fourier coefficients for each j.

$$\hat{g}_j(k) = \sqrt{\frac{2}{m}} \sum_{j=1}^{m} g_{ij} \sin\left(\frac{\pi k_i}{m}\right) \; ; \; 2 \leq j \leq n-2 \qquad (3.49)$$

The appropriate tridiagonal equations with the known right-hand sides are then given by

$$[1 \quad -(2-2\beta^2) - \{\cos(\frac{\pi i}{m})-1\} \quad 1]\hat{f}_j = \Delta y^2 \hat{g}_i(k) \; ; \; 2 \leq j \leq n-2 \qquad (3.50)$$

After solving each of the tridiagonal equations the potential at each mesh point is then recovered by using

$$f_{ij} = \sqrt{\frac{2}{m}} \sum_{k=1}^{m} \hat{f}_j(k) \sin\left(\frac{\pi k_i}{m}\right) \; ; \; 2 \leq j \leq n-2 \qquad (3.51)$$

The Fourier method, described by (3.49 - 3.51) is easy to program and has the major advantage that the solution does not involve any iterative steps. If the number of grids points in one or the other direction can be expressed as a integer of the form 2p then the most expensive element of the computation, the decomposition, can be performed using Fast Fourier Transform (FFT) algorithms. Unfortunately this does not often occur in practical applications of the type discussed in the previous section. More sophisticated procedures have been developed and in particular there is a trend towards combining the Fourier analysis and r steps of cyclic reduction producing composite algorithms which are denoted by FACR(r) (Temperton, 1979; Swarztrauber, 1977).

Each of the above methods were coded and tested on a series of sample problems one example of which is given by

$$\nabla^2 f = -2\pi \sin(\pi x) \sin(\pi y) \; ; \; x,y \in R \qquad (3.52)$$

$$f = 0 \; ; \; x,y \in \partial\Omega \qquad (3.53)$$

This test case has the exact solution

$$f(x,y) = \sin(\pi x) \sin(\pi y) \qquad (3.54)$$

The computational time required to solve (3.52) for each of the three

methods is given in Table 3.1. In the case of the SOR method the optimum relaxation factor was determined to be 1.6 (Figure 3.11) as compared to the value of 1.9 estimated by (3.42). The convergence parameter for the ADI was obtained from a series of numerical experiments the results of which are shown in Figure 3.12. For this and a number of other test problems the ADI method was more efficient than either the SOR or Fourier series methods and so it was selected for initial implementation in the wind field generation procedure. After publication of the paper reprinted in Section 3.7 the computational algorithm was modified to make use of the direct solution scheme described by Swarztrauber (1977). The cyclic reduction technique has proved to be both extremely efficient and reliable.

TABLE 3.1

Results of Test Case Comparing Three Poisson Equation Solving Algorithms

METHOD	CONVERGENCE CRITERION	CONVERGENCE PARAMETER	NUMBER OF ITERATIONS	RELATIVE EXECUTION TIME
Fourier				18.8
SOR	10^{-4}	1.6	50	1.7
	10^{-4}	1.9	139	4.8
ADI	10^{-4}	0.1	9	1.0

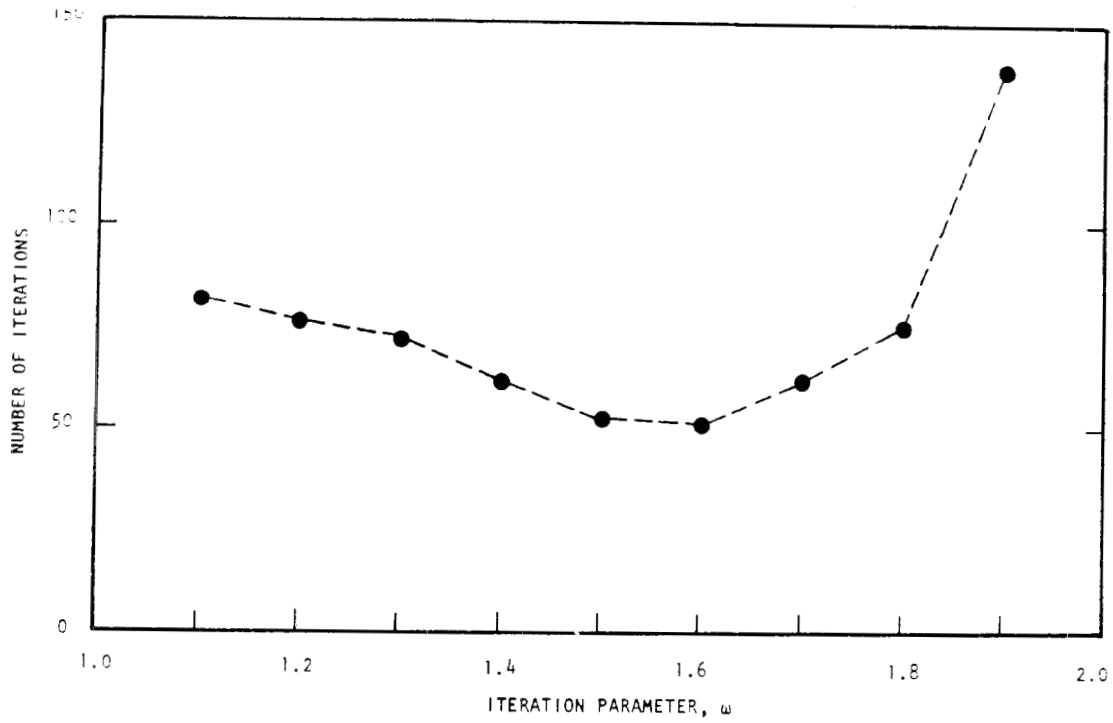

FIGURE 3.11

Number of Iterations Required for Convergence V as a Function of ω of the Successive Over Relaxation (SOR) Method.

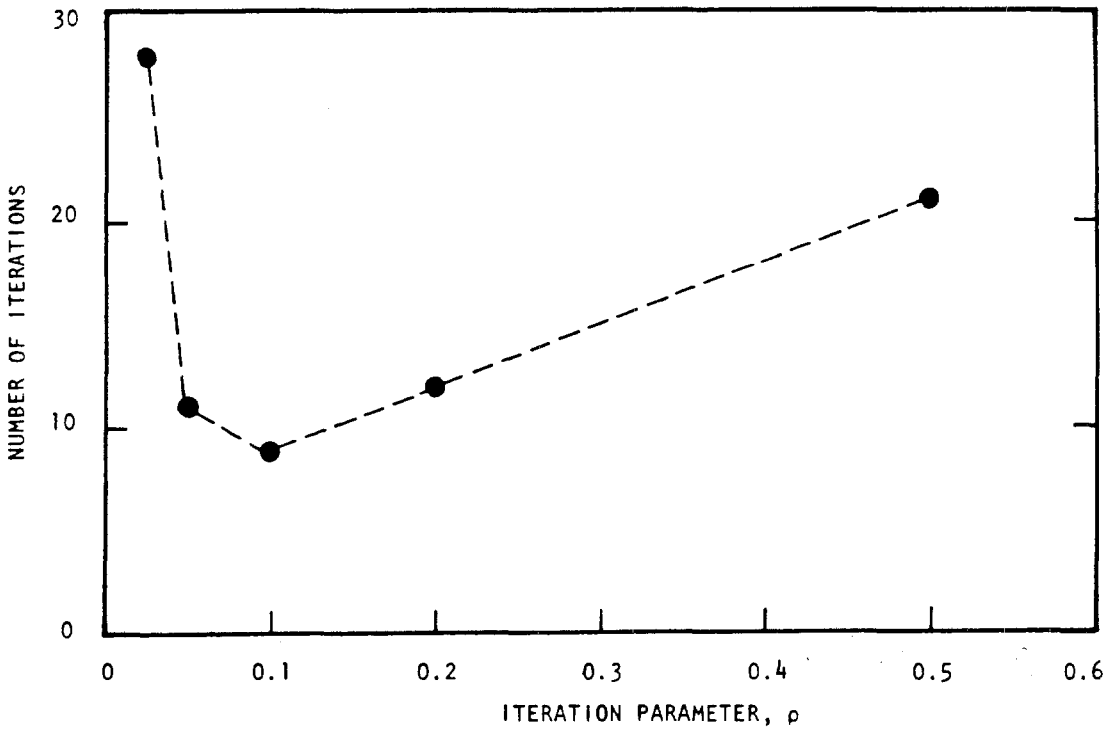

FIGURE 3.12

Number of Iterations Required for Convergence of the Alternating Direction Implicit (ADI) Method as a Function of ρ

3.10 Trajectory Integration Procedure

Once the wind field $\underline{u}(\underline{x},t)$ has been established it is extremely useful to be able to follow the paths of individual air parcels as they traverse the airshed. There are two reasons for this. For the trajectory model introduced in Chapter 2, the spatial location of the column of air is needed to specify the emission inputs and the appropriate meteorological data. A second application of a trajectory integration procedure is to specify the horizontal boundaries for three-dimensional airshed models. For example, by locating the model boundaries beyond the extent of return air flow, in regions subjected to land-sea breeze reversals, the effect of uncertainties in inflow boundary conditions can be minimized as background values are more likely to apply. This section describes a procedure for calculating the movement of air parcels within flow fields generated by objective analysis techniques of the type presented in Section 3.7.

The spatial position of the air parcel at time T relative to an initial starting location $\underline{x}(\underline{0})$ is given by

$$\underline{x}(T) = \underline{x}(0) + \int_0^T \underline{u}(\underline{x},t)\, dt \tag{3.55}$$

Since the velocity field $\underline{u}(\underline{x},t)$ is usually only available at discrete locations, objective analysis procedures of the type discussed in previous section must be used to characterize the flow in between grid points. The method adopted in this study is to calculate the velocity at the current trajectory position $p(\underline{x},t)$ as a distance-weighted

function of the wind field at the nearest grid points. A two-dimensional example is shown in Figure 3.13, where $\underline{u}(\underline{p},t)$ is formed as a weighted mean of the wind field at the four nearest grid points. The velocity components at $p(\underline{x},t)$ are given by

$$\underline{u}_k(\underline{x},t) = \frac{\sum_{i=1}^{n} u_i^k/d_i}{\sum_{i=1}^{n} 1/d_i} \tag{3.56}$$

where n is the number of nearest grid point (=4 for two-dimensional problems and 8 for three-dimensional cases) and $\underline{u}_i^k$ are the k-th components of the velocity field at each of the grid points.

A variety of techniques can be used to integrate the initial value problems (3.55); the simplest numerical scheme is given by

$$\underline{x}(t + \Delta t) = \underline{x}(t) + \Delta t \underline{u}[\underline{x}(t),t] \tag{3.57}$$

Although the Euler integration method is only first-order accurate in time ($O(\Delta t)$), with sufficiently small time steps O(10 minutes) the positional errors using hourly averaged wind fields are negligible. The reasons for this are that Δt is small compared to the averaging time for $\underline{u}(\underline{x},t)$ and the spatial gradients in the velocity field over a distance of $\underline{u}\Delta t$. Figure 3.14 illustrates an application of the procedure to tracking a sulfur hexafluoride (SF_6) tracer release. After 12 hours, the predicted position of the concentration centroid is almost coincident with the field measurements.

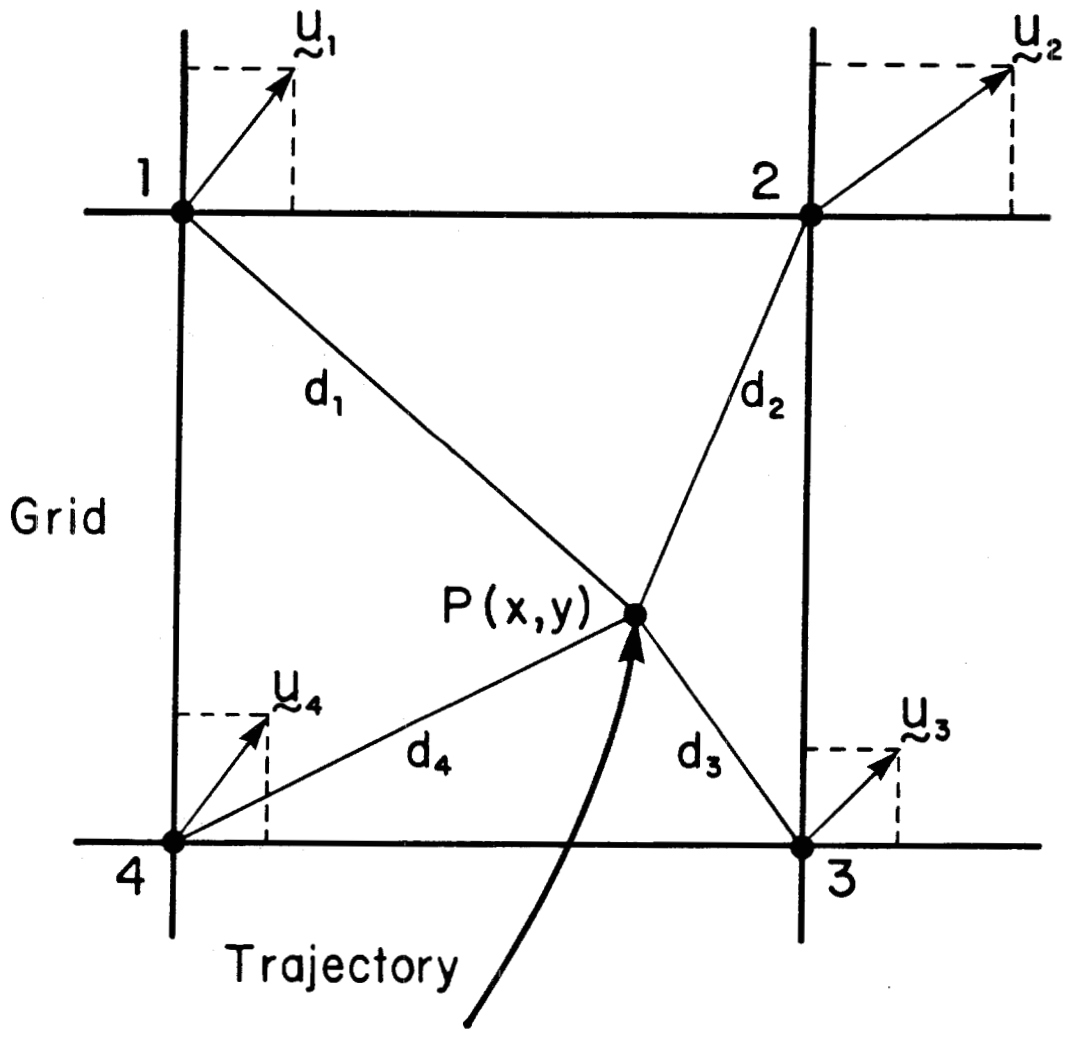

FIGURE 3.13

Velocity at Current Position P(x,y) is Determined as a Distance Weighted Mean of Wind Velocity at the Four Nearest Grid Points.

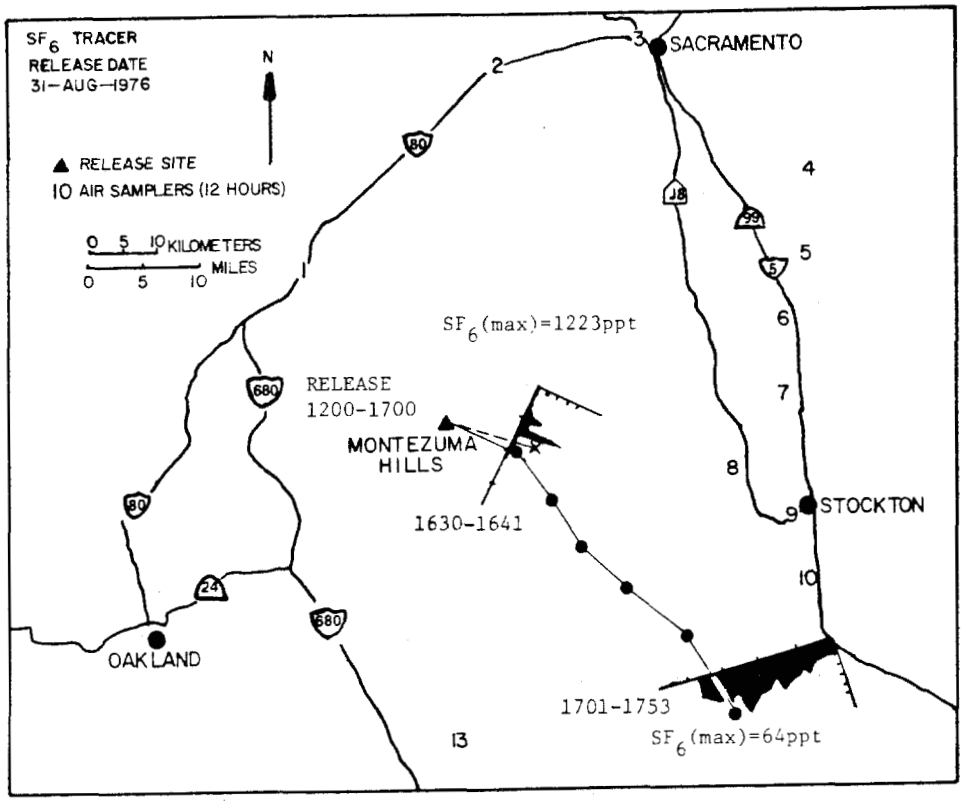

FIGURE 3.14

Forward Air Parcel Surface Trajectories.
Each Point ● Represents One Hour of Transport.
Source: Lamb and Shair (1977)

In order to assess the effects of errors in the wind field a number of numerical experiments were conducted in which grid values were randomly perturbed and the trajectory path recalculated. In these calculations the velocity magnitudes were assumed to be normally distributed about the old field value with a standard deviation of $\pm$ 20%. Angular errors were assumed to be uniformly distributed in a segment of $\pm 11.25^{o}$. The error growth $e(t) = [\underline{x}^{p}(t) - \underline{x}^{o}(t)]$ for these problems is defined as the distance between the nominal path $\underline{x}^{o}(t)$ and the trajectory $\underline{x}^{p}(t)$ calculated with the perturbed wind field. This error is derived from two components, a positional error V_p due to the uncertainty in the wind field $\underline{u}$ and the other arising from spatial gradients in the velocity field V_g i.e.

$$\frac{de(t)}{dt} = V_p + V_g = V_p + \frac{d}{dt}[\underline{x}^{p}(t) - \underline{x}^{o}(t)] \tag{3.58}$$

Sykes and Hatton (1976) assumed that when e(t) is small compared to the large scale features of the flow field, V_g can be approximated by e(t)S where S is the horizontal shear or vorticity.

$$\frac{de(t)}{dt} = V_p + e(t)S \tag{3.59}$$

With this formulation it can be seen that the error growth is linear when $e(t) \ll V_p/S$ and exponential when $e(t) = V/S$. In urban regions where the topography is reasonably flat, the error growth is linear. For example, in Los Angeles a typical velocity error is O(1 m/s) and the vorticity of flows with scales greater than 10 km is $O(10^{-4}$ s) so

the error growth is in the linear regime. This observation is confirmed by the sample calculation displayed in Figure 3.15 where the maximum error at the end of a 24 hr integration is O(5 km), the size of a typical computational cell. When one of the trajectories in Figure 3.15 encountered mountainous terrain the error exhibited an exponential like growth.

3.11 Conclusion

In this chapter a new method for constructing three-dimensional, mass-consistent wind fields has been introduced. Two steps are involved in the generation process. The first involves interpolating irregularly spaced monitoring data to a regular computational mesh. Objective analysis procedures are then employed to adjust the wind vectors at each grid point so that an applied physical constraint such as minimum field divergence is satisfied. A major advantage of the technique is that it only requires, as input, routinely measured information. In addition, the interpolation algorithms can also be used to establish the initial concentration distributions and mixing height over the airshed. The procedures are easy to implement, computationally efficient and can be easily applied to a wide range of other meteorological applications.

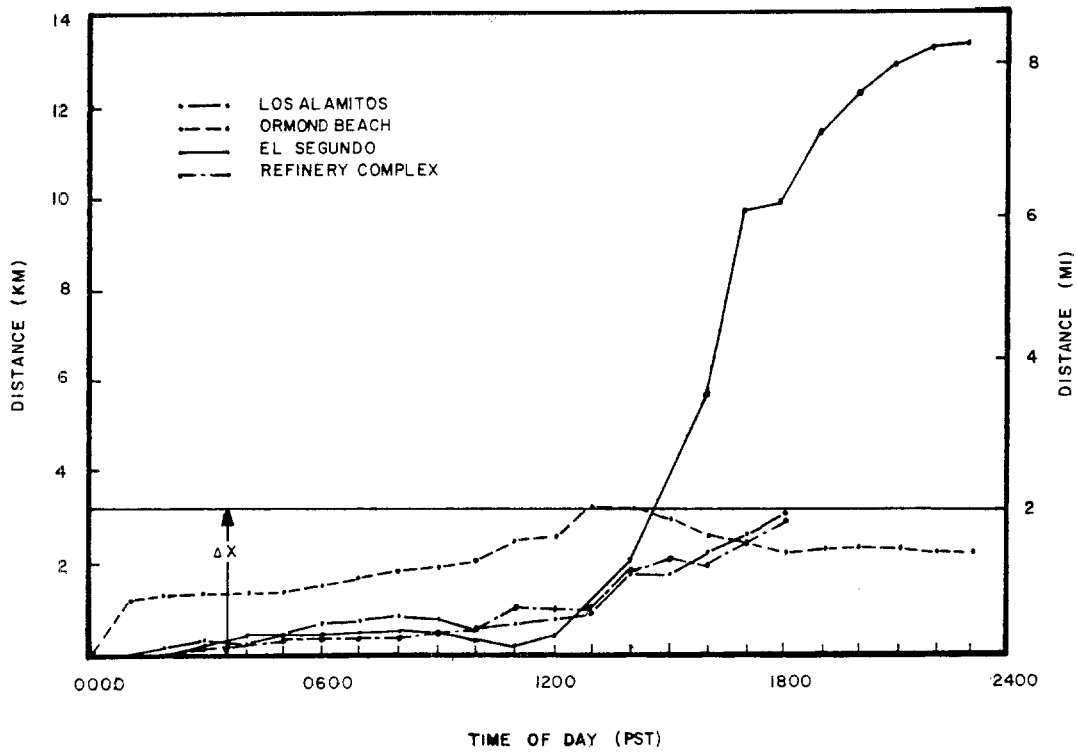

FIGURE 3.15

Plot of Distance Between Actual and Perturbed Trajectories as a Function of Time.

CHAPTER 4

TURBULENT DIFFUSION COEFFICIENTS

4.1 Introduction

Closure of the species continuity equation has been accomplished in the present model by a gradient-diffusion or K-theory hypothesis. This chapter is devoted to a presentation of the formulation adopted for the vertical (K_{zz}) and horizontal (K_{xx},K_{yy}) diffusion coefficients. At the outset it should be remarked that a variety of different formulations exist. Yu (1977), for example, presents a comparative evaluation of 14 different approaches. A particular complication in the selection or development of a model is the lack of suitably detailed measurements of vertical wind shear and temperature profiles. As a result a guiding principle in formulating the present model was to employ only those parameters that are readily available or can be easily estimated.

4.2 Turbulent Diffusion in the Atmosphere

The K-Theory model was introduced to describe the fluxes of material which occur on spatial scales smaller than those which can be resolved either by an observational network of wind stations or by the computational grid points. In this model the fluxes $\langle u'c'_i \rangle$ are assumed to be proportional to the mean concentration gradient $\nabla\langle c_i \rangle$.

$$\langle \underline{u}'c'_i \rangle = K\nabla\langle c_i \rangle \tag{4.1}$$

Specification of the components of the second-rank eddy diffusion tensor K requires an understanding of the turbulent processes occurring in the atmosphere. The planetary boundary layer is commonly divided into three layers. In most models these regions are: the constant flux layer next to the ground, a deeper layer in which the fluxes generally decrease with height and the free atmosphere. These regions are illustrated in Figure 4.1 for an atmospheric state characteristic of daytime conditions. During daytime conditions the mixed layer has a reasonably well defined upper boundary. This height, Z_i, is commonly associated with the base of an elevated temperature inversion. Solar heating causes the convective layer to increase in thickness at a rate determined by the heat flux radiated at the ground. Above the mixed layer there is a quasi-permanent layer of non-turbulent flow. Stable layers can also exist close to the ground as a result of nocturnal cooling.

Many processes are involved in turbulent transport. For example, above the planetary boundary layer, diffusion is associated with internal wind shear and the effect of topography on a scale large enough to cause upward propagation of energy. In the surface or "constant flux" layer the fluxes of heat, momentum and water vapor are approximately constant with height. Over most of the boundary layer the small scale turbulence is induced by wind shear and/or thermal convection. The relationship between mean values and vertical gradients of such properties as wind, temperature, humidity and surface properties was the subject of a major workshop project (Haugen, 1973).

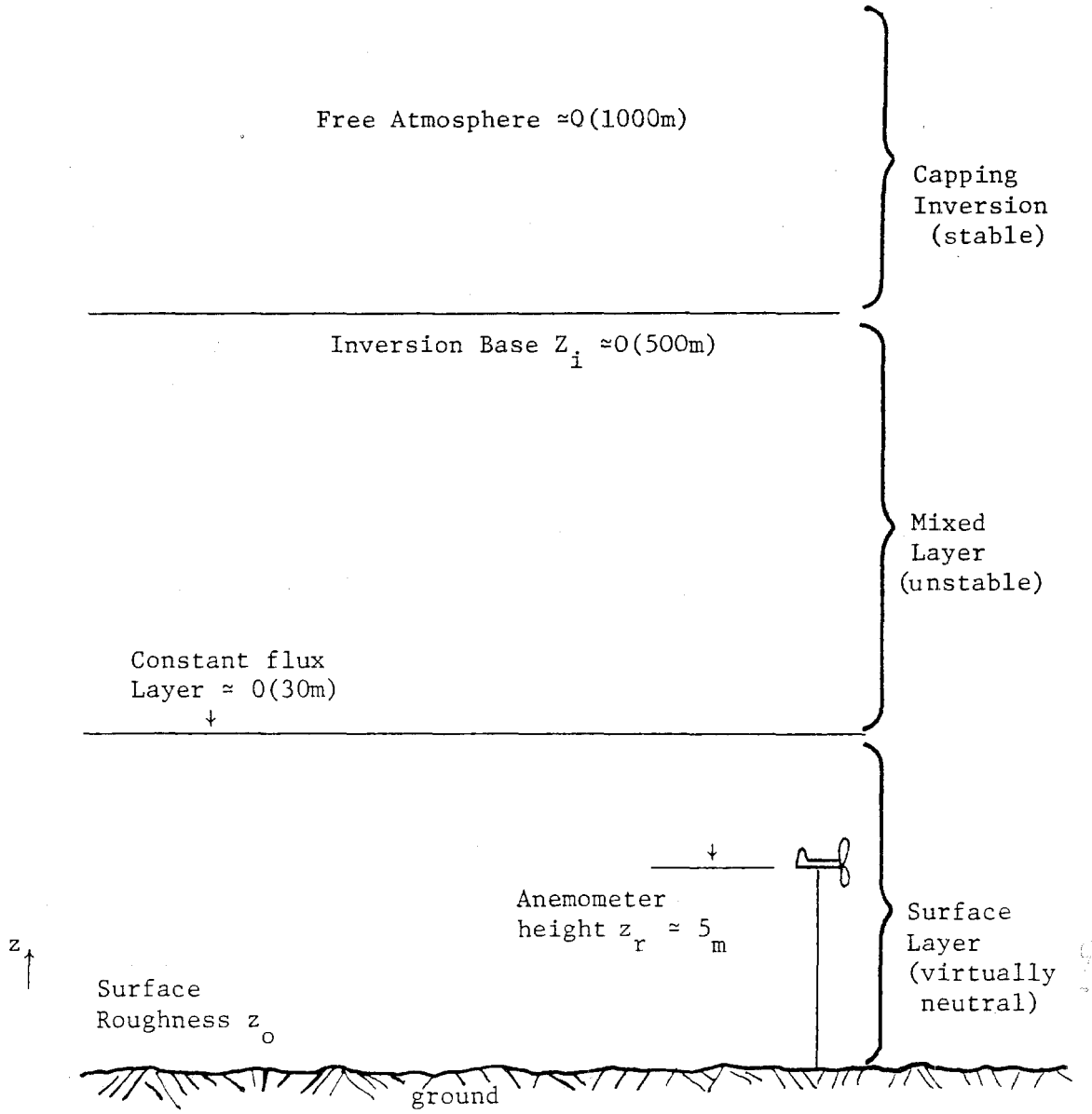

FIGURE 4.1

Structure of the Atmospheric Boundary
for Typical Daytime Conditions

4.3 Turbulent Transport Parameters

In this study primary attention is directed at the turbulent processes that occur in the mixed layer as a result of the interaction between shear and buoyancy driven flows. The flux Richardson number R_f gives a measure of the relative importance of the buoyancy terms in the equations of motion $\frac{g}{T}\overline{w'\theta'}$ as compared to the shear production terms $\overline{u'w'}\frac{\partial \bar{u}}{\partial z}$ i.e.,

$$R_f = \frac{\frac{g}{T}\overline{w'\theta'}}{\overline{u'w'}\frac{\partial \bar{u}}{\partial z}} \tag{4.2}$$

where $\overline{w'\theta'}$ is a measure of the kinematic sensible flux and $\overline{u'w'}$ is the x-component of vertical momentum flux. Clearly when R_f is large the flow is dominated by buoyancy effects. The flux Richardson number is a function of the distance from the ground and is thus a measure of the local stability property of the turbulent flow. Richardson (1920) suggested that turbulence should occur in the atmosphere when the production of turbulent energy by the wind shear is just large enough to counterbalance its consumption by buoyancy forces.

A major deterrent to the use of (4.2) as a measure of atmospheric stability is the need for simultaneous determinations of both the heat and momentum flux. Another approach is to define a quantity similar to (4.2) called the gradient Richardson number R_i.

$$R_i = \frac{\frac{g}{T}\frac{\partial \theta}{\partial z}}{(\frac{\partial \bar{u}}{\partial z})^2} \tag{4.3}$$

where θ is the potential temperature and T the absolute air temperature. The relationship between R_f and R_i is

$$R_f = \frac{K_H}{K_m} R_i \tag{4.4}$$

where K_m and K_H are the eddy diffusion coefficients for momentum and heat respectively. R_i determines the stability of a stratified fluid subjected to small perturbations and so it is a measure of the onset of turbulence (Plate, 1971).

Another stability parameter often used in micro-meteorology is the Monin-Obukhov length

$$L = - \frac{u_*^3 \, c_p \, \rho T}{kHg} \tag{4.5}$$

where c_p is the specific heat at constant pressure, ρ the air density, k the von Karman constant, T the absolute air temperature, g acceleration of gravity, H is the vertical heat flux and u_* is the friction velocity. Physically the Monin-Obukhov length is the approximate height above the surface at which buoyancy effects become comparable to the shear effects. For neutral conditions, L is related to the flux Richardson number R_f by

$$R_f = \frac{z}{L} \tag{4.6}$$

The Monin-Obukhov length, like R_f, provides a measure of the stability of the surface layer since:

$L > 0$	Stable	
$L = \infty$	Neutral	(4.7)
$L < 0$	Unstable	

4.4 Estimation of the Monin-Obukhov Length

The Monin-Obukhov length L is a key parameter in the present model and indeed in many other approaches. Golder (1972) established a relation between the stability classes of Pasquill and Turner, the roughness height and L. The results of his investigation are shown in Figure 4.2 . With this technique, the local wind speed and cloud cover measurements are used to estimate the Pasquill stability class (Table 4.1). In addition, Golder developed a nomogram for relating the gradient Richardson number R_i to the more easily determined bulk Richardson number B

$$B = \frac{g}{T} \frac{\partial \theta}{\partial z} \left[\frac{z}{\overline{u}}\right]^2 \tag{4.8}$$

In order to simplify calculation of 1/L, within the airshed model, each stability class was approximated by a single straight line of 1/L against surface roughness. The error induced by this approximation is quite small, for example, in calculating the convective velocity scale w_*

$$w_* = \left(-\frac{1}{k} \frac{Z_i}{L}\right)^{\frac{1}{3}} u_* \tag{4.9}$$

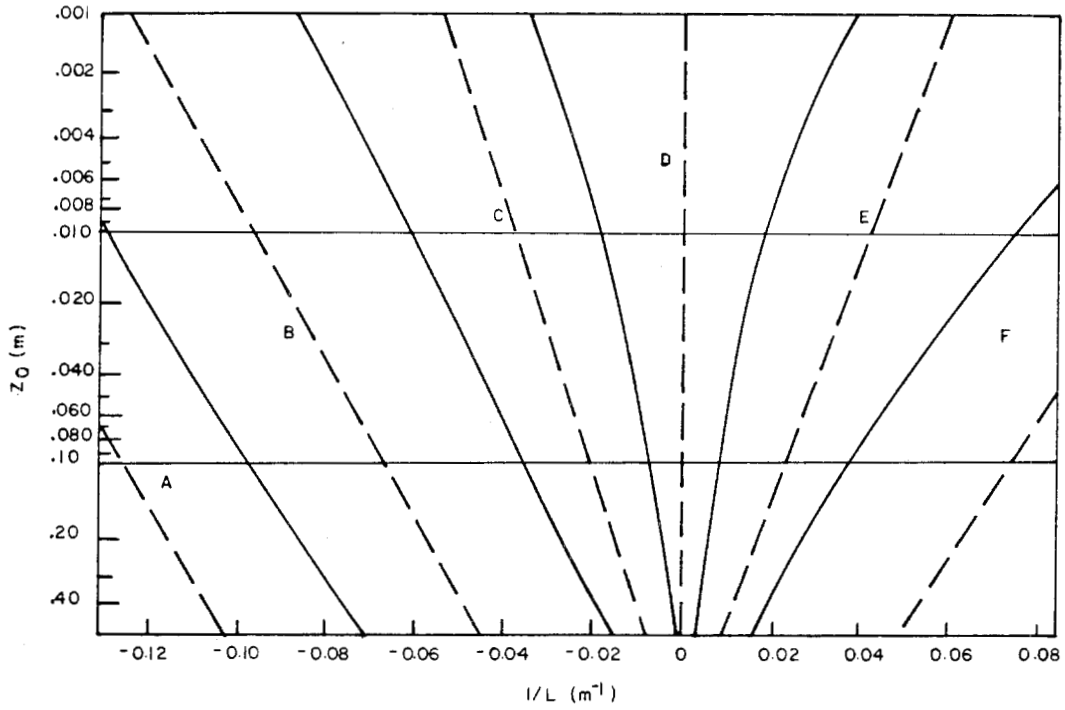

FIGURE 4.2

Relationship between Pasquill Stability Classes, Surface Roughness, and Monin-Obukhov Length. (Solid lines define stability classes, dotted lines used to approximate stability region).

TABLE 4.1

Estimation of Pasquill Stability Classes. (Source: Turner, 1969)

Surface Wind Speed at 10m ($m\text{-}sec^{-1}$)	Solar Radiation*			Night Time Cloud Cover Fraction	
	Strong	Moderate	Slight	Low cloud $\geq \frac{4}{8}$	cloud $\leq \frac{3}{8}$
< 2	A	A - B	B		
2 - 3	A - B	B	C	E	F
3 - 5	B	B - C	C	D	E
5 - 6	C	C - D	D	D	D
> 6	C	D	D	D	D

*

Incoming Radiation (Category)	Solar Insolation (Langley min^{-1})	($W - m^{-2}$)
Strong	$I > 1.0$	$I > 700$
Moderate	$0.5 \leq I \leq 1.0$	$350 \leq I \leq 700$
Slight	$I < 0.5$	$I < 350$

Since the parameter 1/L is raised to the one third power, large variations do not lead to rapid variations in w_*. The parameters for the straight line approximations to the stability classes are shown in Table 4.2.

There is a variety of factors that could influence the location of the lines approximating each stability class. An important factor is the presence of water vapor in the atmosphere. If suitable data are available, the Monin-Obukhov length L can be redefined as

$$L_w = \frac{1}{[1 + \frac{m}{B_o}]} \tag{4.10}$$

where B_o is the Bowen ratio and m is a constant the value of which is given by $m = 0.61\ c_p\ T/\bar{L}$ where $\bar{L}$ is the latent heat of vaporization of water (for $T = 300^oK$, $m \simeq 0.07$, Lumley and Panofsky, 1964). The water vapor flux can exert a considerable influence on diffusion, particularly over the ocean and heavily vegetated areas. Increased levels of evaporation act to shift the lines to the right and so, for a given surface roughness, larger values of $\bar{L}$ can be expected.

4.5 Surface Roughness Estimation

In the present model the effects of small-scale surface irregularities on the boundary layer transfer processes are incorporated only through the surface roughness parameter z_o. As a result, z_o must be specified at each grid point within the modeling region. The range of variation of z_o over different land types is quite large, and the

TABLE 4.2

Coefficients for Straight Line Approximation to Golder's Plot as a Function of Stability Classes

$$\frac{1}{L} = a + b \log_{10} z_o$$

	Pasquill Stability Class	Coefficients a	b
Extremely Unstable	A	-0.096	0.029
Moderately Unstable	B	-0.037	0.029
Slightly Unstable	C	-0.002	0.018
Neutral	D	0	0
Slightly Stable	E	+0.004	-0.018
Moderately Stable	F	+0.035	-0.036

measurements required to estimate the effective roughness are quite complex. As an alternative, Plate (1971) proposed a simple formula that relates z_o to the mean canopy height h_c.

$$z_o = 0.15\ h_c \tag{4.11}$$

Depending on the conditions, the 'constant' 0.15 varied from 1/7 to 1/30. Figure 4.3 presents surface roughness values for a variety of land use categories compiled primarily from the reviews by Myrup and Ranzieri (1976) and Hodgin (1980). The precision implied by some entries on the figure is deceptive because there is considerable scatter in many of the underlying experimental data.

When a modeling region includes a large body of water, the roughness cannot be characterized by simply associating h_c with the wave height. Unlike the land, the effective roughness of the water surface is a dynamic variable whose magnitude is influenced by factors such as the wave state and wind stress. There is a variety of models of the air-sea interaction and its influence on z_o. The studies by Gent, (1977), Hsu (1974) and Kitaigorodskii (1970) illustrate some of the complexities. Arya (1977) has recently reviewed some of the more simple parameterizations that are applicable to the present study. For example, Wipperman (1972) has suggested the following formula for smooth as well as rough conditions:

$$z_o = 0.1 \frac{\nu}{u_*} + b \frac{u_*^2}{g} \tag{4.12}$$

Where ν is the kinematic viscosity of air and b is a constant whose

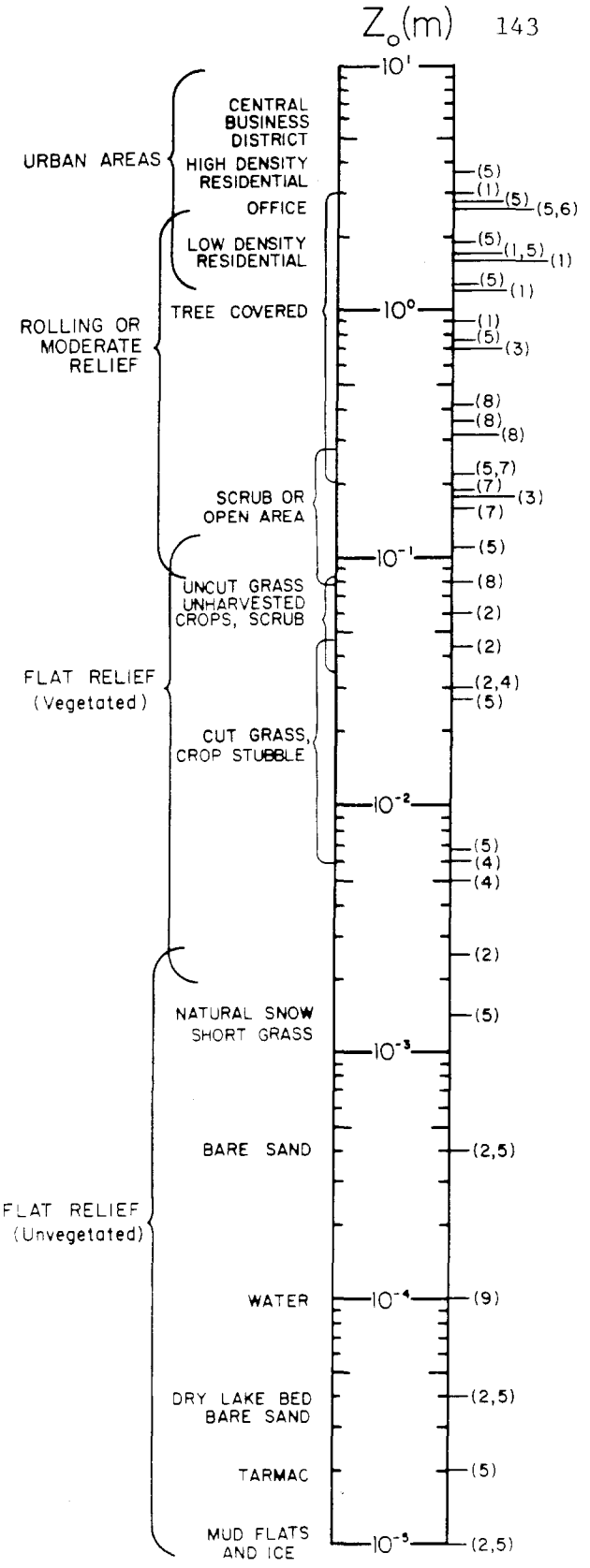

REFERENCES

1. COUNIHAN (1975)
2. DEACON (1949)
3. FICHTL and McVEHIL (1970)
4. GOLDER (1972)
5. MYRUP and RANZIERI (1976)
6. SLADE (1969)
7. TOUMA (1977)
8. WEBER et al. (1975)
9. SEE TEXT

FIGURE 4.3

Variation of Surface Roughness as a Function of Surface Type

magnitude $\simeq 0.02$. The formula implies a considerably increasing trend in z_o; the results of Stewart (1974) and calculations by Gent (1977) imply a more or less constant value of $z_o \simeq 0.01 - 0.02$ cm for 10 m wind speeds in the range 6-12 m s^{-1}. For the purposes of this study, a value of z_o for the ocean was set to be 0.01 cm.

4.6 Determination of the Friction Velocity u_*

Close to the ground, in the constant flux layer, u_* is a measure of the turbulent eddying and of the transfer of momentum due to these fluctuations. The friction velocity u_* is used in many situations and this section presents some simple formulae that can be used under a variety of meteorological conditions. The friction velocity is defined by

$$u_*^2 = \frac{\tau_o}{\rho} = -\overline{u'w'} \tag{4.13}$$

where τ_o is the shear stress per unit area of the boundary and ρ is the density of the fluid. A K-Theory approximation for the momentum flux $\overline{u'w'}$ and a Monin-Obukhov similarity expression can be used to develop the following form.

$$u_* = \frac{k\, u(z_r)}{\int_{z_o}^{z_r} \phi_m\left(\frac{z}{L}\right) \frac{dz}{z}} \tag{4.14}$$

where $u(z_r)$ is the velocity at a reference elevation z_r, typically the elevation of the wind measuring instrument and ϕ_m an experimentally determined function. The velocity at the height of the momentum sink,

z_o, is assumed to be zero. Businger et al. (1971) developed a series of ϕ_m functions from field data, the results of which are given by:

$$\phi_m\left(\frac{z}{L}\right) = \begin{cases} 1 + 4.7\left(\frac{z}{L}\right) & ; \frac{z}{L} > 0 \\ 1 & ; \frac{z}{L} = 0 \\ \left[1 - 15\left(\frac{z}{L}\right)\right]^{-\frac{1}{4}} & ; \frac{z}{L} < 0 \end{cases} \tag{4.15}$$

Substituting these expressions into (4.14) gives the friction velocity. The necessary integrals are summarized in Table 4.3.

4.7 Vertical Diffusivity Profile for Unstable Conditions

Transport of pollutant material in the vertical direction is often dominated by turbulent diffusion. Only diagonal components of the eddy diffusion tensor K are used in the airshed model and, as a consequence, the specification of K_{zz} has an important bearing on the performance of the airshed model. Many approaches have been tried to establish vertical profiles of K_{zz} within the boundary layer. The wide range of meteorological regimes encountered in practice considerably complicates the task. This section is devoted to a discussion of the mathematical model adopted for K_{zz} under unstable conditions, i.e., when $L < 0$.

Monin-Obukhov similarity theory predicts that the surface layer eddy diffusion coefficient is given by Monin and Yaglom (1971)

$$K_{zz} = \frac{k\, u_* z}{\phi\left(\frac{z}{L}\right)} \tag{4.16}$$

TABLE 4.3

Momentum and Pollutant Integrals of Different Stability Conditions

INTEGRAL	STABILITY CONDITION		
	STABLE	NEUTRAL	UNSTABLE
	$\frac{z}{L} > 0$	$\frac{z}{L} = 0$	$\frac{z}{L} < 0$
MOMEMTUM			
$\int_{z_o}^{z_r} \phi_m(\frac{z}{L}) \frac{dz}{z}$	$\ln(\frac{z_r}{z_o}) + \frac{4.7}{L}(z_r - z_o)$	$\ln(\frac{z_r}{z_o})$	$\ln\left[\frac{(1-15\frac{z_r}{L})^{\frac{1}{4}} - 1}{(1-15\frac{z_r}{L})^{\frac{1}{4}} + 1}\right] - \ln\left[\frac{(1-15\frac{z_o}{L})^{\frac{1}{4}} - 1}{(1-15\frac{z_o}{L})^{\frac{1}{4}} + 1}\right] + 2\arctan(1-15\frac{z_r}{L})^{\frac{1}{4}} - 2\arctan(1-15\frac{z_o}{L})^{\frac{1}{4}}$
POLLUTANT			
$\int_{z_o}^{z_r} \phi_p(\frac{z}{L}) \frac{dz}{z}$	$0.74\ln(\frac{z_r}{z_o}) + \frac{4.7}{L}(z_r - z_o)$	$0.74\ln(\frac{z_r}{z_o})$	$0.74\left\{\ln\left[\frac{(1-9\frac{z_r}{L})^{\frac{1}{2}} - 1}{(1-9\frac{z_r}{L})^{\frac{1}{2}} + 1}\right] - \ln\left[\frac{(1-9\frac{z_o}{L})^{\frac{1}{2}} - 1}{(1-9\frac{z_o}{L})^{\frac{1}{2}} + 1}\right]\right\}$

where ϕ is an experimentally determined function that basically corrects for buoyancy effects on the turbulence. Businger et al. (1971) have constructed ϕ expressions for momentum ϕ_m and heat ϕ_H from an analysis of field data. For unstable conditions $z/L<0$ the formulae for ϕ_m and ϕ_H are

$$\phi_m(\frac{z}{L}) = [1 - 15(\frac{z}{L})]^{-\frac{1}{4}} \tag{4.17}$$

$$\phi_H(\frac{z}{L}) = \phi_m^{\,2} \tag{4.18}$$

The findings of Galbally (1971) and Crane et al. (1977) indicate that eddy transport of matter is more closely related to that of heat rather than momentum. Using the above results, an approximate expression for K_{zz} can be derived in terms of the momentum diffusivity K_{zz}^m .

$$K_{zz} = K_{zz}^m[1 - 15\ (\frac{z}{L})]^{\frac{1}{4}} \tag{4.19}$$

This result indicates that the common assumption, adopted in many air pollution studies, that $K_{zz} \simeq K_{zz}^m$ can lead, under typical meteorological conditions, to an underestimate of K_{zz} by a factor of 3. Carl et al. (1973) suggested an expression for K_{zz}^m that closely fits a second order closure model calculation by Zeman and Lumley (1976).

$$K_{zz}^m = 2.5\ w_* Z_i[k\ \frac{z}{Z_i}]^{\frac{4}{3}} \tag{4.20}$$

Combining the last two equations gives the distribution of K_{zz} in the surface layer under unstable conditions.

$$K_{zz} = 2.5\, w_* Z_i [k \frac{z}{Z_i}]^{\frac{4}{3}} [1 - 15 \frac{z}{L}]^{\frac{1}{4}} \qquad (4.21)$$

Above the surface layer there is considerable uncertainty about the magnitude and height dependence of K_{zz}. Some observed features of atmospheric flow, for example, are not consistent with the basic K-Theory formulation of turbulent transport. For example, the difficulty of describing counter gradient fluxes of pollutant material has been discussed by Willis and Deardorff (1976). A basic problem with the K-Theory model, particularly for convectively driven flows, is that the turbulent transport is no longer described by local concentration gradients.

With these limitations in mind, Lamb et al. (1975) derived empirical expressions for K_{zz} using the numerical turbulence model of Deardorff (1970). Their work was directed at finding expressions for the vertical eddy diffusivity that were: positive definite, functions only of the height above the ground and that yielded solutions of the diffusion equation in good agreement with more refined turbulence models. The methodology employed Lagrangian diffusion theory and optimal control techniques to develop the profiles. An optimal K_{zz} was considered to be one for which a solution to the steady state diffusion equation $c_s(x,t)$ minimized the mean square difference from a known concentration field $c_K(x,t)$. Formally the objective was to find a K_{zz} which

minimized the index J where

$$J(t) = \int_D [c_K(\underline{x},t) - c_s(\underline{x},t)]^2 \, dD \qquad (4.22)$$

The data used for determining K_{zz} were limited to the stability conditions z/L = 0 and z/L = -4.5. Recently Lamb and Durran (1978) improved the numerical procedures and extended the stability range to z/L = -1100. The calculations for each of these studies are displayed in Figure 4.4. When scaled with w_* the convective velocity and Z_i, the diffusivity profiles are sufficiently similar in shape to suggest that a single profile of the form

$$\tilde{K}_{zz} = \frac{K_{zz}}{w_* Z_i} = f(\frac{z}{Z_i}) \qquad (4.23)$$

might be applicable. Convective scaling is appropriate because L is small compared with Z_i. The function f can be assumed to be universal under the following conditions: (i) the turbulence structure within the mixed layer is self similar and in equilibrium with the current boundary conditions and (ii) the normalized eddy diffusion K_{zz} is independent of the nature of the pollutant source distribution (Crane et al. 1977). In practice, the equilibrium condition is usually satisfied since it requires that the mixed layer depth varies slowly, i.e. that $\partial Z_i / \partial t \ll w_*$. Willis and Deardorff (1976a) indicate that self similarity occurs after $w_* x / u Z_i$ exceeds 2.5 (where x is the distance covered after the material has been released and u the mean wind speed). This latter condition is satisfied for grid cell spacing O(5Km). Condition

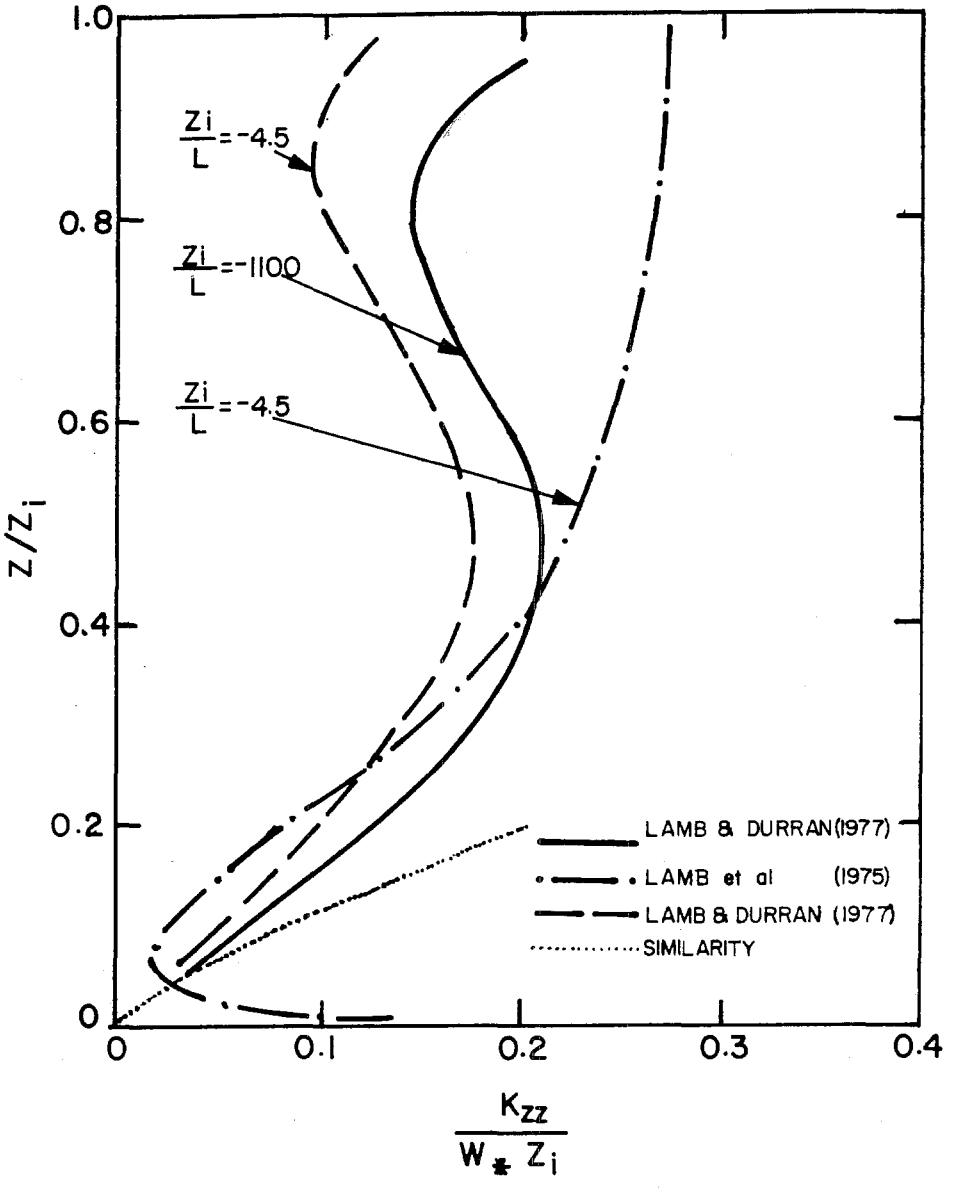

FIGURE 4.4

Vertical Diffusivity Profiles for a Range of Stability Conditions Derived from Turbulence Model of Deardorff (1970)

(ii) is not, in general, satisfied in convectively driven flows. If the eddy diffusivity were truly a local property of the turbulent flow, then K_{zz} would be independent of the height of source emissions. Lamb and Durran (1978) determined that the form of the K_{zz} profile is quite dependent on the source height. With this proviso it can be recognized that most emissions are released at or near ground level and so a single profile is applicable. The numerical form of the profile is given by (4.24) for stability conditions in the range $Z_i/L<-10$. (The same profile may also apply for $-10<Z_i/L<0$.)

$$K_{zz} = w_* Z_i [0.021 + 0.408(\frac{z}{Z_i}) + 1.352(\frac{z}{Z_i})^2 - 4.096(\frac{z}{Z_i})^3 + 2.560(\frac{z}{Z_i})^4] \tag{4.24}$$

Field data for $c_K(x,t)$ were used by Crane et al. (1977) in a similar approach to estimate the optimal diffusivity profile. Their results are shown in Figure 4.5. However, since they neglected the effects of vertical advection and lateral diffusion, K_{zz} was underestimated by a factor of 2. The dotted line in Figure 4.5 is intended to reflect this correction. The shaded region in the center of the plot was excluded because of measurement difficulties when $\partial c/\partial z$ was small and the effective diffusivity was large $O(100\ m^2\ s^{-1})$. An important feature of their results was that the diffusivity was quite small near the top of the mixed layer. The divergence of (4.24) for $z/Z_i>0.8$ is most likely due to the numerical treatment of the profile in the solution process, since no boundary slopes were imposed. There is no a priori reason why the diffusivity should be a maximum at the top of the mixed layer; indeed the results of Zeman and Lumley (1976), and the study of Stull (1973) would tend to suggest a small value.

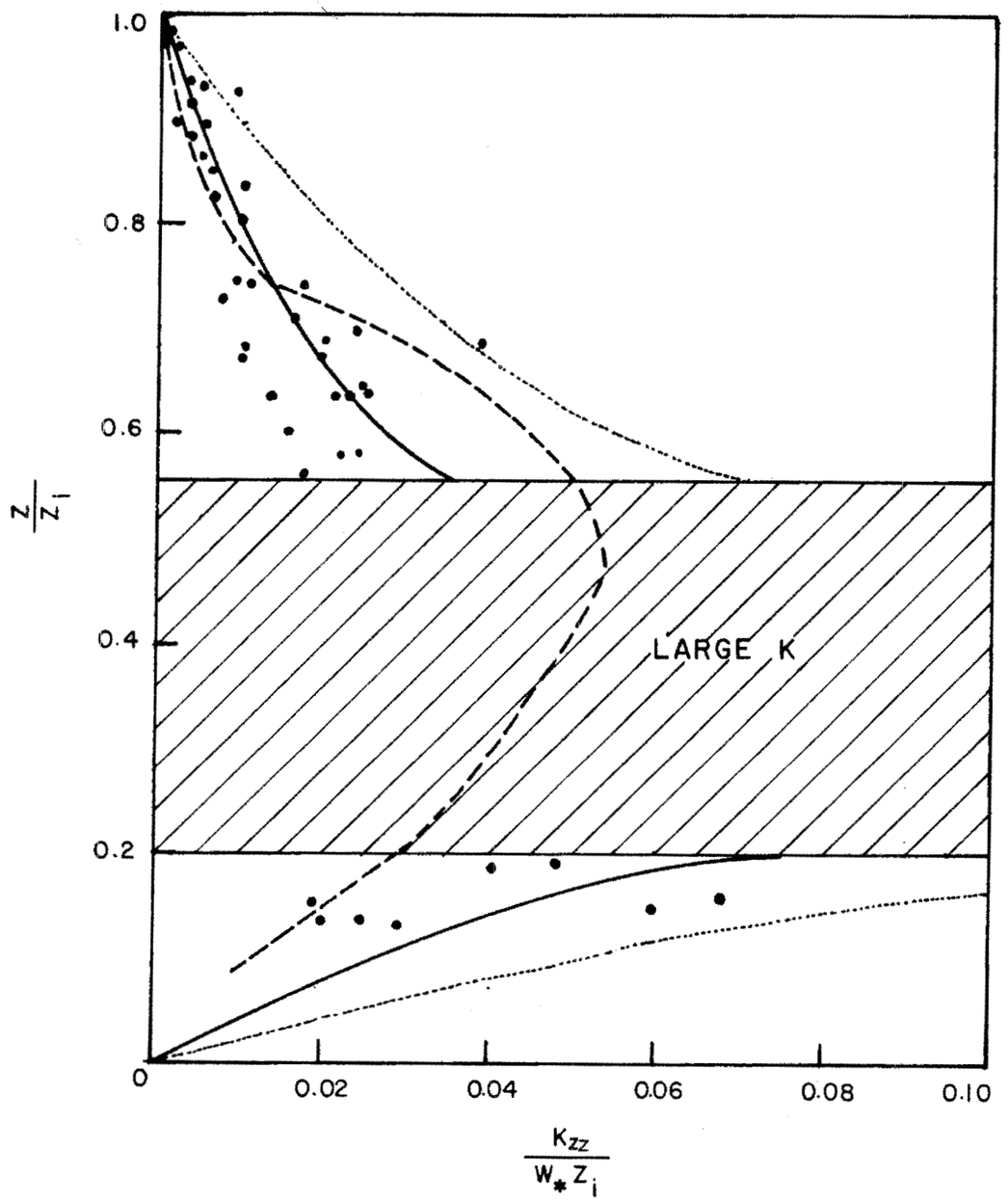

FIGURE 4.5

Vertical Turbulent Diffusivity Profiles, Derived from Field Measurements and a Second Order Closure Calculation.

For this reason (4.24) was modified for $z>Z_i>0.6$ to the following form

$$K_{zz} = 0.2\ w_* Z_i\ \exp[6-10(\frac{z}{Z_i})] \qquad (4.25)$$

This function smoothly reduces the profile to a small value at the top of the mixed layer. For $z>1.1Z_i$ the diffusivity is held constant at a value of $0.0013 w_* Z_i$ which is approximately one percent of the maximum value in the mixed layer.

Summarizing, the vertical eddy diffusivity profile under unstable conditions used in this study is shown in Figure 4.6 and is given by:

$$\frac{K_{zz}}{w_* Z_i} = \begin{cases} 2.5(k\frac{z}{Z_i})^{4/3}[1-15(\frac{z}{L})]^{1/4} & ; \ 0<\frac{z}{Z_i}<0.05 \\ 0.021+0.408(\frac{z}{Z_i})+1.352(\frac{z}{Z_i})^2-4.096(\frac{z}{Z_i})^3+2.560(\frac{z}{Z_i})^4 & ; \ 0.05\leq\frac{z}{Z_i}\leq 0.6 \\ 0.2\ \exp[6-10(\frac{z}{Z_i})] & ; \ 0.6<\frac{z}{Z_i}<1.1 \\ 0.0013 & ; \ \frac{z}{Z_i}\geq 1.1 \end{cases} \qquad (4.26)$$

Near the ground the profile matches the similarity solution quite closely. The maximum value of the diffusivity occurs when $z/Z_i \simeq 0.5$ and has a magnitude $\simeq 0.21 w_* Z_i$. For typical meteorological conditions this corresponds to a diffusivity of $O(100\ m^2\ s^{-1})$ and a diffusion time defined by Z_i^2/K_{zz} of $O(5Z_i/w_*)$. While the diffusivities appear to be high they are in accord with the results of some recent boundary layer

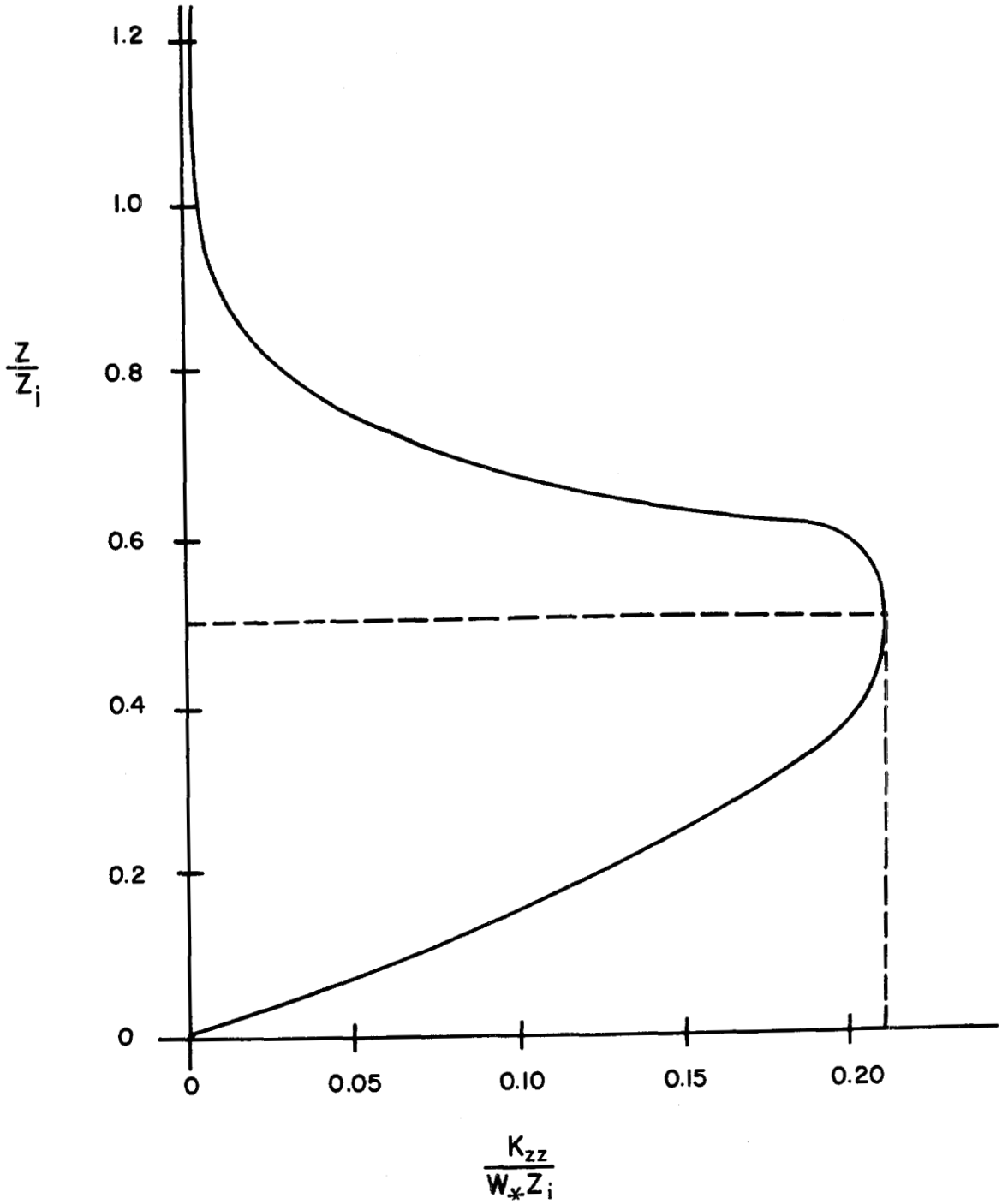

FIGURE 4.6

Vertical Turbulent Diffusivity Profile
Corresponding to (4.26)

models. Yamada (1977), for example, has observed maximum diffusivities of $O(100\ m^2\ s^{-1})$ when modeling the Wangara day 34 field experiment. Above the surface layer the observational evidence is inadequate to verify more than an order of magnitude estimate of the diffusivity. Clearly there is a need for more field data to establish the shape of the profile in the upper portions of the mixed layer.

A number of other models for unstable conditions have been used in airshed modeling studies, notably the formulations of O'Brien (1970) and Myrup and Ranzieri (1976). O'Brien's model defines a cubic polynomial variation of K_{zz} above the surface layer. Boundary conditions are established by matching a similarity solution at the top of the surface layer and fixing profile gradients at $z = |L|$ and Z_i. The expression for the diffusivity is given by

$$K_{zz} = K(Z_i)+\left[\frac{Z_i-z}{Z_i-|L|}\right]^2\left[K(|L|)-K(Z_i)+(z-|L|)\left\{\left.\frac{\partial K}{\partial z}\right|_{z=|L|}+2\left(\frac{K(|L|)-K(Z_i)}{Z_i-|L|}\right)\right\}\right] \tag{4.27}$$

where the height of the top of the surface layer is given by $z = |L|$. The similarity solution can be used to evaluate $K(|L|)$, the gradient $\partial K/\partial z$, and the maximum diffusivity in the mixed layer.

$$K_{zz}(|L|) = 5.0\ w_* Z_i \left(\frac{k|L|}{Z_i}\right)^{\frac{4}{3}} = 2u_*|L| \tag{4.28}$$

$$\left.\frac{\partial K_{zz}}{\partial z}\right|_{z=|L|} = 8.23\ k w_* \left(\frac{k|L|}{Z_i}\right)^{\frac{1}{3}} = 3.3\ u_* \tag{4.29}$$

Assuming $Z_i >> |L|$ the maximum diffusivity occurs at $z/Z_i \simeq 0.3$ and is given by

$$K_{zz}(\max) \simeq \frac{4}{27}\left[K_{zz}(|L|) + Z_i \left.\frac{\partial K}{\partial z}\right|_{z=|L|}\right] = 0.5\, u_* Z_i \tag{4.30}$$

Myrup and Ranzieri (1976) developed an approach based on similarity theory and a set of empirical formulae. For unstable conditions ($z/L<-5$) their profile is specified by

$$K_{zz} = k u_* z\left[1-15 \frac{z}{L}\right]^{\frac{1}{4}} q \tag{4.31}$$

where

$$q = \begin{cases} 1 & ; \frac{z}{Z_i} < 0.1 \\ 1.1 - \frac{z}{Z_i} & ; 0.1 \leq \frac{z}{Z_i} \leq 1.1 \end{cases} \tag{4.32}$$

For the above conditions the maximum diffusivity occurs at $z/Z_i \simeq 0.5$ with a value $K_{zz}(\max) \simeq 0.4 u_* Z_i$. Figure 4.7 presents a comparison of the three different diffusivity models for a set of typical meteorological conditions. A striking feature of the plot is the similarity, in the upper and lower regions of the mixed layer, between (4.27) and the O'Brien model. The maximum diffusivity for all models is quite large which in turn implies that the vertical mixing is quite rapid.

4.8 Vertical Diffusivity Profile for Neutral Conditions

Under neutral conditions the atmospheric lapse rate is adiabatic. Close to the ground the vertical eddy diffusivity profile can be based

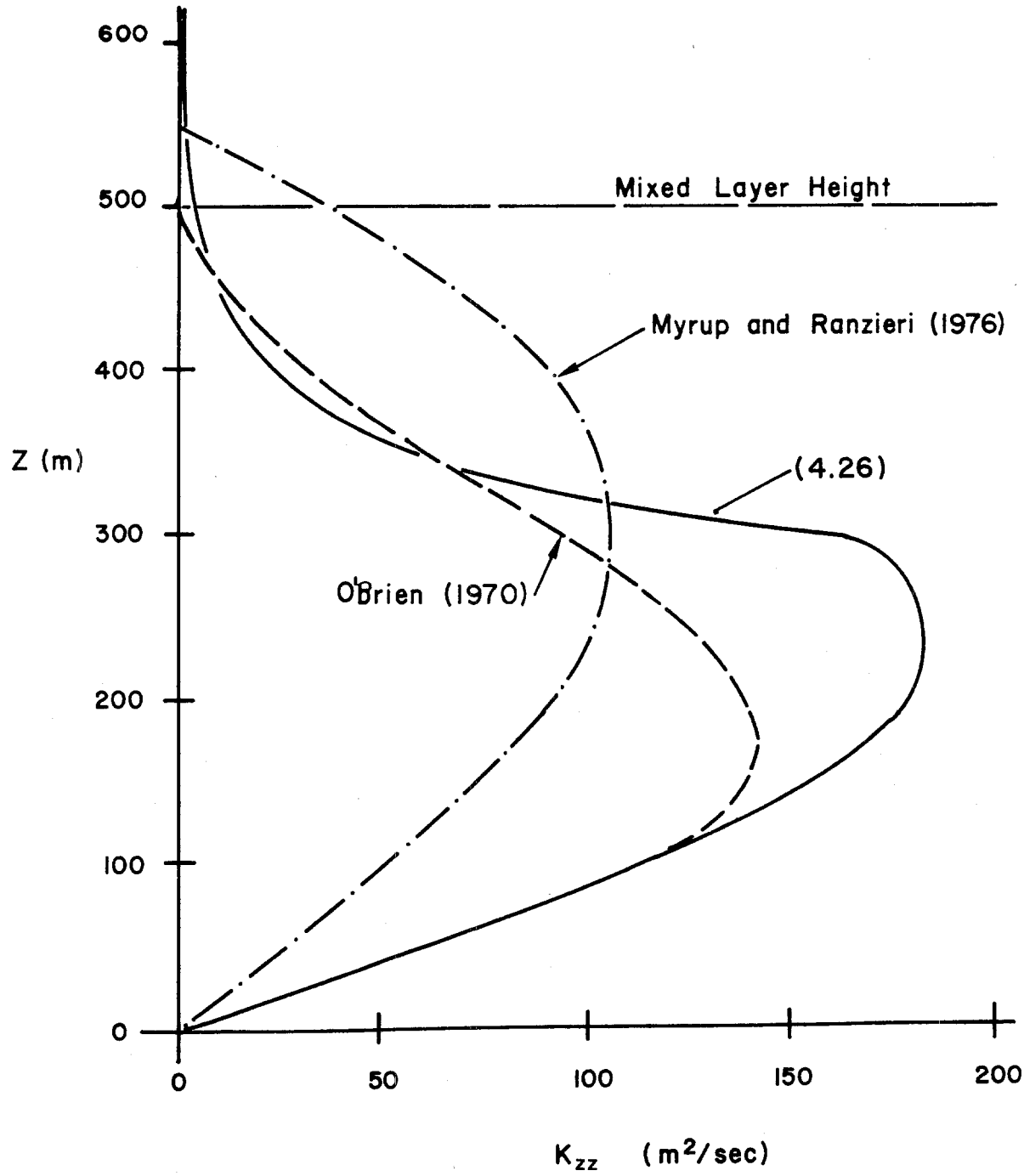

FIGURE 4.7

Comparison of Diffusivity Profiles for Unstable Conditions
(L = -30m, u_* = 0.5m/sec Z_i = 500 m)

on Monin-Obukhov similarity theory in which case $\phi_m = 1$ and $K_{zz}=ku_*z$. With this formulation K_{zz} increases without limit, clearly a physically unrealistic situation. Myrup and Ranzieri (1976) proposed a set of empirical 'roll off' functions for extending the model to altitudes above the surface layer.

$$K_{zz} = \begin{cases} ku_*z & ; \frac{z}{Z_i} < 0.1 \\ ku_*z(1.1 - \frac{z}{Z_i}) & ; 0.1 \leq \frac{z}{Z_i} \leq 1.1 \\ 0 & ; \frac{z}{Z_i} > 1.1 \end{cases} \qquad (4.33)$$

The form implied by (4.33) is some what arbitrary. Shir (1973) developed the following relationship from a study of a one-dimensional version of a turbulent transport model for extrapolation above the surface layer,

$$K_{zz} = ku_*z \exp[-\frac{8fz}{u_*}] \qquad (4.34)$$

where $f = 2\omega\cos(\phi)$is the Coriolis parameter corresponding to the latitude ϕ of the airshed. Under neutral conditions $L = \infty$ and so the Monin-Obkuhov length is not an appropriate choice for the vertical length scale. An alternative is to define the scale in terms of the Ekman layer height u_*/f. Another formulation was proposed by Businger and Ayra (1974) for neutral and stable conditions.

$$K_{zz} = \frac{ku_*z}{1+\alpha\phi_m(\frac{z}{L})} \exp[-|V_g| \frac{zf}{u_*^2}] \qquad (4.35)$$

where V_g is the geostrophic wind component orthogonal to the surface wind and α a constant. Note that if V_g is approximately $8u_*$, as has been predicted by the turbulence models of Wyngaard (1973) and Deardorff (1970), then both (4.34) and (4.35) are very similar. Lamb et al. (1975) calculated the eddy diffusivity of virtual particles by employing the same techniques described in the previous section. Their polynomial form for the neutral case is given by

$$K_{zz} = \begin{cases} \frac{u_*^2}{f}[7.396\text{x}10^{-4} + 6.082\text{x}10^{-2}(\frac{zf}{u_*}) + 2.532(\frac{zf}{u_*})^2 - 12.72(\frac{zf}{u_*})^3 \\ \qquad + 15.17(\frac{zf}{u_*})^4] & ; \ 0 \leq (\frac{zf}{u_*}) \leq 0.45 \\ \simeq 0 & ; \ (\frac{zf}{u_*}) > 0.45 \end{cases} \tag{4.36}$$

The predictions of the various models are shown in Figure 4.8 where the scale height has been replaced with

$$H = \begin{cases} 0.5\,\frac{u_*}{f} & \text{Shir (1973)} \\ Z_i & \text{Myrup and Ranzieri (1976)} \\ \frac{u_*}{f} & \text{Lamb et al. (1975)} \end{cases} \tag{4.37}$$

From an examination of the profiles it is clear that there are substantial differences in the magnitudes of K_{zz} predicted by the various models. Unlike the unstable case discussed in the previous section, the similarity solution and the form proposed by Myrup and Ranzieri (1976) appear to be much larger than the 'optimal' profile.

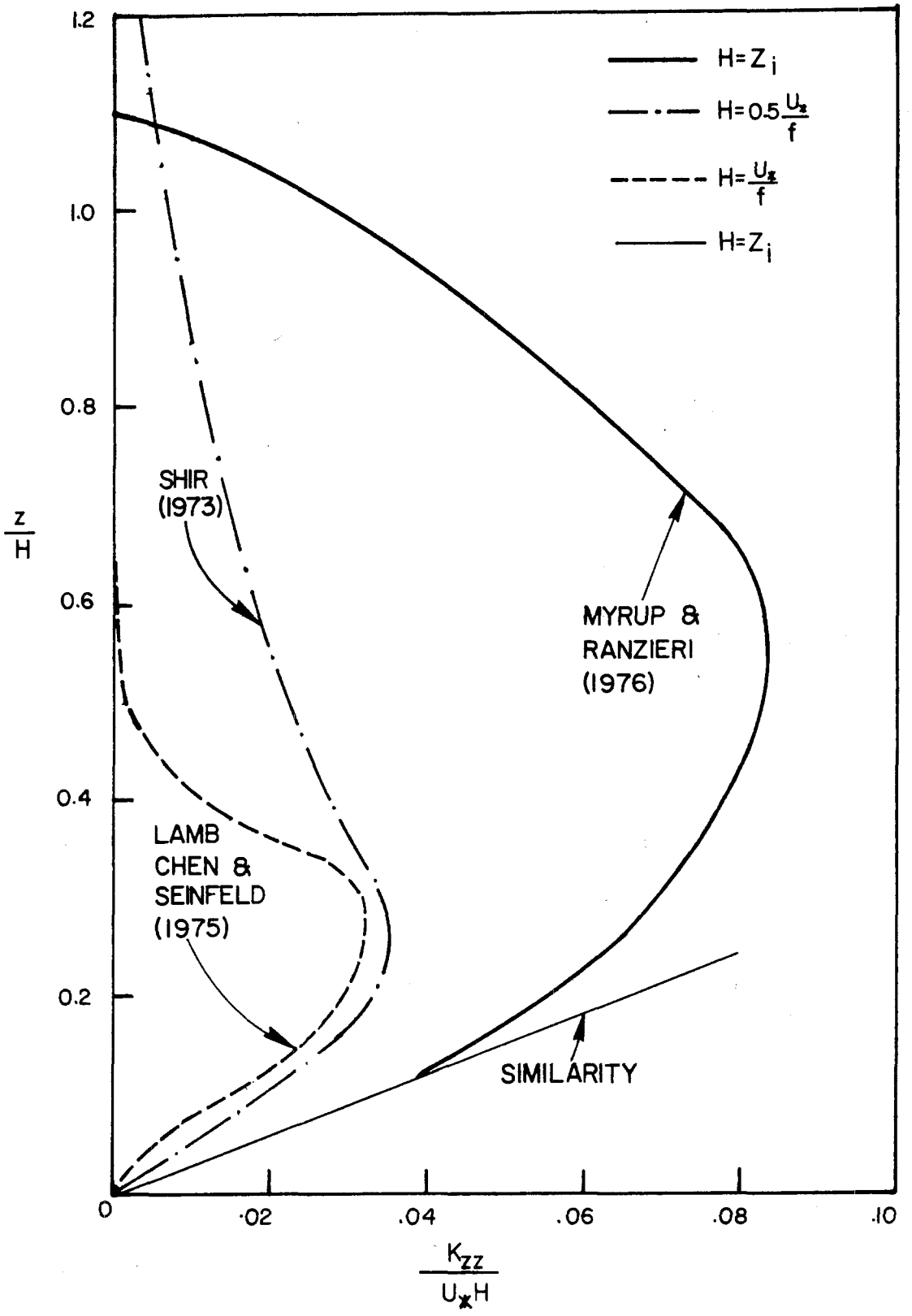

FIGURE 4.8

Comparison of Various Models for Vertical Diffusivity Profile Under Neutral Conditions

The diffusivity estimates at the top of the boundary layer predicted by the similarity solution are excessively large. The profiles of Shir (1973) and Lamb et al. (1975) are in quite close agreement up to a height of $z/H \simeq 0.3$. Above this elevation the polynomial profile is considerably smaller. For the purposes of the present model the vertical diffusivity profile under neutral conditions will be represented by (4.34).

4.9 Vertical Diffusivity Profile for Stable Conditions

Stable conditions, which typically occur at nighttime, are an important determinant of pollutant carryover effects. When $z/L > 0$ the nature of the mixing processes is quite different from either the neutral or unstable cases. For example, in a stably stratified shear flow, turbulent energy can be transferred by internal gravity waves. These waves can become unstable and break into isolated patches of turbulence. Wyngaard (1975) has postulated that wave-induced instabilities are probably responsible for a large fraction of scalar diffusion. The intermittent nature of these instabilities considerably complicates the modeling problem because waves, as well as the turbulent patches, can transport momentum. The models discussed below do not predict these local disturbances since they are intended to represent an ensemble average diffusivity.

Even under the most stable conditions it is likely that turbulent mixing occurs at the surface. For example the maximum shear at the surface under a light geostrophic wind, $V_g \simeq 1$ m-s^{-1}, is given by

$$\frac{\partial \bar{u}}{\partial z} = V_g \sqrt{\frac{f}{2\nu}} \tag{4.38}$$

where $f = 2\omega\cos(\phi)$ is the Coriolis parameter ($\simeq 10^{-4}$-s^{-1}) and ν is the kinematic viscosity ($\simeq 1.5 \times 10^{-5}$ m^2 s^{-1}). Assuming that the critical Richardson number for transition from a turbulent to a laminar flow is 0.25 then (4.3) can be combined with (4.38) to give an expression for the surface temperature gradient.

$$\frac{\partial \theta}{\partial z} > \frac{V_g^2 \, f \, T}{8g\nu} \tag{4.39}$$

For the stated conditions, the temperature gradient must exceed a physically unrealistic value of $\simeq 25^{o}$C/m to maintain a laminar flow. Far from the surface the conditions are much less stringent and laminar regimes can exist. In the surface layer, similarity theory can be used to give an expression for momentum and heat diffusivity. Using the field data of Businger et al. (1971) and (4.16) the expressions are given by

$$K_{zz}^{m} = \frac{ku_{*}z}{1 + 4.7(\frac{z}{L})} \tag{4.40}$$

and

$$K_{zz} = \frac{ku_{*}z}{0.74 + 4.7(\frac{z}{L})} \tag{4.41}$$

Again, as in the previous cases, the above results are not applicable for $z/L > 1$. Under stable conditions, mixing above the surface layer can be expected to be quite different from local free convection where the eddies scale with the depth of the mixed layer Z_i. When $z > L$ the appropriate scale for the eddies is L because buoyancy inhibits vertical excursions of air parcels over larger distances. This emphasizes that under stable conditions there is a minimum of turbulent exchange in the vertical direction. Businger and Ayra (1974) proposed a modification of (4.31) to extend the model above $z = L$.

$$K_{zz} = \frac{ku_* z}{0.74 + 4.7(\frac{z}{L})} \exp\left[-\left|\frac{V_g}{u_*}\right| \frac{fz}{u_*}\right] \tag{4.42}$$

The maximum value of the diffusivity for this model is given by the empirical expression.

$$K_{zz}(\max) \simeq 0.03 \frac{u_*^2}{f} (\frac{fL}{u_*})^{0.9} \tag{4.43}$$

For typical meteorological conditions the maximum diffusivity can be expected to be in the range 0.5 - 5 m^2/sec. The magnitude is considerably smaller than the equivalent values encountered under strongly unstable conditions. A limitation of the above formulation is the need for a knowledge of the geostrophic wind velocity V_g. Unless this is available, (4.42) must be solved simultaneously with the equations of motion for a steady-state barotropic layer. If the assumption $V_g \simeq 8u_*$,

discussed in the previous section, is employed then (4.43) can be written in the form

$$K_{zz} = \frac{ku_* z}{0.74 + 4.7(\frac{z}{L})} \exp\left[-\frac{8fz}{u_*}\right] \tag{4.44}$$

This model is quite similar to the Myrup and Ranzieri (1976) form except that the exponential decay is replaced by the 'roll-off' functions defined by (4.30). An alternative approach is to modify the O'Brien formula noting that the expression (4.27) enables a unique polynomial profile to be established by matching the applied boundary conditions. From (4.41) the slope at z = L is given by

$$\left.\frac{\partial K_{zz}}{\partial z}\right|_{z=L} = 0.025\ ku_* \tag{4.45}$$

Substituting this result into (4.27) and defining the scale height to be H, the vertical diffusivity variation is

$$K_{zz} = K(H)+\left[\frac{H-z}{H-L}\right]^2\left[K(L)-K(H)+(z-L)\left\{\left.\frac{\partial K}{\partial z}\right|_{z=L}+2\left(\frac{K(L)-K(H)}{H-L}\right)\right\}\right] \tag{4.46}$$

where $K(L) = 0.025ku_*L$. If K(H) is set equal to K(L) then (4.46) can be further simplified to

$$K_{zz} = 0.025\ ku_*L\left[1 + 0.025\left(\frac{z}{L} - 1\right)\left(\frac{H-z}{H-L}\right)^2\right] \tag{4.47}$$

The form and magnitude of the scale height H clearly depends on the meteorological conditions. Wyngaard (1975) concluded that turbulence

is confined to a layer of thickness H given approximately by

$$H = 0.22 \frac{u_*}{f} \sqrt{\frac{fL}{u_*}} \tag{4.48}$$

This result is the same form as the power law predicted by Zilitinkevich (1972) and, apart from a different constant $\simeq 0.74$, is identical to the Businger and Ayra (1974) K-Theory model. Within the airshed model the form (4.46) was adopted with $K(H) \simeq 0.05\ K(L) = 0.01\ ku_*L$. Above $z = H$, K_{zz} is held fixed at K(H) which results in diffusivities $0(0.1\ m^2\ s^{-1})$, a value consistent with the modeling studies of Yu (1977). The diffusivity profiles for the above models are very similar to the forms shown in Figure 4.8. Considering the magnitude of the diffusivities, the associated mixing times and grid cell spacing, the simplest profile is a constant value of $K_{zz} = K(L)$ for $0 < z < H$ and $K_{zz} = pK(L)$ for $z > H$ where p is a small fraction $\simeq 0.05$.

Evaluation, selection or development of a model for stable conditions is, at present, considerably hampered by a lack of suitable field data. An interesting topic for further research is to develop an understanding of the role of density stratification in inhibiting turbulent mixing and transport.

4.10 Horizontal Eddy Diffusion Coefficients

Completion of the eddy diffusion model requires specification of the horizontal components K_{xx}, K_{yy}. Unlike the vertical direction, the contribution from turbulent fluxes is small compared to the advection.

For typical urban meteorological conditions and grid cell spacings, a simple scale analysis indicates that:

$$\frac{\partial uc}{\partial x} >> \frac{\partial}{\partial x} K_{xx} \frac{\partial c}{\partial x} \quad ; \quad \frac{\partial vc}{\partial y} >> \frac{\partial}{\partial y} K_{yy} \frac{\partial c}{\partial y} \tag{4.49}$$

With this result it is evident that the model formulation for K_{xx}, K_{yy} is not as critical as in the case for K_{zz}. Liu et al. (1977) studied the influence of changes in K_{xx}, K_{yy} (0 - 500 m^2/sec) and concluded that the effect on concentration predictions for area wide averages is quite small, < 2%. This result should, however, be interpreted in the light of the observation that when simple numerical solution techniques are employed the effective diffusion coefficient K_e is the sum of two terms. One term, K_n, is due to the numerical truncation error and the other is the real physical component, K_p, i.e.

$$K_e = K_n + K_p \tag{4.50}$$

Unless special precautions are taken K_n can exceed K_p and so large changes in K_p do not influence K_e. As an extreme example the simple upwind difference scheme for the advection equation has $K_n = (u\Delta x - u^2\Delta t)/2 \simeq 0(1000\ m^2 s^{-1})$. A consequence of using more refined numerical techniques is that more attention must be given to K_p since $K_p > K_n$.

Many previous studies have either ignored the horizontal diffusion terms or have assumed, as in the case of Reynolds et al. (1973), a constant value $\simeq 50\ m^2\ s^{-1}$. The influence of stability and grid size was incorporated into the MacCracken et al. (1978) model using the scale dependent diffusion approach of Batchelor (1950) and Walton (1973).

The bases for the formulation adopted in this study are the classic work of Taylor (1938), the laboratory studies of Willis and Deardorff (1976b) and some suggestions by Lamb (1977). If $x_i(t)$ is the displacement of a particle in the ith direction due to an eddy velocity $u_i'(t)$ then the rate of change of dispersion is a stationary and homogeneous turbulent field given by

$$\frac{d\langle x_i^2(t)\rangle}{dt} = 2\langle x_i(t)u_i'(t)\rangle = 2\langle u_i'(t)^2\rangle \int_o^t R_{ii}(t-\tau)d\tau \qquad (4.51)$$

where $\langle\ \rangle$ represents an ensemble average and R_{ii} is the Lagrangian velocity correlation coefficient defined as

$$R_{ii}(t-\tau) = \frac{\langle u_i'(t)u_i'(\tau)\rangle}{\langle u_i'^2\rangle} \qquad (4.52)$$

From this expression the integral scale of the turbulence can be defined as

$$T_L = \int_o^\infty R(\xi)d\xi \qquad (4.53)$$

T_L is a measure of the time over which u_i' is correlated with itself. Now integrating (4.52) with respect to time gives

$$\langle x_i^2(t)\rangle = 2\langle u_i'(t)^2\rangle \int_o^t\int_o^{t'} R_{ii}(t-\tau)d\tau dt \qquad (4.54)$$

which in the limit of small and large times leads to the results

$$\langle x_i^2(t)\rangle = \begin{cases} \langle u_i'(t)^2\rangle t^2 & ; \ t \to 0 \ (t < T_L) \\ 2K_{ii}t & ; \ t \to \infty \ (t >> T_L) \end{cases} \tag{4.55}$$

Where

$$K_{ii} = \langle u_i'(t)^2\rangle \lim_{t\to\infty} \int_0^t R(\tau)d\tau \tag{4.56}$$

K_{ii} has the dimensions of a diffusion coefficient, since for $t>>T_L$

$$K_{ii} = \frac{1}{2}\frac{d\langle x_i^2(t)\rangle}{dt} \tag{4.57}$$

Measurements of T_L in the atmosphere are extremely difficult and it is not at all clear whether the condition $t >> T_L$ holds for urban scale flows. The time t in the case of the present model is equal to the numerical time step $\Delta t \sim 0(1000$ sec). Csanady (1973) indicates that a typical eddy which is generated by shear flow near the ground has a Lagrangian time-scale of the order of 100 sec. Lamb and Neiburger (1971) in a series of measurements in the Los Angeles Basin estimated the Eulerian time-scale T_e to be ~ 50 sec. In a discussion of some field experiments Lumley and Panofsky (1964) suggested that $T_L < 4\ T_e$ and so an approximate upper limit of T_L for the Los Angeles data is 200 seconds. If the averaging interval is selected to be equal to the travel time then an approximate value for K_H can be deduced from the

measurements of Willis and Deardorff (1976b). Their data indicate that for unstable conditions (L > 0) and a travel time $t = 3Z_i/w_*$

$$\frac{\langle y(t)^2 \rangle}{Z_i^2} \simeq 0.64 \tag{4.58}$$

Employing the previous travel time estimate and combining this result with (4.58) gives

$$K_H = K_{xx} = K_{yy} = \frac{1}{6} \frac{y(t)^2}{Z_i^2} w_* Z_i \simeq 0.1 \, w_* Z_i \tag{4.59}$$

This latter result can be expressed in terms of the friction velocity, u_* and the Monin-Obukhov length L

$$K_H \simeq 0.1 \, Z_i^{\frac{4}{3}} (-kL)^{-\frac{1}{3}} u_* \tag{4.60}$$

For a range of typical meteorological conditions this formulation results in diffusivities O(50-100 m^2/sec). Some typical results, plotted in Figure 4.9, are in quite close agreement with field measurements and the formulae recommended by Briggs (1974) for city conditions. In the above model K_H varies as a function of the surface conditions at different spatial locations but is assumed to be invariant with height. This latter assumption is based on the observation that the energy dissipation rate $\varepsilon(z)$ is a weak function of elevation with $K_H \sim \varepsilon^{1/3}$ and for most practical purposes can be ignored.

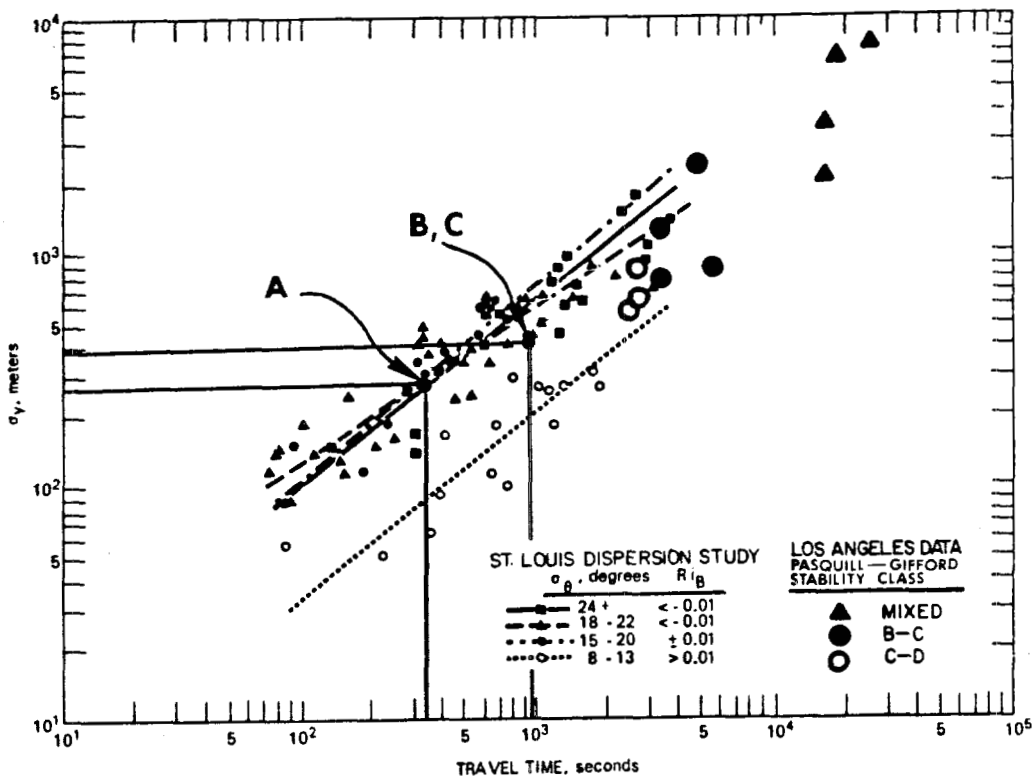

FIGURE 4.9

Cross Wind Standard Deviation σ_y as a Function of Travel Time
(Labeled points correspond to examples in Table 4.4)
(St. Louis data derived from McElroy and Pooler, 1968; Los Angeles data derived from Drivas and Shair, 1975; Shair, 1977)

TABLE 4.4

Typical Horizontal Eddy Diffusivities
and Cross Wind Standard Deviations

Stability Class	z_o (m)	L (m)	$\bar{u}$ (m/sec)	u_* (m/sec)	Z_i (m)	w_* (m/sec)	K_H (m^2/sec)	σ_y (m)	Travel Time (sec)
A	0.5	-14	2	0.42	300	2.44	73	231	368
B	1.08	-29	2	0.43	500	1.58	79	387	949
C	1.75	-250	4	0.83	500	1.48	74	387	1013

4.11 Application and Validity of the Diffusion Coefficients

Previous sections have been devoted to surveys and a detailed discussion of the various diffusivity expressions embedded in the airshed model. The inputs required to calculate the components of K are as follows: surface wind speed u, roughness height z_o, solar intensity I, mixed layer depth Z_i, latitude and vertical extent of the airshed. A summary of the steps in the calculational procedure for each stability regime is presented in Figure 4.10.

In constructing the models for K_{zz} and K_H a number of critical assumptions were invoked. The first was to assume that the temporal variations in the components of K rapidly adjust to changes in the meteorological condition. A formal validation of this condition would be quite complex. As an alternative it is useful to observe that the characteristic time scales for unstable, neutral and stable conditions (Z_i/w_*, Z_i/u_*, L/u_*) are all in the range of 100-500 seconds. The temporal scales of the processes driving the boundary layer dynamics are much longer, particularly if it is noted that most meteorological data used in airshed modeling studies are hourly averaged. An implication of this discussion is that the turbulence levels change with time but in such a way that at any instant the flow can be considered stationary. Certain non-stationary conditions can exist, however, at sunrise and sunset.

An assumption, possibly more restrictive than stationarity, is that within the surface grid cells an equilibrium state has been assumed between the fluxes and gradients. As air parcels move over the airshed they experience the effects of changes in surface roughness. The adjustment process is relatively slow, implying that the transition

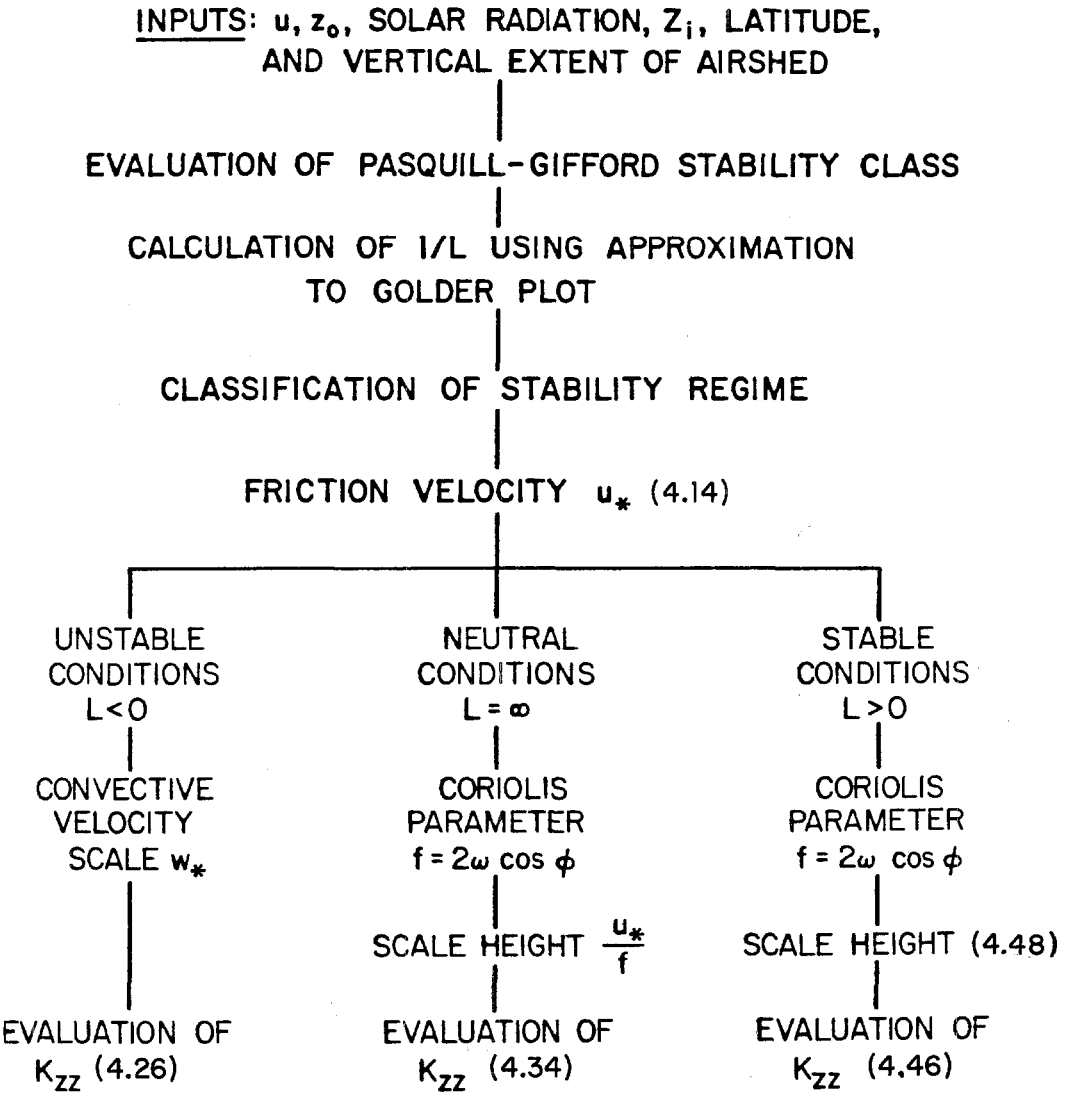

FIGURE 4.10

Summary of Calculational Procedure to Evaluate the Vertical Variation of K_{zz}

region occupies a significant portion of the area above the new surface. In the transition region the diffusivities are a function of the downwind fetch from the edge of the change as well as the parameters discussed previously. Mulhearn (1977) has recently developed a set of relationships between the surface fluxes and mean profiles of concentration downwind of a change in z_o. The results indicate that if horizontal homogeneity is assumed within each computational cell the K_{zz} values will be overestimated for the case of a rough to smooth transition and underestimated for the opposite case. With a sufficiently large grid cell spacing the effects of inhomogeneities are small.

4.12 Conclusions

Turbulent diffusion is an important process which influences the airshed concentration distributions. In this chapter the parameterization of the components of K has been presented. A different model for each of the stable, neutral and unstable conditions was introduced. Particular emphasis was given to developing models for K_{zz}, K_H under convectively driven conditions. In all cases the guiding principle in model formulation was to employ only those data which are commonly available or readily estimated. Within the airshed model the diffusivity expressions have been implemented as separate modules and so incorporation of any modifications is quite straightforward.

CHAPTER 5

CONVECTIVE DOWNMIXING OF PLUMES IN A COASTAL ENVIRONMENT

(Reprinted from J. Applied Meteorology, 20, 1312-1324)

1312 JOURNAL OF APPLIED METEOROLOGY VOLUME 20

Convective Downmixing of Plumes in a Coastal Environment

GREGORY J. MCRAE, FREDRICK H. SHAIR[1] and JOHN H. SEINFELD[1]

Environmental Quality Laboratory, California Institute of Technology, Pasadena 91125

(Manuscript received 30 April 1981, in final form 2 August 1981)

ABSTRACT

This paper describes the results of an atmospheric tracer study in which sulfur hexafluoride (SF_6) was used to investigate the transport and dispersion of effluent from a power plant located in a coastal environment. The field study demonstrated that material emitted into an elevated stable layer at night can be transported out over the ocean, fumigated to the surface, and then be returned at ground level by the sea breeze on the next day. At night when cool stable air from the land encounters the warmer ocean convective mixing erodes the stable layer forming an internal boundary layer. When the growing boundary layer encounters an elevated plume the pollutant material, entrained at the top of the mixed layer, can be rapidly transported in ~20 min to the surface. Various expressions for the characteristic downmixing time ($\lambda = Z_i/w_*$) are developed utilizing the gradient Richardson number, the Monin-Obukhov length and turbulence intensities. Calculations using these expressions and the field data are compared with similar studies of convective mixing over the land.

1. Introduction

A major influence on pollutant dispersion and transport in coastal environments is the presence of land/sea breeze circulation systems. Unfortunately the characterization of turbulent transport is complicated by the presence of flow reversals and differing atmospheric stabilities. Since many large sources are located in shoreline environments, it is important to understand the mixing characteristics within the boundary layer. A field experiment designed to determine the fate of pollutants emitted into the offshore flow associated with a land/sea breeze circulation system, was carried out by Shair *et al.* (1981). In that study it was found that tracer material emitted into an elevated stable layer at night could be transported out over the ocean, fumigated to the surface, and then be returned at ground level by the sea breeze on the next day. The objectives of this work are to examine the vertical transport processes responsible for this rapid downmixing and to characterize the mixing rates within the internal boundary layer formed when cool air from the land is advected out over a warm ocean surface.

2. Description of field experiment

Because of the complexity of atmospheric flows, the only direct way to relate the emissions from a particular source to observed concentrations is to tag the source exhaust gases so they can be uniquely identified. Over the last few years a variety of atmospheric tracers, including sulfur hexafluoride (SF_6), fluorescent particles, halocarbons and deuterated methane, have been used in transport and diffusion studies. Sulfur hexafluoride was used in this experiment because it is gaseous, physiologically inert, chemically stable, and easily detected using electron-capture gas chromatography (Simmonds *et al.*, 1972). Drivas and Shair (1974), Lamb *et al.* (1978a,b) and Dietz and Cote (1973) have successfully demonstrated the utility of SF_6 as a tracer in large-scale field studies. Current analysis techniques have achieved detection limits of 2×10^{-13} parts SF_6 per part of air. From a practical point of view both the release techniques and sampling protocols are well established and reliable.

Each experiment was carried out by injecting the tracer gas into the number 4 stack of the Southern California Edison El Segundo power plant located on the shore of Santa Monica Bay (Fig. 1). This particular chimney is 61 m high and 4.3 m in diameter. The tracer was released at a time when the flow, at the effective stack height, was offshore. Before each experiment an initial estimate of the plume rise was determined using Briggs' formulas (Briggs, 1969; 1975) for neutral conditions. For the particular load conditions (0.57 of capacity), an exhaust gas temperature of 365 K and a gas flow rate of 230 m^3 s^{-1}, the plume rise was estimated to be 250 m. This information, together with the vertical wind distribution obtained from pibal releases, was used to establish the time to initate the tracer injection so that the material was released into the offshore flow. After the experiment a more detailed calculation,

[1] Department of Chemical Engineering.

0021-8952/81/111312-13$07.25

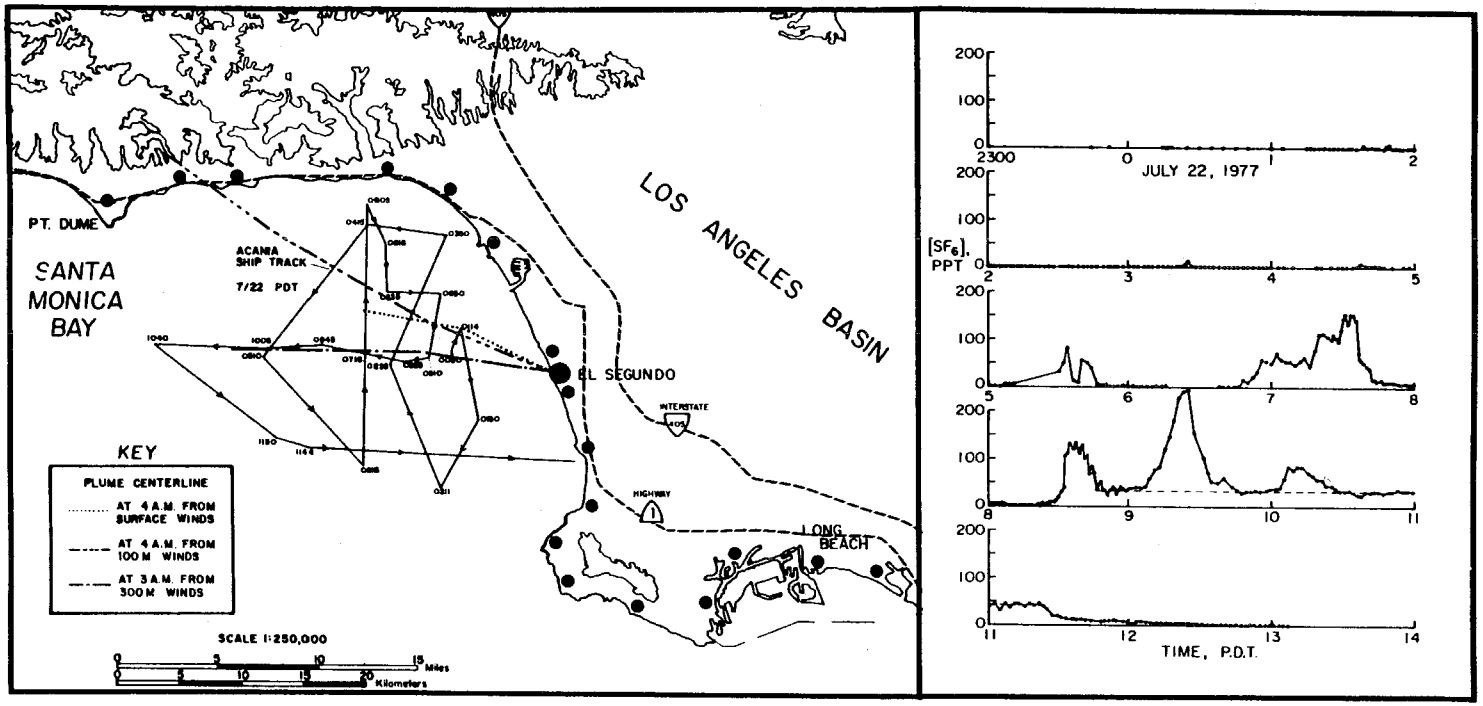

FIG. 1. Sulfur hexafluoride (SF_6) measurements made on board R/V *Acania* 22 July 1977 coordinated with ship course and possible plume trajectories derived from surface and elevated wind measurements: (●), release site; (●) onshore monitoring sites.

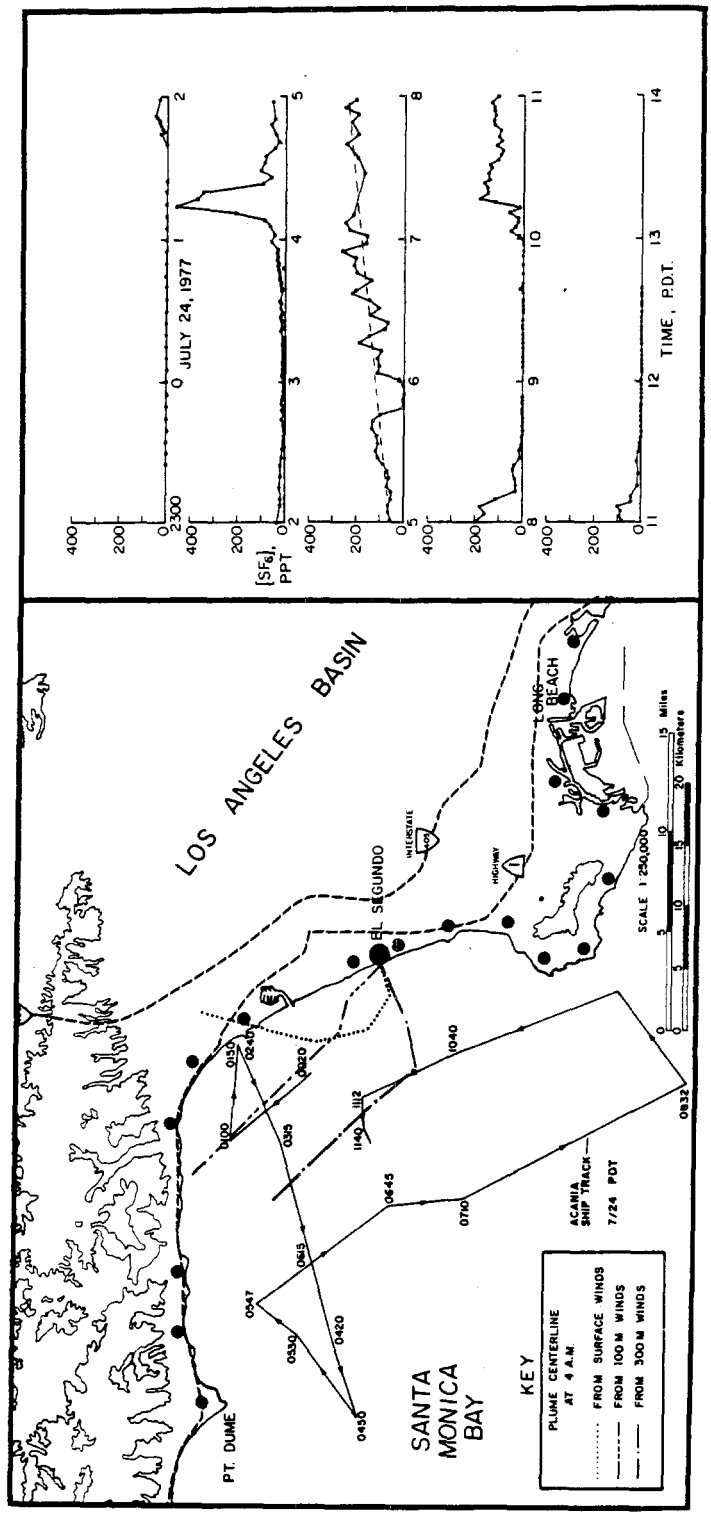

FIG. 2. Sulfur hexafluoride (SF_6) measurements made on board R/V *Acania* 24 July 1977 coordinated with ship course and possible plume trajectories derived from surface and elevated wind measurements: (●) release site; (●) onshore monitoring sites.

accounting for the actual vertical variations in wind and temperature profiles, was carried out using the Schatzmann (1979) integral plume rise model, using meteorological data from Schacher *et al.* (1978). During the first test, on 22 July 1977, 90 kg of SF_6 was released at a rate of 5.0 g s^{-1} from 0005–0500 (all times PDT). During the second test 245 kg of SF_6 were released, at a higher rate of 13.6 g s^{-1}, from 2303 on 23 July 1977 until 0400 on 24 July.

The amount and release rates for each experiment were selected so that there was sufficient material to distinguish the source from the background at the maximum sampling distance. If the total amount of tracer released during each experiment were to be uniformly distributed throughout a volume of 1600 $km^2 \times 300$ m (i.e., the area of Santa Monica Bay times the estimated plume rise above the ocean surface), then the average tracer concentration would have been 50 ppt[2], a value well above both the detection limit and normal background levels. Most of the current world background concentration of <0.5 ppt is a result of leakages from high-voltage power transformers and switching systems where SF_6 is used for corona discharge suppression.

Hourly averaged air samples were collected continuously, from 0500–1700 during each of the test days, at 29 coastal sites located from Ventura to Corona del Mar (Figs. 1 and 2). This was to observe the tracer flux across the coast during the sea breeze on the day following the nighttime release. Subsequent mass balance calculations using these measurements were able to account for virtually 100% of the material released during both experiments (Shair *et al.*, 1981). Samples were analyzed using the methodology described in Lamb *et al.* (1978a,b). In addition, grab samples were collected every 5 min on board a ship traversing Santa Monica Bay and analyzed using portable electron-capture gas chromatographs. This sampling protocol provided rapid feedback on the tracer concentrations and plume position during each experiment. The measurements taken on board the ship are shown in Figs. 1 and 2. Sampling on board the ship was started 1 h before each release so that any possible background levels could be detected. All samples were collected in 30 cm^3 plastic syringes and were analyzed within one day of each experiment. At the coastal monitoring sites battery-powered sequential samplers were used to determine the hourly averaged SF_6 concentration levels. In addition automobile sampling traverses were conducted periodically along coastal highways between 1000–1427 on 22 July and between 0235–1540 on 24 July. Grab samples were collected at 0.8–3.2 km intervals along the coastal highway between Redondo Beach and Malibu. The results from the shore measurements and automobile traverses were used by Shair *et al.* (1981) to calculate the flux of SF_6 across the coast.

The tracer experiments were carried out in collaboration with investigators from the Environmental Physics Group at the Naval Postgraduate School in Monterey, California. The research vessel *Acania* was used as a platform to collect meteorological data in the vicinity of Santa Monica Bay. The ship was equipped with a complete suite of meteorological equipment capable of multilevel measurements (4.2, 7.0 and 22.5 m above the ocean) of mean and fluctuating quantities. Since complete details of the instrumentation can be found in Houlihan *et al.* (1978) and Schacher *et al.* (1978), the material will not be repeated here. For the particular study of the mixing rates over the ocean, measurements were made of sea surface temperature T_s, air temperature T_a, humidity/dew point T_d, true wind speed u, direction θ, and temperature inversion height Z_i. The wind direction θ is particularly useful since it can be used to differentiate local (land and sea breeze) circulations. Both the wind speed and direction have been corrected to account for the ship motion. In addition, during the period 19–26 July, 14 radiosondes were released to examine the vertical temperature structure. During each tracer experiment pibals were released each hour at a site close to the release point so that the horizontal winds as a function of elevation could be determined. Observations made at the 100 and 300 m levels were used to calculate plume trajectories from the release point. Some of these results are superimposed on Figs. 1 and 2. The complete data sets describing the meteorological conditions are contained in the reports by Schacher *et al.* (1978, 1980). For convenience a summary of key information from these sources, together with the calculated virtual heat flux Q_0, is presented in Table 1.

Since the pattern of results observed on board R/V *Acania* on both days were similar it suffices to discuss the experiment conducted on 22 July. A more detailed discussion of the concentration levels measured at the coastal monitoring stations is contained in Shair *et al.* (1981). Prior to 0530 PDT, when the mixing depth was below 200 m, the ship passed under the calculated plume positions at 0100, 0325 and 0438 and no significant concentrations of SF_6 were observed. At 0530, when the ship was 6.4 km south of the plume, the first significant peak (80 ppt) was recorded at a time when the mixed layer was growing above the 200 m level. From 0600 onward all the concentration peaks at 0730, 0835 and 0925 were observed when the ship was in the vicinity of the plume and the mixed-layer height was above 200 m. From 0830 to 1130 the SF_6 exceeded 20 ppt and the ship was always within 3 km of the plume. Lower concentrations were observed when the ship

[2] Parts per trillion.

TABLE 1. Basic meterological data collected during the period 19–26 July 1977.*

Date	Time (PDT)	Humidity (%)	T_s (°C)	T_a (°C)	T_s-T_a (°C)	Q_0 (10^3 m s^{-1} K)	Date	Time (PDT)	Humidity (%)	T_s (°C)	T_a (°C)	T_s-T_a (°C)	Q_0 (10^3 m s^{-1} K)
19	0000	90	16.4	19.1	−2.75	8.7	21	0945	89	17.5	18.8	−1.26	2.8
19	0020	92	16.0	18.5	−2.53	5.6	21	1005	88	17.4	18.2	−0.72	2.1
19	0100	92	16.0	17.6	−1.61	2.4	21	1025	88	17.6	18.5	−0.38	0.8
19	0140	93	15.9	16.7	−0.80	0.7	21	1045	88	17.6	18.4	−0.80	1.6
19	1620	79	18.7	21.1	−2.39	14.9	21	1105	89	17.4	17.7	−0.33	2.1
19	1650	79	18.5	21.1	−2.57	19.4	21	1305	90	17.7	17.7	−0.05	2.2
19	1710	79	18.3	21.0	−2.72	18.8	21	1325	90	17.5	17.7	−0.24	3.0
19	1730	79	18.1	20.9	−2.77	19.4	21	1345	90	17.5	17.9	−0.40	3.0
19	2000	84	18.2	18.8	−0.59	5.8	21	1405	90	17.7	18.2	−0.54	4.6
19	2040	87	17.5	19.8	−2.26	11.8	21	1505	88	18.2	18.9	−0.68	7.9
19	2120	87	17.5	19.8	−2.26	7.3	21	1620	86	18.3	18.8	−0.47	6.6
19	2140	87	17.6	19.9	−2.33	7.5	21	1720	85	18.0	18.7	−0.69	6.4
19	2200	87	17.6	19.8	−2.20	8.9	21	1945	79	18.6	19.9	−1.30	10.4
							21	2030	85	18.2	19.8	−1.66	7.5
20	0700	86	17.0	18.7	−1.67	9.9	21	2110	84	18.3	19.7	−1.35	3.4
20	0740	86	17.3	19.2	−1.93	8.5	21	2130	85	18.3	19.5	−1.21	3.8
20	0900	85	17.8	19.3	−1.46	4.6							
20	0920	85	17.9	19.3	−1.42	4.4	22	0550	93	17.1	17.3	−0.19	0.5
20	1240	78	19.0	20.2	−1.20	5.2	22	0610	94	16.9	17.2	−0.34	0.7
20	1300	79	19.0	19.8	−0.78	3.2	22	0710	96	16.5	17.3	−0.77	0.5
20	1320	88	19.0	19.7	−0.63	2.3	22	0730	97	16.6	17.3	−0.68	0.4
20	1800	84	18.8	18.2	0.56	−3.9	22	0750	97	16.5	17.3	−0.76	0.5
20	1900	83	18.3	17.8	0.48	−4.3	22	0810	97	16.7	17.3	−0.57	0.3
20	1920	84	18.4	17.7	0.65	−6.4	22	0830	96	16.6	17.3	−0.72	2.1
20	1940	84	18.3	18.4	−0.12	2.5	22	0910	97	16.5	17.3	−0.78	1.4
20	2000	85	18.2	18.3	−0.09	2.1	22	0930	97	16.6	17.3	−0.71	0.8
20	2020	86	17.7	18.3	−0.56	3.7	22	1030	96	17.1	18.5	−1.46	4.6
20	2040	87	17.9	18.3	−0.45	2.5	22	1050	94	17.5	18.6	−1.09	1.4
20	2120	88	17.8	18.2	−0.41	2.3							
20	2140	89	17.7	18.2	−0.53	2.8	23	1440	87	19.2	18.2	0.92	−1.4
20	2220	90	17.6	19.0	−1.38	4.8	23	1505	85	19.5	18.7	0.76	−2.9
20	2230	91	17.6	18.4	−0.83	2.7	23	1645	83	19.9	20.4	−0.43	5.1
20	2300	91	17.2	18.2	−1.00	2.9	23	1725	85	19.1	19.2	−0.08	1.9
							23	1745	87	18.8	19.1	−0.28	1.2
21	0000	94	16.6	17.2	−0.63	2.5	23	2340	90	18.5	18.0	0.53	−0.5
21	0040	94	16.2	16.9	−0.70	2.5							
21	0100	93	15.9	16.6	−0.72	2.0	24	0040	91	19.1	18.6	0.50	−0.7
21	0405	98	16.2	17.7	−1.46	6.3	24	0100	90	19.0	18.6	0.39	−0.5
21	0425	97	16.4	18.1	−1.65	6.2	24	0120	90	19.0	18.7	0.28	−0.3
21	0445	96	16.8	18.4	−1.57	6.0	24	0240	87	19.0	18.7	0.25	−0.3
21	0505	94	17.1	18.4	−1.33	4.5	24	0300	86	19.0	18.7	0.28	−0.3
21	0545	91	17.4	18.2	−0.81	2.2	24	0420	88	18.8	18.7	0.06	0.0
21	0605	89	17.4	18.3	−0.84	0.7	24	1000	78	19.3	19.2	0.06	0.5
21	0645	89	17.3	18.3	−0.96	2.0							
21	0705	89	17.3	18.2	−0.86	2.4	25	2220	83	19.3	17.7	1.57	−8.8
21	0845	91	17.7	19.0	−1.31	6.4	25	2320	84	19.1	17.9	1.27	−7.1
21	0905	89	17.8	18.9	−1.14	3.9	26	0420	90	18.6	18.1	0.49	−0.2

* Source: Schacher *et al.* (1980).

and the plume separation increased to more than 15 km. The only major difference between the two tests was the increased wind speeds and mixing heights on 23–24 July. While this, together with the wind shear, enhanced the horizontal dispersion of SF_6 there were no significant differences in the observed vertical mixing rates.

Although the power plant effluent was emitted well above the surface into an elevated stable layer where vertical mixing could be expected to be quite small, large amounts of tracer suddenly appeared at the sampling sites close to the ocean surface. The remaining sections of this work are devoted to a discussion of the reasons for the rapid transport of tracer material to the surface.

3. Vertical mixing over the ocean

The problem of dispersion and transport near coastlines and large lakes has received considerable attention in the literature (See, e.g., Lyons, 1975; Businger, 1975; Misra, 1980; Raynor *et al.*, 1980 Orgill, 1981). The purpose of this section is to examine the results from prior observations applicable to the present field experiment, since few, if any, studies have been made of convective activity over the ocean at night. Since the ocean temperatures during the experiments were greater than that of the air, it can be seen that the conditions are similar to those observed over the land during the day.

Under the action of buoyancy forces induced by

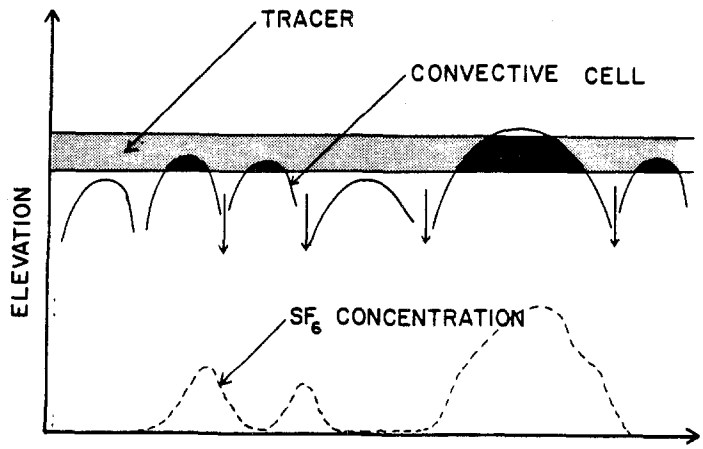

FIG. 3. Intermittent entrainment of tracer material by convective cells.

surface heating, parcels of warm air, displaced by mechanical turbulence, rise all the way through the mixed layer and impinge at the inversion base. To compensate for these vertical motions, zones of sinking air fill the spaces between rising air parcels. Close to the top of the mixed layer the net flux is directed downward. Adiabatic transport of air through the capping inversion would produce the negative flux, which in turn suggests a mechanism for substantial entrainment of air and tracer material into the mixed layer from above (Ball, 1960; Kaimal *et al.*, 1976; Deardorff *et al.*, 1980). The regions of upward flux are obviously thermals which originate near the surface shear layer and the transport is thus occurring over a scale Z_i.

The updraft regions in the thermals resembles the three-dimensional convection patterns observed by Frisch *et al.* (1975) with dual-Doppler radar. Kaimal *et al.* (1976) suggested that the rising air spreads out laterally as it reaches the inversion base, producing a domelike depression at the interface, and returns as a downdraft along the "side wall" of the thermal. These structures can be observed with acoustic sounders and radars. Arnold *et al.* (1975) found that domelike structures are colocated with the thermals detected simultaneously by an acoustic sounder. The strong returns from the side walls indicate the presence of entrained air from the inversion. The inverted U structures in the vertical section and the doughnut-shaped patterns in plan views observed by Hardy and Ottersten (1969), Konrad (1970), Arnold and Rowland (1976) and Agee and Chen (1973) in radar returns indicate the presence of convective cells.

Arnold and Rowland (1976) conclude that most of the entrainment takes place along the top of the dome. Here either the Kelvin-Helmholtz instability or wavelike overturning of the dome structures could provide the mechanism for entrainment. This process is illustrated in Fig. 3 where the tops of the convective cells can rise to the elevation of the SF_6. Entrainment of this material and its subsequent transport to the surface lead to the large concentration increases. Areas of low concentration would then result when the ship went beyond the bounds of the cloud or when the convective cells did not reach the height of the tracer. A detailed examination of the mechanism of entrainment and mixed-layer growth is beyond the scope of this work and for details the reader is referred to Stull (1973), Venkatram (1976), Zeman and Tennekes (1977), Heidt (1977) and Deardorff (1978). Convective entrainment has been studied in the laboratory by Willis and Deardorff (1976a), Manins (1977) and Deardorff *et al.* (1980). The characteristic separation distance of the thermals given by Kaimal *et al.* (1976) is $1.3-1.4Z_i$ with the diameter-to-depth ratio for the Rayleigh cells being of the order of 40:1 (Agee and Chen, 1973).

With this background it is now possible to advance an explanation of the findings from the tracer experiments. When the cool stable air from the land encounters the warmer ocean surface, convective mixing begins to erode the overlying stable layer forming an internal boundary layer (Fig. 4). (The growth of this layer as a function of distance from the shore can be seen in the acoustic sounder traces.) Convective mixing in the surface layer entrains air from the stable layer aloft causing the inversion base to rise from the surface. Heating of the mixed layer is due to the combined effects of an upward heat flux from the ocean and a downward flux from the warmer air in the inversion. Continued growth of the mixed layer ultimately leads to a situa-

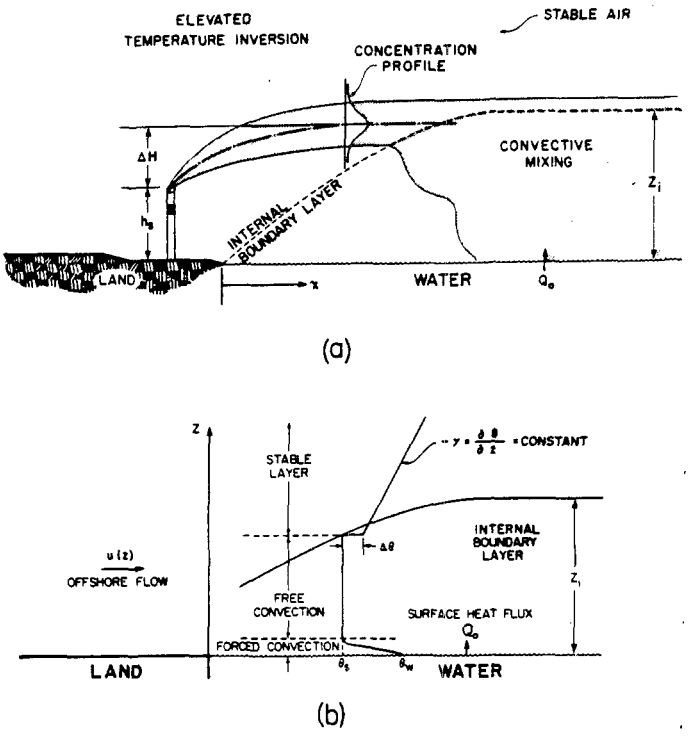

FIG. 4. Schematic representation of (a) fumigation process and (b) notation for mixing model.

tion where the internal boundary layer intercepts the elevated plume and the tracer materials. Since below the inversion base the mixing is rapid, the entrained SF_6 is quickly transported to the surface. Except for the strength of the convective mixing, the conditions of the experiment are similar to those that occur over the land during the day. Subsequent sections of this work are devoted to an estimate of the rate at which the tracer material is transported to the surface.

4. Mixing times under convective conditions

Under convective conditions a variety of interacting processes are involved in the mixing within the boundary layer. The relative role of buoyancy $\overline{w'T_v'}$, in comparison with the transfer of energy from the mean motion $\overline{u'w'}\partial\bar{u}/\partial z$, can be expressed in terms of the flux Richardson number R_f (Monin and Yaglom, 1971; Kraus, 1972), as

$$R_f = \frac{\frac{g}{T}\overline{T_v'w'}}{\overline{u'w'}\frac{\partial \bar{u}}{\partial z}}, \quad (1)$$

where T_v is the virtual temperature. A more commonly used expression is the gradient Richardson number Ri

$$\mathrm{Ri} = \frac{g\left(\frac{\partial \hat{T}_v}{\partial z} + \Gamma\right)}{T_v\left(\frac{\partial \bar{u}}{\partial z}\right)^2} = \frac{g}{\theta_v}\frac{\frac{\partial \hat{\theta}_v}{\partial z}}{\left(\frac{\partial \bar{u}}{\partial z}\right)^2} = \frac{N^2}{\left(\frac{\partial \bar{u}}{\partial z}\right)^2}, \quad (2)$$

where N is the Brunt-Väisälä frequency, θ_v the potential temperature, and Γ the adiabatic lapse rate. The relationship between R_f and the more easily measured Richardson number Ri is simply $R_f = \alpha\,\mathrm{Ri}$, where α is the ratio of the turbulent eddy diffusion coefficients for heat and momentum. Under a spatial homogeneity assumption temporal changes in the total mean kinetic energy are negligible if synoptic and mesoscale forces driving the boundary layer vary slowly (Caughey *et al.*, 1978). In particular, if the time scales for the large-scale processes are long compared to the time required for the boundary layer to adjust then the rate of change of turbulent kinetic energy per unit mass is negligible. If the contribution from the flux divergence term in the energy equation is small,

TABLE 2. Additional data and calculated results for period 19–26 July 1977.*

Date	Time (PDT)	u (m s^{-1})	θ (K)	Z_i/L	u_* (m s^{-1})	T_* (K)	Z_i (m)	w_* (m s^{-1})	λ (min)
19	0000	1.5	283	−4.840	0.060	−0.117	280	0.436	11
19	0020	1.0	308	−8.206	0.044	−0.104	330	0.397	14
19	0100	0.5	317	−18.190	0.025	−0.075	320	0.296	18
19	0140	0.3	11	−29.206	0.014	−0.035	190	0.166	19
19	1620	3.1	294	−1.125	0.112	−0.077	470	0.585	13
19	1650	3.9	272	−0.754	0.142	−0.085	500	0.663	13
19	1710	3.6	275	−0.929	0.132	−0.093	490	0.659	12
19	1730	3.7	285	−0.889	0.136	−0.096	480	0.665	12
19	2000	4.4	277	−0.216	0.156	−0.023	500	0.477	17
19	2040	3.0	280	−1.134	0.108	−0.082	540	0.597	15
19	2120	1.5	5	−4.174	0.060	−0.092	590	0.525	19
19	2140	1.5	318	−4.291	0.060	−0.096	600	0.534	19
20	0700	3.6	285	−0.542	0.129	−0.051	160	0.369	7
20	0740	2.5	260	−1.433	0.089	−0.068	230	0.400	10
20	0900	1.5	250	−2.852	0.058	−0.053	160	0.290	9
20	0920	1.5	250	−2.502	0.058	−0.044	180	0.286	10
20	1240	2.0	195	−1.645	0.071	−0.036	360	0.385	16
20	1300	1.8	206	−1.459	0.064	−0.020	360	0.332	18
20	1320	2.0	220	−0.773	0.069	−0.013	280	0.264	18
20	1800	7.2	186	0.045	0.259	0.036	80		
20	1900	6.2	275	0.079	0.213	0.042	140		
20	1920	7.2	250	0.058	0.257	0.041	160		
20	1940	7.2	270	−0.004	0.267	0.013	260	0.069	
20	2000	5.7	270	−0.024	0.203	0.007	280	0.228	20
20	2020	5.1	270	−0.056	0.183	−0.001	240	0.273	15
20	2040	3.6	280	−0.158	0.123	−0.005	200	0.248	13
20	2120	3.6	270	−0.150	0.123	−0.005	240	0.258	15
20	2140	3.5	260	−0.186	0.120	−0.009	240	0.272	15
20	2220	2.0	280	−1.606	0.071	−0.048	340	0.378	15
20	2230	2.0	290	−0.931	0.069	−0.023	340	0.305	19
20	2300	2.3	302	−0.356	0.080	−0.030	300	0.328	15
21	0000	2.6	255	−0.470	0.087	−0.020	280	0.288	16
21	0040	2.6	259	−0.441	0.087	−0.019	310	0.290	18
21	0100	1.8	305	−0.876	0.063	−0.019	200	0.227	15
21	0120	1.0	141	−1.656	0.039	−0.014	270	0.193	23
21	0405	3.1	85	−0.595	0.108	−0.048	240	0.370	11
21	0425	2.5	125	−1.106	0.088	−0.058	320	0.406	13
21	0445	2.6	142	−0.994	0.090	−0.054	380	0.425	15
21	0505	2.1	125	−1.443	0.073	−0.049	360	0.380	16
21	0545	1.5	160	−1.497	0.056	−0.025	455	0.319	24
21	0605	0.2	160	−43.572	0.012	−0.031	460	0.213	36
21	0645	1.0	100	−3.625	0.040	−0.030	480	0.310	26
21	0705	1.5	100	−1.691	0.055	−0.026	460	0.326	23
21	0845	3.1	95	−0.583	0.108	−0.040	475	0.457	17
21	0905	2.1	91	−1.158	0.072	−0.032	430	0.368	19
21	0945	1.0	129	−4.270	0.041	−0.040	360	0.310	19
21	1005	1.5	135	−1.164	0.055	−0.014	310	0.252	21
21	1025	0.2	200	−39.449	0.012	−0.024	300	0.176	28
21	1045	0.8	235	−3.474	0.033	−0.015	280	0.212	22
21	1105	3.6	270	−0.035	0.120	0.006	260	0.143	30
21	1305	7.2	258	0.006	0.264	0.012	180		
21	1325	7.0	260	0.000	0.256	0.009	210		
21	1345	6.5	280	−0.003	0.237	0.008	200	0.079	42
21	1405	6.7	285	−0.020	0.246	0.000	200	0.244	14
21	1505	6.5	280	−0.045	0.240	−0.007	200	0.318	10
21	1620	7.0	260	−0.021	0.260	0.003	200	0.258	13
21	1720	5.5	270	−0.058	0.198	−0.003	120	0.239	8
21	1945	4.0	250	−0.397	0.144	−0.038	250	0.428	10
21	2030	2.5	225	−1.328	0.089	−0.059	150	0.336	7
21	2110	1.0	220	−5.585	0.042	−0.053	300	0.325	15
21	2130	1.5	220	−2.618	0.056	−0.043	310	0.341	15
22	0550	2.0	130	−0.209	0.065	0.000	205	0.143	24
22	0610	1.5	130	−0.550	0.053	−0.006	220	0.169	22
22	0710	0.2	140	−35.247	0.012	−0.030	240	0.157	26

TABLE 2. (*Continued*)

Date	Time (PDT)	u (m s^{-1})	θ (K)	Z_i/L	u_* (m s^{-1})	T_* (K)	Z_i (m)	w_* (m s^{-1})	λ (min)
22	0730	0.2	120	−29.493	0.012	−0.024	240	0.144	28
22	0750	0.2	140	−32.846	0.012	−0.028	240	0.152	26
22	0810	0.2	150	−21.592	0.011	−0.015	245	0.126	33
22	0830	2.1	180	−0.631	0.070	−0.018	230	0.238	16
22	0910	1.0	307	−2.365	0.040	−0.024	210	0.205	17
22	0930	0.5	270	−6.285	0.023	−0.020	220	0.165	22
22	1010	2.6	260	−0.763	0.089	−0.040	240	0.330	12
22	1030	2.0	250	−1.369	0.071	−0.045	260	0.326	13
22	1050	0.5	305	−10.055	0.024	−0.033	260	0.213	20
23	1440	2.5	250	1.332	0.050	0.031	280		
23	1505	3.9	215	0.285	0.114	0.039	310		
23	1645	4.6	275	−0.086	0.163	0.001	320	0.307	17
23	1725	4.9	262	−0.011	0.170	0.012	355	0.112	
23	1745	2.1	244	−0.268	0.068	0.004	350	0.188	31
23	2340	1.7	260	1.943	0.029	0.017	500		
24	0040	2.1	281	0.527	0.052	0.017	155		
24	0100	1.8	270	0.776	0.043	0.017	120		
24	0120	1.5	236	0.767	0.037	0.014	170		
24	0240	1.7	140	0.381	0.046	0.016	120		
24	0300	1.5	136	0.455	0.041	0.016	160		
24	0420	1.0	210	0.044	0.032	0.011	140		
24	1000	1.0	269	−0.091	0.034	0.021	165		
25	2220	5.0	270	0.340	0.150	0.068	160		
25	2320	5.0	280	0.231	0.157	0.054	160		
26	0420	1.4	340	3.147	0.019	0.012	90		

* Source: Schacher *et al.* (1980).

then, with the above assumptions, the turbulent kinetic energy equation reduces to

$$-\overline{u'w'}\,\frac{\partial \bar{u}}{\partial z}\,(1 - R_f) - \epsilon = 0, \tag{3}$$

where ϵ is the dissipation or the rate of conversion of kinetic into internal energy by the viscous forces in the smallest eddies. Since $\epsilon > 0$ and $-\overline{u'w'}\partial\bar{u}/\partial z$ is practically always greater than zero, stationary, undamped turbulence is possible only if $R_f < 1$. This result is often used as an approximate criterion for defining the transition to turbulence in a stratified medium. For the purpose of analyzing the experimental results within this framework it is useful to identify the appropriate length and velocity scales. A key scaling parameter is the Monin-Obukhov length L defined by

$$\frac{1}{L} = -\frac{kgQ_0}{u_*^3 T} = -\frac{kg}{u_*^3 T}\left(Q + 0.61\frac{TM_0}{\rho}\right) = \frac{1}{L_T} + \frac{1}{L_q}, \tag{4}$$

where $Q_0 = (\overline{T_v'w'})_0$ is the virtual surface heat flux that accounts for the influence of humidity fluctuations on buoyancy, k the von Kármán constant, $u_*^2 = -\overline{u'w'}$ the friction velocity, and L_T and L_q are the Monin-Obukhov lengths calculated from the surface heat and evaporative fluxes. Physically, L is the height at which the two production terms are approximately of equal magnitude. One of the major differences in examining conditions over the ocean or other large bodies of water is that the density stratification is controlled not only by the surface heat flux but also by the water vapor flux. The measurements made by McBean and MacPherson (1975) over Lake Ontario indicate that there can be a significant difference between L_q and L_T, that in turn have a major influence on L.

Above the surface layer a more appropriate length scale for the eddies is the mixed layer depth Z_i. While there is some controversy associated with a formal definition of Z_i, in this work it is defined as the elevation of the lowest inversion base. The studies of Deardorff (1972) and Deardorff *et al.* (1980) indicate that this is an appropriate boundary layer height for momentum and heat. Under convective conditions the appropriate velocity scale, above the surface layer, is given by

$$w_* = \left(\frac{g}{T}Z_iQ_0\right)^{1/3} = \left[\frac{g}{T}Z_i(\overline{w'T_v'})_0\right]^{1/3} = \left(-\frac{1}{k}\frac{Z_i}{L}\right)^{1/3}u_*. \tag{5}$$

The characteristic time scale under convective conditions is then given by $\lambda = Z_i/w_*$. Willis and Deardorff (1976b) have shown that material released instantaneously at the surface becomes nearly well mixed within a travel time of $\sim 3\lambda$. In the field experiment the tracer material was "released" at the top of the mixed layer. Apart from the small contribution due to mechanical mixing the characteristic mixing time can be expected to be similar to that for a surface release. The reason for this is that the effective aerodynamic roughness of the ocean is very small.

There are a variety of means of estimating the fluxes needed to evaluate the above expressions. Three of the more common techniques are 1) the profile or gradient method, 2) the variance budget or dissipation technique, 3) and bulk aerodynamic calculations using air-sea differences. Schacher *et al.* (1978, 1980) employed the latter approach in reducing the meteorological data from the field experiment. A detailed discussion of these and other procedures is presented in Busch (1977). The key results from Schacher *et al.* (1978, 1980) are summarized in Table 2. In particular the frequency distribution of convective mixing times observed during the period 19–23 July is shown in Fig. 5 together with a similar distribution for daytime conditions over the land. The characteristic mixing times for both experiments were very similar. The influence of a much larger surface heat flux during the day is readily apparent.

In the surface layer, the velocity distribution can be expressed in terms of Monin-Obukhov similarity theory as

$$\frac{\partial \bar{u}}{\partial z} = \frac{u_*}{kz}\,\phi_m\left(\frac{z}{L}\right), \tag{6}$$

where ϕ_m is an experimentally determined function that corrects for the effects of buoyancy on turbulence. Businger *et al.* (1971) have constructed expressions for momentum ϕ_m and heat ϕ_h from an analysis of field data. For unstable conditions $z/L < 0$ the formulas are given by

$$\phi_m\left(\frac{z}{L}\right) = \left[1 - 15\left(\frac{z}{L}\right)\right]^{-1/4}, \tag{7}$$

$$\phi_h{}^2\left(\frac{z}{L}\right) = \phi_m\left(\frac{z}{L}\right). \tag{8}$$

These results, together with (3), the definition of u_* and the relation $\mathrm{Ri} = \alpha R_f$, can combined to give

$$u_*{}^3 = \frac{kz}{(1 - \alpha\,\mathrm{Ri})\phi_m\left(\frac{z}{L}\right)}. \tag{9}$$

The characteristic mixing time τ_m can be defined

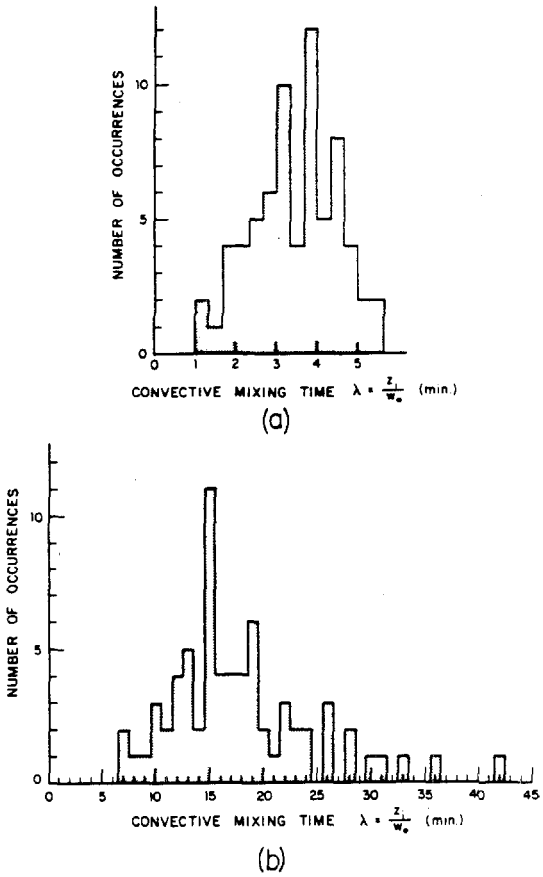

FIG. 5. Distribution of convective mixing times for (a) daytime conditions over land (source, Smith *et al.*, 1976) and (b) nighttime conditions over ocean.

in terms of the convective time scale λ as $\tau_m = 3\lambda = 3Z_i/w_*$. Using (5), and the expression $\phi_m\,\mathrm{R}_f = z/L$, Eq. (9) can be manipulated to give an estimate of the mixing time in terms of the measured dissipation rate and gradient Richardson number Ri:

$$\tau_m = 3\left[\frac{Z_i{}^2}{\epsilon}\left(1 - \frac{1}{\alpha\,\mathrm{Ri}}\right)\right]^{1/3}. \tag{10}$$

For near-neutral conditions, Businger *et al.* (1971) determined that $\alpha = 1.35$; thus a simple upper bound on (10) is $\tau_m \approx 3[-Z_i{}^2/\epsilon\,\mathrm{Ri}]^{1/3}$. For unstable conditions when $|\mathrm{Ri}| \gg 1$, a lower bound is given by $\phi_m = 3[Z_i{}^2/\epsilon]^{1/3}$. Using the data tabulated in Appendix B of Schacher *et al.* (1978) the limits on the convective mixing times can be calculated and are shown in Table 3 for the experiment conducted on 22 July. The important result from the tracer experiments is that the calculated mixing rates using

TABLE 3. Convective mixing times based on turbulence intensities for 22 July 1977.

Date	Time (PDT)	Z_i/L	u_* (m s^{-1})	Z_i (m)	Ri	ϵ (10^{-4} m s^{-3})	$\left[\frac{Z_i^2}{\epsilon}\right]^{1/3}$ (min)	$\left[-\frac{Z_i^2}{\epsilon\,\mathrm{Ri}}\right]^{1/3}$ (min)
22	0550	−0.209	0.065	205	−0.04	1.8	10	30
22	0610	−0.550	0.053	220	−0.09	3.6	8	19
22	0710	−35.247	0.012	240	−0.16	3.6	9	17
22	0730	−29.493	0.012	240	−0.08	4.0	9	20
22	0750	−32.846	0.012	240	−0.18	2.9	10	17
22	0810	−21.592	0.011	245	−0.21	5.1	8	14
22	0830	−0.631	0.070	230	−0.10	4.6	8	17
22	0910	−2.365	0.040	210	−0.02	7.1	7	24
22	0930	−6.285	0.023	220	−0.03	7.3	7	22

either the bulk or dissipation methods produces results consistent with the observed fumigation times. The rapid concentration increases were measured during times when the ship was beneath the plume and the mixed layer height exceeded 200 m.

5. Eddy diffusion coefficients

A basic problem with modeling convectively driven flows is that the turbulent mixing is no longer described by local concentration gradients. Nevertheless, there are some circumstances in which it is desirable to parameterize the diffusive fluxes by a K-theory model. The objective of this section is to present a simple formulation that produces transport times consistent with observed fumigation rates. Some recent work by Crane *et al.* (1977) and McRae *et al.* (1981) indicates that vertical eddy diffusivity profiles for unstable conditions can be scaled by a single profile of the form

$$K_{zz} = w_* Z_i f\left(\frac{z}{Z_i}\right) . \tag{11}$$

Lamb *et al.* (1975) derived an expression for f using the numerical turbulence model of Deardorff (1970). The profile adopted by McRae *et al.* (1981) is given by

$$\frac{K_{zz}}{w_* Z_i} = \begin{cases} 2.5\left(\frac{kz}{Z_i}\right)^{4/3}\left[1 - 15\left(\frac{z}{L}\right)\right]^{1/4}, & 0 < \frac{z}{Z_i} \leq 0.05 \\ 0.021 + 0.408\left(\frac{z}{Z_i}\right) + 1.352\left(\frac{z}{Z_i}\right)^2 - 4.096\left(\frac{z}{Z_i}\right)^3 + 2.560\left(\frac{z}{Z_i}\right)^4, & 0.05 < \frac{z}{Z_i} \leq 0.6 \\ 0.2 \exp\left[6 - 10\left(\frac{z}{Z_i}\right)\right], & 0.6 < \frac{z}{Z_i} \leq 1.1 \\ 0.0013, & \frac{z}{Z_i} > 1.1. \end{cases} \tag{12}$$

As can be seen from Fig. 6 the maximum value of the diffusivity occurs when $z/Z_i \approx 0.5$ and has a magnitude $\sim 0.21 w_* Z_i$. For typical conditions this corresponds to a diffusion time, defined by Z_i^2/K_{zz}, of $\sim 5Z_i/w_*$ that is quite consistent with the bounds shown in Tables 2 and 3.

6. Conclusions

There are a number of important findings from the tracer study that are of direct relevance to air pollution studies, first of which is that close to the shoreline different stabilities can exist above the land and water surfaces. Under these conditions atmospheric stability cannot be easily determined in terms of conventional classifications. A second finding is that the presence of convective activity can cause downmixing or fumigation of material that can return the next day as a significant increment to the onshore ground-level concentration. The process by which this occurs is as follows. During the night, cool stable air is advected out over the ocean. When this air encounters the warmer ocean surface convective mixing begins to erode the stable layer. Once the internal boundary layer has grown to the height of the plume the tracer material, entrained at the top of the mixed layer, is rapidly fumigated to the surface. The characteristic mixing time, inferred from the concentration records, is consistent with an estimate based on the convective time scale $\lambda = Z_i/w_*$ that, for the conditions of the experiment, was ~20 min.

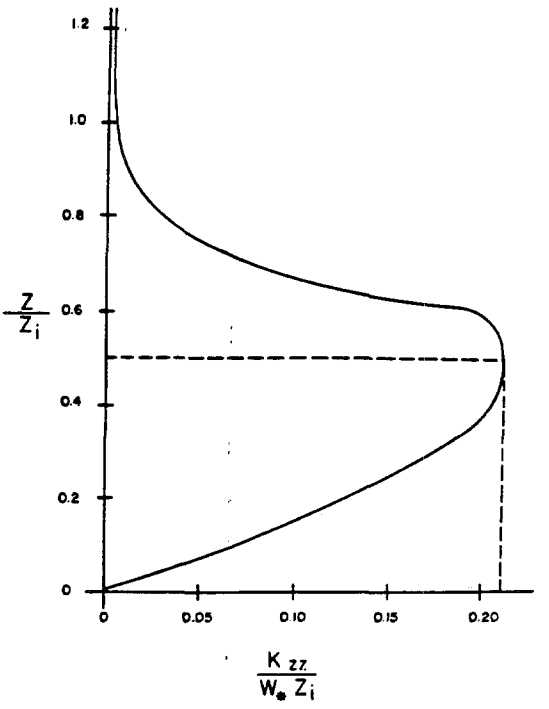

FIG. 6. Vertical turbulent diffusivity profile for unstable conditions (source, McRae *et al.*, 1981).

Understanding of these mixing processes and convective activity over the ocean will improve the ability to predict atmospheric dispersion in coastline environments.

Acknowledgments. This work was supported by the California Air Resources Board under contracts A5-187-30, A5-046-87 and A7-187-30. The assistance of Gordon Schacher of the Naval Postgraduate School, who supplied descriptions of data reduction procedures and measurement equipment, and Charles Bennett of the California Air Resources Board is appreciated.

REFERENCES

Agee, E. M., and T. S. Chen, 1973: A model for investigating eddy viscosity effects on mesoscale convection. *J. Atmos. Sci.*, **30**, 180–189.

Arnold, A., and J. R. Rowland, 1976: Fine scale observation of free convection in the atmospheric boundary layer. *Preprints Third Symp. Atmospheric Turbulence Diffusion and Air Quality*, Raleigh, Amer. Meteor. Soc., 1–8.

——, T. G. Konrad, J. H. Richter, D. R. Jensen and V. R. Noonkester, 1975: Simultaneous observation of clear air convection by a pulse radar, an FM-CW radar, an acoustic sounder and an instrumented aircraft. *Preprints 16th Radar Meteorology Conf.*, Houston, Amer. Meteor. Soc., 290–295.

Ball, F. K., 1960: Control of inversion height by surface heating. *Quart. J. Roy. Meteor. Soc.*, **86**, 483–494.

Briggs, G. A., 1969: *Plume Rise.* Atomic Energy Commission Review Series, 81 pp. [NTIS TID-25075].

——, 1975: Plume rise predictions. *Lectures on Air Pollution and Environmental Impact Analysis*, D. A. Haugen, Ed. Amer. Meteor. Soc., 59–111.

Busch, N. E., 1977: Fluxes in the surface boundary layers over the sea. *Proceedings of a NATO Advanced Study Institute, Urbino, Italy, (1975)*, Pergamon Press, 72–91.

Businger, J. A., 1975: Interactions of sea and atmosphere. *Rev. Geophys. Space Phys.*, **13**, 720–726, 817–822.

——, J. C. Wyngaard, Y. Izumi and E. F. Bradley, 1971: Flux-profile relationship in the atmospheric surface layer. *J. Atmos. Sci.*, **28**, 181–189.

Caughey, S. J., B. A. Crease, D. N. Asmakopoulos and R. S. Cole, 1978: Quantitative bistatic acoustic sounding of atmospheric boundary layer. *Quart. J. Roy. Meteor. Soc.*, **104**, 147–161.

Crane, G., H. A. Panofsky and O. Zeman, 1977: A model for dispersion from area sources in convective turbulence. *Atmos. Environ.*, **11**, 893–900.

Deardorff, J. W., 1970: A three-dimensional numerical investigation of the idealized planetary boundary layer. *Geophys. Fluid Dyn.*, **1**, 377–410.

——, 1972: Numerical investigation of neutral and unstable planetary boundary layers. *J. Atmos. Sci.*, **29**, 91–115.

——, 1978: Prediction of convective mixed-layer entrainment for realistic capping inversion structure. *J. Atmos. Sci.*, **36**, 424–436.

——, G. E. Willis and B. H. Stockton, 1980: Laboratory studies of the entrainment zone of a convectively mixed layer. *J. Fluid Mech.*, **100**, 41–64.

Dietz, R. N., and E. A. Coté, 1973: Tracing atmospheric pollutants by gas chromatographic determination of sulfur hexafluoride. *Environ. Sci. Tech.*, **7**, 338–342.

Drivas, P. J., and F. H. Shair, 1974: A tracer study of pollutant transport and dispersion in the Los Angeles area. *Atmos. Environ.*, **8**, 1155–1163.

Frisch, A. S., R. B. Chadwick, W. R. Moninger and J. M. Young, 1975: Observation of boundary layer convection cells measured by dual-Doppler radar and echosounder and by microbarograph array. *Bound.-Layer Meteor.*, **3**, 199–226.

Hardy, K. R., and H. Ottersten, 1969: Radar investigation of convective patterns in the clear atmosphere. *J. Atmos. Sci.*, **26**, 666–672.

Heidt, F. D., 1977: The growth of the mixed layer in a stratified fluid due to penetrative convection. *Bound.-Layer Meteor.*, **12**, 439–461.

Houlihan, T. M., K. L. Davidson, C. W. Fairall and G. E. Schacher, 1978: Experimental aspects of a shipboard system used in investigation of overwater turbulence and profile relationships. Naval Postgraduate School Rep. No. NPS61-78-001, 254 pp.

Kaimal, J. C., J. C. Wyngaard, D. A. Haugen, O. H. Coté and Y. Izumi, 1976: Turbulence structure in the convective boundary layer. *J. Atmos. Sci.*, **33**, 2152–2169.

Kraus, E. B., 1972: *Atmosphere-Ocean Interaction.* Clarendon Press, 275 pp.

Konrad, T. G., 1970: The dynamics of the convective process in clear air as seen by radar. *J. Atmos. Sci.*, **27**, 1138–1147.

Lamb, B. K., A. Lorenzen and F. H. Shair, 1978a: Atmospheric dispersion within coastal regions—Part I. Tracer study of power plant emissions from the Oxnard Plain. *Atmos. Environ.*, **12**, 2089–2100.

——, F. H. Shair and T. B. Smith, 1978b: Atmospheric dispersion within coastal regions—Part II. Tracer study of industrial emissions in the California Delta region. *Atmos. Environ.*, **12**, 2101–2118.

Lamb, R. G., H. W. Chen and J. H. Seinfeld, 1975: Numerico-empirical analysis of atmospheric diffusion theories. *J. Atmos. Sci.*, **32**, 1754–1807.

Lyons, W. A., 1975: Turbulent diffusion and pollutant transport in shoreline environments. *Lectures on Air Pollution and Environmental Impact Analysis*, D. A. Haugen, Ed., Amer. Meteor. Soc., 59–111.

Manins, P. C., 1977: Fumigation and a laboratory experiment. *Weather*, June, 221–228.

McBean, G. A., and J. I. MacPherson, 1975: Turbulence above Lake Ontario: velocity and scalar statistics. *Bound.-Layer Meteor.*, **10**, 181–197.

McRae, G. J., W. R. Goodin and J. H. Seinfeld, 1981: Development of a second generation mathematical model for urban air pollution: I Model formulation. *Atmos. Environ.*, (in press).

Misra, P. K., 1980: Dispersion from tall stacks into a shore line environment. *Atmos. Environ.*, **14**, 397–400.

Monin, A. S., and A. M. Yaglom, 1971: *Statistical Fluid Mechanics: Mechanics of Turbulence*, Vol. I. MIT Press, 769 pp.

Orgill, M. M., 1981: Atmospheric studies in complex terrain: A planning guide for future studies. Rep. PNL-3656, Pacific Northwest Laboratories, Richland, WA, U.S. Department of Energy Contract DE-AC06-76RLO 1830.

Raynor, G. S., P. Michael and S. SethuRaman, 1980: Meteorological measurement methods and diffusion models for use at coastal nuclear reactor sites. *Nuclear Safety*, **21**, 749–765.

Schacher, G. E., K. L. Davidson and C. W. Fairall, 1980: Atmospheric marine boundary layer mixing rates in the California coastal region. Naval Postgraduate School Rep. No. NPS61-80-003, 115 pp.

——, C. W. Fairall, K. L. Davidson and T. M. Houlihan, 1978: Experimental investigation of the marine boundary layer in support of air pollution studies in the Los Angeles air basin. Naval Postgraduate School Rep. No. NPS61-78-002, 257 pp.

Schatzmann, M., 1979: An integral model of plume rise. *Atmos. Environ.*, **13**, 721–731.

Shair, F. H., E. Sasaki, D. Carlan, G. R. Cass, W. R. Goodin, J. Edinger and G. E. Schacher, 1981: Transport and dispersion of airborne pollutants associated with the land breeze-sea breeze system. *Atmos. Environ.* (in press).

Simmonds, P. G., G. R. Shoemake, J. E. Lovelock and H. C. Lord, 1972: Improvements in the determination of sulfur hexafluoride for use as a meteorological tracer. *Anal. Chem.*, **44**, 860–863.

Smith, T. B., S. L. Marsh, W. H. White, T. N. Jerskey, R. G. Lamb, P. A. Durbin and J. P. Killus, 1976: Analysis of the data from the three-dimensional gradient study. Final Report to the California Air Resources Board under Contracts ARB-4-051 and ARB-4-250, Meteorology Research, Inc., Pasadena, and Systems Applications, Inc., San Rafael, 124 pp.

Stull, R. B., 1973: Inversion rise model based on penetration convection. *J. Atmos. Sci.*, **30**, 1092–1099.

Venkatram, A., 1976: Internal boundary layer development and fumigation. *Atmos. Environ.*, **11**, 479–482.

Willis, G. E., and J. W. Deardorff, 1976a: Visual observations of horizontal planforms of penetration convection. *Preprints Third Symp. Atmospheric Turbulence Diffusion and Air Quality*, Raleigh, Amer. Meteor. Soc., 1–8.

——, and ——, 1976b: A laboratory model of diffusion into the convective planetary boundary layer. *Quart. J. Roy. Meteor. Soc.*, **102**, 427–445.

Zeman, O., and H. Tennekes, 1977: Parameterization of the turbulent energy budget at the top of the daytime atmospheric boundary layer. *J. Atmos. Sci.*, **34**, 111–123.

CHAPTER 6

SURFACE DEPOSITION OF POLLUTANT MATERIAL

6.1 Introduction

A significant process that influences the concentration predictions of the airshed model is the interaction of the pollutants with the ground. Roberts (1975), for example, estimated that in the Los Angeles Basin almost half of the sulfur oxides are removed at the ground before air parcels leave the airshed. The objective of this section is to develop an upper limit expression for the rate at which gaseous material is removed at the surface. In most models the deposition rate is described by a single quantity, the pollutant deposition velocity v_g. The flux of material, F, directed towards the lower boundary surface is defined by

$$F = v_g \, c(z_r) \tag{6.1}$$

where $c(z_r)$ is the concentration of the material at some reference height z_r. A basic problem with (6.1) is that it does not explicitly represent the fact that dry deposition involves a complex linkage between turbulent diffusion in the surface boundary layer, molecular scale motion at the air-ground interface and chemical interaction of the material with the surface. Various physical processes are involved including gravitational settling, turbulent and molecular diffusion, inertial impaction, phoretic and electrical effects. In

addition to these removal phenomena, deposited material can be desorbed or mechanically resuspended. Reviews of the general subject of dry deposition are included in the works of Chamberlain (1966), Hill and Chamberlain (1974), Kneen and Strauss (1969), Liu and Ilori (1974), Sehmel and Hodgson (1974), Slinn (1974), Davidson (1977), National Academy of Sciences (1978), McMahon and Denison (1979), and Sehmel (1980).

As a first step towards improving upon the model (6.1) it is necessary to recognize that there are two basic components associated with pollutant removal: one is the transport of material to the ground and the other is the interaction of the pollutants with the surface. Unless extensive field experiments have been made in the airshed, it is not possible to accurately characterize the second component of the dry deposition process. An alternative approach, and the focus of this chapter, is to develop an upper limit for v_g in terms of the transport processes and the concentration at a reference point above the surface. (Typically the height of the lowest computational grid point in the airshed model.) A secondary goal is to identify the significant meteorological variables and surface properties needed to either correlate different measurements of v_g or to modify the results for different experimental conditions.

6.2 Deposition in the Constant Flux Layer

Consider the idealized representation of the airshed surface shown in Figure 6.1. Within the layer $0 \leq z \leq z_r$ the deposition is assumed to be a one-dimensional, steady-state, constant flux process occurring

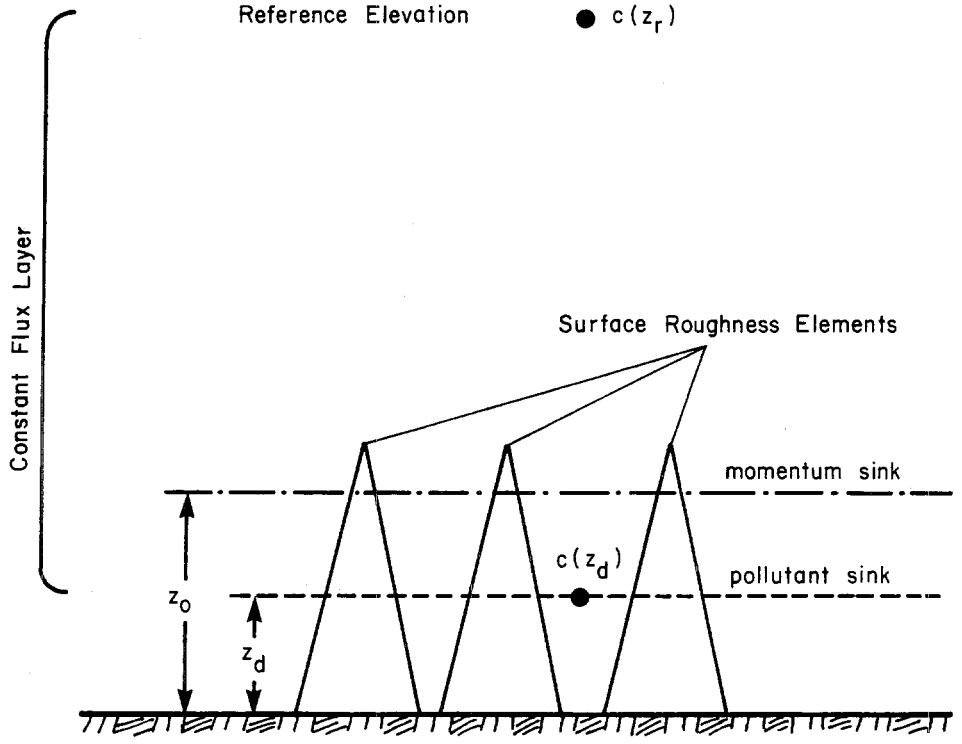

FIGURE 6.1

Idealized Representation of the Airshed Surface

without re-entrainment and, in the case of aerosols, without particle agglomeration. With these assumptions the deposition flux is described by

$$F = [K_p(z) + D] \frac{dc}{dz} + v_t \, c(z) \tag{6.2}$$

where $K_p(z)$ is the pollutant eddy diffusion coefficient, D the molecular diffusion coefficient of the material in air and v_t the terminal settling velocity for particulate material. Equating the fluxes in expressions (6.1) and (6.2) gives

$$\int_{z_d}^{z_r} \frac{dz}{[K_p(z)+D]} = \int_{c(z_d)}^{c(z_r)} \frac{dc}{[v_g c(z_r) - v_t c(z)]} \tag{6.3}$$

The lower limits of integration z_d and $c(z_d)$ refer to the elevation and concentration of material at the effective pollutant sink height. It is important to note that z_d is not in general equal to the surface roughness z_o, a height associated with the momentum sink (Brutsaert, 1975). If the terminal settling velocity is set to zero for the case of gaseous materials then (6.3) can be written in the simpler form

$$v_g = \frac{\left[1 - \frac{c(z_d)}{c(z_r)} \right]}{\int_{z_d}^{z_r} \frac{dz}{[K_p(z) + D]}} \tag{6.4}$$

6.3 Eddy Diffusion of Momentum and Scalar Contaminants in the Surface Layer

Since the model is intended to be used primarily in the surface layer of the atmosphere, an expression for $K_p(z)$ can be developed using Monin-Obukhov similarity theory. The velocity shear and the pollutant eddy diffusion coefficient, $K_p(z)$, are given by

$$\frac{\partial u}{\partial z} = \frac{u_*}{kz} \phi_m\left(\frac{z}{L}\right) \tag{6.5}$$

and

$$K_p(z) = \frac{k\, u_*\, z}{\phi_p\left(\frac{z}{L}\right)} \tag{6.6}$$

where k is the von Karman constant, u_* the friction velocity, L the Monin-Obukhov length and ϕ_p, ϕ_m are universal functions which must be determined by experiment (Monin and Yaglom, 1971). The ϕ functions are basically correct for the effects of buoyancy on turbulence. Businger et al. (1971) have constructed expressions for momentum ϕ_m and heat ϕ_H from an analysis of field data taken under a wide variety of stability conditions. A survey of the results of some experiments directed at developing these functions is shown in Table 6.1. For the present model the expressions adopted for momentum are

$$\phi_m\left(\frac{z}{L}\right) = \begin{cases} \left[1 + 4.7\left(\frac{z}{L}\right)\right] & \text{Stable; } \frac{z}{L} > 0 \\ 1 & \text{Neutral; } \frac{z}{L} = 0 \\ \left[1 - 15\left(\frac{z}{L}\right)\right]^{-\frac{1}{4}} & \text{Unstable: } \frac{z}{L} < 0 \end{cases} \tag{6.7}$$

TABLE 6.1

Estimates of Turbulence Constants from Surface-Layer Measurements
(Source: Busch, 1973)

$$\phi_m = \begin{cases} 1 + \beta_m \frac{z}{L} & ; \frac{z}{L} > 0 \\ (1 - \alpha_m \frac{z}{L})^{-\frac{1}{4}} & ; \frac{z}{L} < 0 \end{cases} \qquad \phi_H = \begin{cases} 1 + \beta_H \frac{z}{L} & ; \frac{z}{L} > 0 \\ (1 - \alpha_H \frac{z}{L})^{-\frac{1}{2}} & ; \frac{z}{L} < 0 \end{cases}$$

REFERENCE	MOMENTUM α_m	MOMENTUM β_m	HEAT α_H	HEAT β_H	$\phi_H(0)$	$\phi_M(0)$
Businger et al. (1971)	15	4.7	9	6.4	0.74	---
Paulson (1970) Badgley et al. (1972)	16	7	16	7	1	1
Webb (1970)	18	5.2	9	5.2	1	1
Dyer and Hicks (1970)	16	---	16	---	1	1

In addition to the transport relations for momentum there are some data for ϕ functions associated with water vapor ϕ_w and heat ϕ_H. Unfortunately, there are few direct experimental measurements of pollutant fluxes in the atmospheric surface layer.

A decision must be made as to the form of the ϕ function for a generalized passive scalar contaminant. For unstable conditions ($z/L < 0$) the experimental evidence of Dyer and Hicks (1970) indicates that ϕ_H, $\phi_w = \phi_m^2$. Galbally (1971) measured ozone profiles and fluxes in the surface layer and concluded that the eddy transport mechanism for O_3 is similar to that for heat rather than momentum. On the basis of these two studies and the data of Businger et al. (1971) the following ϕ functions have been adopted for pollutant transport.

$$\phi_p\left(\frac{z}{L}\right) = \begin{cases} 0.74 + 4.7\left(\frac{z}{L}\right) & \text{Stable;} \quad \frac{z}{L} > 0 \\ 0.74 & \text{Neutral;} \quad \frac{z}{L} = 0 \\ 0.74\left[1-9\left(\frac{z}{L}\right)\right]^{-\frac{1}{2}} & \text{Unstable;} \quad \frac{z}{L} < 0 \end{cases} \tag{6.8}$$

6.4 Upper Limit Deposition Model

Within the surface layer defined by $z_d \leq z \leq z_r$ the bulk contribution to the diffusive transport from molecular diffusion is negligible. Applying this assumption to equation (6.4) and in addition substituting the flux gradient relation (6.6) for $K_p(z)$ gives the following upper limit to the deposition velocity.

$$v_g = \frac{k\left[1 - \frac{c(z_d)}{c(z_r)}\right]}{\int_{z_d}^{z_r} \frac{1}{zu_*}\phi_p(\frac{z}{L})dz} \tag{6.9}$$

Since u_* is approximately constant with height in the surface layer (Busch, 1973) and $\phi_p \simeq 1$ for $z_d \leq z \leq z_o$, the denominator of (6.9) can be expanded to give

$$v_g = \frac{k^2 u(z_r)\left[1 - \frac{c(z_d)}{c(z_r)}\right]}{\left[\int_{z_o}^{z_r} \phi_m(\frac{z}{L})\frac{dz}{z}\right]\left[\ell n(\frac{z_o}{z_d}) + \int_{z_o}^{z_r} \phi_p(\frac{z}{L})\frac{dz}{z}\right]} \tag{6.10}$$

Evaluation of the term $\ell n(z_o/z_d)$ in the denominator of equation (6.10) requires a knowledge of z_d and of the transfer processes at the surface. Based on a survey of the heat transfer literature and in particular the work of Brutsaert (1975), Wesely and Hicks (1977) assumed that

$$\ell n\left(\frac{z_o}{z_d}\right) = 2(\frac{Sc}{Pr})^{\frac{2}{3}} \tag{6.11}$$

where Sc and Pr are the Schmidt and Prandtl numbers associated with the pollutant material in air. The complete model is then

$$v_g = \frac{k^2\, u(z_r)\left[1 - \dfrac{c(z_d)}{c(z_r)}\right]}{\left[\displaystyle\int_{z_o}^{z_r} \phi_m\left(\frac{z}{L}\right)\frac{dz}{z}\right]\left[2\left(\frac{Sc}{Pr}\right)^{\frac{2}{3}} + \displaystyle\int_{z_o}^{z_r} \phi_p\left(\frac{z}{L}\right)\frac{dz}{z}\right]} \tag{6.12}$$

The integrals required to evaluate v_g are shown in Table 6.2.

6.5 Application of Deposition Model

The final result exposes a number of the limitations of the basic model (6.1), in particular, the fact that v_g is directly influenced by the prevailing meteorology and atmospheric stability. The effect of stability is particularly apparent; consider for example, the conditions shown in Table 6.3 for a range of Sc/Pr ratios. With z/L in the range -1.5 to +1.5, the deposition velocities vary by almost a factor of five. This result indicates that under typical conditions there could be a significant diurnal variation in the surface removal of pollutant material. The functional dependence of v_g on the elevation above the surface highlights the need for reporting the reference height z_r in field or laboratory studies. If v_g, z_r, z_o and $u(z_r)$ are measured, then it is possible to evaluate $c(z_d)/c(z_r)$ and, in turn, v_g for elevations other than the reference height. This is a useful approach for developing the deposition velocities for air quality models in which z_r may be of O(10-50 m). The variation of v_g as a function of z/L is shown in Figure 6.2.

TABLE 6.2

Momentum and Pollutant Integrals for Different Stability Conditions

INTEGRAL	STABILITY CONDITION		
	STABLE	NEUTRAL	UNSTABLE
	$\frac{z}{L} > 0$	$\frac{z}{L} = 0$	$\frac{z}{L} < 0$
MOMENTUM			
$\int_{z_o}^{z_r} \phi_m(\frac{z}{L}) \frac{dz}{z}$	$\ln(\frac{z_r}{z_o}) + \frac{4.7}{L}(z_r - z_o)$	$\ln(\frac{z_r}{z_o})$	$\ln\left[\frac{(1-15\frac{z_r}{L})^{\frac{1}{4}} - 1}{(1-15\frac{z_r}{L})^{\frac{1}{4}} + 1}\right] - \ln\left[\frac{(1-15\frac{z_o}{L})^{\frac{1}{4}} - 1}{(1-15\frac{z_o}{L})^{\frac{1}{4}} + 1}\right]$ $+ 2 \arctan (1-15\frac{z_r}{L})^{\frac{1}{4}} - 2 \arctan (1-15\frac{z_o}{L})^{\frac{1}{4}}$
POLLUTANT			
$\int_{z_o}^{z_r} \phi_p(\frac{z}{L}) \frac{dz}{z}$	$0.74 \ln(\frac{z_r}{z_o}) + \frac{4.7}{L}(z_r - z_o)$	$0.74 \ln(\frac{z_r}{z_o})$	$0.74\left\{\ln\left[\frac{(1-9\frac{z_r}{L})^{\frac{1}{2}} - 1}{(1-9\frac{z_r}{L})^{\frac{1}{2}} + 1}\right] - \ln\left[\frac{(1-9\frac{z_o}{L})^{\frac{1}{2}} - 1}{(1-9\frac{z_o}{L})^{\frac{1}{2}} + 1}\right]\right\}$

TABLE 6.3

Deposition Velocity as a Function of Stability and Ratio of Sc/Pr*

	Deposition velocity v_g as a function of stability (z/L)						
$\frac{Sc}{Pr}$	-1.5	-1.0	-0.5	0	0.5	1.0	1.5
0.6	1.36	1.26	1.13	0.51	0.49	0.31	0.21
0.8	1.28	1.20	1.07	0.50	0.47	0.30	0.21
1.0	1.22	1.14	1.02	0.48	0.46	0.29	0.20
1.2	1.17	1.09	0.98	0.47	0.44	0.29	0.20
1.4	1.12	1.05	0.95	0.46	0.43	0.28	0.19
1.6	1.09	0.01	0.92	0.44	0.42	0.27	0.19
1.8	1.05	0.98	0.89	0.43	0.41	0.27	0.19
2.0	1.02	0.95	0.86	0.42	0.41	0.27	0.19
2.2	0.99	0.92	0.84	0.42	0.40	0.26	0.18
2.4	0.96	0.90	0.82	0.41	0.39	0.26	0.18
2.6	0.93	0.87	0.80	0.40	0.38	0.25	0.18
2.8	0.91	0.85	0.78	0.39	0.38	0.25	0.18
3.0	0.89	0.84	0.76	0.39	0.37	0.25	0.17

*Conditions for calculations

$u = 2.5$ m/sec, $z_o = 0.01$m , $z_r = 10$m, $c(z_d) = 0$

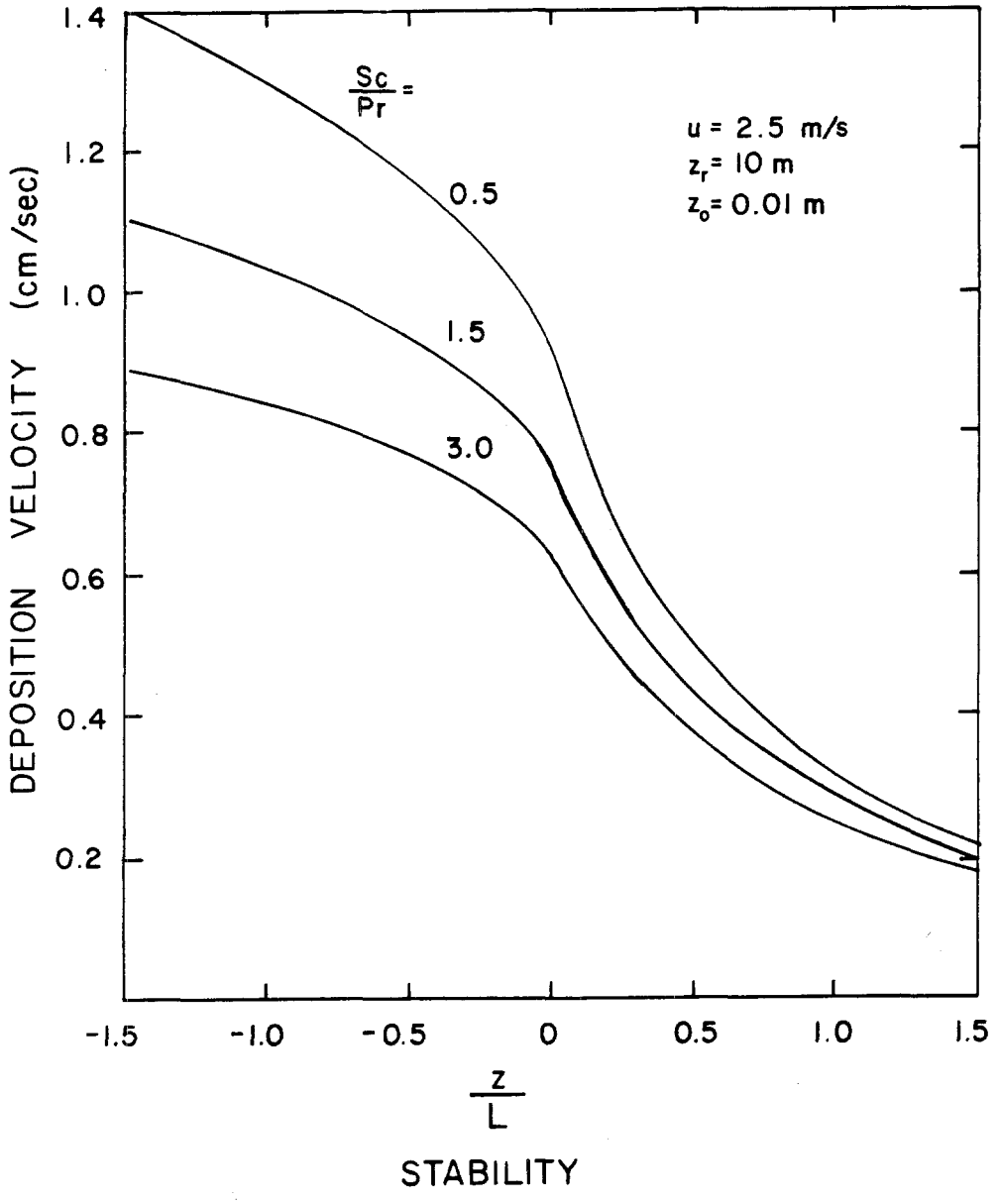

FIGURE 6.2

Variation of Surface Deposition Velocity v_g as a Function of Atmospheric Stability and Pollutant Sc/Pr Ratio

Once the pollutant deposition velocity has been established, either by direct measurement or estimated using the proposed model, the next step is to develop a formal procedure for calculating the amount of material removed at the ground. At the lower surface of the airshed the pollutant removal is typically described by the boundary condition:

$$F \equiv - K_p(z) \left.\frac{\partial c}{\partial z}\right|_{z = z_r} = - v_g(z_r)\ c(z_r) \qquad (6.13)$$

Where z_r is a reference elevation, $v_g(z_r)$ and $c(z_r)$ are the pollutant deposition velocity and concentration at that height. Because of the nonlinear nature of $K_p(z)$, most mathematical descriptions of pollutant transport require numerical solution. This can pose a problem in that the elevation of the lowest computational grid point is typically much higher than the reference height, z_r, used to establish the pollutant deposition velocities. The situation is illustrated in Figure 6.3 where Δz is the height of the bottom cell and $\Delta z >> z_r$. Because of the need to approximate the vertical concentration profile in discrete increments $c(z_r)$ is not readily available. When coupled with the observation that v_g varies with height there is a need to develop an equivalent deposition velocity $\bar{v}_g$ that, when applied to the cell average concentration, c_1, correctly predicts the flux at the lower boundary. One way to develop such a model is to assume that most of the lowest cell is within the surface or constant flux layer. If this is the case then the cell deposition velocity is given by

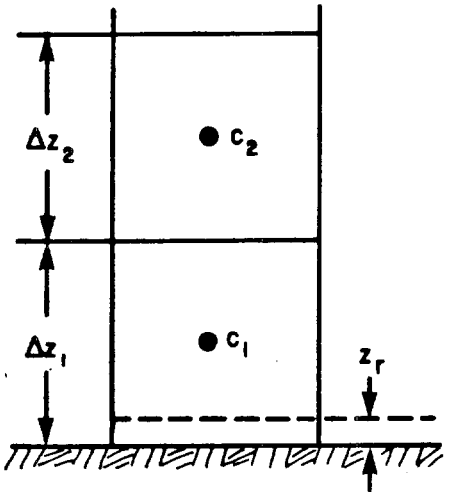

FIGURE 6.3

(a) Computational Cell Nomenclature

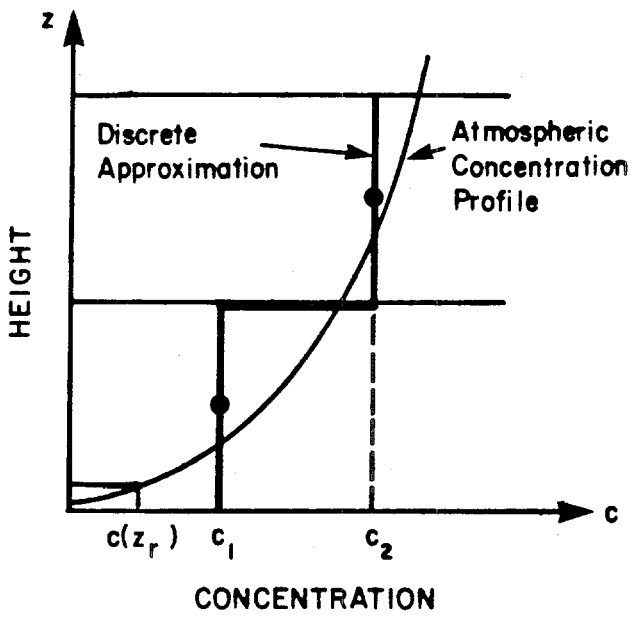

FIGURE 6.3

(b) Discrete Approximation of Vertical Concentration Profile

$$\bar{v}_g = \frac{v_g(z_r)c(z_r)}{c_1} \tag{6.14}$$

If c_1 is to represent the average value of the actual vertical concentration distribution in the range $z_r \leq z \leq \Delta z$ then it must be equivalent to

$$c_1 = \frac{1}{\Delta z - z_r} \int_{z_r}^{\Delta z} c(z)dz \tag{6.15}$$

Within the constant flux layer c(z) is given by

$$c(z) = c(z_r) \left[1 + v_g(z_r) \int_{z_r}^{z} \frac{1}{K_p(z)} \, dz \right] \tag{6.16}$$

The equivalent cell deposition velocity can now be determined by combining (6.16), (6.15), (6.14) and (6.6) to give

$$\bar{v}_g = \frac{v_g(z_r)}{1 + \frac{v_g(z_r)}{ku_*(\Delta z - z_r)} \int_{z_r}^{\Delta z} \int_{z_r}^{z} \phi_p(\frac{x}{L}) \frac{dx}{x} dz} \tag{6.17}$$

The integrals needed to evaluate the denominator of (6.17) are shown in Table 6.3. An example of the variation of $\bar{v}_g$ with cell size and atmospheric stability is shown in Figure 6.4, and, as can be expected, the equivalent deposition velocity becomes smaller as Δz increases. The

TABLE 6.4

Integrals Required to Calculate the Cell Average Deposition Velocity

STABILITY CONDITION	$\phi_p(\frac{z}{L})$	INTEGRAL $I = \int_{z_r}^{\Delta z} \int_{z_r}^{z} \phi_p(\frac{x}{L}) \frac{dx}{x} dz$
Stable $(\frac{z}{L} > 0)$	$\phi_p(\frac{z}{L}) = 0.74 + 4.7(\frac{z}{L})$	$I = 0.74(\Delta z \ \ell n \frac{\Delta z}{z_r} - \Delta z + z_r) + \frac{2.35}{L} (\Delta z - z_r)^2$
Neutral $(\frac{z}{L} = 0)$	$\phi_p(\frac{z}{L}) = 0.74$	$I = 0.74(\Delta z \ \ell n \frac{\Delta z}{z_r} - \Delta z + z_r)$
Unstable $(\frac{z}{L} < 0)$	$\phi_p(\frac{z}{L}) = 0.74[1 - 9 \frac{z}{L}]^{-\frac{1}{2}}$	$I = 0.74 \ \Delta z \ \ell n \left[\left(\frac{\sqrt{1 - 9\frac{\Delta z}{L}} - 1}{\sqrt{1 - 9\frac{z_r}{L}} - 1} \right) \left(\frac{\sqrt{1 - 9\frac{z_r}{L}} + 1}{\sqrt{1 - 9\frac{\Delta z}{L}} + 1} \right) \right]$ $+ 0.104 \ L \left[\sqrt{1 - 9\frac{\Delta z}{L}} - \sqrt{1 - 9\frac{z_r}{L}} \right]$

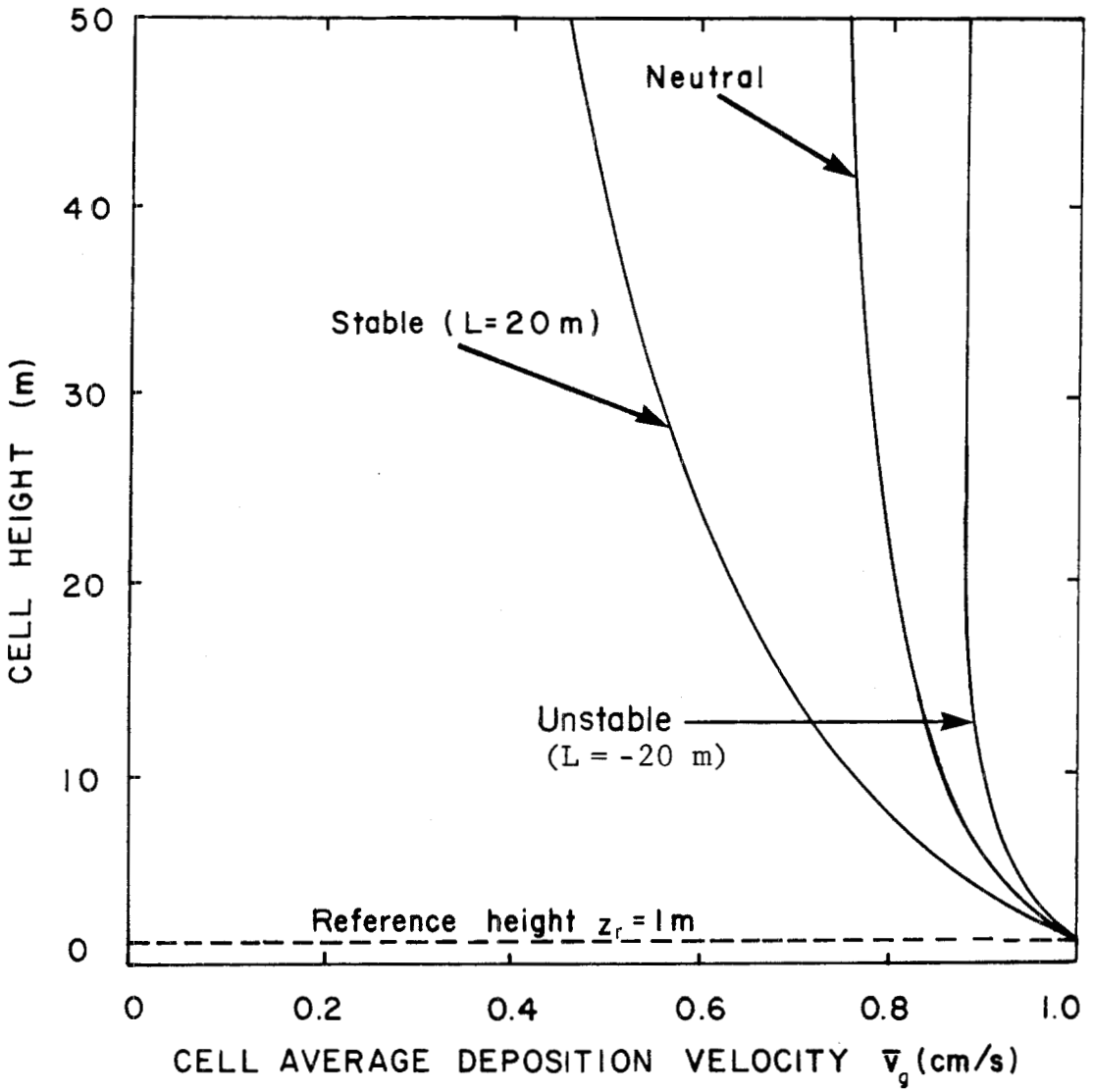

FIGURE 6.4

Variation of Average Deposition Velocity as a Function of Atmospheric Stability and the Cell Height

(z_o = 0.01 m, $\bar{u}$ = 2.5 m/s, $v_g(z_r)$ = 0.01 m/s)

variation is most pronounced under stable conditions because of the reduced vertical mixing. One implication of this result is that if $v_g(z_r)$, rather than $\bar{v}_g$, were to be used in a practical calculation then the surface removal flux would be considerably overestimated.

In order to illustrate how diurnal variations in atmospheric stability influence the surface removal processes consider a column of air of height H containing an initial distribution, c(z,0), of a non-reacting species. If there are no other competing processes the fraction of material remaining in the column at time t is given by

$$M_f(t) = \frac{\int_0^h c(z,t)dz}{\int_0^h c(z,0)dz} \tag{6.18}$$

By neglecting both vertical wind shear and advection the pollutant transport can be described by

$$\frac{\partial c}{\partial t} = \frac{\partial}{\partial z} K_p(z) \frac{\partial c}{\partial z} \tag{6.19}$$

with the boundary conditions at the surface and at the column top given by

$$K_p(z) \frac{\partial c}{\partial z} = 0 \quad ; \quad z = H \tag{6.20}$$

and

$$K_p(z) \frac{\partial c}{\partial z} = v_g c \quad ; \quad z = z_r \tag{6.21}$$

Once the initial conditions $v_g(z_r)$ and $K_p(z)$ have been specified the numerical procedures described in Chapter 8 can be used to predict the evolution of the vertical concentration distribution. As an illustration, Figures 6.5 and 6.6 depict the variations of $c(z,t)$ and $M_f(t)$ within an air parcel as it traverses a typical urban airshed. There is quite a pronounced variation in both the vertical diffusion and surface deposition rate during the diurnal cycle. The surface depletion rate, expressed in terms of the deposition velocity, and the total material loss show a complex dependence on the time of day, the extent of vertical mixing and surface conditions. The point of this calculation is to illustrate that the use of a single diurnal average v_g could lead to a significant over-prediction of the amount of material removed during the nighttime. This conclusion further reinforces the need for careful reporting of atmospheric conditions during field studies directed at establishing surface removal fluxes.

6.6 Experimental Methods for Determining Deposition Velocities

In the previous section primary attention was directed at developing an upper limit estimate of the rate at which pollutants can be transported to the ground. Whether this flux corresponds to the actual removal rate depends to a large extent on the conditions and type of the underlying surface. Garland (1974), for example, has observed an order of magnitude difference in the ozone (O_3) deposition velocity over different soil types. If $c(z_d)$ is the pollutant concentration at the effective sink height, z_d, then the upper and lower limits on v_g correspond to

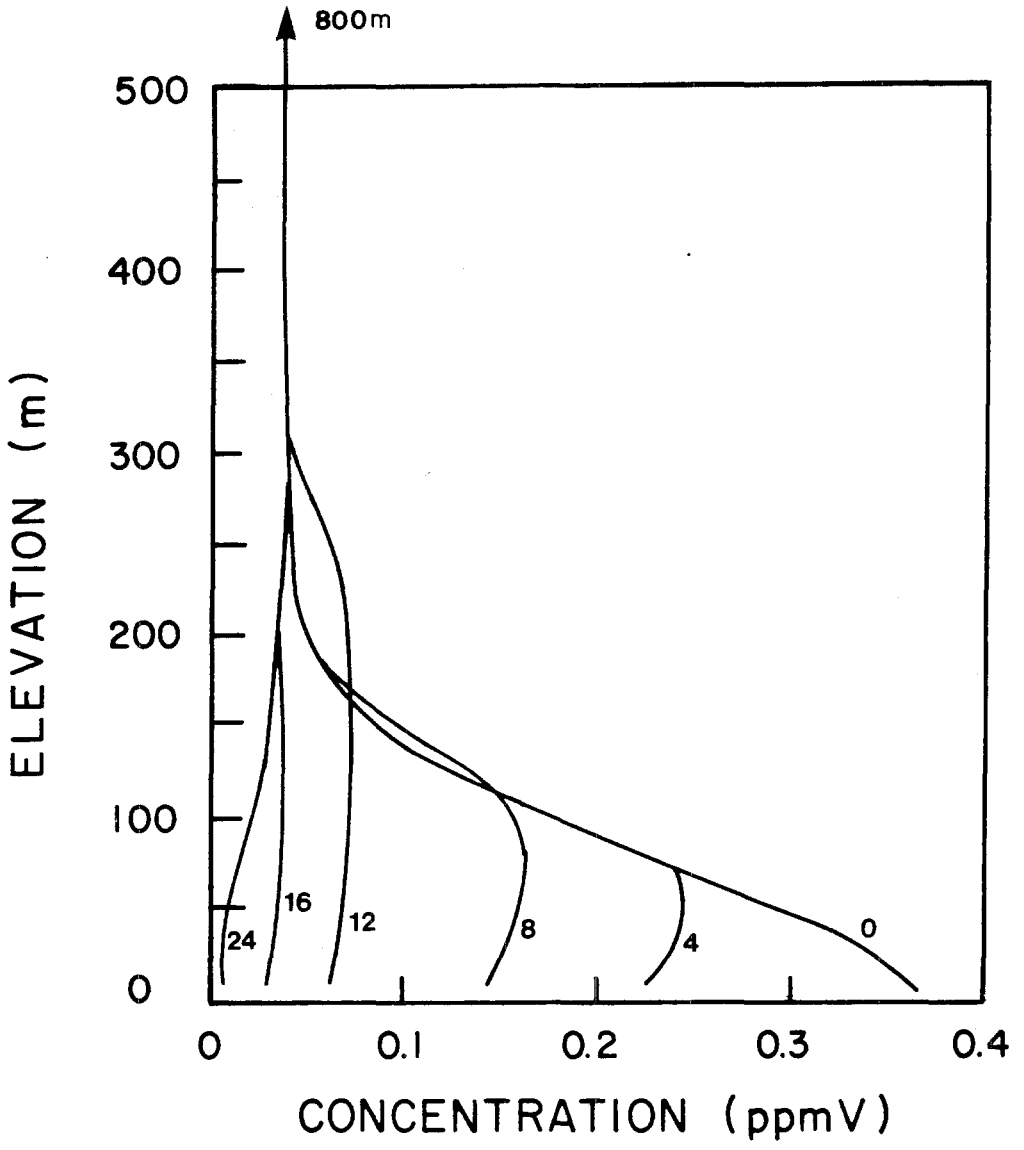

FIGURE 6.5

Time Evolution of a Typical Vertical Concentration Profile for an Air Parcel Traversing an Urban Airshed

(Δz = 20 m, z_o = 0.01 m, z_r = 10 m, v_g = 0.01 m/s)

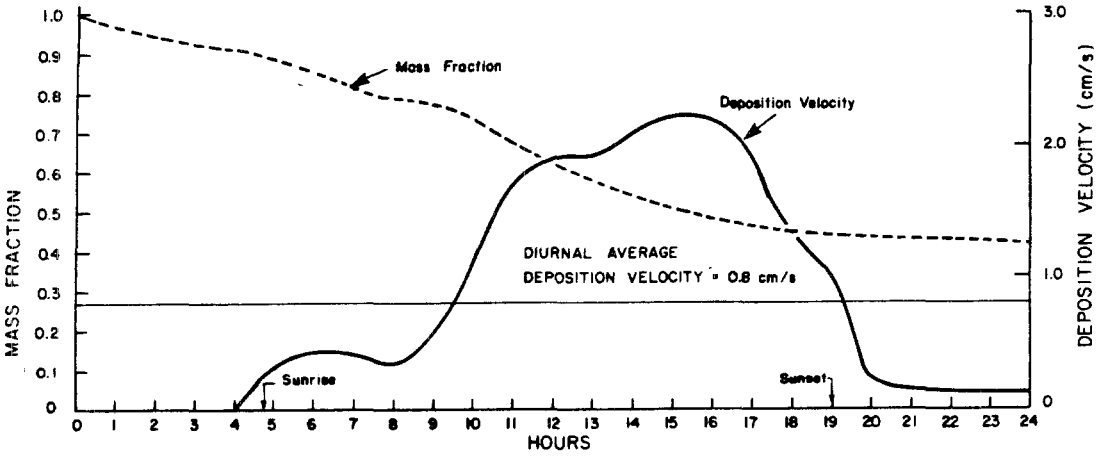

(a)

Diurnal Variation of Column Mass Fraction and
Cell Average Deposition Velocity

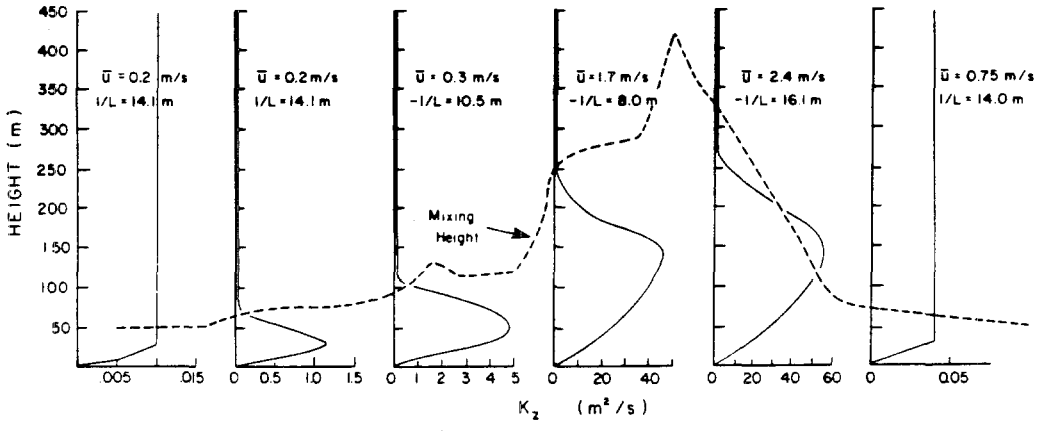

(b)

Diurnal Variation of Vertical Diffusivity
(Profiles are drawn every four hours)

FIGURE 6.6

the conditions $c(z_d) = 0$ and $c(z_r) = c(z_d)$. If a lower bound on v_g is required then it is important to be able to estimate the concentration difference $c(z_r) - c(z_d)$. At present the only satisfactory means for establishing the surface condition is by experimental measurement. This section presents a brief survey of field and laboratory techniques for determining deposition velocities for gaseous species which participate in photochemical reaction processes.

Whether pollutant deposition velocities are measured in the field or under laboratory conditions usually one of three basic techniques is employed. These methods include: the use of radioactive tracers, free stream concentration decay measurements and gradient or profile determinations. The most common laboratory procedure is called the flux method which equates free stream concentration decay rates to the surface removal fluxes. Garland and Penkett (1976) measured the concentration decay of peroxy acetyl nitrate (PAN) as it passed over different surfaces in a wind tunnel. Given the concentration difference, the travel time over the surface and the wind tunnel dimensions, it is a simple task to infer the net deposition flux and in turn determine the deposition velocity. A similar technique was used by Hill and Chamberlain (1974) to establish the pollutant influx required to maintain a constant concentration over different plant canopies. More recently the emergence of fast response pollutant detectors has enabled a direct measurement of the vertical turbulent flux. Wesely et al. (1977) recorded the velocity, w', and concentration, c', fluctuations at a

reference height of z_r = 5 m and evaluated v_g directly using

$$v_g(z_r) = \left. \frac{\overline{w'c'}}{\bar{c}} \right|_{z = z_r} \tag{6.23}$$

where $\overline{w'c'}$ is the time averaged vertical turbulent flux and $\bar{c}$ the average concentration. The averaging time for the results reported in Wesely et al. (1977) was O(10 minutes).

Another means for determining deposition velocities is to employ isotopic labelling techniques. If isotopes, with low natural abundances, are used then the task of differentiating between material previously present at the surface and the amount deposited during the experiment is considerably simplified. Owens and Powell (1974) released sulfur dioxide (SO_2), labelled with the sulfur isotope ${}_{16}S^{35}$, and measured the accumulation of $^{35}SO_2$ at the ground. Given the exposure time, T, and the $^{35}SO_2$ concentration at the reference elevation the deposition velocity is given by

$$v_g(z_r) = \frac{^{35}SO_2 \text{ Activity at the Ground}}{T \quad ^{35}SO_2(z_r)} \tag{6.24}$$

Chamberlain (1966) used thorium - B (${}_{82}Pb^{212}$), in a wind tunnel, to measure the vertical flux of pollutant materials towards grass and similar surfaces as a function of the concentration difference between the reference height and the surface.

The most common technique used in field studies is the gradient or profile method. This procedure utilizes measurements at two or more elevations to establish the vertical concentration gradient $\partial c/\partial z$. If the momentum, heat, water vapor, and pollutant fluxes are constant within the surface layer then the Monin-Obukhov similarity hypothesis, coupled with the measured vertical gradient, gives the pollutant deposition velocity

$$v_g(z_r) = \frac{K_p(z)}{c(z)} \left.\frac{\partial c}{\partial z}\right|_{z = z_r} \tag{6.25}$$

The turbulent eddy diffusivity $K_p(z)$ can be estimated using the methods presented in Chapter 4 or determined from energy budget measurements using a mass transfer analogy. An alternative approach is to assume that the pollutant transport is similar to that of water vapor and employ a stability dependent bulk transfer coefficient to approximate the surface flux. Given the measured concentration profile the deposition velocity is simply

$$v_g(z_r) = C\bar{u}(z_h) \left(\frac{c(z_h) - c(z_d)}{c(z_r) - c(z_d)} \right) \tag{6.26}$$

where C is the aerodynamic transfer coefficient and $\bar{u}(z_h)$ is the mean wind speed at an elevation z_h above the ground. Whelpdale and Shaw (1974) used (6.26) to evaluate SO_2 deposition velocities over different surfaces for a range of stability conditions. Further, more detailed discussions of the profile and other methods are given in Garland (1974) and Droppo and Hales (1974).

6.7 Literature Survey of Deposition Velocity Measurements

A major goal of developing the upper limit deposition model was to establish the surface removal rates for those species which participate in photochemical reactions. A partial list of these species includes nitric oxide (NO), nitrogen dioxide (NO_2), ozone (O_3), peroxy acetyl nitrate (PAN), hydrogen peroxide (H_2O_2), nitrous acid (HONO), nitric acid (HNO_3), carbon monoxide (CO), reactive hydrocarbons, organic and inorganic radicals. An extensive literature search was carried out to identify experimental determinations of ground level deposition velocities for each of these species. The results, presented in Table 6.5, include additional values excerpted from the comprehensive surveys conducted by Droppo (1976), Slinn et al. (1978) and McMahon and Denison (1979). In constructing the table an attempt has been made to summarize those factors which influence the estimates, namely the experimental technique, reference height, type of surface, moisture conditions and the atmospheric conditions.

Considering the important role of deposition in establishing ambient concentration levels the most striking feature of Table 6.5 is the paucity of reported results. The problem is further compounded by inadequate documentation of the atmospheric conditions prevailing during each of the experiments. Unless sufficient meteorological data are reported it is difficult to separate whether the turbulent transport or chemical nature of the underlying surface is controlling the deposition. The limited data reported in the table are, unfortunately, insufficient to adequately verify the quantative performance of the upper limit model.

TABLE 6.5

Literature Survey of Deposition Velocity Data for Species Involved in Photochemical Reaction Processes

SPECIES	DEPOSITION VELOCITY v_g(cm/s)	SURFACE CONDITIONS	MEASUREMENT METHOD	METEOROLOGICAL DATA REPORTED	REFERENCE
O_3	1.67	Alfalfa	Flux	$\bar{u}$	Hill and Chamberlain (1974)
	0.10-2.10	Soil, Short Grass	Profile	$z/L, R_{i_b}, u_*, z_r$=4m, T, RH, z_o	Galbally (1971)
	0.47-0.55	Grass, Soil, Water	Flux	$\bar{u}, u_*, z_o, z_r$=10cm	Garland and Penkett (1976)
	0.20-0.80	Maize	Flux	$\bar{u}, u_*, z_o$, w, T, z_r=4-5m	Wesely et al. (1978)
	0.60-6.30	---	---	---	Droppo (1976)
	0.02-1.80	---	---	---	McMahon and Denison (1979)
	0.29-0.84	Soybean field	Eddy-correlation	$\bar{u}$, z_r=5.2m, L	Wesley et al. (1982)
NO	0.10	Alfalfa	Flux	$\bar{u}$	Hill and Chamberlain (1974)
NO_2	1.90	Alfalfa	Flux	$\bar{u}$	Hill and Chamberlain (1974)
	0.50-2.00	---	---	---	McMahon and Denison (1979)
	0.05-0.56	Soybean field	Eddy-correlation	$\bar{u}$, z_r=5.2m, L	Wesley et al. (1982)
CO	0.00-0.002	Vegetation	---	---	McMahon and Denison (1979)
PAN	0.14-0.30	Grass, Soil	Flux	$\bar{u}, u_*, z_o, z_r$=10cm	Garland and Penkett (1976)
	0.63	Alfalfa	Flux	$\bar{u}$	Hill and Chamberlain (1974)

A qualitative indication can, however, be gained by examining the study of sulfur dioxide (SO_2) deposition carried out by Whelpdale and Shaw (1974). Their results, presented in Table 6.6, clearly demonstrate that the influence of atmospheric stability is consistent with the calculated variation shown in Figure 6.2. During stable conditions the deposition flux is primarily controlled by the rate at which material can be transported to the surface. Such circumstances are likely to occur at night. During the daytime the deposition rate is much more likely to be influenced by the chemical interaction at the surface.

Table 6.7 summarizes the deposition velocities derived from the literature survey. The accompanying concentration ratios, based on a reference elevation z_r = 1 m, are for use in the airshed model. The data should only be considered as estimates.

6.8 Conclusions

In this chapter a simple upper limit model for pollutant deposition velocities has been presented. The principal features of the formulation are: an explicit treatment of atmospheric stability and a formal procedure for determining equivalent cell average deposition velocities for use in numerical calculations. The fact that atmospheric stability has such a pronounced effect on the surface fluxes points to the need for careful reporting of meteorological conditions during field studies. This would enable an independent assessment of whether the limits on v_g are set by the eddy diffusion or by the ability of the underlying surface to assimilate the material. In terms of future work considerably more

TABLE 6.6

Average Deposition Velocity of SO_2 for Different Surface and Stability Conditions[a]

SURFACE	STABILITY	NUMBER OF EXPERIMENTS	DEPOSITION VELOCITY v_g (cm/s)
Grass	$Ri_b < -0.02$	10	2.4
	$-0.02 < Ri_b < 0.02$	3	2.6
	$Ri_b > 0.02$	2	0.5
Snow	$Ri_b < -0.02$	1	1.6
	$-0.02 < Ri_b < 0.02$	3	0.52
	$Ri_b > 0.02$	8	0.05
Water	$Ri_b < -0.02$	7	4.0
	$-0.02 < Ri_b < 0.02$	7	2.2
	$Ri_b > 0.02$	4	0.16

a. Source: Whelpdale and Shaw (1974)

b. Stability is defined in terms of the bulk Richardson Number Ri_b

$$Ri_b = \frac{g}{T} \Delta z \frac{\Delta\theta}{(\Delta\bar{u})^2}$$

where T is the ambient temperature, Δz difference in sampling heights, $\Delta\theta$ the potential temperature difference and $\Delta\bar{u}$ the wind speed.

TABLE 6.7

Summary of Deposition Velocity Data
and Concentration Ratios

SPECIES	DEPOSITION VELOCITY RANGE v_g(cm/s)	CONCENTRATION RATIO $1 - \frac{c(z_d)}{c(z_r)}$
O_3	0.025 - 6.3	0.8
NO_2	0.5 - 2.0	0.6
PAN	0.14 - 0.63	0.25
CO	0.0 - 0.03	0.0
NO	0.0 - 0.10	0.1

attention needs to be given to characterizing the physical and chemical processes occuring in the layer $z_d \leq z \leq z_o$. At present there are no satisfactory theoretical treatments of the mass transfer close to the surface. Even more serious is the limited amount of field data on pollutant uptake at the surface.

A basic limitation of the model is the reliance on Monin-Obukhov similarity theory to characterize the material fluxes. While this formally restricts applications to steady conditions and values $|z/L| < 1$, the model is, nevertheless, capable of producing useful limits for surface deposition fluxes for a range of the species encountered in photochemical applications.

CHAPTER 7

TREATMENT OF POINT AND AREA SOURCE EMISSIONS

7.1 Introduction

A primary determinant of pollutant concentration levels within an urban environment is the emission of contaminant materials into the atmosphere. These emissions, which can be produced from a variety of different activities, enter the airshed model either through the boundary conditions or as source terms in the conservation equations. This chapter describes the procedures used to allocate emissions into the appropriate computational cells. Particular attention is given to: the mode of material injection, effective release height, near source chemistry and the influence of turbulent diffusion. The issues which need to be considered when compiling a comprehensive emission inventory for a specific region are discussed in Chapter 13.

7.2 Point and Area Source Emissions

Despite the diversity of different source types, pollutants and modes of material discharge, most emissions can be considered to be released from either point locations or areal regions. Point sources, by definition, need to be treated as direct inputs to the species continuity equations in much the same manner as the chemical reaction terms. If a point source emits a typical species at the rate $E_p(\underline{x}_p,t)$ from the discharge point $\underline{x}_p$, then the contribution to the rate of concentration change at $\underline{x}$ is given by

$$S(\underline{x},t) = E_p(\underline{x}_p,t)\alpha(\underline{x},\underline{x}_p) \qquad (7.1)$$

where $\alpha(\underline{x},\underline{x}_p)$ is given by

$$\alpha(\underline{x},\underline{x}_p) = \begin{cases} 1 & ; \quad \underline{x} = \underline{x}_p \\ 0 & ; \quad \underline{x} = \underline{x}_p \end{cases} \tag{7.2}$$

Area sources are typically located at the ground and as a result they enter the airshed model through the boundary conditions. For the problem under consideration the flux balance at the surface results in an expression of the form

$$v_g c - K_{zz}\frac{\partial c}{\partial z} = E_a(\underline{x},t) \tag{7.3}$$

where v_g is the deposition velocity of species c, K_{zz} the turbulent diffusivity and $E_a(\underline{x},t)$ is the emission flux at the ground. In a typical urban airshed there are often a very large number of point sources within an area defined by a typical computational cell. Rather than considering each source separately, a common practice is to aggregate all the ground level point sources within each cell and develop a comparable source term. If there are n ground level point sources located within an area, A, then the equivalent, uniformly distributed flux is given by

$$E_a(\underline{x},t) = \frac{1}{n}\sum_{i=1}^{n} E_p(\underline{x}_i,t) \qquad ; \underline{x}_i \in A \tag{7.4}$$

Most airshed models cannot resolve spatial scales smaller than the size of an individual computational cell. Because of this, point and area emissions are often treated as volume source terms. In order

to determine the incremental contribution from emissions into a particular cell consider the one shown in Figure 7.1, which is of arbitrary base area A and uniform height h(t). Given the mass emission rate from either a point source $E_p(\underline{x}_p,t)$ or an area source $E_a(\underline{x},t)$, the corresponding cell mass concentrations $Q_p(t)$ and $Q_a(t)$ are of the form

$$Q_p(t) = \frac{E_p(\underline{x}_p,t)}{h(t)\ A} \tag{7.5}$$

and

$$Q_a(t) = \frac{\iint_A E_a(\underline{x}_p,t)\ d\underline{x}}{h(t)} \tag{7.6}$$

To be useful in comparisons against ambient air quality standards the expressions (7.5 - 7.6) need to be converted to a system of concentration units expressed in terms of parts per million by volume. This is accomplished by assuming that all species can be described by the ideal gas laws. Under these conditions the volume occupied by one mole of an ideal gas is given by RT/P where R is the Universal gas constant, T the absolute temperature in ^{o}K, and P the pressure in standard atmospheres. If M is the molecular weight of species k then the conversion is given by

$$\text{Concentration (ppmv)} = \frac{RT}{MP}\ \text{Concentration } (\mu gm/m^3) \tag{7.7}$$

The source conversion factor, S, expressed in units of ppm sec^{-1} is then given by

$$S = \frac{RT}{MP}\ 10^9\ Q(Kgm/m^3\text{-}s) \tag{7.8}$$

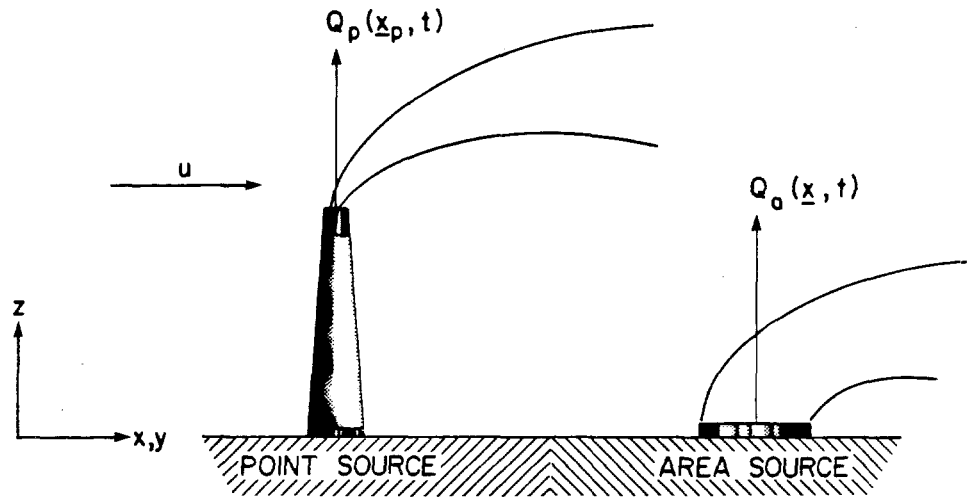

(a)

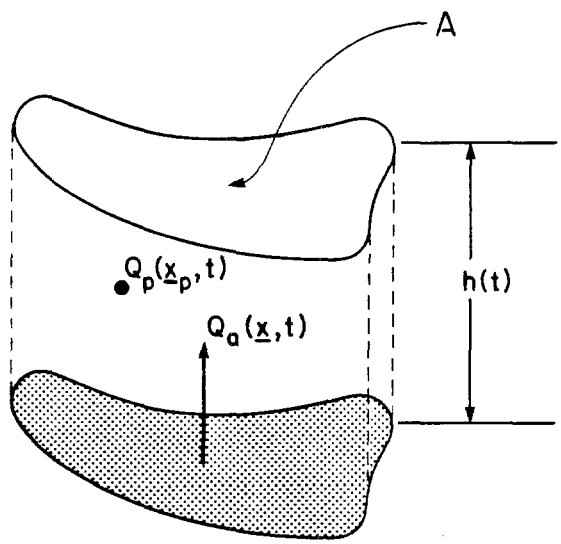

(b)

FIGURE 7.1

Point and Area Source Representation

For the most common case of a regular cell of volume V and source emissions E_p and E_a the above expressions reduce to:

$$S_p(t) = \frac{RT}{MP} \frac{10^9}{V} E_p(\underline{x}_p, t) \tag{7.9}$$

$$S_a(t) = \frac{RT}{MP} \frac{10^9}{h(t)} E_a(\underline{x}, t) \tag{7.10}$$

In order to illustrate an application of the above formulae consider an area source with an emission flux density of $E_a(t) = 1$ Kgm/m^2-s and a point release of $E_p(t) = 1$ Kgm/s. If the ambient conditions are T = 25 ^oC = 298 ^oK, P = 1 atm and R = 8.314 Joule/gm-mole-^oK (RT/P = 0.02450), then the source conversion factors for a unit cell volume and height can be readily calculated from (7.9) and (7.10). Some typical results for a range of different species are shown in Table 7.1.

Both concentration conversion formulae require a knowledge of the molecular weights. This does not pose a problem for most species; however, a difficulty arises when treating hydrocarbons because there are hundreds of them present in a typical urban atmosphere. Since it is not practical to consider the reactions of each individual hydrocarbon, the most common approach is to treat the chemistry of a series of lumped classes. A typical grouping could be aldehydes, olefins, aromatics, alkanes and other non-reactive species.

TABLE 7.1

Conversion Factors for Point and Area Sources[a]

SPECIES (k)	MOLECULAR WEIGHT (gm)	CONVERSION FACTORS[b] ($\frac{\mu gm}{m^3}$ / ppm)	SOURCE EMISSION[c] FACTORS ($S_p^k V$, $S_a^k h$)
CO	28	1143	8.75×10^5
NO	30	1224	8.17×10^5
NO_2	46	1878	5.33×10^5
SO_2	64	2612	3.83×10^5
SO_3	80	3625	3.06×10^5
CH_4	16	653	15.31×10^5
C_3H_8	44	1796	5.57×10^5
HCHO	30	1224	8.17×10^5
NH_3	17	694	14.41×10^5

(a) Ambient conditions p = 1 atm and T = 298°K

(b) Example calculation, 1.5 ppmV of nitric oxide (NO) = 1.5 x 1224 = 1836 $\mu gm/m^3$

(c) The conversion factors are based on E_a = 1 Kgm/m^2-sec and E_p = 1 Kgm/sec. As an example consider a large point source emitting 0.1 Kgm/sec (≃ 10 tons/day) of nitric oxide (NO) into a grid cell of dimension 5000 x 5000 x 30 m, then

$$S_p(NO) = \frac{RT}{MP}\frac{10^9}{V} E_p(NO) = \frac{8.17\times10^5 \times 0.1}{5000\times5000\times30} = 1.14\times10^{-4} \frac{ppm}{sec} \simeq 7 \frac{ppb}{min}$$

In the present study the i-th hydrocarbon class average molecular weight, MW_i, is determined from

$$MW_i = \frac{\sum_{k=1}^{n} E_k}{\sum_{k=1}^{n} E_k / M_k} \qquad (7.11)$$

where E_k and M_k are the emissions and molecular weight of species k in the i-th class.

7.3 Effective Release Height for Emissions

In the previous section no consideration was given to either the physical stack height or the buoyant rise of hot exhaust gases when locating the effective discharge point, $\underline{x}_p$. Within the airshed model the actual height, H, for emission release is considered to be the sum of the stack elevation, h_s, and the plume rise, h_p. Depending upon the value of H and the size of the first computational cell, Δz, the emissions can be treated as either ground level or elevated releases. Clearly when $h_s > \Delta z$ the emissions need to be considered as elevated point sources. When $h_s < \Delta z$ the distinction between ground level and elevated sources, and their mode of numerical treatment, is no longer clear cut. As a result it is necessary to establish selection criteria which can be used to distinguish between the two cases. One approach for creating such a division is shown in Figure 7.2 and illustrates the need to address two basic issues: the computational cost and the magnitude of the concentration increment.

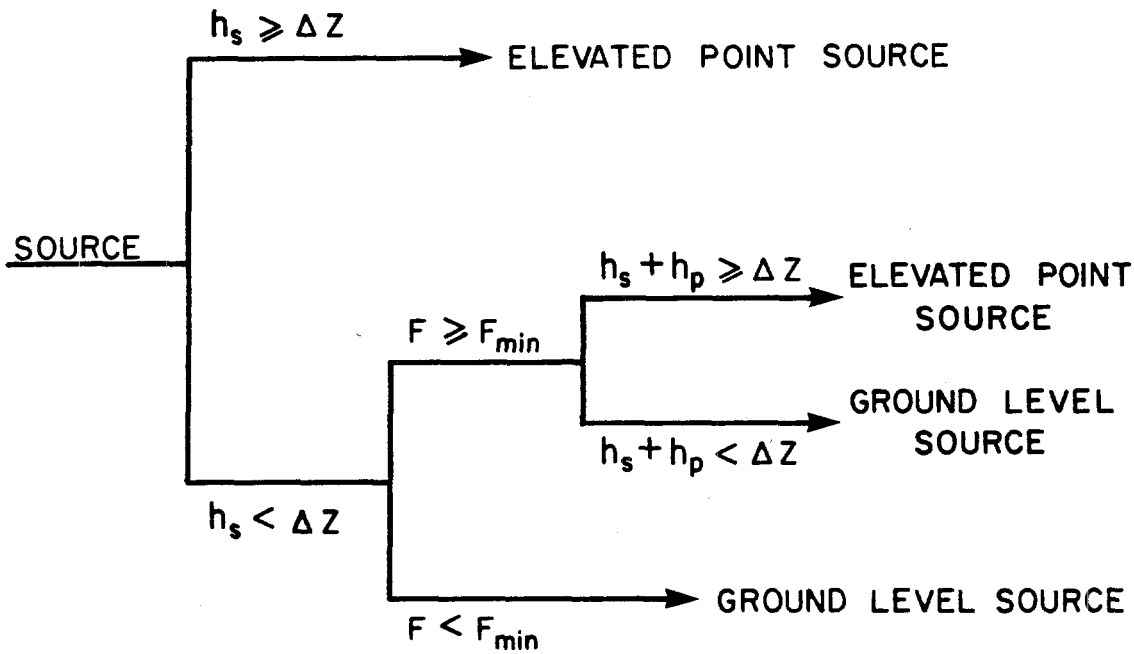

FIGURE 7.2

Selection Criteria for Ground Level and Elevated Sources

The critical problem, in either case, is to determine if the plume rise above the stack top is greater than Δz. Since most of the exhaust plumes encountered in an urban environment are dominated by buoyancy rather than momentum, an initial selection can be made on the basis of the magnitude of the buoyancy flux, F, emitted by the source. This flux is defined as

$$F = \frac{g\, Q_H}{\pi C_p \rho T_s} \tag{7.12}$$

where Q_H is the heat output from the source, T_s the stack gas temperature, C_p and ρ the specific heat and density of the exhaust gases. In the present model the source emissions are treated as ground level releases if the effluent buoyancy is below a minimum value, F_{min}. Assigning a lower value effectively reduces the the number of sources treated as individual point releases. This latter factor is quite important as an extensive set of calculations must be performed in order to correctly account for the material dispersion from each source. In practice the exact value of the cutoff depends on the number of sources and the magnitude of their emissions. Chapter 13 discusses the choice of F_{min} for an urban airshed.

When the source buoyancy exceeds F_{min} the next step is to determine if the equilibrium height of the effluent plume is above the top of the first computational cell. If the plume rise plus the stack height exceeds Δz then the source is treated as an elevated point source. When $h_s + h_p < \Delta z$ the point source is added to the ground level flux term in (7.3). Clearly a crucial element of the selection

process is the determination of h_p and this is the subject of the next section.

7.4 Plume Rise and Effective Stack Height

Characterization of the plume rise above the stack top in terms of the exhaust gas properties and the ambient atmospheric state is a complex problem. A recent review by Briggs (1975) indicates that no single formula adequately predicts plume rise for the range of commonly encountered meteorological conditions; indeed, the predictions of different formulations can vary by factors of 2 to 10. Given such a large range of uncertainty it is natural to ask the question: what procedures can be used in the airshed model to predict the plume rise from individual point sources? The objective of this section is to present the formulae embedded in the airshed model.

As might be expected, there is an extensive literature on plume rise modeling; however, it is beyond the scope of this study to consider the details of the different formulations. This background information is comprehensively reviewed in the works of Briggs (1969,1975), Fischer et al. (1979), Fabrick et al. (1977) and Tesche et al. (1976). An examination of this literature indicates that the approaches can be broadly classified into three basic categories. The most detailed involves solving the coupled conservation equations of mass, momentum, energy and species. This method is generally not used in airshed models because of the prohibitive cost of the numerical solution. An alternative approach, introduced by Morton et al. (1956), is to consider the integrated form of the conservation equations. This method

involves integrating the equations across a section normal to the plume trajectory and assuming that all turbulent transport terms vanish at the plume boundary. Several variations of the general equations for the integral method are available for different flow geometries and the ambient conditions. A thorough discussion of the development of the general equations for a buoyant jet in a density- stratified cross flow are given by Hirst (1972), Omms (1972), Wright (1977), Schatzmann (1979), Koh and Brooks (1975), Csanady (1973), Hoult et al. (1969) and Fischer et al. (1979).

Although there are many plume rise formulae, the ones proposed by Briggs (1969, 1975) are the most widely employed in practice (CRSTER, 1977). Extensive sets of field observations, dimensional analyses and theoretical formulations were used by Briggs in developing the plume models. Near the source h_p is adequately predicted using the momentum conservation equations and a simple entrainment assumption.

For <u>neutral</u> and <u>unstable</u> conditions Briggs developed the following expression:

$$h_p = \frac{1.6\ [F\ x^2]^{1/3}}{u} \qquad (7.13)$$

where x is downwind distance from source (m), and u is the horizontal wind speed (m/s). The buoyancy flux, in $m^4\ s^{-3}$, is defined by

$$F = \frac{g d^2 V_s (T_s - T_a)}{4 T_s} \qquad (7.14)$$

where g is the gravitational acceleration (9.8 m s^{-2}), d is the stack

inside diameter (m), V_s the exhaust gas velocity (m/s), T_a is the ambient air temperature (^oK), and T_s the stack exhaust gas temperature. Based on early experimental evidence, Briggs concluded that the final plume rise, h_p, occurred at a downwind distance of ten stack heights. Later results indicated that the the downwind distance at which the final plume rise occurred was a function of buoyancy. The distances are as follows

$$x_d = \begin{cases} 14\ F^{5/8} & ;\ F < 55 \qquad (7.15) \\ 34\ F^{2/5} & ;\ F \geq 55 \qquad (7.16) \end{cases}$$

The limiting plume rise predictions as a function of the buoyancy flux parameter F are shown in Figure 7.3.

Under stable ambient stratification Briggs (1975) indicates that the plume rise can be described by

$$h_p = \begin{cases} 2.6\ [F/us]^{1/3} & ;\ \text{for windy conditions} \qquad (7.17) \\ 5.0\ [F^2/s^3]^{1/8} & ;\ \text{for near calm conditions} \qquad (7.18) \end{cases}$$

In these expressions s is stability parameter defined in terms of the vertical potential temperature gradient.

$$s = \frac{g}{T} \frac{\partial \theta}{\partial z} \qquad (7.19)$$

When calculating the plume rise h_p, the smaller of the values estimated by (7.17) and (7.18) should be used. The downwind distance

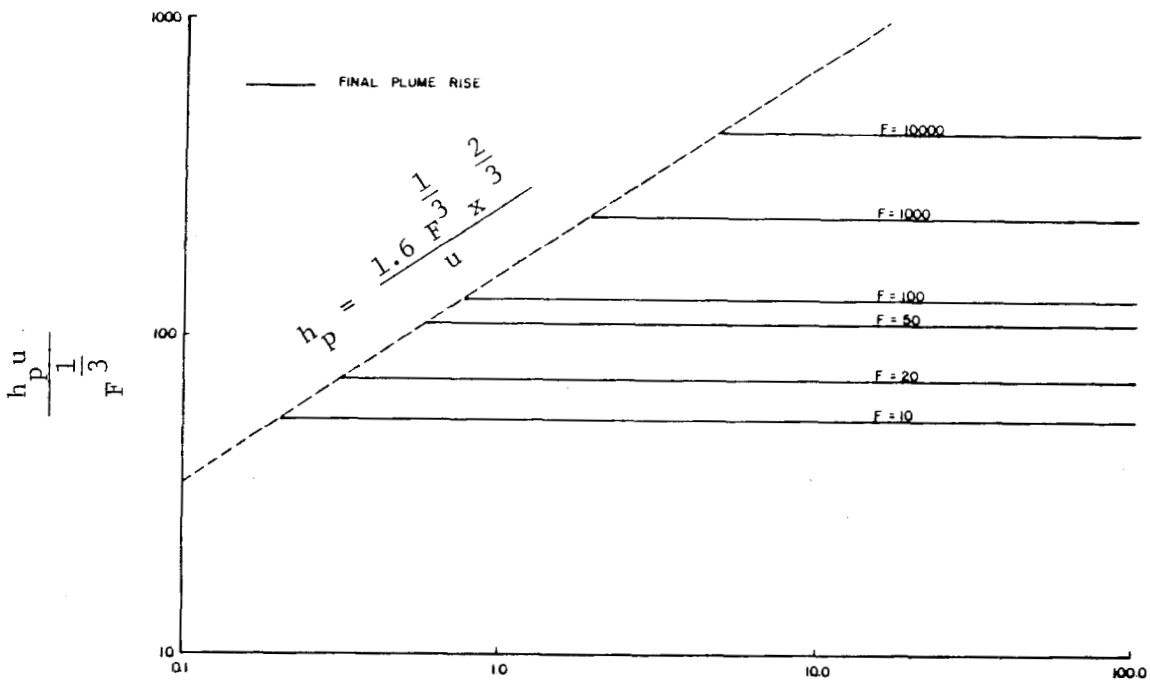

FIGURE 7.3

Limiting Plume Rise as a Function of the Buoyancy Flux Parameter F.

to the final plume rise is given by

$$x_d = \pi u/\sqrt{s} \tag{7.20}$$

In some circumstances the appropriate field data will not be available for direct determination of the stratification parameter; for these situations s can be approximated using the information presented in Table 7.2.

7.5 Plume Penetration Into Elevated Stable Layers

In urban environments the surface layer is often capped by an elevated stable layer. Since the formulae presented in the previous sections are only valid for conditions of uniform stratification they provide little guidance in assessing the ability of buoyant plumes to penetrate into the inversion. This section presents a simple model that enables the study of plume penetration in an environment composed of a surface neutral layer below a stable, elevated temperature inversion. A schematic representation of the problem is shown in Figure 7.4. Note that for the purposes of the following analysis the inversion is considered to be deeper than the final plume rise.

As a first approximation consider the classic Morton et al. (1956) approach to plume rise in which there is no cross flow. If the Boussinesq approximation is invoked then the conservation equations for mass, momentum and buoyancy can be written in the form

$$\frac{d}{dz}(b^2 w) = 2\alpha b w \tag{7.21}$$

TABLE 7.2

Relationship Between Pasquill-Gifford Stability Classes and Temperature Stratification

STABILITY CLASS	AMBIENT TEMPERATURE GRADIENT $\partial T/\partial z$ ($^{o}C/100m$)	POTENTIAL TEMPERATURE* GRADIENT $\partial\theta/\partial z$ ($^{o}C/100m$)
A (extremely unstable)	<-1.9	<-0.9
B (moderately unstable)	-1.9 to -1.7	-0.9 to -0.7
C (slightly unstable)	-1.7 to -1.5	-0.7 to -0.5
D (neutral)	-1.5 to -0.5	-0.5 to 0.5
E (slightly stable)	-0.5 to 1.5	0.5 to 2.5
F (moderately stable)	>1.5	>2.5

*Calculated by assuming $\frac{d\theta}{dz} \simeq \frac{dT}{dz} + \Gamma$ where Γ is the adiabatic lapse rate (0.986 $^{o}C/100m$).

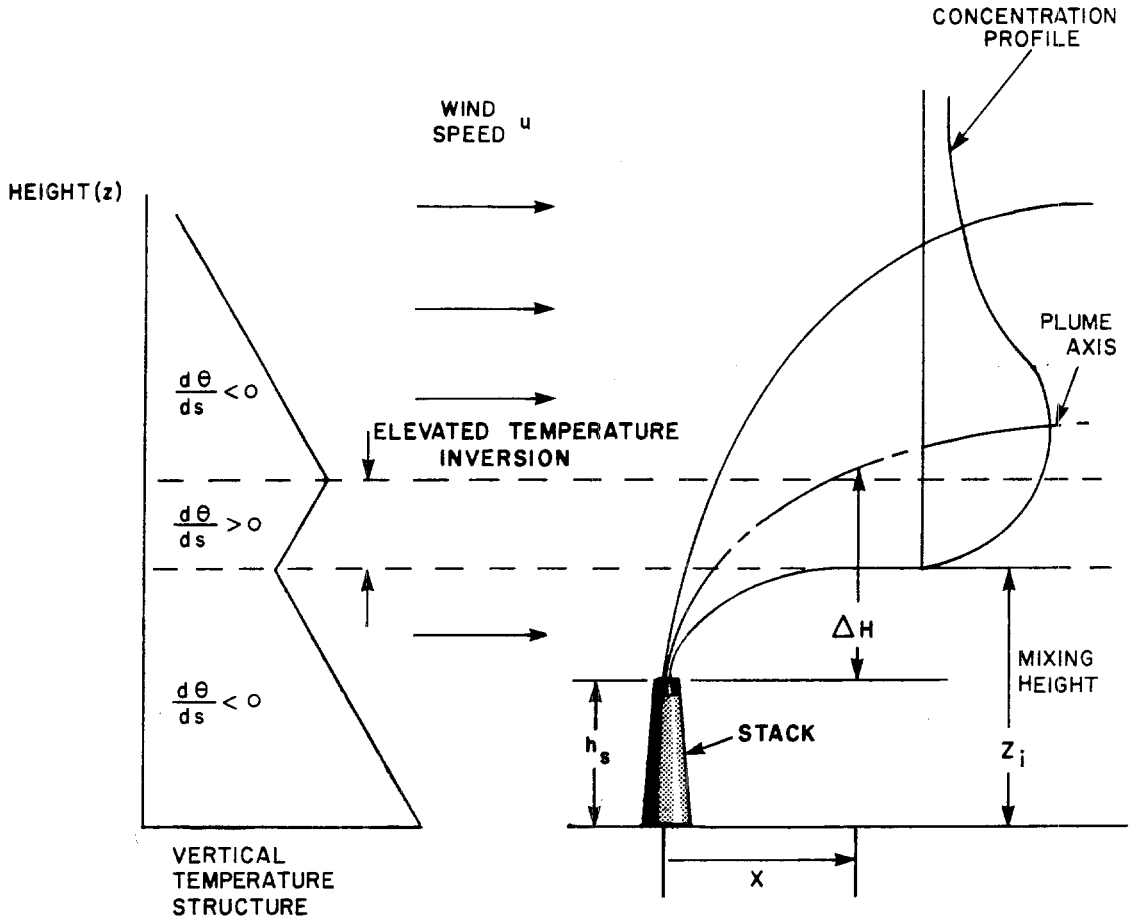

FIGURE 7.4

Nomenclature for Plume Rise Calculations

$$\frac{d}{dz}(b^2w^2) = b^2 g \frac{T_1 - T}{T_a} \tag{7.22}$$

$$\frac{d}{dz}\left(b^2 w g \frac{T_1 - T}{T_a}\right) = b^2 w \frac{g}{T_a} \frac{dTa}{dz} \tag{7.23}$$

where α is the entrainment coefficient, w(z) the vertical velocity component, b(z) the plume radius as a function of elevation z, T and T_1 are the temperatures inside and outside the plume. (T_a is a reference temperature, typically the ambient value at the same elevation as the top of the stack.) In the above formulation the vertical velocity and temperature have been assumed to be constant across the plume at any height. This formulation can be easily extended to the more conventional approaches of Csanady (1973) and Koh and Brooks (1975) in which the profiles are assumed to be Gaussian.

The buoyancy flux in (7.23) is given by

$$F_z = b^2 w g \frac{T_1 - T}{T_a} \tag{7.24}$$

Under neutral conditions $d(F_z)/dz$ is constant and so F_z is equal to F, the buoyancy flux at the stack exit. Equations (7.21) and (7.22) can be solved to give an expression for the change in buoyancy flux as a function of elevation and the temperature stratification parameter s, i.e.

$$\frac{dF_z}{dz} = -\frac{6\alpha}{5}\left(\frac{9\alpha}{10}\right)^{1/3} s^{1/3} F^{1/3} z^{5/3} \tag{7.25}$$

Starting at the stack top, where $F_z = F$, (7.25) can be integrated to find the elevation at which $F_z = 0$. This height defines the vertical extent of the plume rise. Since s=0 for $0 \leq z \leq Z_i$ the integral can be written in the form

$$\int_F^0 dfz = \frac{6\alpha}{5} \left(\frac{9\alpha}{10}\right)^{1/3} s\, F^{1/3} \int_{Z_i}^{z_e} z^{5/3}\, dz \tag{7.26}$$

Where z_e is the height of final plume rise. Evaluating the integral gives

$$z_e = Z_i \left[1 + \frac{20}{9\alpha} \left(\frac{10}{9\alpha}\right)^{1/3} 1/s \left(\frac{F}{Z_i^4}\right)^{2/3} \right]^{3/8} \tag{7.27}$$

Which for a typical value of the entrainment coefficient, $\alpha = 0.124$, (Briggs, 1975) gives the following approximate expression for z_e

$$z_e = Z_i \left[1 + \frac{37}{s} \left(\frac{F}{Z_i^4}\right)^{2/3} \right]^{3/8} \tag{7.28}$$

Considering the finite size of the plume, complete penetration is likely to occur when $z_e = 1.3Z_i$. A similar analysis can be performed for the uniform cross flow case which results in an equilibrium plume rise of the form

$$z_e = Z_i \left[1.8 + \frac{19F}{usZ_i^4} \right]^{1/3} \tag{7.29}$$

A surprising feature of (7.29), also noted by Briggs (1975), is that

50% penetration ($z_e = Z_i$) requires only 1/28 of the buoyancy required for 100% penetration ($z_e > 2Z_i$). Within the airshed model the plume is considered to have penetrated the inversion base if

$$F > 0.3\ us Z_i^3 \tag{7.30}$$

Because of the finite depth of the plume, partial penetration of elevated inversions probably occurs more often than total penetration. In either case it is important to have some estimate of the amount of material injected into the inversion. Manins (1979) presents laboratory results and a theoretical model of the conditions under which plumes can penetrate sharp, elevated temperature inversions. Of particular interest is the fact that his model can be used to predict the fraction of material trapped in the inversion layer and which will be available for subsequent fumigation. One of the more interesting findings of Manins' work was that so long as the plume remains in the inversion layer the amount of material trapped per unit downwind distance is approximately independent of wind speed.

In many situations the boundary layer temperature structure is more complicated than the simple two layer system described above. There are a number of integral plume models which can be used to predict plume dispersion in arbitrarily stratified environments. Some examples are described in the works of Schatzmann (1979), Omms (1972), Briggs (1975) and Hirst (1972). Unfortunately none of these models result in simple analytic expressions and as a result they must be solved numerically.

7.6 Treatment of Elevated Point Sources

Most previous models have either ignored the dispersion of pollutant material from elevated point sources (MacCracken et al., 1978) or treated them in a highly simplified manner (Reynolds et al, 1973). This is unfortunate since the contribution to both local and more distant pollutant levels can be quite significant. For example when the effective stack height is below the top of the mixed layer, the effluents can be rapidly downmixed within a short distance of the source. If the emissions are injected into the inversion the plume material can remain aloft for many hours, effectively isolated from the ground, until convective mixing erodes the stable layer. The point at which the fumigation occurs may be a considerable distance downwind from the source. This phenomenon was discussed in Chapter 5.

The most common allocation scheme for elevated point sources is to add the emissions from the source into the grid cell at the effective stack height. If all the material is injected into one cell the near source air quality impact can be overestimated. An even more serious drawback with this approach is that an isolated source can induce numerical dispersion errors that in turn can produce severe instabilities during numerical solution of the chemical kinetics. These errors can become even more severe when multiple sources are considered because the dispersive waves from each release can interact and be amplified (Figure 7.5). Some of these computational difficulties can be overcome by using the solution procedures described in Chapter 10.

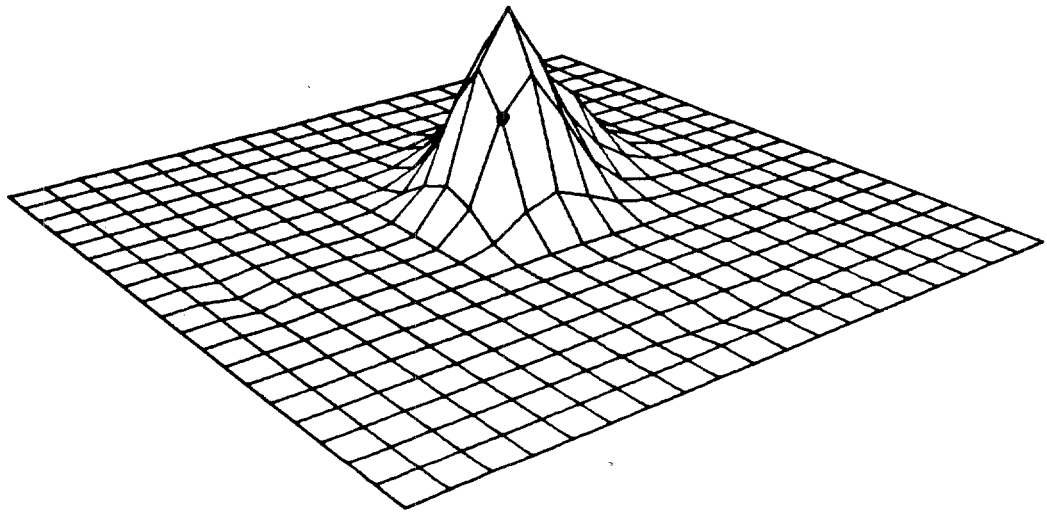

(a)

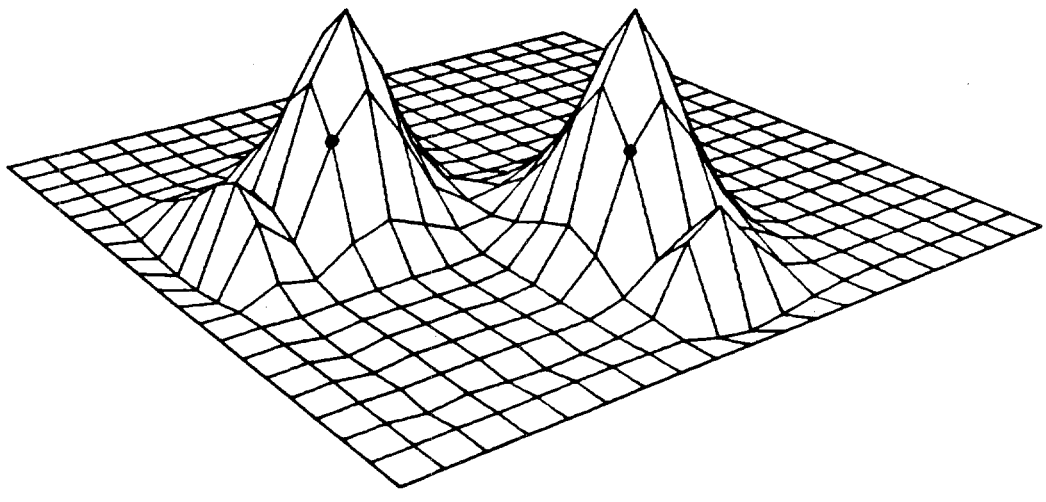

(b)

FIGURE 7.5

Concentration Distributions Resulting from
Direct Point Source Injection into the
Computational Cells indicated by Dots

(u=v=2.2 m/s, t = 1.6 hrs, $\Delta t = \Delta x = \Delta y$ = 3.2 Km, $K_{xx}=K_{yy}$ = 100m^2/sec)

In an earlier effort to avoid some of these problems, Reynolds et al. (1973) allocated the emissions to downwind computational cells on the basis of some Gaussian plume dispersion estimates. During the daytime the plume was considered to be well mixed in the vertical direction within a horizontal distance of two grid cells downwind from the source. Perhaps the most critical limitation of their procedure was that emissions injected above the top of the mixed layer were ignored.

The approach adopted in this study is to disperse the emissions downwind, taking into account the actual vertical and lateral spread of the plume as well as whether the effective stack height is above or below the top of the mixed layer. Lateral and vertical dimensions of the plume are obtained by assuming a Gaussian profile in each direction. In each direction the plume halfwidth is assumed to be 2σ which includes 95% of the plume mass. The dispersion coefficients σ_y and σ_z are functions of solar radiation, cloud cover, wind speed and surface roughness. The plume is assumed to extend downwind for a distance $u\Delta t$ where Δt is the averaging time of the wind data. If the vertical thickness of the plume, $4\sigma_z$, exceeds the mixed layer depth, the vertical thickness is taken to be the mixing height. Over the averaging time of the wind data, the plume is assumed to be uniformly mixed and to be essentially conical (Figure 7.6). With this assumption the fraction, F_{ijk}, of the elliptical cone volume that is within a given downwind grid cell, (i,j,k), can be used to calculate the magnitude of the source contribution

$$S_{ijk} = \frac{E_p \, \Delta t}{\Delta x \, \Delta y \, \Delta z} F_{ijk} \qquad (7.31)$$

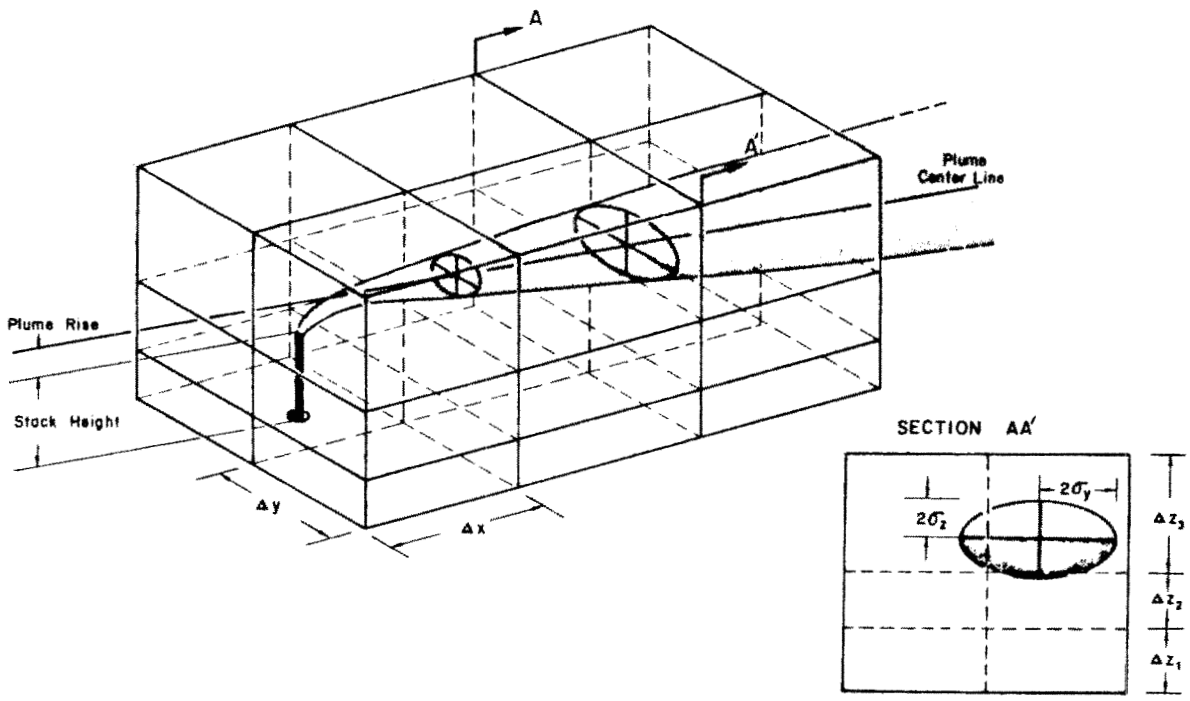

FIGURE 7.6

Plume Dispersion in Computational Grid

Figure 7.7(a) displays the concentration distribution resulting from a single source using this dispersion procedure. The upwind negative concentrations are much smaller than those resulting from the single cell source injection. Figure 7.7(b) shows the concentration distribution resulting from the same computational procedure but with two sources. The upwind dispersion errors, in both cases, are substantially less than those shown in Figure 7.5.

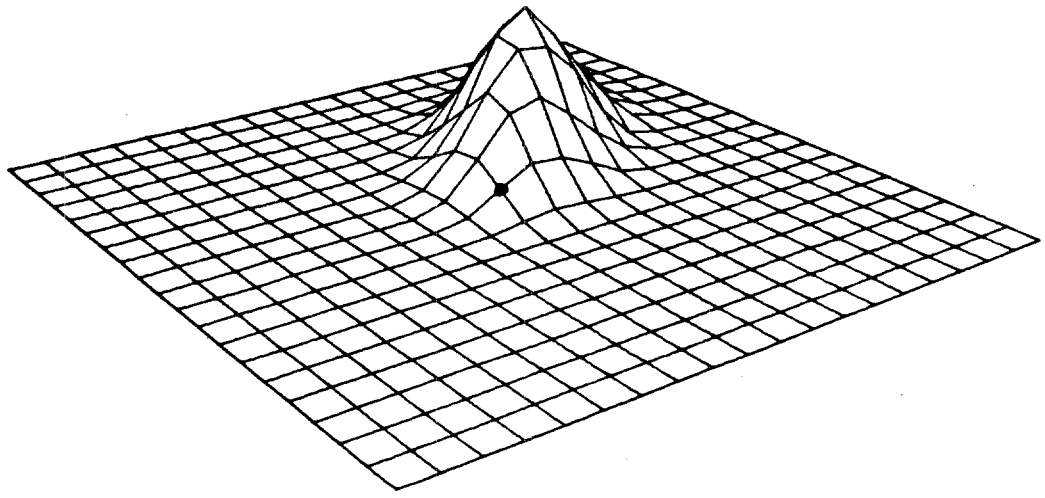

(a)

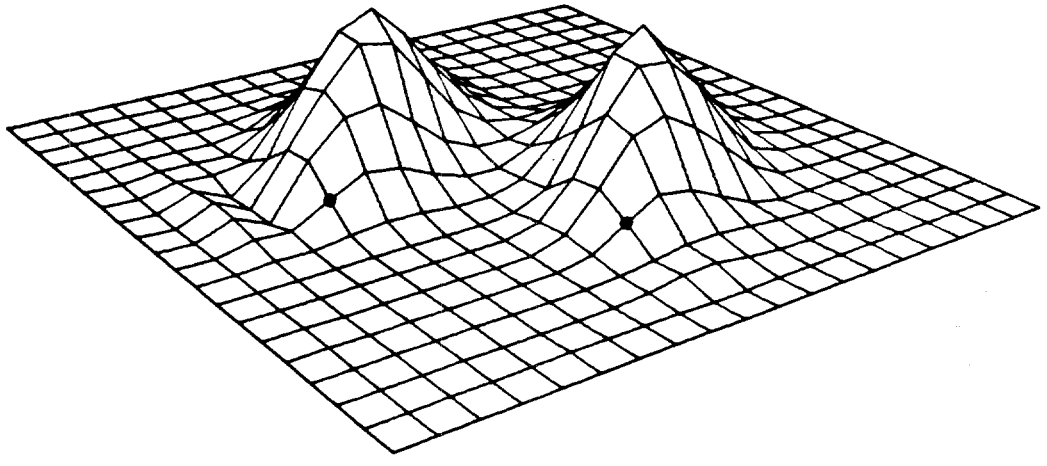

(b)

FIGURE 7.7

Same as Figure 7.6 except that the source injection is performed using the algorithm described in the text

7.7 Plume Dispersion Parameters

A key element of the source allocation procedure introduced in the previous section was the characterization of the plume growth in terms of the dispersion parameters σ_y and σ_z. While there is an extensive literature on procedures for estimating the coefficients, most of the commonly adopted schemes utilize the formulation presented in Turner (1970). Unfortunately the Turner Workbook is based on a limited set of field data and, more importantly, it does not accurately describe dispersion under unstable conditions. (Hanna et al., 1977; Gifford, 1976;and Pasquill, 1975, 1976). The recent work of Willis and Deardorff (1976, 1978), Lewellen and Teske (1975) and Lamb (1978, 1979) indicates that under convectively driven conditions both the mixed layer depth and the convective velocity scale have a significant impact on pollutant diffusion from elevated sources. Neither of these variables are included in typical Gaussian plume calculations. The objective of this section is to present an algorithm for predicting the plume growth in terms of readily available or estimated meteorological information. The procedure supplements the material presented in Chapter 4 and is partly based on the measurements and literature results assembled by Irwin (1979).

When describing the plume geometry it is important to ensure that the averaging times of the turbulence statistics and requirements for the concentration predictions are consistent. The basic problem is illustrated in Figure 7.8. As seen by a stationary observer, the mean concentration is influenced by meandering of the plume during the

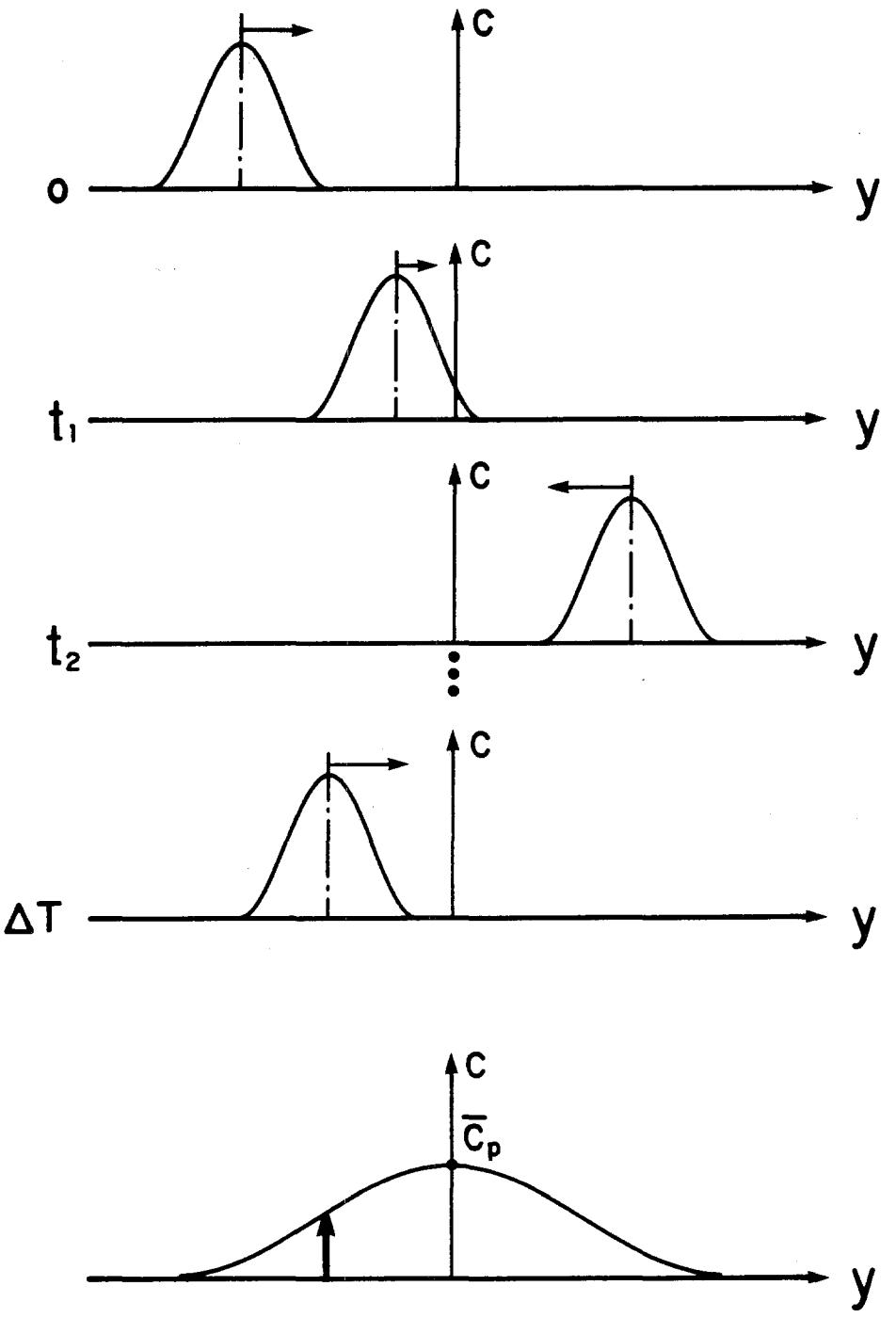

FIGURE 7.8

Instantaneous Concentrations and the Effect of Temporal Averaging

experiment. Taylor (1921) addressed this issue and proposed a model for the average plume dimensions expressed in terms of the motion of single particles released from the point source. At a particular instant, however, the plume outline is defined by the trajectories of two particles released simultaneously by the source. The instantaneous plume width is described by the particle separation and the meander by the position of their center of mass. The need for distinguishing between the two cases becomes apparent when it is recognized that the plume chemistry is controlled by the instantaneous values and the observed ground level concentration by the average profile. Some initial ideas on the relationship between averaging times and particle statistics for different observed wind velocity spectra are presented in Sheih (1980). Further, more definitive work will require field data from a wider range of conditions. For the purposes of the present study it has been assumed that the averaging times for the dispersion coefficients are comparable with those of the meteorological data.

In the atmosphere σ_y and σ_z reflect the influence of the different physical phenomena acting on the plume. If the assumption is made that the various processes are additive (Pasquill, 1975) then the total dispersion in each direction can be represented by

$$\sigma_y^2 = \sigma_{a(y)}^2 + \sigma_{b(y)}^2 + \sigma_{s(y)}^2 \tag{7.32}$$

$$\sigma_z^2 = \sigma_{a(z)}^2 + \sigma_{b(z)}^2 \tag{7.33}$$

where the subscript a refers to the contribution from atmospheric

turbulence, b the fraction induced by the inherent buoyancy of the plume and s the additional cross wind spread arising from vertical wind shear. Since the primary purpose of the source allocation procedure is to maintain the plume integrity only until it has grown to the size of a typical computational cell,the effect on lateral dispersion from changes in the wind direction and speed with elevation can be ignored. Most of the research work and field investigations have been directed at formulating the contribution from atmospheric turbulence.

Under suitable assumptions on atmospheric stationarity and homogeneity Taylor (1921) showed that the diffusion parameters can be written in the general form

$$\sigma^2_{a(y)} = 2\,\overline{v'^2}\int_0^T\int_0^t R_y\,(\xi)\,d\xi dt \tag{7.34}$$

$$\sigma^2_{a(z)} = 2\,\overline{w'^2}\int_0^T\int_0^t R_z\,(\xi)\,d\xi dt \tag{7.35}$$

where T is the diffusion time and $R_{y,z}$ are the Lagrangian autocorrelations associated with the wind fluctuations v′, w′ in the y and z directions. Close to the source $R(\xi) = 1$. In the limits of long diffusion times it is highly likely that the velocity fluctuations are uncorrelated and as a result $R(\xi) = 0$. For intermediate times measurement difficulties complicate characterization of the functional form of $R(\xi)$. In an effort to overcome some of the practical difficulties, Pasquill (1971) suggested an alternative definition that retained the

essential features of the Taylor formulation but which was more amenable to parameterization in terms of readily determined Eulerian quantities. In its most general form, as adopted by Draxler (1976), Hanna et al. (1977), and Irwin (1979), the Pasquill representation results in dispersion coefficients of the form

$$\sigma_{a(y)} = \sigma_v(\underline{P})\ t\ F_y(\underline{P}) \tag{7.36}$$

$$\sigma_{a(z)} = \sigma_w(\underline{P})\ t\ F_z(\underline{P}) \tag{7.37}$$

where the standard deviation of the wind fluctuations σ_v and σ_w and $F_{y,z}$ are universal functions of a set of parameters $\underline{P}$ which specify the characteristics of the atmospheric boundary layer over a range of stability conditions.

The variables which comprise $\underline{P}$ were introduced in Chapter 4 and include the friction velocity u_*, the Monin-Obukhov length L, the Coriolis parameter f, the mixed layer depth Z_i, the convective velocity scale w_*, the surface roughness z_0 and the height of the pollutant release above the ground z, i.e., $\underline{P} = \{ z, Z_i, u_*, w_*, z_0, L, f\}$. Details of the procedures used to determine these variables are discussed in Chapter 4.

For lateral dispersion, the standard deviation of the horizontal wind fluctuations can be written in the form

$$\sigma_v = \begin{cases} 1.78u_* \left[1 + 0.059 \left(- \frac{Z_i}{L} \right) \right]^{\frac{1}{3}} & ; \frac{Z_i}{L} < 0 \qquad (7.38) \\ 1.78u_* & ; \frac{Z_i}{L} \geq 0 \qquad (7.39) \end{cases}$$

Irwin (1979) developed (7.38) by combining the results of Nieuwstadt and van Duuren (1979), Deardorff and Willis (1975), and Draxler (1976). For neutral and stable conditions, σ_v is based on the calculations described in Binkowski (1979).

Normally Monin-Obukhov similarity is valid only for $z/L < -2$; however, for convective conditions mixed-layer scaling can be applied throughout the whole boundary layer (Panofsky et al., 1977; Nieuwstadt, 1980). Using these results Irwin (1979) proposed the following forms for F_y.

$$F_y = \begin{cases} \dfrac{1}{1 + \left(\dfrac{t}{T_i} \right)^{\frac{1}{2}}} \; ; \; \dfrac{1}{T_i} = \dfrac{2.5u_*}{Z_i} \left[1 + 0.0013 \left(- \dfrac{Z_i}{L} \right) \right]^{\frac{1}{3}} \; ; \; \dfrac{Z_i}{L} \leq 0 & (7.40) \\ \dfrac{1}{1 + 0.9 \left(\dfrac{t}{T_0} \right)^{\frac{1}{2}}} \; ; \; \dfrac{1}{T_0} = 1.001 \; ; \; \dfrac{Z_i}{L} > 0 & (7.41) \end{cases}$$

An examination of (7.38-7.41) indicates that they have the same limiting behaviour predicted by the Taylor theory i.e. $\sigma_v \propto t$ for $t \to 0$ and $\sigma_v \propto \sqrt{t}$ for $t \to \infty$. Another interesting feature of the model is that there is no functional dependence on release height.

In contrast, the standard deviation of the vertical velocity fluctuations are closely related to the height of the pollutant release above the surface. The reason for this is that under unstable conditions the appropriate similarity variables are the convective velocity w_* and the mixed layer height Z_i (Willis and Deardorff, 1976). Using these variables a wide range of field and laboratory measurements can be described by a universal function of the form

$$\sigma_w = w_* G(z/Z_i) \tag{7.42}$$

Irwin (1979) has assembled a number of different data sets which characterize $G(z/Z_i)$. His results, shown in Figure 7.9, have been incorporated into the airshed model.

During neutral and stably stratified conditions the formulation developed by Binkowski (1979) can be used

$$\sigma_w = u_* \left[\frac{\phi_m\left(\frac{z}{L}\right) - \frac{z}{L}}{3kf_m} \right]^{\frac{1}{3}} \quad ; \frac{z}{L} \geq 0 \tag{7.43}$$

In (7.43) k is the von Karman constant and $\phi_m(z/L)$ is given by

$$\phi_m\left(\frac{z}{L}\right) = 1 + 4.7\left(\frac{z}{L}\right) \tag{7.44}$$

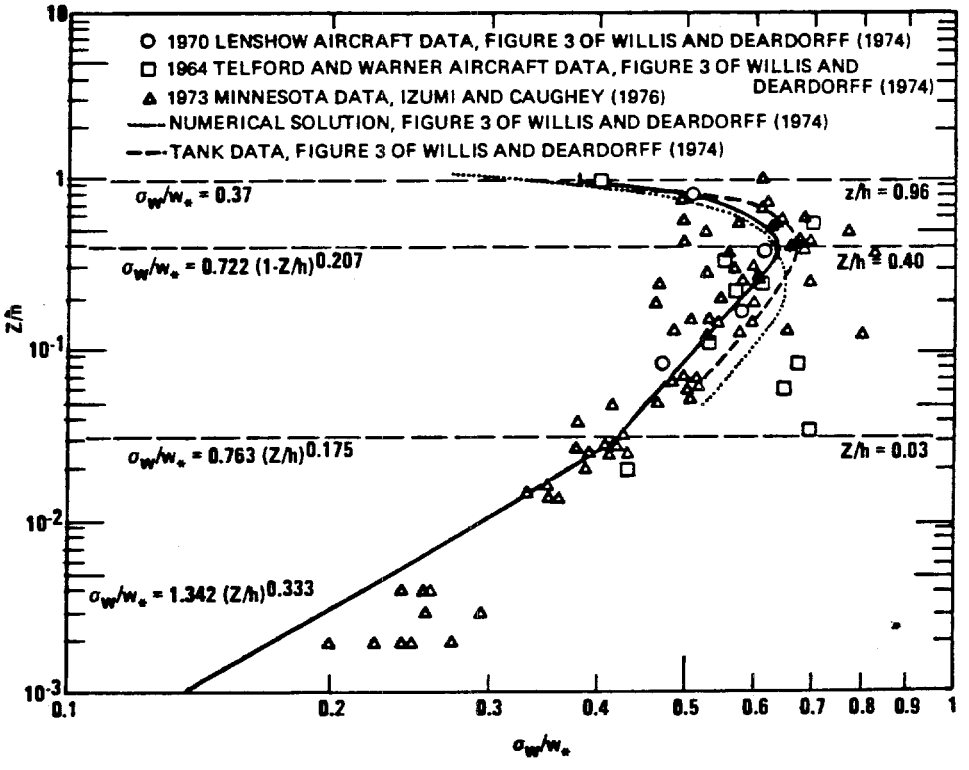

FIGURE 7.9

Vertical Profile of σ_w/w_* for Fully Convective Conditions
(After Irwin, 1979)

The reduced frequency f_m (Busch, 1973) at which the vertical velocity spectrum has its peak is given by

$$f_m = \begin{cases} 0.4 \left[1 + 3.9\left(\frac{z}{L}\right) - 0.25\left(\frac{z}{L}\right)^2\right] & ; \frac{z}{L} \leq 2 \quad (7.45) \\ 0.4 \left[6.78 + 2.39\left(\frac{z}{L} - 2\right)\right] & ; \frac{z}{L} > 2 \quad (7.46) \end{cases}$$

Once the standard deviations of the wind velocity fluctuations have been established the next step is to complete parameterization of the vertical dispersion coefficients by specifying F_z. Some field and laboratory results for unstable conditions are shown in Figure 7.10, where the data have been plotted as a normalized function of the convective time scale Z_i/w_*. From an inspection of these graphs it is apparent that there are two different dispersion regimes, one for discharges above $0.1Z_i$ and the other for surface releases. Lamb (1979) has shown that locus of maximum concentration of a non-buoyant elevated plume ($z_s > 0.1Z_i$) follows a descending path that intercepts the ground at a downwind distance $x \sim 2z_s\underline{u}/w_*$. For a surface source the locus of the maximum concentration ascends beginning at a distance of approximately $x = Z_i\underline{u}/w_*$. The important features of the concentration field can be reproduced by the Gaussian plume model if the actual source elevation is replaced by a "virtual source height" H_e (Lamb, 1979). At present there are, unfortunately, no simple analytic expressions which describe the variation in F_z or H_e as a function of release height and stability. For the present study the data shown in Figure 7.10 are

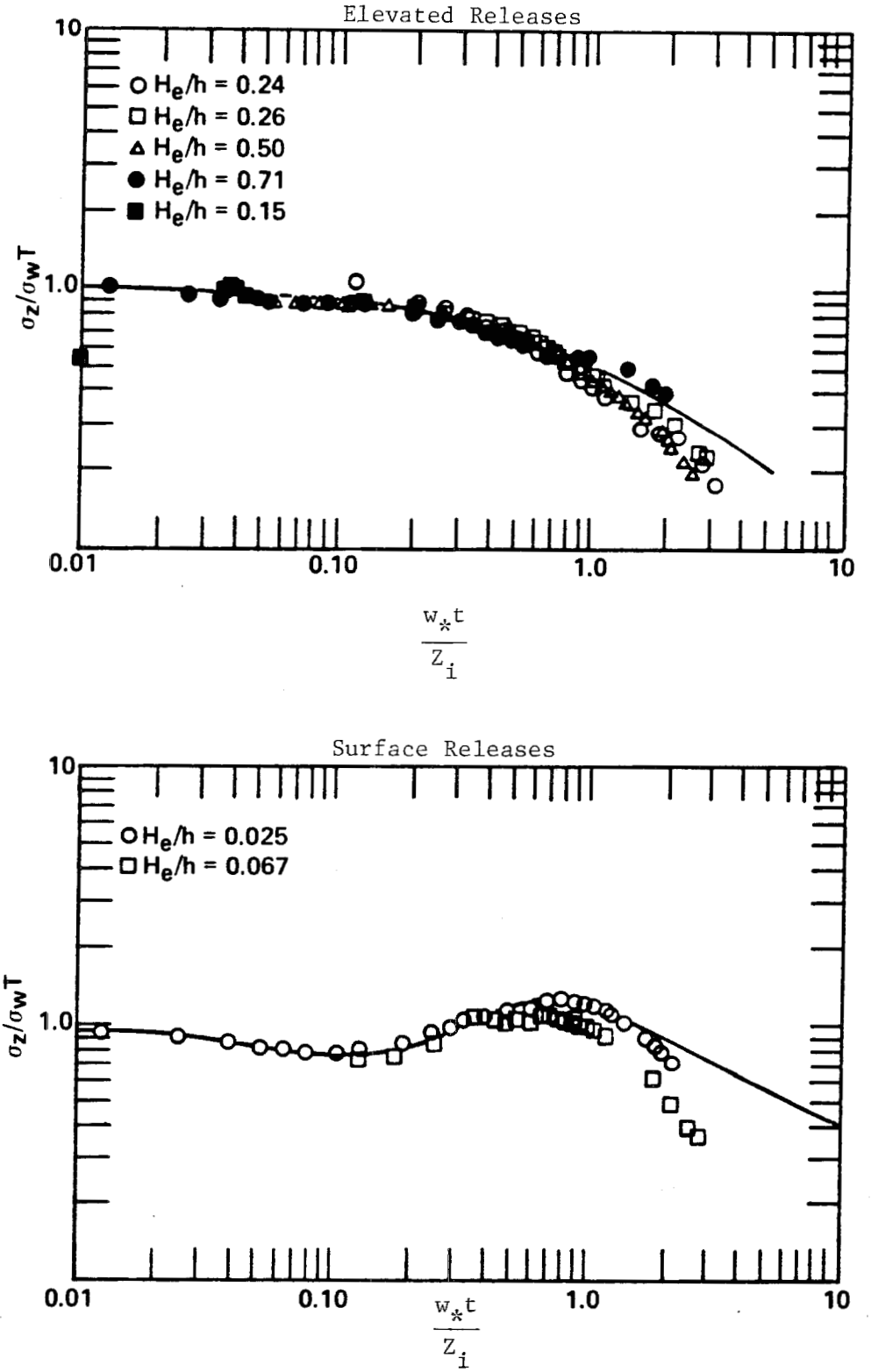

FIGURE 7.10

Values of F_z for Elevated Releases and Near-Surface Releases during Convectively Unstable Conditions (After Irwin, 1979)

employed directly in combination with (7.42). Between neutral conditions and $-Z_i/L$ less than 10 an interpolation formula due to Irwin (1979) is used.

Draxler (1976) developed the following results for neutral and stable conditions.

$$F_z = \begin{cases} \dfrac{1}{1 + 0.9\left(\dfrac{t}{T_0}\right)^{\frac{1}{2}}} & ; \quad z < 50\text{m} \qquad (7.47) \\ \dfrac{1}{1 + 0.945\left(\dfrac{t}{T_0}\right)^{0.8}} & ; \quad z \geq 50\text{m} \qquad (7.48) \end{cases}$$

The field data which formed the basis of (7.47-7.48) are shown in Figure 7.11. Both expressions require specification of the characteristic time T_0. While an initial estimate of 50 seconds was given by Draxler, Irwin (1979) proposed the following functions after an analysis of additional field experiments and laboratory studies

$$T_0(s) = \begin{cases} 50 & ; \quad z < 50\text{m} \\ 1.52 - 25 & ; \quad 50 \leq z < 150\text{m} \\ 200 & ; \quad z \geq 150\text{m} \end{cases} \qquad (7.49)$$

Even though most of the data examined by Irwin were for near neutral conditions the results are likely to have wider applicability because turbulence levels during stable conditions are relatively low.

So far in the discussion the plumes have been considered to be at the same temperature as the environment. If the source effluent is hot then the dispersion is influenced by both the ambient turbulence and

the buoyancy induced entrainment. Unfortunately there are few published studies which assess the relative importance of each process. As a result most descriptions of the source induced dispersion are based on theoretical formulations. Close to the stack the Taylor entrainment hypothesis predicts a linear relationship between the plume radius and the height of ascent. This is partially supported by the data reported in Briggs (1969) which indicate that the vertical spread is comparable to plume rise h_p. Pasquill (1975,1976) used this result to develop an estimate of the dispersion caused by the plume buoyancy. The Pasquill model assumes that the concentration distribution, across any cross section, is uniform. When modified for equivalent Gaussian profiles, the thermal dispersion coefficients utilized in the airshed model are given by

$$\sigma_{b(y,z)} = \frac{h_p}{2\sqrt{3}} \simeq 0.3\ h_p \qquad (7.50)$$

As in all the previous formulations there is a clear need for additional field and laboratory data which can be used to test different models over a wide range of atmospheric conditions. This lack of suitable verification information considerably hampers the development of more refined descriptions of the dispersion of buoyant and passive exhaust gases.

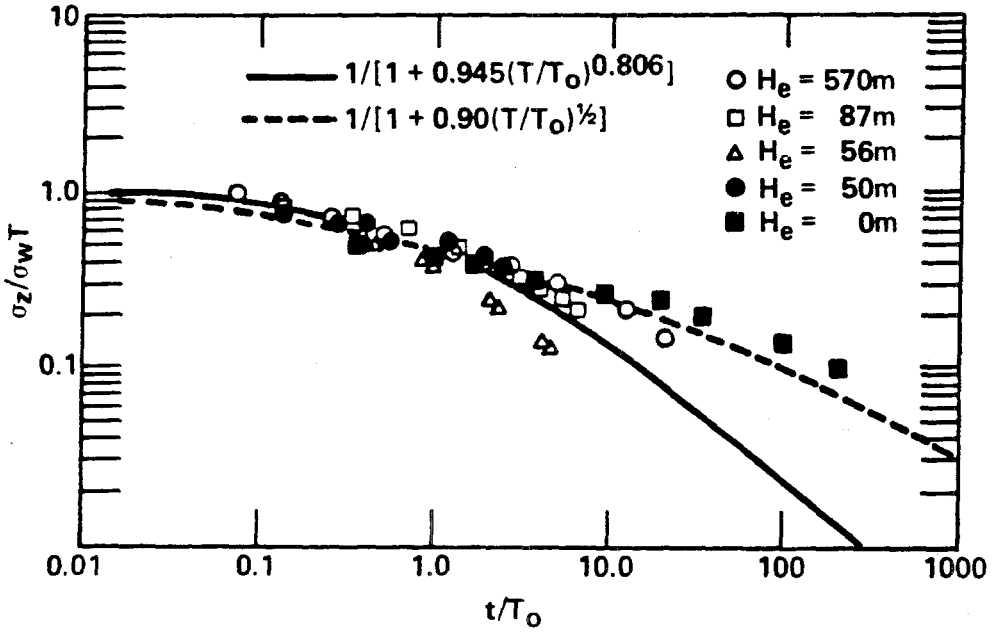

FIGURE 7.11

Values of F_z for Surface and Elevated Releases During Neutral and Stable Conditions

(After Irwin, 1979)

7.8 Near Source Plume Chemistry

The combustion products from large point sources are rich in nitrogen oxides and typically have low concentrations of reactive hydrocarbons. As a result the near source plume chemistry is dominated by the following reactions.

$$NO_2 + h\nu \xrightarrow{k_1} NO + O(^3P) \tag{7.51}$$

$$O(^3P) + O_2 + M \xrightarrow{k_2} O_3 + M \tag{7.52}$$

$$O_3 + NO \xrightarrow{k_3} NO_2 + O_2 \tag{7.53}$$

Once the plume has grown to the size of a typical computational cell the full airshed model reaction mechanism, with its hydrocarbon and radical interactions, is more appropriate. The purpose of this section is to present a simple model which can be used to estimate the fraction of nitric oxide (NO) which is converted to nitrogen dioxide (NO_2) during the initial phase of plume dispersion.

Given a background ozone concentration of 0.04 ppm a simple calculation, using the rate constant data published in Hampson and Garvin (1977), predicts a typical NO half life of a few seconds. This calculation assumes that every available NO molecule in the plume encounters an ozone molecule. In reality the background ozone must diffuse into the NO rich plume. Because the chemical kinetics are so fast, relative to the characteristic mixing times, the overall conversion rates are

limited by the entrainment processes. There have been a number of theoretical studies (Kewley, 1978; Shu et al., 1978; White, 1979) as well as field measurements (White, 1977 and Hegg et al., 1977) which support this hypothesis for the reaction system (7.51 - 7.53).

At night the dominant reaction is (7.53); however, during daylight hours when $k_1 > 0$, an equilibrium is established amongst NO, NO_2, and O_3 which depends on the sunlight intensity. The NO_2 concentration levels are given by the photostationary approximation

$$NO_2 = \frac{k_3 NO\ O_3}{k_1} \tag{7.54}$$

An additional source of NO_2 is the thermal conversion process

$$NO + NO + O_2 \xrightarrow{k_4} 2NO_2 \tag{7.55}$$

In this reaction the NO_2 formation is proportional to $(NO)^2$ and, as a result, (7.55) is only significant when the NO concentration levels are high. This is the rationale for omitting the step in most photochemical reaction mechanisms. There are some circumstances, however, where the thermal oxidation can be important and these conditions are discussed in Section 7.9.

Ignoring, for the present, the NO_2 conversion from reaction (7.55), additional constraints are imposed on the $NO\text{-}NO_2\text{-}O_3$ system because of the fact that $NO_2 + O_3 + O(^3P)$ and $NO + NO_2$ are stoichiometric invariants. If surface removal processes are unimportant and the plume is considered to be well mixed across a transverse section, then the nitrogen and excess oxygen balances require that

Nitrogen:

$$NO_x(t) = NO_2(t) + NO(t) = D(t)NO_x(0) + [1 - D(t)]NO_x^b \qquad (7.56)$$

Excess Oxygen (Ignoring $O(^3P)$):

$$O_x(t) = NO_2(t) + O_3(t) = D(t)[NO_2(0) + O_3(0)] + [1 - D(t)](NO_2^b + O_3^b) \qquad (7.57)$$

In these expressions D(t) refers to the plume dilution at time t, and $NO_x(0)$ to the stack concentrations and the superscript "b" to the background values. The dilution can be defined in terms of the change in the plume cross sectioned area as a function of time. If the initial transverse area is A_0 and is A(t) at some later time t, then D(t) = $A_0/A(t)$. There is a simple relation between the dilution and the growth of a cross sectional segment of unit thickness; this expression is

$$\frac{1}{A(t)} \frac{dA(t)}{dt} = - \frac{1}{D(t)} \frac{dD(t)}{dt} \qquad (7.58)$$

In addition to the dilution D(t), the change in cross section can be expressed in terms of the dispersion coefficients, σ_y and σ_z,

$$\frac{1}{A(t)} \frac{dA(t)}{dt} = \frac{1}{\sigma_y \sigma_z} \frac{d\sigma_y \sigma_z}{dt} \qquad (7.59)$$

If the functional forms given by (7.36 - 7.37) are substituted into (7.59) then the dilution is given by

$$\frac{1}{A(t)} \frac{dA(t)}{dt} = \frac{\sigma_w}{\sigma_z} \left[F_z\left(\frac{t}{T_i}\right) + t \frac{dF_z}{dt} \right] + \frac{\sigma_v}{\sigma_y} \left[F_y\left(\frac{t}{T_i}\right) + t \frac{dF_y}{dt} \right] \qquad (7.60)$$

When using expressions of the form (7.59 - 7.60) it is important to ensure that the dispersion parameters describe the instantaneous plume profile and not the time averaged envelope (White, 1977). The reason for this is that the meandering has no effect on the plume chemistry. The large scale fluctuations in wind direction do, however, influence the time averaged concentrations.

Since the ozone concentration in the stack exhaust gases is usually negligible, (7.57) can be written in the form

$$O_3(t) = b - NO_2(t) \tag{7.61}$$

where

$$b = D(t)NO_2(0) + [1 - D(t)](NO_2{}^b + O_3{}^b) \tag{7.62}$$

and the NO concentration is given by (7.56)

$$NO(t) = a - NO_2(t) \tag{7.63}$$

where

$$a = D(t)NO_x(0) + [1 - D(t)]NO_x{}^b \tag{7.64}$$

Combining (7.54, 7.61-7.64) produces a quadratic expression for $NO_2(t)$, the only physically realistic solution of which is given by

$$NO_2(t) = \frac{1}{2}\left[(a+b+\frac{k_1}{k_3}) - \sqrt{(a+b+\frac{k_1}{k_3})^2 - 4ab}\right] \tag{7.65}$$

The variables a and b can be calculated from measurements of NO/NO_x in the stack exhaust, the dilution and the background concentrations of NO, NO_2 and O_3. Given the rate constant ratio k_1/k_3 the *downwind NO_2 concentration within the plume can be readily evaluated.*

Some of the necessary corrections for the effects of turbulent fluctuations and concentration inhomogeneities are discussed in Shu et al. (1978) and White (1979). A variety of other methods for estimating short-term NO_2 impacts are reviewed in Cole and Summerhays (1979) and Peters and Richards (1977). One advantage of the formulation presented in this section is that it can be used in conjunction with conventional Gaussian plume models.

7.9 An Examination of the Contribution of Thermal NO Oxidation to the Formation of NO_2.

When nitrogen oxides (NO_x) are reported in source inventories they are frequently expressed in terms of equivalent emissions of nitrogen dioxide (NO_2) even though the exhaust NO_x is composed primarily of nitric oxide (NO). Unless the initial NO_2/NO_x ratio is specified from instack measurements it is necessary to establish appropriate fractions for reconstructing the actual emission levels of NO and NO_2. Depending on the source, and the characteristics of its combustion process, the fraction can vary from approximately 1 to 10%. In addition to the NO_2 formed during combustion, some small quantities can be formed in the exhaust gases by the third order reaction

$$NO + NO + O_2 \xrightarrow{k_4} 2NO_2 \tag{7.66}$$

This reaction step is normally ignored in photochemical reaction mechanisms because of the low ambient levels of nitric oxide. The objective of this section is to present a very simple model which can be used to estimate the fraction of NO which is converted to NO_2 in the vicinity of the source. The intent is not to add an additional reaction step to the airshed model chemistry but rather to develop a simple approach for augmenting the emission inventory NO_2/NO_x ratio.

If the plume is considered to be well mixed across each transverse section then the nitric oxide (NO) decay rate is given by

$$\frac{d(NO)}{dt} = -2\, k_4(T)(NO)^2(O_2) + \frac{1}{D(t)} \frac{dD(t)}{dt} (NO - NO^b) \tag{7.67}$$

where D(t) is the plume dilution as defined in Section 7.8 and NO^b is the background concentration of nitric oxide. The nitrogen mass constraint enables the direct calculation of NO_2 from

$$NO_2(t) = D(t)NO_x(0) + [1 - D(t)]NO_x^b - NO(t) \tag{7.68}$$

In (7.67) the second order reaction rate constant, in ppm^{-2}-min^{-1} units, is of the form (Baulch et al.,1978)

$$k_4(T) = \frac{1.066 \times 10^{-5}}{T^2} \exp(530/T) \tag{7.69}$$

Even though the above expressions are straightforward, the NO concentration dynamics downwind from the stack are not immediately obvious. While entrainment of cool ambient air into the plume causes an increase in the magnitude of $k_4(T)$ (Figure 7.12), the plume dilution also results in a reduction of NO. This interplay between cooling and dilution can be described by integrating the species rate equation. If the background contribution in (7.67) is ignored then the NO concentration decay is given by

$$NO(t) = \frac{NO(0)\ D(t)}{1 + 2NO(0)\int_0^t k_4(T)\{D(t)O_2 + [1 - D(t)]O_2^b\}D(t)\ dt} \tag{7.70}$$

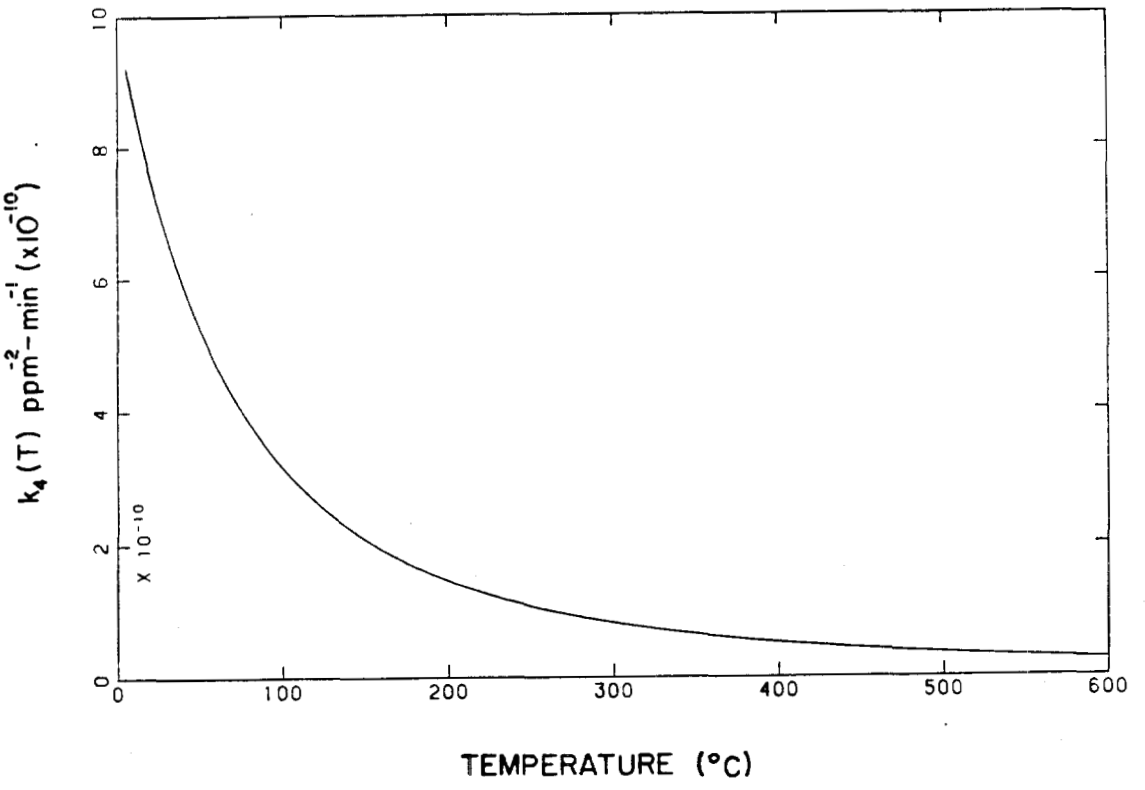

FIGURE 7.12

Variation of $NO+NO+O_2 \xrightarrow{k_4(T)} 2NO_2$ Reaction Rate Constant as a Function of Temperature

Within the plume, the oxygen and temperature distributions are given by

$$O_2(t) = O_2^b + D(t)[O_2(0) - O_2^b] \tag{7.71}$$

$$T(t) = T^b + D(t)[T(0) - T^b] \tag{7.72}$$

While details of near source dilution characteristics can be found in Fischer et al. (1979), an approximate form was adopted in this study

$$D(t) = \exp[-0.15t] \quad ; \; t < 30 \text{ s} \tag{7.73}$$

Given the initial and background conditions for NO_x, T and O_2 the system of equations (7.67 - 7.73) can be solved to give the conversion fractions for short travel times. Figure 7.13 presents the results of one such calculation where the initial $NO_2(0)/NO_x$ ratio was 5.0%, $O_2(0)$ = 3% = 30000 ppmV, and the instack NO was varied from 200 to 2000 ppmV. A comparison between the pure dilution cases and those in which the chemistry was included indicates that between 2 and 12% of the increase in NO_2 concentration at any travel time can be explained by thermal oxidation. Two conclusions are apparent from this investigation. The first is that, close to the source, the reaction step can be significant, which in turn implies that more attention needs to be given to characterizing the stack exhaust gas concentration and temperature distributions when assembling emission inventory information. Since the effects of thermal oxidation are minimal when the dilution is high, there is no need to include the reaction step (7.66) in the airshed model. The incremental conversion can be incorporated by simply increasing the initial NO_2/NO_x emission inventory ratio.

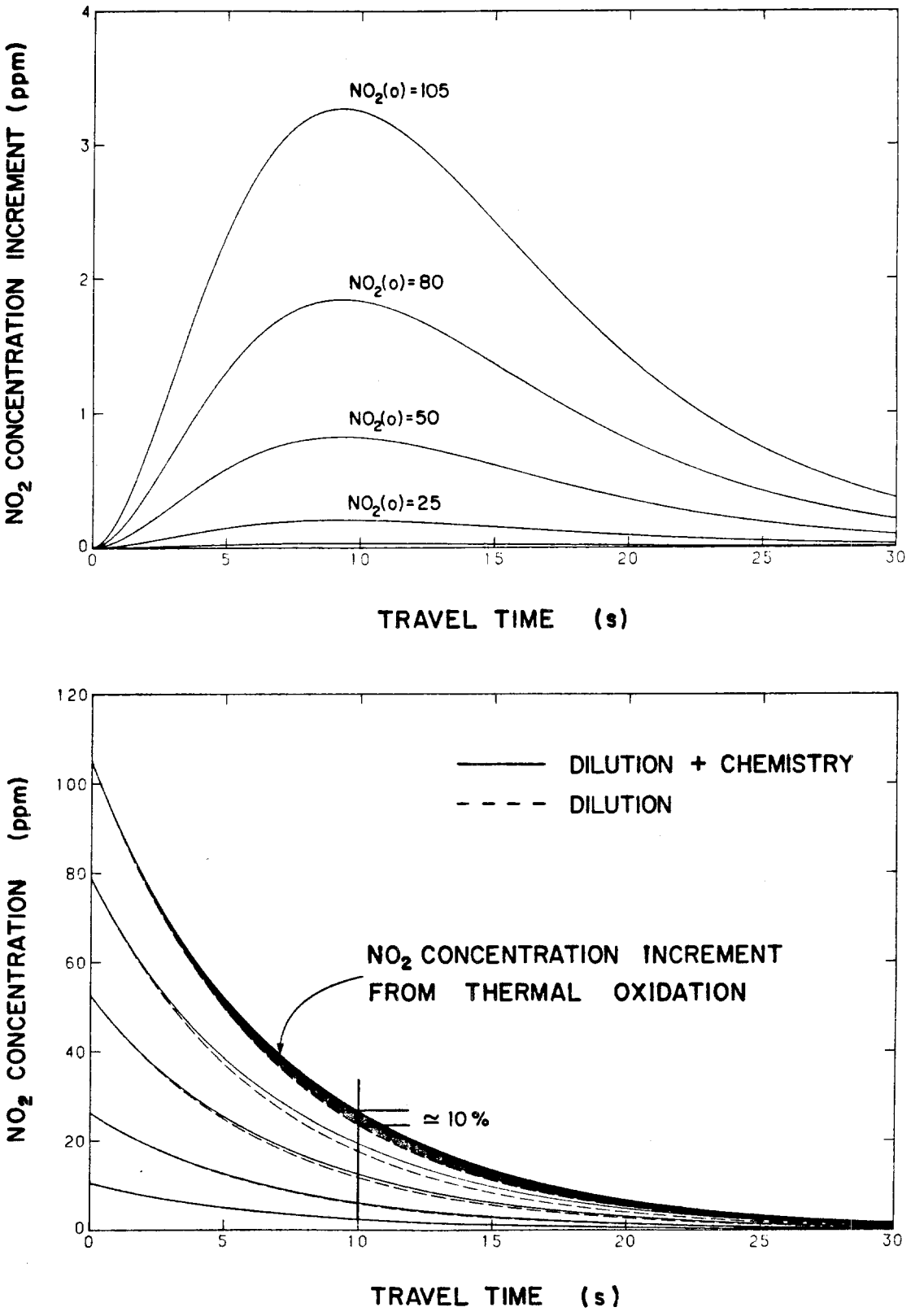

FIGURE 7.13

NO_2 Concentrations as a Function of Travel Time
Stack conditions $T = 250^{o}C$, $O_2 = 3\%$, $NO_2(o)/NO_x = 0.05$, $NO_2^b = 0.02$.

7.10 Conclusions

This chapter has described how both point and area source emissions are treated in the airshed model. Of particular interest is an improved method for allocating elevated emissions discharges into a three-dimensional computational grid. When coupled with suitable selection criteria that identify whether a particular source should be treated as an elevated release, the procedure significantly reduces the numerical dispersion errors associated with conventional allocation schemes. Some preliminary work on the treatment of plume rise in a non-uniformly stratified environment resulted in a simple criterion that establishes whether a plume can penetrate an elevated temperature inversion. In addition to formulating the plume rise models some consideration was given to the characteristics of the near source chemistry and, in particular, the role of thermal oxidation of nitric oxide to NO_2.

There is a critical need for more field measurements which can be used to verify different models of plume dispersion, trapping and subsequent fumigation.

CHAPTER 8

PRACTICAL IMPLEMENTATION OF A PHOTOCHEMICAL REACTION MECHANISM WITHIN AN AIRSHED MODEL

8.1 Introduction

Photochemical air pollution is formed as a result of a complex interaction between sunlight, meteorology and primary emissions of nitrogen oxides and reactive hydrocarbons. The development of a reaction mechanism that accurately describes the atmospheric chemistry and which, at the same time, is computationally tractable is a complex undertaking. The task is complicated by the need to maintain a balance between the level of chemical detail and minimizing, for numerical reasons, the number of species and reaction pathways. This dilemma is particularly apparent when considering hydrocarbon chemistry. In a typical urban atmosphere literally hundreds of different hydrocarbons are present. Under most circumstances it is simply not feasible to incorporate the reaction steps for each species. As a result two basic approaches have been developed to characterize the hydrocarbon chemistry: surrogate and lumped reaction mechanisms.

Surrogate mechanisms are those in which the organic species in a particular class, e.g. olefins, are represented by one or more members of that class, e.g. propylene. In general these mechanisms, typified by Graedel et al. (1976) and Dodge (1977), tend to have a large number of reaction steps and are not practical in situations where the meteorological transport model involves more than a few computational

cells. The second approach to the problem is to use chemical lumping in which one or more reactants, of similar structure and reactivity, are grouped together into a single class. A basic objective is to take advantage of the common features of the hydrocarbons and free radicals in order to minimize the number of species while at the same time maintaining a high degree of detail for the inorganic reactions. In the present study the lumped mechanism, developed by Falls and Seinfeld (1978), has been used. Their mechanism represents the atmospheric hydrocarbon mixture by six classes: ethylene, other olefins, alkanes, aromatics, formaldehyde and higher aldehydes. Other examples of lumped mechanisms are described in Eschenroeder and Martinez (1972), Gelinas and Skewes-Cox (1975), Hecht and Seinfeld (1972), Hecht et al. (1974), MacCracken and Sauter (1975) and Whitten et al. (1979).

The basic objective of this chapter is to provide sufficient information regarding initial conditions, rate constants and stoichiometry to allow an independent verification of the Falls and Seinfeld (1978) mechanism. Their mechanism was selected, for the airshed model, because it incorporates recent information on rate constants, mechanistic structure and, in addition, has been successfully validated against a wide range of smog chamber experiments. Since an extensive analysis of the chemical basis of the reaction scheme is available in the cited reference it will not be repeated here. Subsequent sections of this chapter present the results of a series of tests designed to examine the numerical properties of the kinetics, the adequacy of some

psuedo steady state approximations and the mechanism consistency as evidenced by mass balance checks. While primary emphasis is given to the Falls and Seinfeld (1978) formulation, much of the discussion in subsequent sections can be easily applied to other mechanisms.

8.2 Chemical Reaction Source Term and Mechanism Definition

Within the airshed model the ambient chemistry is represented by the presence of reaction terms, R_i; $i = 1,2,\ldots,n$, in the atmospheric diffusion equation. This section presents the detailed formulation of the mathematical form and structure of these terms. Consider a homogeneous, isothermal, isobaric system in which n single phase species, c_i, $i = 1,2,\ldots,n$, simultaneously participate in m elementary reaction steps. Formally, the reaction set can be written in terms of linear combinations of species called complexes (Horn and Jackson, 1972).

$$\sum_{i=1}^{n} r_{ji}\, c_i \rightarrow \sum_{i=1}^{n} p_{ji}\, c_i \qquad j = 1,2,\ldots,m \tag{8.1}$$

The reactant and product stoichiometry in reaction step j is defined by the coefficients r_{ji}, p_{ji}. In general, these coefficients are such that mass is conserved in each elementary reaction; however, there are circumstances, to be discussed later, in which this condition must be relaxed. Note that the sum in (8.1) extends over all n species to allow for the possibility that a given species can participate in a reaction step as both a product and a reactant. Equation (8.1) can be written

in a more compact matrix notation in which $\{c\}$ is interpreted as a concentration vector $c = [c_1, c_2, \ldots, c_n]^T$ and where the reactant and product stoichiometric matrices [R], [P] are of dimension m x n.

$$[R]\ \{c\} \rightarrow [P]\ \{c\} \tag{8.2}$$

If the rates f_j of the m individual reactions are given, the following set of ordinary differential equations, together with appropriate initial conditions, is a basis for describing the kinetics of the reaction set embedded in the airshed model (Gavalas, 1968; Aris, 1965).

$$\frac{d\{c\}}{dt} \equiv \{\dot{c}\} = [S]^T\{F\} = \underset{\sim}{g}(\underset{\sim}{c}) \tag{8.3}$$

where [S] is the m x n stoichiometric matrix defined by [P] - [R], $\{F\}$ is an m x 1 vector of rate functions f_j, and $\underset{\sim}{g}(\underset{\sim}{c})$ can be interpreted as a non-linear transformation which maps points from $\mathbb{R}^m$ into $\mathbb{R}^n$. In general the matrix [S] has no special properties, such as symmetry, band or block structure, except that the number of differential equations clearly has the upper bound: rank (S) $\leq$ min (m,n).

For definitional purposes the chemical mechanism embedded in the airshed model is reproduced in Table 8.1. Each species and its symbolic representation is shown in Table 8.2. In this latter table the last column indicates whether the species is described by one of the following mathematical types: a differential equation (D), a pseudo steady state approximation (PSSA), a constant (C) or as an uncoupled

TABLE 8.1

CHEMICAL MECHANISM USED WITHIN AIRSHED MODEL

Photolysis of NO_2 and basic $NO-NO_2-O_3$ photolytic cycle

NO_2	+ hν	$\xrightarrow{1}$	NO	+ $O(^3P)$	1*
$O(^3P)$ + O_2	+ (M)	$\xrightarrow{2}$	O_3	+ (M)	2
O_3	+ NO	$\xrightarrow{3}$	NO_2	+ O_2	3
NO_2	+ $O(^3P)$	$\xrightarrow{4}$	NO	+ O_2	4
NO	+ $O(^3P)$	$\xrightarrow{5}$	NO_2		6

Chemistry of NO_3 (nitrogen trioxide)

NO_2	+ $O(^3P)$	$\xrightarrow{6}$	NO_3		5
O_3	+ NO_2	$\xrightarrow{7}$	NO_3	+ O_2	7
NO_3	+ NO	$\xrightarrow{8}$	$2NO_2$		8

Nitrous acid and peroxy nitrous acid chemistry

NO	+ OH	$\xrightarrow{9}$	HONO		22

Photolysis of HONO

HONO	+ hν	$\xrightarrow{10}$	OH	+ NO	24

Nitrous acid chemistry

HO_2	+ NO_2	$\xrightarrow{11}$	HONO	+ O_2	18
HONO	+ OH	$\xrightarrow{12}$	NO_2	+ H_2O	26
NO_2	+ HO_2	$\xrightarrow{13}$	HO_2NO_2		19
	HO_2NO_2	$\xrightarrow{14}$	HO_2	+ NO_2	20

*These numbers correspond to reactions presented in Tables I-III of Falls and Seinfeld (1978)

TABLE 8.1 (Continued)

Conversion of NO to NO_2

HO_2	+ NO	$\xrightarrow{15}$	NO_2	+ OH		21
RO_2	+ NO	$\xrightarrow{16}$	NO_2	+ RO		52
RCO_3	+ NO	$\xrightarrow{17}$	NO_2	+ RO_2	+ CO_2	53

Nitric acid ($HONO_2$) formation

NO_2	+ OH	$\xrightarrow{18}$	$HONO_2$			23

Hydroperoxyl radical formation

CO	+ OH	$\xrightarrow{19}$	HO_2	+ CO_2		25

Photolysis of ozone

O_3	+ hν	$\xrightarrow{20}$	$O(^3P)$	+ O_2		15

Photolysis of formaldehyde

HCHO	+ hν	$\xrightarrow{21}$	$2HO_2$	+ CO		31
HCHO	+ hν	$\xrightarrow{22}$	H_2	+ CO		32

Formaldehyde chemistry

HCHO	+ OH	$\xrightarrow{23}$	HO_2	+ H_2O	+ CO	33

Photolysis of higher aldehydes

RCHO	+ hν	$\xrightarrow{24}$	RO_2	+ HO_2	+ CO	35

Higher aldehyde chemistry

RCHO	+ OH	$\xrightarrow{25}$	RCO_3			36

TABLE 8.1 (Continued)

Olefin chemistry (OLE)

C_2H_4 + OH	$\xrightarrow{26}$	RO_2		42
C_2H_4 + O	$\xrightarrow{27}$	RO_2 + HO_2		43
OLE + OH	$\xrightarrow{28}$	RO_2		37
OLE + O	$\xrightarrow{29}$	RO_2 + RCO_3		38
OLE + O_3	$\xrightarrow{30}$	(a_1) RCHO + (a_2) HCHO + (a_3) HO_2 + (a_4) RO_2 + (a_5) OH + (a_6) RO		39

Alkane chemistry (ALK)

ALK + OH	$\xrightarrow{31}$	RO_2		40
ALK + O	$\xrightarrow{32}$	RO_2 + OH		41

Aromatic chemistry (ARO)

ARO + OH	$\xrightarrow{33}$	RO_2 + RCHO		

Alkoxyl radical chemistry

RO	$\xrightarrow{34}$	(b_1) HO_2 + $(1-b_1)$ RO_2 + (b_2) HCHO + (b_3) RCHO		44

Photolysis and chemistry of RONO

RONO + hν	$\xrightarrow{35}$	NO + RO		46
RO + NO	$\xrightarrow{36}$	RONO		
RO + NO_2	$\xrightarrow{37}$	$RONO_2$		47
RO + NO_2	$\xrightarrow{38}$	RCHO + HONO		48

TABLE 8.1 (Continued)

Peroxy nitrate chemistry

NO_2	+ RO_2	$\xrightarrow{39}$	RO_2NO_2		49
NO_2	+ RO_2	$\xrightarrow{40}$	RCHO	+ $HONO_2$	50
RO_2NO_2		$\xrightarrow{41}$	NO_2	+ RO_2	51

Peroxyacyl nitrate (PAN) chemistry

RCO_3	+ NO_2	$\xrightarrow{42}$	PAN		54
PAN		$\xrightarrow{43}$	RCO_3	+ NO_2	55

Dinitrogen pentoxide (N_2O_5) chemistry

NO_2	+ NO_3	$\xrightarrow{44}$	N_2O_5		9
N_2O_5		$\xrightarrow{45}$	NO_2	+ NO_3	10
H_2O	+ N_2O_5	$\xrightarrow{46}$	2 $HONO_2$		11

Ozone removal steps

O_3	+ OH	$\xrightarrow{47}$	HO_2	+ O_2	29
O_3	+ HO_2	$\xrightarrow{48}$	OH	+ $2O_2$	30

Ozone wall loss term for smog chamber experiments

O_3	$\xrightarrow{49}$	wall loss

Hydrogen peroxide production and photolysis

HO_2	+ HO_2	$\xrightarrow{50}$	H_2O_2	+ O_2	27
H_2O_2	+ $h\nu$	$\xrightarrow{51}$	2OH		--

Recombination Reaction for peroxalkyl radicals

RO_2	+ RO_2	$\xrightarrow{52}$	2RO		--

TABLE 8.2

Chemical Species Participating in Photochemical Reaction Mechanism

	SPECIES[a]	NAME	TREATMENT IN AIRSHED MODEL[b]
1	NO	Nitric Oxide	D
2	NO_2	Nitrogen Dioxide	D
3	O_3	Ozone	D
4	HCHO	Formaldehyde	D
5	RCHO	Higher Aldehydes	D
6	OLE	Lumped Olefins	D
7	ALK	Lumped Alkanes	D
8	ARO	Lumped Aromatics	D
9	C_2H_4	Ethylene	D
10	CO	Carbon Monoxide	D
11	H_2O_2	Hydrogen Peroxide	D
12	PAN	Peroxyactyl nitrate	D
13	HONO	Nitrous Acid	D
14	RONO	Alkyl Nitrite	D
15	RNO_4	Peroxyalkyl Nitrate	D
16	N_2O_5	Dinitrogen Pentoxide	PSSA
17	HNO_4	Peroxynitric Acid (HO_2NO_2)	PSSA
18	RCO_3	Peroxyacyl Radical	PSSA
19	HO_2	Hydroperoxyl Radical	PSSA
20	NO_3	Nitrogen Trioxide	PSSA
21	RO_2	Alkylperoxy Radical	PSSA

TABLE 8.2 (Continued)

	SPECIES[a]	NAME	TREATMENT IN AIRSHED MODEL[b]
22	OH	Hydroxyl Radical	PSSA
23	RO	Alkoxyl Radical	PSSA
24	O	Atomic Oxygen	PSSA
25	CO_2	Carbon Dioxide	P
26	RNO_3	Alkyl Nitrate ($RONO_2$)	P
27	HNO_3	Nitric Acid ($HONO_2$)	P
28	H_2	Hydrogen	P
29	LOSS	Ozone loss term for smog chamber experiments	P
30	H_2O	Water	C
31	O_2	Oxygen	C
32	M	Third Body	C

Notes:

a. Species name is restricted to four characters for computational reasons.

b. Treatment of species within the airshed model chemistry

D - Differential Equation

PSSA - Pseudo Steady State Approximation

C - Constant species during one integration step

P - Product species ignored in some applications.

differential form (P). The structure and interrelation among all elements of the mechanism are shown in Figure 8.1.

The Jacobian matrix of the system of differential equations is frequently required as a component of numerical solution procedures and for sensitivity analyses. For the set of equations defined by (8.3) and (8.4) the Jacobian is given by

$$J \equiv \frac{\partial\{\dot{c}\}}{\partial\{c\}} = [S]^T \frac{\partial\{F\}}{\partial\{c\}} \tag{8.4}$$

A number of species in the mechanism appear only as products and as a result can be treated as uncoupled differential equations. Partitioning the concentration vector to reflect this division, (8.3) can be written as

$$\{\dot{c}\} = \begin{Bmatrix} \dot{c}_c \\ \dot{c}_p \end{Bmatrix} = \begin{Bmatrix} g_c\ (c_c) \\ g_p\ (c_c) \end{Bmatrix} \tag{8.5}$$

where the subscripts refer to the coupled (c) and product (p) species. Since the $\{c_p\}$ can be expressed as functions of $\{c_c\}$, their concentrations are readily determined for any interval $[t_0,T]$ by standard numerical quadrature procedures by evaluating integrals of the form

$$\{c_p(T)\} = \{c_p(t_0)\} + \int_{t_0}^{T} \{g_p(c_c)\}\, dt \tag{8.6}$$

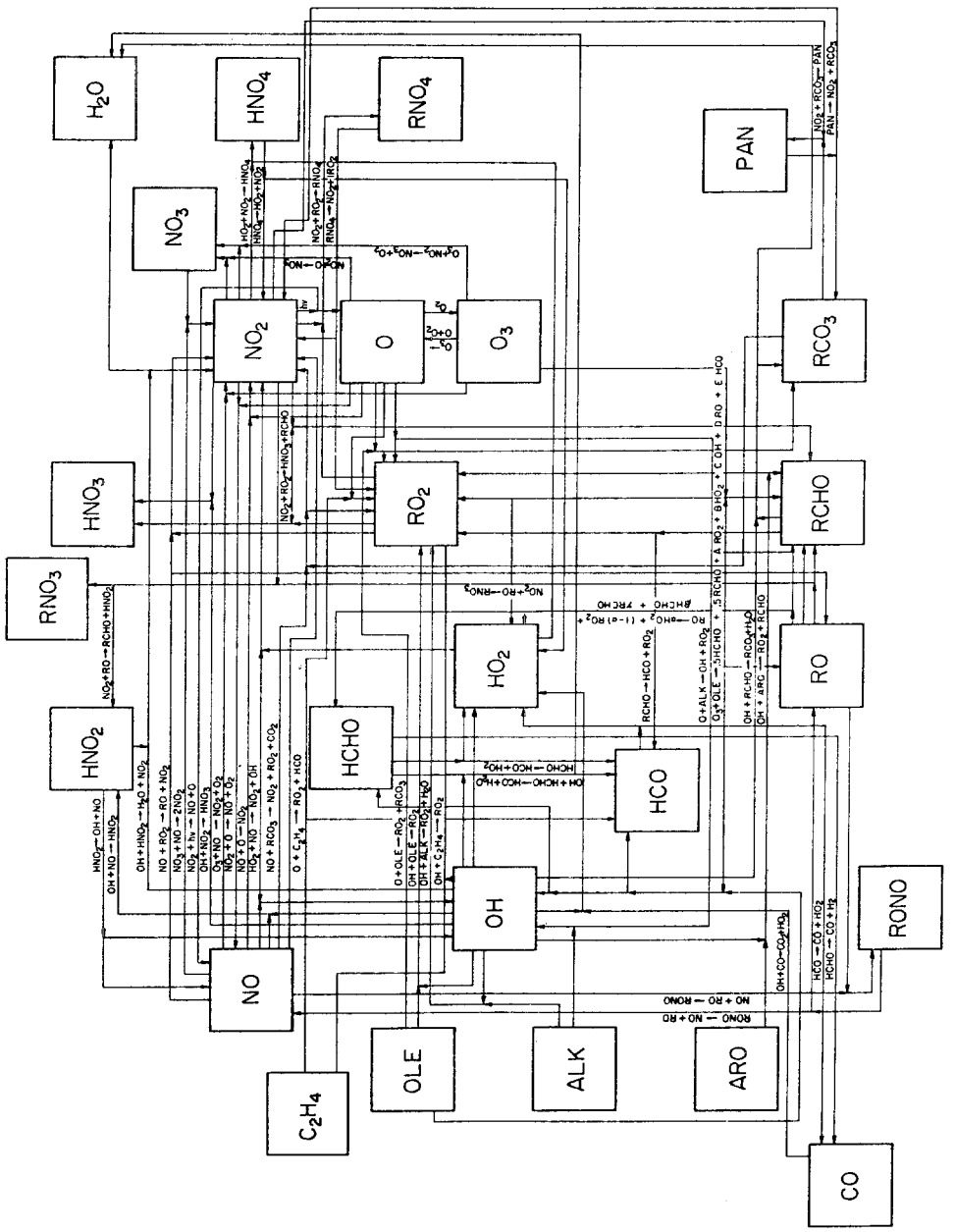

FIGURE 8.1

Structure of the Falls and Seinfeld (1978) Photochemical Reaction Mechanism

8.3 Stoichiometric Coefficients for the Lumped Reactions

Two reactions in the Falls and Seinfeld (1978) mechanism require specification of stoichiometric coefficients. The first is the lumped ozone-olefin chemistry which is shown schematically in Figure 8.2 and can be expressed in the form

$$\begin{aligned} \mathrm{OLE} + \mathrm{O_3} \xrightarrow{30} & (a_1)\mathrm{RCHO} + (a_2)\mathrm{HCHO} + (a_3)\mathrm{HO_2} \\ & + (a_4)\mathrm{RO_2} + (a_5)\mathrm{OH} + (a_6)\mathrm{RO} \\ & + (a_7)\mathrm{HCO} \end{aligned} \tag{8.7}$$

where the stoichiometric coefficients are given by

$$\begin{aligned} a_1 &= (1 - 0.5\delta) \\ a_2 &= 0.5\delta \\ a_3 &= 0.5\,\varepsilon\,(\xi + \eta)\,(1-0.5\delta) + \rho\delta \\ a_4 &= 0.5\,\varepsilon\,(2\xi + \eta)\,(1-0.5\delta) \\ a_5 &= 0.5\,\varepsilon\xi\,(1-0.5\delta) \\ a_6 &= 0.5\,\varepsilon\eta\,(1-0.5\delta) \\ a_7 &= 0.5\,\varepsilon\eta\,(1-0.5\delta) \end{aligned} \tag{8.8}$$

where δ equals the fraction of olefins with terminal double bonds, $1-\varepsilon$ the fraction of RCHOO reactions that proceed by collisional stabilization, ξ and η the fractions of RCHOO to [RCHOO]* and [HOCOR]* respectively. All other splits are assumed to be 50/50 except for the step

$$\cdots \longrightarrow \quad RCHO + [HOCOR] \xrightarrow{70\%} H_2O + CO$$

$$\xrightarrow{20\%} H_2 + CO_2$$

$$\xrightarrow{\rho} 2H + CO_2$$

$$\xrightarrow{O_2} 2HO_2$$

where ρ is 10% (Dodge, 1978). For the purposes of calculating the stoichiometric coefficient for HO_2 production, ρ has been assumed to be 0.1. From a computational point of view, it is desirable to minimize the number of species. Since the formyl radical (HCO) reacts very rapidly with oxygen to form hydroperoxyl (HO_2), HCO can be eliminated with the reaction step

$$HCO + O_2 \longrightarrow HO_2 + CO \tag{8.9}$$

Applying this result, together with the interpretation by Dodge (1978) of the Herron and Huie (1977) ozone-olefin experiments, the stoichiometric coefficients can be calculated from $\varepsilon = 0.8$, $\xi = 0.68$, $\eta = 0.17$, $\delta = 1$, and $\rho = 0.1$. Substituting these values into the expressions for $a_1,\ldots,a_6$ gives

$$\begin{aligned} OLE + O_3 \xrightarrow{30} & 0.5\ RCHO + 0.5\ HCHO + 0.30\ HO_2 \\ & + \ 0.31\ RO_2 + 0.14\ OH \ + 0.03\ RO \end{aligned} \tag{8.10}$$

where the HO_2 coefficient is derived from $a_3 + a_7$, i.e.

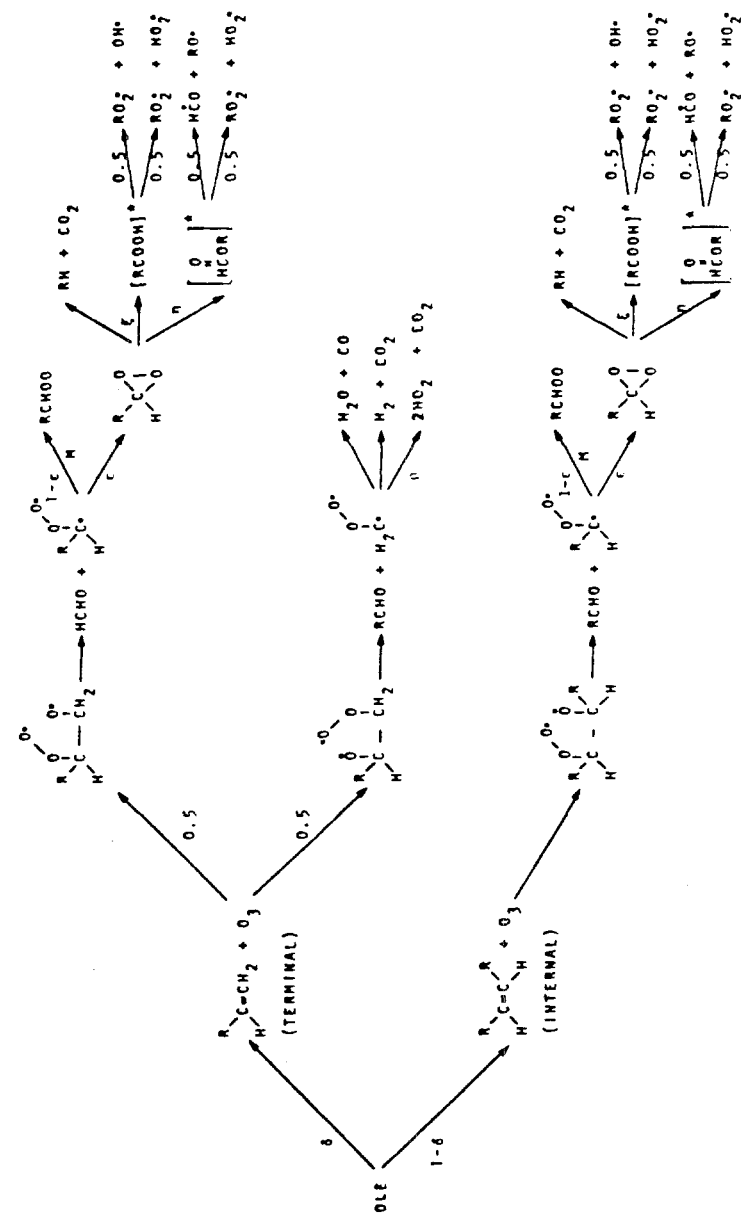

FIGURE 8.2
General Ozone-Olefin Reaction Mechanism
with Reaction Products as Proposed by Dodge (1978)

$$a_3 + a_7 = [0.5\varepsilon(\xi+\eta)(1-0.5\delta) + \rho\delta] + [0.5\varepsilon\eta(1-0.5\delta) = 0.304 \qquad (8.11)$$

The decomposition, reaction with O_2, and isomerization of the alkoxyl and hydro-alkoxyl classes in the airshed mechanism have been concentrated in the reaction step

$$RO \xrightarrow{34} (b_1)HO_2 + (1-b_1)RO_2 + (b_2)HCHO + (b_3)RCHO \qquad (8.12)$$

Since the RO lumped species represents a large class of different-sized radicals and because splits between reaction paths even for specific radicals are unknown, b_1 can have a value in the range 0 to 1. For the present model, the coefficients have been assigned the following values: $b_1 = 1$, $b_2 = 0.5$, and $b_3 = 0.5$, so that (8.12) can be written in the simpler form

$$RO \xrightarrow{34} HO_2 + 0.5\ HCHO + 0.5\ RCHO \qquad (8.13)$$

8.4 Specification of the Reaction Rate Constants

Three basic types of reaction rate data are needed to complete the mechanism kinetics: inorganic, lumped hydrocarbon and photolysis rates. The determination of individual species reaction rates {F} is a major area of experimental and theoretical investigation. For dilute chemical systems, a frequently employed model for correlating experimental data is the so-called 'mass action law' which is based on an analogy to

molecular collision (Pratt, 1969). In its simplest statement this model results in a polynomial expression for the rate, f_j of the form

$$f_j = k_j \prod_{i=1}^{n} c_i^{r_{ji}} \tag{8.14}$$

where k_j is a temperature dependent rate constant given by,

$$k_j(T) = A_j \exp [-B_j/T] \tag{8.15}$$

Expression (8.15) is the Arrhenius equation, the coefficients of which are derived from measurements of individual reaction rates as a function of temperature and pressure. The rate data for the inorganic reactions in the Falls and Seinfeld (1978) are presented in Table 8.3 together with appropriate literature citations. Baulch et al. (1980) have recently published an evaluated review of kinetic data for atmospheric chemistry. In some cases there are differences between their recommendation and the values used in the model evaluation studies described in subsequent chapters of this study. While future work with the mechanism will incorporate the new information, Table 8.3 serves as documentation of the rate constants employed in calculations to date. A discussion of procedures for developing the rate data for the lumped hydrocarbon reaction is presented in the next section. For more detailed analyses of the kinetic model (8.14) the reader is referred to Krambeck (1970), Horn and Jackson (1972) and Bowen (1976).

TABLE 8.3

Summary of Rate Constants Excluding Photolysis and Lumped Hydrocarbon Steps

REACTION	RATE CONSTANTS (ppm-min units)	VALUE AT 298°K	REFERENCE[a]
$O(^3P) + O_2 + M \xrightarrow{2} O_3 + M$	$\frac{0.346}{T^2} \exp(510/T)$	2.16×10^{-5}	[1]
$O_3 + NO \xrightarrow{3} NO_2 + O_2$	$\frac{9.24 \times 10^5}{T} \exp(-1450/T)$	2.39×10^1	[1]
$NO_2 + O(^3P) \xrightarrow{4} NO + O_2$	$\frac{3.99 \times 10^6}{T}$	1.34×10^4	[1]
$NO + O(^3P) \xrightarrow{5} NO_2$	$\frac{1.67 \times 10^5}{T} \exp(584/T)$	3.98×10^3	[1]
$NO_2 + O(^3P) \xrightarrow{6} NO_3$	$\frac{1.07 \times 10^6}{T}$	3.59×10^3	[1]
$O_3 + NO_2 \xrightarrow{7} NO_3 + O_2$	$\frac{5.19 \times 10^4}{T} \exp(-2450/T)$	4.68×10^{-2}	[1]
$NO_3 + NO \xrightarrow{8} 2NO_2$	$\frac{8.05 \times 10^6}{T}$	2.70×10^4	[2]
$NO + OH \xrightarrow{9} HONO$	$\frac{5.07 \times 10^6}{T}$	1.70×10^4	[1]
$HO_2 + NO_2 \xrightarrow{11} HONO + O_2$	$k_{11} = 0.001\ k_{13}$	1.70	[3]
$HONO + OH \xrightarrow{12} NO_2 + H_2O$	$\frac{2.91 \times 10^6}{T}$	9.77×10^3	[1]
$NO_2 + HO_2 \xrightarrow{13} HO_2NO_2$	$\frac{1.73 \times 10^4}{T} \exp(1006/T)$	1.70×10^3	[4]
$HO_2NO_2 \xrightarrow{14} HO_2 + NO_2$	$1.80 \times 10^{15} \exp(-9950/T)$	5.68	[4]
$HO_2 + NO \xrightarrow{15} NO_2 + OH$	$\frac{3.58 \times 10^6}{T}$	1.20×10^4	[1]
$RO_2 + NO \xrightarrow{16} NO_2 + RO$	$\frac{3.58 \times 10^6}{T}$	1.20×10^4	[5]

TABLE 8.3 (Continued)

REACTION		RATE CONSTANTS (ppm-min units)	VALUE AT 298°K	REFERENCE[a]
$RCO_3 + NO \xrightarrow{17}$	$NO_2+RO_2+CO_2$	$\frac{1.13\times10^6}{T}$	3.79×10^3	[6]
$NO_2 + OH \xrightarrow{18}$	$HONO_2$	$\frac{4.53\times10^{6}}{T}$[e]	1.52×10^4	[1]
$CO + OH \xrightarrow{19}$	$HO_2 + CO_2$	$\frac{1.31\times10^5}{T}$	4.40×10^2	[1]
$RO \xrightarrow{34}$	$b_1HO_2 + b_2HCHO + b_3RCHO + (1-b_1)RO_2$	2.0×10^5	2.0×10^5	[7]
$RO + NO \xrightarrow{36}$	$RONO$	$\frac{4.38\times10^6}{T}$	1.47×10^4	[8]
$RO + NO_2 \xrightarrow{37}$	$RONO_2$	$\frac{2.19\times10^6}{T}$	7.35×10^3	[8]
$RO + NO_2 \xrightarrow{38}$	$RCHO+HONO$[b]	$k_{38}=0.087\ k_{37}$	6.39×10^2	[9]
$NO_2 + RO_2 \xrightarrow{39}$	RO_2NO_2	$\frac{1.64\times10^6}{T}$	5.50×10^3	[10]
$NO_2 + RO_2 \xrightarrow{40}$	$RCHO+HONO_2$	$\frac{1.64\times10^3}{T}$	5.50	[10]
$RO_2NO_2 \xrightarrow{41}$	$NO_2 + RO_2$	same as k_{14}	5.68	[5]
$RCO_3 + NO_2 \xrightarrow{42}$	PAN	$\frac{6.17\times10^5}{T}$	2.07×10^3	[6]
$PAN \xrightarrow{43}$	$RCO_3 + NO_2$	$4.77\times10^{16}\ \exp(-12516/T)$	2.74×10^{-2}	[6]
$NO_2 + NO_3 \xrightarrow{44}$	N_2O_5	$\frac{2.20\times10^6}{T}$	7.39×10^3	[13]
$N_2O_5 \xrightarrow{45}$	$NO_2 + NO_3$	$3.44\times10^{16}\ \exp(-10600/T)$	1.22×10^1	[13]

TABLE 8.3 (Continued)

REACTION	RATE CONSTANTS (ppm-min units)	VALUE AT 298°K	REFERENCE[a]
$H_2O + N_2O_5 \xrightarrow{46} 2HONO_2$	$\frac{4.47\times10^{-3}}{T}$	1.50×10^{-5}	[1]
$O_3 + OH \xrightarrow{47} HO_2 + O_2$	$\frac{6.62\times10^{5}}{T}\exp(-1000/T)$	7.75×10^{1}	[1]
$O_3 + HO_2 \xrightarrow{48} OH + 2O_2$	$\frac{4.85\times10^{3}}{T}\exp(-580/T)$	2.32	[11]
$O_3 \xrightarrow{49^c}$ wall loss	0.0	Depends on the equipment	
$HO_2 + HO_2 \xrightarrow{50} H_2O_2 + O_2$	$\frac{3.4\times10^{4}}{T}\exp(1100/T)+\frac{5.8\times10^{-5}}{T^2}\exp(5800/T)[H_2O]^f$	8.28×10^{3}	[11]
$RO_2 + RO_2 \xrightarrow{52} 2RO$	$\frac{2.04\times10^{4}}{T}\exp(223/T)$	1.45×10^{2}	[12]

a) [1] Hampson and Garvin (1978)
[2] Graham and Johnston (1978)
[3] Graham, Winer and Pitts (1977)
[4] Graham, Winer and Pitts (1978)
[5] Estimate
[6] Cox and Roffey (1977)
[7] Baldwin, Barker, Golden and Hendry (1977)
[8] Batt and Rattray (1979)
[9] Baker and Shaw (1965)
[10] Simonaitis and Heicklen (1974)
[11] NASA (1981)
[12] Sander and Watson
[13] Baulch et al. (1980)

b) $\frac{k_{37}}{k_{37}+k_{38}} = 0.92$ for CH_3, $k_{38} = 0.087\ k_{37}$

c) Wall loss term for modeling smog chamber experiments, k_{49} depends on experimental conditions.

d) Rate constants for reactions 39 and 40 are based on the assumption that $k_{16}/(k_{39} + k_{40}) = 2.2$.

e) Determined from $1.477 \times 10^{15} \times 10^{-(\frac{11.6T}{17.4+T})}\sqrt{\frac{280}{T}}$

f) Water concentration in ppm, value at 298°K based on 20,000 ppm.

8.5 Lumped Hydrocarbon Reaction Rate Constants

Most lumped photochemical mechanisms represent atmospheric hydrocarbon chemistry by reactions of the form

$$HC_j + X_m \xrightarrow{\bar{k}_j^m} \text{Products} \tag{8.16}$$

The step (8.16) involves a reaction between X_m, typically atomic oxygen (O), hydroxyl radical (OH) or ozone (O_3), and the jth hydrocarbon class. In the case of the Falls and Seinfeld (1978) mechanism the organics, present in ambient air, are divided into one of four classes: alkanes, olefins, aromatics and oxygenated compounds like aldehydes. Since each class is composed of many different species the lumped reaction rate constant, $\bar{k}_j^m$, is composition dependent. This section describes the procedures used to generate the rate constants for reactions of the type

$$\begin{aligned}
HC_1 &\begin{cases} \text{Olefins} + O \rightarrow \\ \text{Olefins} + OH \rightarrow \\ \text{Olefins} + O_3 \rightarrow \end{cases} \\
HC_2 &\begin{cases} \text{Aromatics} + O \rightarrow \\ \text{Aromatics} + OH \rightarrow \end{cases} \\
HC_3 &\begin{cases} \text{Alkanes} + O \rightarrow \\ \text{Alkanes} + OH \rightarrow \end{cases} \\
HC_4 &\{ \text{Aldehydes} + OH \rightarrow
\end{aligned} \tag{8.17}$$

The basis for calculating the lumped rates are the kinetic data and concentrations of individual species in each class. Consider a typical class, j, which is composed of p_j individual species. The mole weighted lumped rate constant $\bar{k}_j^m$ is given by

$$\bar{k}_j^m = \frac{\sum_{i=1}^{p_j} k_i^m n_i}{\sum_{i=1}^{p_j} n_i} \qquad (8.18)$$

where n_i is the number of moles of species c_i in class j and k_i^m is the rate constant for the reaction between c_i and X_m. The expression (8.18) is the form adopted for use in calculating the lumped rate constants either from emissions data or concentration measurements. In order to evaluate (8.18) an extensive literature search was carried out to identify the basic kinetic data for individual organic species and their reaction with O_3, OH and O. The results of this survey are too voluminous to be presented however. for additional details, the reader is referred to the rate data contained in Hampson and Garvin (1978), Atkinson et al. (1978) and Lloyd et al. (1976).

As an illustration of the procedure consider the calculation of the lumped rates for a typical smog chamber experiment. The composition of the hydrocarbon mixture for the smog chamber experiment SUR-119J (Pitts et al., 1976) is shown in Table 8.4. Individual species concentrations were chosen so that the overall mixture was representative

TABLE 8.4

Hydrocarbon Composition of Smog Chamber Experiment SUR-119J
Excluding Methane, Acetylene, and Acetone

LUMPED HYDROCARBON CLASS	SPECIES	CONCENTRATION ppbV	ppbC
ALKANES	Ethane (C_2H_6)	76.8	154
	Propane (C_3H_8)	17.0	51.0
	Isobutane (C_4H_{10})	0.2	0.8
	N-butane	166	664
	2,3-Dimethyl Butane (C_4H_8-$(CH_3)_2$)	97.6	586
		357.6	1455.8
OLEFINS	Ethene (C_2H_4)	43.2	86.4
		43.2	86.4
	Propene (C_3H_6)	10.6	31.8
	Trans-2-Butene (C_4H_8)	0.7	2.8
	Cis-2-Butene (C_4H_8)	13.0	52.0
	2-methyl Butene-2 (C_4H_7-CH_3)	14.8	74.0
		39.1	160.6
AROMATICS	Benzene (C_6H_6)	1.6	9.6
	Toluene (C_6H_5-CH_3)	16.8	118
	Ethyl Benzene (C_6H_5-C_2H_5)	6.4	51.2
	Meta-xylene (C_6H_4-$(CH_3)_2$)	42.4	339
	Isopropyl Benzene (C_6H_5-C_3H_7)	0.4	3.6
	n-Propyl Benzene ((C_6H_4-$C_3H_7)_n$)	0.1	0.9
	Meta-Ethyl Toluene (C_6H_4-CH_3-C_2H_5)	1.0	9.0
	1,2,3 Trimethyl Benzene (C_6H_3-$(CH_3)_3$)	1.6	14.4
		70.3	545.7

TABLE 8.4 (Continued)

LUMPED HYDROCARBON CLASS	SPECIES	CONCENTRATION ppbV	CONCENTRATION ppbC
ALDEHYDES	Formaldehyde (HCHO)	38.0	38.0
	Acetaldehyde (CH_3CHO)	20.0	40.0
	Propionaldehyde (C_2H_5CHO)	3.2	9.6
		23.2	49.6
	TOTALS FOR MIXTURE	571.4	2336.0

of the 6-9 AM ambient pollutant burden in the Los Angeles atmosphere. Species have been grouped into each of the lumped classes with the concentration, c_i, expressed both in terms of volume as ppbV and by carbon atom as ppbC. Tables 8.5-8.7 present the individual species rate data for reactions with OH, O, and O_3 derived from the literature survey. Given this information and (8.18) the rate constants for the lumped reaction in the Falls and Seinfeld (1978) mechanism are shown in Table 8.8. For comparison purposes the lumped rate constants based on species emission data are also presented in the same table. Details of the emissions inventory and its composition are described in Chapter 13. As a caution it is important to note that in a smog chamber experiment the more reactive components in each class are consumed first. Applying a mole weighted scheme under these circumstances has the effect of underestimating the reaction rates at the beginning of the experiment and overestimating them at the end of a run. This is not a particularly serious problem in urban modeling application because there is a continued injection of source material.

As can be seen from the previous exercise, detailed composition data are required to develop the lumped rate constants. Since most monitoring agencies only report total (THC) and non-methane (NMHC) hydrocarbon concentration levels it is necessary to develop a procedure to partition the broad groupings into the appropriate lumped class for establishing initial conditions. One way to do this is to develop splitting factors from detailed compositional studies and then apply

TABLE 8.5

Rate Constant Data for Reaction with OH

CLASS	SPECIES	RATE CONSTANT (298°K) (cm^3/molecule-sec)	$ppbV_i k_i$	LUMPED RATE CONSTANT (cm^3/molecule-sec)
ALKANES	Ethane (C_2H_6)	2.8×10^{-13}	2.15×10^{-11}	
	Propane (C_3H_8)	1.47×10^{-12}	2.5×10^{-11}	
	Isobutane (C_4H_{10})	2.4×10^{-12}	4.8×10^{-13}	
	N-butane	2.7×10^{-12}	4.48×10^{-10}	
	2,3 Dimethylbutane (C_4H_8-$(CH_3)_2$)	6.54×10^{-12}	6.38×10^{-10}	
			1.14×10^{-9}	$\bar{k} = 3.18 \times 10^{-12}$
OLEFINS	Ethene (C_2H_4)	7.9×10^{-12}	3.41×10^{-10}	$\bar{k} = 7.89 \times 10^{-12}$
	Propene (C_3H_6)	2.5×10^{-11}	2.65×10^{-10}	
	Trans-2-Butene (C_4H_8)	7×10^{-11}	4.9×10^{-11}	
	Cis-2-Butene (C_4H_8)	5.4×10^{-11}	7.02×10^{-10}	
	(2-methyl butene-2) (C_4H_7-CH_3)	8.7×10^{-11}	1.28×10^{-9}	
			2.296×10^{-9}	$\bar{k} = 5.87 \times 10^{-11}$

TABLE 8.5 (Continued)

CLASS	SPECIES	RATE CONSTANT (298°K) (cm^3/molecule-sec)	$ppbV_i k_i$	LUMPED RATE CONSTANT (cm^3/molecule-sec)
AROMATICS	Benzene (C_6H_6)	$1.2x10^{-12}$	$1.92x10^{-12}$	
	Toluene ($C_6H_5-CH_3$)	$6.1x10^{-12}$	$1.02x10^{-10}$	
	EthylBenzene ($C_6H_5-C_2H_5$)	$8x10^{-12}$	$5.12x10^{-11}$	
	Meta-xylene ($C_6H_4-(CH_3)_2$)	$2.4x10^{-11}$	$1.01x10^{-9}$	
	Isopropyl Benzene ($C_6H_5-C_3H_7$)	$6.2x10^{-12}$	$2.48x10^{-12}$	
	n-Propyl Benzene ($C_6H_4-C_3H_7)_n$	$6.2x10^{-12}$	$6.2x10^{-13}$	
	meta-Ethyl Toluene ($C_6H_4-CH_3-C_2H_5$)	$1.95x10^{-11}$	$1.95x10^{-11}$	
	1,2,3 Trimethylbenzene ($C_6H_3-(CH_3)_3$)	$2.64x10^{-11}$	$4.22x10^{-11}$	
			$1.23x10^{-9}$	$\bar{k} = 1.75x10^{-11}$
ALDEHYDES	Formaldehyde	$9.4x10^{-12}$	$3.57x10^{-10}$	$\bar{k} = 9.4x10^{-12}$
	Acetaldehyde (CH_3CHO)	$1.6x10^{-11}$	$3.2x10^{-10}$	
	Propionaldehyde (C_2H_5CHO)	$3.06x10^{-11}$	$9.79x10^{-11}$	
			$4.18x10^{-10}$	$\bar{k} = 1.8x10^{-11}$

TABLE 8.6

Rate Constant Data for Reactions with O

CLASS	SPECIES	RATE CONSTANT (298°K) (cm^3/molecule-sec)	$ppbV_i k_i$	LUMPED RATE CONSTANT (cm^3/molecule-sec)
ALKANES	Ethane (C_2H_6)	8.9×10^{-16}	6.84×10^{-14}	
	Propane (C_3H_8)	8.6×10^{-14}	4.42×10^{-13}	
	Isobutane (C_4H_{10})	1.07×10^{-13}	2.14×10^{-14}	
	N-butane	4.91×10^{-14}	8.15×10^{-12}	
	2,3 Dimethylbutane (C_4H_8-$(CH_3)_2$)	2.11×10^{-13}	2.06×10^{-11}	
			2.93×10^{-11}	$\bar{k} = 8.19 \times 10^{-14}$
OLEFINS	Ethylene (C_2H_4)	8.25×10^{-13}	3.56×10^{-11}	$\bar{k} = 8.25 \times 10^{-13}$
	Propene (C_3H_6)	3.6×10^{-12}	3.82×10^{-11}	
	Trans-2-Butene (C_4H_8)	2.3×10^{-11}	1.61×10^{-11}	
	Cis-2-Butene (C_4H_8)	1.7×10^{-11}	2.21×10^{-10}	
	2-methyl butene-2 (C_4H_7-CH_3)	5.17×10^{-11}	7.65×10^{-10}	
			1.04×10^{-9}	$\bar{k} = 2.66 \times 10^{-11}$

TABLE 8.6 (Continued)

CLASS	SPECIES	RATE CONSTANT (298°K) (cm^3/molecule-sec)	$ppbV_i k_i$	LUMPED RATE CONSTANT (cm^3/molecule-sec)
AROMATICS	Benzene (C_6H_6)	$2.2x10^{-14}$	$3.52x10^{-14}$	
	Toluene ($C_6H_5-CH_3$)	$7.3x10^{-14}$	$1.23x10^{-12}$	
	Ethyl Benzene ($C_6H_5-C_2H_5$)	$5.3x10^{-13}$	$3.39x10^{-12}$	
	Meta-xylene ($C_6H_4-(CH_3)_2$)	$3.4x10^{-13}$	$1.44x10^{-11}$	
	Isopropyl Benzene ($C_6H_5-C_3H_7$)	$6.0x10^{-13}$	$2.40x10^{-13}$	
	n-Propyl Benzene ($C_6H_4-C_3H_7)_n$	$6.0x10^{-13}$	$6.0\ x10^{-14}$	
	meta-Ethyl Toluene ($C_6H_4-CH_3-C_2H_5$)	$4.0x10^{-13}$	$4.0\ x10^{-13}$	
	1,2,3 Trimethylbenzene ($C_6H_3-(CH_3)_3$)	$1.15x10^{-12}$	$1.84x10^{-12}$	
			$2.16x10^{-11}$	$3.07x10^{-13}$

TABLE 8.7

Rate Constant Data for Reactions with O_3

CLASS	SPECIES	RATE CONSTANT (298°K) (cm^3/molecule-sec)	$ppbV_i k_i$	LUMPED RATE CONSTANT (cm^3/molecule-sec)
OLEFINS	Ethylene (C_2H_4)	1.67×10^{-18}	7.21×10^{-17}	$\bar{k} = 1.67 \times 10^{-18}$
	Propene (C_3H_6)	1.04×10^{-17}	1.1×10^{-16}	
	Trans-2-butene (C_4H_8)	1.76×10^{-16}	1.23×10^{-16}	
	Cis-2-butene (C_4H_8)	1.25×10^{-16}	1.63×10^{-15}	
	2-methyl butene-2 (C_4H_7-CH_3)	4.4×10^{-16}	6.51×10^{-15}	
			8.37×10^{-15}	$\bar{k} = 2.15 \times 10^{-16}$

TABLE 8.8

Rate Constants for Lumped Hydrocarbon Reaction Steps

REACTION STEP	RATE CONSTANTS (ppm^{-1} - min^{-1}) Smog Chamber Surrogate Hydrocarbon Mixture SUR-119J	Atmospheric Conditions in Los Angeles 27 June 1974
$HCHO + OH \xrightarrow{23} HO_2 + H_2O + CO$	13890.0	13890.0
$RCHO + OH \xrightarrow{25} RCO_3$	26600.0	25680.0
$C_2H_4 + OH \xrightarrow{26} RO_2$	11660.0	11660.0
$C_2H_4 + O \xrightarrow{27} RO_2 + HO_2$	1219.0	1219.0
$OLE + OH \xrightarrow{28} RO_2$	86800.0	89142.0
$OLE + O \xrightarrow{29} RO_2 + RCO_3$	39300.0	22118.0
$OLE + O_3 \xrightarrow{30} (a_1)RCHO + (a_2)HCHO + (a_3)HO_2$ $(a_4)RO_2 + (a_5)OH + (a_6)RO$	0.317	0.136
$ALK + OH \xrightarrow{31} RO_2$	4700.0	4700.0
$ALK + O \xrightarrow{32} RO_2 + OH$	121.0	99.8
$ARO + OH \xrightarrow{33} RO_2 + RCHO$	25900.0	16112.0

Variable Stoichiometric Coefficients for OLE + O_3 reactions

$a_1 = 0.5$ $a_2 = 0.5$ $a_3 = 0.30$

$a_4 = 0.31$ $a_5 = 0.14$ $a_6 = 0.03$

these values to the routine non-methane hydrocarbon measurements. As an example consider the surrogate mixture in Table 8.4. Given the average carbon numbers for each class, C_j^a, and the carbon fraction, f_j, in each class then it is a straightforward task to develop the volume splitting factors from

$$v_j = \frac{f_j}{C_j^a} \tag{8.19}$$

where the average carbon number of class j is given by

$$C_j^a = \frac{\sum_{i=1}^{p_j} c_i \text{ (ppbC)}}{\sum_{i=1}^{p_j} c_i \text{ (ppbV)}} \tag{8.20}$$

The process is illustrated in Figure 8.3.

8.6 Photolytic Rate Constants

A key process in the formation of photochemical air pollution is the photolysis of such species as nitrogen dioxide (NO_2), formaldehyde (HCHO) and nitrous acid (HONO). In an urban atmosphere it is difficult either to measure the rates directly or to use routine monitoring data as a basis for indirect calculations. This section is devoted to a discussion of a priori methods for determining the diurnal variation of the photolysis rate constants.

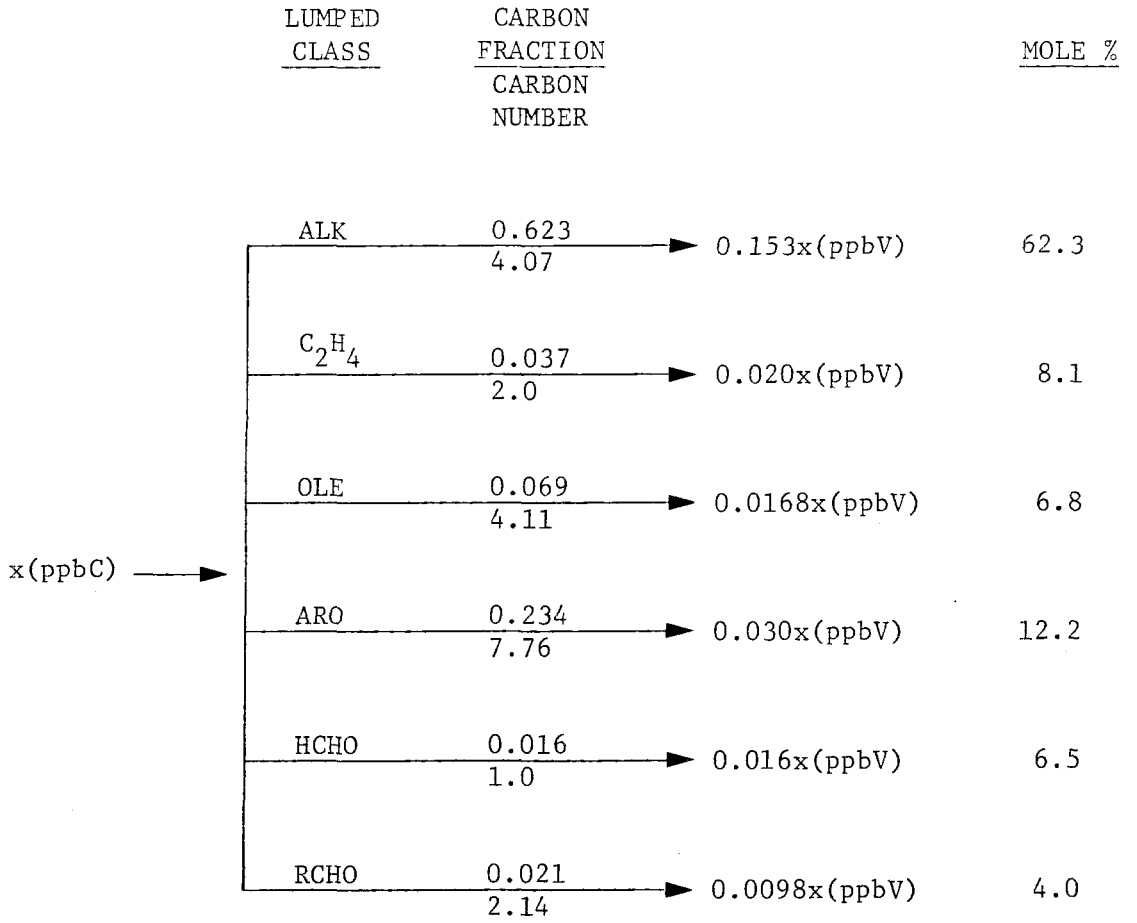

FIGURE 8.3

Conversion of Total Reactive Hydrocarbon Measurements, Expressed in ppbC, to an Equivalent Volumetric Concentration (ppbV) of Lumped Hydrocarbon Species - The Specific Example is for the Atmospheric Surrogate Smog Chamber Experiment SUR-119J

For a typical species, A, the photodissociation step is commonly written in the form

$$A + h\nu \xrightarrow{k} \text{Products} \tag{8.21}$$

with the forward reaction rate, R, given by

$$R \equiv -\frac{dA}{dt} = k[A] \tag{8.22}$$

The photolysis rate constant, k, of any pollutant, present in the atmosphere in small concentrations, is given by

$$k = \int_0^\infty \sigma[\lambda,T(h)]\ \phi[\lambda,T(h)]\ I[\lambda,N(t),\underline{x}]\ d\lambda \tag{8.23}$$

where $\sigma[\lambda,T(h)]$ (cm^2) is the wavelength, λ, dependent absorption cross section for the species at temperature, T, in most applications the atmospheric temperature is a function of the elevation, h. $\phi[\lambda,T(h)]$ is the quantum yield for the reaction and I is the actinic irradiance (photons/cm^2-sec) corresponding to an atmospheric state, N, at spatial location, $\underline{x}$, and time, t. N specifies the temporal variation of those variables which affect the transmission and absorption of solar radiation in the atmosphere. A typical example is the seasonal variation of turbidity.

Since the wavelength dependent absorption coefficients and quantum yields are fixed, the variation of the species rate constant in space and time depends primarily on the variation of the actinic flux.

Actinic irradiance is the radiometric energy incident on single molecules and, as conventionally defined, applies to ultraviolet (uv) wavelengths. This parameter is very difficult to estimate from customary solar radiation measurements; in particular those made with broad band 180^{o} pyroheliometers. As a result most photolysis rate constants are based on theoretical calculations of the solar flux in the spectral band of interest. Many previous modeling studies employed the tabulation, by Leighton (1961), of photolysis rates as a function of zenith angle. His results were based on a radiative transfer calculation which, by necessity, employed many simplifying assumptions. The availability of more sophisticated radiative transfer models and more recent measurements of the upper atmospheric properties has led to considerable refinement in the calculation of solar fluxes.

Duewer et al. (1978) used the model of Luther and Gelinas (1976) as a basis for determining the photodissociation rate constants of the species NO_2, HNO_2, H_2O_2, Aldehydes, RNO_2, NO_3, O_3. For the present study the actinic irradiance, as a function of zenith angle, was obtained from the report by Peterson (1976). The actinic flux at ground level is shown in Table 8.9 for zenith angles in the range 0^{o}-86^{o} as a function of wavelength in the spectral band 290-800 nm. Extrapolation of these values beyond 700 nm were obtained from Schere and Demerjian (1977). The calculations by Peterson were performed with a modified version of the program developed by Braslau and Dave (1973 a, b). It is beyond the scope of this chapter to discuss the details of the

TABLE 8.9

Ground Level Actinic Irradiance as a Function of Zenith Angle and Wavelength (Photons/cm^2-secx10^{-15})

WAVELENGTH RANGE(NM)	ZENITH ANGLES (DEG) 0.0	10.00	20.00	30.00	40.00	50.00	60.00	70.00	78.00	86.00
285 - 295	0.000	0.000	0.0	0.0	0.0	0.0	0.0	0.0	0.0	0.0
295 - 305	0.040	0.038	0.033	0.025	0.016	0.007	0.002	0.000	0.0	0.0
305 - 315	0.439	0.431	0.401	0.351	0.281	0.198	0.110	0.039	0.009	0.001
315 - 325	0.955	0.944	0.901	0.826	0.717	0.571	0.389	0.194	0.064	0.009
325 - 335	1.613	1.594	1.538	1.440	1.292	1.083	0.803	0.463	0.203	0.039
335 - 345	1.713	1.696	1.645	1.555	1.416	1.215	0.936	0.573	0.269	0.061
345 - 355	1.892	1.875	1.824	1.733	1.591	1.383	1.243	0.684	0.328	0.077
355 - 365	1.951	1.933	1.865	1.798	1.662	1.459	1.164	0.749	0.363	0.083
365 - 375	2.397	2.378	2.323	2.224	2.067	1.831	1.480	0.972	0.477	0.107
375 - 385	2.318	2.301	2.251	2.161	2.019	1.803	1.475	0.988	0.491	0.106
385 - 395	2.341	2.325	2.279	2.195	2.059	1.852	1.534	1.047	0.529	0.111
395 - 405	3.174	3.153	3.093	2.984	2.810	2.541	2.125	1.474	0.758	0.156
405 - 415	3.993	3.968	3.896	3.765	3.556	3.232	2.725	1.919	1.003	0.202
415 - 425	4.119	4.095	4.025	3.898	3.696	3.378	2.875	2.059	1.097	0.215
425 - 435	4.222	4.118	4.051	3.930	3.735	3.428	2.938	2.129	1.151	0.223
435 - 445	4.617	4.512	4.442	4.317	4.113	3.793	3.274	2.402	1.321	0.251
445 - 455	5.209	5.182	5.101	4.958	4.728	4.366	3.783	2.800	1.559	0.292
455 - 465	5.615	5.585	5.498	5.344	5.099	4.715	4.099	3.055	1.721	0.319
465 - 475	5.750	5.721	5.636	5.485	5.242	4.848	4.248	3.193	1.821	0.333
475 - 485	5.799	5.771	5.688	5.541	5.304	4.918	4.327	3.277	1.887	0.340
485 - 495	5.784	5.756	5.676	5.533	5.305	4.944	4.352	3.317	1.926	0.342
495 - 505	5.887	5.857	5.773	5.625	5.390	5.022	4.422	3.377	1.970	0.342
505 - 515	5.935	5.905	5.818	5.666	5.425	5.053	4.450	3.405	1.994	0.339
515 - 525	5.932	5.903	5.818	5.669	5.433	5.067	4.472	3.434	2.020	0.338
525 - 535	5.980	5.950	5.866	5.717	5.482	5.116	4.521	3.476	2.045	0.331
535 - 545	5.927	5.899	5.816	5.670	5.439	5.080	4.495	3.462	2.040	0.322
545 - 555	5.910	5.881	5.797	5.650	5.420	5.061	4.479	3.452	2.037	0.315
555 - 565	5.969	5.940	5.853	5.703	5.467	5.103	4.514	3.479	2.052	0.309
565 - 575	6.058	6.028	5.941	5.789	5.551	5.183	4.585	3.534	2.081	0.303
575 - 585	6.174	6.144	6.058	5.905	5.666	5.296	4.714	3.629	2.148	0.311
585 - 595	6.226	6.197	6.111	5.958	5.722	5.354	4.754	3.686	2.194	0.320
595 - 605	6.269	6.240	6.152	5.997	5.758	5.387	4.785	3.714	2.218	0.324
605 - 615	6.312	6.282	6.192	6.036	5.793	5.421	4.815	3.742	2.242	0.327
615 - 625	6.321	6.292	6.205	5.937	5.638	5.452	4.858	3.798	2.303	0.349
625 - 635	6.330	6.301	6.217	5.838	5.482	5.482	4.900	3.854	2.363	0.372
635 - 645	6.421	6.392	6.306	6.039	5.743	5.562	4.979	3.935	2.438	0.400
645 - 655	6.513	6.483	6.395	6.240	6.004	5.641	5.058	4.015	2.512	0.429
655 - 665	6.594	6.563	6.472	6.314	6.074	5.708	5.122	4.079	2.574	0.455
665 - 675	6.674	6.643	6.549	6.388	6.144	5.775	5.187	4.142	2.635	0.481
675 - 685	6.659	6.626	6.537	6.379	6.139	5.777	5.199	4.168	2.671	0.499
685 - 695	6.643	6.610	6.524	6.369	6.134	5.775	5.211	4.193	2.706	0.518
695 - 705	6.460	6.430	6.350	6.200	5.980	5.710	5.150	4.090	2.740	0.530
705 - 715	6.400	6.360	6.290	6.140	5.910	5.650	5.110	4.070	2.750	0.540
715 - 725	6.340	6.320	6.220	6.060	5.870	5.600	5.050	4.050	2.760	0.560
725 - 735	6.370	6.290	6.180	6.020	5.830	5.550	5.030	4.040	2.770	0.560
735 - 745	6.210	6.190	6.100	5.980	5.750	5.490	4.970	4.020	2.780	0.560
745 - 755	6.140	6.120	6.030	5.900	5.660	5.430	4.920	4.000	2.790	0.570
755 - 765	6.050	6.000	5.970	5.840	5.640	5.400	4.900	3.990	2.790	0.590
765 - 775	6.020	6.000	5.910	5.780	5.580	5.340	4.860	3.970	2.790	0.590
775 - 785	5.950	5.940	5.850	5.720	5.530	5.310	4.840	3.960	2.790	0.600
785 - 795	5.890	5.880	5.790	5.660	5.470	5.250	4.800	3.940	2.780	0.600
795 - 805	5.820	5.810	5.730	5.590	5.420	5.220	4.760	3.930	2.780	0.600

algorithms, it suffices to say however, that their model includes aerosol scattering and absorption, Rayleigh scattering, and ozone absorption. The atmospheric state, N, assumed in the model corresponds to annual average U.S. urban conditions, Flowers et al. (1969). This condition corresponds to a cloud-free atmosphere over a typical urban environment.

The photolysis rate constant for a particular species can be determined by evaluating (8.23) and in practice the integral can be approximated, with minimal error, by a finite interval summation of the form

$$k \simeq \sum_{i=1}^{n} \overline{\sigma}\,[\lambda_i, \Delta\lambda_i]\ \overline{\phi}[\lambda_i \Delta\lambda_i]\ \overline{I}\,[\lambda_i, \Delta t_i N(t), h, z] \tag{8.24}$$

where the overbar represents an average over a wavelength interval $\Delta\lambda_i$ centered at λ_i. The actinic irradiance at a particular time and elevation h is specified as a function of the zenith angle z. Compared to the total solar spectrum, the summation interval is quite small ($290 \leq \lambda \leq 800$ nm). The photochemistry of the lower atmosphere is dominated by the fact that virtually no solar radiation of wavelengths less than 290 nm reaches the troposphere . Essentially all the incident solar radiation at wavelengths below 290 nm is absorbed by gases in the upper atmosphere, principally the Hartley band of 220-295 nm and by oxygen in the Schumann continuum 175-145 nm (Coulson, 1975). The upper limit for λ is set by either the reduction of the species absorption cross section or reaction quantum yield as a function of increasing wavelength.

Data for the species absorption class sections and quantum yields as a function of wavelength are required in order to evaluate (8.24). Tables 8.10 and 8.11 contain the appropriate information, compiled from Schere and Demerjian (1977), Demerjian (1977) and Demerjian et al. (1980), for the following reactions

$$
\begin{aligned}
NO_2 &+ h\nu \rightarrow NO &&+ O(^3P) \\
HONO &+ h\nu \rightarrow NO &&+ OH \\
HNO_3 &+ h\nu \rightarrow OH &&+ NO_2 \\
O_3 &+ h\nu \rightarrow O_2 &&+ O(^3P) \\
O_3 &+ h\nu \rightarrow O_2 &&+ O(^1D) \\
O_3 &+ h\nu \rightarrow O &&+ O_2(^1\Delta) \\
HCHO &+ h\nu \rightarrow 2HO_2 &&+ CO \\
HCHO &+ h\nu \rightarrow H_2 &&+ CO \\
HCHO &+ h\nu \rightarrow 2OH &&+ 2OH \\
CH_3CHO &+ h\nu \rightarrow CH_3 &&+ HO_2 + CO \\
CH_3CHO &+ h\nu \rightarrow CH_4 &&+ CO
\end{aligned}
\qquad (8.25)
$$

The tables represent a collation of experimental information and have been assembled to enable an independent verification of the photolysis rate calculations. The species rate constants, as a function of the cosine of the zenith angle, are shown in Figures 8.4-8.14. The diurnal variation of the rate constants for any date or location can be easily evaluated using these figures and a knowledge of the solar declination angle δ. The local zenith angle, Z, can be determined from the expression (Sellers, 1969)

TABLE 8.10

Quantum Yield Data Averaged over 10 nm Wavelength Interval

	Quantum yields for photolytic processes, 10 nm integral averaged, centered about λ for the reactions (8.25)										
λ(nm)	NO_2	HONO	$HONO_2$	O_3[a]	O_3	O_3	HCHO	HCHO	CH_3CHO	CH_3CHO	H_2O_2
290	1.0	1.0	1.0	0.0	1.0	1.0	.73	.28	.46	.31	1.0
300	1.0	1.0	1.0	0.0	1.0	1.0	.77	.23	.60	.19	1.0
310	1.0	1.0	1.0	1.0	.52	1.0	.75	.25	.72	.09	1.0
320	1.0	1.0	1.0	1.0	.01	1.0	.61	.39	.86		1.0
330	1.0	1.0		1.0		1.0	.31	.59	.98		1.0
340	1.0	1.0		1.0		1.0	.01	.42	1.00		1.0
350	1.0	1.0		1.0		1.0					1.0
360	1.0	1.0									
370	.99	1.0									
380	.97	1.0									
390	.91	1.0									
400	.65										
410	.22										
420	.02										
430											

[a] O_3 quantum yield in the 450-750 nm region equal 1.0.

TABLE 8.11

Absorption Cross Section $\sigma(10^{-20} cm^2\ molecule^{-1})$
10 nm integral averaged, centered about λ

λ (nm)	NO_2	HONO	$HONO_2$	O_3	HCHO	CH_3CHO	H_2O_2
290	8.52		0.634	162.	3.18	4.66	1.23
300	12.83		0.276	44.4	3.25	4.09	0.71
310	18.26	0.3	0.095	11.9	3.15	2.96	0.41
320	24.74	3.4	0.018	3.36	2.34	1.69	0.24
330	30.95	6.6		0.88	2.37	0.69	0.14
340	37.39	13.3		0.19	1.98	0.13	0.08
350	44.90	17.0		0.04	0.84		0.05
360	50.11	9.6			0.18		
370	54.05	17.2					
380	56.99	10.9					
390	58.22	2.3					
400	59.52						
410	58.03						
420	54.52						
430	51.46						
440	48.50						
450	45.50			.020			
460				.036			
470				.054			
480				.075			
490				.096			
500				.131			
510				.174			
520				.220			
530				.276			
540				.331			
550				.378			
560				.454			
570				.509			
580				.493			
590				.515			
600				.552			
610				.498			
620				.417			
630				.361			
640				.318			
650				.269			
660				.217			
670				.179			
680				.152			
690				.126			
700				.098			
710				.081			
720				.068			
730				.056			
740				.048			
750				.041			

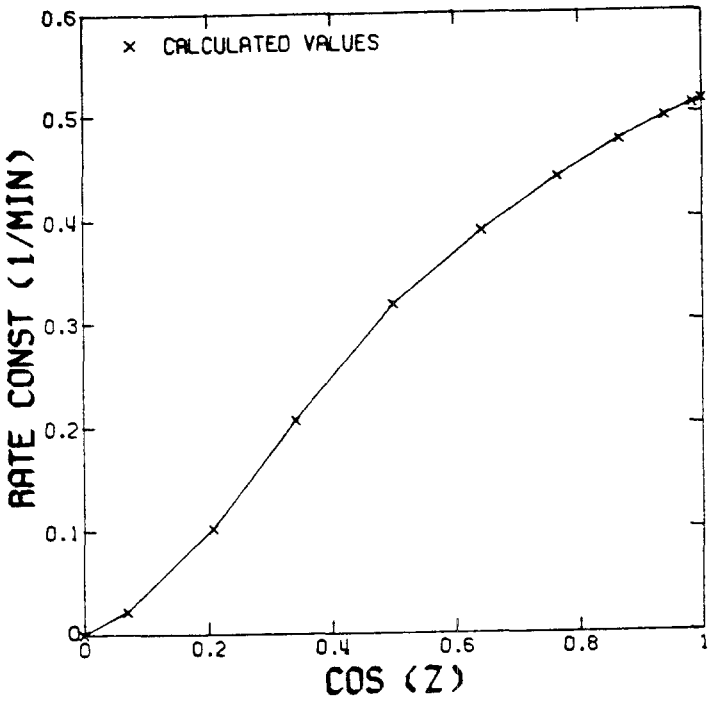

FIGURE 8.4

Photolysis Rate for $NO_2 + h\nu \xrightarrow{k} NO + O(^3P)$ as a Function of Zenith Angle

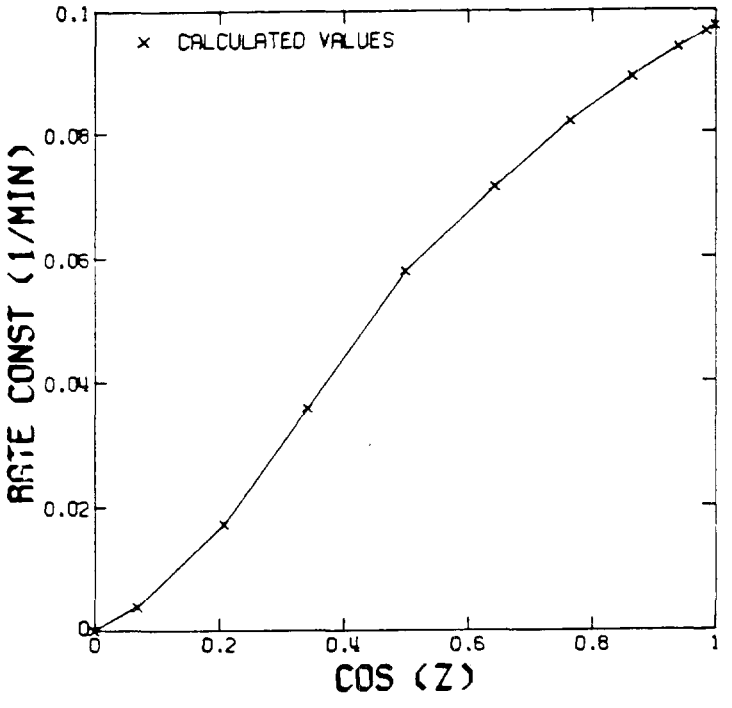

FIGURE 8.5

Photolysis Rate for $HONO + h\nu \xrightarrow{k} OH + NO$ as a Function of Zenith Angle

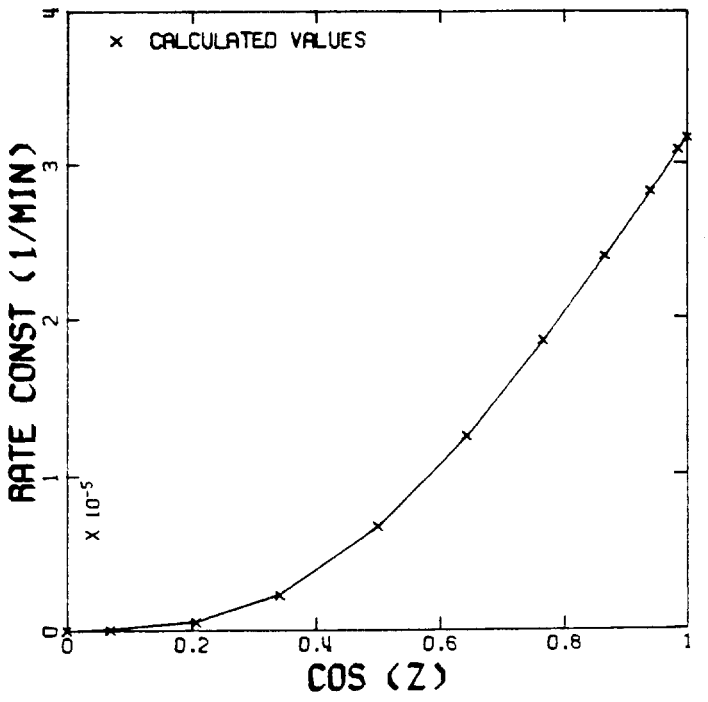

FIGURE 8.6

Photolysis Rate for $HNO_3 + h\nu \xrightarrow{k} OH + NO_2$ as a Function of Zenith Angle

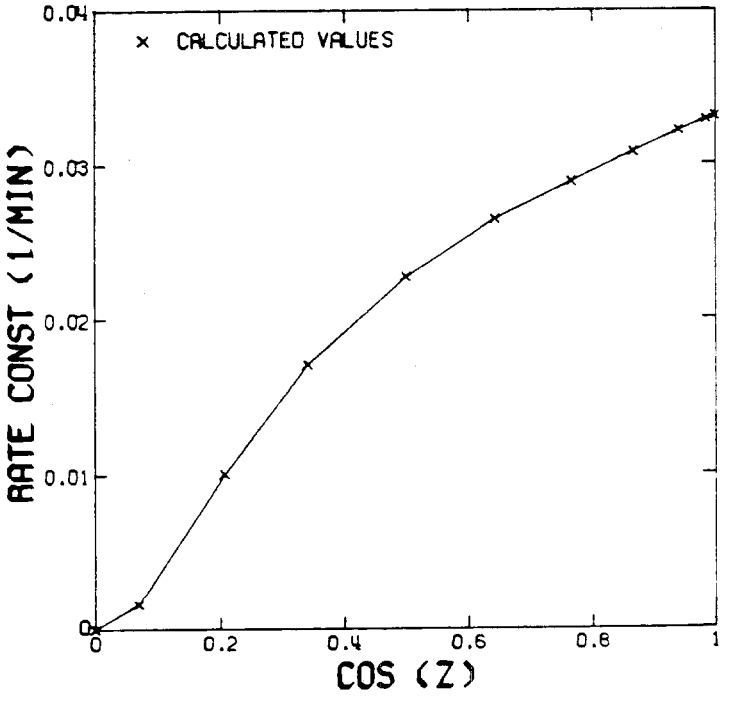

FIGURE 8.7

Photolysis Rate for $O_3 + h\nu \xrightarrow{k} O(^3P) + O_2$ as a Function of Zenith Angle

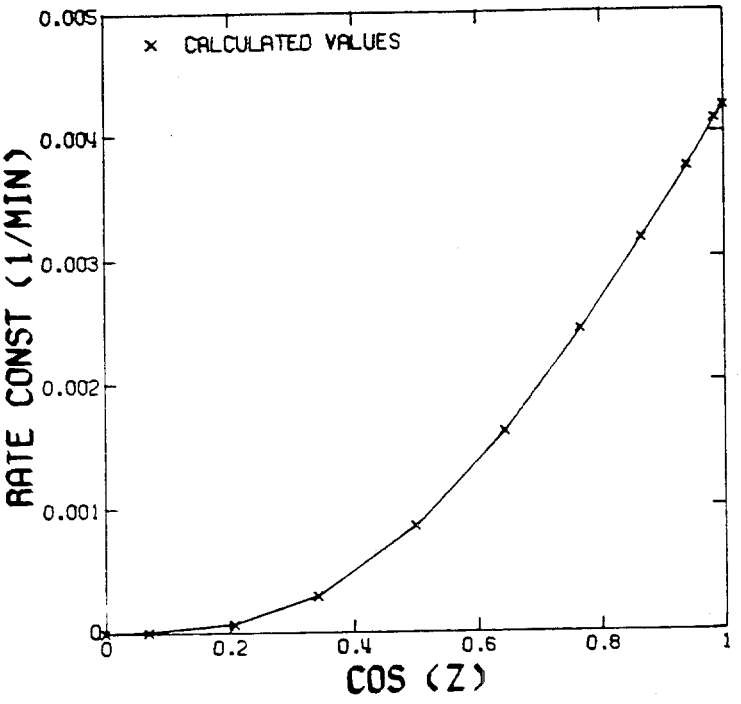

FIGURE 8.8

Photolysis Rate for $O_3 + h\nu \xrightarrow{k} O(^1D) + O_2$ as a Function of Zenith Angle

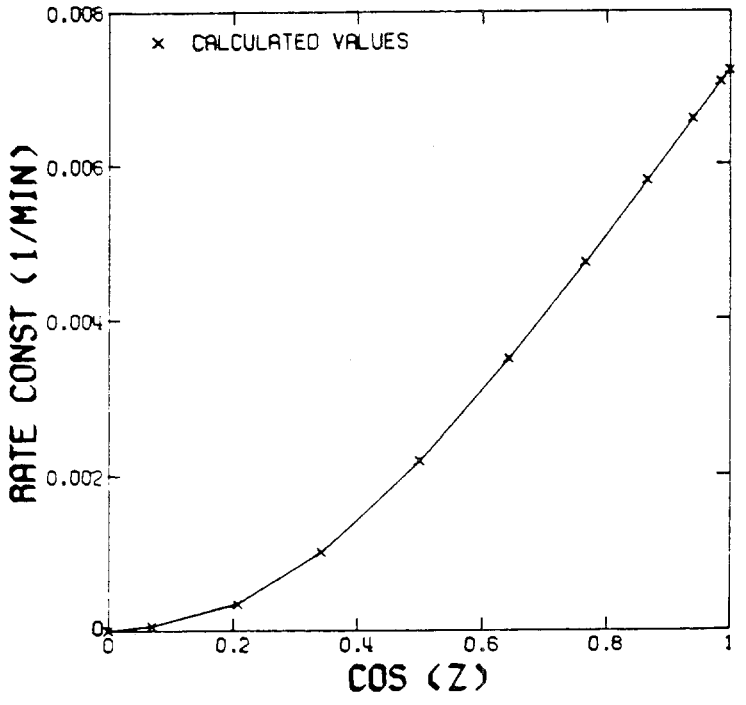

FIGURE 8.9

Photolysis Rate for $O_3 + h\nu \xrightarrow{k} O_2(^1\Delta) + O$ as a Function of Zenith Angle

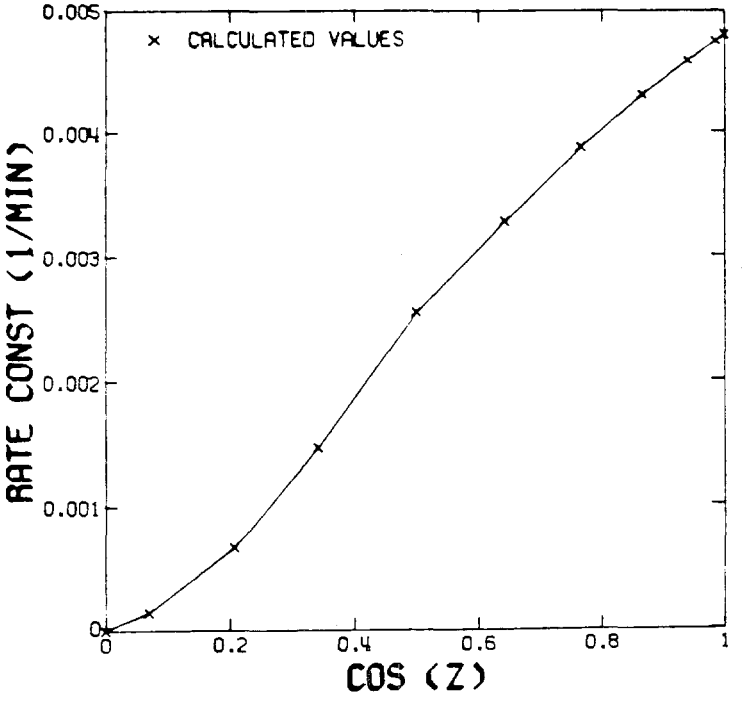

FIGURE 8.10

Photolysis Rate for HCHO + $h\nu \xrightarrow{k} H_2 + CO$ as a Function of Zenith Angle

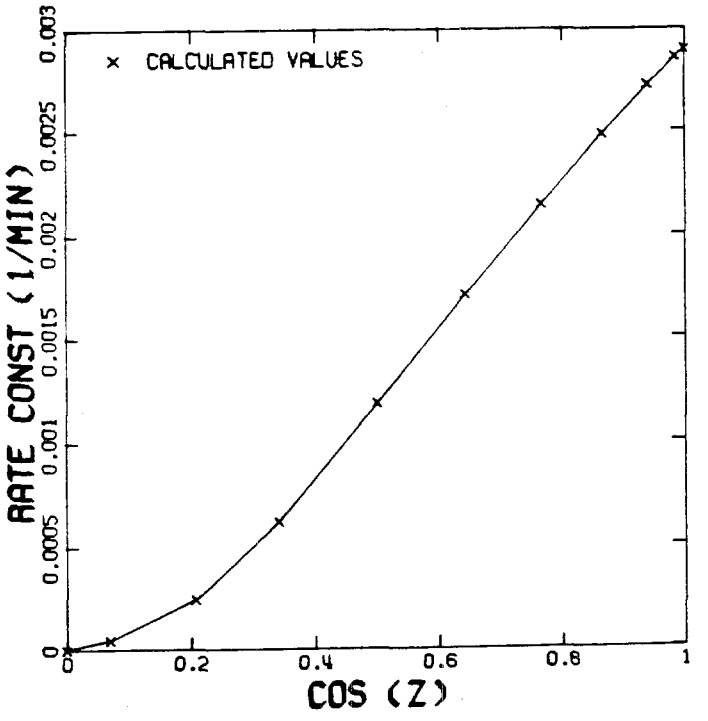

FIGURE 8.11

Photolysis Rate for HCHO + $h\nu \xrightarrow{k} 2HO_2 + CO$ as a Function of Zenith Angle

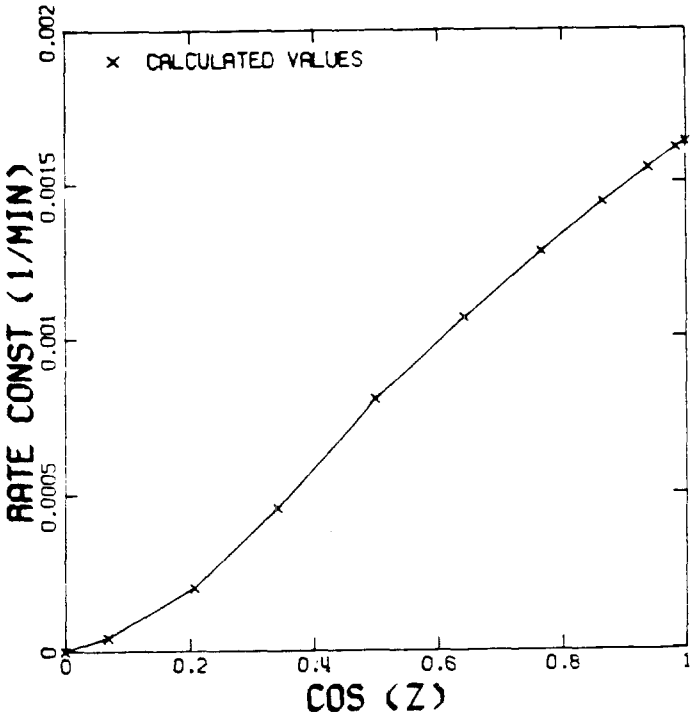

FIGURE 8.12

Photolysis Rate for $H_2O_2 + h\nu \xrightarrow{k} 2OH$ as a Function of Zenith Angle

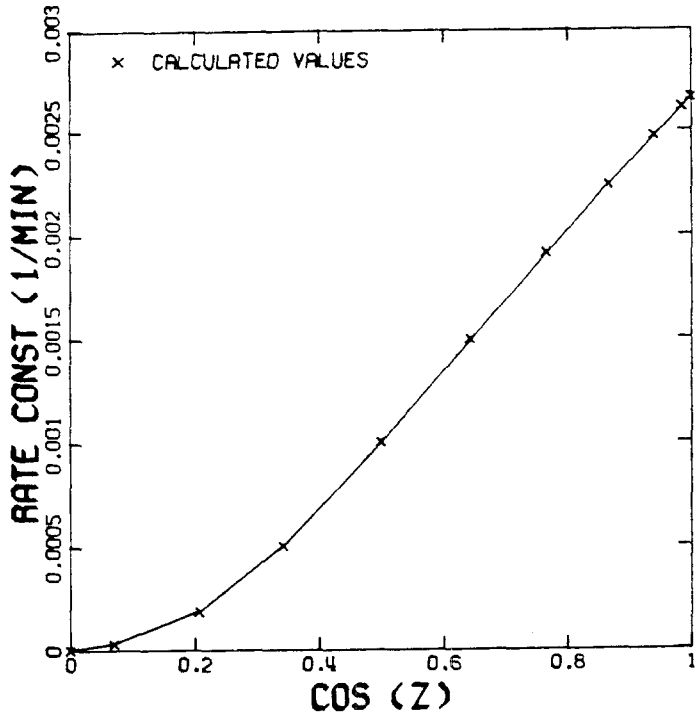

FIGURE 8.13

Photolysis Rate for $CH_3CHO + h\nu \xrightarrow{k} CH_3 + HO_2 + CO$ as a Function of Zenith Angle

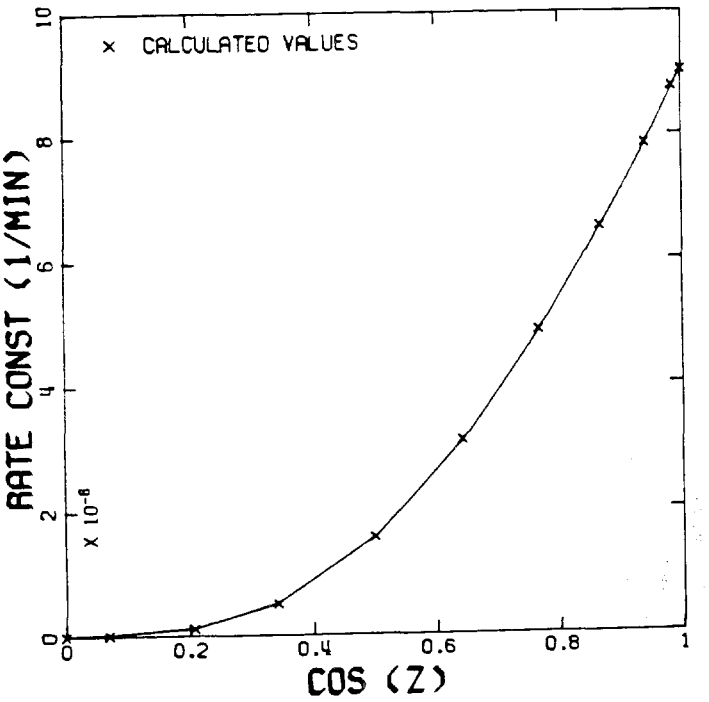

FIGURE 8.14

Photolysis Rate for $CH_3CHO + h\nu \xrightarrow{k} CH_4 + CO$ as a Function of Zenith Angle

$$\cos Z = \sin \phi \sin \delta + \cos \phi \cos \delta \cos h \qquad (8.26)$$

where ϕ is the latitude and h the hour angle. The relationship between these angles is shown in Figure 8.15. At solar noon the hour angle is zero and as a result it is related to the local standard time and the longitude ϕ. The declination angle is a function only of the day of the year and it varies from $23^{o}27'$ on June 21 to $-23^{o}27'$ on December 22nd. Values for each day and hour can be obtained from a nautical almanac or calculated using the algorithm of Woolf (1967). This latter approach, together with a simple interpolation scheme, and Figures 8.4-8.14 is used to evaluate the photolysis rates in the airshed model. The expression (8.26) can also be employed to calculate the day length and in turn the sunrise and sunset times. A knowledge of these times is very useful for controlling the numerical procedures during the rapid chemical changes which take place during initiation or termination of the mechanism photolysis steps.

A typical diurnal variation in the NO_2 photolysis rate and a comparison against the experimental observations of Zafonte (1977), is shown in Figure 8.16. The predicted and measured values agree quite closely over most of the day. Scatter in the experimental measurements was primarily due to the presence of broken high cloud conditions (Zafonte, 1977). Schere and Demerjian (1977) attempted a similar correlation; however, most of the measurements available to them were for non clear sky conditions and, as a result, scaling of the calculated

results was required. Table 8.12 presents a summary of the photodissociation rates for the photolysis steps in the Falls and Seinfeld (1978) mechanism. Some preliminary results for ozone and the appropriate experimental techniques for formaldehyde (HCHO), nitrous acid (HONO), hydrogen peroxide (H_2O_2), and nitric acid (HNO_3) have been described by Stedman et al. (1977). An additional point to note about the results is that the rates have been calculated using ground level actinic irradiance data. Within the lowest 5-10 km of the atmosphere the actinic flux increases with elevation leading to higher photolysis rates. The results of Peterson et al. (1977) for NO_2 and HCHO show a significant increase with height. For example, at an elevation of 0.98 km the photolysis rate for NO_2, depending on the zenith angle, is between 21 and 70% higher than the corresponding ground level value. The photolysis rates should be recalculated if the modeling region is at a high elevation.

Most theoretical calculations of the photolysis rate constants assume 'clear sky' conditions. A critical problem in practice is how to modify the calculated results when there is a perturbation to the basic atmospheric state employed in the radiative transfer calculations. Increased aerosol loadings or the presence of clouds would require scaling of the photodissociation rates.

When only broad band measurements of solar radiation are available correction of the calculated values can be based on the ratio of pyranometer observations to the theoretical clear sky transmission. Because pyranometer data reported by air pollution agencies typically only apply to total solar fluxes and the reaction rates depend on the ultraviolet (uv) flux densities, the scaling ratio may not be a good representation. Scattering is wavelength dependent and as a result the uv flux is more strongly affected than the total solar flux. Offsetting this to some extent, the flux density is much less sensitive to scattering them than is the flux (Duewer et al., 1978).

In situations where uv pyranometer data are available another approach is possible. Zafonte et al. (1977) and Stedman et al. (1977) correlated their NO_2 photodissociation rate measurements with solar radiation in the uv portion of the spectrum. Radiometric data were obtained with Eppley uv pyranometers that have a full bandwidth sensitivity of 295-385 nm, a wavelength interval relevant to many photochemical reactions. The results of the correlations are shown in Figure 8.17. This graph provides a direct means of determining either the photolysis rate from the radiation measurements or the scaling ratios for the calculated values. Schere and Demerjian (1977) used uv measurements and the calculated clear sky solar flux to scale the rate constants. They reported substantial differences in some cases between theoretical clear sky and observed rate constants, however, the uv scaled calculated rates match the observations quite closely as in Figure 8.18.

TABLE 8.12

Photolysis Steps in Photochemical Reaction Mechanism[a]

REACTION				Photolysis Rate (min^{-1})		
				7:24 AM[b]	Average[c]	Peak
NO_2	+ hν $\xrightarrow{1}$	NO	+ $O(^3P)$	0.320	0.339	0.508
HONO	+ hν $\xrightarrow{10}$	OH	+ NO	0.0585	0.0631	0.0963
O_3	+ hν $\xrightarrow{20}$	$O(^3P)$	+ O_2	0.0229	0.0232	0.0328
HCHO	+ hν $\xrightarrow{21}$	$2HO_2$	+ CO	0.00121	0.00163	0.00284
HCHO	+ hν $\xrightarrow{22}$	H_2	+ CO	0.00258	0.00296	0.00473
RCHO	+ hν $\xrightarrow{24}$	RO_2	+ HO_2 + CO	0.00103	0.00145	0.00260
RONO	+ hν $\xrightarrow{35}$	NO	+ RO	0.0704[d]	0.0746[d]	0.1118[d]
H_2O_2	+ hν $\xrightarrow{51}$	2OH		0.00082	0.00098	0.00161

a) All values are for Los Angeles California (latitude 34.06°, longitude 118.25°, time zone = 8.0)

b) Photolysis rates at 7:24 Pacific Standard Time, 26 June 1974.

c) Average of daylight hours.

d) Photolysis rate set to 0.22 of NO_2

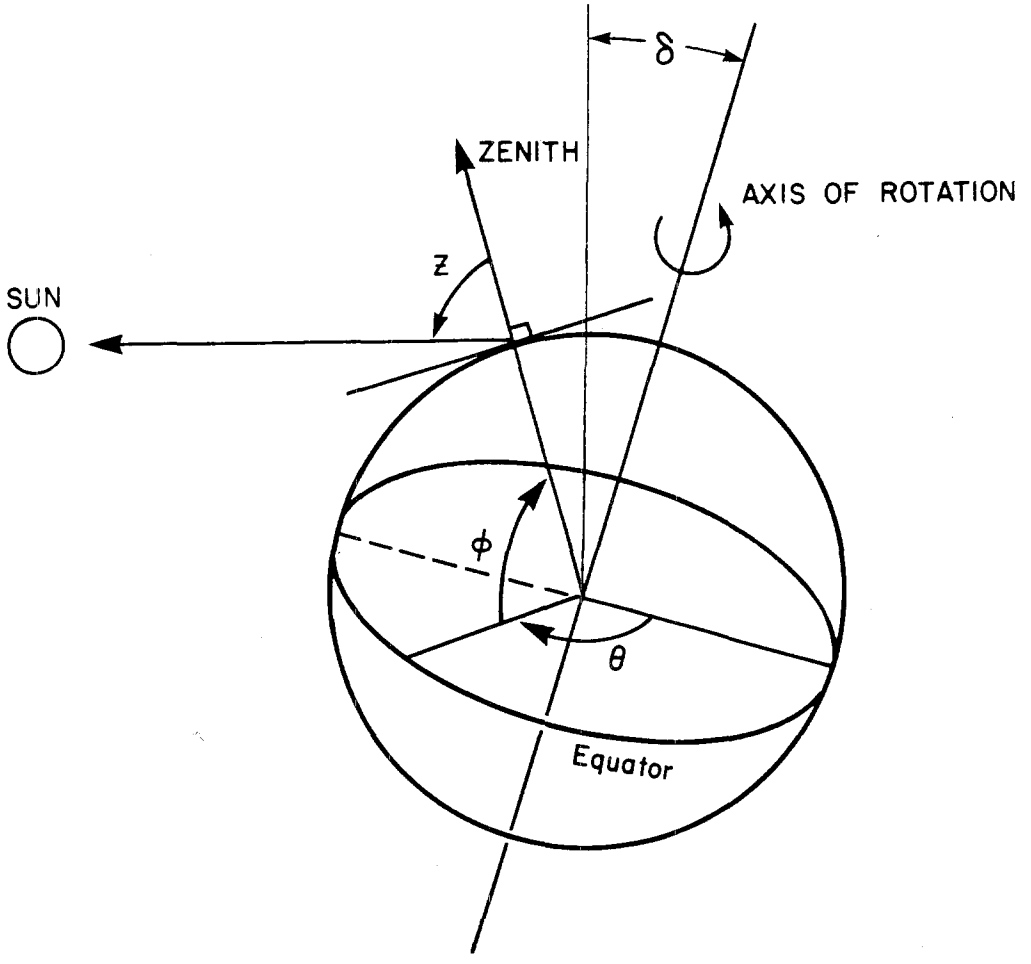

FIGURE 8.15

Relationship Between Latitude, Declination and Zenith Angles.

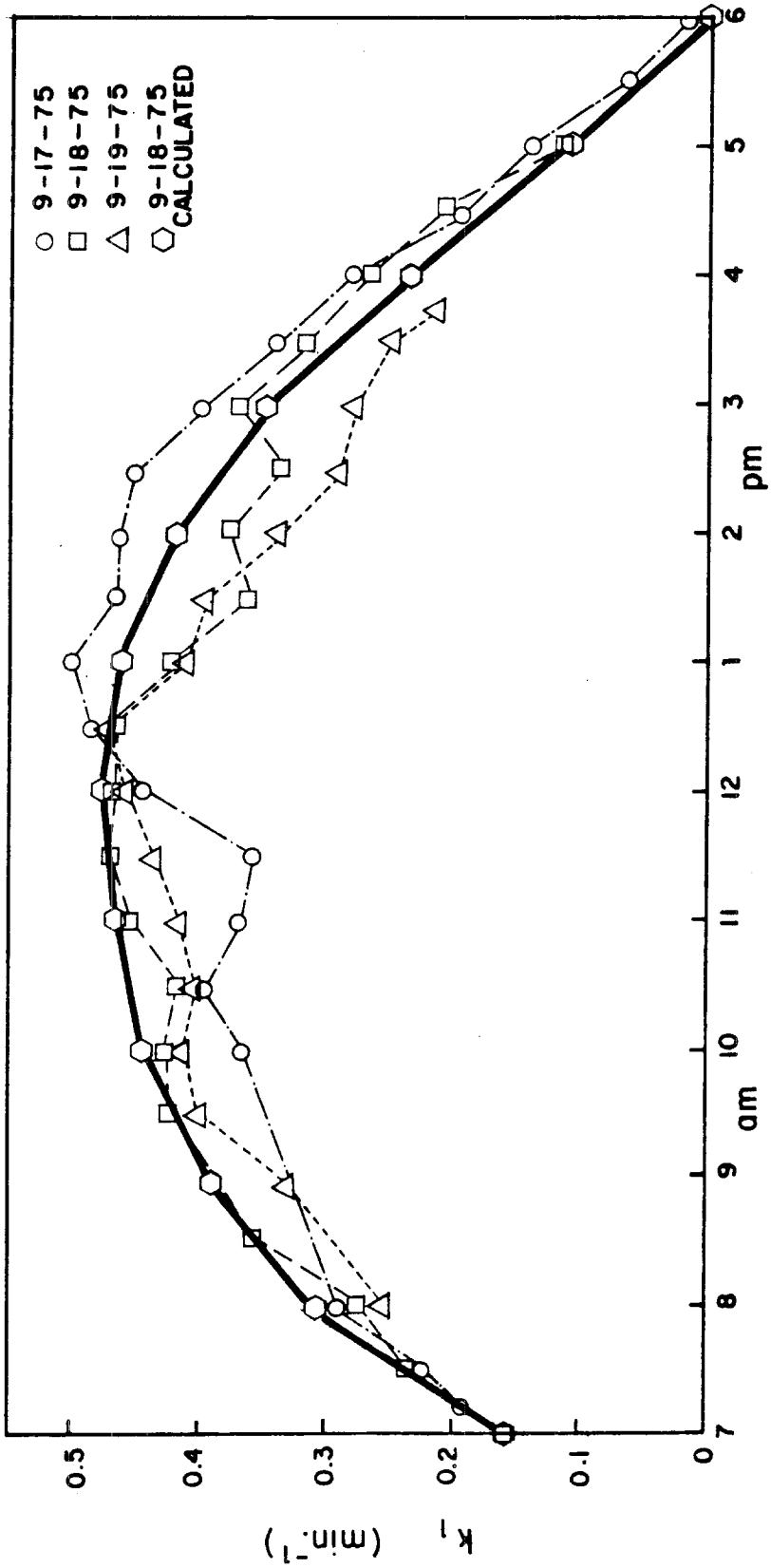

FIGURE 8.16

Comparison of Calculated Diurnal Variation of NO_2 Photolysis Rate with Experimental Measurements of Zafonte et al. (1977)

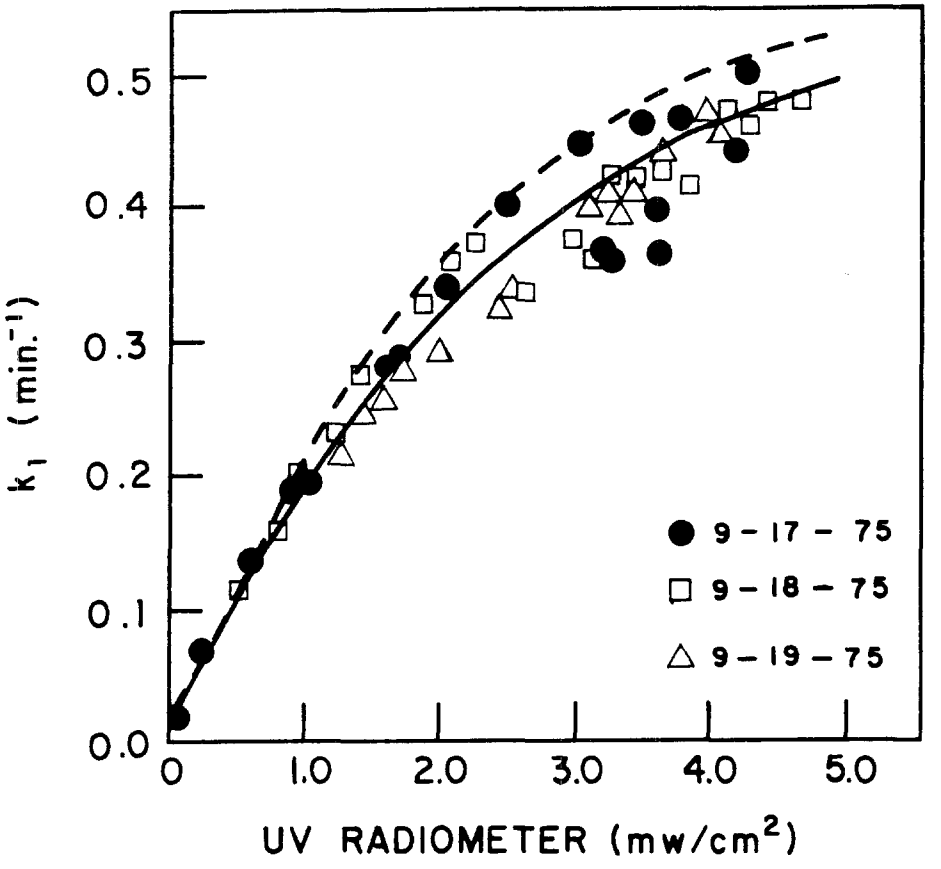

FIGURE 8.17

Correlation Between UV Radiometric Measurements and NO_2 Photolysis Rate - Experimental Points and Solid Line are from Zafonte et al. (1977), Dashed Line is Best Fit to Data of Stedman et al. (1977)

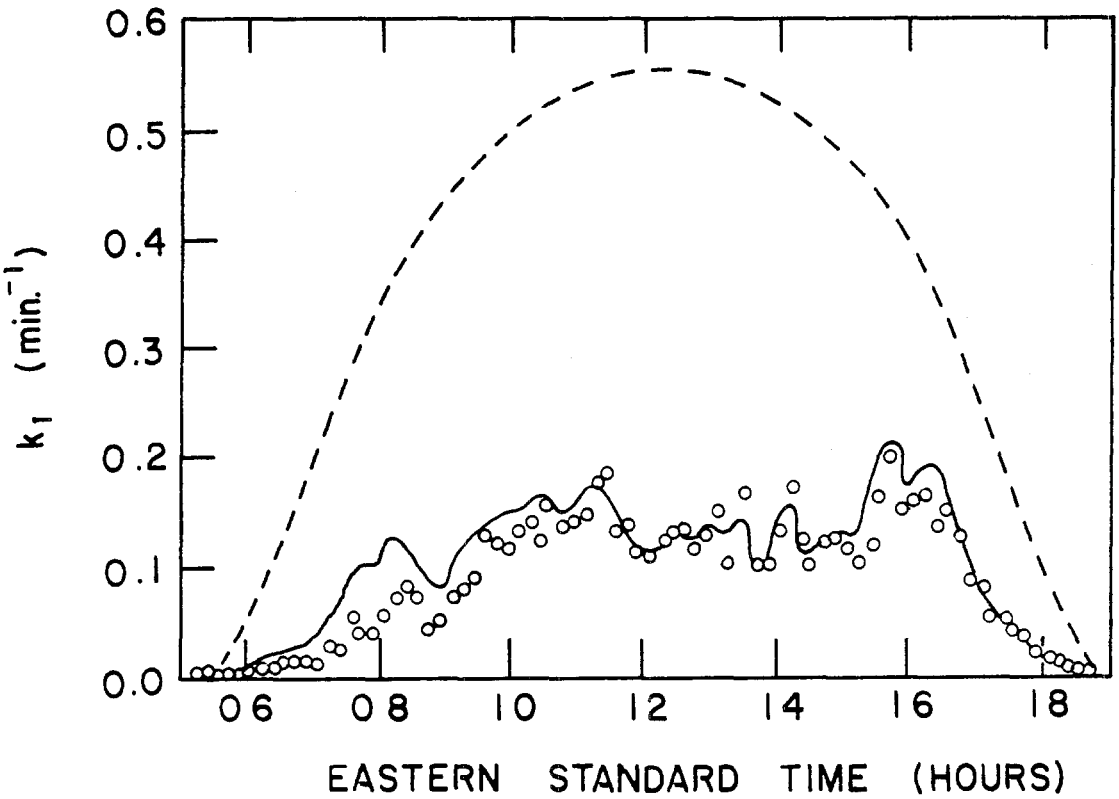

FIGURE 8.18

Comparison of the Experimental (Circles), Theoretical (Dashed Line), and UV Scaled Theoretical (Solid Line) Diurnal Variation of the Photolytic Rate Constant for the Photolysis of NO_2 Near Raleigh, N.C. (35.8°N, 78.6°W) on April 28, 1975 (Source: Schere and Demerjian, 1977).

8.7 Calculation of Atmospheric Water Vapor Concentration

Most photochemical reaction mechanisms require that the water vapor be expressed in terms of concentration units like ppmV or $\mu g/m^3$. While it is a straightforward task to determine the concentration given ambient measurements of temperature, pressure, and relative humidity, the need to employ psychrometric charts or tables considerably complicates automation of the process . This section presents a simple algebraic procedure, based on McRae (1980), which enables the water concentration to be determined to within 0.5% over the range of commonly encountered meteorological conditions.

For a given temperature, T, relative humidity, RH, is defined as the rate of the observed vapor pressure to the saturation vapor pressure at the same conditions. An alternative approach is to define RH in terms of the mole fraction of water vapor in the moist atmosphere, y, to the mole fraction at saturation y_s. In either case the relative humidity is often expressed in percent so that

$$RH = 100 \frac{y}{y_s} \tag{8.27}$$

Since the mole fraction is equivalent to the volume fraction the water concentration in ppmv is given by

$$H_2O(ppmv) = 10^6 y = 10^4 RH\ y_s \tag{8.28}$$

By using the perfect gas laws (8.28) can be written in terms of the saturation vapor pressure $P_s(T)$ and the atmospheric pressure P_a. The

error involved in using Dalton's Law over a temperature range of -50 to 50°C is less than 0.5% (Threlkeld, 1970). With this approximation (8.28) can be written in the form:

$$H_2O(ppmv) = 10^4 RH \frac{P_s(T)}{P_a} \tag{8.29}$$

In order to evaluate this expression, the saturation vapor pressure must be known. While many tabulations and graphical forms exist in the literature relatively few are suitable for direct inclusion in the airshed model; what is required is an explicit algebraic expression. One of the first attempts to describe $P_s(T)$ - T experimental data in a functional form was the work of Goff and Gratch (1945). Their function, while quite accurate ($\sim$ 0.001%), involves a large number of constants and contains highly non-linear terms. An approximate expression for $P_s(T)$ in mb, applicable to a limited temperature range, is given by (Iribarne and Godson, 1973).

$$\log_{10}[P_s(T)] = -\frac{2937.4}{T_a} - 4.9283 \log_{10} T_a + 23.5518 \tag{8.30}$$

This form is sometimes called the Magnus formula and corresponds to the inclusion of second and third terms in the viral equation of state. For the purpose of this study the simple, but relatively unknown, polynomial expression of Richards (1971) was adopted. The functional form is given by:

$$P_s(T) = P_A \exp[13.3185t - 1.9760t^2 - 0.6445t^3 - 0.1299t^4] \qquad (8.31)$$

where P_A is the standard atmospheric pressure of 1013.25 mb, the parameter t is defined in terms of the ambient temperature T_a(^oK) and the steam temperature $T_s \simeq 373.15^oK$ at pressure P_a.

$$t = 1 - \frac{T_s}{T_a} \simeq 1 - \frac{373.15}{T_a} \qquad (8.32)$$

Equation (8.31) is more accurate than (8.30) and is valid to $\pm$ 0.1% over a temperature range of -50 to 140^{o}C. The variation of $P_s(T)$ over the range T_a = -50 to 40^{o}C is shown in Figure 8.19. Table 8.13 illustrates the application of the procedure to some typical atmospheric conditions.

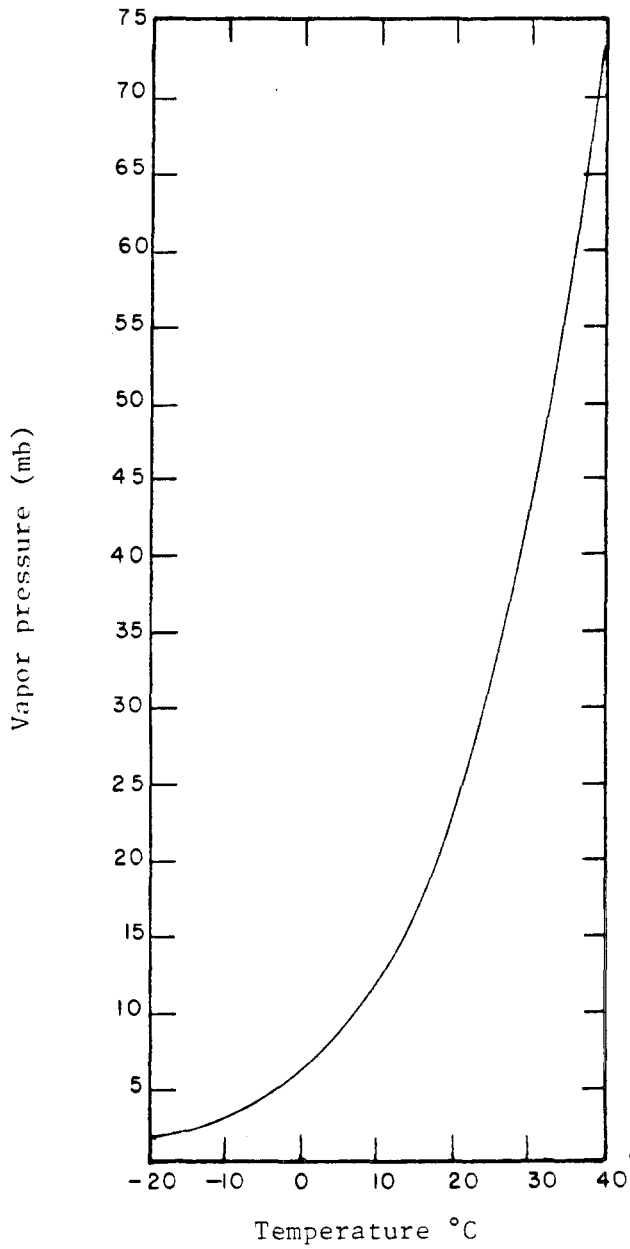

FIGURE 8.19

Saturation Vapor Pressure as a Function of Ambient Temperature Evaluated Using the Polynomial Expression of Richards (1971)

TABLE 8.13

APPLICATION OF PROCEDURE FOR CALCULATING

ATMOSPHERIC WATER VAPOR CONCENTRATION [a]

T_a (°C)	$P_s(T_a)$ (mb)	$\frac{H_2O(ppm)}{RH(\%)}$	H_2O at 50% RH (ppm)
-20	1.25	12.34	617
-15	1.91	18.85	942
-10	2.86	28.23	1411
-5	4.22	41.65	2082
0	6.11	60.30	3015
5	8.72	86.06	4303
10	12.28	121.19	6060
15	17.05	168.27	8413
20	23.39	230.84	11542
25	31.69	312.76	15638
30	42.45	418.95	20947
35	56.26	555.24	27762
40	73.80	728.35	36417
45	95.89	946.36	47318

[a] Ambient conditions assumed for calculation P_a = 1013.25 mb

Steam temperature T_S = 373.15°K.

8.8 A Simple Box Model for Testing Photochemical Reaction Mechanisms

Before a photochemical reaction scheme is used in an airshed model it is necessary to carry out a series of tests to evaluate the performance of the mechanism under a variety of conditions. A common approach is to compare the prediction of the mechanism against observational data from smog chamber experiments. While valuable, these comparisons do not adequately test the kinetics over the range of conditions likely to be encountered in the atmosphere. Specifically, few smog chamber experiments include the effects of continuous injection of source material or diurnal variations of solar radiation. This section presents the formulation of a simple box model in which the effects of different meteorological and surface removal processes can be isolated. When interpreted as a well mixed chemical reactor, the mathematical system can be used to model a wide variety of smog chamber experiments. The range of valid atmospheric applications, however, is restricted by the nature of the assumptions used in the model derivation.

The most elementary form of a box model is a well mixed, variable volume, chemical reactor. A variable volume formulation is needed in atmospheric applications because the vertical extent of pollutant dispersion is controlled by diurnal variations in the depth of the mixed layer. The effects of a capping inversion over an urban area can be best studied if the mixing height is included as an explicit variable.

In order to account for these effects consider a single cell located over a large, horizontally homogeneous, urban area (Figure 8.20).

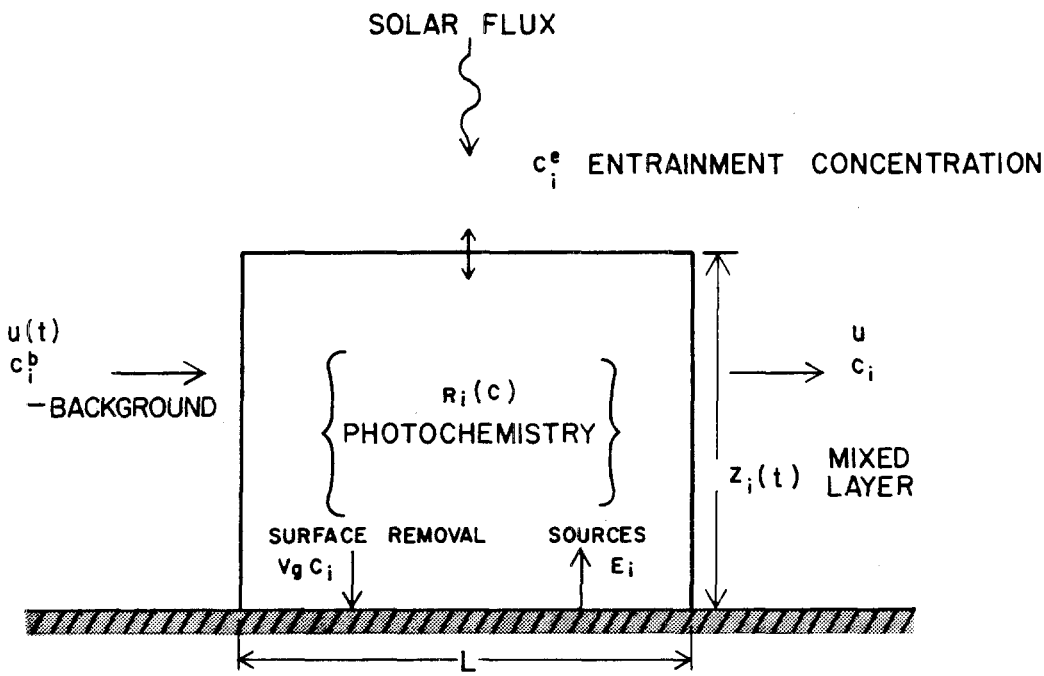

FIGURE 8.20

Schematic Representation of a Simple Box Model

The source strength per unit area for species c_i, i=1,2,...,n is represented by E_i. The box is of dimension $LWZ_i(t)$ where L is the length parallel to the spatially uniform wind field u(t). W is the box width and $Z_i(t)$ the current mixed layer depth. The ventilation cross section is WZ_i and the pollutant flux out of the box is simply $WZ_i uc_i$, where c_i is the average pollutant concentration in the well mixed box. If c_i^b is the background concentration, then the material flux into the box from outside the region is $WZ_i uc_i^b$. Generation or removal of species by chemical reaction is represented by $R_i(c_1,c_2,...,c_n)$. In the present model, surface interactions are parameterized in terms of simple deposition velocity v_g.

If pollutants, left at elevated levels from the previous day, are advected out of the box before sunrise on the current day then the mixed layer will grow into air containing ambient or background conditions. Denoting c_i^e as the concentration left above the current mixed layer, then if $c_i^e > 0$ the entrainment flux into the box is $LWc_i^e dZ_i/dt$. A collapsing mixed layer, however, does not act as an impenetrable lid. Ignoring the contribution from surface sources, the concentration within the box is not affected by the volume change. When the ventilation is weak, then c_i^e should be replaced by c_i so that the current concentration is entrained the next day. In this present study, chemical reactions amongst the species above the mixed layer are not considered.

Given the above assumptions and ignoring the effects of horizontal diffusion, the conservation equations for pollutant material within the box can be written as a set of ordinary differential equations.

$$\frac{d}{dt}(LWZ_i c_i) = LWZ_i R_i(c) + LWE_i + WZ_i u(c_i^b - c_i) + LW\frac{\partial Z_i}{\partial t} c_i^e - LWv_g c_i \qquad (8.33)$$

$$i=1,2,\ldots,n$$

Dividing through by the box volume and taking into account the temporal variations in Z_i, (8.33) can be written in the form

$$\frac{dc}{dt} = R(c) + \frac{E}{Z_i} + \frac{u}{L}(c^b - c) + \frac{(c^e - c)}{Z_i}\frac{dZ_i}{dt} - \frac{v_g c}{Z_i} \qquad (8.34)$$

where the species index i has been dropped for convenience. For numerical solution purposes it is convenient to have the Jacobian of (8.34) which is given by (8.35) where [I] is the identity matrix.

$$J = \frac{\partial}{\partial c}\left(\frac{dc}{dt}\right) = \frac{\partial R(c)}{\partial c} - \frac{u}{L}[I] - \frac{1}{Z_i}\frac{dZ_i}{dt}[I] - \frac{v_g}{Z_i}[I] \qquad (8.35)$$

In the above expression the terms involving dZ_i/dt are set to zero if $dZ_i/dt < 0$. The form (8.35) is quite similar to the expression originally proposed by Lettau (1970). The principal differences are: the parameterization of the turbulent flux caused by entrainment, the chemical reactions and surface deposition terms. If the box moves with mean wind then (8.35) represents a one-dimensional trajectory model.

In view of the simplicity of the model, it is worthwhile to reiterate the basic assumptions used in its formulation. The most critical simplification is that the pollutants are well mixed up to the

capping inversion. Unless the characteristic turbulent mixing time is fast in comparison to the chemical reaction rates, then the box model is not representative of atmospheric conditions.

8.9 Numerical Solution Procedures

The algebraic forms of the ordinary differential equations which describe the kinetics of the mechanism shown in Table 8.1 are presented in Appendix A. This system, subject to the appropriate rate constants and initial conditions, was solved with the variable step, variable order, backward difference scheme of Hindmarsh and Byrne (1975). This method was chosen because it represents one of the best general purpose approaches to numerical integration of stiff ordinary differential equations. Selection of a method that was both robust and highly accurate was important because in a number of cases the numerical results of this appendix were used as standards for comparative evaluation of solution schemes described in Chapter 11.

Except for cases in which steady state approximations were used, the kinetics of each species were described by differential equations. Because of their high concentration, constant values were assigned to oxygen (2.1×10^5 ppmV) and the third body M(1.0×10^6 ppmV) which appears in the ozone formation step. In each case the starting and maximum step sizes were set to 10^{-5} and 10 minutes, respectively. Semi-relative error control, with a convergence tolerance of $\varepsilon = 0.0001$, was selected because some species have an initial concentration of zero. From a

practical point of view there is little to be gained by using smaller values of ε. In fact, setting ε to be less than 10^{-4} in most cases gave no useful additional information and at the same time drastically increased the consumption of computer time.

8.10 Smog Chamber Experiments

A direct way of evaluating photochemical reaction mechanisms is to compare the predictions against carefully controlled laboratory studies. Falls and Seinfeld (1978), for example, tested their model against smog chamber experiments conducted at the Statewide Air Pollution Research Center (SAPRAC) of the University of California at Riverside. Extensive documentation of the experimental protocols, sampling procedures and measurement techniques used at that research center are given in Pitts et al. (1976), Pitts and Winer (1978) and Winer et al. (1980). The initial evaluation of the airshed mechanism employed propylene and n-butane as well as different combinations of the two compounds. Further experiments have been carried out using hydrocarbon mixtures which more closely correspond to atmospheric conditions. A representative sample of these results is presented in this section.

The initial conditions for one smog chamber experiment, SUR-119J (Pitts et al., 1976), are reproduced in Table 8.14. This information together with the photolysis and lumped hydrocarbon rate constants from Tables 8.8 and 8.12 is sufficient to enable an independent duplication of the mechanism performance. Table 8.15 and Figures 8.21 - 8.27

TABLE 8.14

Initial Conditions for Smog Chamber Experiment SUR-119J

SPECIES	CONCENTRATION (ppmv)
NO	0.301
NO_2	0.041
HNO_2	0.012
CO	7.45
HCHO	0.038
RCHO	0.023
ALK	0.358
OLE	0.039
C_2H_4	0.043
ARO	0.07
H_2O	15500.0
O_2	210000.0
M	1000000.0
Total Nitrogen	0.354
RHC(ppmV)	0.548
NO_x/RHC (ppmv/ppmV)	0.642
Relative Humidity (%)	58.5-53.0
Temperature (°C)	30.5-33.1

TABLE 8.15

Initial Conditions for Smog Chamber Experiments

Experiment[a]	Initial Conditions (ppmV)									
	NO	NO_2	OLE	ALK	ARO	ETH	HCHO	RCHO	HONO[b]	k_1 (min^{-1})
119J	0.301	0.041	0.039	0.358	0.070	0.043	0.038	0.023	0.0	0.32
121J	0.044	0.012	0.040	0.370	0.066	0.042	0.06	0.011	0.0	0.32
126J	0.302	0.040	0.039	0.372	0.075	0.046	0.043	0.007	0.0	0.32
132J	0.144	0.018	0.024	0.224	0.045	0.029	--	0.014	0.012	0.32
133J	0.084	0.013	0.023	0.227	0.046	0.032	0.005	0.011	0.012	0.32
134J	0.030	0.008	0.041	0.368	0.067	0.043	0.031	0.013	0.0	0.32
EC-237[c]	0.377	0.106	0.15	1.488	0.177	0.875	0.0	0.0012	0.08	0.30

a Pitts et al. (1976)

b Assumed (see Text)

c Evacuable chamber O_3 wall loss rate = 2.3×10^{-3} min^{-1}, dilution 2.9×10^{-4} min^{-1} (Pitts and Winer, 1978).

document these results as well as a number of other experiments. The model predictions closely match most of the observed data.

There is some evidence that nitrous acid is formed during the loading of smog chambers (Chan et al., 1976). Nitrous acid is produced in the dark by the reactions

$$NO + NO_2 + H_2O \underset{k_r}{\overset{k_f}{\rightleftharpoons}} 2HONO$$

and an equilibrium can be reached given sufficient time. The concentration of nitrous acid achieved in the dark is governed by

$$\frac{d[HONO]}{dt} = 2k_f [NO][NO_2][H_2O] - 2k_r [HONO]^2 \qquad (8.36)$$

Solution of this rate equation subject to $[HONO]_o = 0$ yields the concentration of nitrous acid as a function of time. As $t \to \infty$, the equilibrium concentration,

$$[HONO]_{eq} = \left[\frac{k_f [NO][NO_2][H_2O]}{k_r}\right]^{1/2} \qquad (8.37)$$

is reached. Assuming that $[NO]$, $[NO_2]$ and $[H_2O]$ are constant, (8.36) can be integrated to yield

$$\frac{[HONO]}{[HONO]_{eq}} = \tan\left\{2t\sqrt{k_f k_r [NO][NO_2][H_2O]}\right\} \qquad (8.38)$$

Table 8.16 shows the approach of HONO to the equilibrium value as a function of time for representative values of the rate of reaction. The quantity of nitrous acid that forms in a chamber or atmosphere prior

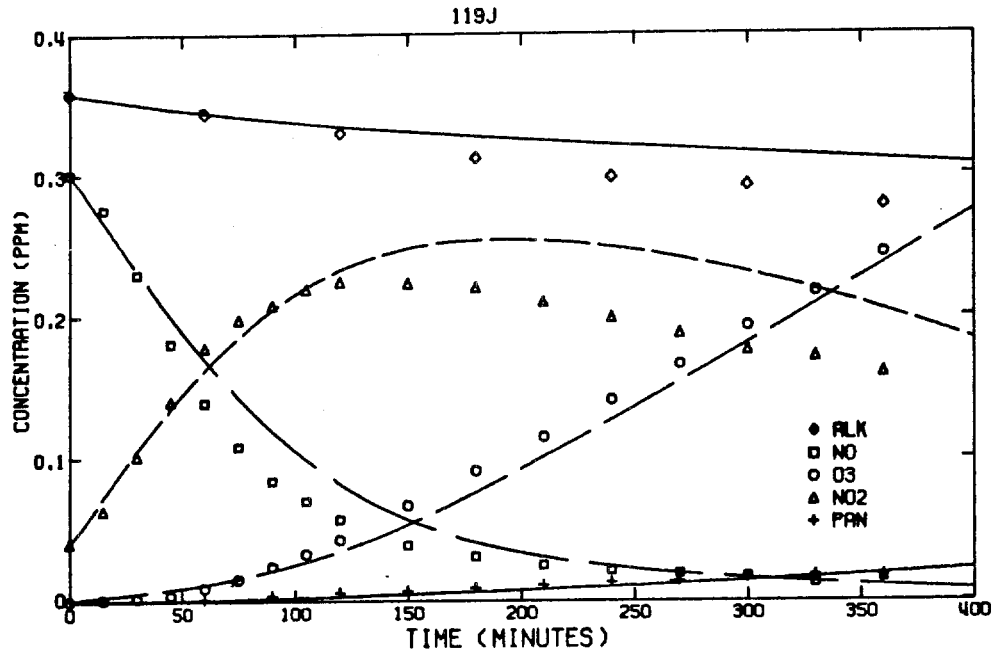

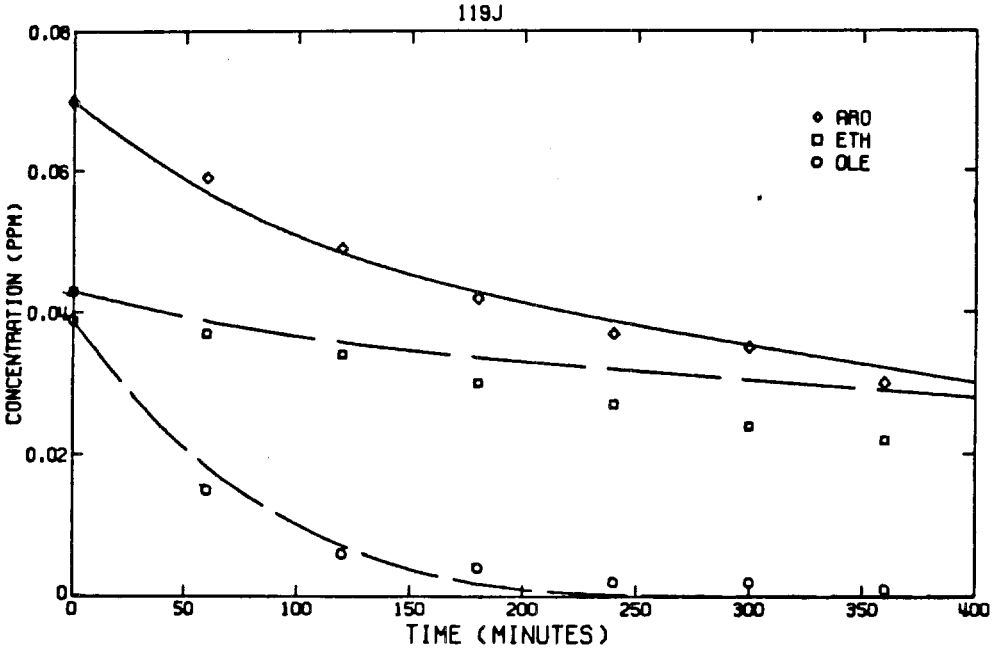

FIGURE 8.21

Predicted and Observed Concentration Profiles for Smog Chamber Experiment 119J

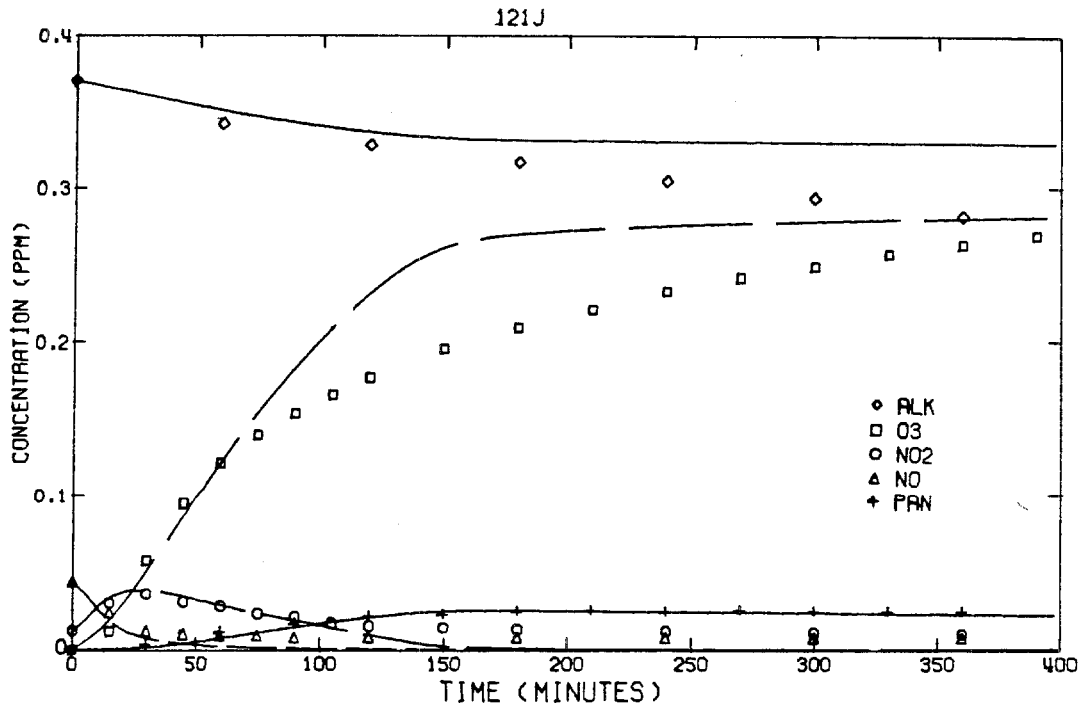

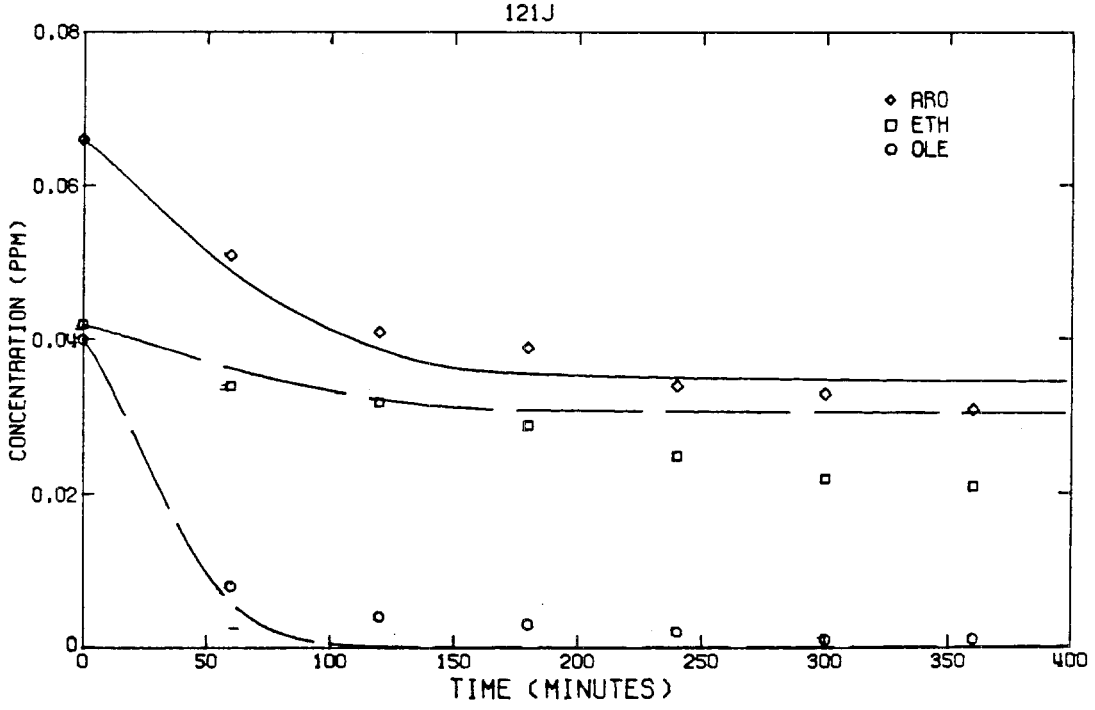

FIGURE 8.22

Predicted and Observed Concentration Profiles for Smog Chamber Experiment 121J

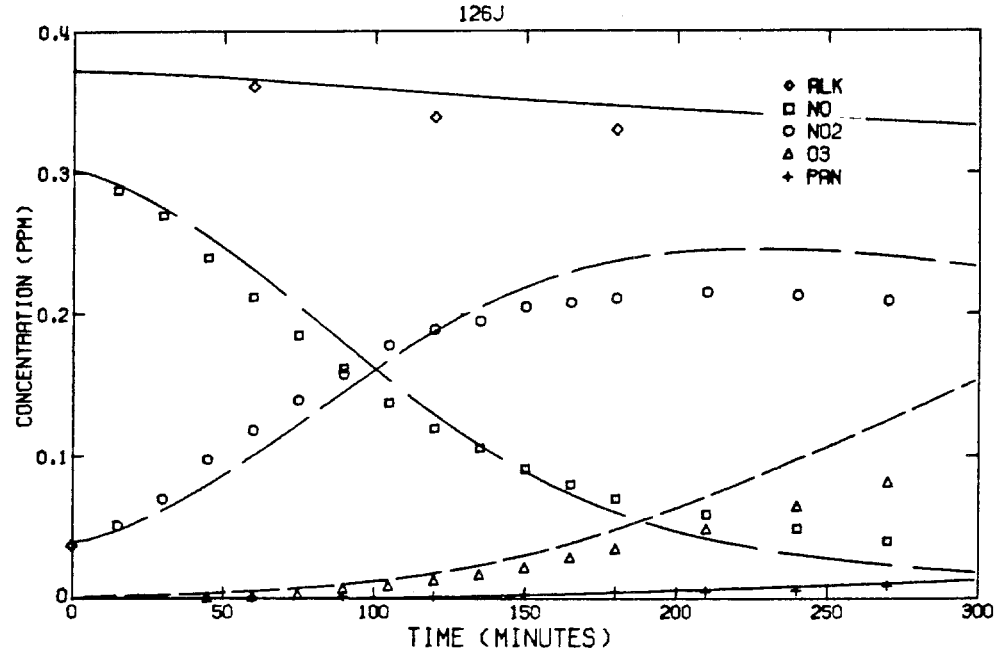

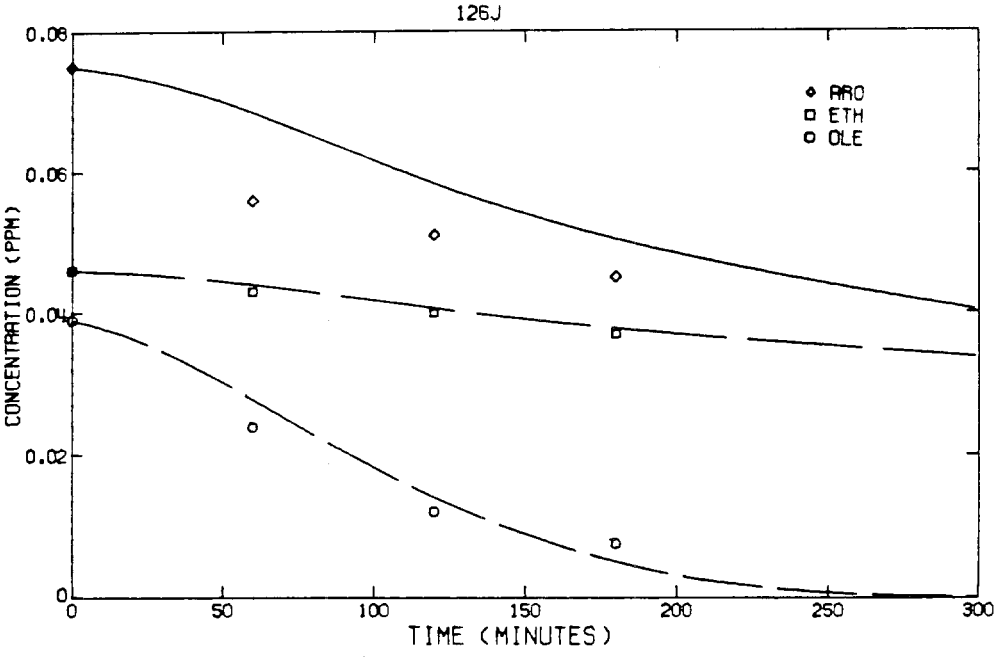

FIGURE 8.23

Predicted and Observed Concentration Profiles for Smog Chamber Experiment 126J

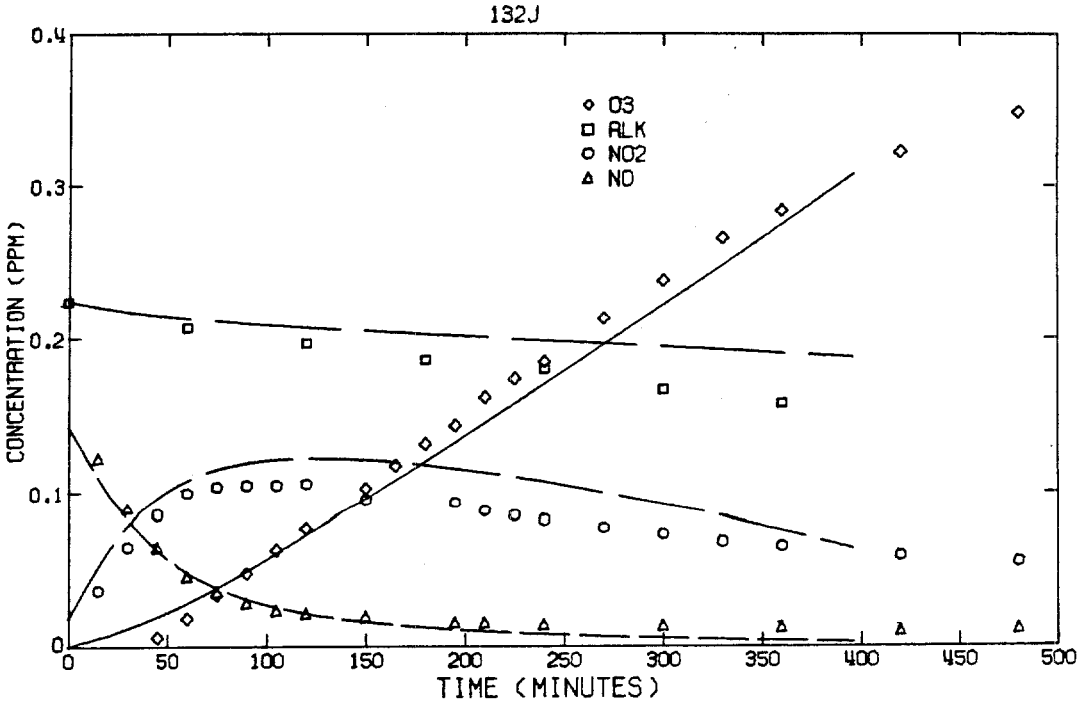

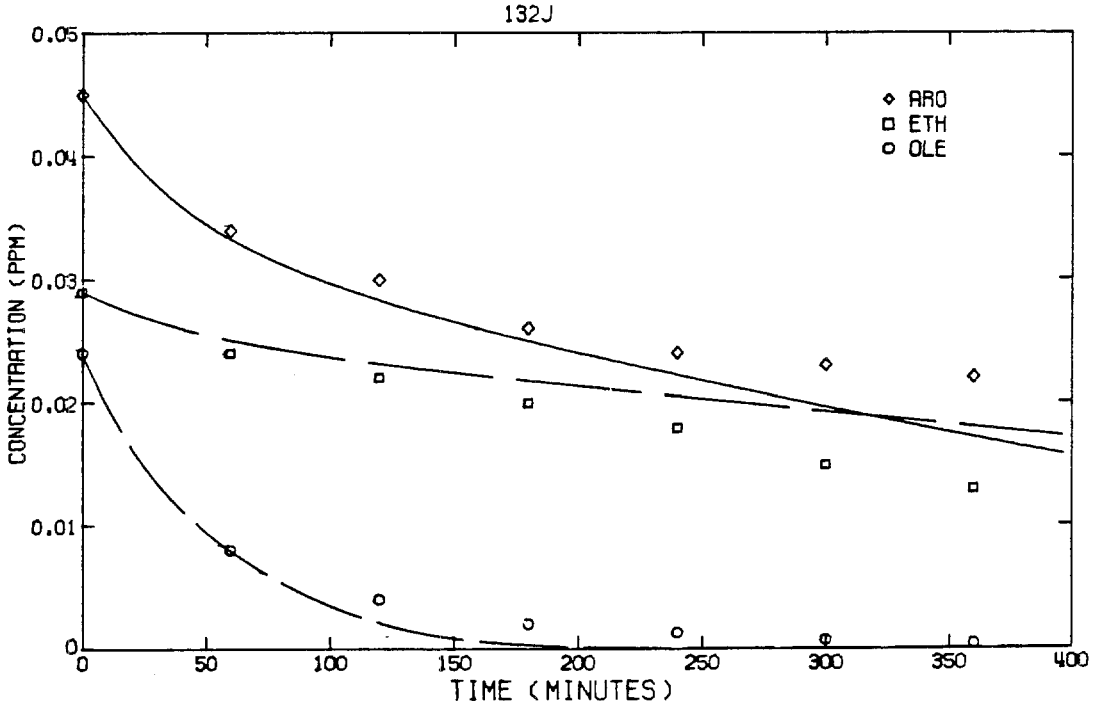

FIGURE 8.24

Predicted and Observed Concentration Profiles for Smog Chamber Experiment 132J

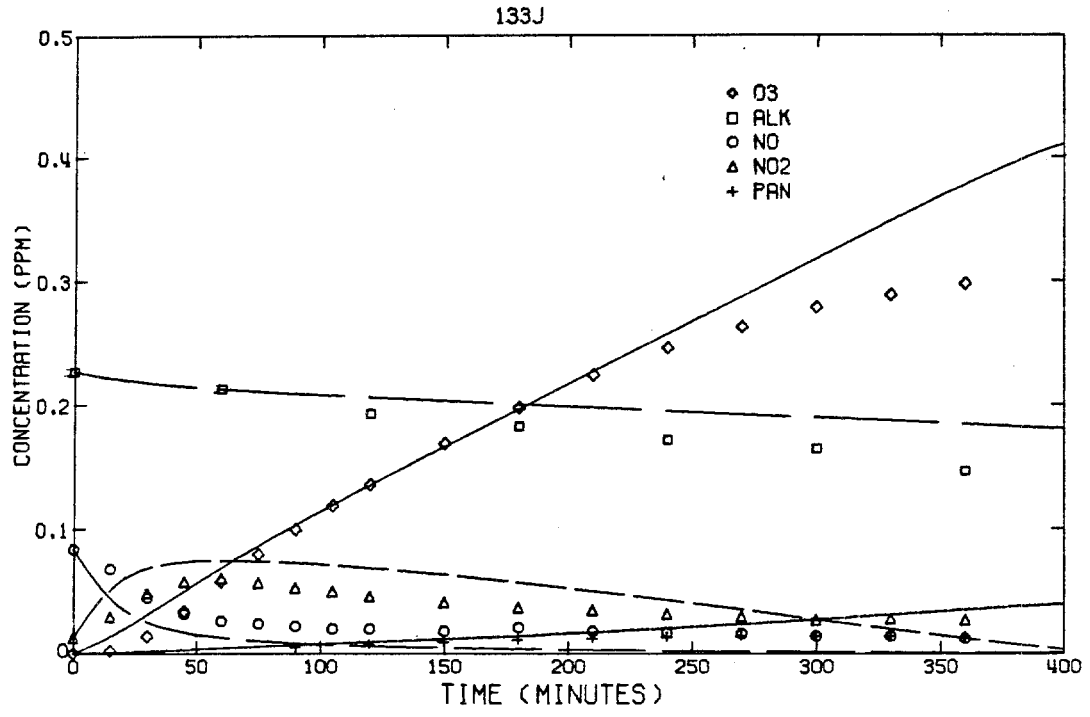

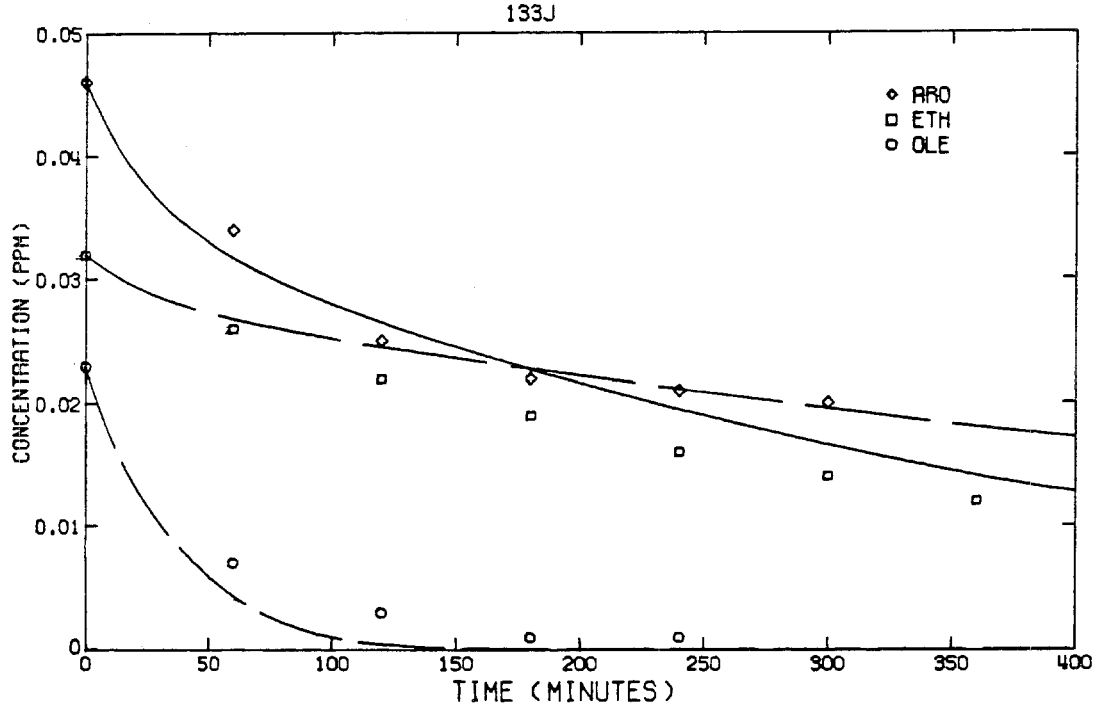

FIGURE 8.25

Predicted and Observed Concentration Profiles for Smog Chamber Experiment 133J

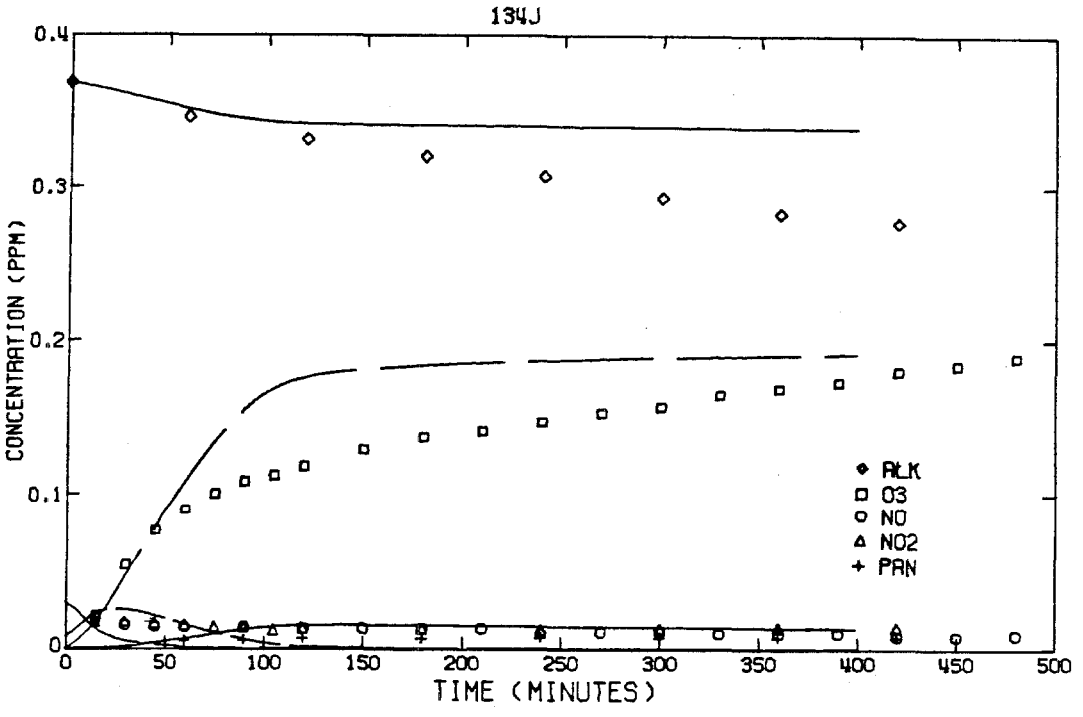

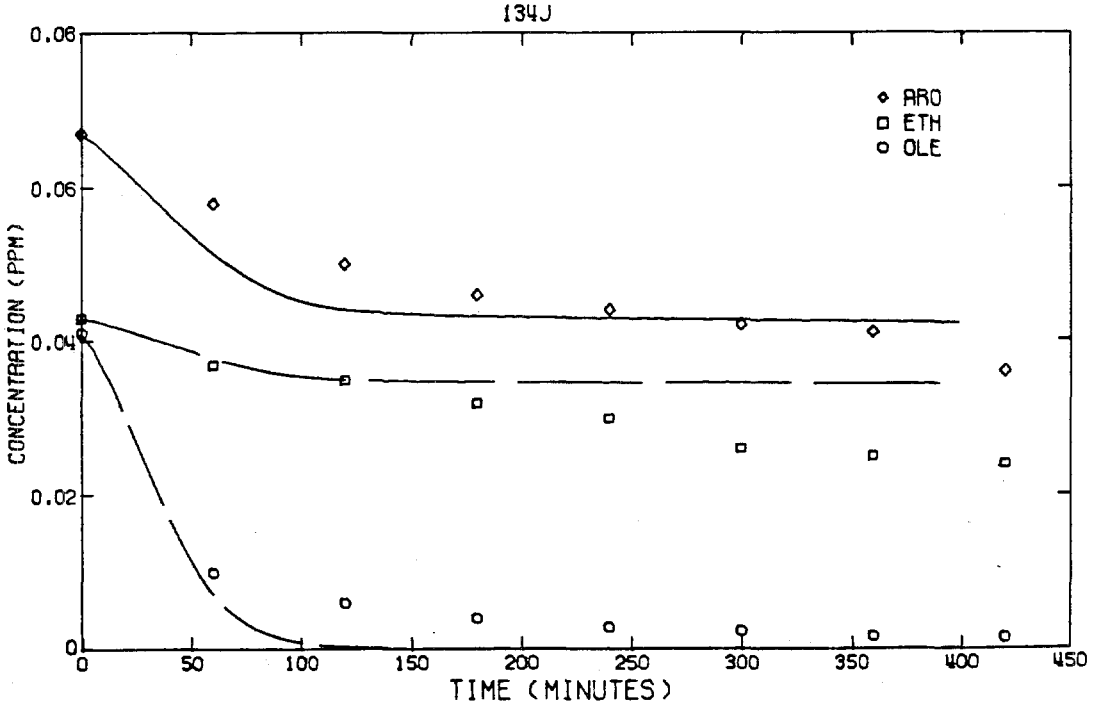

FIGURE 8.26

Predicted and Observed Concentration Profiles for Smog Chamber Experiment 134J

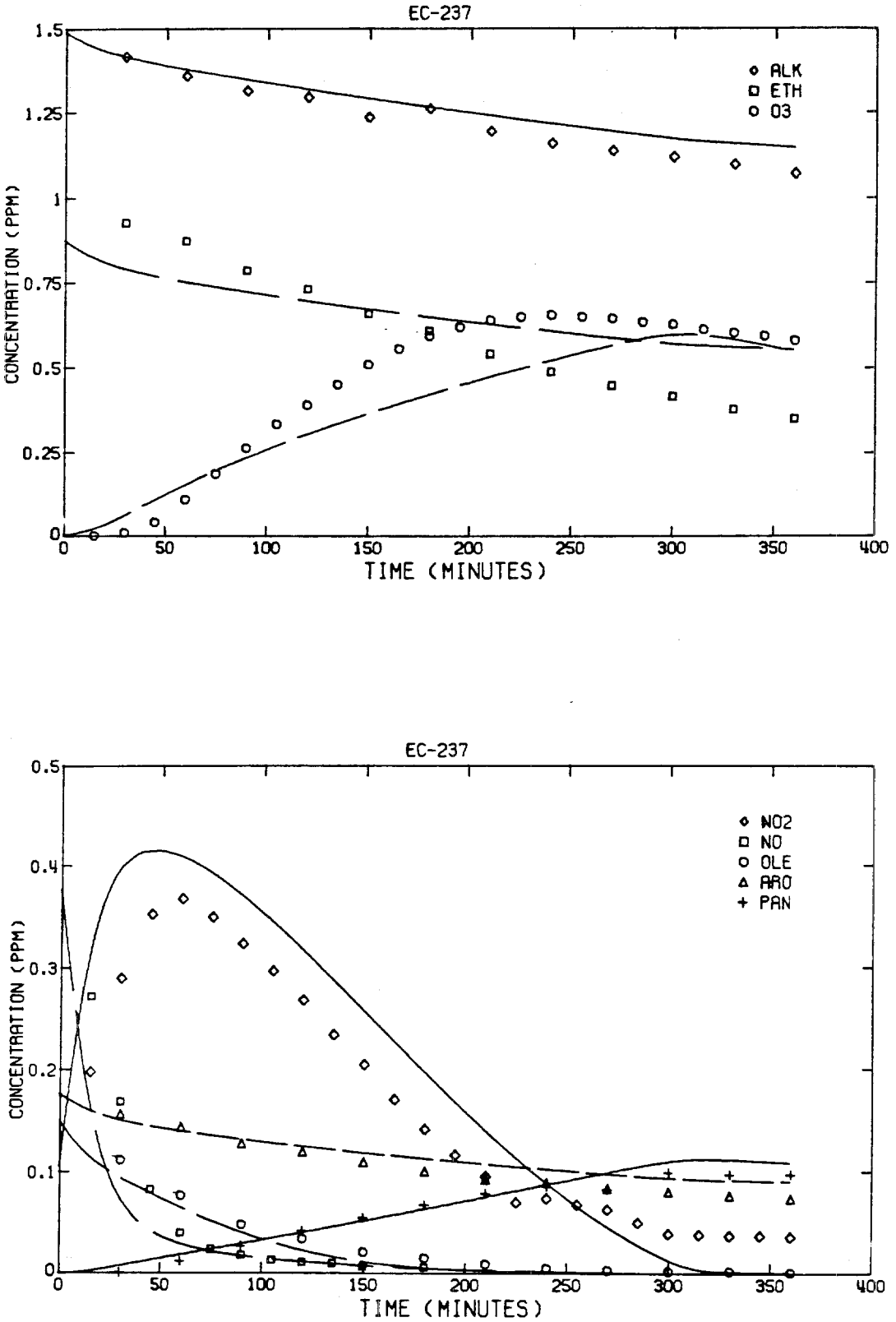

FIGURE 8.27

Predicted and Observed Concentration Profiles for Smog Chamber Experiment EC-237

to irradiation can be estimated from equation (8.36). In their simulation of the SAPRC experiments, Whitten and Hogo (1976) found that about one-third of the equilibrium concentration of nitrous acid was required as an initial concentration. The results in Table 8.16, however, indicate that the time required to reach a substantial fraction of the equilibrium concentration is long compared to that characteristic of the loading and initial mixing in a smog chamber. The predicted values shown in Table 8.16 and 8.17 are also consistent with the recent atmospheric measurements of Platt et al. (1980). In some of the smog chamber experiments increasing the initial HONO concentration tends to decrease the time at which the NO_2 maximum occurs but does not influence the maximum concentration of NO_2 or O_3. In atmospheric simulations it is usually unnecessary to assume an initial concentration of HONO since there is normally sufficient aldehydes present at sunrise to provide an initial radical flux.

TABLE 8.16

Approach to the Equilibrium Nitrous Acid (HONO) Concentration[a]

Case 1	Case 2	Case 3[b]
(NO) = 0.1	(NO) = 1	(NO) = 0.301
(NO_2) = 0.1	(NO_2) = 1	(NO_2) = 0.041
(H_2O) = 10000	(H_2O) = 10000	(H_2O) = 15000
(HONO)eq = 0.0125	(HONO)eq = 0.125	(HONO)eq = 0.0171

Time (min)	Case 1	Case 2	Case 3
100	0.00004	0.0044	0.00008
300	0.00013	0.0132	0.00024
1000	0.00044	0.0423	0.00082
10000	0.00423	0.125	0.00758

(a) $NO+NO_2+H_2O \underset{k_r}{\overset{k_f}{\rightleftarrows}} 2HONO$ $\quad k_f = 2.2\times10^{-9}$ ppm^{-2}min^{-1}, $k_r = 1.4\times10^{-3}$ ppm^{-1}min^{-1}

(b) Initial conditions correspond to smog chamber experiment SUR-119J.

TABLE 8.17

Predicted Concentration of Nitrogen Containing Species for Smog Chamber Experiment SUR-119J

SPECIES	CONCENTRATION (ppm)					
	0(min)	60(min)	120(min)	180(min)	240(min)	300(min)
NO_2	$4.1x10^{-2}$	$1.6x10^{-1}$	$2.3x10^{-1}$	$2.5x10^{-1}$	$2.5x10^{-1}$	$2.3x10^{-1}$
HNO_4	0	$2.2x10^{-5}$	$4.6x10^{-5}$	$8.4x10^{-5}$	$1.3x10^{-4}$	$1.8x10^{-4}$
NO	$3.01x10^{-1}$	$1.7x10^{-1}$	$8.7x10^{-2}$	$4.4x10^{-2}$	$2.6x10^{-2}$	$1.6x10^{-2}$
HNO_2	$1.2x10^{-2}$	$6.9x10^{-3}$	$2.8x10^{-3}$	$1.1x10^{-3}$	$5.4x10^{-4}$	$3.3x10^{-4}$
PAN	0	$8.8x10^{-4}$	$3.1x10^{-3}$	$6.2x10^{-3}$	$1.0x10^{-2}$	$1.4x10^{-2}$
RONO	0	$1.0x10^{-3}$	$8.0x10^{-4}$	$4.6x10^{-4}$	$2.5x10^{-4}$	$1.3x10^{-4}$
NO_3	0	$2.3x10^{-8}$	$1.7x10^{-7}$	$7.8x10^{-7}$	$2.2x10^{-6}$	$4.6x10^{-6}$
RNO_4	0	$6.6x10^{-4}$	$1.4x10^{-3}$	$2.4x10^{-3}$	$3.6x10^{-3}$	$4.9x10^{-3}$
$2N_2O_5$	0	$2.3x10^{-6}$	$2.4x10^{-5}$	$1.2x10^{-4}$	$3.4x10^{-4}$	$6.6x10^{-4}$
RNO_3	0	$2.4x10^{-4}$	$5.7x10^{-4}$	$8.9x10^{-4}$	$1.2x10^{-3}$	$1.4x10^{-3}$
HNO_3	0	$1.2x10^{-2}$	$2.8x10^{-2}$	$4.5x10^{-2}$	$6.2x10^{-2}$	$8.0x10^{-2}$
M [Nitrogen Balance]	0.3540	0.3539	0.3539	0.3539	0.3539	0.3539

8.11 Species Conservation Constraints

If a physical system satisfies one or more conservation laws, then a computational scheme which preserves the same constraint should be used to eliminate at least one source of potential numerical error. The use of numerical methods which do not preserve linear conservation laws can often lead to highly inaccurate solutions. For an initial value problem the basic constraint on conservation of mass can be expressed in the form

$$W^T C = M \tag{8.39}$$

or

$$W^T \frac{dC}{dt} = 0 \tag{8.40}$$

where $W = [w_1, w_2, \ldots, w_n]^T$ is a vector of weights associated with each of the species, $C = [c_1, c_2, \ldots c_n]^T$ and M is a constant depending on the initial conditions. Constraints can be applied to the total mass within the system or to individual atomic components. In the airshed mechanism the presence of lumped reaction steps, unfortunately, precludes the use of total mass balance checks. The conservation constraint does however apply to atomic species such as nitrogen. For the mechanism shown in Table 8.1, M is given by

$$M = NO + NO_2 + NO_3 + HNO_2 + HNO_3 + HNO_4 + RNO_2 + RNO_3 + RNO_4 + 2N_2O_5 + PAN \tag{8.41}$$

The numerical method developed by Hindmarsh and Byrne (1975) and used in this chapter employs a variable step, variable order, backward

difference, multistep method of the form

$$\sum_{j=0}^{k} \alpha_{k-j}^{m} \, c^{m-j} = h_m \sum_{j=0}^{k} \beta_{k-j}^{m} \, \frac{dc}{dt}^{m-j} \qquad (8.42)$$

where $h_m = t_m - t_{m-1}$ is the step size for the mth step, $\{\alpha\}$ and $\{\beta\}$ are the coefficients for the mth step in the variable step method.

Rosenbaum (1977) has shown that such methods are conservative so that, M, defined by (8.41) should be constant. This is indeed the case as shown in Table 8.17 and Figure 8.19. While the use of linear constraints to check on numerical accuracy is often very useful, it is important to be aware of the limitations. In general, while a constant value for M implies that the roundoff errors are small, it gives little information about the magnitude of the truncation errors. Stated another way, it is possible to devise extremely poor numerical solution schemes that conserve mass.

8.12 Steady State Approximations for Ozone

The three principal reaction steps involved in the $NO\text{-}NO_2\text{-}O_3$ photolytic cycle are given by:

$$NO_2 + h\nu \xrightarrow{1} NO + O(^3\underline{P}) \quad ; k_1 \simeq 0.3 \text{ min}^{-1} \qquad (8.43)$$

$$O(^3\underline{P}) + O_2 + M \xrightarrow{2} O_3 + M \quad ; k_2 = 2\text{x}10^{-5} \text{ ppm}^{-2}\text{-min}^{-1} \qquad (8.44)$$

$$O_3 + NO \xrightarrow{3} NO_2 + O_2 \quad ; k_3 = 25.8 \text{ ppm}^{-1}\text{-min}^{-1} \qquad (8.45)$$

Under most conditions these three reactions proceed at a rate nearly two orders of magnitude faster than the kinetics of any of the other steps involving ozone. A sample calculation of the forward reaction

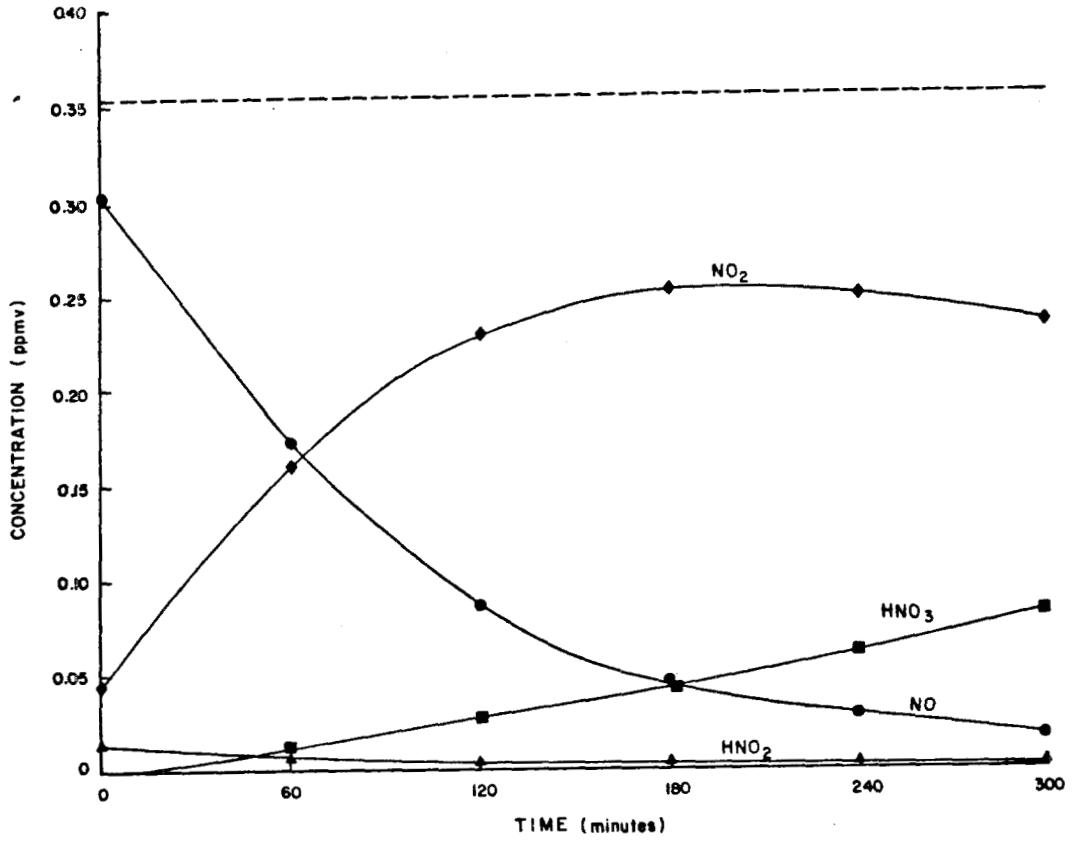

FIGURE 8.28

Concentration Profiles of Major Nitrogen Containing Species for Smog Chamber Experiment 119J

rates is shown in Table 8.18. The main oxidizing reaction (8.45), for typical atmospheric concentrations, has a half life of approximately 30 seconds. Under these conditions many investigators have made the assumption that the ozone production and decay rates are in equilibrium and derived the photostationary state approximation (PSSA)

$$\frac{k_1(NO_2)}{k_3(NO)(O_3)} = 1 \qquad (8.46)$$

Since there is a recurring debate in the literature about the validity of the simple expression (8.46) this section presents a brief evaluation of its validity for smog chamber simulations.

Eschenroeder et al. (1972) and Calvert (1976) have examined experimental data collected in Los Angeles and concluded that time-averaged atmospheric measurements often do not obey the photostationary state approximation. Stedman and Jackson (1975) tested the hypothesis that $k_1(NO_2)/k_3(NO)(O_3)=1$ in a set of carefully controlled measurements of ambient air quality. Using 400 data sets they found that the left-hand side was equal to 1.01 with a standard deviation of 0.2 and a standard error of the mean equal to 0.01. A variety of different explanations have been offered to explain the discrepancies. Eschenroeder et al. (1972), Seinfeld (1977) and Bilger (1977) postulated that inhomogeneities in atmospheric concentrations of NO and O_3 could reduce the effective reaction rates of the system (8.43-8.45). The basic problem is that when using time-averaged data in the photo stationary state equation the product of average concentrations is not equal to the average of the products. In general,

TABLE 8.18

Forward Reaction Rates for Smog Chamber Experiment SUR-119J[a]

Mechanism Component	Reaction Rate (ppm/min) t = 60 min	t = 300 min
dO_3/dt	3.070×10^{-4}	8.732×10^{-4}
$R_2=k_2(O)(O_2)(M)$	5.43×10^{-2}	6.78×10^{-2}
$R_3=k_3(NO)(O_3)$	5.36×10^{-2}	6.02×10^{-2}
$R_7=k_7(NO_2)(O_3)$	1.24×10^{-4}	2.12×10^{-3}
$R_{20}=k_{20}(O_3)$	3.14×10^{-4}	4.61×10^{-3}
$R_{30}=k_{30}(OLE)(O_3)$	3.77×10^{-5}	2.63×10^{-6}
$R_{47}=k_{47}(OH)(O_3)$	1.34×10^{-7}	1.03×10^{-6}
$R_{48}=k_{48}(HO_2)(O_3)$	1.67×10^{-8}	1.63×10^{-6}
$R_1=k_1(NO_2)$	5.41×10^{-2}	6.33×10^{-2}
(a) O_3	0.01364	0.2005
NO	0.1541	0.01178
NO_2	0.1690	0.1978
NO_2/NO	1.096	16.79

unless the atmosphere is well mixed or the averaging times are sufficiently short

$$\frac{k_1(\overline{NO_2})}{k_3(\overline{NO})(\overline{O_3})} \neq \frac{k_1}{k_3}\left[\frac{\overline{(NO_2)}}{(NO)(O_3)}\right] \tag{8.47}$$

The basic problem with testing this explanation is that it is extremely difficult to perform the necessary experiments. Confirmation requires very accurate and rapid determinations of k_1, temperature, (NO), (NO_2) and (O_3).

Part of the variation can be readily explained by considering the kinetics of ozone formation. In the airshed model the balance between ozone formation and decay rates is given by

$$\frac{dO_3}{dt} = R_2 - R_3 - R_7 - R_{20} - R_{30} - R_{47} - R_{48} - R_{49} \tag{8.48}$$

where

$$\begin{aligned}
R_2 &= k_2(O)(O_2)(M) \\
R_3 &= k_3(NO)(O_3) \\
R_7 &= k_7(NO_2)(O_3) \\
R_{20} &= k_{20}(O_3) \\
R_{30} &= k_{30}(OLE)(O_3) \\
R_{47} &= k_{47}(OH)(O_3) \\
R_{48} &= k_{48}(HO_2)(O_3) \\
R_{49} &= k_{49}(O_3)
\end{aligned} \tag{8.49}$$

So that the correct expression for the quasi steady state approximation (QSSA) is given by

$$\frac{k_2(O)(O_2)(M)}{[k_3(NO)+k_7(NO_2)+k_{20}+k_{30}(OLE)+k_{47}(OH)+k_{48}(HO_2)+k_{49}](O_3)} = 1 \qquad (8.50)$$

Both (8.46) and (8.50) were tested using the concentrations predicted in a numerical solution of the smog chamber experiment SUR-119J (Pitts et al., 1976). At the end of a 400 minute simulation the error in the photo stationary state (PSSA) was approximately 5% whereas (8.50) was correct to within 1%. As shown in Table 8.18, early in the run, the ozone kinetics is dominated by the photolytic cycle (8.43-8.45) and as a result both (8.46) and (8.50) are of comparable accuracy. Later in the solution, when $NO_2 >> NO$, the contributions from the terms R_7 and R_{20} become more apparent. These results indicate that in atmospheric applications there could be significant departures from the photo stationary state simply as a result of the chemistry. Future field measurements should be directed at separating the influences of turbulent inhomogeneities and chemistry when evaluating the validity of steady state approximations.

8.13 Conclusions

In this chapter the basic airshed mechanism has been presented together with sufficient information regarding initial conditions, rate constants and stoichiometry to allow an independent duplication of its performance. The mechanism incorporates recent information on rate

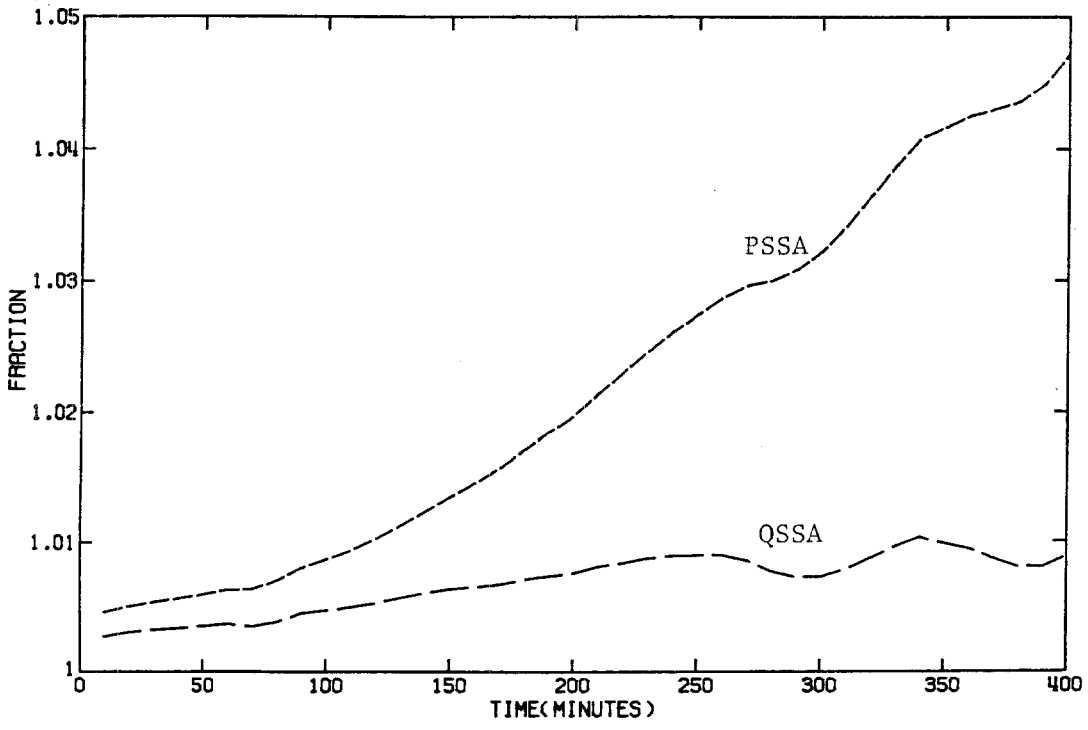

FIGURE 8.29

Errors in the Photo Stationary State (PSSA) and Quasi Stationary State (QSSA) Approximations for Ozone in Smog Chamber Experiment SUR-119J

constants, mechanistic structure and, in addition, has been successfully validated against a wide range of smog chamber experiments. Further discussion of the sensitivity of model predictions to changes in the various inputs is given in Chapter 12.

Note: Subsequent to the publication of the kinetic mechanisms in Falls and Seinfeld (1978) and McRae et al. (1981) a number of modifications were made to some of the reaction rate constants. These changes are documented in Tables 8.3, 8.8 and 8.12 and were made to reflect more recent determinations of the basic kinetic data. In section 8.10 Figures 8.21 and 8.27 show a comparison between observed and predicted concentration profiles for the two sets of rate constants.

CHAPTER 9

NUMERICAL SOLUTION OF THE ATMOSPHERIC DIFFUSION EQUATION FOR CHEMICALLY REACTING FLOWS

(Reprinted from J. Computational Physics, 45, 1-42)

Reprinted from JOURNAL OF COMPUTATIONAL PHYSICS
All Rights Reserved by Academic Press, New York and London

Vol. 45, No. 1, January 1982
Printed in Belgium

Review Article

Numerical Solution of the Atmospheric Diffusion Equation for Chemically Reacting Flows

GREGORY J. MCRAE, WILLIAM R. GOODIN,* AND JOHN H. SEINFELD†

Environmental Quality Laboratory, California Institute of Technology, Pasadena, California 91125

Received May 15, 1981

A comprehensive study of numerical techniques for solving the atmospheric diffusion equation is reported. Operator splitting methods are examined in which the three-dimensional problem is converted into a sequence of one-dimensional problems. A Galerkin, linear finite element scheme with a nonlinear filter is found to be computationally superior to the other methods tested for the advection–diffusion components. The chemical reaction dynamics component, treated within the splitting scheme, is generally highly stiff. A second-order predictor, iterated corrector technique, in combination with an asymptotic treatment of the stiff components, is found to be computationally superior for the chemical kinetics. The validity of the pseudo steady state approximation for certain reactive species is also investigated.

1. INTRODUCTION

Many disciplines in engineering and science depend on the availability of predictive models of chemically reacting fluid flows. One area of considerable practical interest and a source of many challenging problems in numerical analysis is the construction of mathematical descriptions of the formation and transport of urban-scale air pollution. A complete treatment of atmospheric concentration dynamics and chemical interactions involves the full, three-dimensional turbulent planetary boundary layer equations for conservation of mass, momentum and energy. Unfortunately the routine solution of such a system is an enormous undertaking and not feasible on the present generation of computers since a typical calculation might involve $O(10^4)$ grid points, 20–50 chemical species and $O(10^6)$ computer storage locations. A somewhat more limited approach, and the focus of this work, is based on decoupling the mass conservation equations from the equations of motion of the air. This simplification results in a set of coupled parabolic partial differential equations that describe the combined

* *Present address*: Advanced Technology Group, Dames and Moore, 1100 Glendon Avenue, Los Angeles, CA 90024.
† Department of Chemical Engineering.

0021-9991/82/010001-42$02.00/0

influences of advection, turbulent diffusion and chemistry within a prescribed flow field. The presence of nonlinearities and the existence of widely disparate temporal and spatial scales considerably complicate the selection and implementation of suitable solution techniques. In addition the availability and utilization of computational resources are practical considerations equally as important as the requirement for numerical accuracy.

This paper begins with a general statement of the atmospheric diffusion equation and proceeds to describe the use of coordinate transformations and operator splitting techniques for numerical solution. Once the equations have been decomposed into component parts by operator splitting, specially suited procedures for the components (advection, diffusion, and chemical reaction) can be applied. We then describe the choice and testing of appropriate techniques for solving the transport or advection–diffusion components of the equation. The final element involves numerical solution of the chemical kinetics. Although the numerical techniques described in this work have been specifically developed to solve the atmospheric diffusion equation, much of the material is applicable to other problems, particularly those that involve chemically reacting fluid flows.

2. Governing Differential Equations

Consider an arbitrary, time-varying, spatial domain Ω_t located in the Euclidean space E^3 and bounded by $\partial\Omega_t$. In this region, a spatial point is denoted $\mathbf{X} = \{X, Y, Z\} \in \Omega_t$. Within Ω_t the conservation of mass for each of p chemical species $c_i(\mathbf{X}, t)$; $i = 1,..., p$, can be expressed by the following set of coupled, nonlinear, parabolic, partial differential equations,

$$\frac{\partial c_i}{\partial t} + \nabla \cdot (\mathbf{u}c_i) = \nabla \cdot (\mathbf{K} \cdot \nabla c_i) + f_i(c_1,..., c_p), \tag{1}$$

with $(\mathbf{X}, t) \in \Omega_t \times [0, T]$. For this system $\mathbf{u}$ is the prescribed advective velocity field $\mathbf{u}(\mathbf{X}, t) = (u, v, w)$, $\mathbf{K}$ is a second-order, diagonal, eddy diffusivity tensor and f_i a temperature dependent chemical formation (or depletion) rate of species i. In meteorological applications (1) is frequently called the atmospheric diffusion equation [1].

To complete the problem formulation both the initial and boundary conditions need to be specified. For the system (1) the initial conditions $c_i(\mathbf{X}, 0)$, are given by

$$c_i(\mathbf{X}, 0) = c_i^0(\mathbf{X}); \qquad i = 1,..., p; \qquad \mathbf{X} \in \Omega_0. \tag{2}$$

The measured concentration data, from which the initial conditions are normally specified, are sparse, irregularly spaced, and generally limited to ground level values. Under these conditions, a representative initial field can be obtained by interpolation using the techniques described in Goodin *et al.* [2–4]. Boundary conditions simply represent statements of mass continuity across the enclosing surface $\partial\Omega_t$. For this

system most practical cases are described by the inhomogeneous mixed Neumann and Dirichlet boundary conditions

$$a(\mathbf{X}, t)\, c_i + b(\mathbf{X}, t) \frac{\partial c_i}{\partial \sigma} = g_i(\mathbf{X}, t); \qquad (\mathbf{X}, t) \in \partial\Omega_t \times [0, T]. \tag{3}$$

In this equation σ indicates the normal direction to $\partial\Omega_t$, and the functions $a(\mathbf{X}, t)$, $b(\mathbf{X}, t)$ and $g_i(\mathbf{X}, t)$ describe particular cases, the explicit forms of which are presented in Reynolds *et al.* [5].

The difficulties that arise during numerical solution of (1)–(3) stem from the radically different character of the advection, $\nabla \cdot (\mathbf{u}c_i)$, turbulent diffusion, $\nabla \cdot (\mathbf{K} \cdot \nabla c_i)$, and chemical reaction, f_i, operators. Even though (1) is formally parabolic in most atmospheric flows, transport in the horizontal plane is dominated by advection, leading to hyperbolic like characteristics. One of the major sources of difficulty arises during numerical solution of the chemical reaction terms f_i. While complicating the numerical solution, the presence of the nonlinearities in f_i is not as much a problem as the potential for eigenvalues that span a wide range of time scales. In typical photochemical reaction mechanisms of the type described by Falls and Seinfeld [6], it is possible to encounter situations in which individual reaction times differ by $O(10^8$ seconds). That, in turn, virtually dictates an implicit solution procedure for the chemical kinetics.

3. Coordinate Transformations

In typical applications the airshed domain Ω_t is defined by three bounding surfaces; the topography $Z = h(X, Y)$, vertical sides at the horizontal extremes, and a time varying upper boundary, $Z = H(X, Y, t)$. The presence of topographic relief can considerably complicate the numerical implementation of boundary conditions of the form (3). The problem can be avoided to a certain extent by transforming the spatial domain into one of simpler geometry. This can be accomplished by a mapping $\mathbf{F}: \Omega_t \to \Omega_c$, that transforms points in the physical domain Ω_t into the more convenient computational domain Ω_c. Points in Ω_c are denoted by $\mathbf{x} = (x, y, z, t)$.

A variety of functional forms for $\mathbf{F}$ are used in practice; a common one in atmospheric modeling application is the terrain-following coordinate transformation [5, 7, 8],

$$\mathbf{x} = F(\mathbf{X}) = \begin{bmatrix} X \\ Y \\ \dfrac{Z - h(X, Y)}{H(X, Y, t) - h(X, Y)} \end{bmatrix}, \tag{4}$$

that scales the vertical extent of the modeling region into the new domain $z \in [0, 1]$. So long as the time varying upper boundary H, does not intersect the terrain defined

by h, then a unique inverse for (4) exists. The general requirement for a nonzero Jacobian usually precludes the simultaneous use of these transformations in all three coordinate directions.

Once the form of the transformation has been established, the next step is to apply it to the atmospheric diffusion equation. An important characteristic of this equation is that it represents a differential statement of the conservation of mass for each species c_i. Roache [9] indicates that, with few exceptions, the most accurate numerical results are obtained using numerical approximations that are based on the flux or conservative form of the governing equations. With this in mind, it is desirable to preserve the conservative structure of (1) during the coordinate transformation. If this is done, then it is possible to consider each computational cell as a control volume and develop difference expressions that satisfy the physical conservation laws on a macroscopic level, not at the limit of small time steps and spatial dimensions. Methods for manipulating first and second-order partial differential equations that preserve the conservative properties are described in Anderson *et al.* [10], Oberkampf [11], and Vinokur [12]. Lapidus [13], in particular, has shown that with a nonsingular space transformation, the conservative form of the governing differential equations can be maintained. Using these procedures it is possible to develop the following conservative form of the atmospheric diffusion equation,

$$\frac{\partial \Delta H c_i}{\partial t} + \nabla \cdot (\mathbf{V} \Delta H c_i) = \nabla \cdot (\Delta H \mathbf{K}_c \cdot \nabla c_i) + \Delta H f_i, \qquad (\mathbf{x}, t) \in \Omega_c \times [0, T], \quad (5)$$

where Ω_c is now the transformed domain and $\Delta H = H(x, y, t) - h(x, y)$. The components of the transformed velocity field are now $\mathbf{V} = (u, v, W)$, where the new vertical velocity W, is given by

$$W = \frac{1}{\Delta H}\left[w - u\left(\frac{\partial h}{\partial x} + z\frac{\partial \Delta H}{\partial x}\right) - v\left(\frac{\partial h}{\partial y} + z\frac{\partial \Delta H}{\partial y}\right) - z\frac{\partial \Delta H}{\partial t}\right]. \quad (6)$$

One problem arises as a result of the transformation. Initially the eddy diffusivity tensor $\mathbf{K}$ was diagonal, however, the transformed form is given by

$$\mathbf{K}_c = \begin{bmatrix} K_{xx} & 0 & -\frac{K_{xx}}{\Delta H}\left(\frac{\partial h}{\partial x} + z\frac{\partial \Delta H}{\partial x}\right) \\ 0 & K_{yy} & -\frac{K_{yy}}{\Delta H}\left(\frac{\partial h}{\partial y} + z\frac{\partial \Delta H}{\partial y}\right) \\ -\frac{K_{xx}}{\Delta H}\left(\frac{\partial h}{\partial x} + z\frac{\partial \Delta H}{\partial x}\right) & -\frac{K_{yy}}{\Delta H}\left(\frac{\partial h}{\partial y} + z\frac{\partial \Delta H}{\partial y}\right) & \frac{K_{xx}}{\Delta H^2}\left(\frac{\partial h}{\partial x} + z\frac{\partial \Delta H}{\partial x}\right)^2 + \frac{K_{yy}}{\Delta H^2}\left(\frac{\partial h}{\partial y} + z\frac{\partial \Delta H}{\partial y}\right)^2 + \frac{K_{zz}}{\Delta H^2} \end{bmatrix}. \quad (7)$$

While the presence of off-diagonal terms can complicate the numerical solution, their contribution to turbulent transport in most urban scale flows is negligible since it is possible to show, that for all but the most rugged terrain,

$$\frac{1}{\Delta H}\left[\frac{\partial h}{\partial x}+z\frac{\partial \Delta H}{\partial x}\right]\ll 1; \qquad \frac{1}{\Delta H}\left[\frac{\partial h}{\partial y}+z\frac{\partial \Delta H}{\partial y}\right]\ll 1. \tag{8}$$

4. General Approach to the Numerical Solution of the Problem

Once the equations have been transformed, the next step is to formulate an approach for obtaining numerical solutions of the model system. Although the focus of the present work is the atmospheric diffusion equation, the problem can be stated in the more general form,

$$\frac{\partial c_i}{\partial t}=L(\mathbf{x},t)\,c_i(\mathbf{x},t)+f_i(c_1,\ldots,c_p); \qquad (\mathbf{x},t)\in\Omega_c\times[0,T], \tag{9}$$

$$B(\mathbf{x},t)\,c_i(\mathbf{x},t)=g_i(\mathbf{x},t); \qquad (\mathbf{x},t)\in\partial\Omega_c\times[0,T], \tag{10}$$

$$c_i(\mathbf{x},0)=c_i^0(\mathbf{x}); \qquad (\mathbf{x})\in\Omega_0, \tag{11}$$

where L is a multi-dimensional, semi-linear, elliptic differential operator containing first and second-order derivatives, with respect to x, y, and z, but no mixed derivatives, and B is a linear operator.

While there is an extensive literature relevant to obtaining solutions of the homogeneous system there are relatively few numerical treatments of problems that involve *both* chemical reactions and transport in three dimensions. Even though much of what is available is confined to one- and two-dimensional systems, many different techniques have been applied in practice. For example, Margolis [14] used the method of lines to examine the multi-component chemical dynamics of a premixed laminar flame. Chin and Braum [15] employed a discrete analog of the invariant embedding algorithm to solve the two-point boundary value problem associated with a model of oil shale retorting. A variety of schemes were used by Engquist *et al.* [16] to predict the performance of a catalytic converter; a fourth-order dissipative leap-frog difference method for the hyperbolic components, a Dufort–Frankel procedure for the parabolic elements and Newton iteration for the remaining nonlinear equations. Douglas *et al.* [17] utilized an extrapolated Crank–Nicholson–Galerkin procedure when solving a quasilinear parabolic problem. Kansa [18] used a block implicit scheme, modified to include the basic strategies of stiff ordinary differential equation solution algorithms, to model the combustion process in an axisymmetric wick.

There are two basic steps that must be undertaken as part of most approaches to obtaining numerical solutions of systems of the form (9)–(11). One is to identify the means for approximating the spatial derivatives and the other is to select the

procedure for time integration. Spatial discretization techniques are used to convert the system of time-varying partial differential equations into a set of ordinary differential equations. In most cases this can be accomplished by using either classical finite difference or finite element techniques to produce semi-discrete systems of the form

$$\mathbf{M}\frac{d\mathbf{c}_i}{dt} + \mathbf{S}\mathbf{c}_i = \mathbf{f}_i(c_1, ..., c_p, t), \tag{12}$$

where the matrices $\mathbf{M}$ and $\mathbf{S}$ are typically large and sparse, especially for multi-dimensional problems, and $\mathbf{c}_i$ is a vector-valued function representing the concentration distribution at r points in the computational domain. If $\mathbf{M}$ is the identity matrix, as is often the case when finite difference techniques are used, then the system (12) can be solved using the method of lines. Further details of different parameterizations of the elements of $\mathbf{M}$ and $\mathbf{S}$ are discussed subsequently.

One of the major difficulties associated with a solution of (12) is that the set of equations is usually quite stiff. Consider for example, the case of $\mathbf{f} = \mathbf{f}(t)$ only and constant $\mathbf{M}$. Then the analytic solution of (12) is given by

$$\mathbf{c}_i(t) = \exp\{-\mathbf{M}^{-1}\mathbf{S}t\}\,\mathbf{c}_i(0) + \int_0^t \exp\{-(t-\tau)\,\mathbf{M}^{-1}\mathbf{S}\}\,\mathbf{S}^{-1}\mathbf{f}_i(\tau)\,d\tau. \tag{13}$$

If δ is the discretization parameter, either the computational cell size or finite element, then the condition number of $\mathbf{M}^{-1}\mathbf{S}$ is $O(\delta^{-2})$ [19, 20]. In fact, because of the unboundedness of the eigenvalue spectrum as $\delta \to 0$, increasing demands for accuracy simply exacerbate the stiffness problem. What is not often recognized is that the stiffness of the ordinary differential equations may be an artifact of the spatial discretization and, apart from the character of $\mathbf{f}$, is not a property of the governing differential equations. Because the equations are stiff this usually dictates that an implicit solution procedure must be used for the time integration. While not a major restriction for one-dimensional systems, this can create major computational and operational problems when extended to higher dimensions.

In many situations the practical aspects of implementing the computational procedures can impose another set of limitations. Often the number of previous results that can be held in fast core storage, during one solution step, constrains the choice of a time integration procedure. In addition, careful consideration must be given to the way in which arrays are indexed on computers that employ virtual memory systems otherwise the paging overheads can become very large. These issues, and the theoretical considerations discussed above, are some of the major motivations for the use of operator splitting techniques.

5. Operator Splitting and the Method of Fractional Steps

If the spatial discretization procedures are directly applied to the three-dimensional operator L, the resulting matrices, while sparse, usually cannot be economically decomposed or inverted. One way to reduce the magnitude of the computational task is to employ operator splitting and reduce the multidimensional problem to a sequence of one-dimensional equations. If this is done then successive solutions to each component part can be combined to produce a "weak" approximation to the original operator. There are a number of significant advantages to be gained from this approach. Because the matrices arising from the one-dimensional spatial discretizations are usually tridiagonal, the cost of using stable implicit procedures is small. Perhaps the most important benefit is that the numerical solution techniques can be tailored to the physical behavior of each element, a feature that is particularly attractive in applications involving chemically reacting flows. For example, Rizzi and Bailey [21] used the space-marching procedure of Rizzi and Inouye [22], in combination with operator splitting, to examine the chemical dynamics occurring in supersonic flows over complex geometric shapes. Similar approaches were adopted by Kee and Miller [23] in a study of laminar diffusion flames and by Thomas and Wilson [24] for chemically reacting turbulent jets. In each case isolating the reaction kinetics removed the numerical time step restrictions on the transport operators imposed by the chemistry.

The initial step in operator splitting is to decompose L into a sum of simpler terms

$$L = \sum_{j=1}^{3} L_j. \tag{14}$$

Although it is not strictly necessary, each L_j is usually associated with a particular coordinate direction. As an example (9) can be written in the form ($L_1 \equiv L_x$; $L_2 \equiv L_y$; $L_3 \equiv L_z$)

$$\frac{\partial c_i}{\partial t} = (L_x + L_y + L_z)\, c_i(\mathbf{x}, t) + f_i(c_1, \ldots, c_p, \mathbf{x}, t). \tag{15}$$

Once the elemental components L_j have been identified, the next step is to determine their equivalent discrete representation in the computational domain. First, the continuously varying concentration field must be approximated at the r computational points by the values $\mathbf{c}_i = (c_i(\mathbf{x}_j, t);\ j = 1, 2, \ldots, r)$. At each of the grid points, the spatial derivative L_j must be replaced by its discrete approximation. The net result is the replacement of the scalar operation, $L_j c_i$, distributed over the physical domain, by the matrix product $\mathbf{A}_j \mathbf{c}_i$. In this formulation the elements of $\mathbf{A}_j$ depend on the particular discretization scheme and its coupling of adjacent grid point values. Given the numerical equivalents of each L_j, they then must be combined in a sequence that approximates the system as a whole. There are two common ways to accomplish this; one is to use Alternating Direction Implicit (ADI) schemes and the

other employs Locally One-Dimensional (LOD) or fractional step methods. The most widely known splitting procedure is the ADI algorithm which advances the concentration field a single time step Δt from the level n to time level $n+1$ using the sequence [25–27],

$$\mathbf{c}_i^* - \mathbf{c}_i^n = \frac{\Delta t}{2}\mathbf{A}_x\mathbf{c}_i^* + \Delta t[\tfrac{1}{2}\mathbf{A}_x + \mathbf{A}_y + \mathbf{A}_z]\,\mathbf{c}_i^n + \Delta t\,\mathbf{f}_i^n, \tag{16}$$

$$\mathbf{c}_i^{**} - \mathbf{c}_i^n = \frac{\Delta t}{2}[\mathbf{A}_x\mathbf{c}_i^* + \mathbf{A}_y\mathbf{c}_i^{**}] + \Delta t[\tfrac{1}{2}(\mathbf{A}_x + \mathbf{A}_y) + \mathbf{A}_z]\,\mathbf{c}_i^n, \tag{17}$$

$$\mathbf{c}_i^{***} - \mathbf{c}_i^n = \frac{\Delta t}{2}[\mathbf{A}_x\mathbf{c}_i^* + \mathbf{A}_y\mathbf{c}_i^{**} + \mathbf{A}_z\mathbf{c}_i^{***}] + \frac{\Delta t}{2}[\mathbf{A}_x + \mathbf{A}_y + \mathbf{A}_z]\,\mathbf{c}_i^n, \tag{18}$$

where $\mathbf{c}_i^*$, $\mathbf{c}_i^{**}$ are the intermediate results and $\mathbf{c}_i^{***}$ is an $O(\Delta t^3)$ approximation to $\mathbf{c}_i^{n+1}$. An alternate, but equivalent representation, that is more suited to practical problems, especially those involving steady state applications, is to solve for the concentration increment using

$$\left[\mathbf{I} - \frac{\Delta t}{2}\mathbf{A}_x\right](\mathbf{c}_i^* - \mathbf{c}_i^n) = \Delta t[\mathbf{A}_x + \mathbf{A}_y + \mathbf{A}_z]\,\mathbf{c}_i^n + \Delta t\,\mathbf{f}_i^n, \tag{19}$$

$$\left[\mathbf{I} - \frac{\Delta t}{2}\mathbf{A}_y\right](\mathbf{c}_i^{**} - \mathbf{c}_i^n) = \mathbf{c}_i^* - \mathbf{c}_i^n, \tag{20}$$

$$\left[\mathbf{I} - \frac{\Delta t}{2}\mathbf{A}_z\right](\mathbf{c}_i^{***} - \mathbf{c}_i^n) = \mathbf{c}_i^{**} - \mathbf{c}_i^n. \tag{21}$$

By eliminating the intermediate results from (19)–(21) the ADI solution sequence can be written in the factored form [26]

$$\left[\mathbf{I} - \frac{\Delta t}{2}\mathbf{A}_x\right]\left[\mathbf{I} - \frac{\Delta t}{2}\mathbf{A}_y\right]\left[\mathbf{I} - \frac{\Delta t}{2}\mathbf{A}_z\right](\mathbf{c}_i^{n+1} - \mathbf{c}_i^n) = \Delta t[\mathbf{A}_x + \mathbf{A}_y + \mathbf{A}_z]\,\mathbf{c}_i^n + \Delta t\,\mathbf{f}_i^n. \tag{22}$$

Briley and McDonald [27] discuss the computational implementation of these techniques and in particular the use of linearization procedures for solving nonlinear partial differential equations. Apart from accuracy considerations, implicit discretization procedures usually allow arbitrarily large integration steps. When splitting techniques are used to solve transient problems, the maximum allowable time step is often constrained by the treatment of intermediate level boundary conditions. Weare [28] and Briley and McDonald [27] present analyses of the errors arising from different formulations of the boundary conditions. Unfortunately, ADI procedures are not ideally suited to solving the atmospheric diffusion equation because the coupling between the chemistry and transport in (16) imposes unreasonable time step limitations. In addition, since each term of the governing

differential equation is represented in each fractional step the memory paging overheads can become excessive.

An alternative approach is to use the method of fractional steps introduced by Yanenko [29] and described in Marchuk [30, 31] and Yanenko *et al.* [32]. Only the homogeneous Cauchy problem will be considered here. We discuss how nonlinear reactions can be included later. For the transport alone, the locally one-dimensional approximations, using Crank–Nicholson time integration, are given by

$$\mathbf{c}_i^{n+1} = \prod_{j=1}^{3} \left[\mathbf{I} - \frac{\Delta t}{2}\mathbf{A}_j\right]^{-1} \left[\mathbf{I} + \frac{\Delta t}{2}\mathbf{A}_j\right] \mathbf{c}_i^n \equiv \prod_{j=1}^{3} \mathbf{T}_j^n \mathbf{c}_i^n \equiv \mathbf{T}^n \mathbf{c}_i^n. \tag{23}$$

The principal difference between this formulation and the ADI scheme (20)–(22) is that the solution is advanced only in one coordinate direction at a time. Detailed discussions of the relationships between the two approaches are presented in Morris [33], Gourlay and Mitchell [34], Gourlay [35], and Gottlieb [36]. One important observation that can be made is that there are two sources of error in the fully discrete fractional step algorithm—the intrinsic error involved with operator splitting and the discretization errors associated with the operator approximations. In general these errors interact in a complex fashion. Crandall and Majda [37] have analyzed the stability, accuracy, and convergence of the basic fractional step algorithm when used to obtain discontinuous solutions of scalar conservation equations.

The formal order of the temporal approximation (23) can be developed by expanding the operators $\mathbf{T}_j^n$ in powers of Δt to give [31]

$$\mathbf{T}_j^n = \mathbf{I} - \Delta t\, \mathbf{A}_j^n + \frac{\Delta t^2}{2!}(\mathbf{A}_j^n)^2 - \frac{\Delta t^3}{3!}(\mathbf{A}_j^n)^3 + \cdots. \tag{24}$$

If $\mathbf{A}^n = \mathbf{A}_x^n + \mathbf{A}_y^n + \mathbf{A}_z^n$ then $\mathbf{T}^n$ is given by

$$\mathbf{T}^n = \mathbf{I} - \Delta t\, \mathbf{A}^n + \frac{\Delta t^2}{2!}\left[(\mathbf{A}^n)^2 + \sum_{\alpha=1}^{3}\sum_{\beta=\alpha+1}^{3} (\mathbf{A}_\alpha^n \mathbf{A}_\beta^n - \mathbf{A}_\beta^n \mathbf{A}_\alpha^n) + \cdots\right] + O(\Delta t^3). \tag{25}$$

Thus the split operator difference scheme will be second order accurate only if the split operators $\mathbf{A}_\alpha^n$ and $\mathbf{A}_\beta^n$ commute; otherwise, it is only of first order. To obtain second order accuracy, it is necessary to reverse the order of the operators each alternate step to cancel the two noncommuting terms. The consecutive cycles are then

$$\mathbf{c}_i^n = \prod_{j=1}^{3} \mathbf{T}_j^n \mathbf{c}_i^{n-1} \tag{26}$$

and

$$\mathbf{c}_i^{n+1} = \prod_{j=3}^{1} \mathbf{T}_j^n \mathbf{c}_i^n. \tag{27}$$

The proof of the stability of these approximations is considerably simplified using the following lemmas [31].

LEMMA 1. *Consider a positive semi-definite matrix* $\mathbf{A}$, *i.e.*, $\langle \mathbf{A}\mathbf{c}_i, \mathbf{c}_i \rangle \geqslant 0$, *on the Euclidean space, then for any value of the parameter* $\lambda \geqslant 0$,

$$\|(\mathbf{I} + \lambda\mathbf{A})^{-1}\| \leqslant 1, \tag{28}$$

where $\mathbf{I}$ *is the identity matrix and* $\|\cdot\|$ *is the appropriate norm.*

LEMMA 2. *For any positive semi-definite matrix* $\mathbf{A}$ *and* $\lambda \geqslant 0$ *then*

$$\|(\mathbf{I} - \lambda\mathbf{A})(\mathbf{I} + \lambda\mathbf{A})^{-1}\| \leqslant 1. \tag{29}$$

Using (28) *and* (29) *it is possible to show that*

$$\|\mathbf{c}_i^{n+1}\| \leqslant \|\mathbf{c}_i^{n}\| \leqslant \cdots \leqslant \|\mathbf{c}_i^{0}\|. \tag{30}$$

These results ensure absolute stability and boundness of the solution provided that the discrete operator approximation $\mathbf{A}$ *is also positive semi-definite.*

Implementation of operator splitting for the atmospheric diffusion equation (neglecting chemistry) can be accomplished by further separation of the material transport into advection $(\mathbf{T})_a$, and diffusive components $(\mathbf{T})_d$. If this is done, then a second-order accurate solution is given by

$$\mathbf{c}_i^{n+1} = (\mathbf{T}_x)_a(\mathbf{T}_x)_d(\mathbf{T}_y)_a(\mathbf{T}_y)_d(\mathbf{T}_z)_a(\mathbf{T}_z)_d(\mathbf{T}_z)_d(\mathbf{T}_z)_a(\mathbf{T}_y)_d(\mathbf{T}_y)_a(\mathbf{T}_x)_d(\mathbf{T}_x)_a\,\mathbf{c}_i^{n-1}. \tag{31}$$

Depending on the numerical scheme chosen, it is possible to combine the advection and diffusion into one transport step in each direction. For the remainder of this section and Sections 6 and 7 we focus on the atmospheric diffusion equation in the absence of chemistry to develop the solution procedure for the advection and diffusion components. Equation (31) indicates that the atmospheric diffusion equation can be decomposed, by operator splitting, into a series of simpler one-dimensional problems. Consequently, primary attention will be given to the one-dimensional transport problem (the subscript i denoting species i is dropped for convenience),

$$\frac{\partial c}{\partial t} = Lc = \frac{\partial}{\partial x}\left(K_{xx}\frac{\partial c}{\partial x} - uc\right) \tag{32}$$

and its component parts over the same domain

$$\text{Advection:} \qquad \frac{\partial c}{\partial t} = L_a c = -\frac{\partial uc}{\partial x} \tag{33}$$

and

$$\text{Diffusion:} \qquad \frac{\partial c}{\partial t} = L_d c = \frac{\partial}{\partial x}K_{xx}\frac{\partial c}{\partial x}. \tag{34}$$

The basic objective of the remainder of this work is to identify numerical solution techniques that are compatible with the characteristics of the physical problem, computationally efficient, stable, and accurate. In addition it is important, from a practical point of view, that the methods can be easily implemented and minimize core storage requirements.

6. Formulation of the Numerical Solution

A wide class of numerical approximations to the spatial derivatives in (32) can be expressed in the form $\mathbf{H}(\partial v/\partial x) = \mathbf{B}v$, where $\mathbf{v}$ is the material flux at the r computational grid points. The matrices $\mathbf{H}$ and $\mathbf{B}$ are of dimensions $r \times r$ with elements set by the particular discretization scheme. For example, the standard second-order, centered difference formula would have $\mathbf{H} = \mathbf{I}$ and $\mathbf{B}$ the tridiagonal form $[-1\ 0\ 1]$. Given the material flux

$$\mathbf{v} = \mathbf{K}_{xx}\frac{\partial \mathbf{c}}{\partial x} - \mathbf{U}\mathbf{c} \tag{35}$$

then (32) can be written as an equivalent set of first-order problems

$$\begin{aligned} \mathbf{H}\frac{\partial \mathbf{c}}{\partial x} &= \mathbf{B}\mathbf{c}, \\ \mathbf{P}\frac{\partial \mathbf{c}}{\partial t} &= \mathbf{Q}\mathbf{v}, \end{aligned} \tag{36}$$

where $\mathbf{B}$, $\mathbf{H}$, $\mathbf{P}$, $\mathbf{Q}$ are large sparse matrices resulting from the particular discretization formulation and $\mathbf{K}_{xx}$ and $\mathbf{U}$ are diagonal matrices corresponding to the turbulent diffusion coefficients and advective velocity components at each grid point. Eliminating $\mathbf{v}$ the system can be expressed in the partitioned matrix form,

$$\left(\begin{array}{c|c} \mathbf{H} & \mathbf{0} \\ \hline \mathbf{Q}\mathbf{K}_{xx} & -\mathbf{P} \end{array}\right) \left\{\begin{array}{c} \dfrac{\partial \mathbf{c}}{\partial x} \\ \hline \dfrac{\partial \mathbf{c}}{\partial t} \end{array}\right\} = \left\{\begin{array}{c} \mathbf{B}\mathbf{c} \\ \hline \mathbf{Q}\mathbf{U}\mathbf{c} \end{array}\right\}. \tag{37}$$

The relationship between this formulation and the operator splitting approach introduced in Section 5 can be seen in the explicit representations

$$\text{Advection:} \qquad \frac{\partial \mathbf{c}}{\partial t} = -\mathbf{P}^{-1}\mathbf{Q}\mathbf{U}\mathbf{c} \equiv (\mathbf{T}_x)_a\mathbf{c}, \tag{38}$$

$$\text{Diffusion:} \qquad \frac{\partial \mathbf{c}}{\partial t} = \mathbf{P}^{-1}\mathbf{Q}\mathbf{K}_{xx}\mathbf{H}^{-1}\mathbf{B}\mathbf{c} \equiv (\mathbf{T}_x)_d\mathbf{c}. \tag{39}$$

These two results can be combined to give the complete numerical approximation for $\partial \mathbf{c}/\partial t$,

$$\frac{\partial \mathbf{c}}{\partial t} = \mathbf{P}^{-1}\mathbf{Q}\{\mathbf{K}_{xx}\mathbf{H}^{-1}\mathbf{B} - \mathbf{U}\}\mathbf{c} \equiv \mathbf{T}_x\mathbf{c}. \tag{40}$$

While easy to implement, a direct solution of (40) has a number of drawbacks, the most serious of which is the need to evaluate $\mathbf{H}^{-1}$ and $\mathbf{P}^{-1}$. Normally both $\mathbf{H}$ and $\mathbf{B}$ are tridiagonal, unfortunately there is no guarantee that this property is preserved under the inverse transformation. If $\mathbf{H}^{-1}$ and $\mathbf{P}^{-1}$ are full matrices, then the operation count for evaluating the matrix products becomes quite large. The choice of whether to use a direct solution or a block tridiagonal LU decomposition depends to a large extent on the number of right-hand sides. A single evaluation of $\mathbf{T}_x$ followed by many products of the form $\mathbf{T}_x\mathbf{c}_i$, $i = 1, 2, \ldots, p$, may be more economical. The decision as to which is the more appropriate approach depends on the number of grid points, chemical species and a detailed operation count for each procedure. For the tests to be described in this paper block tridiagonal solution procedures were applied to the system (37). The resulting set of equations, subject to the appropriate boundary conditions, can be solved by standard methods. In subsequent sections the vector notation for $\mathbf{c}$, indicating the numerical approximations to $c(x, t)$ at the r grid points, will be omitted for clarity.

7. Solution of the Advective Transport Step T_a

There is an extensive literature that describes techniques suitable for solving the hyperbolic problem (33) [9, 38–41]. Most of the approaches fall into five basic categories: finite difference, variational, particle-in-cell, spectral and special purpose procedures. On the basis of a preliminary survey, seven methods were identified for detailed evaluation. These schemes were: the flux corrected transport algorithm (SHASTA) [42–44], compact differencing methods [45–50], finite element methods [51–53], the zero-average phase-error technique [54], upwind differencing [9], the Crowley [55] technique and finally the scheme of Price *et al.* [56]. These methods were used as described in the literature except for the finite element scheme that was applied to the conservative formulation of the advection equation.

The particular finite element model used in this study employs a Galerkin formulation and linear basis functions. With this technique, approximations to the concentration and velocity fields are expressed in terms of time-varying coefficients $\alpha_j(t)$, $\beta_j(t)$ and piecewise continuous basis function $\phi_j(x)$,

$$c(x, t) = \sum_{j=1}^{r} \alpha_j(t)\,\phi_j(x), \tag{41}$$

$$u(x, t) = \sum_{j=1}^{r} \beta_j(t)\,\phi_j(x), \tag{42}$$

where

$$\begin{aligned}\phi_j(x) &= \frac{x - x_{j-1}}{x_j - x_{j-1}}; \qquad x_{j-1} \leqslant x \leqslant x_j, \\ &= \frac{x_{j+1} - x}{x_{j+1} - x_j}; \qquad x_j \leqslant x \leqslant x_{j+1}, \\ &= 0; \qquad x < x_{j-1} \text{ or } x > x_{j+1}.\end{aligned} \tag{43}$$

Equation (43) describes a set of linear basis function that vanish outside the interval $[x_{j-1}, x_{j+1}]$. Using these functions, the Galerkin method requires that for all ϕ_j,

$$\left\langle \phi_j, \left\{ \frac{\partial \alpha_q \phi_q}{\partial t} + \frac{\partial}{\partial x}(\beta_s \phi_s \alpha_q \phi_q) \right\} \right\rangle = 0. \tag{44}$$

By expanding the inner product (44), the following set of ordinary differential equations in the dependent variable $\alpha_q(t)$ can be derived *

$$M_{jq} \frac{d\alpha_q(t)}{dt} + \beta_s(t)\, N_{jqs}\, \alpha_q(t) = 0, \tag{45}$$

where

$$M_{jq} = \int \phi_j(x)\, \phi_q(x)\, dx, \tag{46}$$

$$N_{jqs} = \int \left[\phi_j(x)\, \phi_q(x) \frac{\partial \phi_s(x)}{\partial x} + \phi_j(x)\, \phi_s(x) \frac{\partial \phi_q(x)}{\partial x} \right] dx. \tag{47}$$

To compare the solution schemes, some idealized test problems with known solutions were selected. Particular attention was given to the harmonic content of each test case. A concentration distribution containing components with wavelengths shorter than the characteristic grid spacing represents a difficult test for any advection scheme. If little numerical or physical diffusion is present, an initial profile with sharp corners and steep sides should remain intact as it is transported by the velocity field. Test problems were also chosen to allow simultaneous and individual solutions of both transport components. In addition to the accuracy considerations judged by the important attributes of mass conservation, minimal dispersion and minimal pseudo-diffusion, additional constraints in choosing a numerical method arise as a result of the availability of computational resources. Execution time, storage requirements, ease of understanding, and implementation must also be considered since the most accurate scheme may also be the least efficient.

A series of test problems, listed in Table I was used to evaluate the schemes. The velocity was constant at 5 km/hr, the time step at 0.1 hours. The Courant number, C,

* The algebraic details are contained in Appendix B.

TABLE I

Test Problems for Advection Equation

Wave form	Function	Fourier spectrum
Square	$c(x,0)=\begin{cases}1 & \lvert x\rvert \leqslant \frac{\theta}{2}\\ 0 & \lvert x\rvert > \frac{\theta}{2}\end{cases}$	$\dfrac{\sin\frac{\omega\theta}{2}}{\frac{\omega\theta}{2}}$
Triangle	$c(x,0)=\begin{cases}1-\lvert x\rvert/\theta & \lvert x\rvert \leqslant \theta\\ 0 & \lvert x\rvert > \theta\end{cases}$	$\dfrac{\theta\sin\left(\frac{\omega\theta}{2}\right)}{\left(\frac{\omega\theta}{2}\right)^2}$
Gaussian	$c(x,0)=\exp\left[-\Pi\left(\frac{x}{\theta}\right)^2\right]$	$\theta\sqrt{\Pi}\exp\left[-\frac{1}{2}(\theta\omega)^2\right]$

θ—Volume/unit width ratio for the wave form.

was 0.25, which is less than the stability limit for all schemes. These parameters were chosen to be representative of meteorological conditions over a typical urban airshed. The results of the tests are summarized in Table II and shown in Figs. 1–3. Further detailed testing with a range of sample problems narrowed the solution methods to the SHASTA technique and a class of techniques that use linear finite elements or compact differences together with Crank–Nicholson time integration.

7.1. *Preservation of Positive Quantities and Filtering Schemes*

During the course of the testing it became obvious that in order to develop a scheme that preserves peaks, retains positive quantities, and does not severely diffuse sharp gradients, an additional step must be performed to minimize the effect of dispersive waves. As noted by Kreiss and Oliger [57], the basic problem with conventional Galerkin formulations is that they result in nondissipative, discrete approximations when applied to hyperbolic equations. What is required is a procedure for damping out the small scale perturbations before they can corrupt the basic solution. There are several different filtering procedures that can be applied: (1) adding diffusions terms to the basic equation [58], (2) expansion of the concentration field in orthogonal functions with a recombination that omits high wave numbers [59], (3) numerical filtering where the grid point value is replaced by an average formed from surrounding values, (4) inclusion of a dissipative term in the problem formulation [60, 61].

At the simplest level, one approach is to set any negative concentration to zero or a very small positive number following each advection step. This procedure is demonstrated using the finite element method with a square wave in Fig. 4a. While trivial to implement, this correction scheme can induce violations of mass conser-

TABLE II

Summary of Results of Advection Tests for Different Initial Distributions*

Numerical scheme	Test Square (S) Gaussian (G) Triangle (T)	Extreme value		Change in mass (%)	Relative computational time
		Maximum	Minimum		
Upwind [9]	S	0.755	0.0	0.0	1.0
	T	0.693	0.0	−0.03	
	G	0.635	0.0	−0.01	
Price [56]	S	1.463	−0.390	−0.93	1.2
	T	0.971	−0.086	−0.50	
	G	1.108	−0.216	0.26	
Fromm [54]	S	1.084	−0.067	−0.05	1.8
	T	0.918	−0.015	0.28	
	G	0.964	−0.006	0.07	
Crowley [55]	S	1.219	−0.222	−2.02	2.0
	T	0.932	−0.017	0.28	
	G	0.990	−0.001	0.07	
Finite element [Text]	S	1.218	−0.382	−10.27	2.0
	T	0.953	−0.025	0.17	
	G	0.999	−0.001	0.16	
SHASTA [42–44]	S	0.997	0.0	0.0	5.2
	T	0.875	0.0	0.20	
	G	0.900	0.0	0.04	

* Results are at the end of 80 time steps.

vation. Mahlman and Sinclair [62] attempted to correct this problem by using a method called "downstream borrowing." In this scheme, implemented at the end of each time step, negative values are reset to zero by borrowing material from the downstream grid cell so that mass is conserved. In the event that the downstream cell does not contain an adequate amount of material to prevent both cell concentrations from becoming negative, the deficit is borrowed from the upstream cell. With higher-order schemes it is occasionally necessary to borrow mass from the second cells away from the one containing negative c. Although this filling procedure always acts to preserve the total mass in the system, it systematically acts to reduce the mean square concentration. Filling is thus equivalent to adding a nonlinear diffusion term. An example of the application of this procedure is shown in Fig. 4b again using the finite element method with a square wave initial condition.

Boris and Book [42, 43] and van Leer [63] have introduced different approaches to the design of filtered second-order schemes. Their algorithms substantially inhibit

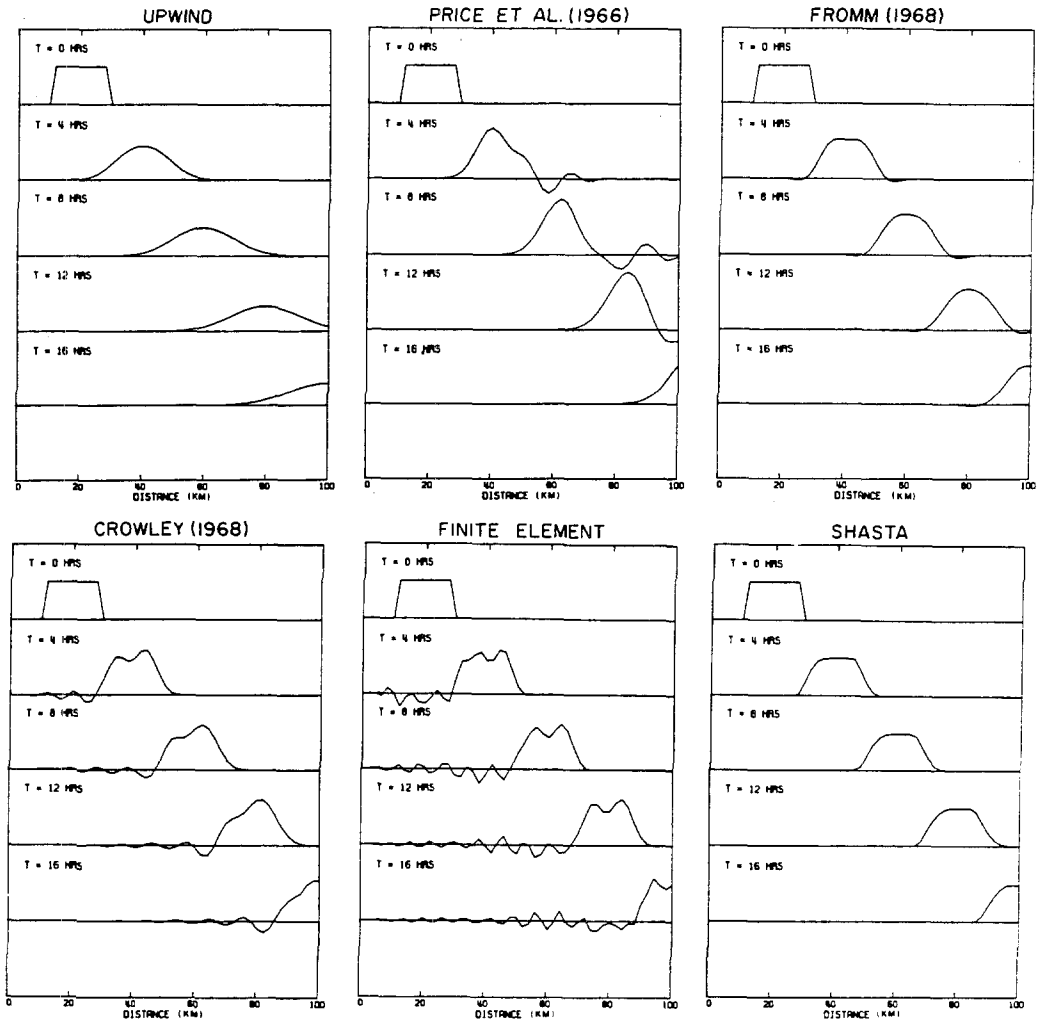

FIG. 1. Results of advection tests using square wave form.

or eliminate computational noise in regions of sharp gradients by using nonlinear smoothing techniques. The principal disadvantage of both methods is that there are substantial amplitude penalties associated with sharply peaked waves. When the SHASTA scheme of Boris and Book is used to advect a triangle, after a few steps the apex is typically severely truncated. However, once this has occurred, the distribution is transported with little change.

Recently Forester [64] introduced a very simple nonlinear filter designed to be used in conjunction with second and higher-order methods. Computational noise is

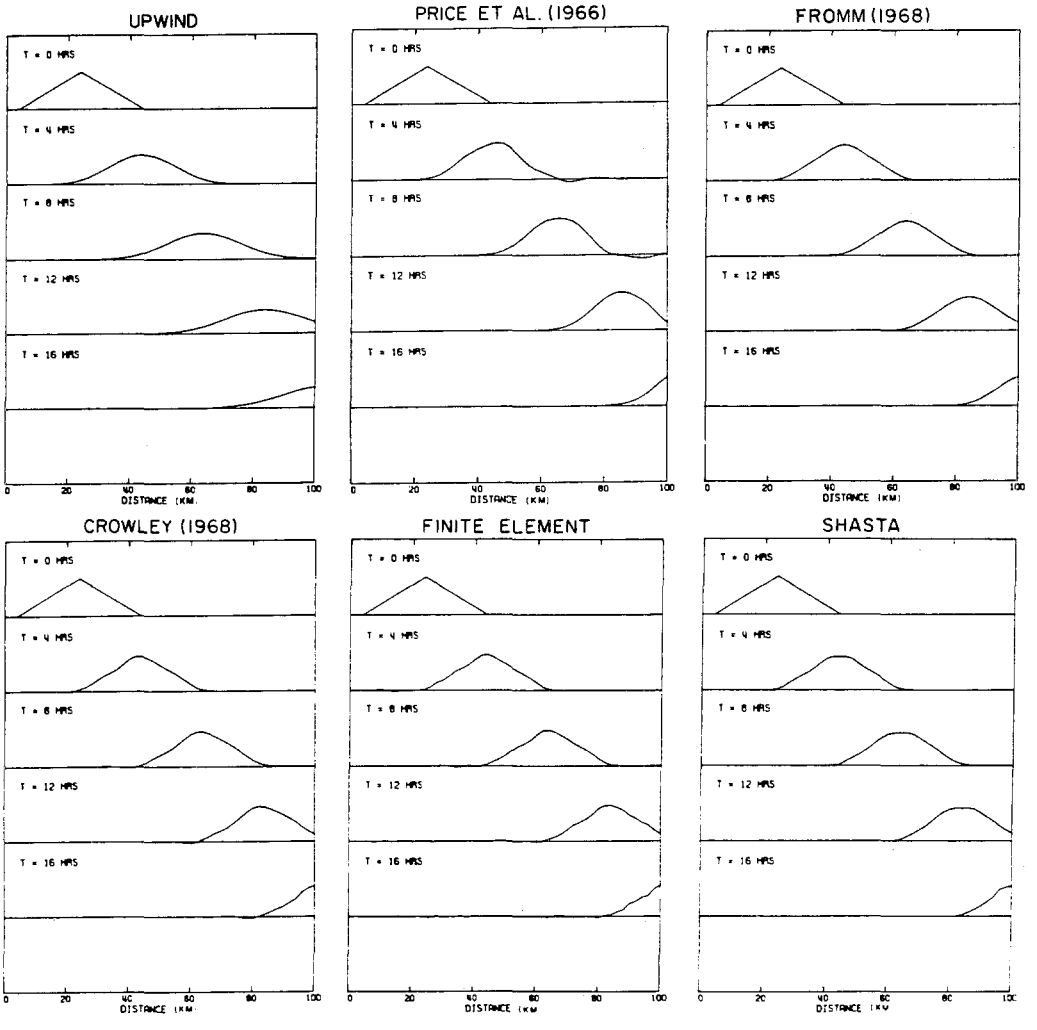

FIG. 2. Results of advection tests using triangular wave form.

minimized without incurring the amplitude penalty of either the SHASTA or van Leer techniques. When coupled with high-order schemes, the Forester method requires less than one-third of the mesh points of the SHASTA scheme to treat the extremes of sharply peaked waves. Positive concentrations are also preserved. The noise generated by the finite difference approximations of (33) is suppressed in the Forester method by a nonlinear filter that locally transforms (33) into

$$\frac{\partial c}{\partial t} + \frac{\partial uc}{\partial x} = \frac{\partial}{\partial x} K_n \frac{\partial c}{\partial x}, \tag{48}$$

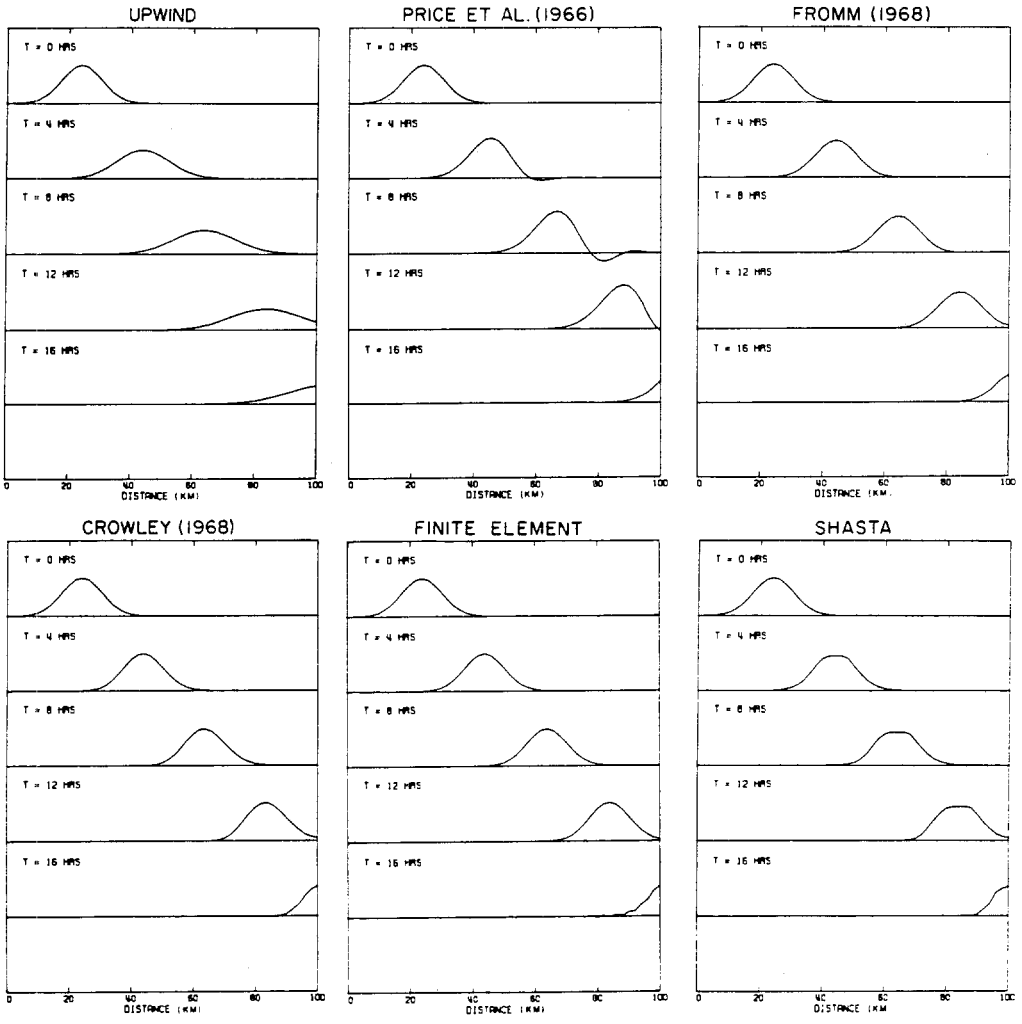

FIG. 3. Results of advection tests using Gaussian wave form.

where K_n is the diffusion coefficient associated with the filtering process. After the solution is advanced a time step, a set of empirically based criteria is used to decide if the term should remain or be removed. The filter for (33) is given by

$$c_j^{k+1} = c_j^k + \frac{K_f}{2}[(c_{j+1} - c_j)(\psi_j + \psi_{j+1}) - (c_j - c_{j-1})(\psi_j + \psi_{j-1})]^k, \tag{49}$$

where c_j^{k+1} is the value of c_j after k applications of the filter and K_f is the weighting coefficient associated with the filtering process. The ψ_j's can only assume a value of 0

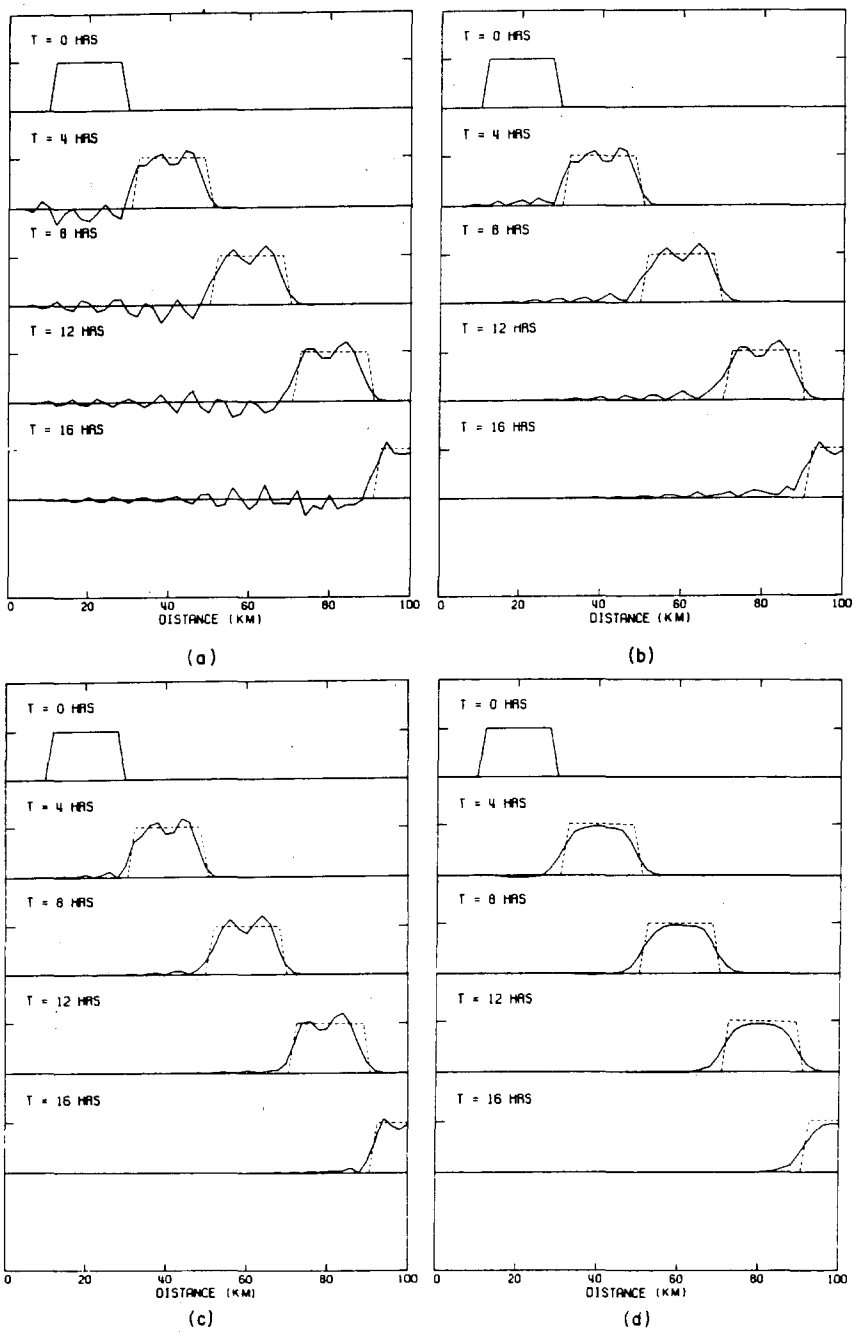

FIG. 4. Application of difference schemes to maintain concentration positivity. (a) Original linear finite element solution. (b) Absolute value $|c|$. (c) Downstream borrowing. (d) Nonlinear filter.

or 1 and determine the points at which smoothing occurs. Clearly if all are zero, no filtering takes place. For the condition $\psi_j = 1$, (51) takes a form that is analogous to the three-point difference expression for the diffusion term,

$$c_j^{k+1} = c_j^k + K_f[c_{j+1} - 2c_j + c_{j-1}]^k. \tag{50}$$

A key element of the filter application is the selection of the points in the grid mesh at which to set $\psi = 1$. Initially, all ψ are set to zero. Consider a point j and an interval $[j-m, j+m+1]$. On this interval the function S_e is evaluated using

$$S_e = \operatorname{sgn}[c_e - c_{e-1}]; \qquad e = j-m, j-m-1, \ldots, j, j+1, \ldots, j+m+1, \tag{51}$$

where

$$\begin{aligned} \operatorname{sgn}(c) &= +1, \qquad \frac{c}{|c|} \geqslant 0, \\ &= -1, \qquad \frac{c}{|c|} < 0. \end{aligned} \tag{52}$$

At mesh point j there is an extremum of c_j if S_j and S_{j+1} are of opposite sign. The distribution of c on the interval $[j-m, j+m+1]$ is considered to be smooth if $S_{j+1}, \ldots, S_{j+m+1}$ have the same sign and all $S_{j-1}, \ldots, S_{j-m}$ are of opposite sign to S_{j+1}. If this occurs, the values of ψ are left unchanged and no smoothing is applied to c_j. No tests for sign continuity of $S_j, \ldots, S_{j-m-1}$ are performed unless c_j is an extremum. These cases are illustrated in Fig. 5. If the slope or sign continuity does not hold for the m values of S on each side of the extremum in c_j, ψ is reset to 1 for the range of i from $i-l$ to $i+l$. To ensure that the mesh points at which ψ is nonzero in fact denote regions that contain computational noise, it is necessary to select the proper magnitudes for l and m. The value of m is chosen to be representative of one-half the wavelength of the lowest-frequency noise waves; l simply must be large enough to permit nonzero c values to be continuous.

For many high-order advective schemes nonlinear effects tend to drive the wavelength of the computational noise toward the limit of two mesh intervals, this can be seen in the results shown in Figs. 1–4. In general, the structure of the dispersive waves depends on the advection algorithm, its performance for different Courant numbers, and the nature of the concentration gradients. Values of m, l, K_f and the number of iterations required to satisfy the error tolerance must be determined empirically. For the above fourth-order schemes the values chosen were $m = 4$, $l = 2$, $K_f = 0.2$, and the number of iterations set to 2 and 3 for local Courant numbers less than 0.5 and greater than 0.5, respectively. An application of the filter, together with the finite element scheme, to the square-wave propagation problem is shown in Fig. 4d. There is clearly a significant improvement over the results displayed in Fig. 1.

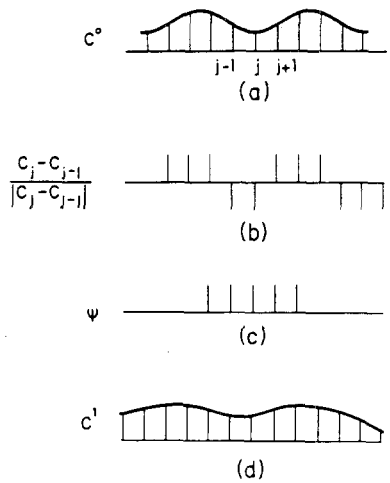

FIG. 5. Steps in the application of the discrete noise filter. (a) Initial distribution c^0. (b) Evaluation of the normalized derivatives. (c) Establishment of ψ function. (d) Resulting distribution after one filter application c^1.

7.2. *Conservation Properties of Different Advection Methods*

With the addition of the nonlinear filter, the performance of the finite element scheme improved to the point where it was useful to perform a quantitative comparison between it and the SHASTA method. In particular, it was important to assess the ability of each scheme to preserve mass, concentration gradients etc. A variety of initial distribution and velocity fields were used to test the techniques. The triangle test problem used in previous sections of this work has the property that

$$\frac{\partial}{\partial t}\int c\,dx = 0, \tag{53}$$

$$\frac{\partial}{\partial t}\int c^2\,dx = 0, \tag{54}$$

$$\frac{\partial}{\partial t}\int c^4\,dx = 0, \tag{55}$$

$$\frac{\partial}{\partial t}\int \left(\frac{\partial c}{\partial x}\right)^2 dx = 0, \tag{56}$$

$$\frac{\partial}{\partial t}\int \left(\frac{\partial^2 c}{\partial x^2}\right)^2 dx = 0. \tag{57}$$

Each of these integrals was evaluated numerically using, in the case of (56) and (57), standard finite difference approximations to the derivatives. While a numerical scheme should ideally conserve both mass (53) and mean square mass (54), diffusive

TABLE III

Results of Advection of Triangular Wave Form after 80 Time Steps

Numerical scheme	ERROR (%) = 100 (calculated/exact − 1)				
	$\int c\,dx$	$\int c^2\,dx$	$\int c^4\,dx$	$\int \left(\frac{\partial c}{\partial x}\right)^2 dx$	$\int \left(\frac{\partial^2 c}{\partial x^2}\right)^2 dx$
Fourth order	0.20	0.00	−0.44	−3.15	−28.17
SHASTA	0.20	−0.92	−5.51	−12.40	−97.75

effects tend to damp the latter quantity. The ability of a numerical scheme to maintain peak values is measured by (55), growth or decay of local gradients by (56) and change of profile curvature by (57). In a more general context, it should be noted that integrals (53) and (54) are analytically conserved in more complex source-free and nondiffusive flows. If gradient reducing diffusion terms are not included in calculations with more complicated flows, (56) and (57) tend to increase with time from either numerical distortion or from a physically real cascade to smaller spatial scales [62]. In practice, it is often difficult to establish which of these two effects is dominant. Since (56) and (57) are conserved in the test problem, any increase in their magnitude with time must be attributed to numerical errors. If this occurs, extra damping would be required to suppress the growth of the errors.

Errors in preserving the conservation properties for the SHASTA and fourth-order schemes are displayed in Table III. The SHASTA scheme performs poorly at maintaining peak values and, in addition, has the most diffusive effect on the profile. By comparison, the finite element method exhibits little diffusion.

A test of the capability of each scheme to handle variable velocity fields was also devised for the system

$$\frac{\partial c}{\partial t} + \frac{\partial uc}{\partial x} = 0; \qquad x \in [0, 100], \tag{58}$$

where the velocity field $u(x)$ is given by

$$u(x) = \frac{x+1}{20}. \tag{59}$$

The exact solution, $c_e(x, t)$ of this system is

$$c_e(x, t) = 0.1(x+1)\exp\left[-\frac{t}{10}\right]. \tag{60}$$

Initial and boundary condition for the problem are $c(x, 0) = c_e(x, 0)$ and $c(0, t) = c_e(0, t)$. Each numerical scheme used a grid size $\Delta x = 2$ km, and a time step $\Delta t = 0.2$ hours. Under these conditions, the maximum Courant number is 0.5. After

TABLE IV

Errors in Concentration Predictions after 120 Time Steps for a Spatially Varying Velocity Field

Numerical scheme	Error (%) at $x = 24$	$x = 50$	$x = 76$	$x = 100$
Fourth order	0.87	−0.08	0.01	0.03
SHASTA	1.18	1.20	1.20	1.87
Exact solution	0.0338	0.0690	0.1042	0.1367

120 time steps (24 hours), the errors were calculated and the results are shown in Table IV. While each scheme performed reasonably well, the finite element method produced better predictions at all spatial locations.

A rather difficult advection calculation, in two dimensions, is the rotating cone problem introduced by Crowley [55] and Molenkamp [65]. The test consists of solving the axisymmetric advection problem

$$\frac{\partial c}{\partial t} + \omega \frac{\partial c}{\partial \theta} = 0, \tag{61}$$

where θ is the angular coordinate, and ω the angular velocity around the axis of rotation. The exact solution of (61) is given by $c(r, \theta, t) = c^0(r, \theta - \omega t)$, where c^0 is the initial distribution of c. Since there is no physical diffusion, the shape c^0 should remain unchanged upon rotation. The Crowley problem consists of solving (61) in rectangular coordinates where the rotation is anticlockwise about the origin.

TABLE V

Summary of Results of Two-Dimensional Cone in a Circular Wind Field ($C_x = C_y = 0.5$)

Numerical scheme	1/4 Revolution		1 Revolution	
	Maximum value	Minimum value	Maximum value	Minimum value
Fromm	0.7400	−0.0218	0.5466	−0.0288
Crowley	0.8478	−0.0586	0.7283	−0.1279
Finite element	0.8731	−0.0335	0.8645	−0.0545
SHASTA	0.6670	0.0	0.5118	0.0
Exact solution	1.0000	0.0	1.000	0.0

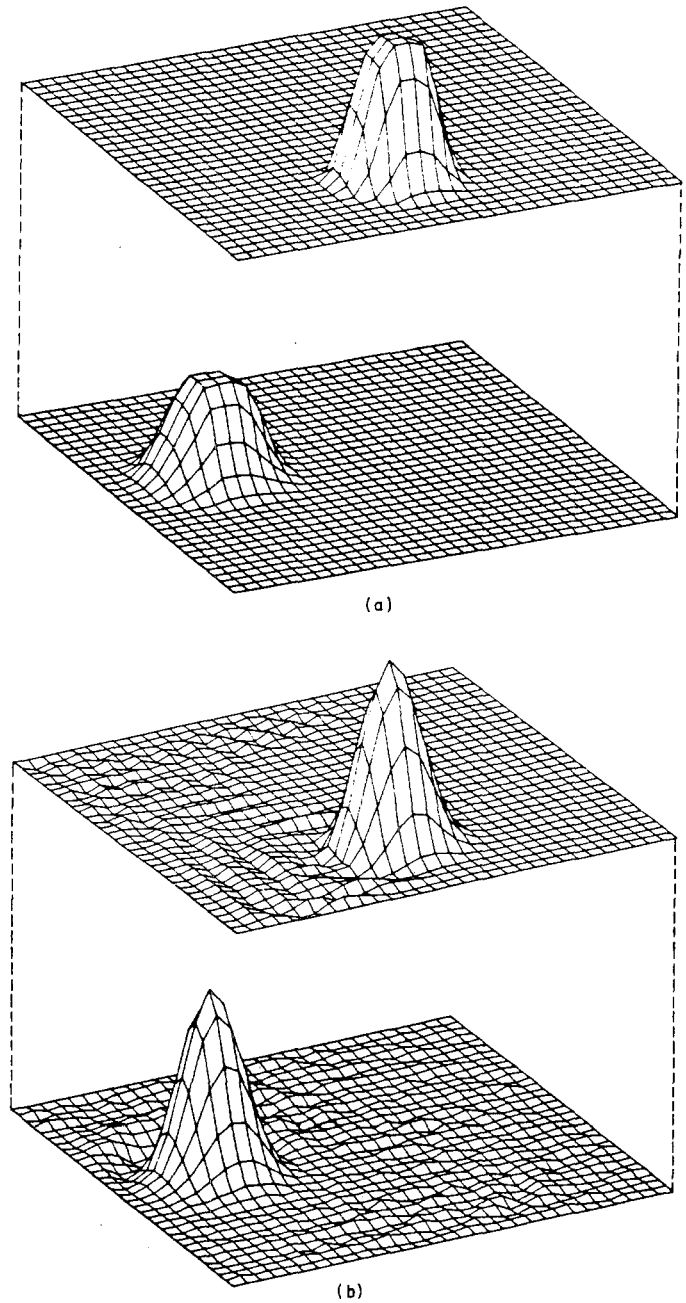

FIG. 6. Results of Crowley test problem for a quarter and complete revolution of a cone using (a) SHASTA method and (b) linear finite element scheme (without filtering step).

Under these conditions, the velocity components are given by $u = -y\omega$, $v = x\omega$ and

$$\frac{\partial c}{\partial t} - \frac{\partial \omega y c}{\partial x} + \frac{\partial \omega x c}{\partial y} = 0. \tag{62}$$

The method of fractional steps was used to solve the problem on a 32×32 grid with $\Delta x = \Delta y = 1$ km, $\Delta t = 0.5$ hrs and $\omega = 0.0626$ rad/hr. A conical distribution, centered initially at $(-8, 0)$, of base radius 4 and with $c_{max} = 1$, $c_{min} = 0$ was used to describe c^0. The results of the experiment, summarized in Table V, are displayed in Fig. 6; the conclusions are similar to the last test case. The peak truncation problem, characteristic of SHASTA, is particularly apparent. From a practical point of view, it is encouraging to note that the amplitudes of the dispersive waves associated with unfiltered finite element scheme are quite small.

8. Solution of the Diffusive Transport Step T_d and Boundary Condition Treatment

Previous sections were devoted to the implementation and testing of a suitable scheme for the advection equation. The contribution to species transport from turbulent diffusion depends on the coordinate direction. In the horizontal plane, transport is dominated by advection and so a simple, explicit three-point finite difference form [9] can be adopted for $(\mathbf{T}_x)_d$ and $(\mathbf{T}_y)_d$. A linear finite element scheme, with Crank–Nicholson time differencing, was used for $(\mathbf{T}_z)_d$. This removed the time step limitation of an explicit method and enabled the use of variable mesh spacing to resolve vertical concentration gradients.

The boundary of the grid is usually placed at the limits of the available data or far from the main calculation area. Boundary conditions are termed either inflow or outflow, depending on the direction of flow relative to the grid region. Often in fluid flow problems, the concentration at the inflow boundary is known and can be specified as a function of time. The outflow boundary is generally not known and therefore must be calculated. This boundary condition is sometimes called a "computational boundary condition" for this reason. Some helpful discussions of boundary conditions exist in the literature [66–73]. The boundary conditions used with (32) are

$$\text{inflow:} \qquad uc - K_{xx}\frac{\partial c}{\partial x} = uc_{in}, \tag{63}$$

$$\text{outflow:} \qquad -K_{xx}\frac{\partial c}{\partial x} = 0, \tag{64}$$

where c_{in} is the known concentration just outside of the inflow boundary. If it is assumed that advection is the dominant transport mechanism at the outflow

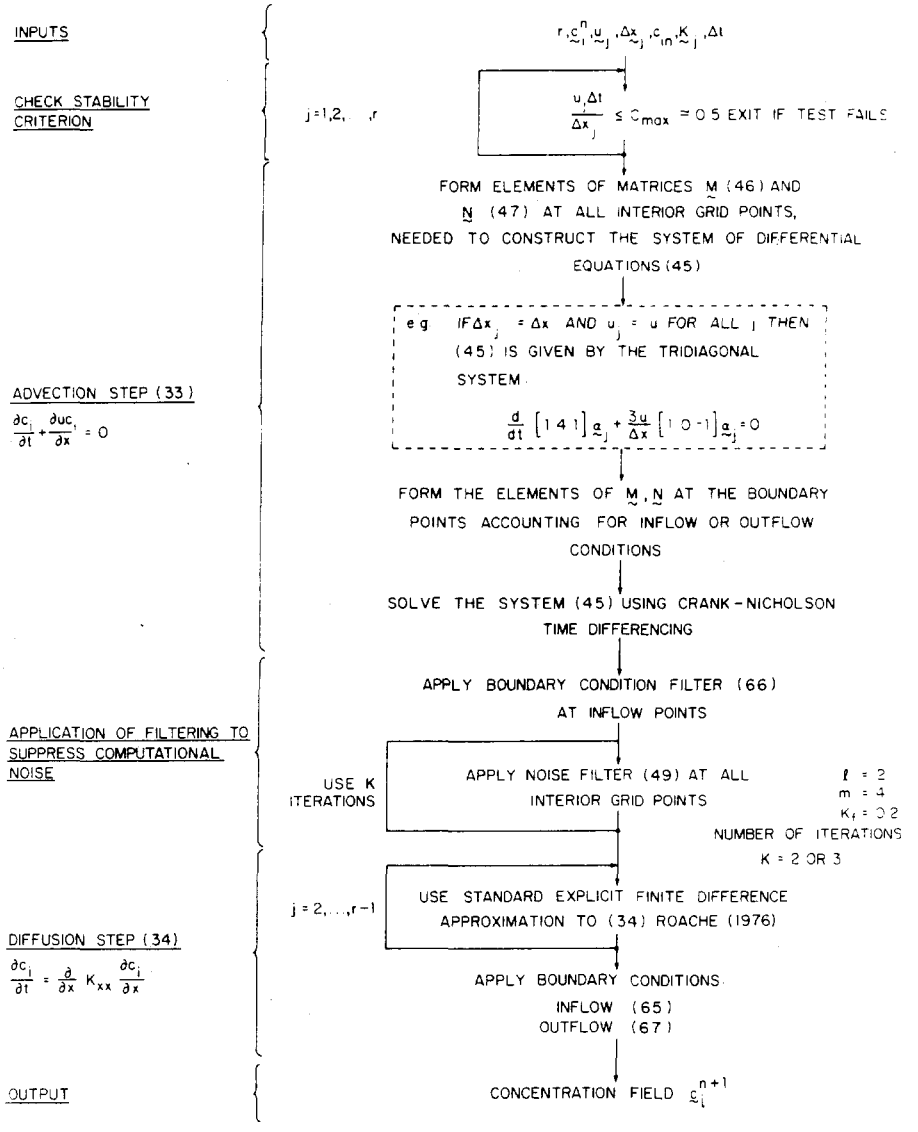

FIG. 7. Structure of the algorithm for solving the advection–diffusion equation for species transport in the x-direction.

boundary, then diffusive transport can be neglected. If the left end of the grid is an inflow boundary, then (63) can be represented as

$$u_1 c_1^{n+1} - \tfrac{1}{2}[(K_{xx})_1 + (K_{xx})_2] \frac{c_2^{n+1} - c_1^{n+1}}{\Delta x} = u_1 c_{\text{in}}^{n+1}, \tag{65}$$

which, in turn, can be solved explicitly for c_1^{n+1} since all other quantities are known. When using a multiple-step, advection–diffusion algorithm, (65) is used following the second (diffusion) step. A boundary value must also be set following the first (advection) step. The single condition $u_1 c_1 = u_1 c_{\text{in}}$ is used for this step in conjunction with a smoothing procedure at the point adjacent to the boundary point. This smoothing damps any waves that may be generated by the inflow boundary point. The simplest smoothing algorithm is

$$c_2^* = \tfrac{1}{2} c_2^{n+1} + \tfrac{1}{4}(c_1^{n+1} + c_3^{n+1}), \tag{66}$$

where c_2^* is the smoothed value of c^{n+1} at $j = 2$. A procedure analogous to the above can be applied to the right boundary. The concentration at an outflow boundary is influenced by information from the interior of the grid. Concentration gradients that are advected to the boundary must be preserved as they pass out of the grid. The simple choice of representing (64) by a zero gradient, i.e., $c_1 = c_2$ or $c_r = c_{r-1}$, where r is the right boundary point, was discarded due to its inability to preserve gradients. The approach adopted was to solve the advection equation (with zero diffusion) using a one-sided difference at the boundary:

$$\frac{c_r^{n+1} - c_r^n}{\Delta t} + \frac{u_r c_r^{n+1} - u_{r-1} c_{r-1}^{n+1}}{\Delta x} = 0. \tag{67}$$

This procedure preserves concentration gradients as they move out of the grid system as can be seen in the previous figures for the one dimensional test problems.

Figure 7 shows a flow diagram of the numerical solution of the advection and diffusion components of the atmospheric diffusion equation.

9. Numerical Solution of the Chemical Kinetics

In the previous two sections primary emphasis was placed on the transport components of the atmospheric diffusion equation. Equation (1) contains terms, f_i, $i = 1, 2, \ldots, p$, that describe the contributions to the rates of change of the p chemical species concentrations, $c_1, c_2, \ldots, c_p$, due to chemical reactions. At any one spatial point the rate of change of each species concentration resulting only from the

chemical kinetics can be described by a set of coupled, nonlinear ordinary differential equations,

$$\frac{dc_i}{dt} = f_i(c_1, c_2, ..., c_p, t); \qquad i = 1, 2, ..., p, \tag{68}$$

and associated initial conditions $c_i(0) = c_i^0$, $i = 1, 2, ..., p$.

There are two sources of difficulty that arise during the numerical solution of (68). One is minor and caused by the nonlinearities resulting from the polynomial form of the mass action rate laws. The more serious problem, however, arises as a result of the fact that in atmospheric systems there are reactions whose characteristic time scales differ by orders of magnitude. Such systems are often referred to as being "stiff." There are various definitions of what constitutes stiffness, the most common is of the form:

DEFINITION. The system (68) is said to be *stiff* if

(a) $\mathrm{Re}(\lambda_i) < 0; \qquad i = 1, 2, ..., p,$

and

(b) $(\max_i |\mathrm{Re}\, \lambda_i|)/(\min_i |\mathrm{Re}\, \lambda_i|) = R \gg 1,$

where R is the stiffness ratio and λ_i are the eigenvalues of the Jacobian matrix $\mathbf{J} = \partial \mathbf{f}/\partial \mathbf{c}$. A way to view the problem of stiffness is to write (68) in the form

$$\frac{dc_i}{dt} = a_i - b_i c_i, \tag{69}$$

where a_i is the production rate for species c_i and $b_i c_i$ is the loss rate. The reciprocal of b_i can be interpreted as the characteristic time for decay of species i. If a_i and b_i are constants then (69) can be solved to give

$$c_i(t) = \frac{a_i}{b_i} + \left[c_i(0) - \frac{a_i}{b_i} \right] \exp(-b_i t). \tag{70}$$

Expressed in this way, it can be seen that $1/b_i$ describes how quickly species c_i reaches its equilibrium value. Figure 8 presents a typical eigenvalue spectrum for atmospheric reaction mechanisms together with the characteristic reaction times $1/b_i$. Two features are readily apparent: one is the close correspondence, for many species, between the eigenvalues and the characteristic reaction times and the other is the extreme range $O(10^{12}$ min) of the spectrum.

In passing it is worthwhile to comment on the reason why some of the eigenvalues are so closely matched to the corresponding reaction times. Consider atomic oxygen (O), which has the fastest reaction time of any species in the system. An examination

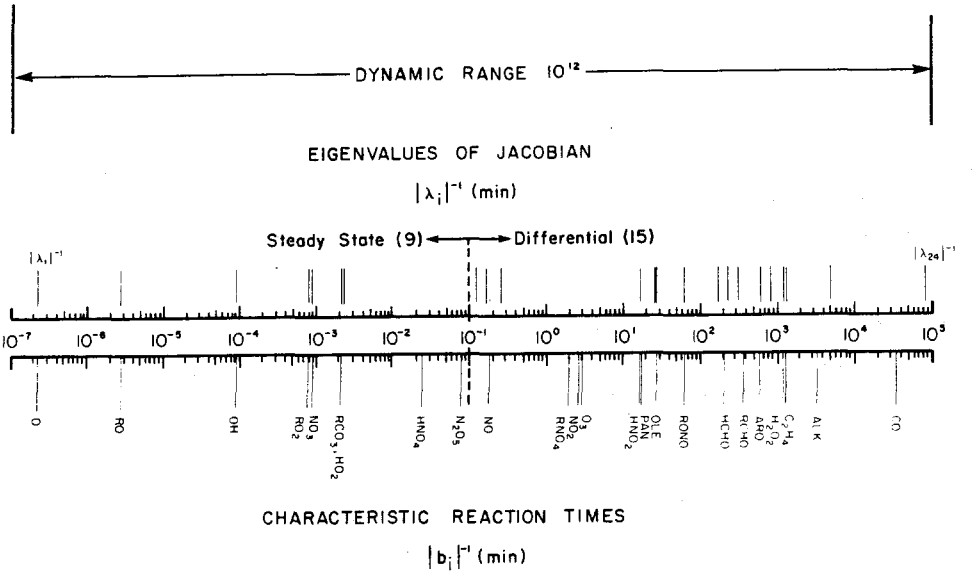

FIG. 8. Typical eigenvalue spectrum and characteristic reaction times for the photochemical mechanism of McRae *et al.* [89].

of O atom production and decay rates under typical conditions indicates that the predominant removal step (by four orders of magnitude) is reaction with molecular oxygen

$$O + O_2 + M \rightarrow O_3 + M. \tag{71}$$

Since the concentration of both molecular oxygen (O_2) and the third body (M), are fixed, the kinetics of O are described to a very good approximation by (69) with a_i and b_i constant. Under these conditions the eigenvalues and characteristic reaction times can be expected to be similar. This behavior was also observed for most of the free radicals: RO, OH, RO_2, NO_3, RCO_3, and HO_2. When there is coupling between species, and the rate terms are of comparable magnitude, the a_i's and b_i's are no longer constant and the analytic solution (70) is inappropriate.

9.1. *Selection of a Suitable Solution Scheme*

In the last few years considerable effort has been devoted to developing general purpose algorithms for solving stiff ordinary differential equations [74–79].

In applications involving simultaneous transport and chemistry such as that of interest here, the reaction rate equations must be integrated at a large number of grid points for relatively short periods of time between transport steps. As a consequence, self starting methods with low overheads are highly desirable. As mentioned earlier, the large size of the computational grid usually precludes storing more than the

results of the previous time step. From a pragmatic point of view it is important to recognize that errors associated with the transport steps are rarely smaller than a few percent so in general there is little to be gained by requiring highly accurate solutions of the kinetics. Summarizing, the desirable requirements of a solution scheme for the chemical kinetics are low start up costs, minimal computer memory requirements, and extreme computational speed.

Given the above considerations, two different solution schemes were sought; one capable of providing highly accurate benchmark standards of predictions and the other, an extremely fast algorithm for use in the airshed model. Since the factors influencing the choice of the method use in the model are discussed in Section 9.3 they will not be discussed here. The method chosen to establish the standard of accuracy for judging other methods was the implementation of the Gear technique by Hindmarsh and Byrne [80] and Byrne *et al.* [81]. Their program, called EPISODE, is extremely well documented and has been subjected to extensive testing by a number of different investigators [79, 81]. Unlike the original Gear method, the program employs a true variable step, variable order approximation that is ideally suited to problems with time varying parameters. Another reason for choosing this particular code was the ease with which different treatments of the Jacobian could be tested. In the version of EPISODE used in this study the Jacobian could be evaluated in either of four ways: functional iteration, analytic evaluation, finite differences, or diagonal approximations. The ability to exercise easily these options considerably simplified the task of identifying the most efficient means for solving the chemical kinetics.

9.2. *Pseudo Steady State Approximation*

Even with fast integration schemes the computational cost of solving the atmospheric diffusion equation is extremely high. There is a need to reduce both the number of active chemical species, to minimize storage requirements, and the stiffness, to lower the computational cost. One approach, commonly used in chemical kinetics, is to alleviate some of these difficulties by employing the pseudo steady state approximation [82, 83]. The basic idea behind this approximation is that the transients associated with the stiff variables decay very rapidly to their equilibrium values. If the concentrations are partitioned into two components, one associated with the nonstiff components $\mathbf{c}_d$ and the other comprising the stiff species, $\mathbf{c}_s$, then if the pseudo steady state approximation is used, (68) is replaced by the systems

$$\dot{\mathbf{c}}_d = \mathbf{f}_d(\mathbf{c}_d, \mathbf{c}_s) \tag{72}$$

and

$$\mathbf{0} = \mathbf{f}_s(\mathbf{c}_d, \mathbf{c}_s). \tag{73}$$

The two main difficulties associated with the valid use of pseudo steady state approximations are the identification of those species that can be treated in this way and the determination of the time after which the approximation is valid. For simple systems there is an extensive literature that utilizes singular perturbation theory to establish

TABLE VI

Comparison between the Exact Calculation and the Pseudo Steady State Approximation for Different Chemical Species

Time (min)	% Error								
	OH	O	RCO_3	RO_2	RO	HO_2	HNO_4	NO_3	N_2O_5
60	-2.5×10^{-3}	-4.3×10^{-6}	$+8.3 \times 10^{-3}$	-3.4×10^{-3}	-1.2×10^{-2}	$+8.6 \times 10^{-3}$	$+8.5 \times 10^{-2}$	-3.5×10^{-2}	-3.7×10^{-1}
120	-2.7×10^{-3}	$+2.1 \times 10^{-6}$	-2.0×10^{-3}	-4.2×10^{-3}	$+8.6 \times 10^{-3}$	$+4.1 \times 10^{-3}$	$+3.8 \times 10^{-2}$	$+2.6 \times 10^{-2}$	$+3.3 \times 10^{-1}$
180	$+2.6 \times 10^{-2}$	-5.6×10^{-6}	$+7.3 \times 10^{-3}$	-1.0×10^{-2}	$+1.5 \times 10^{-2}$	-1.1×10^{-2}	$+2.1 \times 10^{-2}$	-1.6×10^{-1}	$+1.6 \times 10^{-1}$
240	$+7.0 \times 10^{-2}$	$+4.7 \times 10^{-6}$	-2.8×10^{-3}	-1.5×10^{-2}	$+1.8 \times 10^{-1}$	-4.5×10^{-2}	$+3.0 \times 10^{-3}$	$+9.1 \times 10^{-2}$	$+1.4 \times 10^{-1}$
300	$+1.2 \times 10^{-1}$	$+3.2 \times 10^{-6}$	-2.0×10^{-2}	$+2.2 \times 10^{-3}$	$+4.3 \times 10^{-1}$	-7.3×10^{-2}	-3.0×10^{-2}	-2.1×10^{-1}	$+7.0 \times 10^{-2}$
360	-8.8×10^{-2}	-1.9×10^{-5}	$+1.9 \times 10^{-3}$	-1.8×10^{-2}	-5.6×10^{-1}	$+7.9 \times 10^{-2}$	$+3.7 \times 10^{-2}$	$+1.7 \times 10^{-2}$	$+2.9 \times 10^{-2}$

* Percentage Error = 100 [PSSA/EXACT − 1].

the appropriate bounds [78, 82–84]. Unfortunately, there is as yet no well-developed theory for systems as complex as the photochemical reaction mechanism utilized in this study. Thus, an approximate way to identify candidate species was developed.

The particular approach adopted in this study was to analyze the behavior of the kinetic equations by performing an eigenvalue–eigenvector analysis of the mechanism Jacobian under a wide variety of test conditions. The reason for doing this is that the eigenvalues all have negative real parts that can be ranked into two distinct subsets. The first set of largest negative eigenvalues generally have eigenvectors containing only one or two components. These elements as noted above usually correspond to those species that have very fast reaction times. These λ's typically have magnitudes as large as 10^7, corresponding to species half-lives as short as 10^{-6} seconds. The second set of eigenvalues has corresponding eigenvectors that each involve many, if not most, of the species in the reaction set. These represent the relatively slowly reacting species.

Using the eigenvalue analysis procedure, nine species were identified as candidates for the steady state approximation: O, RO, OH, RO_2, NO_3, RCO_3, HO_2, HNO_4, and N_2O_5. The solutions using the steady state approximation and one where all species were treated by differential equations were compared over a wide range of conditions. Typical examples of the results of these tests are shown in Tables VI and VII. Table VI is an assessment of the validity of each approximation. An inspection

TABLE VII

Comparison between Predictions of Complete System and Kinetics Using Pseudo Steady State Approximations

Time (min)	Species	Concentration (parts-per-million by volume) Complete system	Kinetics with 9 PSSA species	% Difference*
30	NO	0.0566	0.0567	0.18
	NO_2	0.4034	0.4070	0.89
	O_3	0.0830	0.0834	0.48
60	NO	0.0202	0.0202	0.00
	NO_2	0.3869	0.3889	0.51
	O_3	0.2189	0.2191	0.09
90	NO	0.0110	0.0110	0.00
	NO_2	0.3338	0.3329	−0.27
	O_3	0.3379	0.3383	0.12
120	NO	0.0066	0.0066	0.00
	NO_2	0.2628	0.2652	0.91
	O_3	0.4358	0.4391	0.75

* Percentage difference = 100 [PSSA/complete − 1].

of the results indicates that there are negligible differences between the species being treated by differential or algebraic equations. The most important comparison, however, is the influence of the use of the approximation on the predicted concentrations, $\mathbf{c}_d$. Even after 120 minutes the maximum error shown in Table VII is less than 0.5%. The conclusion reached from an analysis of these and other test cases was that the species identified from the eigenvalue analysis could be treated in steady state with minimal effects on the predicted concentrations of the primary species, $\mathbf{c}_d$.

Once the concentration vector has been partitioned into stiff and nonstiff components, there are a variety of algorithms that can take advantage of the problem structure. For example, Robertson [85] utilized the division in the iterations involved with the use of implicit multistep formulas. During any single step, by fixing the part of the iteration matrix corresponding to the nonstiff components and only updating the elements arising from the transients, significant computational economies were achieved. Techniques that achieve these efficiencies without prior knowledge about the problem structure are relatively rare. Enright and Kamel [86] have developed a general purpose computer code for systems where the stiffness is due to a few components of a large system.

One other approach for minimizing the influence of stiffness is to choose the initial conditions for $\mathbf{c}_s$ so that the complete system does not have the initial transient behavior. While it is extremely difficult to develop a general theory some initial steps in this direction have been made by Watkins [87] and Lambert [88]. The approach of Watkins [87] is particularly relevant because his algorithm has been developed to set initial conditions for transport problems. Unfortunately the cost of the proposed iteration scheme, when applied to systems of the size encountered in this study, is likely to be prohibitive. Kreiss [78] has addressed a similar situation in an attempt to set the initial conditions in a way that would eliminate the rapidly oscillating terms associated with large, purely imaginary eigenvalues. At this time there is no satisfactory means for a priori specification of the initial values for $\mathbf{c}_s$ that will remove or reduce the stiffness of systems of the type considered here.

9.3. *Asymptotic Integration Scheme*

In the previous section the size and stiffness of the reaction mechanism was reduced by employing the pseudo steady state approximation. Even with these changes it was still not feasible to economically use the EPISODE program in the solution of the full atmospheric diffusion equation. A variety of other alternatives were investigated in an attempt to significantly lower the computational cost but without substantially compromising the solution accuracy. The trapezoidal rule was rejected because of the overheads associated with the matrix decompositions. Even with the use of sparse matrix packages and infrequent Jacobian updating, the cost of Newton-type schemes was still excessive. The particular approach finally decided upon with the asymptotic integration method of Young and Boris [89, 90]. Designed to solve the reaction kinetics embedded in very large hydrodynamic problems, the method is self starting, extremely fast and requires minimal storage; as such, it satisfies most of the selection criteria discussed above.

A particularly attractive feature of the method is that it has a very low start up overhead because all that is required to begin a new integration step are the current values of the variables and the derivatives. A second-order predictor–corrector scheme that takes special notice of those equations determined at the beginning of the step to be stiff is employed to continue the integration process. When applied to stiff equations, the method is suited to situations where the solution is slowly changing or nearly asymptotic yet the time constants are prohibitively small. This occurs when the formation and loss rates are large, nearly equal, and there is strong coupling among the equations. Thus, the stiff equations are treated with a very stable method that damps out the small oscillations caused by the very small time constants.

The predictor–corrector algorithm provides enough information to choose the subsequent timestep size once convergence has been achieved. For efficiency, an initial timestep is chosen that approximates the timestep that will be determined after convergence of the predictor–corrector scheme. This initial trial timestep is chosen independently of the stiffness criterion and is determined such that none of the variables will change by more than a prescribed amount. If the formation rate is much larger than the loss rate, it is reasonable to assume that a_i and b_i will remain relatively constant for large changes in c_i. Often the initial change in c_i may be large enough to equilibrate the formation and loss rates. Thus the initial trial timestep $\Delta\tau$, is chosen in two ways:

$$\Delta\tau = \varepsilon \min_i \left[\frac{c_i}{f_i}\right] \tag{74}$$

or if $a_i \gg b_i c_i$ then

$$\Delta\tau = \varepsilon \min_i \left[\frac{1}{b_i}\right]. \tag{75}$$

The second criterion is needed when the initial conditions, for some species, are unknown or set to zero. Here ε is a scale factor, the selection of which is discussed shortly. The timestep dictated by (74) may be larger than some or all of the equilibrium times, in which case the corresponding equations would be classified as stiff. Nevertheless, when solved by the asymptotic method, this timestep ensures that accuracy can be maintained. When a stiff equation is close to equilibrium, the changes in the functional values over the timestep will be small even though the adjustment rate toward equilibrium can be very much shorter than the timestep. When the stiff equation is far from a dynamic equilibrium, the timestep should be scaled down proportionally to the equilibrium time to ensure that the transition to equilibrium will be followed accurately. This readjustment, because of the very fast rate, generally takes place rapidly after which much longer timesteps may be taken.

After a timestep has been chosen, all of the equations are separated into two classes, stiff and nonstiff, according to the values of the b_i. The two types of equations are then integrated by separate predictor–corrector schemes. A simple asymptotic formula is used for those equations determined to be stiff.

The predictor part of the step is performed as follows:

$$\text{Nonstiff:} \qquad c_i(1) = c_i(0) + \Delta\tau f_i(0), \tag{76}$$

$$\text{Stiff:} \qquad c_i(1) = c_i(0) + \frac{\Delta\tau f_i(0)}{1 + \Delta\tau f_i(0)}, \tag{77}$$

where $f_i(0) = f_i[t(0), c_i(0)]$ and $c_i(k)$ is the kth iterated value of c_i, or an approximation to $c_i[t(0) + \Delta\tau]$. The zeroth iteration, $c_i(0)$, is the initial value at $t(0)$ and $c_i(1)$ is the result of the predictor step. Also note that $f_i(k) = f_i[t(0) + \Delta\tau, c_i(k)]$. The corrector formulas are:

$$\text{Nonstiff:} \qquad c_i(k+1) = c_i(0) + \frac{\Delta\tau}{2}[f_i(0) + f_i(k)], \tag{78}$$

$$\text{Stiff:} \qquad c_i(k+1) = c_i(0) + \frac{2\Delta\tau[a_i(k) - b_i(0)\, c_i(0) + f_i(0)]}{4 + \Delta\tau[b_i(k) + b_i(0)]}. \tag{79}$$

By comparing $c_i(k+1)$ with $c_i(k)$ on successive iterations using the relative error criterion ε to satisfy

$$\max_i \left[\frac{|c_i(k+1) - c_i(k)|}{c_i(k+1)}\right] \leqslant \varepsilon \tag{80}$$

the convergence of each of the individual equations can be determined. As applied in the present application, ε is typically $O(10^{-3})$ and if the formation and loss rates are nearly equal ε is scaled down slightly, to allow quicker convergence for equations that are nearly in equilibrium.

In practice, c_i is constrained by a minimum value when c_i is decaying exponentially toward zero. This lower bound must be selected to insure that its value in no way affects the physics but yet decouples the equation from accurate integration. Decoupling is accomplished by avoiding applying (80) to all equations that have decayed to values corresponding to their lower bounds. Convergence for these equations is then trivial and the function no longer affects the size of the timestep. For equations that are decaying exponentially to zero, with time constants that are small enough to control the timestep, it is important for efficiency reasons to decouple these equations at the largest lower bound possible.

In practical application the maximum solution speed is realized by keeping the allowed number of corrector iterations small, typically one or two. If satisfactory convergence of all equations has not been obtained before or during the last iteration, the step is started over with a smaller timestep. By keeping the maximum number of iterations small, a minimum amount of time is wasted on an unstable or nonconvergent step. When nonconvergence is encountered, it is more efficient to reduce the timestep sharply (a factor of 2 or 3). On the other hand, when increasing the timestep, as, for example, when convergence is achieved on the first or second

iteration, it is best to increase only by 5–10% each step. The asymptotic integration scheme was compared against the program EPISODE [80, 81] to evaluate the characteristics of the algorithm when applied to the photochemical reaction mechanism. For all EPISODE calculations semi-relative error control was used with a convergence tolerance of 0.0001. The starting and maximum step sizes were set to 10^{-5} and 10 minutes, respectively.

Both programs were exercised over a wide range of initial conditions, pseudo steady state approximations, photolysis rates and diurnal cycles. Two features were apparent in all the tests, and they are illustrated in Table VIII. First, and perhaps most important, is that there were negligible differences in the predictions of both schemes over solution steps comparable to the maximum expected transport times. For example, after 30 minutes the maximum discrepancy between the two schemes for the species NO, NO_2, and O_3 was $O(0.2\%)$.

The most striking difference between the two schemes is the high start up costs associated with the EPISODE algorithm. During the initial 30 minutes there is a factor of 7 difference in the computation time. Once started, however, the incremental cost, per time interval, of using EPISODE becomes successively smaller. From a

TABLE VIII

Comparison of Start Up Times for EPISODE and Hybrid Solution Scheme for Typical Smog Chamber Experiment

Time (min)	Species	Concentration (parts-per-million by volume) Episode	Hybrid solver	Computer time (ms) per 30 minute step Episode	Hybrid
30	NO	0.0567	0.0567 (0.00)*	1014	152
	NO_2	0.4070	0.4077 (0.17)		
	O_3	0.0834	0.0832 (−0.24)		
60	NO	0.0202	0.0203 (0.50)	175	104
	NO_2	0.3889	0.3914 (0.64)		
	O_3	0.2191	0.2194 (0.14)		
90	NO	0.0110	0.0107 (−2.73)	79	81
	NO_2	0.3329	0.3290 (−1.17)		
	O_3	0.3383	0.3450 (1.98)		
120	NO	0.0066	0.0062 (−6.06)	47	70
	NO_2	0.2652	0.2557 (−3.58)		
	O_3	0.4391	0.4497 (2.41)		
				1315 ms	407 ms

* Percentage difference between EPISODE and Hybrid solution technique = 100 [Hybrid/EPISODE − 1].

practical point of view, considering the short integration intervals in an operator splitting solution, the asymptotic scheme is clearly preferable to the EPISODE algorithm for the present application.

9.4. *Implementation of Asymptotic Integration Scheme*

Using the operator splitting procedures described earlier, (9) can be written in the form

$$\text{Transport} \qquad \frac{\partial c_i}{\partial t} = L(\mathbf{x}, t)\, c_i, \tag{81}$$

$$\text{Chemistry} \qquad \frac{\partial c_i}{\partial t} = f_i(c_1, \ldots, c_p, t). \tag{82}$$

If $\mathbf{T}_x$, $\mathbf{T}_y$, $\mathbf{T}_z$ and $\mathbf{C}_c$ are the numerical approximations to the transport and chemistry operators then a complete solution can be obtained from the sequence

$$\mathbf{c}_i^{n+1} = \mathbf{T}_x \mathbf{T}_y \mathbf{T}_z \mathbf{C}_c(2\Delta t)\, \mathbf{T}_z \mathbf{T}_y \mathbf{T}_x \mathbf{c}_i^{n-1}, \tag{83}$$

where $\mathbf{C}_c$ symbolically denotes the means of solving (82) at each of the grid points given a set of initial conditions. Most of the computer time required for each cycle (83) is consumed by the chemical solution $\mathbf{C}_c$. Two advantages of operator splitting are apparent, the chemistry is decoupled from the transport and it can be solved for a period $2\Delta t$. This latter feature is particularly important because most of the overhead associated with solving (82) occurs at the start of each initial value problem; subsequent time increments can be obtained at minimal expense.

The actual sequence of operations used to obtain a solution of (83) is as follows. Solve

$$\frac{\partial c_i^*}{\partial t} = L_x c_i^*, \tag{84}$$

$$\frac{\partial c_i^{**}}{\partial t} = L_y c_i^{**}, \tag{85}$$

$$\frac{\partial c_i^{***}}{\partial t} = L_z c_i^{***}, \tag{86}$$

on the interval $t^{n-1} \leqslant t \leqslant t^n$,

$$\frac{\partial c_i}{\partial t} = f_i(c_1, \ldots, c_p, t) \tag{87}$$

on the interval $t^{n-1} \leqslant t \leqslant t^{n+1}$, and then solve the system (84)–(86) in the reverse order, i.e., in z, y, and x directions. The initial conditions for each of the problems (84)–(86) are: $c_i^*(t^{n-1}) = c_i(t^{n-1})$, $c_i^{**}(t^{n-1}) = c_i^*(t^n)$, $c_i^{***}(t^{n-1}) = c_i^{**}(t^n)$ and for (87) $c_i(t^{n-1}) = c_i^{***}(t^n)$.

Unfortunately, there is little guidance in the literature relevant to establishing a priori bounds on the maximum value of Δt. Within the airshed model it has been observed that the convergence of the sequence (83), during the photochemically active daylight hours, is controlled more by the rate of vertical turbulent mixing than by the Courant limit of the horizontal advection schemes. As a result of considerable experimentation with successively smaller time steps it was found that if $2\Delta t$ was limited to be less than 10 minutes, the predicted results were comparable to cases in which the two-dimensional coupled problem (9) was solved directly. At night when there is little or no chemical activity, the chemical time steps are controlled by the stability limits of the advection schemes. The total computer time required to simulate the concentration dynamics of 15 species at 3000 grid points for a 24-hour period is $O(50$ minutes) on an IBM 370/168. The interested reader is referred to McRae *et al.* [91] for a description of the air pollution model.

10. Conclusions

In this paper, a variety of numerical methods were studied in order to identify a solution scheme for the atmospheric diffusion equation. As a result of this investigation, a composite technique was developed in which operator-splitting was first used to segment the three-dimensional system of equations into a sequence of one-dimensional problems. Each transport step was further simplified to three basic components: an advection step, application of a nonlinear filter and finally a diffusion step. A Galerkin, linear finite element scheme was adopted for the critical advection step. The results of numerous numerical experiments indicate that this algorithm, together with the filter step, preserves extreme values, gradients, total mass and mean square concentration. The solution of the chemical kinetics component is carried out by a second-order predictor, iterated corrector technique, in combination with an asymptotic treatment of the stiff components of the problem [90, 91]. Computational economies are achieved by implementation of the pseudo steady state approximation.

APPENDIX: Notation

$a(\mathbf{X}, t), b(\mathbf{X}, t)$	Coefficients associated with boundary conditions (3)
a_i	Production rate for species i, $i = 1, 2,..., p$
$\mathbf{A}$	An $r \times r$ matrix representing the discrete approximation to L at r computational grid points. ($\mathbf{A}_j$ is the discrete representation of L_j)
b_i	First-order coefficient for removal rate of species i, $i = 1, 2,..., p$
B	Linear boundary operator
$\mathbf{B}, \mathbf{H}, \mathbf{M}, \mathbf{P}, \mathbf{Q}, \mathbf{S}$	Matrices of dimension $r \times r$ associated with different spatial discretization techniques
$\mathbf{c}_d$	Concentration vector of nonstiff components
$c_i(k)$	kth iterate of c_i

$c_i(\mathbf{X}, t), c_i(\mathbf{x}, t)$	Concentrations of species i in the physical and computational domains; $i = 1, 2,..., p$
$\mathbf{c}_i(\mathbf{x}, t)$	Concentration vector of species i at r computational points $\mathbf{c}_i(\mathbf{x}, t) = (c_i(\mathbf{x}_j, t); j = 1, 2,..., r)$
$\mathbf{c}_s$	Concentration vector of stiff components
C	Courant number
$\mathbf{C}_c$	Symbol representing solution of the chemical kinetics
f_i	Chemical formation (or depletion) rate of species i $\mathbf{f}_i = (f_i(c_1(\mathbf{x}_j, t),..., c_p(\mathbf{x}_j, t)); j = 1, 2,..., r)$
$\mathbf{F}$	Mapping function that transforms points from $\mathbf{X}$ into $\mathbf{x}$
$g_i(\mathbf{X}, t)$	Species specific boundary condition coefficient
$h(X, Y)$	Topographic surface (lower boundary of region)
$H(X, Y, t)$	Time varying upper surface of region
$\mathbf{I}$	Unit matrix of dimension $r \times r$
$\mathbf{J}$	Jacobian matrix with elements $\partial f_i/\partial c_j$, $i, j = 1, 2,..., p$
k_l	Rate constant for reaction l
K_f	Coefficient in noise filter
K_n	Diffusion coefficient associated with noise filter
$\mathbf{K}$	Second-order turbulent eddy diffusion tensor (usually a diagonal matrix with elements K_{xx}, K_{yy}, K_{zz}). In the computational domain $\mathbf{K}_{xx}$ are the values of K_{xx} at each of the r grid points.
L	Three-dimensional, semi-linear, elliptic differential operator (L_x, L_y, L_z are the components in x, y and z directions).
R	Stiffness ratio
r	Radial coordinate for Crowley problem
t	Time
T	Extent of time interval for solution
$\mathbf{T}$	Composite transport operator (T_j is the transport operator for the jth direction)
$\mathbf{u}(\mathbf{X}, t)$	Velocity field in physical domain $\mathbf{u} = (u, v, w)$
$\mathbf{U}$	Velocity field in computational domain $\mathbf{U} = (u_j; j = 1, 2,..., r)$
$\mathbf{V}(\mathbf{x}, t)$	Velocity field in transformed domain $\mathbf{V} = (u, v, W)$
$\mathbf{x}$	Point in computational domain $\mathbf{x} = (x, y, z) \in \Omega_c$
$\mathbf{X}$	Point in physical domain $\mathbf{X} = (X, Y, Z) \in \Omega_t$

Greek Symbols

α, β	Time varying coefficients associated with the concentration and velocity distributions employed in the Galerkin formulation
δ	Discretization unit (either finite element or grid size)
ε	Relative error criterion
Δt	Basic time step of atmospheric diffusion equation
$\Delta\tau$	Time step for solution of the chemical kinetics
Δx	Size of computational grid element
ΔH	$= H(X, Y, t) - h(X, Y)$

θ Volume to width ratio for test wave forms or angular coordinate
λ An arbitrary parameter with $\lambda \geqslant 0$
λ_i Eigenvalue of Jacobian matrix $\mathbf{J}$, $i = 1, 2, ..., p$
σ Normal direction to $\partial\Omega$
$\mathbf{v}$ Material flux $= \mathbf{K}_{xx}(\partial \mathbf{c}/\partial x) - \mathbf{U}\mathbf{c}$
ϕ_j Basis functions for Galerkin formulation
ψ_j Filter function variable (0, 1)
ω Fourier frequency for test wave forms and angular velocity for Crowley problem
Ω_c Time invariant computational domain
Ω_t Time varying physical domain (Ω_0 initial extent)
$\partial\Omega$ Domain boundary

Sub- and Superscripts

a Advective transport step
c Indicates computational domain
d Diffusive transport step or nonstiff component of concentration vector
e Grid point subscript for testing sign changes during filter application
i Species index
j Index to denote coordinate direction ($x = 1$, $y = 2$, $z = 3$) or computational grid point ($j = 1, 2, ..., r$)
k Iteration counter during one time step
l Domain of final filter application (number of grid points)
m Half width of enveloping interval for testing slope change in filtering scheme
n Time level
o Initial conditions
p Number of chemical species
q Spatial integration index for Galerkin formulation
r Number of computational grid points
s Spatial integration index for Galerkin formulation or stiff component of concentration vector

ACKNOWLEDGMENTS

This work was supported by the State of California Air Resources Board under Contracts A5-046-87 and A7-187-30. Additional funding was provided by a Department of Energy Institutional Grant EY-76-G-03-1305. The assistance of Dr. T. R. Young of the Naval Research Laboratory, and Dr. J. W. Tilden of the Environmental Quality Laboratory is appreciated.

REFERENCES

1. J. H. SEINFELD, "Air Pollution: Physical and Chemical Fundamentals," McGraw–Hill, New York, 1975.
2. W. R. GOODIN, G. J. MCRAE, AND J. H. SEINFELD, *J. Appl. Meteorol.* 18 (1979a), 761.

3. W. R. GOODIN, G. J. MCRAE, AND J. H. SEINFELD, *J. Appl. Meteorol.* **19** (1979b), 98.
4. W. R. GOODIN, G. J. MCRAE, AND J. H. SEINFELD, *J. Appl. Meteorol.* **20** (1981), 92.
5. S. D. REYNOLDS, P. M. ROTH, AND J. H. SEINFELD, *Atmospheric Environment* **7** (1973), 1033.
6. A. H. FALLS AND J. H. SEINFELD, *Environ. Sci. Technol.* **12** (1978), 1398.
7. T. GAL-CHEN AND R. C. SOMERVILLE, *J. Comput. Phys.* **17** (1975), 209.
8. T. L. CLARK, *J. Comput. Phys.* **24** (1977), 186.
9. P. J. ROACHE, "Computational Fluid Dynamics," Second ed., Hermosa Publications, Albuquerque, 1976.
10. J. L. ANDERSON, S. PREISER, AND E. L. RUBIN, *J. Comput. Phys.* **2** (1968), 279.
11. W. L. OBERKAMPF, *Int. J. Numer. Methods Engrg.* **10** (1976), 211.
12. M. VINOKUR, *J. Comput. Phys.* **14** (1974), 105.
13. A. LAPIDUS, *J. Comput. Phys.* **2** (1967), 154.
14. S. B. MARGOLIS, *J. Comput. Phys.* **27** (1978), 410.
15. R. C. Y. CHIN AND R. L. BRAUN, *J. Comput. Phys.* **34** (1980), 74.
16. B. ENGQUIST, B. GUSTAFSSON, AND J. VREEBURG, *J. Comput. Phys.* **27** (1978), 295.
17. J. DOUGLAS, T. DUPONT, AND R. EWING, *SIAM J. Numer. Anal.* **16** (1979), 503.
18. E. J. KANSA, *J. Comput. Phys.* **42** (1981), 152.
19. J. DESCLOUX, *SIAM J. Numer. Anal.* **9** (1972), 260.
20. A. ISERLES, *SIAM J. Numer. Anal.* **18** (1981), 1.
21. A. W. RIZZI AND H. E. BAILEY, *AIAA J.* **14** (1976), 621.
22. A. W. RIZZI AND M. INOUYE, *AIAA J.* **11** (1973), 1478.
23. R. J. KEE AND J. A. MILLER, *AIAA J.* **16** (1978), 169.
24. P. D. THOMAS AND K. H. WILSON, *AIAA J.* **14** (1976), 629.
25. J. DOUGLAS AND J. E. GUNN, *Numer. Math.* **6** (1964), 428.
26. J. E. DENDY, *SIAM J. Numer. Anal.* **14** (1977), 313.
27. W. R. BRILEY AND H. MCDONALD, *J. Comput. Phys.* **34** (1980), 54.
28. T. J. WEARE, *Int. J. Numer. Methods Engrg.* **14** (1979), 921.
29. N. N. YANENKO, "The Method of Fractional Steps," Springer-Verlag, New York, 1971.
30. G. I. MARCHUK, *in* "Numerical Solution of Partial Differential Equations, II," Academic Press, New York, 1971.
31. G. I. MARCHUK, "Methods of Numerical Mathematics," Springer-Verlag, New York, 1975.
32. N. N. YANENKO, V. M. KOVENYA, V. D. LISEJKIN, V. M. FOMIN, AND E. V. VOROZHTSOV, *Comput. Methods Appl. Mech. Engrg.* **17** (1979), 659.
33. J. L. MORRIS, *J. Comput. Phys.* **5** (1970), 219.
34. A. R. GOURLAY AND A. R. MITCHELL, *SIAM J. Numer. Anal.* **6** (1969), 37.
35. A. R. GOURLAY, *Proc. Roy. Soc. London Ser. A* **323** (1971), 219.
36. D. GOTTLIEB, *SIAM J. Numer. Anal.* **9** (1972), 650.
37. M. CRANDALL AND A. MAJDA, *Numer. Math.* **34** (1980), 285.
38. E. S. ORAN AND J. P. BORIS, *Prog. Energy Combustion Sci.* **7** (1981), 1.
39. D. ANDERSON AND B. FATTAHI, *J. Atmospheric Sci.* **31** (1974), 1500.
40. C. Y. LIU, W. R. GOODIN, AND C. M. LAM, *Comput. Methods Appl. Mech. Engrg.* **9** (1976), 281.
41. G. R. CARMICHAEL, T. KITADA, AND L. K. PETERS, *Computers and Fluids* **8** (1980), 155.
42. J. P. BORIS AND D. L. BOOK, *J. Comput. Phys.* **11** (1973), 38.
43. J. P. BORIS AND D. L. BOOK, *J. Comput. Phys.* **20** (1976), 397.
44. D. L. BOOK, J. P. BORIS, AND K. HAIN, *J. Comput. Phys.* **18** (1975), 248.
45. Y. ADAM, *Comput. Math. Appl.* **1** (1975), 393.
46. Y. ADAM, *J. Comput. Phys.* **24** (1977), 24.
47. R. S. HIRSH, *J. Comput. Phys.* **19** (1975), 90.
48. F. THIELE, *J. Comput. Phys.* **27** (1978), 1.
49. M. CIMENT AND S. H. LEVENTHAL, *Math. Comp.* **32** (1978), 143.
50. M. CIMENT, S. H. LEVENTHAL, AND B. C. WEINBERG, *J. Comput. Phys.* **28** (1978), 135.
51. J. J. CONNOR AND C. A. BREBBIA, "Finite Element Techniques for Fluid Flow," Butterworth, London, 1976.

52. G. STRANG AND G. J. FIX, "An Analysis of the Finite Element Method," Prentice-Hall, Engelwood Cliffs, N.J.
53. K. W. MORTON AND A. K. PARROTT, *J. Comput. Phys.* **36** (1980), 249.
54. J. E. FROMM, *J. Comput. Phys.* **3** (1968), 176.
55. W. P. CROWLEY, *Monthly Weather Rev.* **96** (1968), 1.
56. H. S. PRICE, R. S. VARGA, AND J. E. WARREN, *J. Math. Phys.* **45** (1966), 301.
57. H. KREISS AND J. OLIGER, "Methods for the Approximation Solution of Time Dependent Problems," GARP Publication Series No. 10, World Meteorological Organization.
58. H. J. P. CULLEN, *Quart. J. Roy. Meteorol. Soc.* **102** (1976), 77.
59. H. STORCH, *Beiträge Phys. Atmosphare* **51** (1978), 189.
60. W. H. RAYMOND AND A. GARDNER, *Monthly Weather Rev.* **104** (1976), 1583.
61. L. B. WAHLBIN, *in* "Mathematical Aspects of Finite Elements in Partial Differential Equations," Academic Press, New York, 1974.
62. J. D. MAHLMAN AND R. W. SINCLAIR, "Advances in Environmental Science and Technology," Vol. 8, Wiley, New York, 1977.
63. B. VAN LEER, *J. Comput. Phys.* **14** (1974), 361.
64. C. K. FORESTER, *J. Comput. Phys.* **23** (1977), 1.
65. C. R. MOLENKAMP, *J. Appl. Meteorol.* **7** (1968), 160.
66. T. NITTA, *J. Meteorol. Soc. Japan* **40** (1962), 13.
67. J. M. VARAH, *SIAM J. Numer. Anal.* **8** (1971), 569.
68. J. M. VARAH, *SIAM J. Numer. Anal.* **8** (1971), 598.
69. J. H. CHEN, *J. Comput. Phys.* **13** (1973), 522.
70. B. GUSTAFSSON, H. O. KREISS, AND A. SUNDSTROM, *Math. Comp.* **26** (1972), 649.
71. B. GUSTAFSSON, *J. Comput. Phys.* **34** (1980), 108.
72. D. GOTTLIEB AND E. TURKEL, *J. Comput. Phys.* **26** (1978), 181.
73. D. M. SLOAN, *Int. J. Numer. Methods Engrg.* **15** (1980), 1113.
74. R. A. WILLOUGHBY, "Stiff Differential Systems," Plenum, New York, 1974.
75. J. D. LAMBERT, *in* "Computational Techniques for Ordinary Differential Equations," Academic Press, London, 1976.
76. D. D. WARNER, *J. Phys. Chem.* **81** (1977), 2329.
77. A. R. CURTIS, *in* "Numerical Software—Needs and Availability," Academic Press, London, 1978.
78. H. O. KREISS, *SIAM J. Numer. Anal.* **16** (1979), 980.
79. L. F. SHAMPINE AND C. W. GEAR, *SIAM Rev.* **21** (1979), 1.
80. A. C. HINDMARSH AND G. D. BYRNE, "EPISODE: An Experimental Program for the Integration of Systems of Ordinary Differential Equation Systems," Lawrence Livermore Laboratory Report UCID-30112, 1975.
81. G. D. BYRNE, A. C. HINDMARSH, K. R. JACKSON, AND H. G. BROWN, *Comput. Chem. Engrng.* **1** (1977), 133.
82. R. C. AIKEN AND L. LAPIDUS, *AIChE J.* **21** (1975a), 817.
83. R. C. AIKEN AND L. LAPIDUS, *AIChE J.* **21** (1975b), 1227.
84. P. V. KOKOTOVIC, J. J. ALLEMONG, J. R. WINKELMAN, AND J. H. CHOW, *Automatica* **16** (1980), 23.
85. H. H. ROBERTSON, *J. Inst. Math. Appl.* **18** (1976), 249.
86. W. H. ENRIGHT AND M. S. KAMEL, *ACM Trans. Math. Software* **5** (1979), 374.
87. D. S. WATKINS, *SIAM J. Numer. Anal.* **18** (1981), 13.
88. J. D. LAMBERT, *SIAM J. Numer. Anal.* **18** (1981), 83.
89. T. R. YOUNG, "CHEMEQ—A Subroutine for Solving Stiff Ordinary Differential Equations," NRL Memorandum Report 4091, Naval Research Laboratory, Washington, D.C. (1980).
90. T. R. YOUNG AND J. P. BORIS, *J. Phys. Chem.* **81** (1977), 2424.
91. G. J. MCRAE, W. R. GOODIN, AND J. H. SEINFELD, *Atmospheric Environment*, in press.

Printed by the St. Catherine Press Ltd., Tempelhof 41, Bruges, Belgium

CHAPTER 10

SENSITIVITY AND UNCERTAINTY ANALYSIS OF URBAN SCALE AIR POLLUTION MODELS

10.1 Introduction

When complex systems are described by mathematical models a natural question arises: what are the influences of uncertainties in the characterization of physical processes? While a variety of means can be employed to answer the question considerable insight can often be gained from formal studies of the effects of parameter variations. Such sensitivity analyses can provide a direct means for revealing how the predictions vary as a result of changes in model or input variables. Information derived from these investigations is useful for defining limits of valid applications and identifying those areas which might require additional development work.

This chapter presents a technique, the Fourier Amplitude Sensitivity Test (FAST), which can be used to assess the relative influence of parameter variations on the model predictions. A major advantage of this procedure is that, unlike conventional methods, it readily accommodates arbitrarily large variations in the parameters. This feature is exploited in two practical applications. One example involves a combined sensitivity/uncertainty analysis of a photochemical reaction mechanism for the polluted troposphere and the other, a study of a simplified form of the atmospheric diffusion equation. Both cases, and a description of the computational procedure, have been previously published as Koda et al. (1979b), Falls et al. (1979) and McRae and Tilden (1980); these articles form sections of this chapter.

10.2 Methods for Sensitivity Analysis of Mathematical Models

An inevitable consequence of using mathematical models to describe complex systems is that some approximations are involved. These uncertainties arise either from the characterization of the physical processes or from the measurement errors inherent in model input variables. Leaving aside the conceptual question of model validity, the essential problem in sensitivity analysis is to examine the changes in system outputs which result from variations in either the input or structural parameters. This section presents a brief literature survey of different sensitivity analysis methods. While some of the techniques are well known in control theory (Cruz, 1973; Tomovic, 1963; Tomovic and Vucobratovic, 1972; and Frank, 1978) they have not, as yet, been extensively employed in atmospheric modeling. Gelinas and Vajk (1978) have, however, examined the suitability of some methods for air quality applications.

In order to provide a framework for the survey consider a general system of the form

$$F(\underline{u},\underline{k}) = 0 \qquad (10.1)$$

where F is a general algebraic or differential operator, $\underline{u}$ is a vector of n output variables and $\underline{k}$ a set of m parameters. Given such a model there are four basic factors which need to be considered when selecting a method or an approach for performing a sensitivity analysis of a model system. The issues are: the extent of the parameter domain, the sensitivity measure or criterion, the combined roles of parameter sensitivity and uncertainty, and finally, the computational cost.

From a practical point of view a dominant consideration in selecting a sensitivity analysis method is the computational cost. When comparing different techniques it is important to keep in mind two basic considerations: one is simply the number of times that the model must be solved to obtain the desired sensitivity information. The second factor is the amount of time required to implement the particular technique. In many situations it is this latter factor which has a major influence on the selection process. For example some techniques do not require extensive programming beyond that needed to solve the basic model while others can require considerable additional effort on the part of the investigator. While the cost of each method can be expressed in terms of the number of required solutions the final choice will often be dictated by the complexity of the basic system being analysed. Gelinas and Vajk (1978) have carried out an extensive study of the expected cost of applying different sensitivity analysis methods to some different mathematical models of environmental processes.

Perhaps the most fundamental constraint which dictates the choice of a sensitivity analysis method is the extent of parameter variations to be considered. All the feasible values of the parameter vector $\underline{k}$ define the parameter space. Varying the parameters over their full domain produces the m-dimensional surface $\underline{u}(\underline{k})$. A typical example is depicted in Figure 10.1 where the response of one model output, $u_i(t)$, to variations in $\underline{k}$, is shown. In this case the extent of parameter space is defined by the upper and lower limits for each of the variables k_1 and k_2. The point Q on the solution surface represents the magnitude of u_i

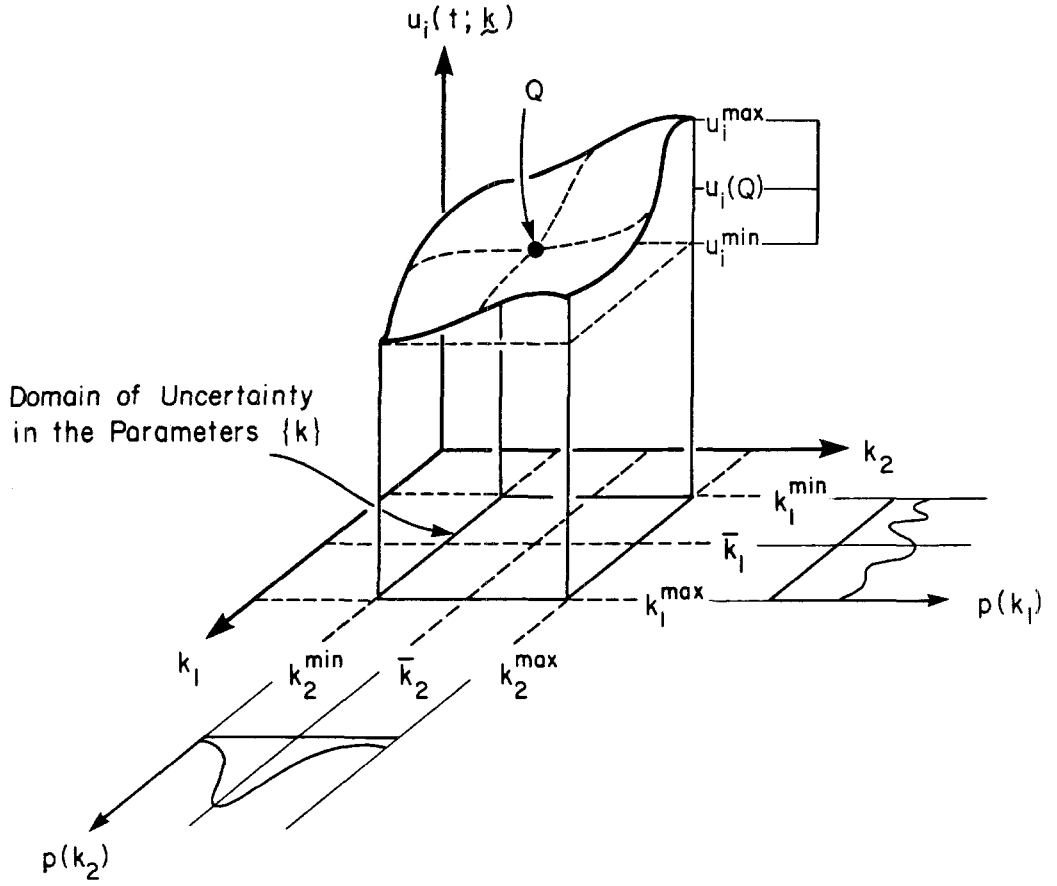

FIGURE 10.1

Schematic Representation of the Parameter Space k and the Response Surface for State Variable $u_i(t;\underset{\sim}{k})$

resulting from the parameter combination $(\bar{k}_1, \bar{k}_2)$. These nominal values typically represent the best a priori estimates of the parameters.

The ultimate goal of any sensitivity analysis is to determine the form of the system output resulting from the parameter variations. Since most models will require numerical solution, the outputs needed to define the response surface will only be available for a finite set of parameter combinations. Given this situation the basic problem then becomes how to sample the parameter space with sufficient regularity to adequately characterize $\underline{u}(\underline{k})$. An analysis which accounts for simultaneous variations in all the parameters over their full range of uncertainties is called a global method. Conversely, local analyses attempt to infer the shape or value of the response surface at a particular point. The limitations of local approaches are readily apparent, particularly if the model is highly nonlinear or the range of parameter variations is large. A typical case is shown in Figure 10.2. For small variations in $\underline{\bar{k}}$ the tangent plane approximation differs from the actual surface by only a small amount. Unfortunately this simplification does not contain useful information on the behavior of a u away from $\underline{\bar{k}}$. This example highlights a critical limitation of local methods when they are applied to problems which involve large uncertainties in the parameters. For example, a variable to which the model predictions are not especially sensitive at say $\underline{\bar{k}}$, may have such a large range of uncertainty that, when all possible variations are considered, its influence on the results may be quite large. Information of this type is very useful in the design of experimental programs because more effort can be devoted to elucidating

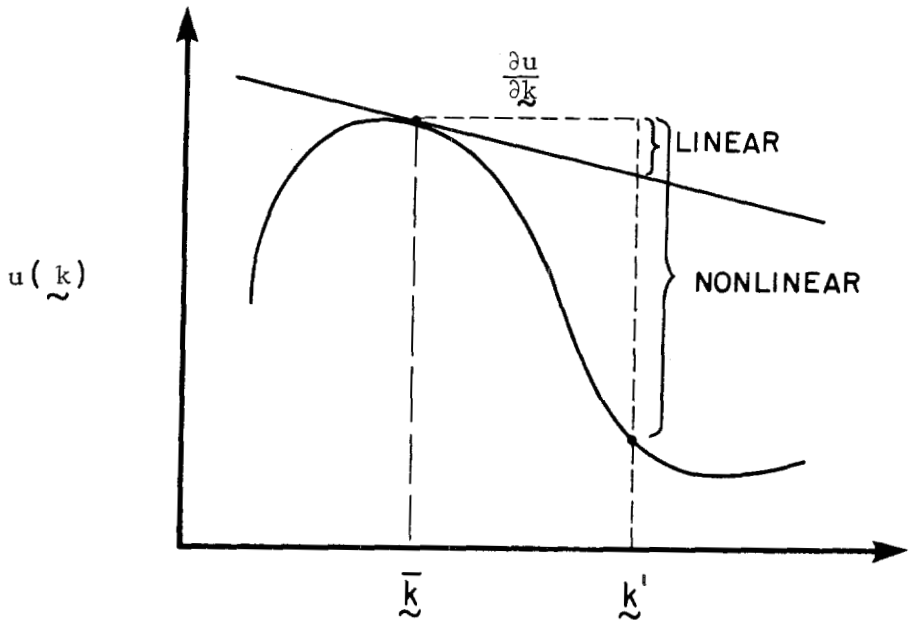

FIGURE 10.2

Linear and Nonlinear Sensitivity Analysis

the important phenomena and eliminating potentially unproductive measurements.

So far in the discussion all values of $\underline{k}$ have been considered to be equally likely; however, in practice, the parameters often have non-uniform probability distributions. While the response surface, $\underline{u}(\underline{k})$, is independent of all assumptions about the likely parameter combinations, the expected value or mean sensitivity, $\langle \underline{u}(\underline{k}) \rangle$, depends on both the probability distribution for $\underline{k}$ and the form of the model. A sensitivity analysis then refers to the influence of parameter variations on the model predictions whereas a combined sensitivity/uncertainty analysis considers the additional factor of the parameter distributions. Regardless of refinements in knowledge of parameter accuracy the global sensitivity of the model remains the same. In Figure 10.1 the probability distributions associated with k_1 and k_2 are independent and denoted by $p(k_1)$ and $p(k_2)$. By considering $\underline{k}$ to be a random vector with probability density $P(\underline{k})$ the ensemble mean sensitivity can be expressed in the form

$$\langle u_i(k) \rangle = \int_{\underline{k}} \cdots \int u_i(k_1,\ldots,k_m)\ P(k_1,\ldots,k_m)\ dk_1,\ldots,dk_m \qquad (10.2)$$

In general (12.2) does not correspond to the solution obtained when the parameters are set to their nominal values $\bar{\underline{k}}$. A variety of other sensitivity measures are available for assessing the system performance. Some of the more common criteria are listed below and in Table 10.1; further details can be found in Frank (1978). Perhaps the most elementary criterion is the change in system output, $\delta\underline{u}$, which results from an arbitrary variation, $\delta\underline{k}$, in the parameters away from some nominal value $\bar{\underline{k}}$ i.e.

TABLE 10.1

Summary of Sensitivity Measures

SENSITIVITY MEASURE	DEFINITION
Response from arbitrary parameter variation $\underline{k}$	$\underline{u} = \underline{u}(\bar{\underline{k}} + \delta\underline{k}) - \underline{u}(\underline{k})$
Normalized Response	$D_i = \dfrac{\delta u_i}{u_i(\bar{\underline{k}})}$; $i=1,2,\ldots,n$
Local Gradient Approximation	$\delta \underset{\sim}{u} \simeq [S]\delta\underline{k}$; $S_{ij} = \dfrac{\partial u_i}{\partial k_j}$
Normalized Gradient	$S^n_{ij} = \dfrac{\bar{k}_j}{u_i(\bar{\underline{k}})} \dfrac{\partial u_i}{\partial k_j}$
Average Response	$\overline{u_i(\bar{\underline{k}})} = \dfrac{\int_{\underline{k}}\cdots\int u_i(\bar{\underline{k}})\,d\underline{k}}{\int_{\underline{k}}\cdots\int d\underline{k}}$
Expected Value	$\langle u_i(\underline{k})\rangle = \int_{\underline{k}}\cdots\int u_i(\underline{k})P(\underline{k})\,d\underline{k}$
Variance	$\delta_i^2(\underline{k}) = \langle u_i(\underline{k})^2\rangle - \langle u_i(\underline{k})\rangle^2$
Extrema	$\max\,[u_i(\underline{k})]$, $\min[(u_i(\underline{k})]$

$$\delta \underline{u} = \underline{u}(\bar{\underline{k}} + \delta \underline{k}) - \underline{u}(\bar{\underline{k}}) \tag{10.3}$$

This difference measure is often expressed in the normalized form

$$D_i = \frac{\delta u_i}{u_i(\bar{\underline{k}})} = \frac{u_i(\bar{\underline{k}} + \delta \underline{k})}{u_i(\bar{\underline{k}})} - 1 \tag{10.4}$$

If the parameters are varied one at a time then (10.4) is given by

$$D_{ij} = D_i(\delta k_j) = \frac{u_i(\bar{\underline{k}} + \delta k_j)}{u_i(\bar{\underline{k}})} - 1 \tag{10.5}$$

Both of these criteria are essentially point estimates. If a sufficiently large number of $\underline{k}$ combinations are considered then it is possible to develop estimates of some of the important response statistics, namely: the mean, variance and extrema of $\underline{u}(\underline{k})$. The extreme values are often of critical importance in environmental applications. In the interests of computational economy it is desirable to obtain as much information as possible from each parameter combination. One means is to extrapolate the results away from the nominal solution $\underline{u}(\bar{\underline{k}})$. A wide class of methods can be represented by the form

$$\delta \underset{\sim}{u} \simeq [S]\ \delta \underline{k} \tag{10.6}$$

The most simple case corresponds to the well known Taylor series expansion for which the elements of the matrix [S] are given by

$$S_{ij} = \frac{\partial u_i}{\partial k_j} \quad ; \quad i=1,2,\ldots,n \qquad j=1,2,\ldots,m \tag{10.7}$$

Equation (10.7) is often written in the normalized form

$$S_{ij}^{n} = \frac{\partial \ \ell n(u_i)}{\partial \ \ell n(k_j)} = \frac{\bar{k}_j}{u_i(\bar{k})} \frac{\partial u_i}{\partial k_j} \tag{10.8}$$

Methods which neglect the higher order terms in the expansion are referred to as first order or linear techniques. In space and time dependent models the linear sensitivities are more appropriately defined in terms of operator or Frechet derivatives.* These derivatives are linear continuous and have the usual properties of the classical differentials of functions of one or more variables. In particular the chain rule holds (Nashed, 1971). This latter result is extremely useful in practical applications.

Once the basic model has been formulated and an appropriate sensitivity measure identified the next step is to actually solve the sensitivity problem. As noted previously there are two basic approaches: local or global techniques. In order to illustrate how local methods

---

*Consider a mapping $F:X \to Y$ where both X and Y are complete, normed linear spaces. Given that $x \in X$, then if a bounded linear map, F', exists such that

$$\lim_{||\underline{h}|| \to 0} \frac{||F(\underline{x}+\underline{h}) - F(\underline{x}) - F'(\underline{x})\underline{h}||_Y}{||h||_X} = 0$$

then F is said to be Frechet differentiable at $\underline{x}$ and $F'(\underline{x})$ is the Frechet derivative of F at $\underline{x}$. Under certain conditions the continuous, linear operator $F'(\underline{x})$ is represented by the Jacobian matrix at $\underline{x}$ (Dieudonné, 1960; Tapia, 1971).

are applied, consider the following set of ordinary differential equations and initial conditions.

$$F(\underline{u},\underline{k}) \equiv \frac{d\underline{u}}{dt} - \underline{f}(\underline{u},\underline{k}) = 0 \tag{10.9}$$

$$\underline{u}(o) = \underline{u}^{o} \tag{10.10}$$

A very wide class of practical problems can be described by systems of the form (10.9-10). The change in $\underline{u}$ away from some nominal parameter values $\bar{\underline{k}}$ can be expressed, using operator derivatives in the form

$$\frac{d}{dt}\left(\frac{\partial \underline{u}}{\partial \underline{k}}\right) - \frac{\partial \underline{f}}{\partial \underline{u}}\left(\frac{\partial \underline{u}}{\partial \underline{k}}\right) - \frac{\partial \underline{f}}{\partial \underline{k}} = 0 \tag{10.11}$$

or more compactly as the matrix differential equation

$$\dot{[Z]} = [J][Z] + [B] \tag{10.12}$$

where

$$Z_{ij} = \frac{\partial u_i}{\partial k_j} \qquad \begin{matrix} i=1,2,\ldots,n \\ j=1,2,\ldots,m \end{matrix} \tag{10.13}$$

$$J_{ij} = \left.\frac{\partial f_i}{\partial u_j}\right|_{f_i[\underline{u}(\bar{\underline{k}}),\bar{\underline{k}}]} \qquad \begin{matrix} i=1,2,\ldots,n \\ j=1,2,\ldots,n \end{matrix} \tag{10.14}$$

$$B_{ij} = \left.\frac{\partial f_i}{\partial k_j}\right|_{f_i[\underline{u}(\bar{\underline{k}}),\bar{\underline{k}}]} \qquad \begin{matrix} i=1,2,\ldots,n \\ j=1,2,\ldots,m \end{matrix} \tag{10.15}$$

A typical column of [Z], defined by $\partial u_i/\partial k_j$; i=1,2,...,n, denotes the sensitivity of $\underline{u}$ with respect to the jth parameter. The initial conditions for (10.12) are given by [Z(o)] = [o] unless any $u_i(o)$ are included in $\bar{\underline{k}}$

in which case the appropriate elements of [Z] are set to one. Because there is no direct coupling in (10.12) each of the m vector differential equations can be solved independently.

There is a variety of ways to obtain the desired sensitivity information. The simplest involves a direct solution of the coupled systems of n(m+1) ordinary differential equations (10.9-10 and 10.12). This method was used by Dickinson and Gelinas (1976) and Atherton et al. (1975). Operationally it is sometimes more convenient to consider the parameters one at a time; if this is done then the number of required solutions increases to 2nm. This number can be reduced, at some loss of numerical accuracy, to n(m+1) if the nominal solution $\underset{\sim}{u}(\bar{\underline{k}},t_p)$, p=1,2,... are retained and used for constructing interpolated approximations to the $\underline{u}(\underline{k},t)$ needed in the evaluation of (10.14 and 10.15). While the three approaches produce similar results they can involve considerably different computational costs: $0[n^3(m+1)^3]$ for the coupled system, $0[m(2n)^3]$ for the one parameter at a time case and $0[(m+1)n^3]$ for the interpolated solution. Since the equations of interest are usually stiff, and m(>n) is in general quite large, the above procedures can be quite expensive. Another approach, which is the focus of work by Hwang et al. (1978), Dougherty et al. (1979) and Hwang and Rabitz (1979), is to make use of the associated Green's function matrix.

An nxn Green's function matrix $[K(t,\tau)]$ can be constructed which satisfies

$$\frac{d}{dt}[K(t,\tau)] - [J][K(t,\tau)] = [0] \quad ; \; t > \tau \tag{10.16}$$

with

$$[K(t,t)] = I \tag{10.17}$$

The sensitivity information is then given by the following set of integrals (Hwang et al., 1978)

$$[Z(t)] = [K(t,0)][Z(0)] + \int_0^t [K(t,\tau)][B(\tau)]d\tau \tag{10.18}$$

In practice [K] is determined by first solving (10.9-10) to obtain $\underset{\sim}{u}(\underline{\bar{k}},t_p)$ p=1,2,..., at an adequate number of grid points so that [J(t)] can be determined by interpolation. Operationally it is more convenient to solve the adjoint system (10.19-20) backwards in time.

$$\frac{d[K^*(\tau,t)]}{dt} + [K^*(\tau,t)][J(\tau)] = [0] \; ; \; \tau < t \tag{10.19}$$

$$[K^*(\tau,\tau)] = I \tag{10.20}$$

with

$$[K^*(\tau,t)] = [K(t,\tau)] \tag{10.21}$$

The major advantage of the adjoint formulation is that the sensitivity integrals (10.18) can be more easily evaluated row by row as functions of τ at a fixed time t. Another good feature of the Green's function approach is that the calculations needed to evaluate $\underline{u}(\underline{k},t_p)$ and $[K^*(\tau,t)]$ are independent of the number of parameters m. If m > n this can result in a very large savings in computational time over the direct methods.

In passing it is important to emphasize that the procedure produces a local approximation to the system sensitivity $\underline{u}(\underline{k})$. Section 10.3 presents a procedure valid for global analyses.

The remaining class of methods are global sensitivity analysis techniques in which the major concern is to characterize the response surface $\underline{u}(\underline{k})$ over the full range of parameter variations. In carrying out such analyses, the basic consideration to keep in mind is to minimize the number of model solutions. Conceptually the simplest approach is to solve the system repeatedly, varying one parameter at a time. Without careful prescreening this "brute force" approach can become prohibitively expensive. For example consider a model system of m parameters and r different values for each k_j. The systematic evaluation would require $0(m^r)$ solutions and even relatively small values of m could render the procedure impractical. The key to a successful global sensitivity method is then to devise an economical means for sampling the parameter space. Similar problems arise in locating starting points for optimization algorithms or in the evaluation of multi-dimensional integrals.

Perhaps the most well known sampling procedure is the Monte-Carlo method. In this procedure the parameter combinations are selected at random. A random number generator is used to select values of the parameters from the $\underline{k}$ space which are then used to evaluate $\underline{u}(\underline{k})$. What is often not realized is that the value of Monte-Carlo methods is not the randomness of the sampling but the resulting equidistribution properties of the sets of points in the parameter space. Once it is recognized that the main goal of a Monte-Carlo procedure is to produce a uniform distribution of points in the parameter space, then pattern search methods

become a viable global sensitivity method. The brute force method for distributing points is far from optimal. Consider the two-dimensional cases shown in Figure 10.3 which correspond to N=16, r=4, and m=2. If $u(k_1,k_2)$ depends strongly on one of the variables the first distribution (Figure 10.3a) yields only 4 essentially different values each repeated four times while the second set produces 16 values of either $u_i(k_1)$ or $u_i(k_2)$. An algorithm which generates sequences of points that uniformly fill the parameter space is described in Sobol (1979). Aird and Rice (1977) compared two systematic search procedures with the standard random assignment technique and found that the pattern methods consistently performed better than the Monte-Carlo procedure. Unfortunately pattern and Monte-Carlo methods are not well suited to non-rectangular parameter spaces because of difficulties associated with locating points inside the boundaries.

One major advantage of the Monte-Carlo procedure is that it can be readily adapted to situations in which one or more of the parameters have known distributions. Stolarski et al. (1978) used a Monte-Carlo procedure to study the propagation of reaction rate uncertainties in the strospheric ozone depletion model of Rundel et al. (1978). The uncertain rate constants were assumed to be lognormally distributed about the mean measured values. The computational procedure adopted in their work was to continue to sample from the parameter space until the model output statistics stabilized. For the criteria established by Stolarski et al. (1978) 2000 separate combinations were required to assess the effects of fifty-five parameters. Freeze (1975) used a similar approach in a study of two ground water flow problems and in addition considered the

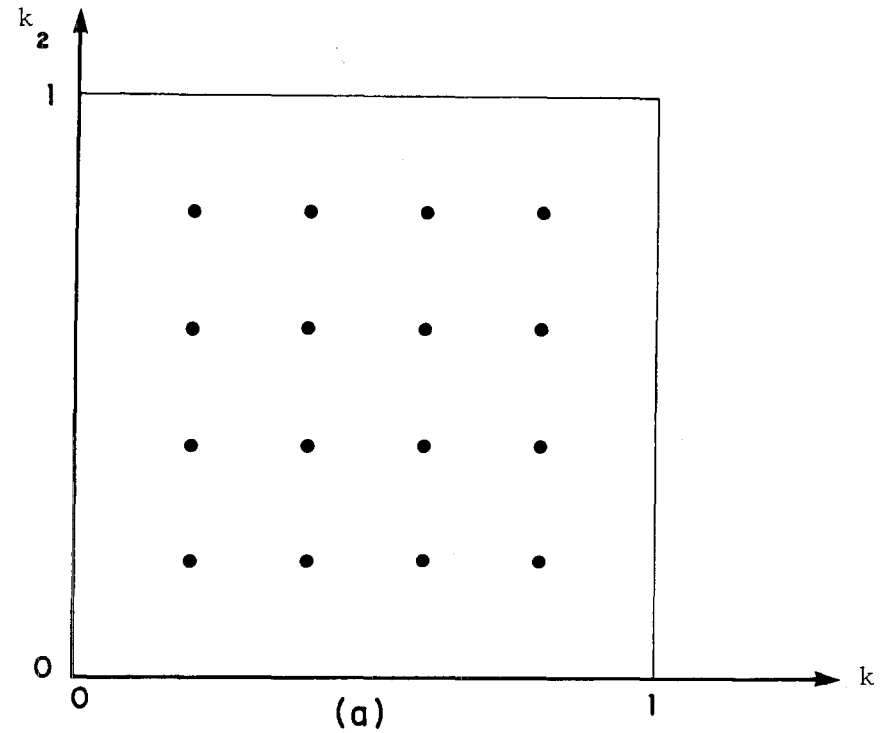

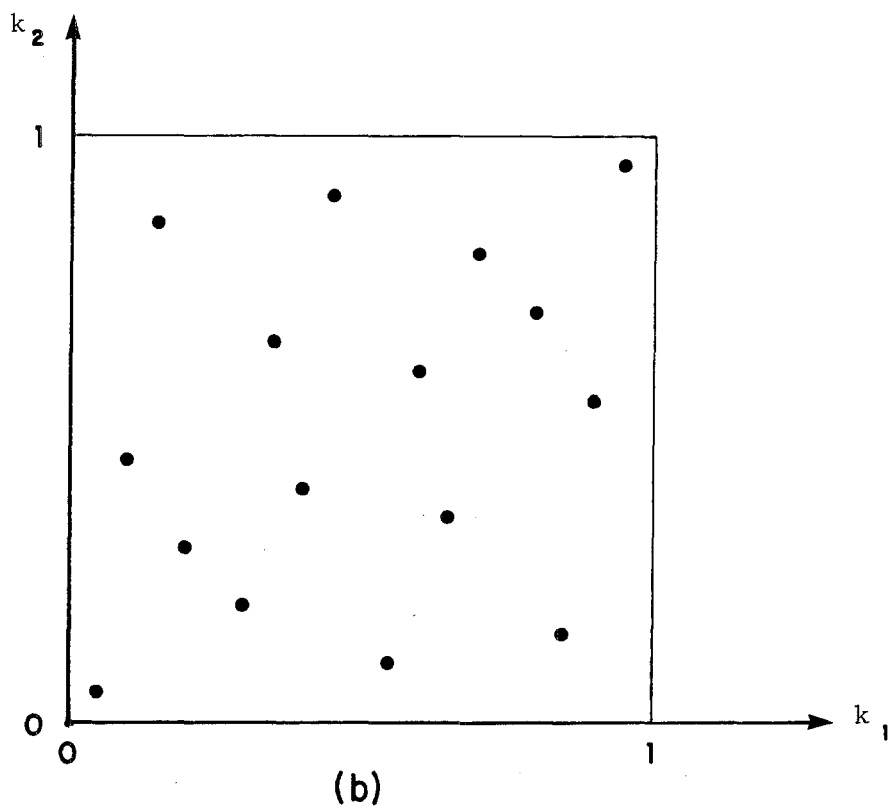

FIGURE 10.3

Systematic Search Patterns of Parameter Space

effects of parameter coupling by using multivariate distributions. Both studies encountered the problem of developing a priori estimates of the number of trials required to produce stable results.

An alternative method for global sensitivity analyses, and the focus of Section 10.3, is the Fourier Amplitude Sensitivity Test (FAST) introduced by Cukier et al. (1973). The essence of this procedure is to assign periodic functions of a new variable, s, to each of the parameters. Under certain conditions each new value of s defines a unique parameter combination $\underline{k}(s)$, along a search curve which can be made to pass arbitrarily close to any point in the $\underline{k}$ space (Weyl, 1938). By sampling $\underline{u}(\underline{k})$ along the search curve and performing a discrete Fourier analysis it is possible to determine the contribution of individual parameters to the global sensitivity of the model (Beauchamp and Yuen, 1979).

In this section the basic issues involved in selecting sensitivity analysis methods have been discussed. Since for some of the techniques there is an extensive literature Figures 10.4 and 10.5 summarize the results of a survey directed at identifying representative treatments of local and global methods. For details of particular applications the reader is referred to the original papers. Subsequent sections of this chapter are directed at developing and applying global methods to components of the atmospheric diffusion equation.

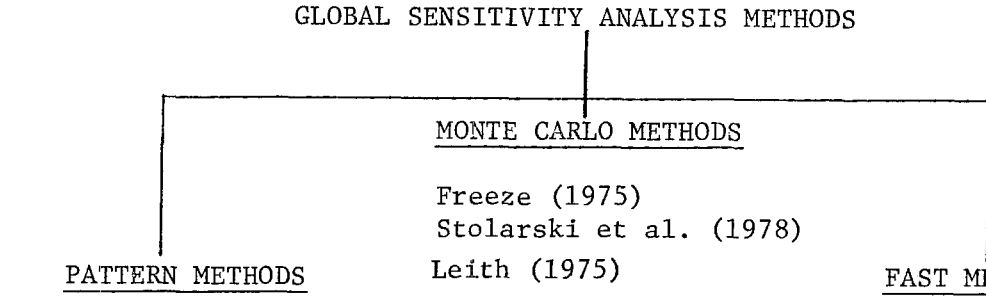

FIGURE 10.4

Survey of Global Sensitivity Analysis Methods

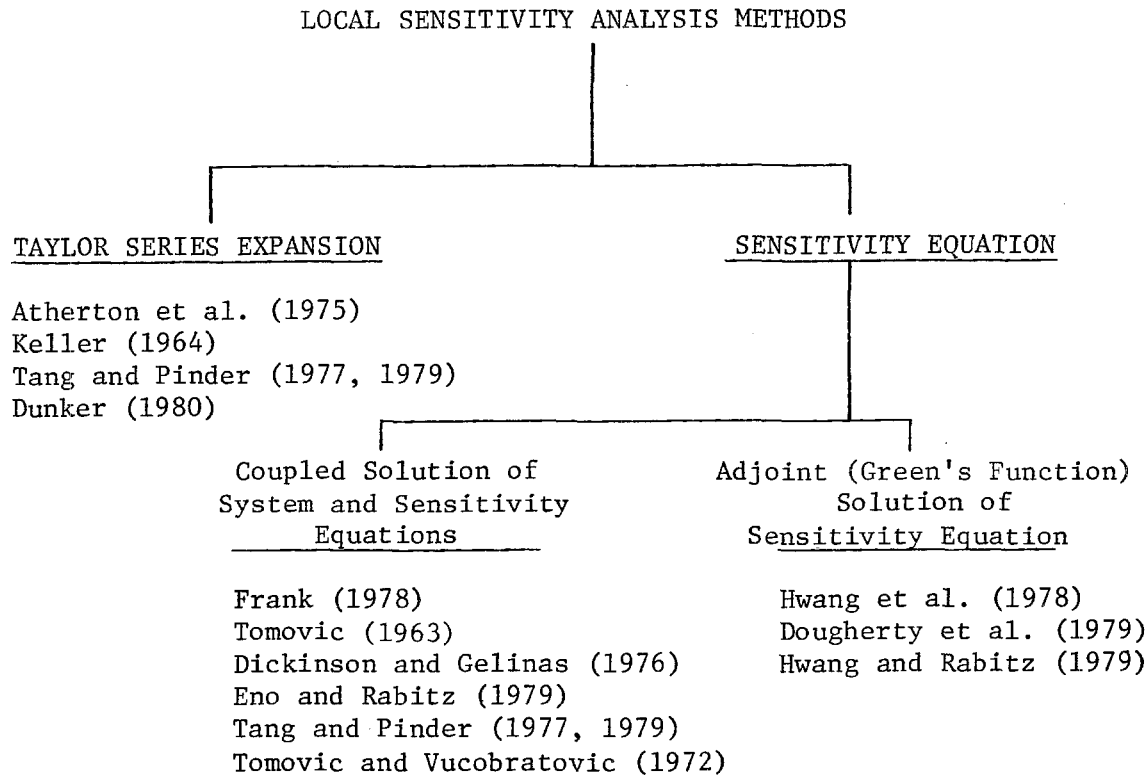

FIGURE 10.5

Survey of Local Sensitivity Analysis Methods

10.3 Automatic Sensitivity Analysis of Kinetic Mechanisms

(Reprinted from Int. Journal of Chemical Kinetics, 11, 427-444.)

Automatic Sensitivity Analysis of Kinetic Mechanisms

MASATO KODA, GREGORY J. MCRAE, and JOHN H. SEINFELD

Department of Chemical Engineering, California Institute of Technology, Pasadena, California 91125

Abstract

An algorithm for the automatic sensitivity analysis of kinetic mechanisms based on the Fourier amplitude sensitivity test (FAST) method of Shuler and co-workers is reported. The algorithm computes a measure of the relative sensitivity of each concentration to each parameter of interest, such as rate constants, Arrhenius parameters, stoichiometric coefficients, and initial concentrations. Arbitrary variations in the magnitude of the parameters are allowable. The algorithm is illustrated for the simple example of computing the sensitivity of the concentration of species A to variation of the two Arrhenius parameters for the hypothetical reaction $A + A \rightarrow$.

Introduction

A variety of chemical phenomena are described by lengthy and complex reaction mechanisms. It is often desirable to determine the effect of uncertainties in rate constants and other parameters on the predictions of the mechanism and to ascertain which parameters are most influential. When a measure of the sensitivity of the concentrations to variations of a parameter is combined in an appropriate manner with a measure of the degree of uncertainty in the parameter's value, one may then determine which parameters, through both their sensitivity and uncertainty, have the most influence on the predicted concentrations.

Conceptually the simplest approach to a sensitivity analysis is to solve the system repeatedly while varying one parameter at a time and holding the others fixed. This type of analysis soon becomes impractical as the number of parameters subject to variation increases. Most of the theories for sensitivity analysis of sets of differential equations containing parameters are linearized ones, valid strictly only for small variations of the parameter value [1]. Recently a new sensitivity analysis method has been developed by Shuler and co-workers [2–5] that is not restricted to small parameter variations. The method is particularly attractive for chemical kinetics applications because order of magnitude uncertainties in rate constant values are not uncommon.

International Journal of Chemical Kinetics, Vol. XI, 427–444 (1979)
 0538-8066/79/0011-0427$01.00

The object of this paper is to report a computational method for the automatic sensitivity analysis of systems of differential equations based on the Fourier amplitude sensitivity test (FAST) method of Shuler and co-workers [2–5]. The computational method processes the concentration–time histories from integration of the system to produce a measure of the sensitivity of each concentration to each parameter. An arbitrary choice of the range of variation of each parameter is possible. The mathematical foundation of the FAST method has been described in detail previously [5]. Thus we present here only a concise discussion of those elements of the method necessary for the understanding and implementation of the computational algorithm. We have extended the basis of the FAST method in one respect; that is, we have developed a way to treat parameters that are constrained by a relationship of the form $H(k_1, k_2, \cdots, k_m) \leq 0$. Such a constraint is important in chemical kinetics applications. Parameters in a chemical reaction mechanism are frequently related to each other. For example, the ratio of two rate constants k_i/k_j may be fixed with k_i or k_j subject to individual uncertainty. Also, if a species may decompose by two paths, the fractional occurrences of which are k_1 and k_2, one may wish to examine the sensitivity of the mechanism's predictions to k_1 and k_2, subject to the constraint that $k_1 + k_2 = 1$.

In the next section we summarize the key elements of the FAST method. The computation of the partial variances, the basic sensitivity measure, is then outlined, followed by a description of the practical implementation of the method. Finally, we illustrate its application in the case of a single reaction.

Mathematical Basis of the FAST Method

We consider a system described by the set of ordinary differential equations

$$\frac{d\boldsymbol{u}(t)}{dt} = \boldsymbol{F}(\boldsymbol{u},\boldsymbol{k}) \tag{1}$$

$$\boldsymbol{u}(0) = \boldsymbol{u}_0 \tag{2}$$

where $\boldsymbol{u}(t)$ is the n-dimensional vector of state variables (concentrations) and $\boldsymbol{k}$ is the m-dimensional vector of parameters (rate constants, Arrhenius parameters, stoichiometric coefficients, etc.) We assume that eq. (1) can be solved numerically subject to the initial condition of eq. (2) to give $\boldsymbol{u}(t)$ for any choice of $\boldsymbol{k}$.

We are interested in determining the sensitivity of each concentration u_i, $i = 1, 2, \cdots, n$, to variation of each parameter k_j, $j = 1, 2, \cdots, m$. We consider the parameter vector $\boldsymbol{k}$ to be a random vector with probability density function $P(\boldsymbol{k})$. In reality the k_j are not, of course, random variables. However, their precise values are uncertain and it is advantageous to treat

them as if they were random variables with a presumed distribution for the purpose of computing the sensitivities. If the k_j are random variables, then the u_i resulting from the solution of eq. (1) are also random variables. The (ensemble) mean value of the concentration of species i at any time t is then given by

$$\langle u_i(t)\rangle = \int \cdots \int u_i(t; k_1, \cdots, k_m) P(k_1, \cdots, k_m)\, dk_1 \cdots dk_m \tag{3}$$

where $u_i(t; k_1, \cdots, k_m)$ denotes the solution of eq. (1). The key concept of the FAST method is to convert the m-dimensional integral of eq. (3) into an equivalent one-dimensional integral.

The method uses the transformations

$$k_l = G_l(\sin \omega_l s), \qquad l = 1, 2, \cdots, m \tag{4}$$

where G_l, $l = 1, 2, \cdots, m$, are a set of known functions, ω_l, $l = 1, 2, \cdots, m$, are a set of frequencies, and s is a scalar variable. By means of this transformation variations of the m parameters are transformed into variations of the single scalar variable s. By variation of s over the range $-\infty \leq s \leq \infty$, eq. (4) traces out a space-filling curve in the m-dimensional parameter space. For a suitable choice of the G_l, which transforms the probability density $P(\boldsymbol{k})$ into s space, Weyl [6] demonstrated that

$$\bar{u}_i(t) = \lim_{T\to\infty} \frac{1}{2T} \int_{-T}^{T} u_i(t; k_1(s), \cdots, k_m(s))\, ds \tag{5}$$

is identically equal to $\langle u_i(t)\rangle$ from eq. (3). Equation (5) is the fundamental expression in the FAST method for computing the mean value, variance, and other properties of the concentration u_i.

The set of frequencies $\{\omega_l\}$ should be incommensurate, in that

$$\sum_{l=1}^{m} \gamma_l \omega_l = 0 \tag{6}$$

for an integer set $\{\gamma_l\}$ if and only if $\gamma_l = 0$, $l = 1, 2, \cdots, m$. If the frequencies $\{\omega_l\}$ are, in fact, incommensurate, the search curve in s space is space-filling in that it passes arbitrarily close to any point in the m-dimensional parameter space of $\boldsymbol{k}$. Unfortunately the set of $\{\omega_l\}$ used in actual computation cannot be truly incommensurate. As discussed by Shuler and coworkers [3–5], we select $\{\omega_l\}$ as an appropriate set of integer frequencies. The use of integer frequencies in eq. (4) implies that the parameters k_l, $l = 1, 2, \cdots, m$, are periodic in s on the finite interval $(-\pi, \pi)$, in which case eq. (5) becomes

$$\bar{u}_i(t) = \frac{1}{2\pi} \int_{-\pi}^{\pi} u_i(t; k_1(s), \cdots, k_m(s))\, ds \tag{7}$$

The variance of concentration i is then

$$\sigma_i^2(t) = \frac{1}{2\pi} \int_{-\pi}^{\pi} u_i^2(t; k_1(s), \cdots, k_m(s))\, ds - \bar{u}_i^2 \tag{8}$$

Henceforth we will replace $\bar{u}_i(t)$ by $\langle u_i(t)\rangle$, representing the s-space average. Then $\bar{u}_i = \langle u_i\rangle$ and $\sigma_i^2 = \langle u_i^2\rangle - \langle u_i\rangle^2$. In addition, for convenience, we will denote $u_i(t; k_1(s), \cdots, k_m(s))$ by $u_i(t; s)$.

The evaluation of σ_i^2 can be carried out by using the s-space Fourier coefficients of u_i. From Parseval's theorem we have

$$\langle u_i^2(t)\rangle = \frac{1}{2\pi}\int_{-\pi}^{\pi} u_i^2(t; s)\, ds = \sum_{j=-\infty}^{\infty} \{A_j^{(i)}(t)^2 + B_j^{(i)}(t)^2\} \tag{9}$$

where the Fourier coefficients $A_j^{(i)}$ and $B_j^{(i)}$ are defined as

$$A_j^{(i)}(t) = \frac{1}{2\pi}\int_{-\pi}^{\pi} u_i(t; s)\cos js\, ds \tag{10}$$

$$B_j^{(i)}(t) = \frac{1}{2\pi}\int_{-\pi}^{\pi} u_i(t; s)\sin js\, ds \tag{11}$$

Thus, from eqs. (10) and (11),

$$\langle u_i(t)\rangle^2 = A_0^{(i)2} + B_0^{(i)2} = A_0^{(i)2} \tag{12}$$

Using eqs. (9)–(12) we can express the variance $\sigma_i^2(t)$ in terms of the Fourier coefficients as

$$\sigma_i^2(t) = 2\sum_{j=1}^{\infty} (A_j^{(i)}(t)^2 + B_j^{(i)}(t)^2) \tag{13}$$

If the Fourier coefficients (10) and (11) are evaluated for the fundamental frequencies of the transformation (4) or its harmonics, that is, $j = p\omega_l$, $p = 1, 2, \cdots$, the variance

$$\sigma_{\omega_l}(t)^2 = 2\sum_{p=1}^{\infty} (A_{p\omega_l}^{(i)}(t)^2 + B_{p\omega_l}^{(i)}(t)^2) \tag{14}$$

is the part of the total variance σ_i^2 that corresponds to the variance of u_i arising from the uncertainty in the lth parameter. The ratio $S_{\omega_l}^{(i)} = \sigma_{\omega_l}^2/\sigma_i^2$ is the so-called partial variance, which serves as the basic measure of sensitivity for the FAST method. We note that $S_{\omega_l}^{(i)}$ is a normalized sensitivity measure, so that the $S_{\omega_l}^{(i)}$ may be ordered with respect to l to indicate to which parameters concentration u_i is most sensitive.

We can now summarize the essential elements of the FAST method. The sensitivity measures are the partial variances $S_{\omega_l}^{(i)}$, $i = 1, 2, \cdots, n$, $l = 1, 2, \cdots, m$. The relative magnitudes of the m partial variances for each concentration reflect the relative influence of each of the m parameters on that concentration. The partial variances are calculated from the ratio of eqs. (14) and (13), the main computation involved being the evaluation of the integrals (10) and (11). To evaluate the Fourier coefficients from eqs. (10) and (11) requires that the solution of the system of eq. (1) be obtained for enough values of s so that the integrals in eqs. (10) and (11) can be calculated with sufficient accuracy. Thus, with the parameter values being

determined by eq. (4), the system of differential equations, eq. (1), is solved repeatedly for each value of s needed to calculate the Fourier coefficients in eqs. (10) and (11). Therefore the FAST method only requires that the set of eq. (1) be solved numerically a certain number of times to produce the concentrations $u_i(t; s)$ needed to determine the Fourier coefficients and subsequently the partial variances. By contrast, the common linearized methods frequently require that eqs. (1) be differentiated with respect to the k_l to produce an auxiliary set of nm differential equations for the sensitivity coefficients $\partial u_i/\partial k_l$, $i = 1, 2, \cdots, n$, $l = 1, 2, \cdots, m$. Thus whereas the linearized methods require the one-time solution of nm differential equations (in addition to the original n differential equations), the FAST method requires a certain number, N_s, solutions of the original set of n differential equations. The relative solution times depend, of course, on the values of n, m, and N_s. The choice of N_s for the FAST method will be discussed shortly.

The basic sensitivity measure in the FAST method is the partial variance $S_{\omega l}^{(i)}$, whereas in the direct, linearized methods the measure is the sensitivity coefficient $\partial u_i/\partial k_l$. The relation between these two measures is developed in Appendix A. Appendix B indicates how the case of correlated parameters can be treated.

Exploitation of Symmetry Properties

Before describing the practical implementation of the FAST method it is worthwhile to reexamine the search curves and the Fourier integrals, eqs. (10) and (11). As discussed in the previous section, the FAST method requires the repeated evaluation of the model system for each parameter combination. As this generally represents the major component of the computational cost, it is clearly desirable to minimize the required number of model solutions. One way to do this is to exploit the symmetry properties of the search curves. As defined by eq. (4) the search curves have a period of 2π. By choosing the frequency set $\{\omega_l\}$ so that it is composed entirely of odd integers, the functions $G_l(\sin \omega_l s)$, $l = 1, 2, \cdots, m$, become symmetric about $\pm\pi/2$. Consequently the following symmetry properties hold:

$$\boldsymbol{u}(t; \pi - s) = \boldsymbol{u}(t; s)$$

$$\boldsymbol{u}(t; -\pi + s) = \boldsymbol{u}(t; -s)$$

$$\boldsymbol{u}(t; \pi/2 + s) = \boldsymbol{u}(t; \pi/2 - s)$$

$$\boldsymbol{u}(t; -\pi/2 + s) = \boldsymbol{u}(t; -\pi/2 - s)$$

Thus eqs. (10) and (11) become

$$(15)\quad A_j^{(i)}(t) = \begin{cases} 0, & j \text{ odd} \\ \dfrac{1}{\pi}\displaystyle\int_0^{\pi/2} [u_i(t;s) + u_i(t;-s)] \cos js \, ds, & j \text{ even} \end{cases}$$

$$(16)\quad B_j^{(i)}(t) = \begin{cases} 0, & j \text{ even} \\ \dfrac{1}{\pi}\displaystyle\int_0^{\pi/2} [u_i(t;s) - u_i(t;-s)] \sin js \, ds, & j \text{ odd} \end{cases}$$

Exploitation of the symmetry properties has therefore reduced the range of integration and, more importantly, the required number of solutions of the differential equations by one half.

Computation of the Partial Variances

The key sensitivity measure in the FAST method is the partial variance which, suppressing the dependence on t, can be written in the form

$$(17)\quad S_{\omega l}^{(i)} = \frac{2}{\sigma_i^2} \sum_{p=1}^{\infty} [|A_{p\omega l}^{(i)}|^2 + |B_{p\omega l}^{(i)}|^2]$$

where the amplitudes $A_{p\omega l}^{(i)}$, $B_{p\omega l}^{(i)}$ are now determined by the integrals, eqs. (15) and (16). The principal idea behind the partial variance concept of sensitivity is to examine the output $u_i(t;s)$ and isolate the effects of variations in parameter k_l from the influence of changes in all the other parameters. When evaluating eq. (17) it is important to recognize, however, the limitations imposed by the use of integers to define the frequency set $\{\omega_l\}$. In the summation, interferences from the effects of parameters other than ω_l can lead to meaningless situations in which $S_{\omega l}^{(i)} > 1$. The interference problem is readily illustrated by selecting two arbitrary parameters k_l, k_j and their associated frequencies ω_l, ω_j. In evaluating the terms contributing to $S_{\omega l}^{(i)}$ two or more values, say r and q, of the harmonic index p will be encountered such that $r\omega_l = q\omega_j$, which in turn implies that

$$(18)\quad |A_{r\omega l}^{(i)}|^2 + |B_{r\omega l}^{(i)}|^2 = |A_{q\omega j}^{(i)}|^2 + |B_{q\omega j}^{(i)}|^2$$

This result indicates that the calculation of $S_{\omega l}^{(i)}$ is being influenced by terms arising from variations in the other parameter, ω_j. A similar problem arises when the FAST method is applied numerically. In most circumstances algebraic complexities or computational costs restrict the availability of the output $u_i(t;s)$ to discrete values of s in the range $\pm\pi/2$. Unless the integration points are chosen carefully, aliasing errors can cause interferences similar to eq. (18). Ordinarily the Fourier amplitudes decrease as p increases. We expect, therefore, that most of the contributions to the

summation in eq. (17) should occur with the first few values of p. At this point the key question to address is simply: how many harmonics can be included in the summation without causing interference problems.

To answer this question we start by considering the choice of the frequency set $\{\omega_l\}$ and the number N_s of sample points in the s domain used to approximate the integrals, eqs. (15) and (16). We note first of all that if we select $\omega_l = 1$, eq. (17) yields $S_{\omega l}^{(i)} = 1$, which yields no information. The frequency set $\{\omega_l\}$ used in this paper is developed recursively using

$$\begin{aligned} &\omega_1 = \Omega_n \\ &\omega_i = \omega_{i-1} + d_{n+1-i}, \qquad i = 2, 3, \cdots, n \end{aligned} \tag{19}$$

The Ω_n and d_n, tabulated in Cukier and co-workers [4] for n varying from 3 to 50, have been augmented for the two-parameter case with $\{\omega_l\} = 3, 5$ ($\Omega_2 = 3$, $d_1 = 2$), and for $n = 6$, ω_1 has been reset to 13. The maximum frequency $\omega_{\max}$ is given by ω_m if eq. (19) is used to generate the set $\{\omega_l\}$. Also, then the minimum frequency $\omega_{\min}$ is ω_1. If the amplitudes A, B could be determined exactly, the maximum number of terms that can be included in the summation without the possibility of interferences is simply $\omega_{\min} - 1$. This is another reason for avoiding the choice $\omega_l = 1$. The simplest numerical integration procedure for evaluating the amplitudes, which exploits the symmetry properties of $u_i(t; s)$, requires $N_s = N\omega_{\max} + 1$ ($N \geq 2$) uniformly spaced points in the interval $\pm\pi/2$. Several factors influence the choice of N. The lower limit, $N = 2$, is imposed by the Nyquist criterion [7, 5], which indicates that the output $u_i(s)$ needs to be sampled at least twice as often as the highest frequency $\omega_{\max}$. For convenience, it is useful to choose N to be divisible by 2, and so the minimum number of integration points is $2\omega_{\max} + 1$. The numerical approximation of the Fourier integrals can be improved by using $N > 2$ at the expense of increasing the computational cost. As mentioned above, the numerical approximation of the Fourier integrals leads to another type of interference problem commonly called aliasing. These interferences occur when

$$q\omega_n \equiv p\omega_l (\text{mod } \{N\omega_{\max} + 1\}) \tag{20}$$

This generally imposes a lower limit to the number of terms that can be included before interferences occur. The aliasing problem in the computation of $S_{\omega l}^{(i)}$ can be minimized if, using the previous example, we restrict the higher harmonics to satisfy the conditions $r\omega_l < N\omega_{\max} + 1$. The natural choice for r is N, in which case eq. (17) can be rewritten as

$$S_{\omega l}^{(i)} = \frac{2}{\sigma_i^2} \sum_{p=1}^{N} [|A_{p\omega l}^{(i)}|^2 + |B_{p\omega l}^{(i)}|^2] \tag{21}$$

If N is chosen to be 2, then, since $B_{2\omega_l}^{(i)} = 0$, eq. (21), with eq. (12), can be written as

$$S_{\omega l}^{(i)} = \frac{2}{\sigma_i^2} [|B_{1\omega l}^{(i)}|^2 + |A_{2\omega l}^{(i)}|^2] \tag{22}$$

The variance σ_i^2 is given by eq. (13).

Practical Implementation of the FAST Method

While applicable to any problems that are described by a set of differential equations, the FAST method is particularly useful in the analysis of chemical kinetics. The parameters k_j may include rate constants, Arrhenius parameters, stoichiometric coefficients, branching ratios, and initial conditions $\boldsymbol{u}_0$. Application of the FAST method to the sensitivity analysis of reaction mechanisms is illustrated in Figure 1.

Several steps are involved. First the rate laws must be specified. Having established the basic set of differential equations, the next step is to select the parameters to be varied. For each parameter that is to be studied a range of uncertainty must be established and a search curve selected from the options presented in Table I. Given this information and the times

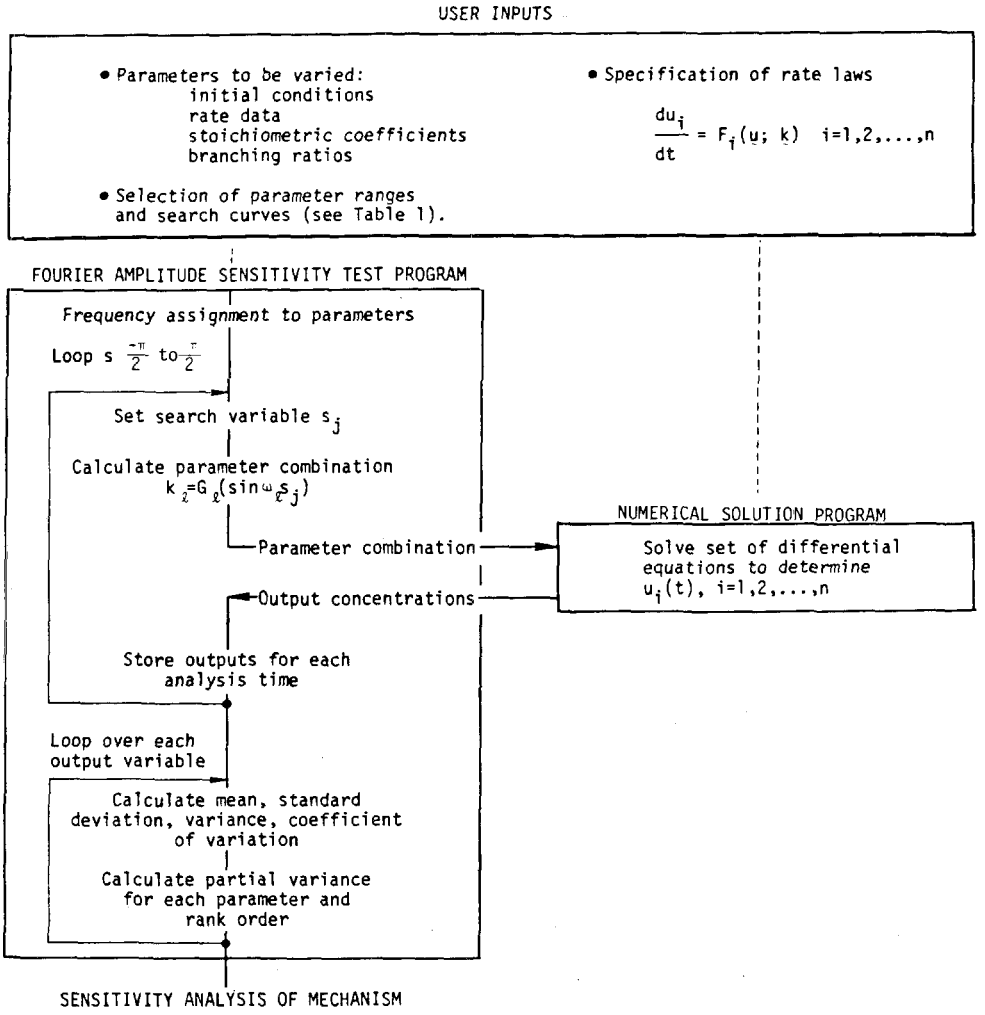

Figure 1. Application of the FAST method to chemical kinetics.

TABLE I. Search curves for different parameter variations.

Application	$k_j(s)$	Mean Value[a] $\bar{k}_j$	Nominal Value $\bar{\nu}_j$
Additive variation	$k_j(s) = \bar{k}_j[1 + \bar{\nu}_j \sin \omega_j s]$	$\frac{k_j^u + k_j^\ell}{2}$	$\frac{k_j^u - k_j^\ell}{k_j^u + k_j^\ell}$
Exponential variation	$k_j(s) = \bar{k}_j \exp[\bar{\nu}_j \sin \omega_j s]$	$\sqrt{k_j^u k_j^\ell}$	$\frac{1}{2} \ln\left(\frac{k_j^u}{k_j^\ell}\right)$
Proportional variation $k_j^u = a\bar{k}_j$, $k_j^\ell = \left(\frac{\bar{k}_j}{a}\right)$	$k_j(s) = \bar{k}_j \exp[\bar{\nu}_j \sin \omega_j s]$	$\bar{k}_j$	$\ln(a)$
Skewed variation $\left(\bar{k}_j > \frac{k_j^u + k_j^\ell}{2}\right)$	$k_j(s) = \nu_j\left[\frac{\alpha_j + \beta_j \sin\omega_j s - 1}{\alpha_j + \beta_j}\right]$	$\nu_j\left(\frac{\alpha_j - 1}{\alpha_j}\right)$	$\alpha_j = \frac{1}{2}\left[\frac{r^u}{r^u - 1} + \frac{r^\ell}{r^\ell - 1}\right]$[b] $\beta_j = -\frac{\alpha_j(r^u + r^\ell - 2)}{(r^u - r^\ell)}$ $\nu_j = -\bar{k}_j\left[\frac{r^u + r^\ell - 2r^u r^\ell}{r^u + r^\ell - 2}\right]$

[a] k_j^u—upper limit for parameter; k_j^l—lower limit for parameter.
[b] $r^u = k_j^u/\bar{k}_j$, $r^l = k_j^l/\bar{k}_j$.

for the analysis of the concentrations, the FAST program automatically evaluates the model system for each parameter combination. The concentration outputs at each time are then processed to determine the partial variances and sensitivity ranking for each of the parameters. The detailed computational procedure is as follows:

(a) Assign to each of the m parameters a different frequency ω_l, $l = 1, 2, \cdots, m$.

(b) Based on some knowledge of the expected range of variation for each parameter, select appropriate search curves from Table I.

(c) Select the number of parameter combinations to be evaluated. For N_s points, a symmetric and uniform spacing in s, including $s = 0$, is given by

$$s_j = \frac{\pi}{2}\left[\frac{2j - N_s - 1}{N_s}\right], \qquad j = 1, 2, \cdots, N_s \tag{23}$$

(d) Solve the set of differential equations, eq. (1), for each parameter combination s_j defined by $k = \bar{k}_l G_l(\sin \omega_l s_j)$, $j = 1, 2, \cdots, N_s$. In many applications, particularly in chemical kinetics, where stiffness is a problem, the computation time per solution can be minimized by using a variable-order method, such as the well-known Gear algorithm [8].

Once the model system has been evaluated for each parameter combi-

nation, the influence of the lth parameter k_l on the ith concentration at time t can be examined by calculating the partial variance $S_{\omega_l}^{(i)}(t)$,

$$S_{\omega_l}^{(i)}(t) = \frac{2 \sum_{p=1}^{N} [|A_{p\omega_l}^{(i)}(t)|^2 + |B_{p\omega_l}^{(i)}(t)|^2]}{\sigma_i^2(t)} \tag{24}$$

The variance $\sigma_i^2(t)$ can be approximated numerically by

$$\frac{1}{N_s} \sum_{j=1}^{N_s} \{u_i(t; s_j) - \langle u_i(t) \rangle\}^2 \tag{25}$$

and the mean value $\langle u_i(t) \rangle$ by

$$\langle u_i(t) \rangle = \frac{1}{N_s} \sum_{j=1}^{N_s} u_i(t; s_j) \tag{26}$$

Simple quadrature formulas can be used to evaluate the amplitudes $A_{p\omega_l}^{(i)}(t)$ and $B_{p\omega_l}^{(i)}(t)$. The following expressions were derived directly from eqs. (15) and (16):

(27) $A_{p\omega_l}^{(i)}(t)$

$$= \begin{cases} 0, & p\omega_l \text{ odd} \\ \dfrac{1}{N_s}\left\{u_i(t; N_0) + \displaystyle\sum_{q=1}^{N_q} [u_i(t; N_0 + q) + u_i(t; N_0 - q)] \times \cos \dfrac{p\omega_l q \pi}{N_s}\right\}, & p\omega_l \text{ even} \end{cases}$$

(28) $B_{p\omega_l}^{(i)}(t)$

$$= \begin{cases} 0, & p\omega_l \text{ even} \\ \dfrac{1}{N_s}\left\{\displaystyle\sum_{q=1}^{N_q} [u_i(t; N_0 + q) - u_i(t; N_0 - q)] \sin \dfrac{p\omega_l q \pi}{N_s}\right\}, & p\omega_l \text{ odd} \end{cases}$$

where $N_q = (N_s - 1)/2$ and $N_0 = N_q + 1$. (The index notation in eqs. (26) and (27) has been chosen to simplify the computer implementation using programming languages such as FORTRAN that do not allow negative or zero indices.)

Figure 2 with $\{\omega_l\} = [3, 5]$ and Figure 3 with $\{\omega_l\} = [11, 13]$ illustrate the two basic approximations involved in the FAST method. The first is that the frequency sets $\{\omega_l\}$ are commensurate, that is, the search curves do not completely cover the parameter space. The second approximation involves the use of a finite number of points in the numerical quadrature. Both of these considerations have been quantitatively examined by Cukier and co-workers [4] and for this reason will not be repeated here.

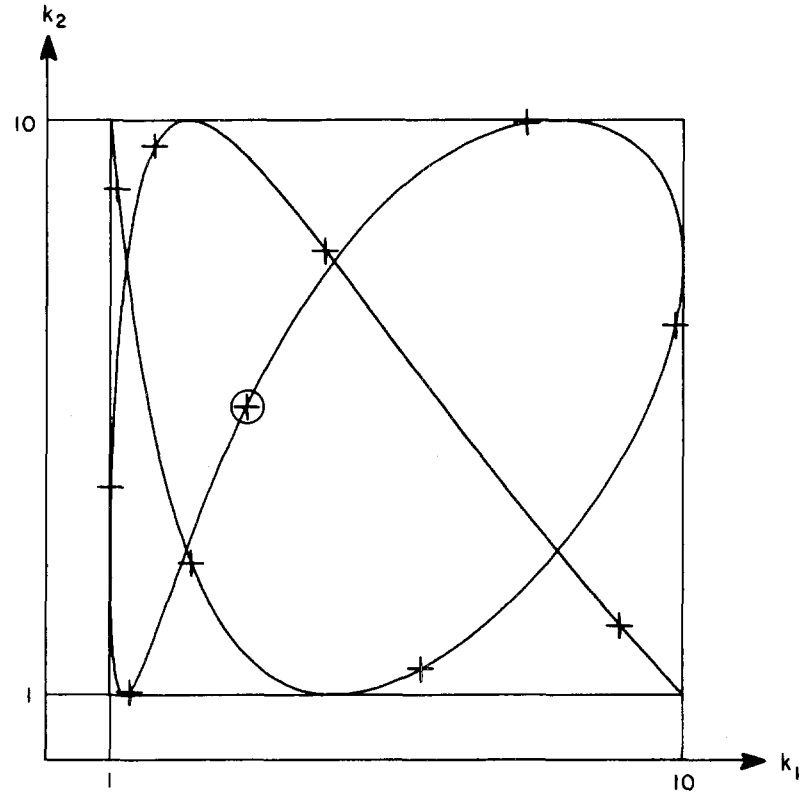

Figure 2. Space-filling search curve for case $\{\omega_i\} = [3,5]$ where $k_1 = \bar{k}_1 \exp(\bar{\nu}_1 \sin \omega_1 s)$ and $k_2 = \bar{k}_2[1 + \bar{\nu}_2 \sin \omega_2 s]$. +—integration points for $N_s = 2\omega_{max} + 1$; ⊕—nominal value of k_1 and k_2.

Example—Application to a Single Reaction

In this section we wish to present an example of the use of the FAST method. We have purposely chosen a very simple system so that the interpretation of the results can be easily discussed; an application involving a larger number of parameters is described in Boni and Penner [9]. Consider a hypothetical recombination reaction

$$A + A \rightarrow$$

with rate constant $\kappa = k_1 \exp(-k_2/T)$. We wish to examine the sensitivity of the concentration of A to variations in the Arrhenius parameters k_1 and k_2 at $T = 298°K$. We let $u = [A]/[A_0]$, the normalized concentration. The nominal values of k_1 and k_2 are chosen as 1.79×10^{10} l/mol-sec and 500°K, respectively. The (arbitrary) ranges of uncertainty and initial concentration were chosen as $8.97 \times 10^9 \leq k_1 \leq 3.59 \times 10^{10}$, $0 \leq k_2 \leq 1000$, $[A_0] = 1$ mol/l.

We use the transformations (see Table I) $k_1 = \bar{k}_1 \exp \nu_1$ and $k_2 = \bar{k}_2 (1 + \nu_2)$, where $\nu_1 = (\ln 2) \sin \omega_1 s$ and $\nu_2 = \sin \omega_2 s$. For this particular problem the sensitivity coefficients can be calculated analytically, $\partial u/\partial k_1 = -2[A_0]\kappa t u^2/\bar{k}_1$ and $\partial u/\partial k_2 = 2[A_0]\kappa t u^2/T$. The FAST method essentially

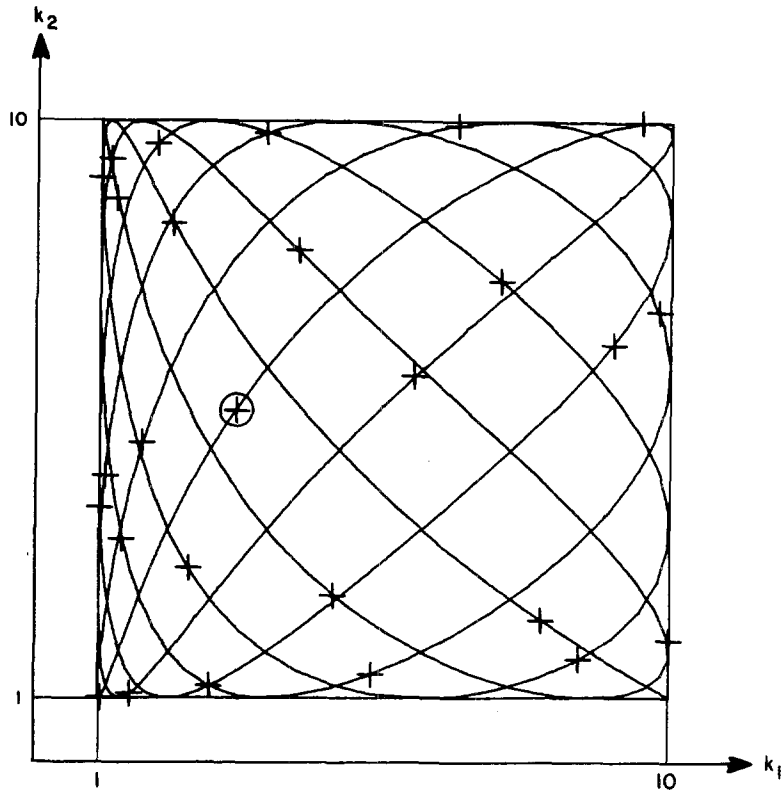

Figure 3. Space-filling search curve for case $\{\omega_l\} = [11,13]$ where $k_1 = \bar{k}_1 \exp(\bar{v}_1 \sin \omega_1 s)$ and $k_2 = \bar{k}_2[1 + \bar{v}_2 \sin \omega_2 s]$. +—integration points for $N_s = 2\omega_{\max} + 1$; ⊕—nominal value of k_1 and k_2.

calculates the Fourier amplitude B_{ω_l} which is proportional to $\langle \partial u/\partial v_l \rangle$, which is the relative sensitivity with respect to the nondimensional v_l for the transformations exp $v_l = k_l/\bar{k}_l$ or $1 + v_l = k_l/\bar{k}_l$ (see Appendix A).

In Figure 4 the concentration u, partial variances S_{ω_1} and S_{ω_2}, fundamental Fourier coefficients B_{ω_1} and B_{ω_2}, and the relative sensitivity coefficients $\bar{k}_1 \partial u/\partial k_1$ and $\bar{k}_2 \partial u/\partial k_2$ are plotted for $\{\omega_1, \omega_2\} = (3, 5)$ and $N_s = 21$. (The results were found to be insensitive to the choice of the frequency set and number of dividing points.) The fundamental Fourier coefficients B_{ω_1} and B_{ω_2} follow quite well the general trends of the relative sensitivity coefficients $\bar{k}_1 \partial u/\partial k_1$ and $\bar{k}_2 \partial u/\partial k_2$, demonstrating the fundamental relationship in the FAST method, $B_{\omega_l} \propto \langle \partial u/\partial v_l \rangle$. The partial variance S_{ω_2} follows the trends of B_{ω_2} and $\bar{k}_2 \partial u/\partial k_2$. On the other hand, the partial variance S_{ω_1} does not follow the trends of B_{ω_1} or $\bar{k}_1 \partial u/\partial k_1$. It decreases when the absolute values of B_{ω_1} and $\bar{k}_1 \partial u/\partial k_1$ increase and increases when the absolute values of $B_{\omega 1}$ and $\bar{k}_1 \partial u/\partial k_1$ decrease. We observe the following relationship between the partial variances;

$$S_{\omega_1} + S_{\omega_2} \simeq 0.96 \pm 0.03 \tag{29}$$

This implies that if the relative importance of the effects of the parameter

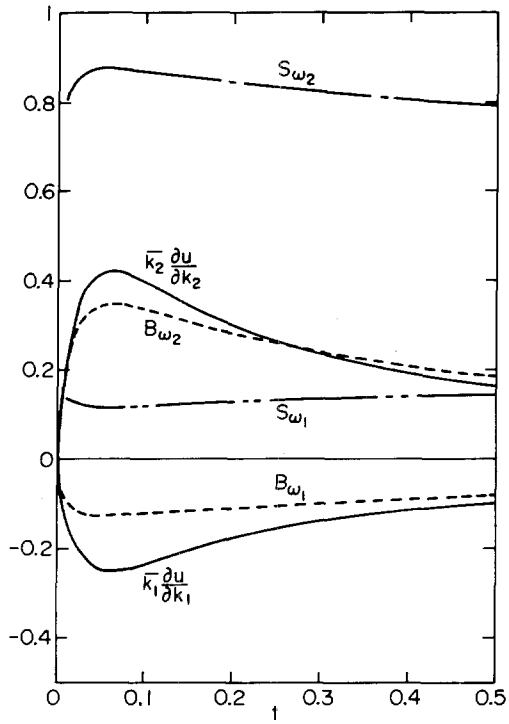

Figure 4. Comparison of the analytical sensitivity coefficients $\bar{k}_i\, \partial u/\partial k_i$ and the fundamental Fourier coefficients B_{ω_i} and partial variance S_{ω_i} as calculated by the FAST method ($i = 1, 2$). Plots are based on the normalized concentration, that is, $u = [A]/[A_0]$. The parameters used are $\omega_1 = 3$, $\omega_2 = 5$, and $N_s = 4\omega_{\max} + 1 = 21$.

uncertainty in k_1, that is, the partial variance S_{ω_1} increases, then S_{ω_2}, the measure of relative importance for k_2, automatically decreases. For the more general multiparameter examples studied by Cukier and co-workers [5], we can observe the same relationship, namely, $\Sigma_{l=1}^{m} S_{\omega_l} \simeq$ constant when the coupling terms like $S_{\omega_i+\omega_j}$ are small. For the parameter range we have studied, all the sensitivity measures including the analytical sensitivity coefficients agreed and gave consistent results, indicating that the concentration of A is more sensitive to changes in k_2 than to changes in k_1.

To test the FAST method further, we increased the range of uncertainty for the parameter k_1 as follows: $0 \leq k_1 \leq 3.59 \times 10^{10}$.[1] To take account of this range of uncertainty we use the transformation (see Table I) $k_1 = \bar{k}_1 (1 + \sin \omega_1 s)$. The range of uncertainty of k_2 is held fixed.

The results of calculations are plotted in Figure 5. Since the parameter uncertainty for k_1 is increased, we observe that the relative importance of the parameter uncertainty in k_1 is increased and $S_{\omega_1} > S_{\omega_2}$ for $t > 0.08$. This fact, is also reflected in the fundamental Fourier coefficients B_{ω_1} and B_{ω_2}. The fundamental Fourier coefficient B_{ω_1} does not agree with the trend

[1] Such a range of variation is, of course, physically implausible. We have chosen it only to illustrate the ability of the method to handle extreme limits of variation.

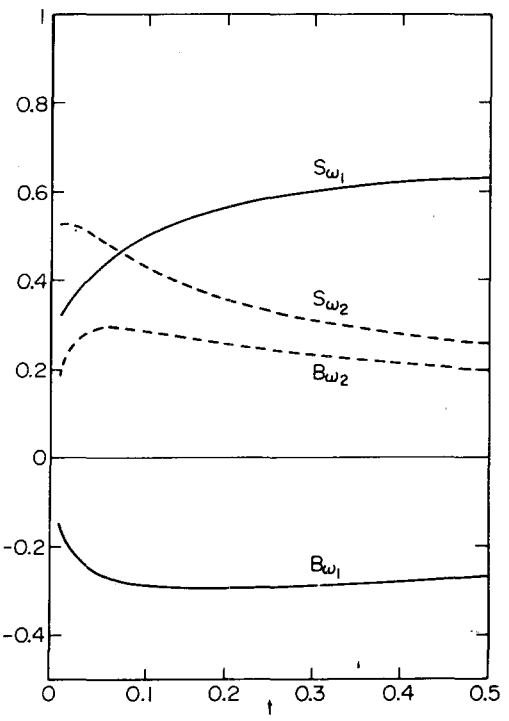

Figure 5. Fundamental Fourier coefficients B_{ω_i} and partial variances S_{ω_i} ($i = 1, 2$) for the case of increased range of uncertainties in the parameter k_1. The parameters used in the FAST method are $\omega_1 = 3$, $\omega_2 = 5$, and $N_s = 4\omega_{max} + 1 = 21$.

of the analytical sensitivity solution of $\bar{k}_1 \, \partial u/\partial k_1$. This behavior is due to the characteristics of the Fourier amplitude sensitivity test and the sensitivity coefficient. The FAST method takes account of the very large variations about the nominal values, while the sensitivity coefficient $\bar{k}_1 \, \partial u/\partial k_1$ is computed at the nominal values for infinitesimal variations. Thus for the case of the increased range of uncertainty of k_1, we conclude that the concentrations of A is more sensitive to k_1 than to k_2. We observe from this example that the partial variances essentially propagate the uncertainties in the parameters.

Summary

An algorithm for the automatic sensitivity analysis of kinetic mechanisms based on the FAST method of Shuler and co-workers [2–5] has been described, and a simple example illustrating its use has been given. With this method assessment of the relative influence of kinetic parameters on the predicted concentrations from a chemical mechanism becomes a relatively routine undertaking. A complete code for the sensitivity analysis of mechanisms includes three routines: 1) one that forms the kinetic rate equations based on the set of chemical reactions, 2) one that integrates the ordinary differential (ODE) rate equations, and 3) one that processes the

concentrations to produce the partial variances of the FAST method. This paper has focused on the third routine. The authors have prepared a complete code consisting of an algebraic manipulation routine to form the rate equations for any set of chemical reactions, the ODE solver EPISODE [10, 11], and the FAST method described here. Interested readers may contact the authors to obtain a copy of the code.

Acknowledgment

This work was supported by the Environmental Protection Agency under Grant No. R805537.

Appendix A

Relation of the FAST Method to Sensitivity Coefficients

In this appendix we summarize the relationship of the FAST method to the generalized sensitivity coefficients $\langle \partial u_i/\partial k_l \rangle$ and to the customary linear sensitivity measures $\partial u_i/\partial k_l|_{\bar{k}}$, $i = 1, 2, \cdots, n$ and $l = 1, 2, \cdots, m$. Cukier and co-workers [4, 5] have considered the problem in somewhat more detail. Here we illustrate the results, using as an example the parameter representation.

$$k_l = G_l(\sin \omega_l s) = \bar{k}_l \exp \nu_l \tag{30}$$

$$\nu_l = g_l(\sin \omega_l s) \tag{31}$$

where $\bar{k}_l$ is the nominal value for the parameter k_l. The function g_l is determined to satisfy

$$\cos^2\theta_l \frac{\partial g_l(\sin \theta_l)}{\partial \sin \theta_l} = \frac{1}{a_l} \tag{32}$$

where $\theta_l = \omega_l s \pmod{2\pi}$ and a_l is a constant parameter. From eq. (3) and Weyl's theorem, we can write

$$\begin{aligned} B_{\omega l}^{(i)}(t) &= \langle u_i(t; s) \sin \theta_l \rangle \\ &= \int_0^{2\pi} \cdots \int_0^{2\pi} u_i(t; \theta_1, \cdots, \theta_m) \sin \theta_l \, P(\theta_1, \cdots, \theta_m) \, d\theta_1 \cdots d\theta_m \end{aligned} \tag{33}$$

where $P(\theta_1, \cdots, \theta_m) = (2\pi)^{-m}$. Then using eqs. (30)–(33) and integrating by parts, we obtain the desired relationship between $B_{\omega l}^{(i)}$ and $\langle \partial u_i/\partial \nu_l \rangle$,

$$B_{\omega l}^{(i)} = \frac{1}{a_l} \left\langle \frac{\partial u_i}{\partial \nu_l} \right\rangle \tag{34}$$

where

$$\left\langle \frac{\partial u_i}{\partial \nu_l} \right\rangle = \frac{\int_{-\infty}^{\infty} \cdots \int_{-\infty}^{\infty} \frac{\partial u_i}{\partial \nu_l} \prod_{j=1}^{m} p(\nu_j, a_j) \, d\nu_j}{\int_{-\infty}^{\infty} \cdots \int_{-\infty}^{\infty} \prod_{j=1}^{m} p(\nu_j, a_j) \, d\nu_j} \tag{35}$$

and where $p(\nu_j, a_j) = a_j/\cosh a_j\nu_j$. The function

$$P(\nu_1, \cdots, \nu_m) = \prod_{j=1}^{m} p(\nu_j, a_j) \tag{36}$$

can be interpreted as a probability density in ν space. Thus the Fourier coefficient $B_{\omega_l}^{(i)}$ is related to a generalized average of the sensitivity $\langle \partial u_i/\partial \nu_l \rangle$. (For an alternative transformation, $G_l(\sin \omega_l s) = \bar{k}_l(1 + \nu_l)$, the same result is obtained.) The relationship of eq. (34) to the linear sensitivity measure can be seen by expanding $\partial u_i/\partial \nu_l$ in a MacLaurin series about $\nu = 0$ and substituting the results into eq. (35) to give

$$\left\langle \frac{\partial u_i}{\partial \nu_l} \right\rangle = \left. \frac{\partial u_i}{\partial \nu_l} \right|_{\nu=0} + \frac{\int_{-\infty}^{\infty} \cdots \int_{-\infty}^{\infty} \prod_{j=1}^{m} p(\nu_j, a_j) \sum_{r=1}^{\infty} \frac{\nu_l^r}{r!} \left[\frac{\partial^r}{\partial \nu_l^r} \left(\frac{\partial u_i}{\partial \nu_l} \right) \right]_{\nu=0} d\nu_1 \cdots d\nu_m}{\int_{-\infty}^{\infty} \cdots \int_{-\infty}^{\infty} \prod_{j=1}^{m} p(\nu_j, a_j)\, d\nu_1 \cdots d\nu_m} \tag{37}$$

From eq. (37) it is clear that unless the $u_i(t; s)$ are linear functions of the parameters $k_1, \cdots, k_m$, the generalized form eq. (34) is not equivalent to $\partial u_i/\partial \nu_l|_{\nu=0}$. If the second and higher order terms can be neglected, then the following approximate relationship holds:

$$B_{\omega_l}^{(i)} \simeq \frac{1}{a_l} \left. \frac{\partial u_i}{\partial \nu_l} \right|_{\nu=0} \tag{38}$$

Appendix B

Extension to Correlated Parameters

In the preceding development the parameters k_l, $l = 1, 2, \cdots, m$, have been assumed to be uncorrelated. Thus a range of uncertainty can be assigned to each parameter independent of the uncertainty range assigned to the other parameters. Relationships may exist, however, among two or more parameters. For example, if k_1 and k_2 represent fractional paths for a single reaction, then $k_1 + k_2 = 1$.

We assume that the parameters are subject to the following constraint:

$$H(k_1, k_2, \cdots, k_m) \leq 0 \tag{39}$$

To employ the FAST method it is necessary to find a set of transformations $k_l = h_l(\alpha_1, \alpha_2, \cdots, \alpha_m)$ such that eq. (39) is satisfied for a set of independent α_l. The fundamental Fourier coefficient for α can be called B_{ω_α}. We need

to relate B_{ω_α} to the Fourier coefficients B_{α_1} and B_{ω_2}. This can be done by considering the sensitivity coefficients

$$\frac{\partial u_i}{\partial k_j} = \sum_{l=1}^{m} \frac{\partial \alpha_l}{\partial k_j} \frac{\partial u_i}{\partial \alpha_l} \tag{40}$$

where $\partial \alpha_l / \partial k_j$ is evaluated at the nominal values $\bar{k}_j$. The material in Appendix A is now needed. By using the ν-space average, eq. (35), we can approximate eq. (40) by

$$\frac{\partial u_i}{\partial k_j} \cong \sum_{l=1}^{m} \frac{1}{a_l} \frac{\partial \alpha_l}{\partial k_j} \left| \frac{\partial u_i}{\partial \nu_l} \right| \tag{41}$$

Then, from eq. (41),

$$B_{\omega j}^{(i)} \cong \sum_{l=1}^{m} \frac{\partial \alpha_l}{\partial k_j} B_{\omega_\alpha l}^{(i)} \tag{42}$$

To illustrate the approach consider, for example, the case of the constraint

$$\frac{k_2}{a} + \frac{k_1}{b} = 1 \tag{43}$$

where $0 < k_1 < b$, $0 < k_2 < a$, and $\bar{k}_1 = b/2$ and $\bar{k}_2 = a/2$. To apply the FAST method to k_1 and k_2 we represent k_1 and k_2 by

$$k_1 = b - \frac{b}{\sqrt{a^2 + b^2}} \alpha \tag{44}$$

$$k_2 = \frac{a}{\sqrt{a^2 + b^2}} \alpha \tag{45}$$

Thus for $0 < \alpha < \sqrt{a^2 + b^2}$, the constraint eq. (43) is satisfied. The search for α is chosen as

$$\alpha = \frac{\sqrt{a^2 + b^2}}{2} (1 + \sin \omega_\alpha s) \tag{46}$$

and the FAST method is applied to α rather than to k_1 and k_2. For example, the constraint (44) becomes

$$B_{\omega_1} \cong \frac{\partial \alpha}{\partial k_1} \left| \frac{\partial u}{\partial k_1} \right| \cong \frac{\sqrt{a^2 + b^2}}{b} B_{\omega_\alpha}$$

$$B_{\omega_2} \cong \frac{\partial \alpha}{\partial k_2} \left| \frac{\partial u}{\partial k_2} \right| \cong \frac{\sqrt{a^2 + b^2}}{a} B_{\omega_\alpha} \tag{47}$$

We note that $-bB_{\omega_1} \cong aB_{\omega_2}$, which is consistent with the relationship between the sensitivity coefficients $\partial u / \partial k_1$ and $\partial u / \partial k_2$.

Bibliography

[1] J. H. Seinfeld and L. Lapidus, "Mathematical Methods in Chemical Engineering," vol. III, Process Modeling, Estimation and Identification, Prentice-Hall, Englewood Cliffs, NJ, 1974.
[2] R. I. Cukier, C. M. Fortuin, K. E. Shuler, A. G. Petschek, and J. H. Schaibly, *J. Chem. Phys.*, **59,** 3873 (1973).
[3] J. H. Schaibly and K. E. Shuler, *J. Chem. Phys.*, **59,** 3879 (1973).
[4] R. I. Cukier, J. H. Schaibly, and K. E. Shuler, *J. Chem. Phys.*, **63,** 1140 (1975).
[5] R. I. Cukier, H. B. Levine, and K. E. Shuler, *J. Comp. Phys.*, **26,** 1 (1978).
[6] H. Weyl, *Am. J. Math.*, **60,** 889 (1938).
[7] R. A. Cadzow, "Discrete Time Systems," Prentice-Hall, Englewood Cliffs, NJ, 1973.
[8] C. W. Gear, "Numerical Initial Value Problems in Ordinary Differential Equations," Prentice-Hall, Englewood Cliffs, NJ, 1971.
[9] A. A. Boni and R. C. Penner, *Combust. Sci. Technol.*, **15,** 99 (1976).
[10] A. C. Hindmarsh and G. D. Byrne, "EPISODE: An Experimental Package for the Integration of Systems of Ordinary Differential Equations," Lawrence Livermore Laboratory Rep. UCID-30112, May 1975.
[11] G. D. Byrne, A. C. Hindmarsh, K. R. Jackson, and H. G. Brown, *Computers and Chem. Eng.*, **1,** 133 (1977).

Received June 30, 1978
Revised August 28, 1978

10.4 Global Sensitivity Analysis - A Computational Implementation of the Fourier Amplitude Sensitivity Test (FAST)

(Reprinted from Computers and Chemical Engineering, 6, 15-25.)

Computers & Chemical Engineering Vol. 6, No. 1, pp. 15–25, 1982
Printed in Great Britain.

0098-1354/82/010015-11$03.00/0
Pergamon Press Ltd.

GLOBAL SENSITIVITY ANALYSIS—A COMPUTATIONAL IMPLEMENTATION OF THE FOURIER AMPLITUDE SENSITIVITY TEST (FAST)

GREGORY J. MCRAE, JAMES W. TILDEN and JOHN H. SEINFELD*
Environmental Quality Laboratory, California Institute of Technology, Pasadena, CA 91125, U.S.A.

(*Received August* 18, 1980; *received for publication* 6 *January* 1981)

Abstract—This paper describes a computational implementation of the Fourier Amplitude Sensitivity Test (FAST) and illustrates its use with a sample problem. The FAST procedure is ideally suited to the task of determinating the global sensitivity of nonlinear mathematical models subjected to variations of arbitrary size in either the system parameters or initial conditions. A FORTRAN computer program, capable of performing sensitivity analyses of either algebraic or differential equation systems is described.

Scope—In virtually all branches of science and engineering, descriptions of phenomena lead to differential equations of substantial complexity. The complexity of such models makes it difficult to determine the effect uncertainties in physical parameters have on their solutions. Traditionally, the analysis of the sensitivity of models to small perturbations in parameters is called *local sensitivity analysis*. When a measure of the sensitivity of the solution to variations of a parameter is combined in an appropriate manner with a measure of the actual degree of uncertainty in the parameter's value, it may then be determined which parameters, through both their sensitivity and uncertainty, have the most influence on the solution. Such a procedure can be called a *global sensitivity analysis*.

Conventional global sensitivity analysis techniques have generally been based on either a pattern search or Monte Carlo technique. Pattern search and Monte Carlo approaches can become extremely time consuming and expensive as the number of parameters become large.

The Fourier Amplitude Sensitivity Test (FAST) technique associates each uncertain parameter with a specific frequency in the Fourier transform space of the system. The system sensitivities are then determined by solving the system equations for discrete values of the Fourier transform variable and then computing the Fourier coefficients associated with each parameter frequency. This approach allows nonlinear global sensitivities of systems subjected to large parameter variations to be determined in a practical and efficient manner.

Conclusions and Significance—Because of the complex nature of many physical and chemical systems, an integral element of any modeling study should be a formal assessment of the effects of uncertainties in the parameterization of the physical processes. In this paper particular attention is given to the Fourier Amplitude Sensitivity Test (FAST) for examining the global sensitivity of nonlinear mathematical models. The FAST technique allows arbitrarily large variations in either system parameters or initial conditions.

The computer program presented here provides a general framework for implementation of the FAST method. When combined with a user supplied subroutine for the specific system of interest, the FAST program computes the sensitivities of the system outputs to the parameter variations specified by the user. The method is illustrated on an example involving a simple autocatalytic reaction mechanism.

1. INTRODUCTION

A variety of chemical engineering phenomena are described by lengthy and complex mathematical models. It is often desirable to determine the effect of uncertainties in system parameters on the system behavior and to determine which parameters are most influential. The complexity of many models makes it difficult to determine the effect uncertainties in physical and chemical parameters have on solutions. When a measure of the sensitivity of the solution to variations of a parameter is combined in an appropriate manner with a measure of the degree of uncertainty in the parameter's value, one may then determine which parameters, through both their sensitivity and uncertainty, have the most influence on predicted system behavior. Such a study can be termed a *sensitivity/uncertainty analysis* or *a global sensitivity analysis*.

Consider a system that is described by a set of n coupled ordinary differential equations containing m parameters, $k_1, k_2, \ldots, k_m$,

$$\frac{d\mathbf{x}}{dt} = \mathbf{f}(\mathbf{x}; \mathbf{k}) \tag{1}$$

where $\mathbf{x}$ is the n-dimensional vector of the system state and $\mathbf{k}$ is the m-dimensional parameter vector. A basic measure of the effect of uncertainties in $\mathbf{k}$ on $\mathbf{x}(t)$ is the deviation in $\mathbf{x}$ caused by a variation in $\mathbf{k}$, $\Delta\mathbf{x}(t; \mathbf{k}) = \mathbf{x}(t; \bar{\mathbf{k}} + \Delta\mathbf{k}) - \mathbf{x}(t; \bar{\mathbf{k}})$, where $\mathbf{x}(t; \bar{\mathbf{k}})$ denotes the solution of (1) at time t with $\mathbf{k} = \bar{\mathbf{k}}$. Taylor's theorem can be invoked

*Author whom correspondence should be addressed.

to express the deviation in state variable i as

$$x_i(t;\bar{\mathbf{k}}+\Delta\mathbf{k}) = x_i(t;\bar{\mathbf{k}}) + \sum_{j=1}^{m} \frac{\partial x_i}{\partial k_j}\Delta k_j + 0((\max \Delta k_j)^2). \quad (2)$$

The partial derivatives $\partial x_i(t)/\partial k_j$, $i = 1, 2, \ldots, n, j = 1, 2, \ldots, m$ are the so-called *sensitivity coefficients*. Much of the work on sensitivity analysis has been concerned with calculation of these sensitivity coefficients. Sensitivity analysis techniques that rely on calculation of the sensitivity coefficients are strictly applicable only to small parameter variations since the higher order terms in (2) are neglected.

Although the sensitivity coefficients $\partial x_i/\partial k_j$ provide direct information on the effect of a small variation in each parameter about its nominal value $\bar{k}_j$ on each state variable, they do not indicate the effect of simultaneous, large variations in all parameters on the state variables. An analysis that accounts for simultaneous parameter variations of arbitrary magnitude can be termed a global sensitivity analysis. The sensitivity coefficients are local gradients in the multidimensional parameter space at the nominal value $\mathbf{k}$. A technique that considers the effect of simultaneous parameter variations over their actual expected ranges of uncertainty produces an average measure of sensitivity over the entire admissible region of variation and thus provides an essentially different measure of sensitivity than that of the sensitivity coefficients. Therefore, both types of analysis are useful in studying the behavior of a system.

Figure 1 shows schematically a hypothetical solution surface $x_i(t;\mathbf{k})$ over the domain of uncertainty of two parameters, k_1 and k_2. The nominal parameter values are $\bar{k}_1$ and $\bar{k}_2$, and the assumed upper and lower limits of variation are indicated producing the domain of uncertainty in the $k_1 - k_2$ plane. The resulting range of uncertainty in x_i is also indicated. The surface shown in Fig. 1 is that at a certain time t. Generally the variations in the solutions $x_i(t)$, $i = 1, 2, \ldots, n$ must be considered as a function of time. The point Q on the solution surface represents the magnitude of the solution x_i at time t with both parameters at their nominal, or best guess, values. Varying both parameters over the full domain of uncertainty generates the two-dimensional solution surface that changes as t changes. The sensitivity coefficients, $\partial x_i/\partial k_1$ and $\partial x_i/\partial k_2$, evaluated at $\bar{k}_1$ and $\bar{k}_2$ represent the slopes of the surface in the two coordinate directions at point Q. A local sensitivity analysis would focus on calculation of these two derivatives and their time variation. For small displacements about the nominal values, the tangent plane at Q differs from the actual solution surface only by a small amount. In this regime the sensitivity coefficients indicate to which parameter the solution is most sensitive. The sensitivity coefficients at point Q do not contain information on the behavior of the surface away from Q nor do they indicate the full range of variation of x_i in the domain of uncertainty of the parameters. The global sensitivity analysis is concerned with assessing the behavior of the entire solution surface of x_i over the domain of uncertainty of the two parameters.

If we have some knowledge of the probability distributions of the two parameters, $p_1(k_1)$ and $p_2(k_2)$, the probability disribution for x_i can in principle be computed. From the probability distribution of x_i, certain statistical properties such as the expected value,

$$\langle x_i(t)\rangle = \int_{k_2\min}^{k_2\max}\int_{k_1\min}^{k_1\max} x_i(t;k_1,k_2)p_1(k_1)p_2(k_2)\,dk_1\,dk_2 \quad (3)$$

and the variance,

$$\sigma_i^2(t) = \langle x_i(t)^2\rangle - \langle x_i(t)\rangle^2 \quad (4)$$

where

$$\langle x_i(t)\rangle^2 = \int_{k_2\min}^{k_2\max}\int_{k_1\min}^{k_1\max} x_i(t;k_1,k_2)^2 p_1(k_1)p_2(k_2)\,dk_1\,dk_2 \quad (5)$$

can be computed.

In Fig. 2 given assumed probability distributions for each parameter, a hypothetical probability distribution for the solution is shown. Note that the best value of each parameter, the nominal value, may differ in general from either the most likely value or the mean value. Likewise, the mean value of the solution, $\langle x_i(t)\rangle$ may not correspond to the value at the nominal parameter values, i.e. point Q.

Whether or not the probability distributions for k_1 and k_2 are given, the solution surface for x_i can be determined by systematically selecting points in the domain of uncertainty of k_1 and k_2 and solving the system to

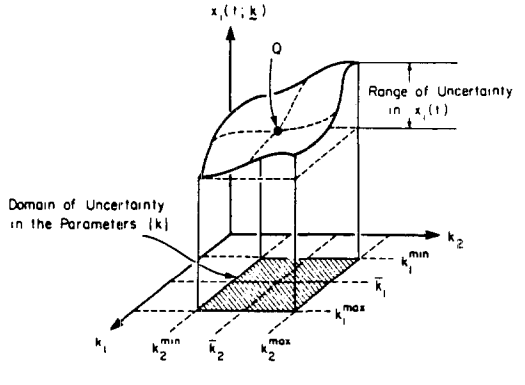

Fig. 1. Hypothetical solution surface over the domain of uncertainty of two parameters (after Gelinas and Vajk[8]).

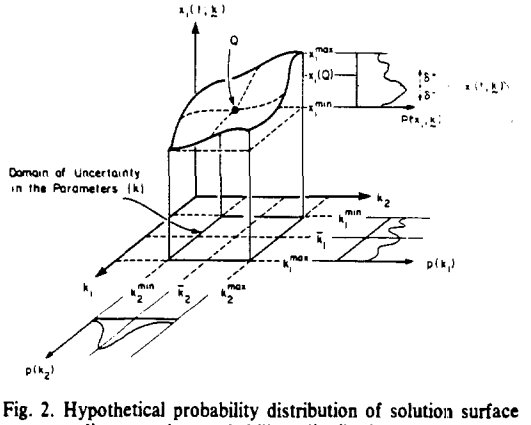

Fig. 2. Hypothetical probability distribution of solution surface corresponding to the probability distributions of the two parameters (after Gelinas and Vajk[8]).

determine $x_i(t; k_1, k_2)$. This approach is indicated in Fig. 3. A sensitivity/uncertainty analysis necessitates some form of sampling over the domain of uncertainty of the parameters.

Figure 3 is a schematic illustration of the Monte Carlo method of sensitivity analysis. A random number generator is used to select values of the uncertain parameters within the domain of uncertainty. The system is then solved for each of the parameter combinations randomly selected. The values of $x_i(t; \mathbf{k})$ thus computed are analyzed by standard statistical methods. The distribution of values obtained is shown in Fig. 3 as a histogram with mean value $\langle x_i \rangle$. The randomly selected points in the domain of uncertainty of the parameters can be chosen according to any prescribed probability density functions for the parameters. No special programming is required, only that needed to select the parameter values and analyze the solutions statistically.

This paper is devoted to a pattern search procedure for global sensitivity analysis that is an alternative to the Monte Carlo method illustrated in Fig. 3. The method is called the Fourier Amplitude sensitivity Test (FAST) and was originally developed by Shuler *et al.*[1–4].

In the next section the mathematical basis of the FAST method is outlined. Then in Section 3 its computational implementation is described. Section 4 contains the description of the computer program and its operation. An example drawn from chemical kinetics is given in Section 5 to illustrate the use of the program.

2. MATHEMATICAL BASIS OF THE FAST METHOD

The basic problem is to determine the sensitivity of each x_i to simultaneous variations in all the parameters $\{k_j\}$. This is done by considering that the $\{k_j\}$ have a distribution of values resulting from either imprecision or uncertainty in their definition. Under these conditions, the ensemble mean for x_i is given by the generalization of (3),

$$\langle x_i \rangle = \int \cdots \int x_i(k_1, k_2, \ldots, k_m) p(k_1, k_2, \ldots, k_m) \, dk_1 \, dk_2, \ldots, dk_m \quad (6)$$

where p is the m-dimensional probability density for $\mathbf{k}$.

The central idea of the FAST method is to convert the m-dimensional integral (6) into a one dimensional form by using the transformation,

$$k_l = G_l[\sin(\omega_l s)]; \; l = 1, 2, \ldots, m. \quad (7)$$

For an appropriate set of functions $\{G_l\}$, it can be shown that[5]

$$\bar{x}_i = \langle x_i \rangle = \lim_{T \to \infty} \frac{1}{2T} \int_{-T}^{T} x_i[k_1(s), k_2(s), \ldots, k_m(s)] \, ds. \quad (8)$$

This relationship will hold only if the frequency set, $\{\omega_l\}$, is incommensurate, i.e.

$$\sum_{i=1}^{m} \gamma_i \omega_i = 0. \quad (9)$$

for an integer set of $\{\gamma_i\}$ if and only if $\gamma_i = 0$ for every i. The functions $\{G_l\}$ need to be chosen so that the arc length, ds, is proportional to $p(k_1, k_2, \ldots, k_m) \, dk_l$ for all l. The transformation then results in a search curve that samples the parameter space in a manner consistent with the statistics described by $p(k_1, k_2, \ldots, k_m)$.

The parametric curve defined by (7) is termed a search curve, and s is termed the search variable. As s is varied, (7) traces out a space filling curve in the parameter space. If it were possible to use an incommensurate frequency set, the curve would never close upon itself and would pass arbitrarily close to every point in the parameter space. This result is a consequence of Weyl's theorem. When integer frequencies are used, it is not possible to obtain a truly incommensurate frequency set and the search curves take on the appearance of multi-dimensional Lissajous curves. The use of higher frequencies results in successively longer search curves. Two examples are shown in Fig. 4 and 5. The length of the search curve and the density of sample points is considerably greater in the second case.

Practical considerations dictate that an integer rather than an incommensurate frequency set must be used. This introduces two types of error. First, the search curve is no longer space-filling, i.e. it does not pass

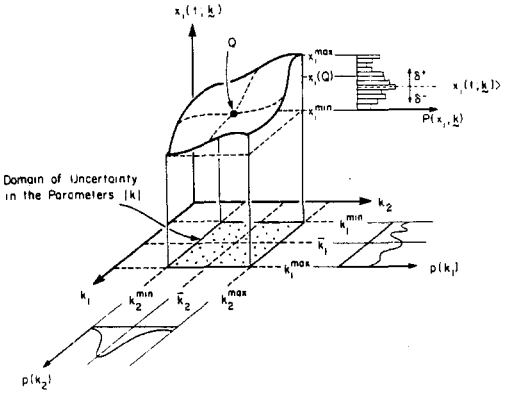

Fig. 3. Monte Carlo approach to generating the solution surface (after Gelinas and Vajk[8]).

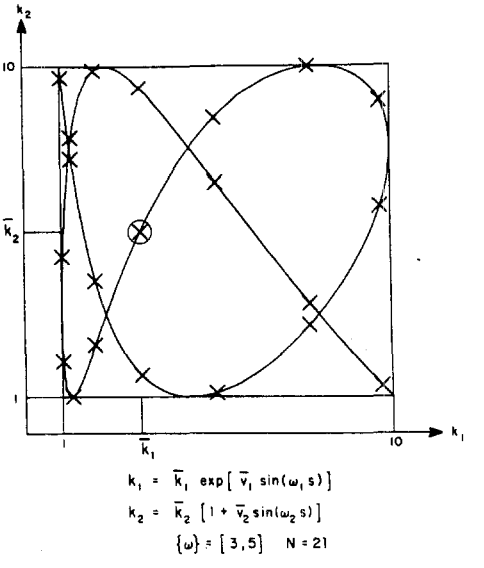

Fig. 4. Search curve with frequencies $\omega_1 = 3$, $\omega_2 = 5$.

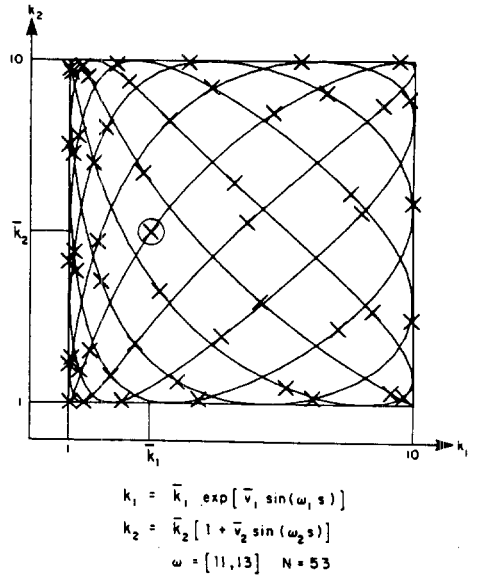

Fig. 5. Search curve with frequencies $\omega_1 = 11$, $\omega_2 = 13$.

arbitrarily close to any point in the k-space; secondly, the fundamental frequencies used to describe the set $\{k_i\}$ will have harmonics that interfere with one another. However, the differences between $\bar{x}$ and $\langle x\rangle$ for a well chosen integer frequency set can be made arbitrarily small[2, 3].

An integer frequency set results in a periodic search curve that becomes a closed path in the s-space. When s is varied between $-\pi$ and $+\pi$, the entire search curve is traversed. The periodicity of the $\{k_i\}$ then implies that the Fourier coefficients

$$A_{p\omega_l}^{(i)} = \frac{1}{2\pi}\int_{-\pi}^{\pi} x_i[k_1(s),\ldots,k_m(s)]\cos(p\omega_l s)\,ds \qquad p = 0, 1, 2, \ldots \quad (10)$$

$$B_{p\omega_l}^{(i)} = \frac{1}{2\pi}\int_{-\pi}^{\pi} x_i[k_1(s),\ldots,k_m(s)]\sin(p\omega_l s)\,ds \qquad p = 1, 2, \ldots \quad (11)$$

are a measure of the sensitivity of the x_i output function to the kth uncertain parameter. For instance, in the case where x_i is totally insensitive to a given parameter, the coefficients corresponding to that parameter would be zero.

The ensemble average,

$$\langle x_i\rangle = \frac{1}{2\pi}\int_{-\pi}^{\pi} x_i[k_1(s),\ldots,k_m(s)]\,ds \quad (12)$$

can be expressed in terms of the Fourier coefficients as

$$\langle x_i\rangle^2 = A_0^{(i)2} + B_0^{(i)2} = A_0^{(i)2}. \quad (13)$$

The variance of x_i is then

$$\sigma_i^2 = \frac{1}{2\pi}\int_{-\pi}^{\pi} x_i^2\,ds - \langle x_i\rangle^2. \quad (14)$$

Parseval's theorem can then be used to determine the variance of x_i, i.e.

$$\langle x_i^2\rangle = \frac{1}{2\pi}\int_{-\pi}^{\pi} x_i^2(s)\,ds = \sum_{j=-\infty}^{\infty}\{A_j^{(i)2} + B_j^{(i)2}\}. \quad (15)$$

The variance and harmonics due to ω_l are expressed by

$$\sigma_{\omega_l}^{(i)2} = 2\sum_{p=1}^{\infty}[A_{p\omega_l}^{(i)2} + B_{p\omega_l}^{(i)2}]. \quad (16)$$

The normalized sensitivity measure, the partial variance, $S_{\omega_l}^{(i)}$, is then defined by the ratio of the variance due to frequency ω_l to the total variance,

$$S_{\omega_l}^{(i)} = \frac{(\sigma_{\omega_l}^{(i)})^2}{(\sigma^{(i)})^2}. \quad (17)$$

Thus the $\{S_{\omega_l}^{(i)}\}$ represent an ordered measure of the sensitivity of the system to each of the $\{k_i\}$ parameters.

The FAST method requires that the system be solved to produce the output state variable values, the Fourier coefficients and subsequently the partial variances.

3. COMPUTATIONAL IMPLEMENTATION OF THE FAST ALGORITHM

Application of the FAST method requires the numerical evaluation of the Fourier coefficients, $A_{p\omega_l}^{(i)}$ and $B_{p\omega_l}^{(i)}$. This in turn requires the x_i be evaluated as s ranges over $[-\pi, \pi]$. Restricting the frequency set to odd integers reduces the range of s to $[-\pi/2, \pi/2]$. In this case

$$\begin{aligned} x(\pi - s) &= x(s) \\ x(-\pi + s) &= x(-s) \\ x\left(\frac{\pi}{2} + s\right) &= x\left(\frac{\pi}{2} - s\right) \\ x\left(-\frac{\pi}{2} + s\right) &= x\left(-\frac{\pi}{2} - s\right) \end{aligned} \quad (18)$$

and the Fourier coefficients can be expressed as:

$$A_j^{(i)} = \begin{cases} 0 & ;\ j \text{ odd} \\ \dfrac{1}{\pi}\displaystyle\int_0^{\pi/2}[x_i(s) + x_i(-s)]\cos js\,ds & ;\ j \text{ even} \end{cases} \quad (19)$$

and

$$B_j^{(i)} = \begin{cases} 0 & ;\ j \text{ even} \\ \dfrac{1}{\pi}\displaystyle\int_0^{\pi/2}[x_i(s) - x_i(-s)]\sin js\,ds & ;\ j \text{ odd}. \end{cases} \quad (20)$$

The actual number of points at which the system must be evaluated can be derived from the Nyquist criterion[6], and is found to be

$$r \geq N\omega_{\max} + 1. \quad (21)$$

Where r is the number of solution points and N an even integer. For convenience in calculating the Fourier coefficients, the additional condition

$$2r = 4q + 2 \quad (22)$$

where q is an integer is also imposed. The values of s are taken to be equally spaced throughout the range $[-\pi/2,$

$\pi/2]$, and the discrete points at which x_i is calculated in the Fourier space are given by

$$s_j = \frac{\pi}{2}\left[\frac{2j-r-1}{r}\right] \quad j = 1, 2, \ldots, r. \tag{23}$$

The following difference expressions for Fourier coefficients can be derived by a simple numerical quadrature technique[4, 7],

$$A_j^i = 0 \ (j \text{ odd}) \tag{24}$$
$$B_j^i = 0 \ (j \text{ even}) \tag{25}$$

$$A_j^i = \frac{1}{2q+1}\left[x_0{}^i + \sum_{k=1}^{q}(x_k{}^i + x_{-k}^i)\cos\left(\frac{\pi jk}{2q+1}\right)\right]; \ (j \text{ even}) \tag{26}$$

$$B_j^i = \frac{1}{2q+1}\left[\sum_{k=1}^{q}(x_k{}^i - x_{-k}^i)\sin\left(\frac{\pi jk}{2q+1}\right)\right]; \ (j \text{ odd}) \tag{27}$$

where x^i replaces x_i for notational purposes.

Interference between the frequencies will occur as a result of this numerical evaluation when

$$q\omega_j = p\omega_l[\text{Mod}\,(N\omega_{\max}+1)] \tag{28}$$

which results in

$$|A^{(i)}_{p\omega_l}|^2 + |B^{(i)}_{p\omega_l}|^2 = |A^{(i)}_{q\omega_j}|^2 + |B^{(i)}_{q\omega_j}|^2 \tag{29}$$

since

$$\sin\left[\frac{\pi q\omega_j}{N\omega_{\max}+1}\right] = \pm\sin\left[\frac{\pi p\omega_l}{N\omega_{\max}+1}\right] \tag{30}$$

and

$$\cos\left[\frac{\pi q\omega_j}{N\omega_{\max}+1}\right] = \pm\cos\left[\frac{\pi p\omega_l}{N\omega_{\max}+1}\right]. \tag{31}$$

This interference, called aliasing, is eliminating when

$$r\omega_l \le N\omega_{\max}+1\ . \tag{32}$$

N is therefore the maximum number of Fourier coefficients that may be retained in calculating the partial variances without interferences between the assigned frequencies. The expression for $S^{(i)}_{\omega_l}$ then becomes

$$S^{(i)}_{\omega_l} = \frac{2}{\sigma_i^2}\sum_{j=1}^{N}\left[|A^{(i)}_{j\omega l}|^2 + |B^{(i)}_{j\omega_l}|^2\right]. \tag{33}$$

Interference will also result from the use of an integer frequency set if the number of Fourier coefficients N used in the summation (33) is greater than or equal to the smallest frequency. To illustrate this consider (33) for the frequencies ω_l and $\omega_{l'}$,

$$S^{(i)}_{\omega_l} = A^{(i)2}_{\omega_l} + B^{(i)2}_{\omega_l} + \cdots + A^{(i)2}_{N\omega_l} + B^{(i)2}_{N\omega_l}$$

$$S^{(i)}_{\omega_{l'}} = A^{(i)2}_{\omega_{l'}} + B^{(i)2}_{\omega_{l'}} + \cdots + A^{(i)2}_{N\omega_{l'}} + B^{(i)}_{N\omega_{l'}}.$$

If $N \ge \omega_1$, terms in the series for $S^{(i)}_{\omega l}$ and $S^{(i)}_{\omega l'}$ become identical. For example, if $N = \omega_1$, and if $\omega_{l'} > \omega_l$, there will be a term in the $S^{(i)}_{\omega_{l'}}$ series for which

$$A^{(i)}_{\omega_l|\omega_l} = A^{(i)}_{j\omega_{l'}}.$$

In such a case, the effect of the variation of parameter l enters spuriously into the partial variance for the variation of parameter l'.

In general, the interference between the higher harmonics will be eliminated when

$$N < \omega_{\min} - 1. \tag{37}$$

N is also related to the number of function evaluations required by (21), so it is desirable to use the minimum possible value, which is $N = 2$. Then a minimum frequency of at least three is sufficient to remove any harmonic interference effects from the partial variances. The final expression for the partial variances then becomes

$$S^{(i)}_{\omega_l} = \frac{2}{\sigma_i^2}\{|B^{(i)}_{1\omega_l}|^2 + |A^{(i)}_{2\omega_l}|^2\}. \tag{38}$$

The choice of $N = 2$ restricts the number of terms in the series to two. This is generally sufficient because the magnitude of the higher order terms in the Fourier series tend to decrease rapidly.

Implementation of the FAST technique also requires the selection of a frequency set, which can be done recursively using

$$\omega_1 = \Omega_n \tag{39}$$
$$\omega_i = \omega_{i-1} + \mathrm{d}_{n+1-i} \tag{40}$$

as described in Cukier *et al.*[4]. The Ω_n and d_n we have used are tabulated in Table 1.

The final step in the FAST implementation is the determination of the transformation function $\{G_l\}$ that determine the actual search curve traversed in s-space. If the probabilities of occurrence for the parameters $\{k_l\}$ are independent, the probability density describing their effects has the form,

$$P(k_1, k_2, \ldots, k_m) = P_1(k_1)P_2(k_2)\ldots P_m(k_m). \tag{41}$$

In this case it can be shown that the transformation functions must obey the relation[5]

$$\pi(1-x^2)^{1/2}P_l(G_l)\frac{\mathrm{d}G_l(x)}{\mathrm{d}x} = 1 \tag{42}$$

with the initial conditions $G_l(0) = 0$. A tabulation of four different search curve formulations and their transformation functions is given in Table 2.

The parameter probability distributions used to derive these curves are described in Cukier *et al.*[3]. The first search curve is suitable for cases with small variations in the uncertain parameters while the second and third are applicable to cases with large variations.

4. PROGRAM DESCRIPTION AND OPERATION

A flowchart of the FAST program is shown in Fig. 6. There are two user interfaces with the program. One is the input data set which contains the following information; program description cards, control cards, analysis times (optional), and parameter cards. The second interface is a user supplied subroutine, called F, that calculates the state variable values for a given parameter combination. When the state variables must

Table 1. Parameters used in calculating frequency sets free of interferences to fourth order

N	Ω_n	d_n	N	Ω_n	d_n
1	0	4	26	385	416
2	3	8	27	157	106
3	1	6	28	215	208
4	5	10	29	449	328
5	11	20	30	163	198
6	1	22	31	337	382
7	17	32	32	253	88
8	23	40	33	375	348
9	19	38	34	441	186
10	25	26	35	673	140
11	41	56	36	773	170
12	31	62	37	875	284
13	23	46	38	873	568
14	87	76	39	587	302
15	67	96	40	849	438
16	73	60	41	623	410
17	85	86	42	637	248
18	143	126	43	891	448
19	149	134	44	943	388
20	99	112	45	1171	596
21	119	92	46	1225	216
22	237	128	47	1335	100
23	267	154	48	1725	488
24	283	196	49	1663	166
25	151	34	50	2019	0

Table 2. Search curves for Fourier Amplitude Sensitivity Test computer program

APPLICATION	$k_j(s)$	MEAN VALUE $\bar{k}_j$	NOMINAL VALUE $\tilde{r}_j$
ADDITIVE VARIATION	$k_j(s) = \bar{k}_j[1 + \tilde{r}_j \sin \omega_j s]$	$\frac{k_j^u + k_j^l}{2}$	$\frac{k_j - k_j^l}{k_j + k_j^l}$
EXPONENTIAL VARIATION	$k_j(s) = \bar{k}_j \exp[\tilde{r}_j \sin \omega_j s]$	$\sqrt{k_j^u k_j^l}$	$\frac{1}{2} \ln\left(\frac{k_j^u}{k_j^l}\right)$
PROPORTIONAL VARIATION $k_j^u = a\bar{k}_j$, $k_j^l = \left(\frac{\bar{k}_j}{a}\right)$	$k_j(s) = \bar{k}_j \exp[\nu_j \sin \omega_j s]$	$\bar{k}_j$	$\ln(a)$
SKEWED VARIATION $k_j > \left(\frac{k_j^u + k_j^l}{2}\right)$	$k_j(s) = \nu_j\left[\frac{a_j + \beta_j \sin \omega_j s - 1}{a_j + \beta_j \sin \omega_j s}\right]$	$\nu_j\left(\frac{a_j - 1}{a_j}\right)$	$a_j = \frac{1}{2}\left[\frac{r^u}{r^u - 1} + \frac{r^l}{r^l - 1}\right]^b$ $\beta_j = -\frac{a_j(r^u + r^l - 2)}{(r^u - r^l)}$ $\nu_j = -\bar{k}_j\left[\frac{r^u + r^l - 2r^u r^l}{r^u + r^l - 2}\right]$

[a] k_j^u – upper limit for parameter; k_j^l – lower limit for parameter

[b] $r^u = k_j^u/\bar{k}_j$, $r^l = k_j^l/\bar{k}_j$

be calculated numerically, the user must also provide a subroutine to perform this function. For chemical kinetic applications several existing differential equation solvers can be easily adopted.

The input information is stored in an array called *P*. Subroutine *F* must access *P* in the same sequence that the parameters were specified on the input cards. The state variables calculated in the *F* subroutine are returned in an array named *C*. The structure of this array is shown in Fig. 7. An example of subroutine *F* for the sample problem in Section 5 is given in Fig. 8. The detailed fields and formats for the input file are shown in Table 3.

The default for the number of analysis times is one, and the default for the number of terms in the partial variance series is two. If this latter default is to be changed, care must be exercised to be sure that the number of points at which x and the Fourier coefficients are evaluated is also modified so that interferences between the parameters will not occur.

Five files can be accessed during execution of the program. These are described in Table 4. Whenever the option to save the results is used, both file IDOUT and file IDISC must be allocated. IDOUT must be allocated when the reanalysis option is specified, and IDPLT must be allocated when the option to plot the partial variances is used. ICARD and IPRIN must be allocated at all times.

Several of the arrays used in the FAST program can become quite large for problems involving several parameters, output state variables and/or analysis times. The default sizes for the program arrays are given in Table 5. The program tests the input requests to determine if the fault storage is sufficient, if not, the program

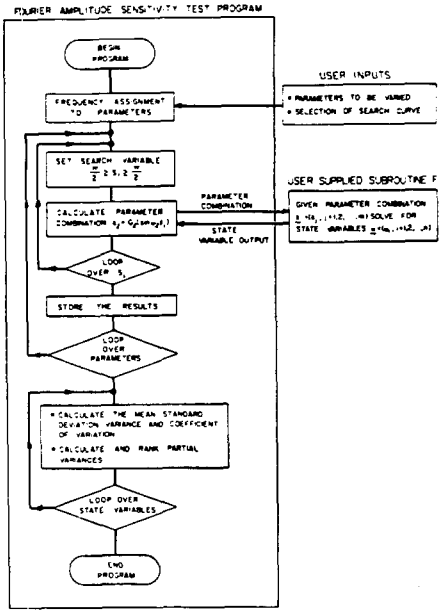

Fig. 6. Fourier Amplitude Sensitivity Test program.

```
      SUBROUTINE F(NT,TIME,NPC,NPARM,P,NSTAT,C)
C
C
C  INPUT VARIABLE        DESCRIPTION                        VARIABLE TYPE
C
C    NT                  NUMBER OF ANALYSIS TIMES           INTEGER
C    TIME                ARRAY OF ANALYSIS TIMES            REAL ARRAY
C    NPC                 CURRENT PARAMETER                  INTEGER
C                        COMBINATION NUMBER
C    NPARM               NUMBER OF PARAMETERS               INTEGER
C    P                   ARRAY OF PARAMETER VALUES          REAL ARRAY
C    NSTAT               NUMBER OF OUTPUT VARIABLES         INTEGER
C
C  OUTPUT VARIABLE        DESCRIPTION                        VARIABLE TYPE
C
C    C                   ARRAY OF STATE VARIABLE            REAL ARRAY
C                        VALUES FOR EACH ANALYSIS TIME
C
      DIMENSION TIME(NT), P(NPARM), C(NSTAT)
C
C     F FOR TEST PROBLEM A + X = 2X
C
C
C
C     UNLOAD THE PARAMETERS
C
      XO=P(1)
      AO=P(2)
      A =P(3)
      B =P(4)
      TA=P(5)
C
C     SOLVE THE SYSTEM
C
      DO 10 J=1,NT
C
      T=TIME(J)
C
      RATE = A*EXP(-B/TA)
C
      S = 1.0 /
          (1.0 + (1.0 - XO )*EXP( -RATE * AO *T )/XO )
C
C     STORE THE SOLUTION IN THE OUTPUT ARRAY
C
      INT=(J-1)*NSTAT
      C(INO+1)=S
   10 CONTINUE
C
      RETURN
      END
```

Fig. 8. Description of subroutine *F*.

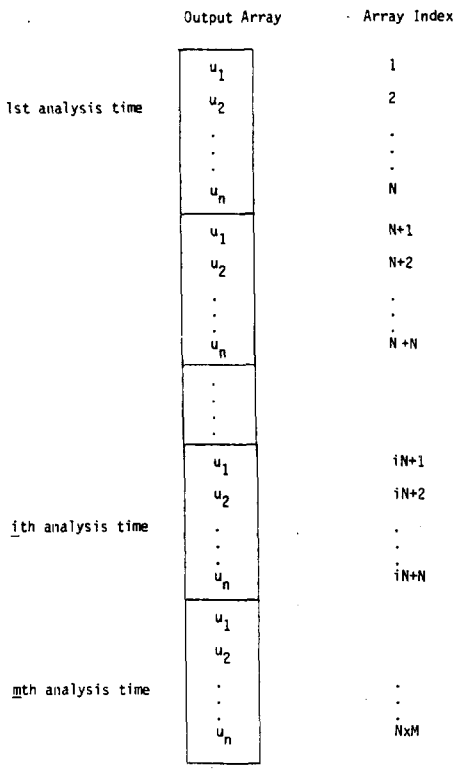

Fig. 7. Structure of the output array *C*

will terminate and write an error message describing which arrays rquire enlargement.

5. SAMPLE PROBLEM

To illustrate the use of the FAST program, a simple example consisting of a single, autocatalytic reaction,

$$A + X \underset{k_r}{\overset{k_f}{\rightleftarrows}} 2X$$

is considered. The concentration of X is governed by

$$\frac{d[X]}{dt} = k_f[A][X] - k_r[X]^2$$
$$[X(0)] = [X]_0.$$

If we assume that $[A]$ is constant, the dimensionless concentration

$$[\hat{X}] = \frac{k_r[X]}{k_f[A]}$$

can be defined, and the differential equation solved to yield

$$[\hat{X}] = [1 - (1 - [\hat{X}]_0^{-1})\, e^{-k_f[A]t}]^{-1}.$$

For the purposes of sensitivity analysis, we express k_f in the Arrhenius form,

$$k_f = B_f\, e^{-C_f/T}.$$

Table 3. Input fields and formats

Problem Description Cards

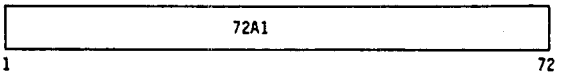

Col 1-72. Descriptive text. Number of cards is optional. The end of the text is indicated by a * in col 1 of the last description card.

Control Card

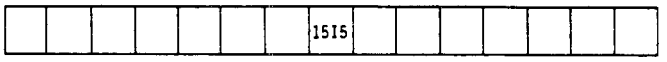

Col.	Description
1-5	number of analysis times
6-10	number of input parameters
11-15	number of output state variables
16-20	number of terms in the partial variance sum (default 2)
21-25	option to print amplitudes
26-30	option to print parameter combinations
31-35	option to print state variable outputs
36-40	multiplier N in $N=Nw_{max}+1$ (default 2)
41-45	option to print unsorted partial variances
46-50	option to save state variable outputs on disc file
51-55	option to reanalyze state variable outputs
56-60	option to plot partial variances
61-65	option to renormalize partial variances for plotting
66-70	option to print partial variances during reanalysis
71-75	option to print sorted partial variances during plotting

Analysis Times (Optional)

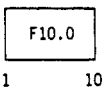

Col	Description
1-10	Analysis time. Number of cards required is determined by the number of analysis times entered in the control card. (These cards may be omitted if the number of analysis times entered on the control card is zero.)

Parameter Card

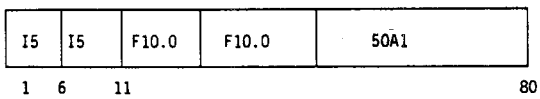

Col	Description
1-5	Parameter number. This number is the array index used for the P array in Subroutine F. The frequency assignment is done in the order in which the parameter cards are input. If an alternative frequency assignment is desired, the order in which the parameter cards are input should be changed, but not the parameter number.
6-10	Search curve type 0 = Fixed Parameter 1 = Small Parameter Variation 2 = Large Parameter Variation 3 = Parameter Variation Expressed as Fractional Change
11-20	Lower parameter limit or fixed parameter value
21-30	Upper parameter limit (type 1) or scale factor (types 2 and 3).
31-80	Parameter Description.

Table 4. Files used by FAST program

Name	Unit Number	Description
IDOUT	1	Reanalysis file. When the option to save the results is used, the output values are stored on this file. When the reanalysis option is used, the state values from this file are read as input.
IDISC	2	Save file. When the save option is on, all other program information including the partial variances is written to this file for later use.
IDPLT	3	Plot file. All information required for plotting is stored on this file during program execution and read back during the execution of the plot routine.
ICARD	5	User's input file.
IPRIN	6	Output print file.

Table 5. FAST program array default sizes

Array	Description	Default Size	Size Variable
IVARB	Variable Numbers	100	NVMAX
ITYPE	Variable Types	100	NVMAX
UBAR	Nominal Values	100	NVMAX
PBAR	Mean Values	100	NVMAX
PV	Variances	100	NVMAX
INDEX	Sort Array	100	NVMAX
PARM	Parameter Combinations	100	NVMAX
DESC	Parameter Descriptions	(48,100)	NVMAX
IW	Frequency Set	50	NPMAX
TIME	Analysis Times	50	NTMAX
OUTPT	Parameter Output	200	NOMAX
FI	Output for All Parameter Combinations	2000	NSMAX

NVMAX	Max Number of Input Parameters	100
NPMAX	Max Number of Variable Parameters	50
NTMAX	Max Number of Analysis Times	50
NOMAX	Max Storage for Each Parameter Combination	200
NSMAX	Max Storage for All Parameter Combinations	2000
NEQN	Number of Solutions for Each Combination	no limit
NSTAT	Number of State Variable Outputs	no limit

We wish to examine the sensitivity of $[\hat{X}]$ to $[\hat{X}]_0$, $[A]$, B_f, C_f, and T from $t = 0$ to $t = 2$. The nominal values and ranges of variation of these five parameters are given in Table 6.

Figure 9 shows the first-order normalized sensitivity coefficients as a function of time evaluated at the nominal values of Table 6. These are defined by

$$\rho_i(t) = \frac{\left|\frac{\partial \hat{x}}{\partial k_i}\Delta k_i\right|}{\sum_{j=1}^{m}\left|\frac{\partial \hat{x}}{\partial k_j}\Delta k_j\right|}.$$

Figure 10 presents the partial variances for the 5 parameters as determined by the FAST method with the

Table 6. Parameter variations for autocatalytic system

Parameter	Nominal Value	Range of Uncertainty (±5%)
$[\hat{X}]_0$	0.15	0.1425 - 0.1575
[A]	1.73	1.644 - 1.817
B_f	1.0	0.95 - 0.105
C_f	165.0	156.8 - 173.3
T	300.0	285.0 - 315.0

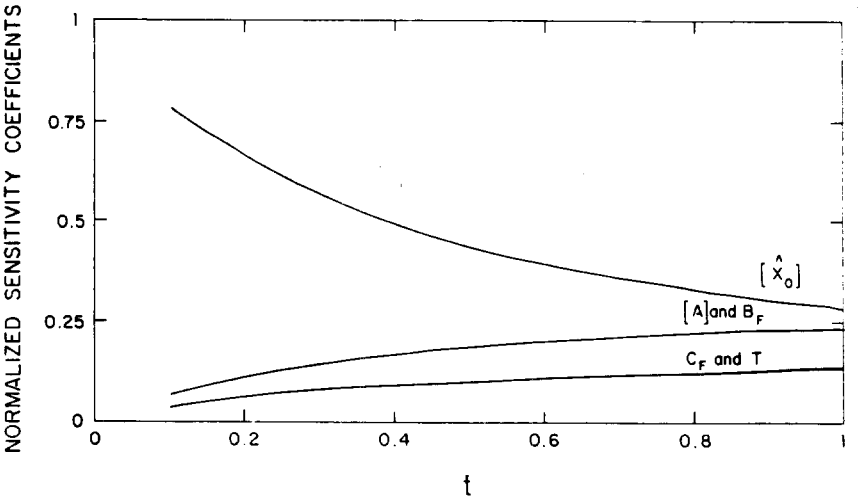

Fig. 9. First-order sensitivity coefficients for the reaction $A + X \rightleftarrows 2X$.

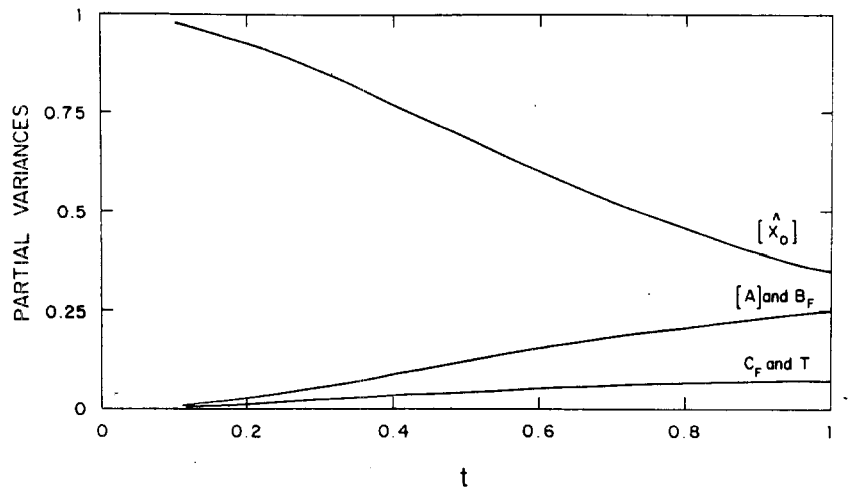

Fig. 10. Partial variances from the FAST method for the reaction $A + X \rightleftarrows 2X$.

± 5% variations of Table 6 using search curve 1 of Table 2. We note first that the first-order sensitivities of $[\hat{X}]$ to variations in $[A]$ and B_f are identical because these two parameters appear as a product in $[\hat{X}]$. The same behavior is noted for C_f and T. As long as the uncertainty ranges chosen for these two sets of parameters are the same, the partial variances of $[A]$ and B_f and C_f and T are identical, as seen in Fig. 10. The qualitative results of both the first-order sensitivity coefficients and the FAST partial variances are the same, although the relative magnitudes differ somewhat. A difference in relative magnitudes is expected since the first-order sen-

sitivity coefficients are computed at the nominal values, whereas the FAST partial variances involve simultaneous variation of all five parameters over their range of uncertainty, in this case ±5%. Both sets of calculations show that $[\hat{X}]$ is most sensitive to $[A]$ and B_f. Note that the FAST method shows that the sensitivity of $[\hat{X}]$ to $[\hat{X}]_0$ close to $t = 0$ is larger than indicated by the first order sensitivity coefficient.

Acknowledgement—This work was supported by U.S. Environmental Protection Agency grant R805537.

NOMENCLATURE

- A constant chemical species
- $A_j^{(i)}$ jth Fourier cosine coefficient for the ith state variable
- B_f pre-Arrhenius rate term
- $B_j^{(i)}$ jth Fourier sine coefficient for the ith state variable
- C_f activation energy term
- d_n frequency set generation parameter
- $f(\mathbf{x};\mathbf{k})$ general system function
- G_i transformation function
- k_f forward rate constant
- k_i ith uncertain parameter
- k_i^l lower limit of ith uncertain parameter
- k_i^u upper limit of ith uncertain parameter
- k_r reverse rate constant
- m number of uncertain parameters
- n number of state variables
- N number of Fourier coefficients
- $p(\mathbf{k})$ probability distribution of the uncertain parameters $\mathbf{k}$
- q quadrature index
- r number of numerical solution points
- r^l ratio of parameter lower limit and mean value
- r^u ratio of parameter upper limit and mean value
- s Fourier space variable
- s_j discrete Fourier space variable
- $S_i^{(j)}$ partial sensitivity of the ith state variable to the jth uncertain parameter
- T temperature
- x state variable
- x_k^i the value of the ith state variable at the kth numerical solution point
- X chemical species
- $\hat{X}$ normalized chemical species
- α_j search curve parameter
- β_j search curve parameter
- σ_i^2 partial variance of the ith state variable
- ρ_i normalized linear sensitivity coefficient for the ith state variable
- ω_j Fourier frequency assigned to the jth parameter
- $\bar{\nu}_j$ nominal value of the jth uncertain parameter
- Ω_n frequency set generation parameter
- $\langle\rangle$ ensemble average quantity
- $-$ time average quantity

REFERENCES

1. R. I. Cukier, C. M. Fortuin, K. E. Shuler, A. G. Petschek & J. H. Schaibly, *J. Chem. Phys.* **59**(8), 3873 (1973).
2. J. H. Schaibly & K. E. Shuler, *J. Chem. Phys.* **59**(8), 3879 (1973).
3. R. I. Cukier, J. H. Schaibly & K. E. Shuler, *J. Chem. Phys.* **63**(3), 1140 (1975).
4. R. I. Cukier, H. B. Levine & K. E. Shuler, *J. Comp. Phys.* **26**(1), 1 (1978).
5. H. Weyl, *Amer. J. Math.* **60**, 889 (1938).
6. K. G. Beauchamp & C. K. Yuen, *Digital Methods for Signal Analysis*. George Allen and Unwin, London (1979).
7. M. Koda, G. J. McRae & J. H. Seinfeld, *Int. J. Chem. Kinetics* **11**, 427 (1979).
8. R. J. Gelinas & J. P. Vajk, *Systematic Sensitivity Analysis of Air Quality Simulation Models*, Final Report to U.S. Environmental Protection Agency under Contract No. 68-02-2942, Science Applications, Inc., Pleasanton, California (1978).

10.5 Application of the Fourier Amplitude Sensitivity Test to Atmospheric Dispersion Problems

A major advantage of the Fourier Amplitude Sensitivity Test (FAST), introduced in the previous section, is that it enables a formal study of the relative influences of large parameter variations in nonlinear systems. As such the method is ideally suited for examining the effects of parameter uncertainties on the predictions of atmospheric dispersion models. In this research the system of most interest is the atmospheric diffusion equation.

$$\frac{\partial c}{\partial t} + \nabla\cdot(\underline{u}c) = \nabla\cdot(\underline{K}\nabla c) + R(c) \qquad (10.22)$$

This equation describes the formation and transport of photochemical air pollution. The parameters and processes of most importance are: advective transport by the flow field, $\underline{u}$, turbulent diffusion characterized by the eddy diffusivities, $\underline{K}$, and the chemical reactions R(c). In addition the source emissions, which enter the system (10.22) through the boundary conditions, have a major impact on the calculated results. This section discusses the application of two sensitivity analysis methods to a simplified representation of the full, three-dimensional airshed model.

While a complete sensitivity analysis of (10.22) has not as yet been undertaken, some preliminary steps have been made by studying individual elements of the basic model. For example, Falls et al. (1979)

investigated the influence of parameter variations on the predictions of a photochemical reaction mechanism. The results of that study are presented in Section 10.6. Koda et al. (1979a) used the FAST method to examine the effects of uncertainties in specification of the vertical turbulent transport. The system considered in their work was the one-dimensional form of (10.22)

$$\frac{\partial c}{\partial t} = \frac{\partial}{\partial z} K_{zz} \frac{\partial c}{\partial z} \tag{10.23}$$

with the boundary and initial conditions given by

$$K_{zz} \frac{\partial c}{\partial z}\bigg|_{z = 0} = Q \tag{10.24}$$

$$\frac{\partial c}{\partial z}\bigg|_{z = Z_i} = 0 \tag{10.25}$$

$$c(z,0) = 0 \tag{10.26}$$

The principal finding from their study was that the concentration predictions were most sensitive to variations of the turbulent diffusivity, K(z), close to the surface. In passing it is worthwhile to mention that this physically realistic result was also found when the direct and variational sensitivity analysis methods were applied to the problem.

Perhaps the most commonly employed form of (10.22) is the simple Gaussian plume approximation introduced by Pasquill (1961) and implemented in the well known workbook of Turner (1970). This formulation

is a good example to illustrate an application of the FAST method because the model can be solved analytically, it is widely used in practice and has not been subjected to extensive sensitivity analyses. The model can be derived from (10.22) by invoking the following assumptions: steady conditions, a uniform wind speed, u, in the x-direction, constant diffusivities, no chemical reaction and that transport in the flow direction is dominated by advection. Under these restrictions (10.22) can be written in the form

$$u \frac{\partial c}{\partial x} = K_{yy} \frac{\partial^2 c}{\partial y^2} + K_{zz} \frac{\partial^2 c}{\partial z^2} \tag{10.27}$$

A suitable set of boundary conditions for an initially pollutant free, unbounded atmosphere with no absorption at the ground is given by

$$- K_{zz} \left. \frac{\partial c}{\partial z} \right|_{z=0} = 0 \tag{10.28}$$

$$c(x,y,z)=0; \; x,y \to \pm \infty \tag{10.29}$$

If a single source of strength Q is located at an elevation H above the surface then the solution of the system (10.27- 10.29) is given by

$$c(x,y,z) = \frac{Q}{4\pi x \sqrt{K_{yy} K_{zz}}} \exp\left\{ - \frac{uy^2}{4xK_{yy}} \right\} \left[\exp\left\{ - \frac{u(z-H)^2}{4xK_{zz}} \right\} + \exp\left\{ - \frac{u(z+H)^2}{4xK_{zz}} \right\} \right] \tag{10.30}$$

In most applications the plume spreading is characterized in terms of the distance downwind from the source and as a result the diffusivities employed in (10.30) are often replaced by expressions of the form

$$\sigma_y^2 = 2K_{yy}t \tag{10.31}$$

$$\sigma_z^2 = 2K_{zz}t \tag{10.32}$$

The basic Gaussian plume model for the ground level concentration is then given by

$$c(x,y) = \frac{Q}{\pi u \sigma_y \sigma_z} \exp\left\{-\frac{1}{2}\left(\frac{y}{\sigma_y}\right)^2\right\}\exp\left\{-\frac{1}{2}\left(\frac{H}{\sigma_z}\right)^2\right\} \tag{10.33}$$

The dispersion coefficients σ_y and σ_z are determined from field experiments and are typically expressed in the form (Gifford, 1976)

$$\sigma = ax^b \tag{10.34}$$

where a and b are constants which depend on the atmospheric stability.

The coefficients used in the Turner Workbook are based on the initial work of Pasquill (1961) and Gifford (1961). While the values are often applied to a large range of stability and wind speed conditions, they were originally intended for use only under rather limited conditions: wind speeds greater than 2 m/s, nonbuoyant plumes, flow over open country and downwind distances of only a few kilometers (Gifford, 1976; Pasquill, 1976). In a study of the Gaussian model, Weber (1976) has

shown that the dispersion coefficients and the release height are some of the most critical parameters. Miller et al. (1979) reached a similar conclusion after an examination of field measurements. In an attempt to improve the predictions Lamb (1979) used Lagrangian similarity theory to describe the dispersion under unstable conditions. So far relatively few systematic studies have been made of the influence of parameter uncertainties on the predictions of the Gaussian model.

Because of the simple form of (10.33) it allows a straightforward evaluation of the partial derivatives of the concentration with respect to the different model parameters. These expressions are given by:

$$\frac{\partial c}{\partial Q} = \frac{c}{Q} \tag{10.35}$$

$$\frac{\partial c}{\partial u} = \frac{c}{u} \tag{10.36}$$

$$\frac{\partial c}{\partial H} = \frac{cH}{z^2} \tag{10.37}$$

$$\frac{\partial c}{\partial \sigma_y} = \frac{c}{\sigma_y}\left[\left(\frac{y}{\sigma_y}\right)^2 - 1\right] \tag{10.38}$$

$$\frac{\partial c}{\partial \sigma_z} = \frac{c}{\sigma_z}\left[\left(\frac{H}{\sigma_z}\right)^2 - 1\right] \tag{10.39}$$

and if $\sigma = ax^b$ then

$$\frac{\partial c}{\partial a} = \left(\frac{\partial c}{\partial \sigma}\right) x^b \tag{10.40}$$

$$\frac{\partial c}{\partial b} = \left(\frac{\partial c}{\partial \sigma}\right) abx^{b-1} \qquad (10.41)$$

where σ can be either σ_y or σ_z. Given the system (10.35 - 10.41) it is possible to define a set of normalized sensitivities at each downwind distance.

$$\rho_i(x) = \frac{\left| \frac{\partial c(x)}{\partial k_i} \Delta k_i \right|}{\sum_{j=1}^{m} \left| \frac{\partial c(x)}{\partial k_j} \Delta k_j \right|} ; \; i=1,2,\ldots,m \qquad (10.42)$$

The expressions, $\rho_i(x)$, are analogous to the partial variances associated with the FAST method, however it is important to note that the partial derivatives are a local representation of the model sensitivity. The conditions chosen for the study are shown in Table 10.2.

Figures 10.6-10.8 depict the results of three calculations, two involve small perturbations and the other large variations in the model parameters. The first two cases were chosen to provide a means of comparing the FAST method with the linearized approximation (10.35 - 10.41). As expected both approaches produced similar results. Close to the source the major influence on the ground level concentration is from the vertical dispersion and in particular the coefficient $b(\sigma_z)$. Further downwind, at the location of maximum impact, the model predictions are most influenced by the horizontal dispersion and the source height.

TABLE 10.2

Parameters Studied in Gaussian Plume Model

PARAMETER (k)		NOMINAL VALUE k(0)	LARGE PARAMETER RANGE
Source Strength (g/s)		100	50 - 200
Wind Speed (m/s)		5	2.5 - 10
Release Height (m)		10	5 - 20
$\sigma_z(m) = ax^b$	a	32.0	16 - 64
	b	0.84	0.42- 1.68
$\sigma_y(m) = ax^b$	a	67.9	34 - 136
	b	0.93	0.47- 1.86

Note: the σ_z and σ_y values correspond to Pasquill-Gifford stability class D and have been extrapolated from Turner (1970).

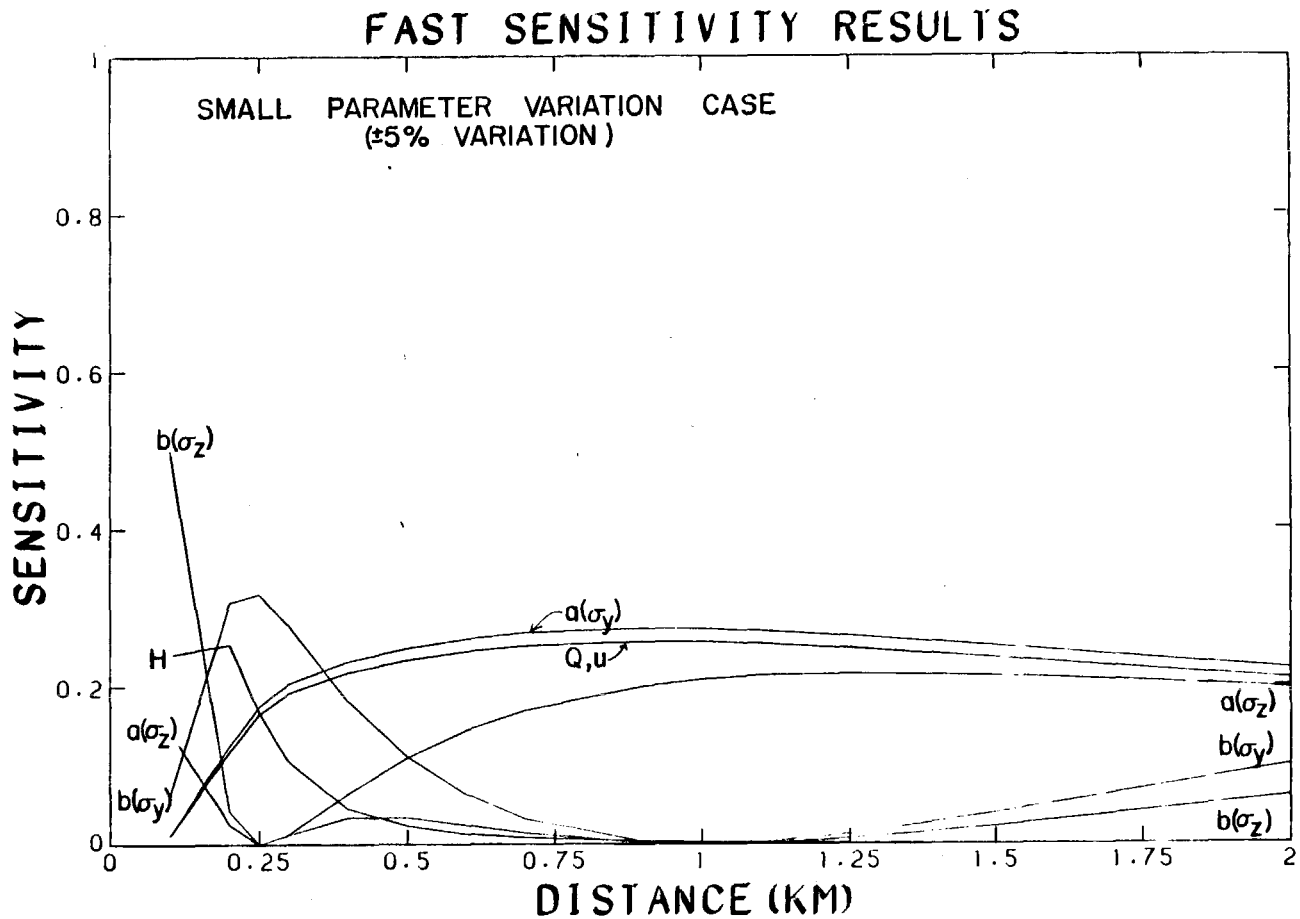

FIGURE 10.6

Linearized Sensitivity Analysis of a Gaussian Plume Model
(± 5% Parameter Variation)

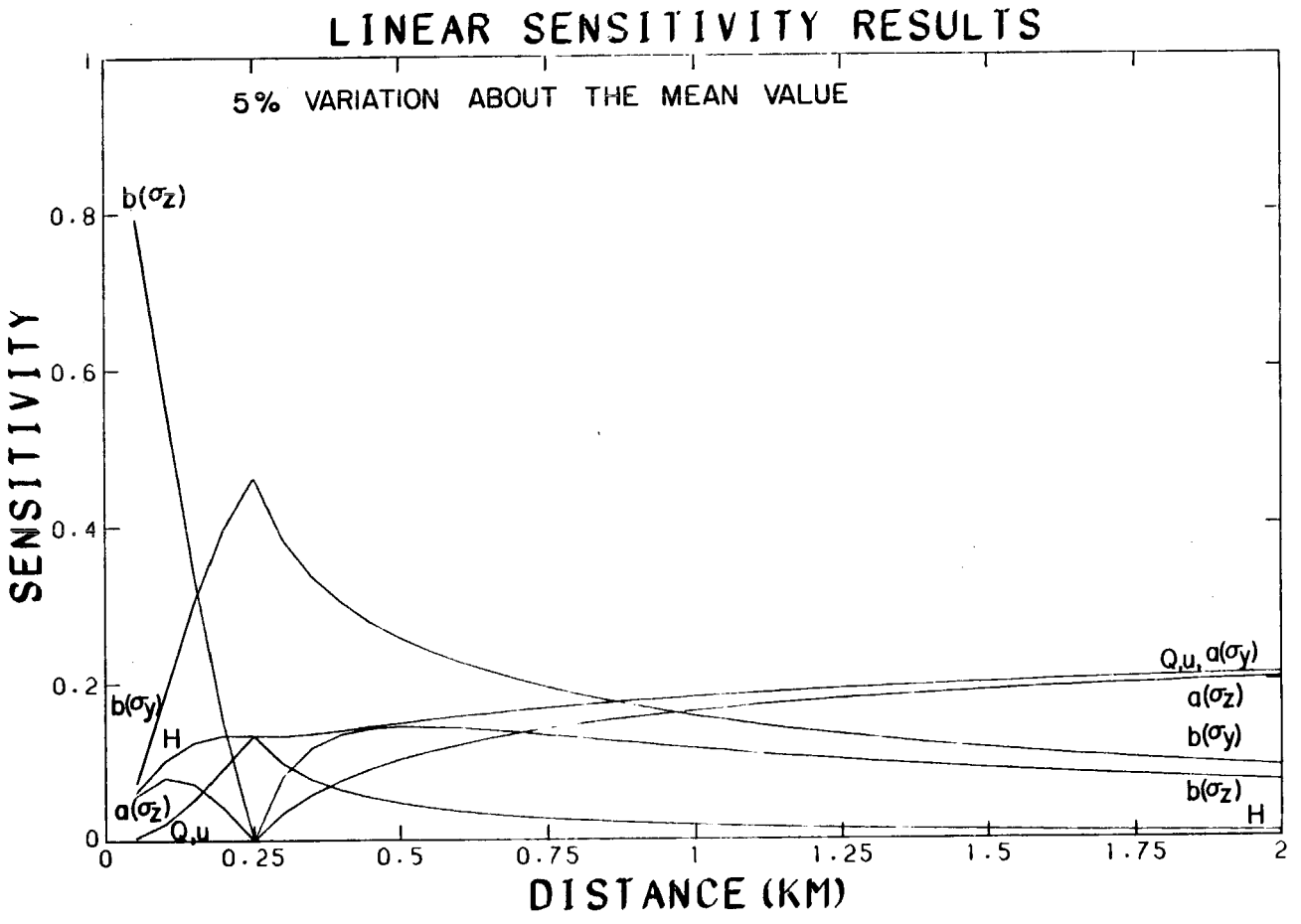

FIGURE 10.7

Fourier Amplitude Sensitivity Test (FAST) Analysis of a Gaussian Plume Model
(± 5% Parameter Variation)

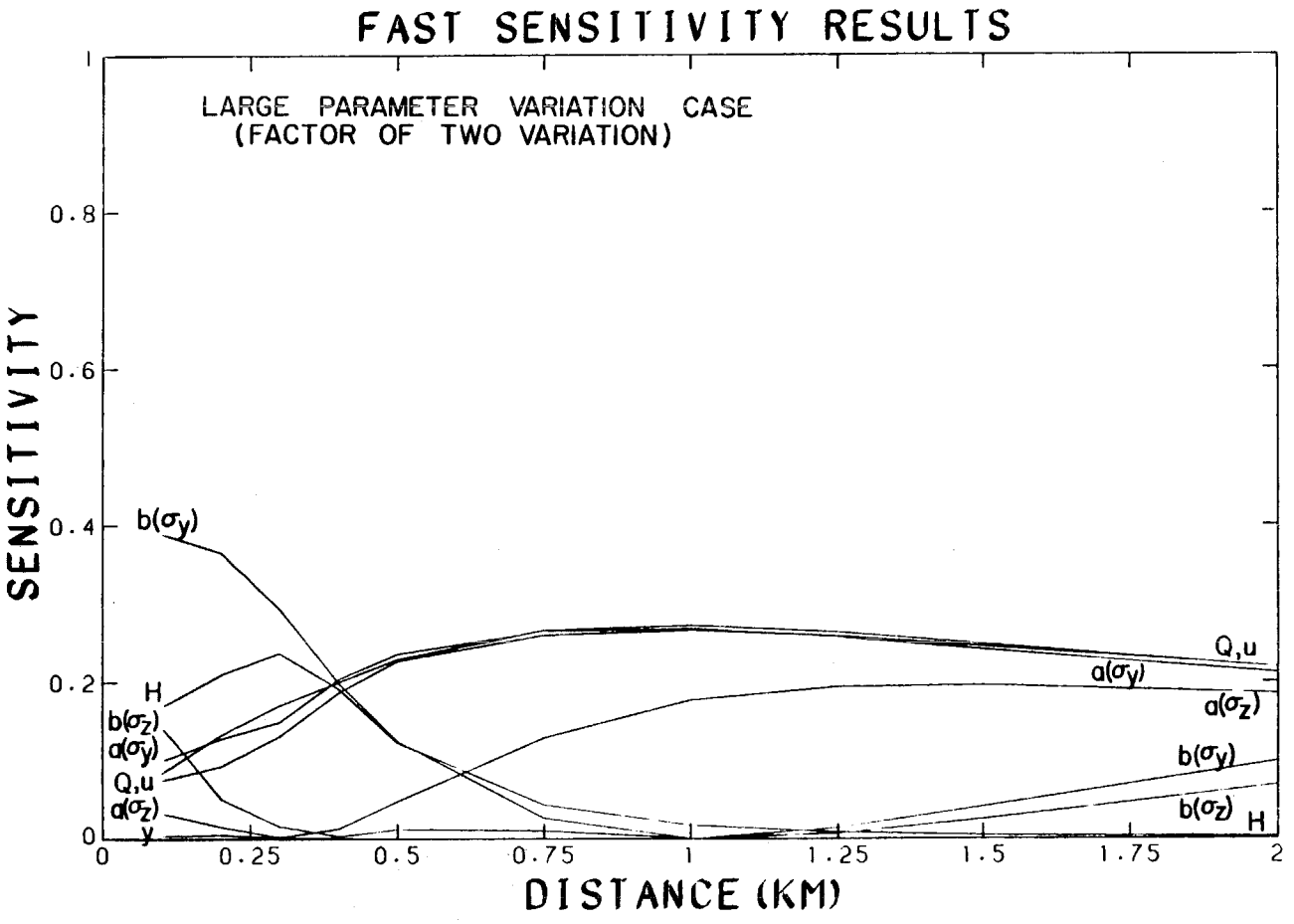

FIGURE 10.8

Fourier Amplitude Sensitivity Test (FAST) Analysis of a Gaussian Plume Model
(Factor of Two Parameter Variation)

In the far field, dispersion still dominates the concentration levels however the effects of wind speed and source strength are more apparent. The oscillation in the sensitivity coefficients associated with σ_z arise from the sign change which occurs in (10.42) when the downwind distance, x, exceeds the value $(H/a)^{1/b}$. The only major difference between the small and large variation cases is that the relative roles of σ_y and σ_z are reversed.

The results of the sensitivity analyses have important practical consequences. For the chosen condition both the effective release height and the dispersion coefficients have a major impact on the ground level concentration. Each of these parameters is strongly influenced by the vertical temperature structure. As a result the parameters, and in turn the model prediction, are quite dependent on the accuracy of the procedures adopted to characterize the atmospheric stability. Considering the known limitations of the Pasquill-Gifford stability classification scheme the findings of this study suggest that more attention needs to be given to developing better estimates of the plume rise and turbulent dispersion coefficients. Additional work is required to analyze the sensitivity of the complete atmospheric diffusion equation. The following section presents a detailed evaluation of the chemical reactions embedded in the airshed model.

10.6 Sensitivity and Uncertainty of Reaction Mechanism for Photochemical Air Pollution

(Reprinted from Int. Journal of Chemical Kinetics, 11, 1137-1162.)

Sensitivity and Uncertainty of Reaction Mechanisms for Photochemical Air Pollution

ANDREW H. FALLS, GREGORY J. McRAE, and JOHN H. SEINFELD

Department of Chemical Engineering, California Institute of Technology, Pasadena, California 91125

Abstract

A sensitivity/uncertainty analysis is performed on a mechanism describing the chemistry of the polluted troposphere. General features of the photochemical reaction system are outlined together with an assessment of the uncertainties associated with the formulations of mechanistic details and rate data. The combined effects of sensitivity and uncertainty are determined using the Fourier amplitude sensitivity test (FAST) method. The results of this analysis identify the key parameters influencing the chemistry of NO_2, O_3, and PAN. Based on these findings, a series of recommendations are made for future experimental kinetic studies.

Introduction

A key problem underlying the development and evaluation of kinetic mechanisms for atmospheric chemistry is determining the sensitivity of the concentration predictions to those uncertain aspects of the reaction scheme. Such a determination can serve as a valuable guide for future experimental studies and for identifying those parameters that, when varied within accepted bounds, will be most influential on the predictions of the mechanism.

Although the qualitative aspects of the chemistry of the polluted troposphere appear to be reasonably well understood, there are many important details that still need to be investigated before a complete quantitative understanding of the photochemical smog system is possible. Several groups [1–7] have formulated chemical reaction mechanisms for polluted tropospheric chemistry. Some of these are based on specific surrogate hydrocarbon chemistries [1–4]. In others, attempts have been made to simulate the complex ambient atmospheric system by representing the general features of the hydrocarbon chemistry [2,5–7]. All mechanisms contain aspects of uncertainty, whether in unknown rate constants, in the importance of competing reaction paths, or in the manner of representing

International Journal of Chemical Kinetics, Vol. XI, 1137–1162 (1979)

0538-8066/79/0011-1137$01.00

the reaction of a generalized species. The measure of the accuracy of a mechanism is usually based on the extent of agreement between predicted concentration profiles and those generated experimentally in smog chambers.

Even though the mechanisms [1–7] currently under study differ in details, the basic structure and qualitative behavior of each is similar. Thus, a separate study of the sensitivity of each of the mechanisms is unnecessary.

The object of this work is to examine closely the sensitivity of mechanisms for photochemical smog to those aspects of the chemistry that are currently uncertain. In doing so, it is hoped that certain general features of the photochemical system will emerge; features that are common to all mechanisms and for which estimates of the effect of uncertain parameters will be valuable. A similar study was carried out by Dodge and Hecht [8] in 1975 using the Hecht–Seinfeld–Dodge mechanism [9]. The mechanism of Falls and Seinfeld [7], which includes the latest available information on rate constants, reactions, and has all of the major features present in the lumped mechanisms of Whitten and Hogo [2], Gelinas and Skewes–Cox [5], and Martinez et al. [6] is used in this work. Sensitivity analyses are carried out using the Fourier amplitude sensitivity test (FAST) method of Shuler et al. [10], as described by Koda et al. [11]. Only a brief discussion of the method is given here; extensive details are available in the cited references.

This work begins with a brief discussion of the chemistry of photochemical smog, aimed at elucidating the general structure of the system within which mechanistic and kinetic uncertainties will be evaluated. Next, based on published reports of measured rate constants and product distributions for individual reactions, the uncertainty associated with each element of the Falls and Seinfeld mechanism [7] is estimated. The sensitivity analysis method is then described briefly, with emphasis on the implementation of the parameter uncertainty bounds and interpretation of the results. Finally, the results of the sensitivity analysis are presented and discussed in detail, leading to a ranking of the most influential elements of the mechanism based on the combined effects of uncertainty and sensitivity.

Photochemical Smog Chemistry

NO_2, NO, and O_3 participate in the well-known cyclic set of reactions

$$NO_2 + h\nu \xrightarrow{1} NO + O(^3P)$$

$$O(^3P) + O_2 + M \xrightarrow{2} O_3 + M$$

$$NO + O_3 \xrightarrow{3} NO_2 + O_2$$

In the absence of significant competing reactions, a photostationary state is reached among reactions (1)–(3) in which the steady-state ozone concentration is given by $[O_3]_{ss} = k_1[NO_2]/k_3[NO]$. However, if a process other than that in reaction (3) can convert NO to NO_2 without consuming a molecule of O_3, the ozone concentration will increase due to the increase in the NO_2/NO concentration ratio.

The two main processes by which NO is converted to NO_2, without the loss of ozone, involve the hydroperoxy radical HO_2 and peroxyalkyl radicals RO_2 via

$$HO_2 + NO \rightarrow OH + NO_2$$

$$RO_2 + NO \rightarrow RO + NO_2$$

Hydroperoxy and peroxyalkyl radicals arise in the photochemical smog system from the photolysis and oxidation of hydrocarbon species.

One source of peroxy radicals is from the photolysis of aldehydes that originate in the atmosphere both from emissions and as the products of chemical reactions. Formaldehyde photolysis, at wavelengths less than 370 nm, proceeds by either a molecular or a radical path:

$$HCHO + h\nu \rightarrow H_2 + CO$$

$$\rightarrow H + HCO$$

Both hydrogen atoms and formyl radicals react rapidly with O_2 to produce HO_2 and HO_2 + CO, respectively. (There is still some disagreement concerning the HCO–O_2 reaction products; however, most evidence indicates that the products are HO_2 and CO.) Higher aldehydes also photodissociate to give alkyl and formyl radicals:

$$RCHO + h\nu \rightarrow R + HCO$$

In addition to their photolysis, the reaction of aldehydes with OH serves as an important radical source and chain carrier. Hydroxyl radicals are generally thought to abstract the aldehydic H atom from aldehydes:

$$OH + RCHO \rightarrow RCO + H_2O$$

Oxidation of hydrocarbon species provides another source of hydroperoxy and peroxyalkyl radicals in the atmospheric system. The key species in the initial oxidation of hydrocarbons is the hydroxyl radical, the major sources of which are indirect chain-related processes such as the photolysis of aldehydes and the reaction of O_3 with olefins which lead to OH radicals through the reaction of HO_2 with NO. Minor sources of the hydroxyl radical include the photolysis of nitrous acid, the photolysis of hydrogen

peroxide, and the reaction of water with singlet oxygen atoms ($O(^1D)$) which originate from the photolysis of ozone:

$$HONO + h\nu \rightarrow OH + NO$$

$$H_2O_2 + h\nu \rightarrow 2OH$$

$$O_3 + h\nu \rightarrow O(^1D) + O_2(^1\Delta_g)$$

$$O(^1D) + H_2O \rightarrow 2OH$$

Hydroxyl radical attack on hydrocarbons leads eventually to a variety of peroxy radicals, such as peroxyalkyl, peroxyacyl, and hydroxy-peroxyalkyl radicals. These radical species convert NO to NO_2, thereby producing ozone, and also serve as sources of alkoxyl, acyl, hydroxy-alkoxyl, and hydroperoxy radicals.

Major Uncertainties in Photochemical Smog Chemistry

With the recent elucidation of the chemistry of the reactions of OH and HO_2 with NO and NO_2 [12,14,15], the inorganic portion of the photochemical smog mechanism is now, by and large, well understood. Table I lists the mechanism under study along with its associated uncertainties. Figure 1 shows the structure and species interaction within the reaction mechanism. Uncertainties to be discussed here include:

(a) Photolysis rates
(b) Alkane–OH product distributions
(c) Olefin–OH and olefin–O_3 product distributions
(d) Aromatic chemistry
(e) Alkoxyl radical reactions
(f) RO_x/NO_x reactions

A major uncertainty in the mechanism lies in the values of the photolysis rate constants. For analyzing smog chamber data, photolysis rate constants relative to the reported value for NO_2 are frequently used. Photolysis rate constants as a function of wavelength can be calculated from

$$k_j = \int_0^\infty \sigma_j(\lambda)\phi_j(\lambda)I(\lambda)\, d\lambda$$

where

k_j = photolysis rate constant for species j
$\sigma_j(\lambda)$ = absorption cross section of species j
$\phi_j(\lambda)$ = quantum yield for the photolysis of species j
$I(\lambda)$ = actinic irradiance

Data applicable to some atmospheric systems have been compiled by Schere and Demerjian [26]. For species such as NO_2, HONO, and O_3, for which extensive experimental determinations of absorption cross sections

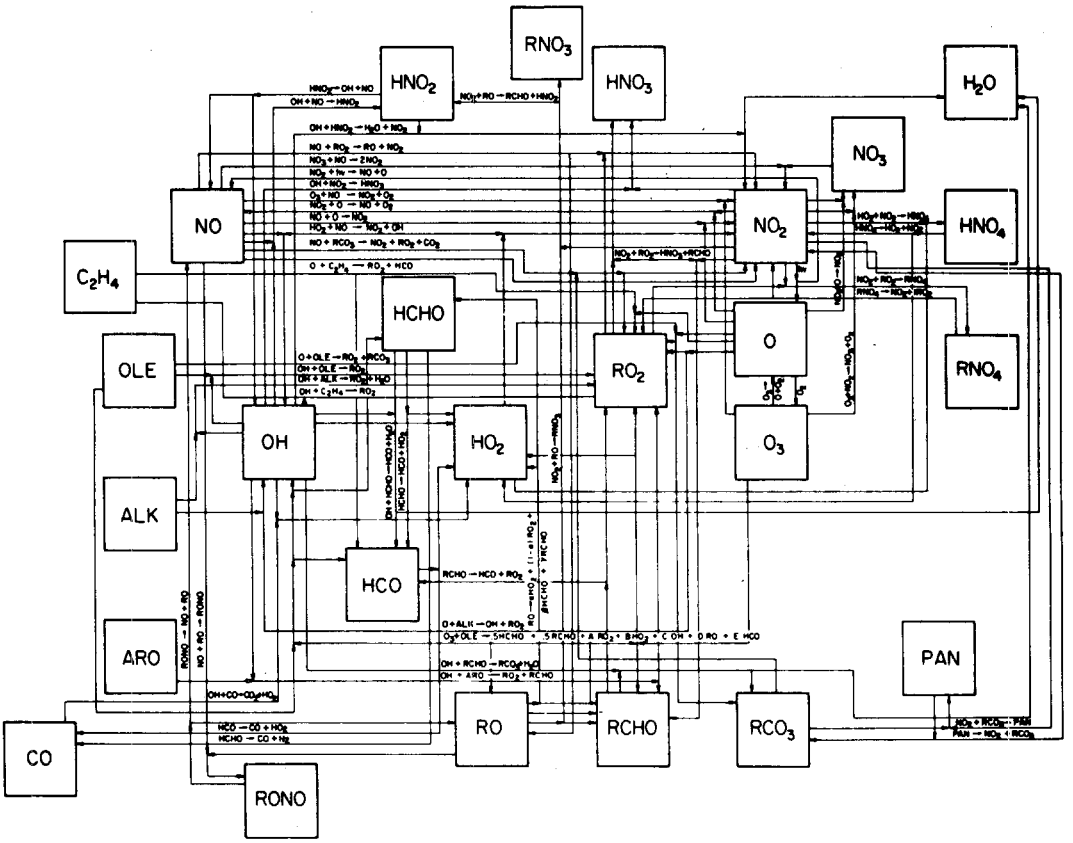

Figure 1. Flow diagram of Falls and Seinfeld reaction mechanism.

and quantum yields have been accomplished, photolysis rate constants are thought to be fairly reliable. However, since cross section and quantum yield data for formaldehyde, higher aldehydes, and alkyl nitrites are much less well characterized, many photolysis rate constants are subjected to large uncertainty. Of course, even if absorption cross sections and quantum yields could be determined accurately for all photosensitive species, uncertainties in atmospheric photolysis rate constants would still exist, as meteorological conditions, clouds, dust, and aerosols cause unknown variances in actinic irradiance.

Whereas rate constants in the inorganic portion of the mechanism are known fairly well, many more uncertainties, both in reaction rate constants and products, are associated with the organic reaction steps. Still to be determined are product distributions and reaction rate constants for the initial steps of the reactions of OH and hydrocarbon species, the largest uncertainties lying in the routes of the various radical species produced. For example, although rate constants for alkane–OH reactions are well established, the ratio of internal to external abstraction for all alkanes is not known. Addition to O_2 to form peroxyalkyl (RO_2) radicals can be

considered as the sole fate of the alkyl radicals first produced in alkane–OH reactions, but after the formation of alkoxyl radicals through the conversion of NO to NO_2, the reaction mechanism becomes uncertain. Alkoxyl radicals can decompose, react with O_2, isomerize, or react with NO or NO_2, with the importance and rate of each reaction path depending on the nature of the alkoxyl group. Even for the most studied of the alkane–OH reactions, the relative rates between decomposition, isomerization, and reaction with O_2, NO, and NO_2 for alkoxyl radicals have not been measured, but must be estimated [3]. The *n*-butane–OH reaction mechanism, for which the ratio of internal to external abstraction is known to be about 86–14 [3], gives rise to *sec*-butoxy and *n*-butoxy radicals. Various possible reaction pathways for these two radicals are:

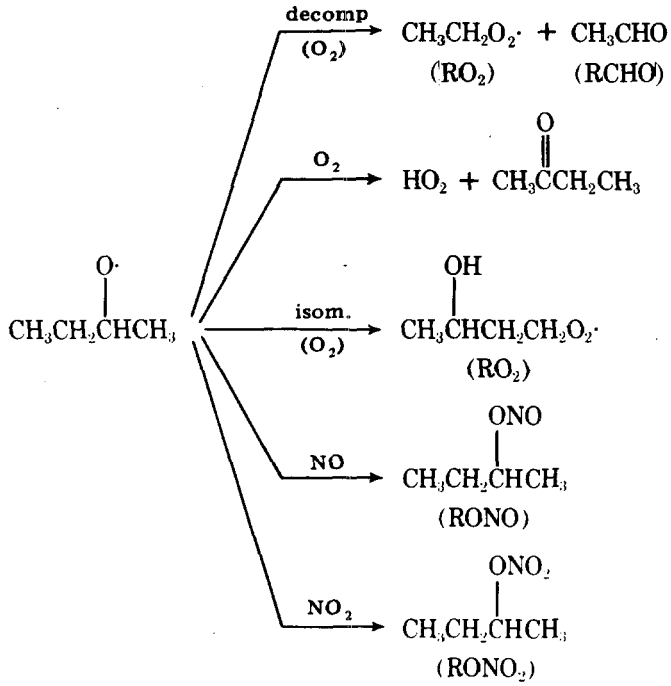

and

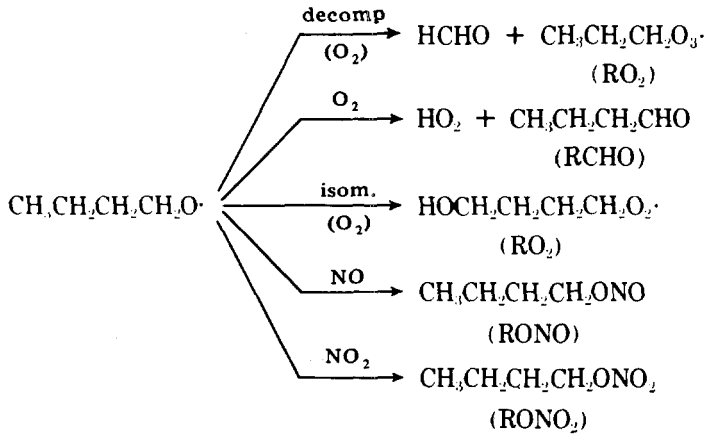

Less well understood than alkane reaction mechanisms are olefin oxidation processes. Whereas reactions of alkanes with O_3 could be neglected, both olefin–OH and olefin–O_3 reactions occur to a significant extent. Olefin–OH reactions may proceed by addition or abstraction [35]. For smaller olefins, the addition path predominates. However, the abstraction fraction increases with the size of the olefin. Along the addition path for terminally bonded olefins, there is uncertainty as to the ratio of internal-to-external addition. Similar to alkyl radicals, the hydroxy-alkyl radicals formed in the initial OH addition to olefins are thought to immediately add O_2 to form hydroxy-peroxyalkyl radicals and thereafter react with NO to give NO_2 and hydroxy-alkoxyl species. The fate of the hydroxy-alkoxyl radicals is subject to speculation, although the analogous alkoxyl reaction paths of decomposition, isomerization, and reaction with NO, NO_2, and O_2 are the most likely possibilities:

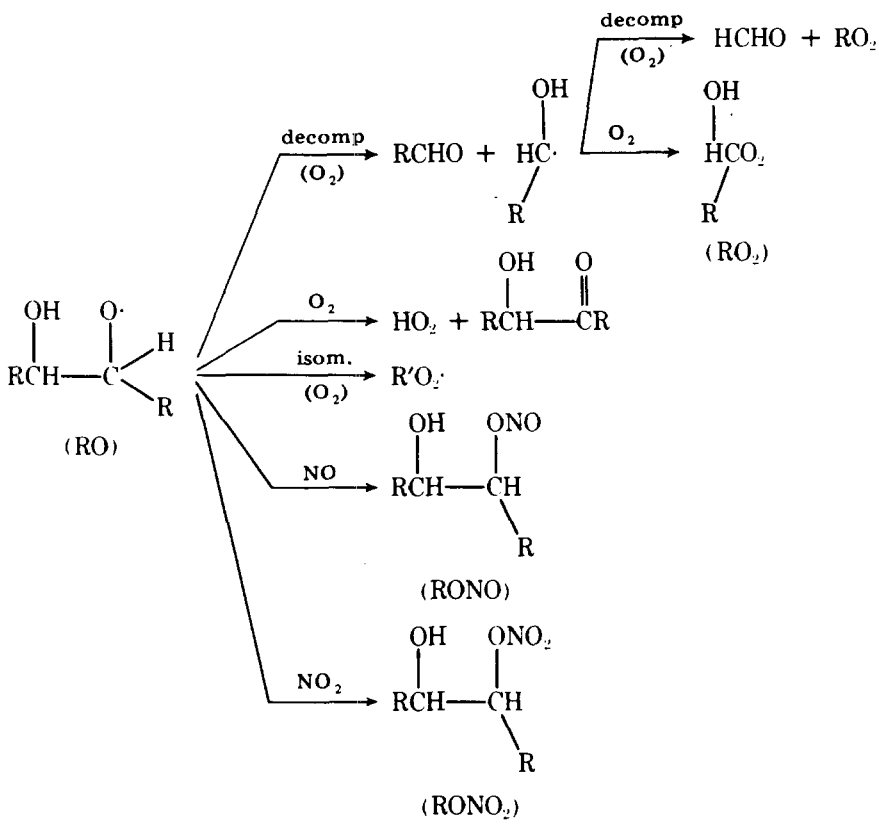

Of some importance in the photochemical smog system is the oxidation of olefins by ozone. The initial rate-determining step in the attack of ozone on the double bond of olefins is the formation of a molozonide, which, as the ring opens, results in a rapid equilibrium between the two possible forms of the oxy-peroxy biradical. The primary uncertainty in the olefin–ozone reaction mechanism lies in the fate of the oxy-peroxy biradical. Currently

it is thought that for lower olefins the biradical decomposes according to the Criegee mechanism of solution phase ozonolosis. However, α- and β-hydrogen abstraction mechanisms have also been proposed [27]. Figure 2 depicts the Criegee mechanism for the gas-phase ozonolosis of a general olefin, with reaction products analogous to those proposed by Dodge [28] for the propylene–O_3 mechanism.

Although much work has been devoted to the understanding of alkane and olefin systems, comparatively little research has been devoted to the study of atmospheric aromatic mechanisms. Recently, absolute rate constants have been determined for the reaction of OH with a series of aromatic hydrocarbons over a range of temperatures [29]. The initial aromatic–OH reaction step can be either abstraction or addition to the ring. At room temperature, the percentage of reaction proceeding by abstraction is on the order of 2–20%, depending on the individual hydrocarbon [29]. The aromatic–OH adduct presumably reacts with other atmospheric species such as O_2, NO, or NO_2. In addition, opening of the aromatic ring presumably occurs at some point in the atmospheric chemistry. Hendry [30] has postulated an aromatic mechanism that accounts for ring cleavage as well as for the formation of oxygenated species such as glyoxal, $H_2C_2O_2$, seen in smog chambers.

The aromatic–OH reaction products in Table I have been represented simply as RO_2 and an oxygenated species that is lumped with the aldehydes. Because the atmospheric chemistry of aromatics is poorly understood, little can be accomplished by speculating on reaction products and mechanisms at this point. For this reason, a sensitivity/uncertainty analysis associated with aromatic species has not been incorporated into this study.

The inherent uncertainty of the decomposition, reaction with O_2, and isomerization of the alkoxyl and hydroxy-alkoxyl radical class in the present mechanism [7] has been concentrated into one reaction step:

$$RO \rightarrow \alpha HO_2 + (1 - \alpha)RO_2 + \beta HCHO + \gamma RCHO$$

As seen from the earlier discussions of alkoxyl radical behavior, RO always gives rise to either HO_2 or RO_2 in any of the decomposition, isomerization, or O_2 reaction pathways. Hence, the stoichiometric coefficients representing the fraction of HO_2 and RO_2 found in the lumped RO reaction should add to 1. Since the RO lumped species represents a large class of different-sized radicals and because splits between reaction paths for even specific radicals are unknown, α can have a value in the range 0 to 1. Many RO reaction routes produce aldehydes with some yielding two, as the one suggested by Martinez et al. [6]. Thus, $0 \leq \beta \leq 1$ and $0 \leq \gamma \leq 1$. Since the composition of the RO radical pool is continually changing during the course of a photooxidation, the actual values of α, β, and γ are functions of time. Thus, the selection of constant values of these coefficients introduces uncertainty.

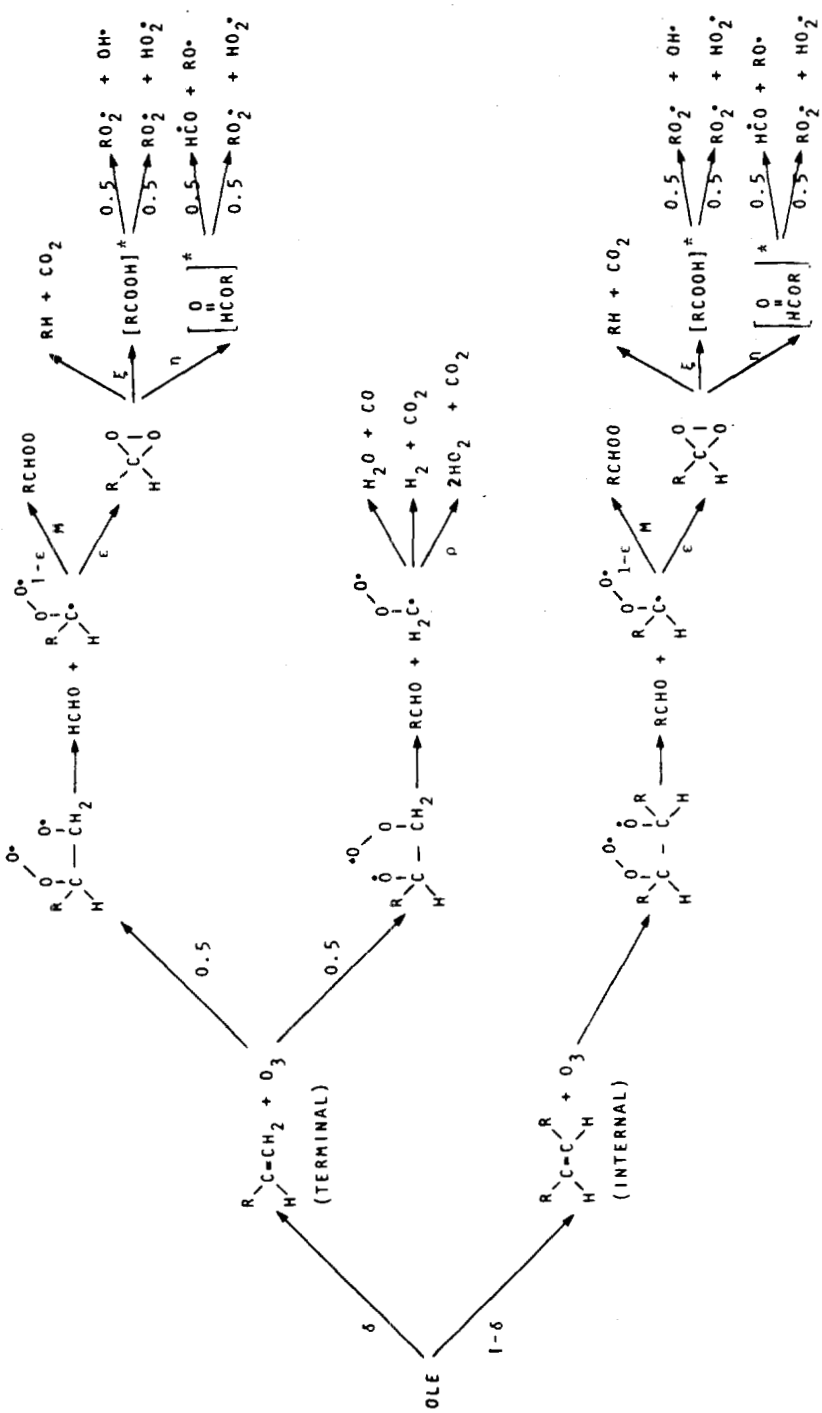

Figure 2. General olefin–ozone reaction mechanism, with reaction products as proposed by Dodge [28].

TABLE I. Uncertainties associated with reaction rate constants in the Falls and Seinfeld mechanism [7].

	Reaction	Nominal rate constant ppm-min units (30°C)	Uncertainty Range[a]	Reference	Sensitivity Uncertainty Analys
1.	$NO_2+h\nu \rightarrow NO+O(^3P)$	variable	$k_1 = \pm 20\%$	(est.)	*
2.	$O(^3P)+O_2+M \rightarrow O_3+M$	2.03×10^{-5} [b]	$1.72\times10^{-5} \leq k_2 \leq 2.38\times10^{-5}$	12	
3.	$O_3+NO \rightarrow NO_2+O_2$	2.55×10^{1}	$1.80\times10^{1} \leq k_3 \leq 3.60\times10^{1}$	12	
4.	$NO_2+O(^3P) \rightarrow NO+O_2$	1.32×10^{4}	$1.15\times10^{4} \leq k_4 \leq 1.52\times10^{4}$	12	
5.	$NO_2+O(^3P) \rightarrow NO_3$	3.52×10^{3} [c]	$2.22\times10^{2} \leq k_5 \leq 5.58\times10^{3}$	12	
6.	$NO+O(^3P) \rightarrow NO_2$	3.87×10^{3}	$2.45\times10^{3} \leq k_6 \leq 6.13\times10^{3}$	12	
7.	$NO_2+O_3 \rightarrow NO_3+O_2$	5.37×10^{-2}	$4.26\times10^{-2} \leq k_7 \leq 6.76\times10^{-2}$	12	
8.	$NO_3+NO \rightarrow 2NO_2$	2.72×10^{4}	$2.12\times10^{4} \leq k_8 \leq 3.31\times10^{4}$	13	
9.	$NO_3+NO_2 \rightarrow N_2O_5$	3.69×10^{3} [c]	$1.06\times10^{3} \leq k_9 \leq 1.21\times10^{4}$	13	
10.	$N_2O_5 \rightarrow NO_3+NO_2$	1.21×10^{1}	-	13	
11.	$N_2O_5+H_2O \rightarrow 2HONO_2$	$<1.45\times10^{-5}$	-	12	
12.	$NO+NO_2+H_2O \rightarrow 2HONO$	2.11×10^{-9} [b]	-	12	
13.	$HONO+HONO \rightarrow NO+NO_2+H_2O$	1.38×10^{-3}	-	12	
14.	$O_3+h\nu \rightarrow O_2+O(^1D)$	variable	$k_{14} = \pm 30\%$	(est.)	
15.	$O_3+h\nu \rightarrow O_2+O(^3P)$	variable	$k_{15} = \pm 30\%$	(est.)	*
16.	$O(^1D)+M \rightarrow O(^3P)+M$	4.14×10^{4}	$3.29\times10^{4} \leq k_{16} \leq 5.21\times10^{4}$	12	
17.	$O(^1D)+H_2O \rightarrow 2OH$	3.34×10^{5}	$2.65\times10^{5} \leq k_{17} \leq 4.21\times10^{5}$	12	
18.	$HO_2+NO_2 \rightarrow HONO+O_2$	$<10^{-3}\ k_{19}$	-	14	
19.	$HO_2+NO_2 \rightarrow HO_2NO_2$	1.58×10^{3}	-	15	
20.	$HO_2NO_2 \rightarrow HO_2+NO_2$	7.5	$3.3 \leq k_{20} \leq 17.1$	15	
21.	$HO_2+NO \rightarrow NO_2+OH$	1.18×10^{4}	$9.59\times10^{3} \leq k_{21} \leq 1.39\times10^{4}$	12	
22.	$OH+NO \rightarrow HONO$	1.74×10^{4} [c]	-	12	
23.	$OH+NO_2 \rightarrow HONO_2$	1.5×10^{4} [c]	$1.31\times10^{4} \leq k_{23} \leq 2.07\times10^{4}$	12	*
24.	$HONO+h\nu \rightarrow OH+NO$	variable	$k_{24} = \pm 30\%$	(est.)	*
25.	$CO+OH \rightarrow CO_2+HO_2$	4.36×10^{2}	$3.46\times10^{2} \leq k_{25} \leq 5.49\times10^{2}$	12	
26.	$OH+HONO \rightarrow H_2O+NO_2$	9.59×10^{3}	$9.15\times10^{2} \leq k_{26} \leq 1.00\times10^{4}$	12	
27.	$HO_2+HO_2 \rightarrow H_2O_2+O_2$	3.63×10^{3}	$1.82\times10^{3} \leq k_{27} \leq 7.26\times10^{3}$	12	
28.	$H_2O_2+h\nu \rightarrow 2OH$	variable	$k_{28} = \pm 30\%$	(est.)	
29.	$OH+O_3 \rightarrow HO_2+O_2$	8.04×10^{1}	$4.03\times10^{1} \leq k_{29} \leq 1.6\times10^{2}$	12	
30.	$HO_2+O_3 \rightarrow OH+2O_2$	3.04	$1.52 \leq k_{30} \leq 6.08$	12	
31.	$HCHO+h\nu \rightarrow 2HO_2+CO$	variable	$k_{31} = \pm 30\%$	(est.)	*
32.	$HCHO+h\nu \rightarrow H_2+CO$	variable	$k_{32} = \pm 30\%$	(est.)	*
33.	$HCHO+OH \rightarrow HO_2+CO$	2.03×10^{4}	$1.62\times10^{4} \leq k_{33} \leq 2.56\times10^{4}$	12	

TABLE I. (*Continued*)

Reaction	Nominal rate constant ppm-min units (30°C)	Uncertainty Range[a]	Reference	Sensitivity/ Uncertainty Analysis
34. $RCHO+h\nu \rightarrow RO_2+HO_2+CO$	variable	$k_{34} = \pm 50\%$	(est.)	*
35. $RCHO+OH \rightarrow RCO_3$	2.1×10^4	-	16	
36. $OLE+OH \rightarrow RO_2$	variable[d]	-	17	
37. $OLE+O \rightarrow RO_2+RCO_3$	variable[d]	-	17	
38. $OLE+O_3 \rightarrow 0.5\delta RCHO + (1-0.5\delta)HCHO + [0.5\varepsilon(1-0.5\delta)(\xi+2\eta)+\rho\delta]HO_2 + 0.5\varepsilon(2\xi+\eta)(1-0.5\delta)RO_2 + 0.5\varepsilon\xi(1-0.5\delta)OH + 0.5\varepsilon\eta(1-0.5\delta)RO$	variable[d]	$0 \le \varepsilon \le 1$, $0 \le \xi \le 1$, $0 \le \eta \le 1$, $0 \le \rho \le 1$ Nominal values $\varepsilon = 0.8, \xi = 0.68, \eta = 0.17$ $\delta = 1.0, \rho = 0.1$	17	*
39. $ALK+OH \rightarrow RO_2$	variable[d]	-	17	
40. $ALK+O \rightarrow RO_2+OH$	variable[d]	-	17	
41. $C_2H_4+OH \rightarrow RO_2$	1.14×10^4	$7.06\times10^3 \le k_{41} \le 1.87\times10^4$	12	
42. $C_2H_4+O \rightarrow RO_2+HCO$	1.24×10^3	$1.03\times10^3 \le k_{42} \le 1.49\times10^3$	12	
43. $ARO+OH \rightarrow RO_2+RCHO$	variable[d]	-		
44. $RO \rightarrow \alpha HO_2+(1-\alpha)RO_2 + \beta HCHO+\gamma RCHO$	3.6×10^5	Nominal Values $0 \le \alpha \le 1$ $\alpha=1$ $0 \le \beta \le 1$ $\beta=1$ $0 \le \gamma \le 1$ $\gamma=0$	3	*
45. $NO+RO \rightarrow RONO$	4.9×10^4	$k_{45} = (3.1\times10^4 - 1.55\times10^5)$	18-20	*
46. $RONO+h\nu \rightarrow RO+NO$	variable	$k_{46} = \pm 30\%$	(est.)	*
47. $NO_2+RO \rightarrow RONO_2$	1.55×10^4	$k_{45}/(k_{47}+k_{48}) = (1.2\text{-}2.7)$	21-23	*
48. $NO_2+RO \rightarrow RCHO+HONO$	1.35×10^3	$k_{47}/k_{48} = (0.08\text{-}0.23)$	21-23	*
49. $NO_2+RO_2 \rightarrow RO_2NO_2$	5.5×10^3	$k_{49} = (1600\text{-}5500)$	(est.)	*
50. $NO_2+RO_2 \rightarrow RCHO+HONO_2$	5.5 (est.)	-		
51. $RO_2NO_2 \rightarrow NO_2+RO_2$	0.5 (est.)	$0.55 \le k_{51} \le 40.0$	37	*
52. $NO+RO_2 \rightarrow NO_2+RO$	1.18×10^4 (est.)	$3000 \le k_{52} \le 12000$	(est.)	*
53. $NO+RCO_3 \rightarrow NO_2+RO_2$	3.77×10^3	$k_{54}/k_{53} = 0.54\pm0.17$	25	
54. $NO_2+RCO_3 \rightarrow PAN$	2.03×10^3		25	
55. $PAN \rightarrow NO_2+RCO_3$	0.055	$0.0039 \le k_{55} \le 0.78$	25	
56. $O_3 \rightarrow$ wall loss	variable[e]			
57. $RO_2+RO_2 \rightarrow 2RO+O_2$	196.0	$50.0 \le k_{57} \le 600.0$	38	*

[a] Uncertainties determined from reliabilities in rate constant measurements given in original references. Where no uncertainty was reported, either an estimate was made or the uncertainty neglected.

[b] Units of rate constant are $ppm^{-2}min^{-1}$.

[c] Pseudo-second-order rate constant for 1 atm air.

[d] Rate constants for the reactions of lumped olefins, alkanes, and aromatics with OH, O, and O_3 were taken to be average mole-weighted ratio, based on initial compositions of each hydrocarbon class. Thus $k_l = \Sigma_i k_i n_i / \Sigma_i n_i$ where k_l is the lumped hydrocarbon rate constant, k_i the individual rate constant for hydrocarbon i, and n_i the number of moles of hydrocarbon i in the initial lumped mix.

[e] Depends on smog chamber experiment, Winer [36].

TABLE II. Reactions in the RO_x–NO_x system.

	NO	NO_2
RO	$RO + NO \rightarrow RONO$[a] $\overset{\leftarrow}{h\nu}$ $\rightarrow RCHO + HNO$	$RO + NO_2 \rightarrow RONO_2$[b] $\rightarrow RCHO + HONO$
RO_2	$RO_2 + NO \rightarrow NO_2 + RO$[c] $\rightarrow RONO_2$	$RO_2 + NO_2 \rightleftarrows RO_2NO_2$[d] $\rightarrow RCHO + HONO_2$
RCO_3	$RCO_3 + NO \overset{O_2}{\rightarrow} NO_2 + RO_2 + CO_2$[e]	$RCO_3 + NO_2 \rightleftarrows PAN$[f]

[a] The primary pathway for the alkoxyl–NO reaction is RO + NO → RONO. Rate constants for this series of reactions have not been measured directly, but have been calculated from measured rates of the reverse reaction and thermodynamic estimates. Batt and co-workers [18] obtained rate constants for several of the above reactions that fall in the range of 3.1–6.2 $\times 10^4$ $ppm^{-1}min^{-1}$. Both Mendenhall and co-workers [19] and Batt and Milne [20] determined the rate constant for *t*-butoxyl + NO, obtaining 1.55×10^5 and 6.2×10^4 $ppm^{-1}min^{-1}$, respectively. Thus the probable uncertainty in an estimated value of a particular RO-NO rate constant is a factor of 2–4. In addition to the path shown above there is an abstraction reaction, the fractional occurrence of which depends on the alkyl group. The abstraction fraction can be estimated based on the data of Batt and co-workers [18].

[b] Two reaction paths for alkoxyl–NO_2 reactions exist, addition and abstraction. For methoxyl + NO_2 the abstraction fraction has been estimated by Weibe and co-workers [21] to be 0.08 and by Barker and co-workers [23] to be 0.23. Rate constants for alkoxyl–NO_2 reactions have been inferred from measured values of the ratio of the rate constants of alkoxyl–NO to akoxyl–NO_2 reactions. Wiebe and co-workers [21] reported that for methoxyl radicals this ratio is 1.2, whereas Baker and Shaw [22] obtained 2.7 for the same ratio. Baker and Shaw [22] determined a ratio of 1.7 for *t*-butoxyl radicals. Absolute rate constants for RO–NO_2 reactions are then obtained on the basis of RO–NO rate constants.

[c] The peroxyalkyl radical–NO reaction may proceed as shown. Conversion to NO to NO_2 occurs primarily by the first reaction. It has been postulated that the second reaction will occur a fraction of the time for longer chain peroxyalkyl radicals [$n > 4$]. Darnall and coworkers [32] estimated the ratio k_2/k_1 to be 0.09 and 0.16 for $n = 4$ and 5, respectively. Aside from the HO_2–NO reaction, rate constant values have not been measured for RO_2–NO reactions. A lower limit for the rate constants for these reactions can be estimated as 3×10^3 $ppm^{-1}min^{-1}$ based on theoretical considerations.

[d] Rate constants for the RO_2–NO_2 reaction and the RO_2NO_2 decomposition must be estimated.

[e] Hendry and Kenley [31] report a value of 4900 $ppm^{-1}min^{-1}$ for $CH_3C(O)O_2$+ NO, whereas Cox and Roffey [25] found 3800 $ppm^{-1}min^{-1}$.

[f] The rate constant for the PAN formation step is determined by Hendry and Kenley [31] to be 1500 $ppm^{-1}min^{-1}$ and by Cox and Roffey [25] to be 2070 $ppm^{-1}min^{-1}$. PAN thermal decomposition rates are also reported by the two investigators.

Reactions in the RO_x/NO_x subsystem (Table II) are subject to degrees of uncertainty for two reasons. First, the rate constants reported for spe-

cific reactions in each lumped group differ among investigators. For instance, different PAN formation and decomposition rates have been determined by Cox and Roffey [25] and Hendry and Kenley [31]. Second, since the composition of the lumped radical classes changes throughout the degradation process of the different atmospheric hydrocarbon species, it is difficult to select accurate rate constants for reactions of the RO_x/NO_x system. The uncertainties associated with each reaction in the RO_x/NO_x network are summarized in Table II.

Sensitivity/Uncertainty Analysis

A sensitivity/uncertainty analysis can provide two different but related types of information. By individually perturbing parameters a small amount from their nominal values, say ±5%, the absolute sensitivity of the predictions of the mechanism can be ascertained. A sensitivity/uncertainty analysis incorporates the same information and, in addition, takes into account the degree of uncertainty associated with each parameter, thereby generating a combined measure of sensitivity and uncertainty. Both types of analyses are important. For example, a parameter to which the predictions of the mechanism are not especially sensitive may have such a large range of uncertainty that, when all possible variations are considered, its influence on the predictions is rather substantial. On the other hand, a very sensitive parameter may have a small range of uncertainty, and therefore its overall influence on the mechanism, considering both sensitivity and uncertainty, may be lower than that of other parameters.

In many problems the uncertainties are such that linearized methods are no longer applicable. The FAST method, which overcomes this restriction, has been developed by Shuler et al. [10]. The particular advantage of this approach is that order of magnitude changes in parameter values can be easily accommodated. Basically the procedure involves a simultaneous variation of all the parameters over their individual ranges of estimated uncertainty. Formally the parameters are ranked in the order of importance by using normalized statistical measures called partial variances. These variances indicate the relative contribution of individual parameters to uncertainties in model predictions. The FAST analysis identifies the contribution of individual parameters to the total variance in each predicted species concentration. To determine the sensitivity of the mechanism, the method can be used with each parameter varied a small amount from its nominal value. Detailed descriptions of the technique are available elsewhere [10,11] and will not be repeated here.

Discussion of Results

Two types of the sensitivity/uncertainty analysis were performed on simulations of three different surrogate hydrocarbon smog chamber experiments carried out at the Statewide Air Pollution Research Center at the University of California, Riverside [33,34]. First, in order to ascertain the absolute sensitivity of the predictions of the mechanism to each of the reaction parameters being studied, runs were made in which all parameters of interest were perturbed from their nominal values by ±5%. In a second set of cases, the parameters were permitted to vary over their entire uncertainty range, thus providing combined sensitivity and uncertainty information. The parameter values for these two cases are shown in columns 2 and 3 of Table I. Many of the reactions have been shown to have relatively little influence on concentration behavior [8]. Thus, only those rate constants of reactions for which an asterisk(*) exists in column 4 of Table I were subject to variation in the studies to be described.

Effects of the parameter variations on predictions of NO_2, O_3, and PAN were monitored. These output variables were chosen because air quality standards exist for NO_2 and O_3, and because NO_2 and O_3 reflect the major features of the chemistry. To explore the effects of varying initial hydrocarbon–NO_x mixtures on the results of the study, smog chamber simulations with a wide range of initial conditions were examined. Tables III–VIII list the parameters and their partial variances, ranked according to their effect on each of the output variables, for each of the analyses performed.

TABLE III. Parameter rankings for case 1,[a] small parameter variations.

Time	60 min.		120 min.		180 min.		240 min.		300 min.	
Rank	Parameter	Partial Variance	Parameter	Partial Variance	Parameter	Partial Variance	Parameter	Partial Variance	Parameter	Partial Variance
OUTPUT VARIABLE: NO_2										
1	α	0.310	k_{23}	0.472	k_{23}	0.583	k_{31}	0.354	α	0.320
2	k_{23}	0.309	α	0.310	k_1	0.310	α	0.233	k_{31}	0.286
3	k_{24}	0.193	k_{31}	0.080	α	0.073	β	0.200	β	0.203
4	k_{31}	0.111	β	0.051	k_{31}	0.026	k_1	0.077	k_{23}	0.074
5	β	0.030	k_1	0.025	k_{34}	0.017	k_{34}	0.056	k_{34}	0.051
OUTPUT VARIABLE: O_3										
1	k_1	0.363	k_{23}	0.317	α	0.328	α	0.340	α	0.345
2	α	0.196	α	0.297	k_{23}	0.305	k_{23}	0.278	k_{23}	0.254
3	k_{23}	0.181	k_{31}	0.130	k_{31}	0.148	k_{31}	0.159	k_{31}	0.163
4	k_{24}	0.120	k_1	0.102	β	0.106	β	0.131	β	0.150
5	k_{31}	0.083	β	0.071	k_1	0.038	k_{34}	0.032	k_{34}	0.035
OUTPUT VARIABLE: PAN										
1	k_{23}	0.391	k_{23}	0.485	k_{23}	0.432	k_{23}	0.386	k_{23}	0.350
2	k_{24}	0.212	α	0.187	α	0.213	α	0.230	α	0.245
3	k_{31}	0.153	k_{31}	0.161	k_{31}	0.171	k_{31}	0.181	k_{31}	0.183
4	α	0.128	β	0.078	β	0.110	β	0.135	β	0.153
5	β	0.035	δ	0.026	δ	0.025	k_{34}	0.019	k_{34}	0.020

[a] Simulation: UCR 119J [32]. Initial conditions: $[NO_2]$ = 0.041; [NO] = 0.301; [OLE] = 0.039; [ALK] = 0.358; [ARO] = 0.070; [ETH] = 0.043; [HCHO] = 0.038; [RCHO] = 0.023; [HONO] (assumed) = 0.0; k_1 = 0.32; simulated NO_2 peak time = 200 min; $[HC/NO_x]_0$ = 1.7

TABLE IV. Parameter rankings for case 2,[a] small parameter variations.

Time	60 min.		120 min.		180 min.		240 min.		300 min.	
Rank	Parameter	Partial Variance	Parameter	Partial Variance	Parameter	Partial Variance	Parameter	Partial Variance	Parameter	Partial Variance
OUTPUT VARIABLE: NO_2										
1	k_{31}	0.264	k_{31}	0.378	k_{31}	0.377	α	0.459	α	0.575
2	k_1	0.191	α	0.194	α	0.321	k_{31}	0.338	k_{31}	0.265
3	δ	0.139	k_1	0.112	β	0.104	β	0.105	β	0.095
4	k_{23}	0.128	β	0.091	k_1	0.054	δ	0.023	k_{34}	0.015
5	ϵ	0.086	k_{23}	0.066	δ	0.039	k_{23}	0.020	δ	0.013
OUTPUT VARIABLE: O_3										
1	k_1	0.473	k_1	0.584	k_1	0.696	k_1	0.778	k_1	0.839
2	α	0.274	α	0.243	α	0.187	α	0.134	α	0.086
3	k_{23}	0.086	k_{23}	0.072	k_{23}	0.071	k_{23}	0.069	k_{23}	0.068
4	k_{31}	0.056	k_{31}	0.043	β	0.021	β	0.009	k_{52}	0.003
5	β	0.032	β	0.035	k_{31}	0.016	k_{31}	0.003	β	0.002
OUTPUT VARIABLE: PAN										
1	k_{23}	0.270	k_{31}	0.290	k_{23}	0.334	k_{23}	0.380	k_{23}	0.404
2	k_1	0.216	k_{23}	0.284	k_{31}	0.306	k_{31}	0.320	k_{31}	0.344
3	k_{31}	0.186	k_1	0.219	k_1	0.199	k_1	0.145	k_1	0.082
4	δ	0.184	δ	0.112	δ	0.091	δ	0.084	δ	0.082
5	ϵ	0.062	β	0.043	β	0.043	β	0.046	β	0.018

[a] Simulation: UCR-121J [32]. Initial conditions: $[NO_2] = 0.012$; [NO] = 0.044; [OLE] = 0.04; [ALK] = 0.37; [ARO] = 0.066; [ETH] = 0.042; [RCHO] = 0.06; [HCHO] = 0.011; [HONO] (assumed) = 0.0; $k_1 = 0.32$; simulated NO_2 peak time = 30 min; $[HC/NO_x]_0 = 10.5$.

TABLE V. Parameter rankings for case 3,[a] small parameter variations.

Time	60 min.		120 min.		180 min.		240 min.		300 min.	
Rank	Parameter	Partial Variance	Parameter	Partial Variance	Parameter	Partial Variance	Parameter	Partial Variance	Parameter	Partial Variance
OUTPUT VARIABLE: NO_2										
1	α	0.289	α	0.423	α	0.433	α	0.441	α	0.445
2	k_{31}	0.167	β	0.226	β	0.238	β	0.240	β	0.232
3	β	0.164	k_{31}	0.197	k_{31}	0.198	k_{31}	0.198	k_{31}	0.200
4	δ	0.112	k_{23}	0.035	k_{23}	0.051	k_{23}	0.048	k_{23}	0.040
5	ϵ	0.084	δ	0.031	δ	0.015	ϵ	0.096	δ	0.009
OUTPUT VARIABLE: O_3										
1	α	0.464	α	0.463	α	0.458	α	0.448	α	0.401
2	k_{23}	0.295	k_{23}	0.210	β	0.190	β	0.189	k_1	0.205
3	β	0.083	β	0.155	k_{23}	0.165	k_{23}	0.136	β	0.149
4	k_{31}	0.042	k_{31}	0.094	k_{31}	0.120	k_{31}	0.120	k_{23}	0.117
5	δ	0.027	k_1	0.025	k_1	0.034	k_1	0.075	k_{31}	0.088
OUTPUT VARIABLE: PAN										
1	k_{23}	0.521	k_{23}	0.348	α	0.287	α	0.297	α	0.284
2	α	0.169	α	0.249	k_{23}	0.263	k_{23}	0.227	k_{31}	0.225
3	δ	0.084	β	0.160	β	0.203	β	0.214	k_{23}	0.224
4	β	0.074	k_{31}	0.148	k_{31}	0.188	k_{31}	0.209	β	0.207
5	k_{31}	0.070	δ	0.042	δ	0.026	δ	0.021	δ	0.021

[a] Simulation: EC-237s [32]. Initial conditions: $[NO_2] = 0.021$; [NO] = 0.075; [OLE] = 0.030; [ALK] = 0.298; [ARO] = 0.035; [ETH] = 0.175; [HCHO] = 0.0; [RCHO] = 0.001; [HONO] (assumed) = 0.020; $k_1 = 0.30$; simulated NO_2 peak time = 30 min; $[HC/NO_x]_0 = 5.57$.

TABLE VI. Parameter rankings for case 4,[a] large parameter variations.

Time	60 min.		120 min.		180 min.		240 min.		300 min.	
Rank	Parameter	Partial Variance	Parameter	Partial Variance	Parameter	Partial Variance	Parameter	Partial Variance	Parameter	Partial Variance
OUTPUT VARIABLE: NO_2										
1	α	0.933	α	0.831	α	0.854	α	0.846	α	0.826
2	k_{23}	0.018	β	0.055	β	0.091	β	0.105	β	0.122
3	k_{24}	0.011	k_{51}	0.031	k_{51}	0.018	k_{51}	0.009	k_{32}	0.013
4	β	0.010	k_{23}	0.019	δ	0.008	k_{31}	0.009	k_{31}	0.010
5	k_{31}	0.005	ε	0.010	k_{31}	0.006	k_{32}	0.008	δ	0.007
OUTPUT VARIABLE: O_3										
1	α	0.861	α	0.861	α	0.855	α	0.849	α	0.834
2	β	0.033	β	0.065	β	0.086	β	0.097	β	0.106
3	k_{51}	0.029	k_{51}	0.023	k_{51}	0.015	k_{51}	0.010	k_{32}	0.013
4	δ	0.015	δ	0.011	δ	0.008	k_{23}	0.008	k_{23}	0.009
5	ε	0.009	k_{31}	0.007	k_{23}	0.007	δ	0.006	k_{51}	0.006
OUTPUT VARIABLE: PAN										
1	α	0.643	α	0.624	α	0.634	α	0.633	α	0.618
2	β	0.112	β	0.203	β	0.243	β	0.265	β	0.286
3	δ	0.061	δ	0.048	δ	0.031	k_{31}	0.027	k_{31}	0.027
4	k_{51}	0.031	k_{31}	0.030	k_{31}	0.028	δ	0.023	k_{23}	0.020
5	k_{23}	0.028	k_{23}	0.027	k_{23}	0.022	k_{23}	0.020	δ	0.018

[a] Simulation: UCR 119J [32]. Initial conditions: $[NO_2] = 0.041$; [NO] = 0.301; [OLE] = 0.039; [ALK] = 0.358; [ARO] = 0.070; [ETH] = 0.043; [HCHO] = 0.038; [RCHO] = 0.023; [HONO] (assumed) = 0.0; $k_1 = 0.32$; simulated NO_2 real time = 200 min; $[HC/NO_x]_0 = 1.7$.

TABLE VII. Parameter rankings for case 5,[a] large parameter variations.

Time	60 min.		120 min.		180 min.		240 min.		300 min.	
Rank	Parameter	Partial Variance	Parameter	Partial Variance	Parameter	Partial Variance	Parameter	Partial Variance	Parameter	Partial Variance
OUTPUT VARIABLE: NO_2										
1	α	0.535	α	0.677	α	0.695	α	0.685	α	0.665
2	δ	0.223	β	0.139	β	0.158	β	0.169	β	0.173
3	β	0.085	δ	0.085	δ	0.052	k_{51}	0.037	k_{51}	0.030
4	ε	0.046	k_{31}	0.038	k_{31}	0.036	δ	0.037	k_{31}	0.030
5	ρ	0.041	ρ	0.015	k_{51}	0.019	k_{31}	0.033	δ	0.028
OUTPUT VARIABLE: O_3										
1	α	0.453	α	0.523	α	0.466	α	0.394	α	0.417
2	k_{51}	0.298	k_{51}	0.219	k_{51}	0.198	k_1	0.256	k_1	0.269
3	k_{52}	0.066	k_1	0.097	k_1	0.169	k_{51}	0.150	k_{52}	0.142
4	k_1	0.064	k_{52}	0.078	k_{52}	0.112	k_{52}	0.149	k_{51}	0.073
5	δ	0.032	β	0.037	β	0.015	k_{23}	0.017	β	0.035
OUTPUT VARIABLE: PAN										
1	α	0.454	α	0.505	α	0.568	α	0.644	α	0.699
2	δ	0.229	δ	0.165	δ	0.123	β	0.116	β	0.111
3	k_{51}	0.144	k_{51}	0.105	β	0.122	δ	0.097	δ	0.084
4	β	0.035	β	0.104	k_{51}	0.083	k_{51}	0.053	k_{31}	0.035
5	ρ	0.031	k_{31}	0.040	k_{31}	0.042	k_{31}	0.038	k_{51}	0.027

[a] Simulation: UCR-121J [32]. Initial conditions: $[NO_2] = 0.012$; [NO] = 0.044; [OLE] = 0.04; [ALK] = 0.37; [ARO] = 0.066; [ETH] = 0.042; [HCHO] = 0.06; [RCHO] = 0.011; [HONO] (assumed) = 0.0; $k_1 = 0.32$; simulated NO_2 peak time = 30 min; $[HC/NO_x]_0 = 10.5$.

TABLE VIII. Parameter rankings for case 6,[a] large parameter variations.

Time	60 min.		120 min.		180 min.		240 min.		300 min.	
	Parameter	Partial Variance	Parameter	Partial Variance	Parameter	Partial Variance	Parameter	Partial Variance	Parameter	Partial Variance
OUTPUT VARIABLE: NO_2										
1	α	0.697	α	0.691	α	0.649	α	0.237	α	0.240
2	β	0.161	β	0.207	β	0.267	k_{51}	0.205	k_{51}	0.200
3	λ	0.074	k_{51}	0.047	k_{51}	0.031	k_{23}	0.119	k_{23}	0.120
4	k_{51}	0.041	λ	0.028	k_{31}	0.021	k_{31}	0.109	k_{31}	0.110
5	k_{31}	0.125	k_{31}	0.016	λ	0.020	λ	0.098	λ	0.090
OUTPUT VARIABLE: O_3										
1	α	0.718	α	0.742	α	0.716	α	0.650	α	0.589
2	k_{51}	0.161	β	0.098	β	0.149	β	0.227	β	0.285
3	β	0.043	k_{51}	0.092	k_{51}	0.061	k_{51}	0.044	k_1	0.040
4	k_{52}	0.035	k_{52}	0.025	k_{52}	0.022	k_1	0.028	k_{51}	0.034
5	δ	0.018	k_1	0.013	k_1	0.016	k_{52}	0.019	k_{52}	0.020
OUTPUT VARIABLE: PAN										
1	k_{51}	0.280	β	0.417	β	0.495	α	0.239	α	0.230
2	λ	0.259	α	0.212	α	0.230	k_{51}	0.204	k_{51}	0.119
3	β	0.224	k_{51}	0.144	k_{51}	0.101	k_{23}	0.121	k_{23}	0.118
4	α	0.107	λ	0.130	λ	0.081	k_{31}	0.105	k_{31}	0.100
5	k_{23}	0.080	k_{23}	0.046	k_{31}	0.051	λ	0.091	λ	0.099

[a] Simulation: EC-237s [32]. Initial conditions: $[NO_2] = 0.021$; $[NO] = 0.075$; [OLE] = 0.030; [ALK] = 0.298; [ARO] = 0.035; [ETH] = 0.175; [HCHO] = 0.0; [RCHO] = 0.001; [HONO] (assumed) = 0.020; $k_1 = 0.30$; simulated NO_2 peak time = 30 min; $[HC/NO_x]_0 = 5.57$.

NO_2 Behavior

The results of the FAST sensitivity/uncertainty analyses help to point out and affirm observations about the qualitative aspects of the chemical mechanism and also provide some new insight into the essential features of the system. The ranking of those parameters to which the predictions of NO_2 behavior are most sensitive highlights the most important of the many mechanisms by which NO_2 is produced. In all the small parameter variation cases, the parameters dominating NO_2 behavior around the time of the NO_2 peak are the photolysis rate, k_1, and the nitric acid formation step. Before and after the predicted peak time, variations in the rates of those reactions forming peroxy radicals, especially the aldehyde photolysis rates, have the most marked effect. In the simulation with the high hydrocarbon to NO_x ratio (case 2), the production of RO_2 and HO_2 from the ozone–olefin reaction is also important.

As discussed earlier, peroxy radicals act to convert NO to NO_2 by

$$RO_2 + NO \xrightarrow{52} RO + NO_2$$

$$HO_2 + NO \xrightarrow{21} OH + NO_2$$

Hence, the rate constants associated with the above reactions, as well as the quantities of RO_2 and HO_2 available, should have a distinct effect on NO_2 concentration levels. The fact that aldehyde photolysis, alkoxyl radical decomposition, and ozone–olefin reactions all produce peroxy radicals explains the large partial variances associated with these parameters. Relative to competing reactions, small variations in k_{52}, the RO_2-NO rate constant, do not produce a large effect on NO_2 predictions. The reason for this is that the RO_2-NO rate constant is so large that other reactions cannot effectively compete for RO_2.

The differences in chemistry brought about by changes in initial conditions are evident from a close examination of the outcome of the larger parameter variation studies, cases 4–6. When the initial hydrocarbon to NO_x ratio is low (case 4), α, the fraction of times that HO_2 is produced from RO, makes the largest contribution to variations in NO_2 predictions. Where initial HC/NO_x levels were higher (case 5), uncertainties in ozone–olefin product distribution and in the production of aldehydes from alkoxyl radicals also contributed significant variances. In systems where initial HC/NO_x ratios are small, or in which fairly unreactive species comprise the hydrocarbon mix, there are not enough radicals present to convert all the available NO to NO_2. As a result, in smog chamber experiments of these systems NO_2 peaks are broad and occur later in the test. For those initial mixtures which are richer in hydrocarbons, or contain very reactive species, there are a larger number of peroxy radicals for the NO_x in the chamber. As the fraction of time that RO_2 is produced from alkoxyl radical reactions is increased (represented by decreasing α), the number of peroxy radicals in the simulation increases. This occurs as a result of the cyclic effect of producing RO_2 from alkoxyl radical reactions and subsequent reconversion to RO through reaction with NO:

$$RO \xrightarrow{44} (1 - \alpha)RO_2 + \alpha HO_2 + \beta HCHO + \gamma RCHO$$

$$RO_2 + NO \xrightarrow{52} RO + NO_2$$

Since simulations with low initial HC/NO_x levels can be thought to be radical deficient, α varied over its entire range of uncertainty has a large influence on NO_x predictions. However, α has much less effect on cases in which the initial HC/NO_x ratio is large than when it is small, as other modes of radical production besides RO reactions occur to a significant extent in the high HC/NO_x situation.

O_3 Behavior

Much of the interest in mechanisms for photochemical smog is focused on understanding the avenues for the production of ozone. The results

of the sensitivity analyses are extremely pertinent to this understanding.

Time-varying plots of the partial variances of the major parameters affecting the production of ozone are given in Figures 3–8. As was the case for NO_2 behavior, the results are substantially different for the various initial conditions. For the higher $[HC]/[NO_x]_0$ simulations of cases 2 and 3, small variations in the NO_2 photolysis rate have the biggest impact on ozone formation. On the other hand, at times in the analysis of the low $[HC]/[NO_x]_0$ run (case 1), ozone concentrations are more influenced by peroxy radical production routes. In the large parameter variation cases α dominates the ranked list for low initial HC/NO_x ratios, whereas the other parameters in the alkoxyl radical reaction and the decomposition of the peroxynitrates are also important for high initial HC/NO_x ratios.

The effects of the parameter variations on ozone behavior can be ex-

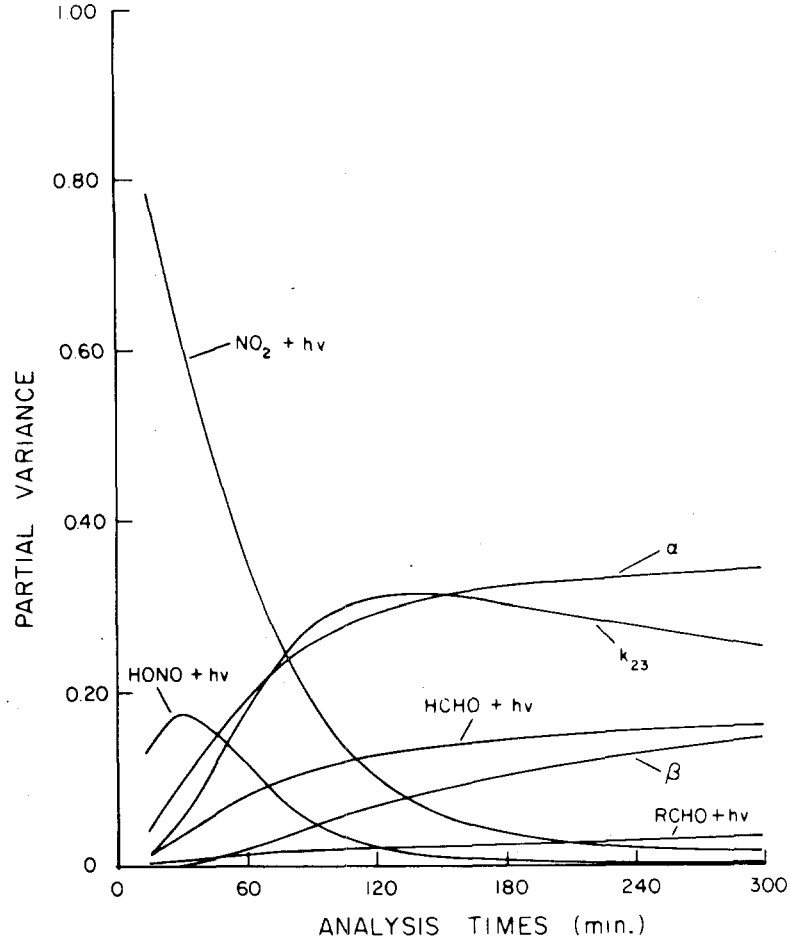

Figure 3. Time-varying partial variances of the major parameters affecting ozone for case 1 (small parameter variation).

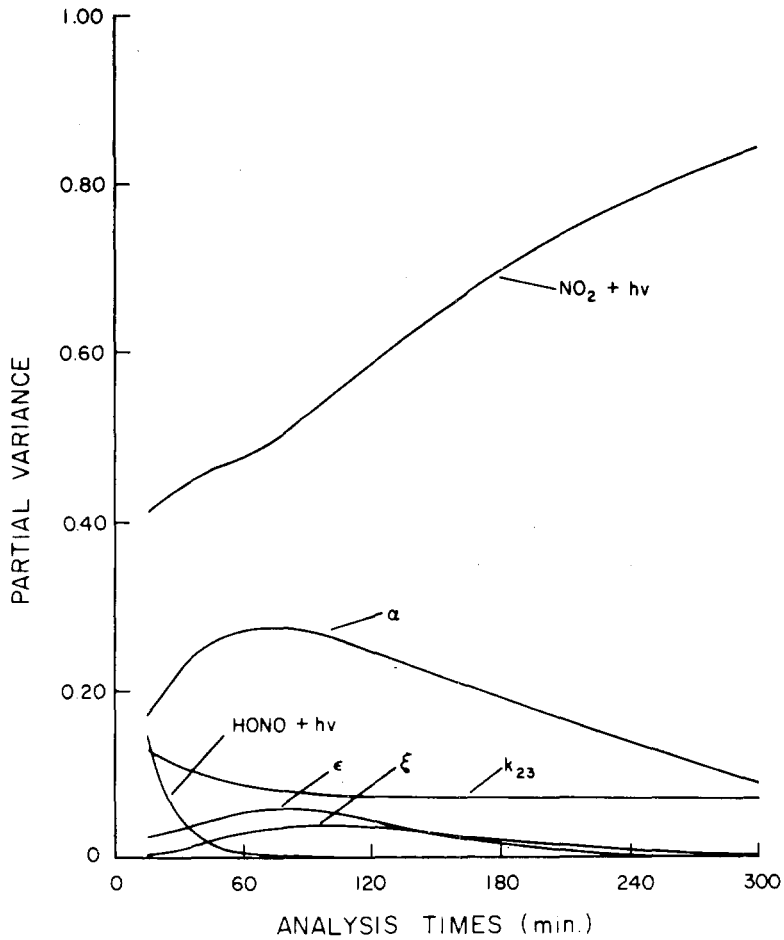

Figure 4. Time-varying partial variances of the major parameters affecting ozone for case 2 (small parameter variation).

plained in much the same fashion as the NO_2 discussion earlier. As can be seen from Figure 1, the ozone level at any time is the result of the complex interplay between NO and NO_2, peroxy radicals, and ozone. Ozone builds up as NO is converted to NO_2 without consuming O_3. When concentration levels of peroxy radicals are low, as in simulations with a lean initial hydrocarbon mix, reactions (1)–(3) exist in a photostationary state. As peroxy radical levels rise, however, the rates of reactions that convert NO to NO_2 without consuming O_3 become comparable to or surpass the rate of reaction (3), modifying the equilibrium set up by reactions (1)–(3). Simulations with low peroxy radical levels will therefore show a much larger sensitivity to those parameters, such as α, which substantially affect the concentrations of the peroxy radicals. When RO_2 levels are higher, as in simulations of high initial HC/NO_x mixtures, there already exists an adequate number of free radicals present to convert NO to NO_2. Hence, the sensitivity of

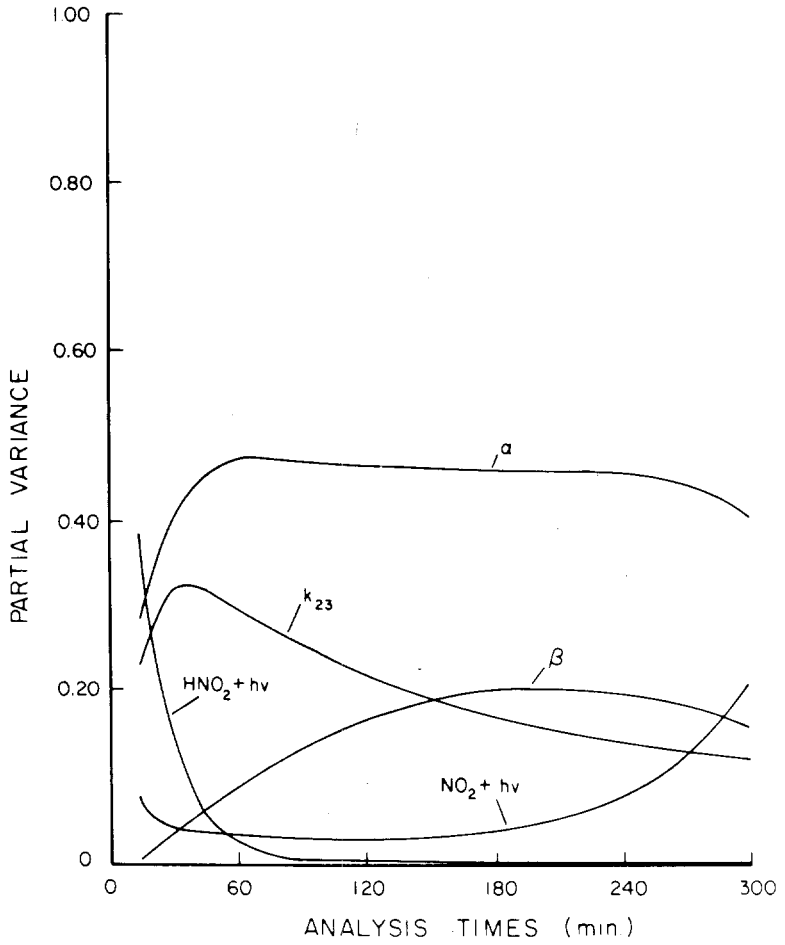

Figure 5. Time-varying partial variances of the major parameters affecting ozone for case 3 (small parameter variation).

the system lies in NO_2 photolysis rates. Moreover, in these systems, the effects of the large variation cases are divided between other parameters which affect the levels of both peroxy radicals and NO_2.

PAN Behavior

PAN predictions are influenced by both NO_2 and RCO_3 concentration levels. Results of the sensitivity/uncertainty analysis can be explained in this light. For case 1, the parameters which highly influence the rate of PAN formation are the nitric acid formation rate constant k_{23} which directly affects the NO_2 level, and the two coefficients α and γ associated with RO decomposition which influences the concentration of RCHO. PAN is affected by RCHO levels because peroxyacyl radicals RCO_3 are formed primarily through the reaction of OH with aldehydes. RCO_3 then

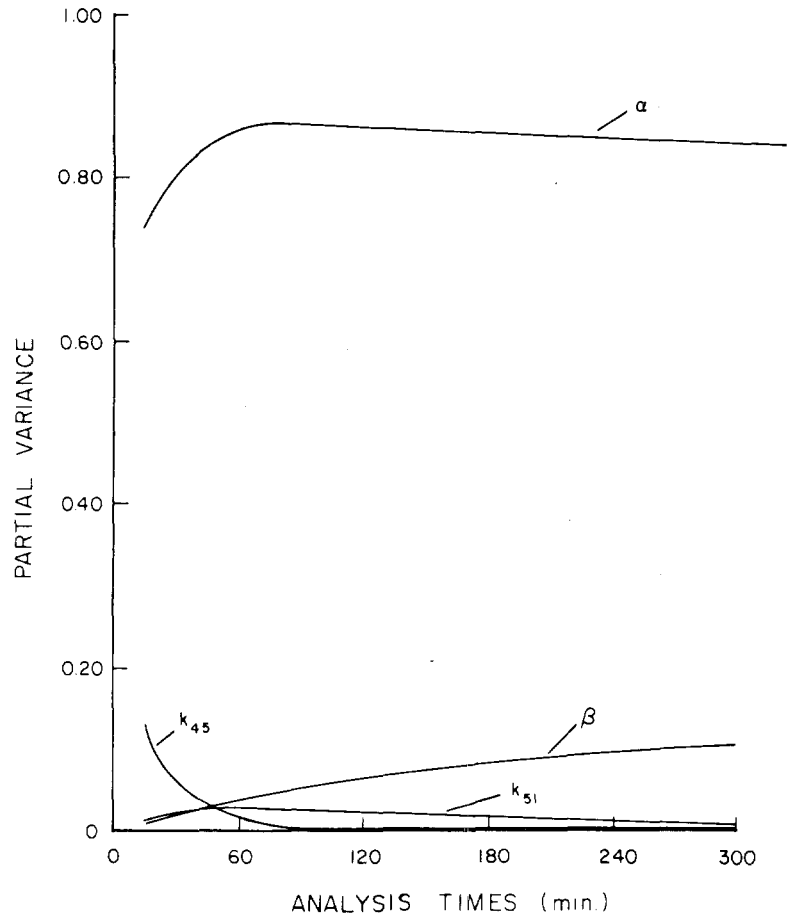

Figure 6. Time-varying partial variances of the major parameters affecting ozone for case 4 (large parameter variation).

reacts with NO_2 to form PAN through a competing reaction with NO. Thus, those parameters that affect RCO_3 production and the availability of OH radicals in the mechanism will subsequently influence PAN levels. For the small parameter variation cases 2 and 3, in which the initial HC/NO_x ratios are higher, parameters perturbing NO_2 levels are much more important in PAN production.

These results are seen even more clearly in the combined sensitivity/uncertainty analyses in cases 4–6. For the low HC/NO_x simulation, the parameters k_{23} and α have large partial variances. The same results are observed in the higher HC/NO_x cases.

Conclusions and Recommendations

Sensitivity and sensitivity/uncertainty analyses have been performed on a representative photochemical smog reaction mechanism. These

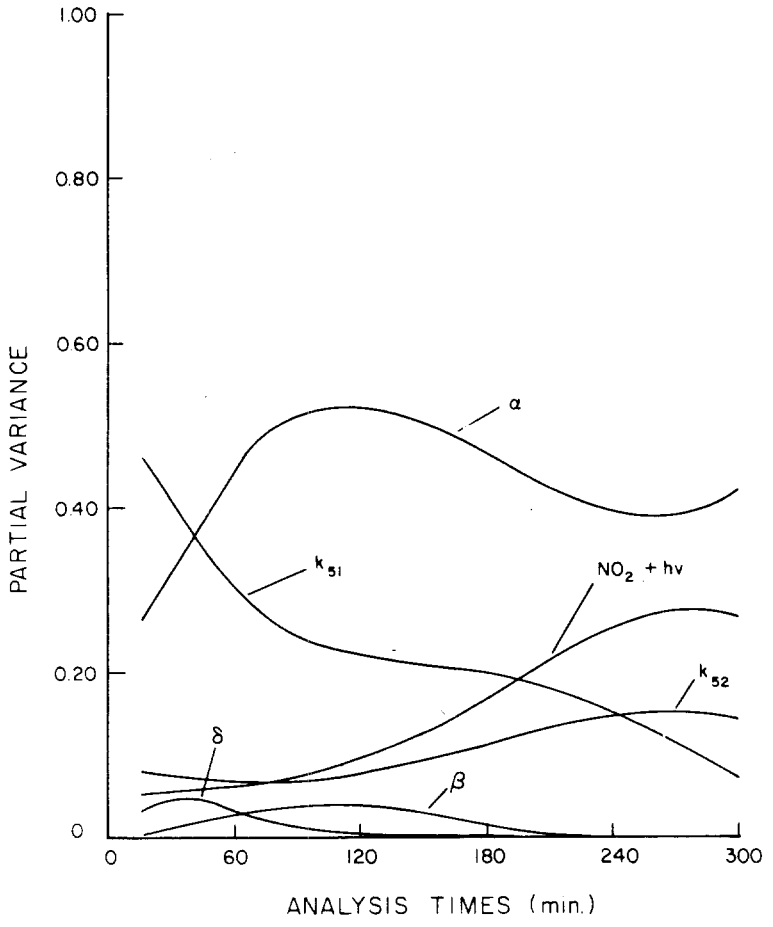

Figure 7. Time-varying partial variances of the major parameters affecting ozone for case 5 (large parameter variation).

studies have shown that the major sensitivity of the NO_2, O_3, and PAN concentrations lies in photolysis rates for NO_2 and aldehydes. On the other hand, when all parameters studied are allowed to vary over their entire ranges of uncertainty, generalized stoichiometric coefficients and certain rate constants have been shown to exert the most influence on the predictions of the mechanism.

Within present experimental uncertainties, the current mechanism for photochemical smog provides a good representation of the chemistry of the major species in the polluted troposphere as evidenced by comparisons of predicted and observed concentrations in smog chamber studies [7]. Based on the sensitivity studies presented here, the level of detail in the treatment of free radical and hydrocarbon chemistry in the mechanism seems to be consistent with the current level of understanding of these processes. However, as additional fundamental studies of alkoxyl radical chemistry, shown by the sensitivity/uncertainty portion of this study to

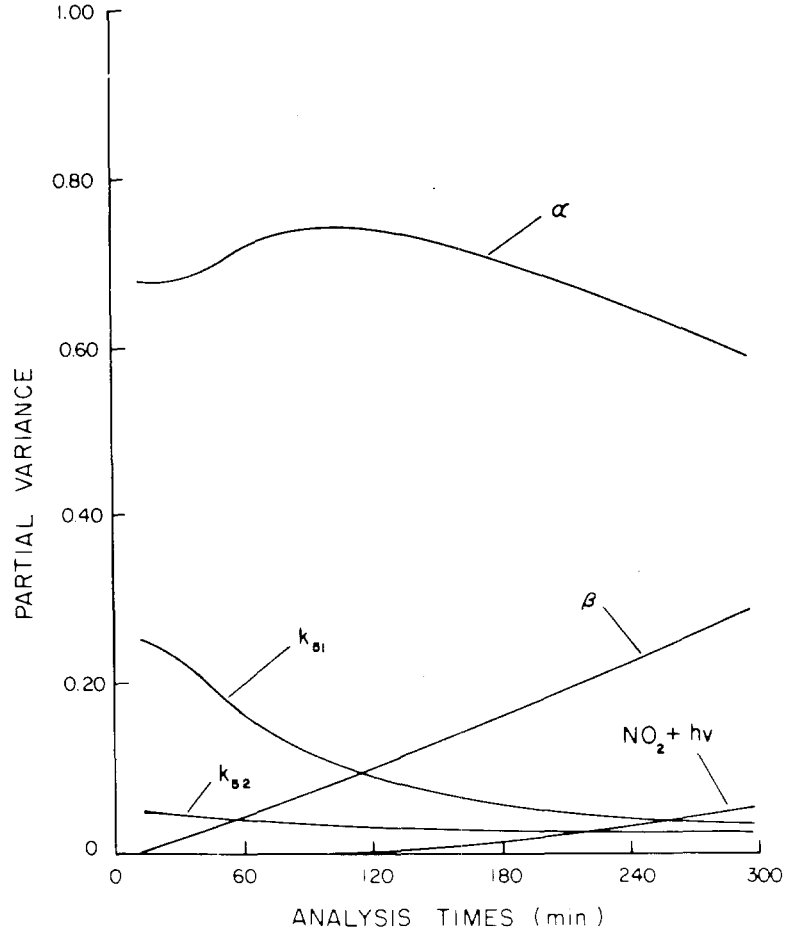

Figure 8.. Time-varying partial variances of the major parameters affecting ozone for case 6 (large parameter variation).

be highly important in the reaction network, are carried out, a more highly resolved radical lumping procedure than is used here may be necessary to improve the accuracy of the mechanism. In addition, when a detailed reaction mechanism for aromatic compounds becomes available, lumped aromatic reaction steps will undoubtedly need to be refined. Because no investigation into the role of aromatics has been attempted in this work, little can be said about the effects such improvements would have on the overall predictions.

In summary, based on these findings, we recommend that experimental work in atmospheric chemistry be concentrated in the following areas:

(a) Studies of decomposition, isomerization, and O_2 reaction pathways of alkoxyl and hydroxyalkoxyl radicals

(b) Improvements in knowledge of the spectral distribution and level

of actinic irradiance for both atmospheric studies and smog chamber experiments

(c) Better measurements of quantum yields and absorption cross sections for aldehydes

and, less importantly, that work be done on:

(d) Olefin–ozone product distributions, needed for accurately modeling systems in which olefins comprise a large fraction of the hydrocarbon mix

(e) Determination of rate parameters associated with the formation and decomposition of peroxynitrates

(f) Determination of emission levels and routine atmospheric measurements of aldehydes, because of their pronounced influence on radical concentrations.

Acknowledgment

This work was supported by the Environmental Protection Agency under grant R805537. Computational resources were provided by the California Air Resources Board under contract A7-187-30. Comments and assistance by Dr. Marcia Dodge and Dr. James Tilden are gratefully appreciated.

Bibliography

[1] T. E. Graedel, L. A. Farrow, and T. A. Weber, *Atmos. Environ.*, **10,** 1095 (1976).

[2] G. Z. Whitten and H. Hogo, "Mathematical Modeling of Simulated Photochemical Smog," Environmental Protection Agency Rep. EPA-600/3-77-011, 1977.

[3] A. C. Baldwin, J. R. Barker, D. M. Golden, and D. G. Hendry, *J. Phys. Chem.*, **81,** 2483 (1977).

[4] W. P. Carter, A. C. Lloyd, J. L. Sprung, and J. N. Pitts, Jr., *Int. J. Chem. Kinet.*, **11,** 45 (1979).

[5] R. J. Gelinas and P. D. Skewes-Cox, *J. Phys. Chem.*, **81,** 2468 (1977).

[6] J. R. Martinez, K. T. Tran, A. C. Lloyd, and G. M. Hidy, "Development of an Atmospheric Model for Sulphate Formation," Environmental Research and Technology, Inc., 1977, Doc. P-1534.

[7] A. H. Falls and J. H. Seinfeld, *Environ. Sci. Technol.*, **12,** 1398 (1978).

[8] M. C. Dodge and T. A. Hecht, *Int. J. Chem. Kinet.*, **1,** 155 (1975).

[9] T. A. Hecht, J. H. Seinfeld, and M. C. Dodge, *Environ. Sci. Technol.*, **8,** 327 (1974).

[10] R. I. Cukier, H. B. Levine, and K. E. Shuler, *J. Comp. Phys.*, **26,** 1 (1978).

[11] M. Koda, G. J. McRae, and J. H. Seinfeld, *Int. J. Chem. Kinet.*, **11,** 427 (1979).

[12] R. J. Hampson, Jr., and D. Garvin, "Reaction Rate and Photochemical Data for Atmospheric Chemistry—1977," NBS Special Rep. Publ. 513, National Bureau of Standards, Washington, DC, 1978.

[13] R. A. Graham and H. S. Johnston, *J. Phys. Chem.*, **82,** 254 (1978).

[14] R. A. Graham, A. M. Winer, and J. N. Pitts, Jr., *Chem. Phys. Lett.*, **51,** 215 (1977).

[15] R. A. Graham, A. M. Winer, and J. N. Pitts, Jr., *J. Chem. Phys.*, **68,** 4505 (1978).

[16] A. C. Lloyd, Workshop on Chemical Kinetic Data Needs for Modeling the Lower Troposphere, Environmental Protection Agency and National Bureau of Standards, Reston, VA, May 15–17, 1978.

[17] G. J. McRae, W. R. Goodin, and J. H. Seinfeld, "Development of a Second Generation Mathematical Model of Photochemical Air Pollution," California Air Resources Board, contract A5-046-87, Final Rep. 1979.
[18] L. Batt, R. D. McCulloch, and R. T. Milne, *Int. J. Chem. Kinet.*, **S1**, 441 (1975).
[19] G. Mendenhall, D. M. Golden, and S. W. Benson, *Int. J. Chem. Kinet.*, **7**, 725 (1975).
[20] L. Batt and R. T. Milne, *Int. J. Chem. Kinet.*, **8**, 59 (1976).
[21] H. A. Wiebe, A. Villa, T. M. Hillman, and J. Heicklen, *J. Am. Chem. Soc.*, **95**, 7 (1975).
[22] G. Baker and R. Shaw, *J. Chem. Soc. (London)*, 6965 (1965).
[23] J. R. Barker, S. W. Benson, and D. M. Golden, *Int. J. Chem. Kinet.*, **9**, 31 (1977).
[24] R. Simonaitis and J. Heicklen, *J. Phys. Chem.*, **78**, 2417 (1974).
[25] R. A. Cox and M. J. Roffey, *Environ. Sci. Technol.*, **11**, 382 (1977).
[26] K. L. Schere and K. L. Demerjian, "Calculation of Selected Photolytic Rate Constants over a Diurnal Range," Environmental Protection Agency Rep. EPA-600/4-77-015, 1977.
[27] H. E. O'Neal and C. Blumstein, *Int. J. Chem. Kinet.*, **5**, 397 (1973).
[28] M. C. Dodge, Workshop on Chemical Kinetic Data Needs for Modeling the Lower Troposphere, Environmental Protection Agency and National Bureau of Standards, Reston, VA, May 15–17, 1978.
[29] R. A. Perry, R. Atkinson, and J. N. Pitts, Jr., *J. Phys. Chem.*, **81**, 296 (1977).
[30] D. G. Hendry, Workshop on Chemical Kinetic Data Needs for Modeling the Lower Troposphere, Environmental Protection Agency and National Bureau of Standards, Reston, VA, May 15–17, 1978.
[31] D. G. Hendry and R. A. Kenley, *J. Am. Chem. Soc.*, **99**, 3198 (1977).
[32] K. R. Darnall, W. P. L. Carter, A. M. Winer, A. C. Lloyd, and J. N. Pitts, Jr., *J. Phys. Chem.*, **80**, 1948 (1976).
[33] J. N. Pitts, Jr., A. M. Winer, K. R. Darnall, G. J. Doyle, and J. M. McAffe, "Chemical Consequences of Air Quality Standards and of Control Implementation Programs: Roles of Hydrocarbons, Oxides of Nitrogen and Aged Smog in the Production of Photochemical Oxidant," California Air Resources Board, contract 4-214, Final Rep., 1976.
[34] A. M. Winer, personal communication, 1978.
[35] J. G. Calvert and R. D. McQuigg, *Int. J. Chem. Kinet.*, **S1**, 113 (1975).
[36] A. M. Winer, personal communication, 1978.
[37] M. C. Dodge, personal communication, 1979.
[38] C. J. Hochanadel, J. A. Ghormley, J. W. Boyle, and P. J. Ogren, *J. Phys. Chem.*, **81**, 3 (1977).

Received September 12, 1978
Revised May 25, 1979
Accepted June 5, 1979

10.7 Conclusions

Because of the complex nature of the planetary boundary layer an integral element of any air quality modeling study should be a formal assessment of the effects of uncertainties in the parameterization of the physical processes. In this chapter a variety of methods for performing such sensitivity analyses have been discussed. Particular attention was given to Fourier Amplitude Sensitivity Test (FAST). Unlike conventional methods the FAST procedure is ideally suited to the task of examining the global sensitivity of nonlinear mathematical models. The reason for this is that the technique allows arbitrarily large variations in either system parameters or input variables. This characteristic was exploited in two practical applications involving components of the atmospheric diffusion equation.

CHAPTER 11

EVALUATION OF MODEL PERFORMANCE

11.1 Introduction

Previous Chapters of this study described the formulation and testing of the individual components of the atmospheric diffusion equation. The most critical test however, is the ability of the system as a whole to satisfactorily describe the concentration dynamics occurring in an airshed. This Chapter presents an assessment of the model performance when applied to one urban region, the South Coast Air Basin of Southern California. The particular period to be studied, for which detailed emissions and meteorological information have been assembled, is 26-27 June 1974.

11.2 Performance Evaluation of the Airshed Model

There are three steps that need to be undertaken when evaluating the performance of a model: (1) A basic assessment of model validity; (2) comparison of predictions and observations for past events; and (3) analysis of the sensitivities of the predictions to uncertainties in model components.

Model validity refers to the essential correctness of the model in terms of its representation of the basic chemistry and physics as well as to its accuracy of numerical implementation as measured by adherence to certain necessary conditions such as conservation of mass.

Discrepancies in validity arise as a consequence of the need to employ simplifying assumptions during the mathematical formulation. As the model described in previous chapters was developed, each component, advection and turbulent diffusion, chemical kinetics, emissions and surface removal, was formulated taking into account the latest relevant data and information (Table 11.1). In each section of the report an attempt has been made to test individual model components in a manner that would assess the validity of the basic representation of the atmospheric physics and chemistry. Every effort has been made to include as much state-of-the-art information as possible, and, given the present generation of computing capabilities, the model represents the most valid practical one for an accurate description of urban air pollution.

Most emphasis in model performance evaluation has traditionally been given to step (2), comparison of predictions and observations for past events. Usually it is impossible to ascertain whether discrepancies between predictions and observations are due to errors in input data, such as emissions inventories, or in the representation of the basic physical and chemical processes. While it is imperative to separate the influences of these uncertainties, the practical problems associated with obtaining the necessary emissions and meteorological information virtually precludes a definitive assessment of the formal validity of a model using field data. Nevertheless, comparisons of predictions and observations for past events is probably the crucial component of the model evaluation. If the test conditions are to be

TABLE 11.1

Summary of Model Components, Their Input Data Requirements and Testing Procedures

MODEL COMPONENT	DETAILED ELEMENTS AND INPUT DATA	TESTING PROCEDURES (REFERENCES REPORTING DETAILED RESULTS)
Chemical Kinetics	Reaction mechanism Photolytic rate constants Thermochemical rate constants Hydrocarbon lumping procedures	The chemical mechanism was evaluated by comparing its predictions against data obtained from carefully controlled smog chamber studies. In addition, the mechanism was subjected to a detailed sensitivity analysis that examined the effects of uncertainties in rate constants and stoichiometric coefficients (Falls et al., 1979). The procedures for generating photolytic rate constants were tested against field measurements of NO_2 dissociation rates (McRae et al., (1982a).
Meteorology	Deposition velocities Mixing height Relative humidity Three-dimensional wind field Temperature Topography Turbulent diffusivities Solar insolation Surface roughness Ultraviolet flux	Much of the basic data used in the model is derived from sparse and discrete ground level observations. The objective analysis procedures that are used to interpolate the data were tested against analytic problems and observed concentration distributions of tracer gases (Goodin et al., 1979a,b, 1981; McRae et al., 1981 and McRae, 1981). Predicted turbulent mixing rates, under convective conditions, were compared against field experiments (McRae et al., 1981). Estimates of surface removal rates, derived from the deposition module, were compared against field and laboratory data.
Numerical Integration Procedures	Solution of advection-diffusion equation for chemically reactive flows Initial and boundary conditions	Problems with known solutions and properties similar to conditions encountered in the atmosphere were used to test the basic numerical technique. In addition, simplified numerical schemes were compared against more detailed approaches (McRae et al., 1982b). The computational procedures were tested for numerical stability, convergence, and mass conservation.

representative of those occuring in an actual airshed then it is important to recognize that the data collection requirements can involve an enormous expenditure of time and resources. Some of the needed information is summarized in Table 11.2. The present chapter is devoted, in large part, to an assessment of the application of the model in reproducing the important features of a two-day smog episode in the South Coast Air Basin (SCAB) of Southern California. This basin, in many respects, is the ideal one for evaluating the performance of an urban model since it has considerable variations in meteorology and emission flux densities and has the most persistently severe photochemical air pollution in the world.

One way to attempt to understand the causes of discrepancies between predictions and observations is to analyze the model to determine to what input parameters and variables the model is most sensitive. When combined with estimates of the levels of uncertainty associated with each input parameter and variable, this analysis, a so-called sensitivity analysis, will indicate how much of the overall uncertainty of the model output is associated with the individual uncertainty in each model input. Then the overall estimated uncertainty in the model predictions can be compared with the differences between predictions and observations in specific applications. Chapter 10, for example, presents the results from a sensitivity analysis of the kinetic mechanism. There have recently been several studies of the sensitivity of photochemical air quality models to input parameter variations or uncertainties (Falls et al., 1979; Dunker, 1980, 1981;

TABLE 11.2

Summary of Input Data Needed to Carry Out
A Model Performance Evaluation Study

BASIC INPUT	DETAILED COMPONENTS	RELEVANT CHAPTERS
Meteorology	Three dimensional wind field Mixing depth Topography and surface roughness Turbulent diffusion coefficients Solar insolation Ultraviolet radiation Temperature Relative humidity	3,4,6
Chemical Kinetics	Reaction mechanism Reaction rate constants Reaction stoichiometry Surface deposition velocities Hydrocarbon lumping procedure	6,8
Air Quality Data	Initial and boundary conditions Verification data	3
Emission Inventory	Mobile sources Stationary sources Area sources	7

Seigneur et al., 1981; Tilden and Seinfeld, 1982). These studies, although carried out on models somewhat different from that under analysis here, do indicate the variables to which large photochemical models are most sensitive. Rather than repeating these calculations in this chapter, relevant results from these earlier studies will be cited where appropriate. One aspect of the input uncertainty question did, however, appear to warrant consideration, that of assessing the accuracy of the emissions inventory. For this reason a new technique for evaluating the influence of errors in individual source categories on the overall inventory is presented.

11.3 Definition of the Region of Interest

The SCAB boundaries are shown in Figure 11.1. The grid system origin can be defined accurately on the Universal Transverse Merator (UTM) system. For the present study the origin is located in UTM zone 11 at E 560 km and N 3680 km. The region extends 400 km in a westerly (x) direction and 160 km north (y). The lower right hand corner was chosen for the origin because of the UTM zone change 60 km inside the western border of the modeling region. For the purposes of locating sources, the region has been further subdivided into 5x5 km cells. Once the grid system has been established then it is possible to process much of the model input data. for example, Figure 11.2 is a perspective view of the topography of the South Coast Air Basin. This information is needed for the wind field generation procedures. Extensive use was made of these three-dimensional displays to check data consistency and orientation.

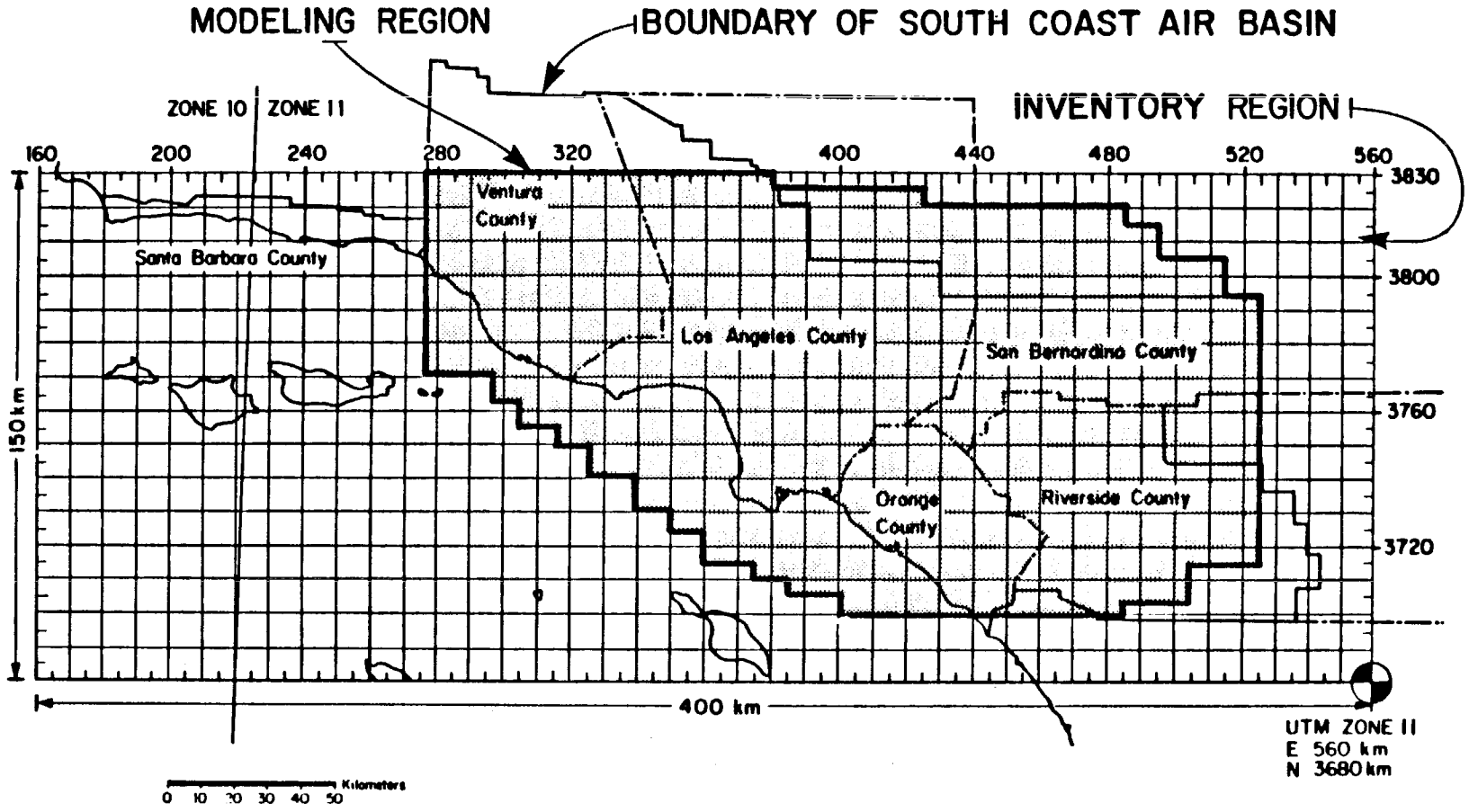

FIGURE 11.1

Definition of Computational Grid System Over the South Coast Air Basin
The shaded portion corresponds to the area used
in the model performance evaluation.

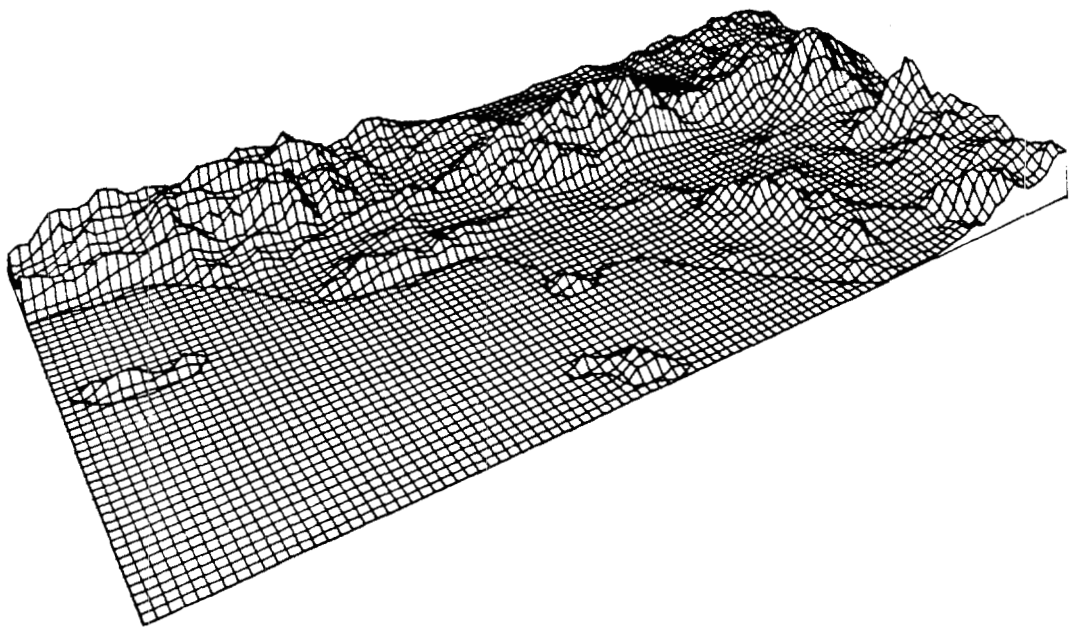

FIGURE 11.2

Perspective View of the Topography of the
South Coast Air Basin. (Vertical Scale 1:10)

11.4 The Episode of 26-28 June 1974 in the South Coast Air Basin

During the week of 26-28 June 1974, a severe air pollution episode was experienced in the South Coast Air Basin of California (CARB, 1974a). Hourly averaged ozone concentrations reached 0.50 ppm in the Upland-Fontana area, and values above 0.35 ppm were reported at 10 other stations. During the period 23-28 June, 1974 wind speeds were considerably lower than normal. (Radiosonde data from Pt. Mugu indicated that the wind speeds averaged about 1.6 m s^{-1} between the surface and 750 mb height; the normal June averaged is about 4.2 m s^{-1}.) At El Monte, the maximum depth of the mixed layer was approximately 750 m on each of the days 26-27 June. This value is unseasonably low. Temperatures between the 300 and 900 m levels reached 30°C during 27 and 28 June, while the surface temperatures dropped as low as 15°C during the night. The intense nocturnal inversion was caused partly by subsidence and partly by radiation from the surface since the dry air aloft kept the sky cloudless (CARB, 1974b). In summary, the low wind speeds, high temperatures and low inversion base produced conditions conducive to the accumulation of precursor emissions, and in turn, to the production of high ozone levels. These high ozone levels provide a stringent test of the ability of the model to reproduce extreme events. Another important reason for choosing the 1974 period was that detailed emissions inventories, commissioned by the State of California Air Resources Board, were available for that year.

11.5 Meteorological Fields Needed for Model Evaluation

The basic meteorological inputs to the atmospheric diffusion equation are shown in Table 11.2. Two of the dominant processes that influence pollutant dispersion over the airshed are advective transport and turbulent mixing. In the model they are characterized by the velocity field, the height of the mixed layer, the surface aerodynamic roughness, solar insolation and vertical temperature structure. These fields were generated, for the period June 26-28, 1974 using the procedures described in Chapters 3 and 4. Figure 11.3 shows a typical surface wind field distribution and Figure 11.4 the spatial variation of the mixing height over the airshed. The basic meteorological input data needed for the model were derived primarily from the South Coast Air Quality Management District (SCAQMD) monitoring stations (APCD, 1974).

11.6 Emissions Inventory for South Coast Air Basin

The most important input to any airshed model is a comprehensive detailed and accurate emission inventory, constructed at a level of detail consistent with the required spatial, temporal and chemical resolution of the model. In this study emissions from 130 different source categories were spatially distributed over the region shown in Figure 11.1. A summary of the daily totals and the distribution between mobile and stationary source classes is shown in Table 11.3, a more detailed breakdown is presented in Table 11.4. Diurnal variations in emission rates were resolved to within one hour in order that the

(a)

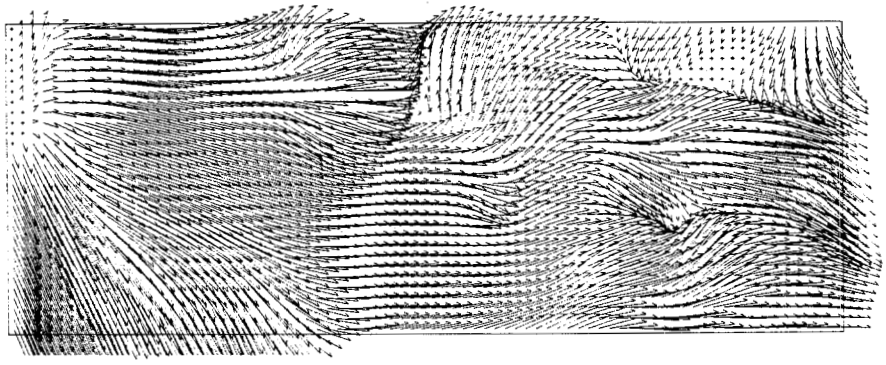

(b)

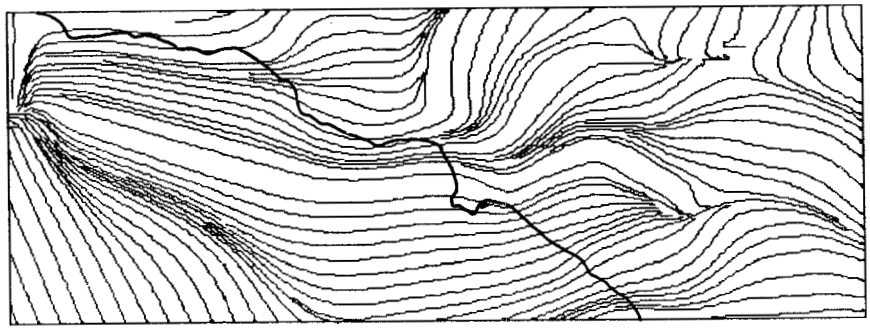

(c)

FIGURE 11.3

Typical Surface Wind Field Distribution for 27 June 1974
(a) Direction and Magnitudes at Monitoring Sites
(b) Generated Ground Level Flow Field
(c) Streamlines for Generated Flow Field

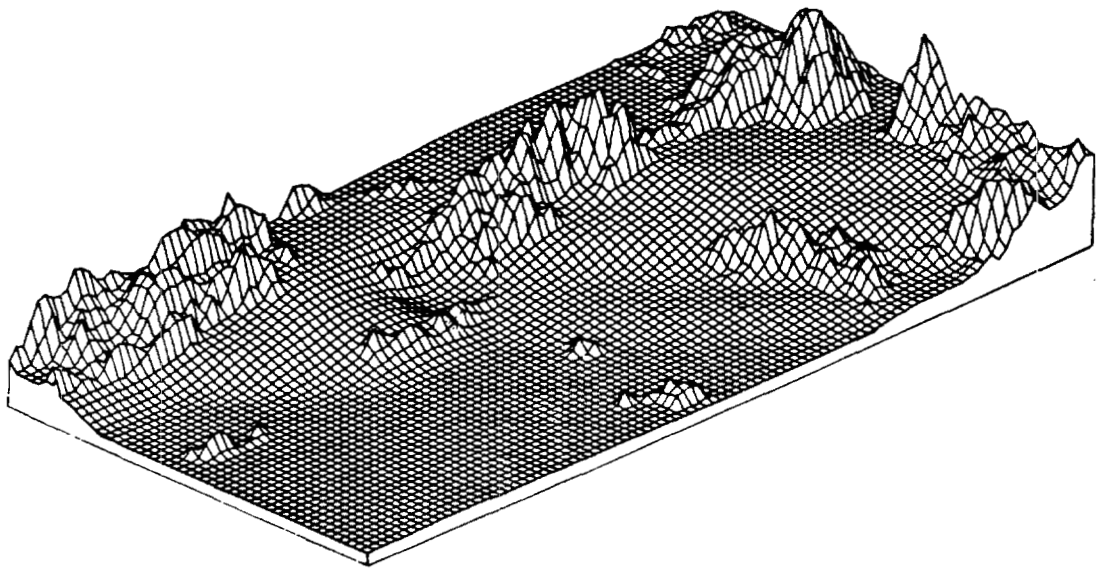

FIGURE 11.4

Mixing Height Distribution Above Sea Level
(16:00 PST 26 June 1974)

TABLE 11.3

Summary of Total Emissions Into South Coast Air Basin*

SPECIES	TOTAL EMISSIONS (Kg/day)	SOURCE CLASS CONTRIBUTION (%) MOBILE	STATIONARY
Carbon Monoxide (CO)	8,610,000	98.8	1.2
Nitrogen Oxides (NO_x)	1,320,000	62.3	37.7
Sulfur Oxides (SO_x)	427,000	13.7	86.3
Reactive Hydrocarbons (RHC)	1,240,000	71.0	29.0

*June 26, 1974

TABLE 11.4

Emissions Inventory for South Coast Air Basin

CATEGORY OF EMISSIONS (CES)	CES NUMBER	EMISSIONS (kg/day) CO	NO_x	TOTAL HYDROCARBONS	REACTIVE HYDROCARBONS
Emission	1	89	497	5,692	3,688
Transportation	130	0	0	0	0
Motor Vehicle	2	7,991,884	704,064	871,864	810,833
Catalyst Gasoline Exhaust	14	0	0	0	0
Non Catalyst Gasoline Exhaust	29	0	0	0	0
Gasoline Evap. Loss Carb	23	0	0	0	0
Gasoline Evap. Fuel Tank	122	0	0	52,461	52,461
Gasoline Crankcase	21	0	0	0	0
Diesel Exhaust	34	0	0	0	0
Diesel Evaporative	37	0	0	0	0
Motorcycle Exhaust	123	0	0	0	0
Subtotals		7,991,973	704,561	930,016	866,982
Off Road Motor Vehicle	38	265,643	7,103	19,204	16,861
Industrial	58	0	0	0	0
Construction	59	11,215	48,859	3,619	3,515
Recreational	60	0	0	0	0
Farm	61	0	0	0	0
Subtotals		276,858	55,962	22,822	20,376
Shipping	3	0	0	0	0
Purging	30	0	0	0	0
Off Loading	33	0	0	0	0
Ballasting	28	0	0	814	731
Transit	39	0	0	0	0
Boilers Non Tankers	119	790	7,144	605	376
Boilers Tankers	120	293	2,760	199	124
Pleasure Craft	121	3,777	1,682	844	760
Subtotals		4,859	11,568	2,462	1,991

TABLE 11.4 (continued)

CATEGORY OF EMISSIONS (CES)	CES NUMBER	EMISSIONS (kg/day) CO	NO_x	TOTAL HYDROCARBONS	REACTIVE HYDROCARBONS
Railroad	4	9,637	28,094	7,029	6,827
Subtotals		9,637	28,094	7,029	6,827
Aircraft	8	0	0	0	0
Jet Exhaust	20	92,310	22,387	43,404	43,300
Jet Fuel Evaporation	63	0	0	0	0
Piston Exhaust	19	125,107	493	8,373	7,574
Piston Fuel Evaporation	129	0	0	0	0
Rocket	50	0	0	0	0
Subtotals		217,417	22,880	51,777	50,873
Stationary	65	0	0	0	0
Petroleum	6	0	0	0	0
Production	13	0	0	0	0
Ext. Combustion Boilers	78	19	2,431	102	54
Int. Combustion Engines	83	3,371	19,228	2,190	370
Industrial Processes	87	2,283	33,271	42,819	27,370
Seeps	118	0	0	9,947	8,057
Crude Oil Evap. Fixed Roof	88	3,216	12	37,487	35,148
Crude Oil Evap. Floating Roof	89	0	0	14	14
Refining	12	0	0	0	0
Ext. Combustion Boilers	77	0	0	0	0
Boilers Residual Oil	73	22	982	41	25
Boilers Distillate Oil	74	110	15,089	1,541	958
Boilers Natural Gas	75	598	9,367	1,283	564
Boilers Process Gas	76	91	7,982	432	399
Internal Combustion Engines	84	3,334	20,616	3,023	725
Industrial Processes	90	923	59,168	13,146	11,479
Storage Evap.	91	0	0	5,974	3,870
Crude Oil Evap. Fixed Roof	93	0	0	4,694	4,281

TABLE 11.4 (continued)

CATEGORY OF EMISSIONS (CES)	CES NUMBER	EMISSIONS (kg/day) CO	NO_x	TOTAL HYDROCARBONS	REACTIVE HYDROCARBONS
Crude Oil Evap. Float Rm	95	0	0	6,955	6,343
Gasoline Evap. Fixed Roof	92	0	0	1,673	1,673
Gasoline Evap. Float Roof	94	0	0	28,039	28,039
Marketing	10	0	213	81,877	13,403
Storage Evap.	100	0	0	4,569	3,100
Crude Oil Evap. Fixed Roof	97	0	0	1,495	1,456
Crude Oil Evap. Float Roof	99	0	0	984	958
Gasoline Evap. Fixed Roof	96	0	0	126	126
Gasoline Evap. Float Roof	98	0	0	3,218	3,218
Loading and Unloading	103	0	0	1,230	830
Gasoline Evap.	101	0	0	6,031	6.031
Crude Oil	102	26	190	3,092	2,777
Underground Storage at Sta.	40	0	0	32,102	32,105
Vehicle Refueling at Sta.	45	0	0	0	0
Subtotals		13,993	168,550	294,085	193,375
Commercial and Institutional	7	0	103	444	257
Internal Combustion Engines	82	1,034	7,498	1,173	1,000
Ext. Comb. Boilers & Space Heat	124	0	89	0	0
Residual Oil	125	88	1,471	44	8
Distillate Oil	126	91	12,544	439	226
Natural Gas	127	94	7,259	178	78
Process Gas	128	36	0	0	0
Printing	113	0	7	417	235
Flexigraphic	112	0	0	6,202	0
Gravure	114	0	0	14,536	11,607
Surface Coating Air Dried Achit.	16	0	0	0	0
Oil Base Incl. Solvent	110	0	0	73,562	39,356
Water Base	111	0	0	10,513	5,625
Dry Cleaning	22	0	0	0	0
Petroleum Base Perchlorethylene	46	0	142	3,668	0
Synthetic	43	0	2	3,112	2,260
Degreasing	11	0	0	186	0
Halogenated	42	2	26	4,912	0
Non-Halogenated	47	0	0	14,090	14,090
Subtotals		1,344	29,141	133,476	74,741

TABLE 11.4 (continued)

CATEGORY OF EMISSIONS (CES)	CES NUMBER	EMISSIONS (kg/day) CO	NO_x	TOTAL HYDROCARBONS	REACTIVE HYDROCARBONS
Industrial	5	1,831	9,049	4,159	1,277
Internal Combustion Engines	81	2,006	13,308	0	493
External Comb. Boilers & Heaters	49	0	0	0	0
Residual Oil	69	286	1,060	21	4
Distillate Oil	70	157	26,861	566	352
Natural Gas	71	380	14,597	458	202
Process Gas	72	4,310	1,416	703	650
Chemical	15	0	17	2,722	1,484
Metallurgical	35	0	0	0	0
Primary Metals	85	54,232	15,713	10,325	4,337
Secondary Metals	86	1,662	5,291	2,750	1,741
Mineral	31	11,728	33,043	1,174	432
Wood Processing	25	0	0	0	0
Elec. Generation Boiler	18	0	0	0	0
Residual Oil	56	7,236	121,409	6,513	4,051
Distillate Oil	67	36	326	36	19
Natural Gas	55	2,506	47,307	1,438	633
Process Gas	68	0	0	0	0
Coal	57	0	0	0	0
Elec. Generation Inter. Comb.	79	677	7,134	549	468
Surface Coating	44	2	6	440	147
Heat Treated	48	303	396	6,432	2,155
Air Dried	41	0	0	0	0
Paint	80	0	349	10,348	7,706
Varnish and Shellac	104	0	72	6,904	197
Lacquer	105	17	183	15,371	3,949
Enamel	106	0	137	13,941	8,984
Primer	107	0	1	1,686	948
Solvent	108	0	0	10,901	4,105
Adhesives	109	26	7	7,887	5,331
Incineration	51	23	127	172	17
Land Fills	117	0	0	846,090	8,461
Subtotals		87,408	297,808	953,594	58,142

TABLE 11.4 (continued)

CATEGORY OF EMISSIONS (CES)	CES NUMBER	EMISSIONS (kg/day) CO	NO_x	TOTAL HYDROCARBONS	REACTIVE HYDROCARBONS
Agricultural	9	0	0	0	0
Agricultural Control Burn	17	0	0	0	0
Vegetative Forest and Citrus	115	0	0	884,026	0
Animal Wastes	116	0	0	65,715	13,143
Pesticides	24	0	0	3,629	3,266
Food Processing	32	30	895	2,467	186
Orchard Heating	36	0	0	0	0
Waste Burning or Wildfires	27	0	0	0	0
Wine Processing	66	0	0	0	0
Subtotals		30	895	955,837	16,595
Domestic	54	0	0	0	0
Solvent Use	26	0	0	27,491	2,859
Utility Equipment 2 stroke	53	0	0	0	0
Utility Equipment 4 stroke	52	0	0	0	0
Fuel Combustion	62	5	1,214	998	0
Structural Fires	64	0	0	0	0
Subtotals		5	1,214	28,490	2,859
TOTALS		8,603,526	1,320,691	3,379,587	1,292,760

model predictions would be compatible with the averaging time used in making ambient air quality measurements. The spatial and temporal variations of pollutant emissions are shown in Figures 11.5-11.7. To avoid any ambiguity, all data times for input of information to the airshed model were defined in terms of the standard time (PST) of the region. For the South Coast Air Basin the standard time corresponds to time zone eight (8) which covers the longitudinal range 105-120°W. Table 11.5 gives the estimated 1974 composition of reactive hydrocarbon emissions in the SCAB grouped according to the chemical lumping scheme introduced in Chapter 8. The detailed hydrocarbon inventory is documented in Table 11.6. These results were derived from detailed composition profiles developed for each source category. For further details of the emission inventory the reader is referred to AQMP (1978).

11.7 Assessment of the Accuracy of the Emissions Inventory

In order to become confident in making decisions based on an inventory, it is not sufficient merely to assemble the basic data. What is required is a quantitative evaluation of the likely errors.

The development of emissions data for a large urban area is an extremely complex undertaking and involves considerable resource commitments. From a practical point of view many simplifications and approximations must be invoked during the compilation of a spatially, chemically and temporally resolved inventory. The assessment of the level of uncertainty in a particular emission inventory is obviously a

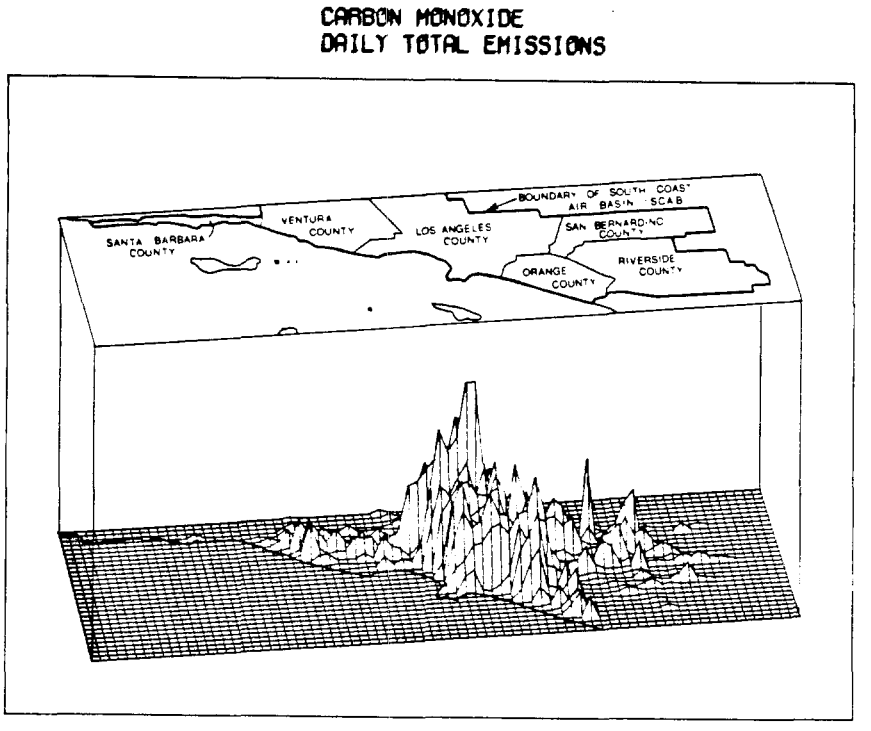

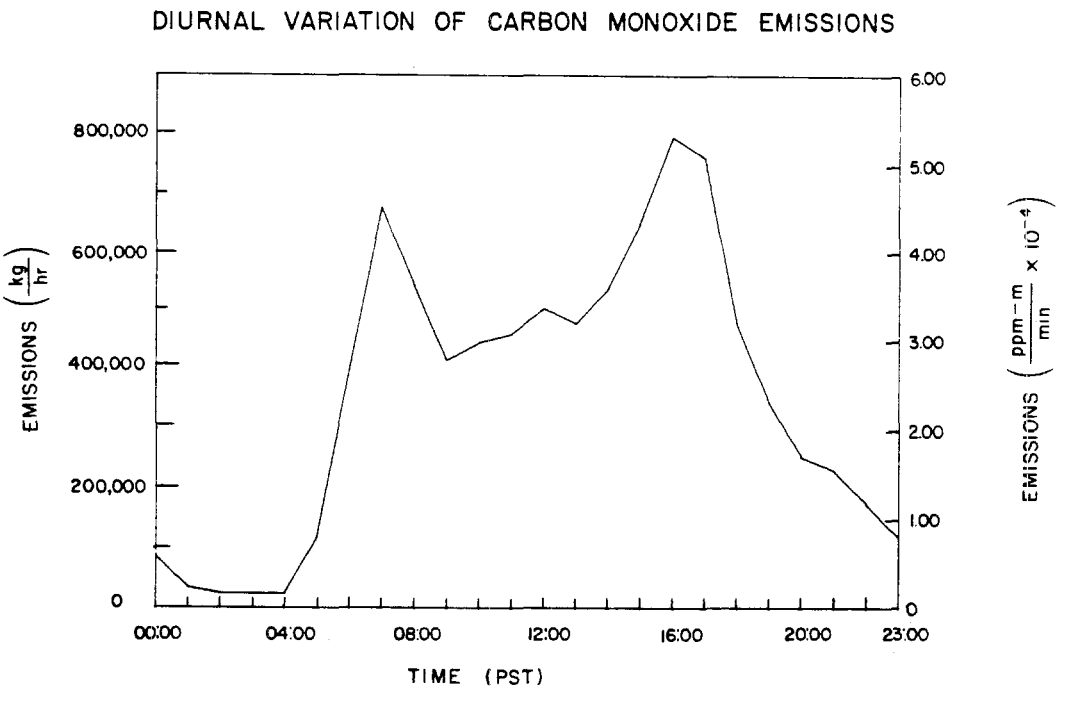

FIGURE 11.5

Spatial and Diurnal Variations in Carbon Monoxide (CO) Emissions

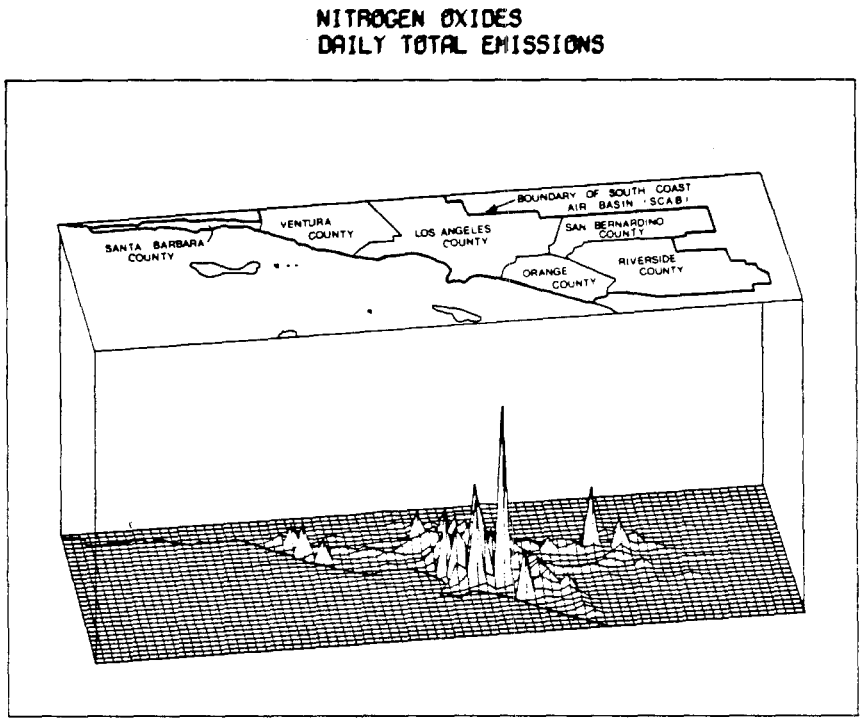

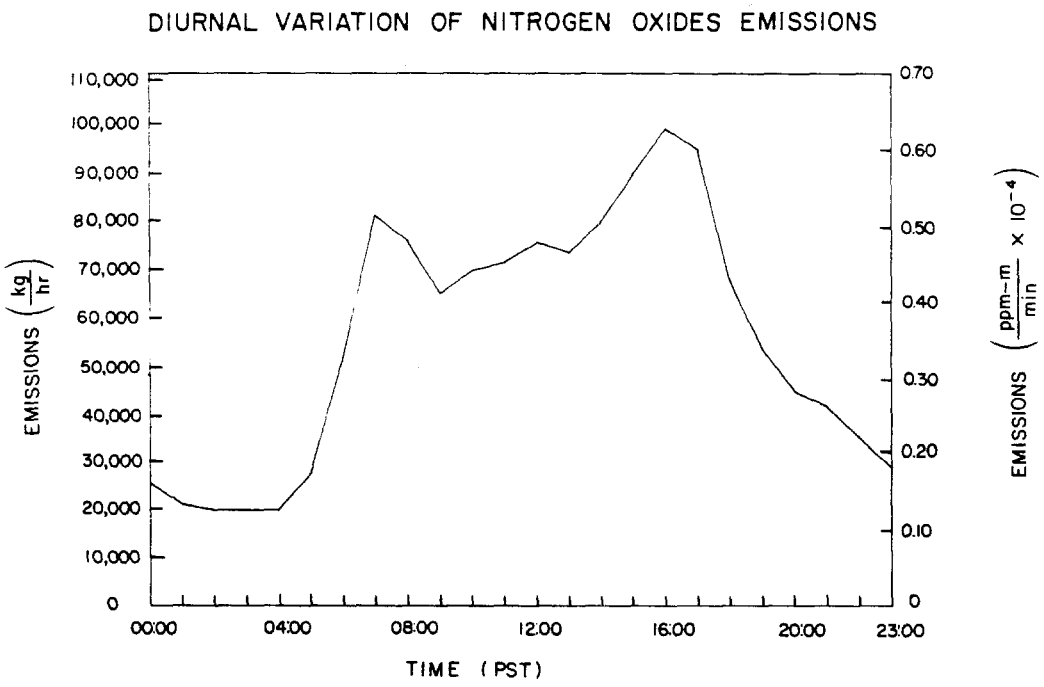

FIGURE 11.6

Spatial and Diurnal Variations in Nitrogen Oxides (NO_x) Emissions

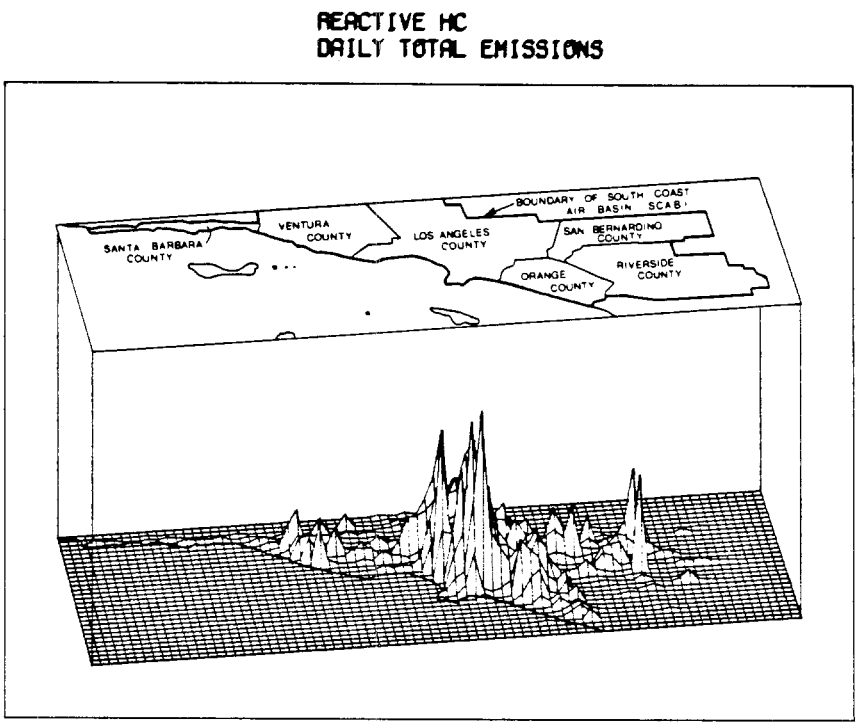

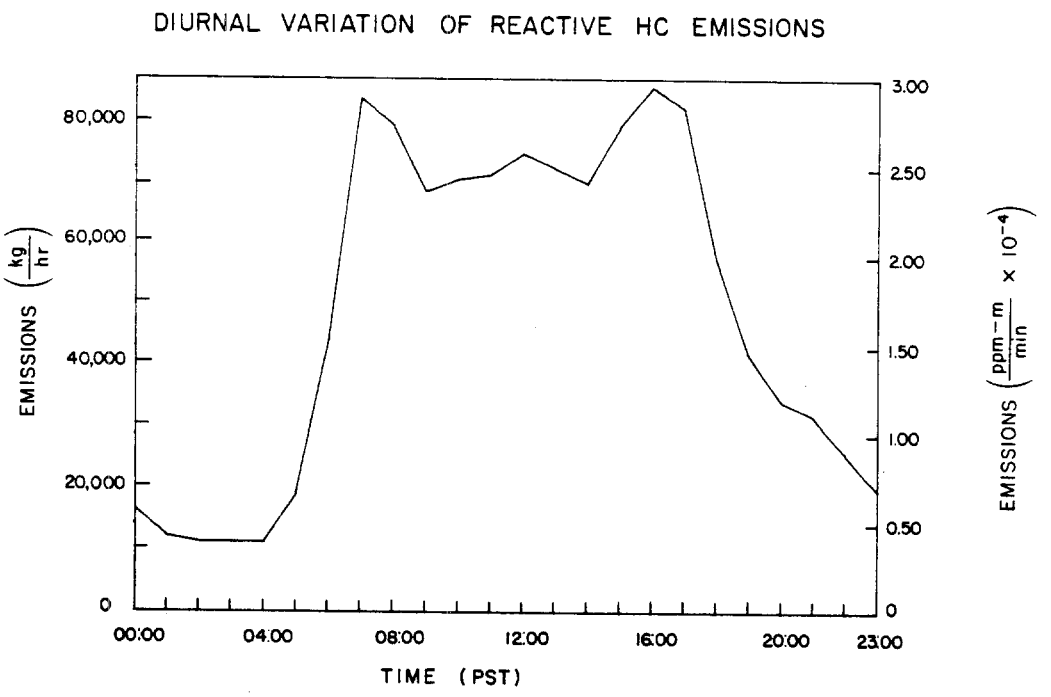

FIGURE 11.7

Spatial and Diurnal Variations in Reactive hydrocarbon (RHC) Emissions

TABLE 11.5

Composition of Reactive Hydrocarbons in Inventory Region

SPECIES	EMISSIONS kg s^{-1}	COMPOSITION(%) WEIGHT	MOLE	MOLE WEIGHTED MOLECULAR WEIGHT	AVERAGE CARBON NUMBER
Formaldehyde (HCHO)	0.18	1.25	2.88	30.0	1.00
Other Aldehydes (RCHO)	0.25	1.74	2.22	63.1	3.36
Ethylene (C_2H_4)	0.82	5.73	13.4	28.0	2.00
Other Olefins (OLE)	1.98	13.8	14.2	67.4	4.83
Aromatics (ARO)	2.03	14.2	9.4	100.2	7.56
Alkanes (ALK)	9.04	63.3	57.9	83.5	5.82
TOTALS	14.30	100.0	100.0		

TABLE 11.6

Reactive Hydrocarbon Emissions for the South Coast Air Basin

CATEGORY OF EMISSIONS (CES)	CES NUMBER	REACTIVE HYDROCARBONS (kg/day) FORMALDEHYDE	OTHER ALDEHYDES	AROMATICS	ETHYLENE	OLEFINS	ALKANES
Emission	1	0	0	0	2,100	438	1,150
Transportation	130	0	0	0	0	0	0
Motor Vehicle	2	22,668	15,693	212,735	91,546	150,832	317,358
Catalyst Gasoline Exhaust	14	0	0	0	0	0	0
Non Catalyst Gasoline Exhaust	29	0	0	0	0	0	0
Gasoline Evap. Loss Carb	23	0	0	0	0	0	0
Gasoline Evap. Fuel Tank	122	0	0	7,607	0	7,659	37,195
Gasoline Crankcase	21	0	0	0	0	0	0
Diesel Exhaust	34	0	0	0	0	0	0
Diesel Evaporative	37	0	0	0	0	0	0
Motorcycle Exhaust	123	0	0	0	0	0	0
Subtotals		22,668	15,694	220,341	93,646	158,930	355,703
Off Road Motor Vehicle	38	595	403	4,263	2,362	3,399	5,838
Industrial	58	0	0	0	0	0	0
Construction	59	186	536	431	223	231	1,908
Recreational	60	0	0	0	0	0	0
Farm	61	0	0	0	0	0	0
Subtotals		782	939	4,694	2,585	3,630	7,746
Shipping	3	0	0	0	0	0	0
Purging	30	0	0	0	0	0	0
Off Loading	33	0	0	0	0	0	0
Ballasting	28	0	0	0	0	0	731
Transit	39	0	0	0	0	0	0
Boilers Non-Tankers	119	1	0	24	65	24	262
Boilers Tankers	120	0	0	8	21	8	86
Pleasure Craft	121	0	0	211	40	149	360
Subtotals		1	0	243	126	181	1,440

TABLE 11.6 (continued)

CATEGORY OF EMISSIONS (CES)	CES NUMBER	REACTIVE HYDROCARBONS (kg/day) FORMALDEHYDE	OTHER ALDEHYDES	AROMATICS	ETHYLENE	OLEFINS	ALKANES
Railroad	4	362	1,040	836	432	449	3,706
Subtotals		362	1,040	836	432	449	3,706
Aircraft	8	0	0	0	0	0	0
Jet Exhaust	20	0	4,926	18,099	0	8,624	11,650
Jet Fuel Evaporation	63	0	0	0	0	0	0
Piston Exhaust	19	571	1,130	2,003	0	0	3,870
Piston Fuel Evaporation	129	0	0	0	0	0	0
Rocket	50	0	0	0	0	0	0
Subtotals		571	6,056	20,102	0	8,624	15,520
Stationary	65	0	0	0	0	0	0
Petroleum	6	0	0	0	0	0	0
Production	13	0	0	0	0	0	0
Ext. Comb. Boilers	78	15	0	5	0	0	34
Int. Comb. Engines	83	0	0	0	160	11	199
Industrial Processes	87	0	0	5,117	3,250	0	19,003
Seeps	118	0	0	0	0	0	8,057
Crude Oil Evap. Fixed Roof	88	0	0	41	0	0	35,107
Crude Oil Evap. Floating Roof	89	0	0	0	1	0	13
Refining	12	0	0	0	0	0	0
Ext. Combustion Boilers	77	0	0	0	0	0	0
Boilers Residual Oil	73	0	0	2	4	2	18
Boilers Distillate Oil	74	2	0	62	165	62	669
Boilers Natural Gas	75	103	0	77	0	0	385
Boilers Process Gas	76	33	0	0	0	76	291
Internal Combustion Engines	84	30	0	0	30	0	665
Industrial Processes	90	1,484	0	51	17	1,572	8,354
Storage Evap.	91	3	0	725	1	14	3,127
Crude Oil Evap. Fixed Roof	93	0	0	178	127	0	3,976
Crude Oil Evap. Floating Roof	95	0	0	264	188	0	5,891
Gasoline Evap. Fixed Roof	92	0	0	243	0	244	1,186
Gasoline Evap. Floating Roof	94	0	0	4,066	0	4,094	19,880

TABLE 11.6 (continued)

CATEGORY OF EMISSIONS (CES)	CES NUMBER	REACTIVE HYDROCARBONS (kg/day) FORMALDEHYDE	OTHER ALDEHYDES	AROMATICS	ETHYLENE	OLEFINS	ALKANES
Marketing	10	24	0	16	25	0	13,338
Storage Evap.	100	6	0	361	4	10	2,719
Crude Oil Evap. Fixed Roof	97	0	0	0	0	0	1,456
Crude Oil Evap. Floating Roof	99	0	0	0	0	0	958
Gasoline Evap. Fixed Roof	96	0	0	18	0	18	89
Gasoline Evap. Floating Roof	98	0	0	467	0	470	2,282
Loading and Unloading	103	0	0	57	0	0	773
Gasoline Evap.	101	0	0	344	0	483	5,205
Crude Oil	102	0	0	0	111	0	2,665
Underground Storage at Sta.	40	0	0	2,520	0	2,472	27,113
Vehicle Refueling at Sta.	45	0	0	0	0	0	0
Subtotals		1,700	0	14,613	4,083	9,526	163,453
Commercial and Institutional	7	0	0	144	0	0	113
Internal Combustion Engines	82	41	122	52	144	54	587
Ext. Comb. Boilers & Space Heat	124	0	0	0	0	0	0
Residual Oil	125	0	0	0	0	0	8
Distillate Oil	126	1	0	0	0	0	225
Natural Gas	127	14	0	11	0	0	53
Process Gas	128	0	0	0	0	0	0
Printing	113	38	0	0	5	104	87
Flexigraphic	112	0	0	0	0	0	0
Gravure	114	0	0	5,774	0	0	5,833
Surface Coating Air Dried Achit.	16	0	0	0	0	0	0
Oil Base Incl. Solvent	110	0	0	8,901	0	0	30,455
Water Base	111	0	0	1,272	0	0	4,352
Dry Cleaning	22	0	0	0	0	0	0
Petroleum Base Perchlorethylene	46	0	0	0	0	0	0
Synthetic	43	0	0	0	0	0	2,260
Degreasing	11	0	0	0	0	0	0
Halogenated	42	0	0	0	0	0	0
Non Halogenated	47	0	0	0	0	0	14,090
Subtotals		94	122	16,154	149	158	58,064

TABLE 11.6 (continued)

CATEGORY OF EMISSIONS (CES)	CES NUMBER	REACTIVE HYDROCARBONS (kg/day) FORMALDEHYDE	OTHER ALDEHYDES	AROMATICS	ETHYLENE	OLEFINS	ALKANES
Industrial	5	389	0	79	0	393	415
Internal Combustion Engines	81	36	0	0	20	0	437
External Comb. Boilers & Heaters	49	0	0	0	0	0	0
Residual Oil	69	0	0	0	0	0	4
Distillate Oil	70	0	0	23	61	23	246
Natural Gas	71	37	0	28	0	0	137
Process Gas	72	53	0	0	0	123	473
Chemical	15	13	12	524	166	202	567
Metallurgical	35	0	0	0	0	0	0
Primary Metals	85	6	0	1,397	1,859	281	794
Secondary Metals	86	494	0	73	0	0	1,173
Mineral	31	5	0	47	18	41	321
Wood Processing	25	0	0	0	0	0	0
Elec. Generation Boiler	18	0	0	0	0	0	0
Residual Oil	56	7	0	261	697	261	2,827
Distillate Oil	67	0	0	0	0	0	18
Natural Gas	55	115	0	86	0	0	431
Process Gas	68	0	0	0	0	0	0
Coal	57	0	0	0	0	0	0
Elec. Generation Inter. Comb.	79	19	57	24	68	25	275
Surface Coating	44	0	0	0	9	0	139
Heat Treated	48	0	0	0	128	0	2,026
Air Dried	41	0	0	0	0	0	0
Paint	80	0	0	7,275	0	0	430
Varnish and Shellac	104	0	0	188	0	0	9
Lacquer	105	0	0	1,911	0	0	2,038
Enamel	106	0	0	1,646	0	0	7,337
Primer	107	0	0	539	0	0	408
Solvent	108	0	0	2,276	0	0	1,829
Adhesives	109	0	0	4,337	0	0	994
Incineration	51	0	0	3	3	5	7
Land Fills	117	0	0	1,692	0	0	6,769
Subtotals		1,175	69	22,410	3,028	1,354	30,106

TABLE 11.6 (continued)

CATEGORY OF EMISSIONS (CES)	CES NUMBER	REACTIVE HYDROCARBONS (kg/day) FORMALDEHYDE	OTHER ALDEHYDES	AROMATICS	ETHYLENE	OLEFINS	ALKANES
Agricultural	9	0	0	0	0	0	0
Agricultural Control Burn	17	0	0	0	0	0	0
Vegetative Forest and Citrus	115	0	0	0	0	0	0
Animal Wastes	116	0	0	0	0	0	13,143
Pesticides	24	0	0	1,172	0	0	2,094
Food Processing	32	3	0	2	34	52	95
Orchard Heating	36	0	0	0	0	0	0
Waste Burning or Wildfires	27	0	0	0	0	0	0
Wine Processing	66	0	0	0	0	0	0
Subtotals		3	0	1,174	34	52	15,332
Domestic	54	0	0	0	0	0	0
Solvent Use	26	165	0	1,237	0	0	1,457
Utility Equipment 2 Stroke	53	0	0	0	0	0	0
Utility Equipment 4 Stroke	52	0	0	0	0	0	0
Fuel Combustion	62	0	0	0	0	0	0
Structural Fires	64	0	0	0	0	0	0
Subtotals		165	0	1,237	0	0	1,457
TOTALS		27,522	23,919	301,805	104,083	182,904	652,526

substantial undertaking and, most properly, should be carried out when the inventory itself is compiled. The objective of this section is to present a methodology for assessing the accuracy of existing emission inventories given estimates of errors in individual source categories. The procedure uses chemically weighted sensitivity analysis methods that distribute both percentage and physical errors in accordance to their total contribution to photochemical oxidant production. By applying the techniques to the present inventory, those sources contributing most to the uncertainty in total emissions can be identified. This information can then be used to help design field and source test programs that will provide improved data bases for control strategy development.

Emissions from each source class can be characterized according to level of spatial resolution, level of temporal resolution, and source activity or emission factor. The level of spatial resolution achievable is in principle as fine as one desires since the locations of all sources can presumably be specified (although traffic count data may not be available on a street-by-street basis). Temporal emission rates will fluctuate some from day to day and the output from some stationary sources may vary with ambient temperature. Even with these variations the major problem in properly specifying source emissions is still the uncertainty in emissions quantities derived from source activities and emission factors. Goklany (1980) presents a detailed discussion of emission inventory errors and suggests various engineering checks that

can be made to insure that the basic data are reliable, accurate and self consistent.

Two basic factors are involved in emission specification, the quantity emitted and its composition. Emission compositions are typically estimated from engineering or source tests. Recent studies aimed at establishing NO_x and SO_x emission inventories for stationary sources in the South Coast Air Basin have presented estimates of the level of accuracy of the overall inventories (Bartz et al., 1974). These reports estimate that a $\pm$20% uncertainty in the total emissions is reasonable, whereas, uncertainties in individual source emissions can range as high as $\pm$300%. A compensating factor is that generally the large uncertainties are associated with small absolute emission levels. Probably the most serious emission inventory problems are those associated with hydrocarbon emissions. Given the existence of uncertainties in the inventory, one must develop methodologies for identifying the major errors.

The basic goal of this analysis is to develop a procedure that will place error bounds on emissions of reactive hydrocarbons (RHC), nitrogen oxides (NO_x) and carbon monoxide (CO). With the exception of CO, these groupings represent the sum of many individual species. In order to generalize the methodology consider a chemical grouping, j, composed of emissions of n_j species. If there are m source classes in the emissions inventory then the total emissions from group j, E_T^j, is given by

$$E_T^j = \sum_{k=1}^{m} \sum_{i=1}^{n_j} w_i E_i^k \qquad (11.1)$$

where D_T^k is the emission of species i from source class k and w_i is a weighting factor that can be used to account for differences in chemical reactivity of the individual species. The choice of suitable forms for w_i is discussed subsequently. In (11.1), for example, $n_j = 1$ for CO and $n_j = 2$ for NO_x since $E_{NO_x} = E_{NO} + E_{NO_2}$. If the E_i^k are considered to be statistically independent then the variance of the total emissions, $(\sigma_T^j)^2$, for a linear model is simply the sum of the individual components $\sigma^2_{E_i}$ k (Feller, 1968)

$$(\sigma_T^j)^2 = \sum_{k=1}^{m} \sum_{i=1}^{n_j} w_i^2 \, (\sigma^2_{E_i^k})^2 \qquad (11.2)$$

In practice the standard deviation of the emissions from a particular source is normally expressed as some fraction f_i^k of the total, i.e. $\sigma_{E_i}^k = f_i^k E_i^k$. If a further assumption is made that each source class k contributes to the total error an amount proportional to the total emissions then the right hand side of (2) can be manipulated to give the fractional uncertainty f_T^j in emission group j as

$$f_T^j = \left\{ \sum_{k=1}^{m} \sum_{i=1}^{n_j} w_i^2 \left[f_i^k \frac{E_i^k}{E_T^j} \right]^2 \right\}^{1/2} \qquad (11.3)$$

One obvious conclusion that can be drawn from this analysis is that the fractional error in the total emissions is <u>less</u> than the sum of the

errors associated with the individual components. Ditto et al. (1976) present a similar analysis including a generalization that accounts for the case when one or more of the $\sigma_{E_i^k}$ are fixed.

In the above derivation the only assumption made about each of the E_i^k was that they were independent and so the uncertainty bounds on E_T^j are simply $E_T^j(1 \pm f_T^j)$. In developing the fractions f_j for each source type it is important to consider the types of errors that might be involved in calculating the emission data.

When error distributions deviate significantly from normality a theorem due to Chebyshev (Feller, 1968) can be used to estimate upper bounds on the confidence intervals. This theorem states that for a random variable E_T^j that has a mean $\bar{E}_T^j$, and standard derivation $(f_T^j \bar{E}_T^j)$, the probability that $|E_T^j - \bar{E}_T^j| > r(f_T^j \bar{E}_T^j)$ is less than $1/r^2$. Thus a $(1-s)$ x 100% confidence interval is given by $(\bar{E}_T^j (1 \pm rf_T^j))$ where $r(f_T^j) = 1/s$. An important feature of the theorem is that it is independent of the distribution of the random variable $\bar{E}_T^j$. While the inequality is true for any value of $r > 1$, the bounds are not sharp, and, as a result, the estimate of the confidence intervals is conservative.

One of the most important reasons for incorporating the weightings w_i in (11.1) is to account for differences in the chemical reactivity of individual species. The need for weighting can be illustrated by considering the emissions of methane from landfills. While there are typically very large uncertainties associated with estimating the mass fluxes, the contribution of methane to oxidant production within an

urban airshed is small. Unless the methane emissions are appropriately weighted, the uncertainties place unrealistically large error bounds on the hydrocarbon inventory. Given this situation it is clearly desirable to develop a weighting scheme that accounts for differences in chemical reactivity. From a practical view point there are two important considerations that any proposed scheme must satisfy. First it must be able to be applied in an a priori manner and secondly, the procedure should not require the numerical solution of kinetic rate equations. Primary attention in this section will be given to characterizing the weighting scheme for the reactive hydrocarbon grouping (RHC).

As might be expected there are many different ways to characterize the chemical reactivity of hydrocarbons including: organic consumption rate, peak oxidant levels, NO_2 formation rate and the time to the ozone peak (Dimitriades, 1974; Trijonis and Arledge, 1975; CARB, 1976; Darnall et al., 1976; and Bufalini et al., 1976). The scheme adopted here is to weight the emissions of individual hydrocarbon species on the basis of their rate of removal by reactions involving the hydroxyl radical (OH) (Darnall et al., 1976).

The normalized weighting factors in (11.1) for the hydrocarbon group are given by

$$w_i = \frac{\sum_{p=1}^{n_j} \frac{r_p k_p (OH)}{MW_p}}{\sum_{j=1}^{m} \sum_{p=1}^{n_j} \frac{r_p k_p (OH)}{MW_p}} \qquad (11.4)$$

where $k_p(OH)$ is the rate constant for the reaction HC_p + OH. MW_p is

the molecular weight of hydrocarbon species p and r_p is the weight fraction; together MW_p and r_p convert the emissions from a mass to a molar basis. The reactivity weights for some different source classes are shown in Table 11.7.

Now consider the 1974 SCAB emissions inventory, a summary version of which is shown in Figure 11.8. Estimates of source class errors derived from engineering analyses and personal interviews (Grisinger, 1981); Bradley, 1981) were used to derive the f fractions. The error in the total emissions were derived using equation (11.3). One of the most striking results from Table 11.7 is the difference between class rankings based on mass emissions and net chemical reactivity.

This section has introduced a technique for establishing overall uncertainty limits on the emissions for a region such as the South Coast Air Basin. For the particular case studied the calculations suggest the following ranges: CO $\pm$ 20%, NO_x $\pm$ 15%, Reactive Hydrocarbons $\pm$ 25% and Total Hydrocarbons $\pm$ 120%.

11.8 Initial and Boundary Conditions for Model Evaluation

The initial concentration field was established using the procedures described in Goodin et al. (1979a, 1981). Hourly averaged data from the monitoring sites (APCD, 1974) shown in Figure 11.9, were interpolated to the computational grid. Since most of these monitoring sites did not report ozone concentrations, but rather oxidant levels, the air quality data were converted to the form required by the model using: $[O_3] = [OX] - 0.2[NO_2] + [S_2]$ (Eldon and Trijonis, 1977). In

TABLE 11.7

Reactivity Weighted Inventory of Emissions from Major Hydrocarbon Source Categories in the South Coast Air Basin

RANK ON A REACTIVITY BASIS	CATEGORY OF EMISSIONS (CES)	CES NUMBER	TOTAL HYDROCARBON EMISSIONS (kg/day)	REACTIVE HYDROCARBON EMISSIONS (kg/day)	REACTIVITY WEIGHT	WEIGHTED EMISSIONS	RANK ON MASS BASIS
1	Motor Vehicle	2	871,864	810,833	0.03464	30,203	1
2	Jet Exhaust	20	43,404	43,300	0.07426	3,223	7
3	Gasoline Evap. (Fuel Tank)	122	52,461	52,461	0.02845	1,492	6
4	Gasoline Evap. (Floating Roof)	94	28,039	28,039	0.02845	798	11
5	Off Road Motor Vehicle	38	19,204	16,861	0.03563	684	13
6	Underground Storage at Stations	40	32,102	32,105	0.01632	524	10
7	Oil Base Including Solvent	110	73,562	39,356	0.00582	428	4
8	Industrial Processes (Pet. Refining)	87	42,819	27,370	0.00811	347	8
9	Industrial Processes (Pet. Refining)	90	13,146	11,479	0.02103	276	18
10	Crude Oil Evap. (Fixed Roof)	88	37,487	35,148	0.00696	261	9
11	Railroad	4	7,029	6,827	0.03127	220	26
12	Piston Exhaust	19	8,373	7,574	0.02199	184	24
13	Land Fills	117	846,090	8,461	0.00018	149	2
	TOTALS (% Contribution to the total SCAB emission Inventory)		2,075,580 (61%)	1,119,814 (87%)		38,789 (95%)	

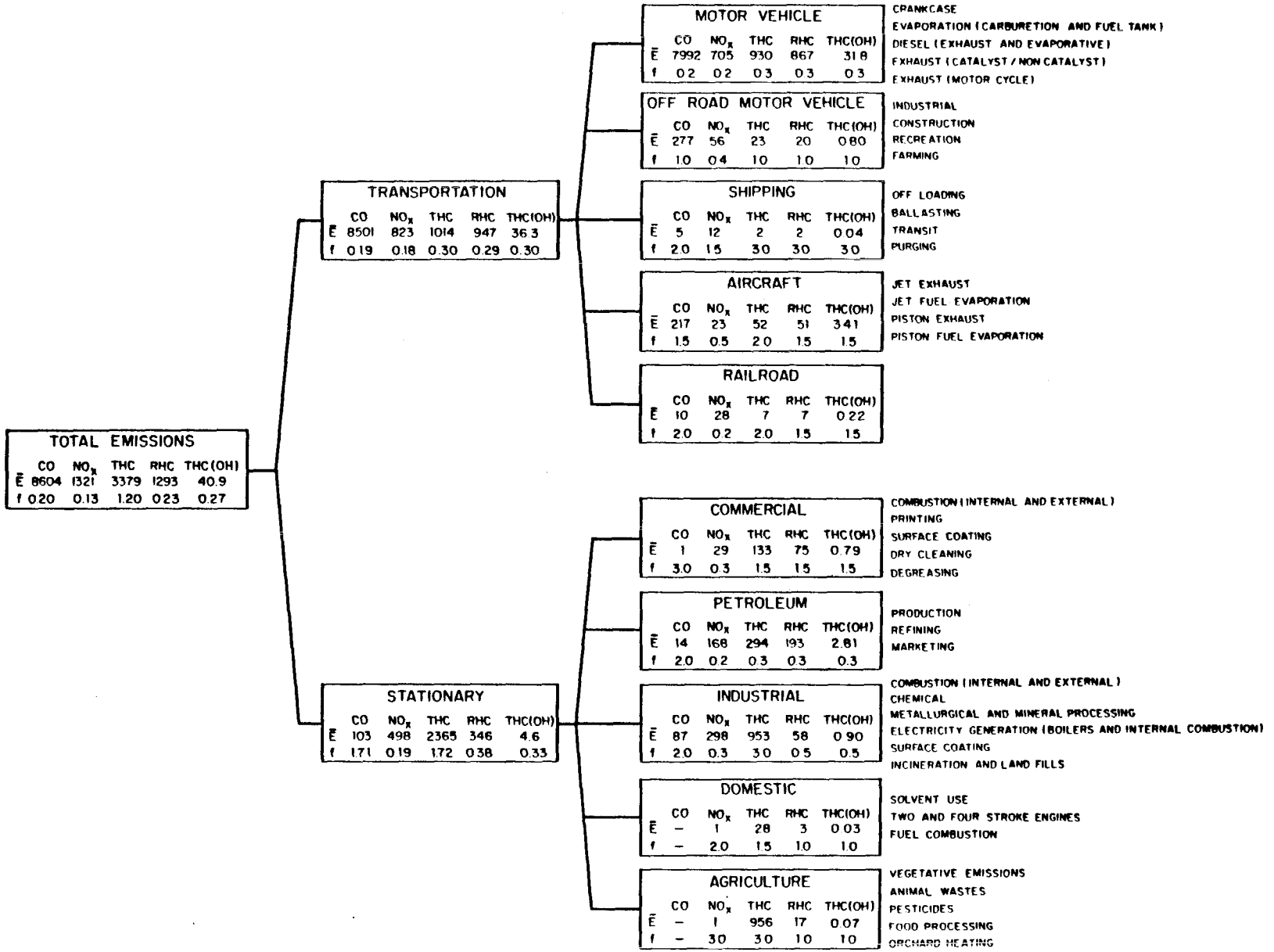

FIGURE 11.8

Simplified Structure of the Inventory Used in this Study Together with an Assessment of the Uncertainty of Pollutant Emissions from Different Source Categories ($\bar{E}$ is the pollutant emission rate in kg $day^{-1} \times 10^{-3}$ and f is the fractional uncertainty in the inventory category).

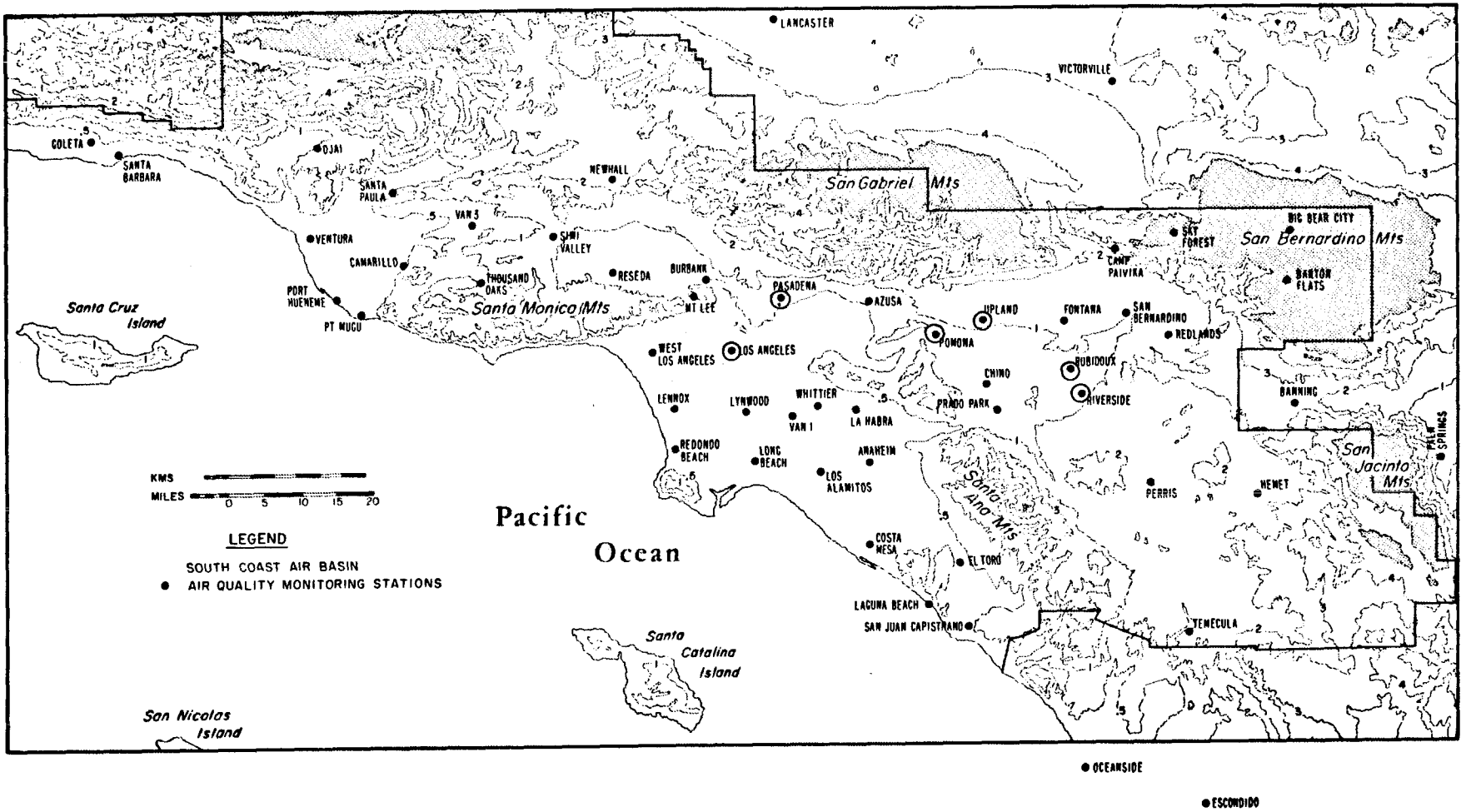

FIGURE 11.9

Location of Air Quality Monitoring Stations in the South Coast Air Basin
(Air quality predictions and observations at the circled locations are shown in Figures 5-9)

this expression [OX] is the oxidant concentration corrected for any calibration errors. (0.8 for data outside of Los Angeles County). The remaining terms in the conversion formula correct for the effects of interferences. Because of the poor quality of most reactive hydrocarbon measurements, a set of splitting factors was developed for converting total hydrocarbon readings into the components needed for the chemical mechanism. These factors were derived from emissions data and from the results of detailed field measurements reported in Altshuller et al. (1974), Cavanagh et al. (1969), Kopczynski et al. (1972), Lamb et al. (1980), Mayrsohn and Crabtree (1976), and Stephens and Burleson (1969). Given a total hydrocarbon measurement, expressed in ppmC, the factors shown in Table 11.8 enables the partitioning of this value into the equivalent ppmv amounts needed for the reaction mechanism.

A three-dimensional model requires initial and boundary concentrations aloft. Unfortunately, few pollutant concentration measurements have been taken above urban regions. One of the most comprehensive measurement programs conducted over the Los Angeles basin was that performed by Blumenthal et al. (1978). The results of that study indicated that on days with light winds aloft, polluted air that has been carried into the inversion layer can remain there overnight to be mixed down the following day. Figure 11.10 shows the measured ozone concentrations from Burbank and Mt. Lee, which are only 5 km apart but differ in elevation by about 300 m. The ozone concentration at Mt. Lee remains high during the night sine little of the NO released at the surface is able to mix vertically under nighttime stable conditions.

TABLE 11.8

Splitting Factors for Converting Total Hydrocarbon Measurements into Hydrocarbon Classes for Chemical Mechanism*

CLASS	URBAN CONDITIONS	RURAL CONDITIONS
Ethylene	0.0247	0.0057
Paraffins	0.0419	0.00967
Olefins	0.0110	0.00253
Aromatics	0.0075	0.00173
Formaldehyde	0.0433	0.0100
Aldehydes	0.0118	0.00273

* ppmv of individual class = Splitting factor x THC in ppmC

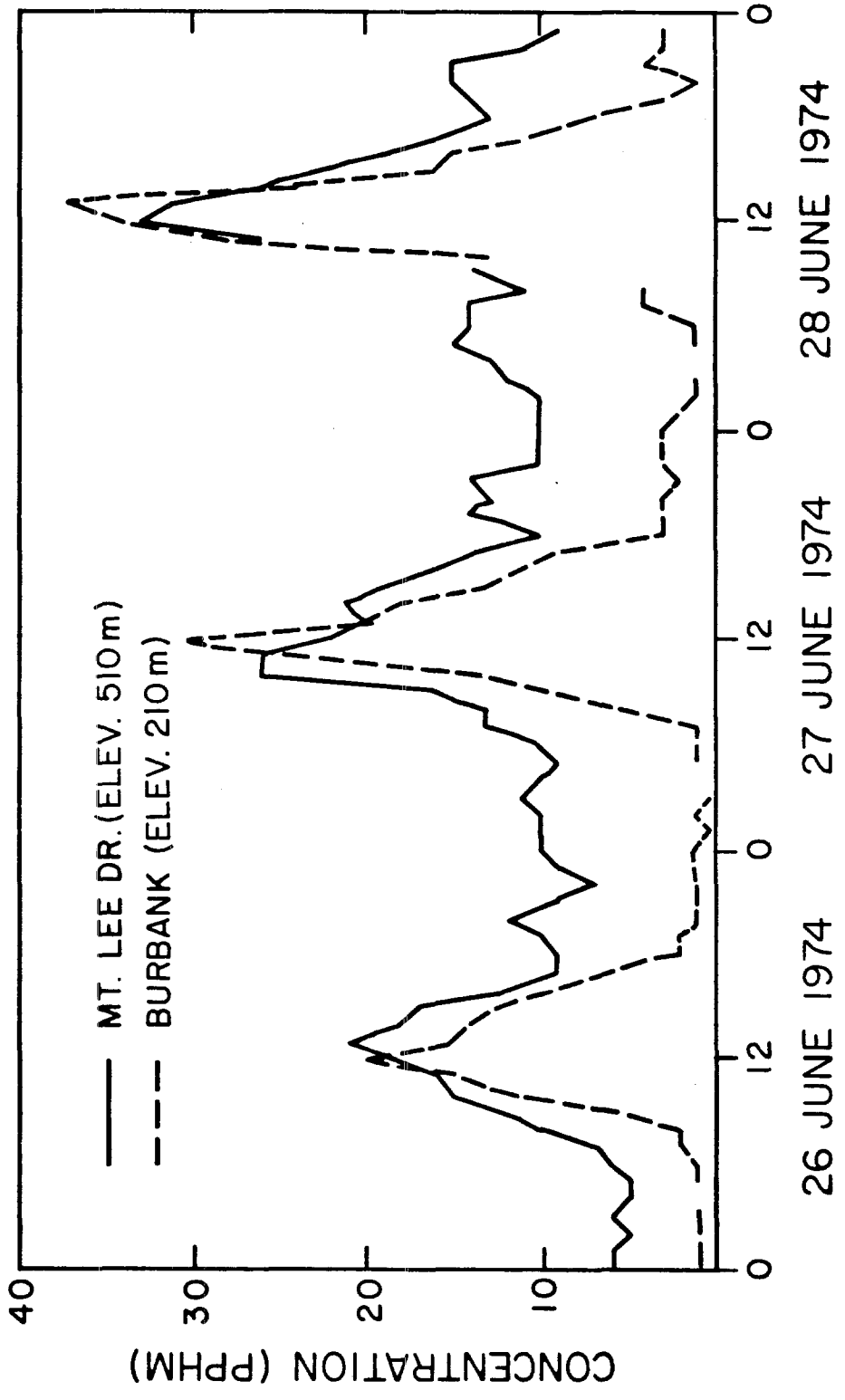

FIGURE 11.10

Measured Ozone Concentrations at Mt. Lee (elevation 510 m) and Burbank (elevation 210 m) During the Period 26-28 June 1974

The maximum hourly averaged concentration at Burbank increased from 0.20 ppm to 0.37 ppm during the episode. This increase of about 0.10 ppm on successive days is approximately the same magnitude as the overnight level at Mt. Lee, indicating that the downward mixing of polluted air from the inversion layer could account in part for the increased pollutant levels observed during this episode.

The procedure adopted in this study for constructing initial and boundary concentrations aloft is to assume a uniform value within the mixed layer using the surface concentration. The concentration then is assumed to decrease linearly to the background value at the top of the modeling region. Table 11.9 summarizes the results of a literature survey carried out to establish background levels and it also presents the values used in the present study. One of the major reasons for carrying out multi-day simulations was to minimize the influence, on the second day, of assumptions about initial conditions on the first day. The initial conditions for the second and subsequent days are simply the model outputs from the preceding day.

11.9 Location of the Airshed Boundaries of the Modeling Region

When choosing the location of the boundary of a modeling region, tradeoffs must be made among factors such as computer storage, computational costs and the accuracy of the results. Important physical phenomena that occur near the edge of the current study region are the land-sea breeze and mountain-valley flow regimes. Polluted air masses carried out to sea by the night time land breeze often return the next

TABLE 11.9

Natural (Unpolluted), Rural and Airshed Background Concentrations

SPECIES	NATURAL BACKGROUND CONCENTRATION (ppm)	REFERENCE	RURAL BACKGROUND CONCENTRATION (ppm)	REFERENCE	VALUE USED FOR BACKGROUND CONDITIONS
CH_4	1.5 1.4	Robinson and Robbins (1968) Rasmussen et al. (1974)	>1.4	Rasmussen et al. (1977)	1.0 (THC)
Reactive HC	<0.002 ppmC	Rasmussen et al. (1974)	0.05-0.18ppmC	Rasmussen et al. (1977)	
CO	0.1 0.01-0.26	Robinson and Robbins (1968) Cavanaugh et al. (1969) Junge (1963)	0.2-0.7	RTI (1975)	0.1
O_3	0.04-0.055 0.01	Chatfield and Harrison (1976) Jerskey et al. (1976)	0.0-0.2	RTI (1975)	0.04*
NO	0.001 0.0002-0.002	Robinson and Robbins (1968) Rasmussen et al. (1974)	<0.05 <0.01	Spicer et al. (1975) RTI (1975)	0.01*
NO_2	0.001 0.0009-0.0013	Robinson and Robbins (1968) Rasmussen et al. (1974)	<0.05 0.005-0.01	Spicer et al. (1975) RTI (1975)	0.01*

*During daylight hours NO, NO_2 and O_3 are in photolytic equilibrium.

day with the sea breeze as shown in Chapter 5. Upslope flows caused by heating of mountain slopes can inject pollutant-laden air into the inversion layer, to be subsequently fumigated down to the surface. At night, downslope or drainage flows can bring contaminated air, which is different from the surrounding surface air, into the basin. Since Eulerian or fixed-grid numerical procedures do not follow material that leaves the airshed, it is desirable to locate the grid boundary farther from the main calculation area than the greatest extent of significant return flows. In view of the importance of these flows, trajectory studies were conducted to locate suitable boundaries for the airshed model.

Numerical experiments were performed for 27 June 1974, in order to choose the location of the boundary of a subgrid area to be analyzed within the 400 x 150 km study area. Parcels of air leaving the coast with the land breeze were followed to determine their seaward extent. Figure 11.11 illustrates the problem in a simple manner. These trajectory calculations were begun at 00:00 PST on 27 June, the approximate start of the land breeze. The calculations were performed using the surface wind fields generated from measured data. Six parcels were tracked from coastal origins between Santa Barbara and San Juan Capistrano. The seaward extent of polluted air leaving the coastline on this day ranged from 0 to 25 km. Thus, if a western boundary for a subgrid region were to be stablished parallel to the coastline, it should be set approximately 25 km offshore in order to avoid loss of polluted air that might return following a flow reversal. Similar

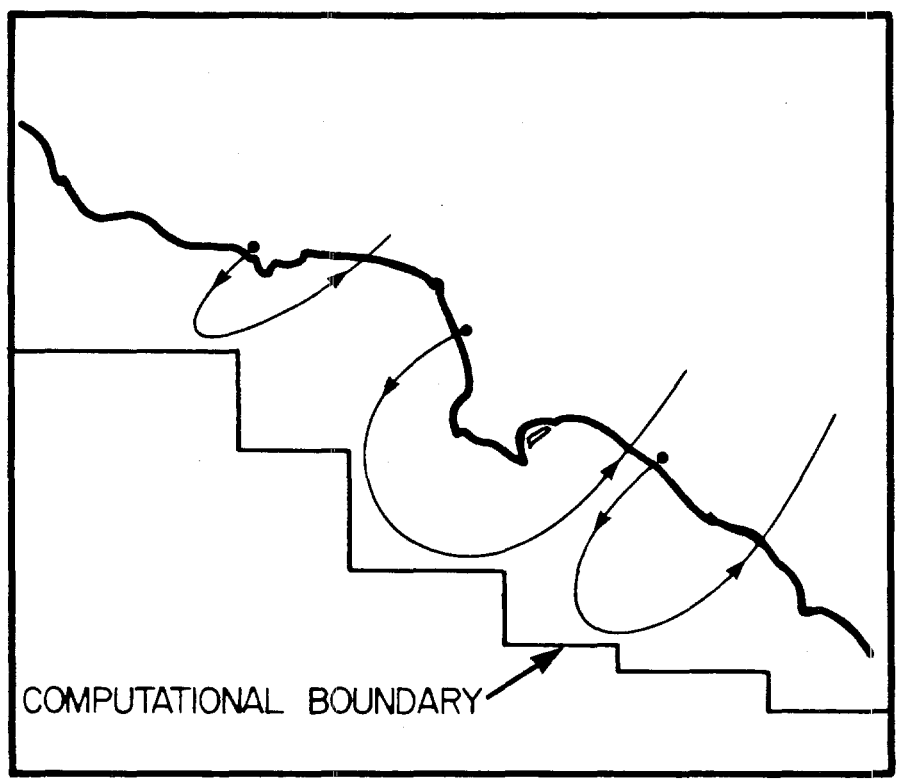

FIGURE 11.11

Illustration of Procedure Used to Define Computational Region that Minimizes the Effects of Inflow Boundary Conditions

calculations were performed to study inland flow patterns. Trajectories were initiated at Newhall, San Bernardino, Pomona and Perris at 00:00 at 27 June 1974. These studies indicated that during the night, air travels only a short distance (2 to 10 km) toward downtown Los Angeles from these locations. The horizontal extent of the computational domain employed is shown as the shaded region in Figure 11.12.

After an examination of mixing depth and vertical temperature structure data for the 26-28 June 1974 episode, the height of the top of the modeling region was set at 1525 m above the terrain. When a mixed layer existed, it was less than 1100 m deep at all points in the basin and so material trapped aloft could be satisfactorily tracked. On those occasions when the mixed layer was destroyed by heating, its depth was assumed to be 1100 m. After a series of detailed calculations the number of computational cells in the vertical direction was set equal to 5, representing a compromise between computational cost and the ability to resolve vertical concentration gradients.

11.10 Summary

Table 11.10 shows a summary of aerometric and emissions information available for 26-28 June 1974 for the study region.

11.11 Predicted and Observed Concentrations for 26-27 June 1974

The model was applied to simulate the two-day period 26-27 June 1974 in the SCAB. The concentrations of 15 species (NO, NO_2, O_3, CO, PAN, HONO, RO_2NO_2, RONO, H_2O_2, C_2H_4, OLE, ALK, ARO, HCHO and RCHO) are

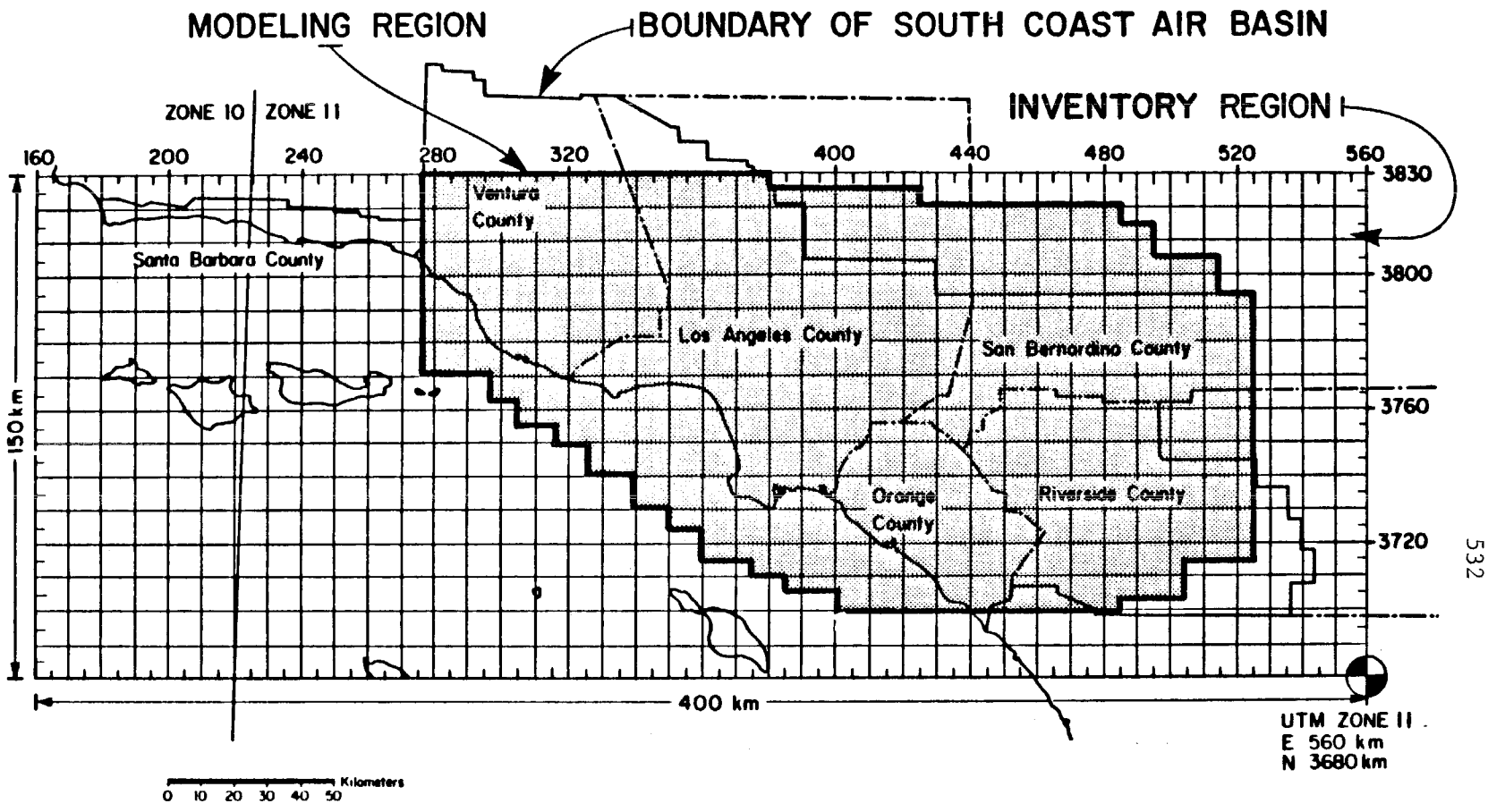

FIGURE 11.12

Definition of Computational Grid System Over the South Coast Air Basin
The shaded portion corresponds to the area used
in the model performance evaluation.

TABLE 11.10 Summary of Aerometric and Emissions Information Available for 26-28 June 1974 for the South Coast Air Basin

TYPE OF DATA	NATURE OF DATA COLLECTED	REMARKS	SOURCE OR ORGANIZATION(S) COLLECTING DATA
AIR QUALITY DATA			
Surface pollution concentration	55 air quality monitoring stations	Data are hourly averaged and include measurements of CO, NO, NO_2, O_3, THC, RHC and SO_2.	SCAQMD, ARB, CALTRANS, USFS
Pollution concentrations aloft	None	Estimates of vertical concentration profiles were derived from detailed field measurements collected from different periods.	
METEOROLOGICAL DATA			
Surface Winds	63 surface wind monitoring stations	Data include hourly averaged and instantaneous values.	SCAQMD, ARB, NWS, USN, USAF
Upper level winds	Radiosondes at Edwards AFB (0400 PST), Pt. Mugu (0400, 1000, and 1500 PST), and San Nicholas Island (0930 and 1500 PST). Pibals at LAX (0530 and 1130 PST) and El Monte (0600 and 1230 PST). Aircraft spiral at Riverside (0600 PST).		SCAQMD, USN, USAF, NWS
Mixing depths	Aircraft spiral at Riverside (0600 PST). Radiosondes at LAX (0530, 1030 PST), El Monte (0600, 1230 PST), Pt. Mugu (0400, 1000, 1500 PST), and San Nicholas Island (0930, 1500 PST), and Edwards AFB (0400 PST). Continuous acoustic sounder at El Monte.	Data are instantaneous except for continuous acoustic sounder at El Monte.	ARB, NWS, USN, USAF
Surface temperatures	Temperatures at 14 stations.	Data are hourly averaged values.	NWS, SCAQMD
Solar radiation	Radiation measurements at UCLA and LAX.	Data are hourly averaged and daily averaged values.	NWS, SCAQMD
Humidity	Humidity at 14 stations	Data are hourly averaged values	NWS, SCAQMD
Cloud cover	Cloud cover at 7 airports and 2 other locations.	Data are instantaneous values recorded every hour.	NWS, SCAQMD
EMISSIONS DATA			
Traffic	Emissions estimates derived from the LARTS transportation model and the ARB FWY011 emissions model.	Peak, off-peak and total emissions rates for THC SO_2, NO_x and CO are available. Percentage of hot and cold starts are included in the inventory, but they are not spatially or temporally distributed; vehicle speed distributions and types (four classes) are included.	ARB, CALTRANS
Refinery	Emissions for organic gases, NO_x, CO and particulates estimated for 28 facilities		SCAQMD

TABLE 11.10 Summary of Aerometric and Emissions Information Available for 26-28 June 1974 for the South Coast Air Basin (Continued)

TYPE OF DATA	NATURE OF DATA COLLECTED	REMARKS	SOURCE OR ORGANIZATION(S) COLLECTING DATA
EMISSIONS DATA (Cont)			
Aircraft	Gridded emissions estimates for all major airports in inventory region.		CALTRANS, SCAQMD
Power plants	Emissions estimates of NO, NO_2 and CO for each plant in inventory region.	Diurnal distribution of emissions based on inspection of daily operating logs.	SCE, LADWP
Distributed area sources	Emissions estimates for organic gases, NO_x and CO.		SCAQMD
Other stationary sources	Emissions estimates for organic gases, NO_x and CO.		SCAQMD

predicted in each of the grid cells as a function of time commencing at 0:00 hours 26 June. Of the 15 species calculated, two for which there exist both monitoring data and National Ambient Air Quality Standards, and the two that provide the most stringent test of a model to simulate photochemical air pollution, are NO_2 and O_3. Therefore, we confine our attention here to these two species.

The computed concentration field may be presented in several ways:

1. One-hour-average ground-level concentration fields at each hour
2. Isopleths (contour lines of constant concentrations) at each hour
3. Concentrations as a function of time for various grid cells, in particular those containing a monitoring station.

Each of these three ways of presenting predicted concentrations is useful and informative. For economy of space and because we are especially interested in comparisons with observations, we only show here the temporal behavior of the concentrations in the grid cells containing monitoring stations.

Figures 11.13-11.17 show predicted and observed concentrations of NO_2 and O_3 during 26-27 June 1974 at several monitoring stations in the SCAB. Results at all the monitoring sites are shown in Appendix C.

In the early morning both NO and reactive hydrocarbons peak due to traffic emissions. The NO_2 peak concentrations are delayed a few hours, consistent with the time required to oxidize NO. Observed and predicted ozone concentrations increase with distance toward the east. Ozone concentrations gradually increase until the time of the peak

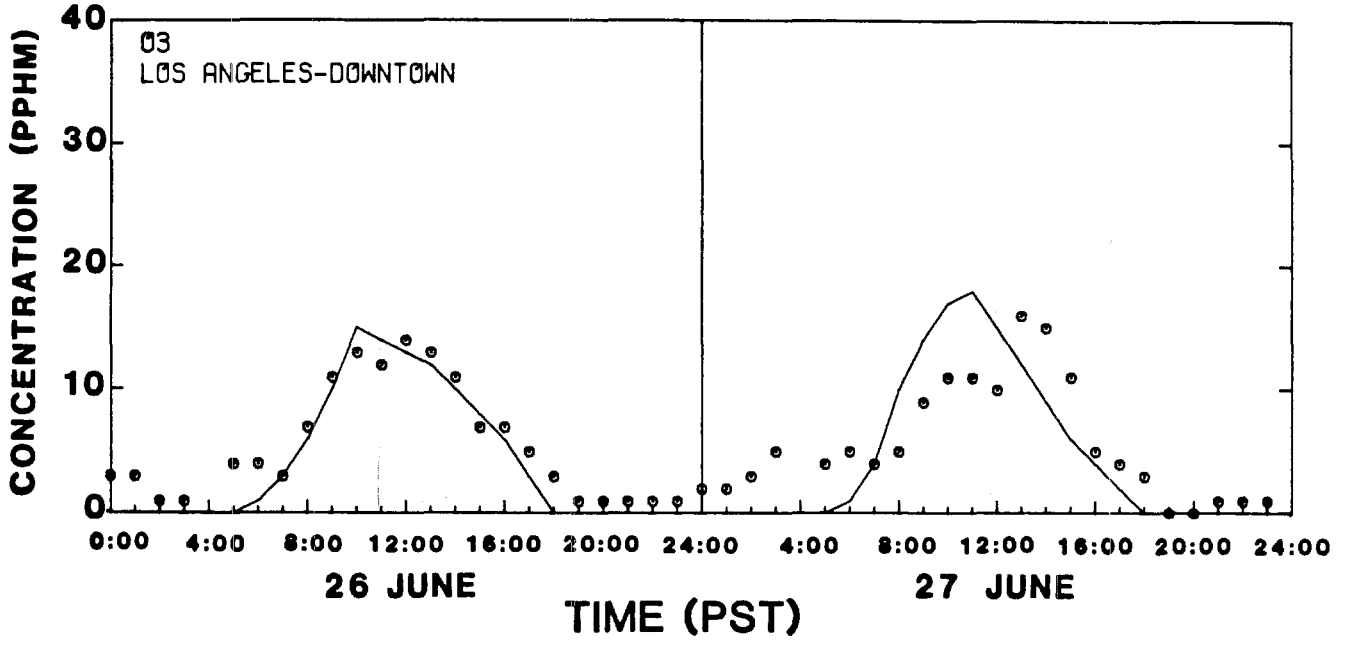

(a)

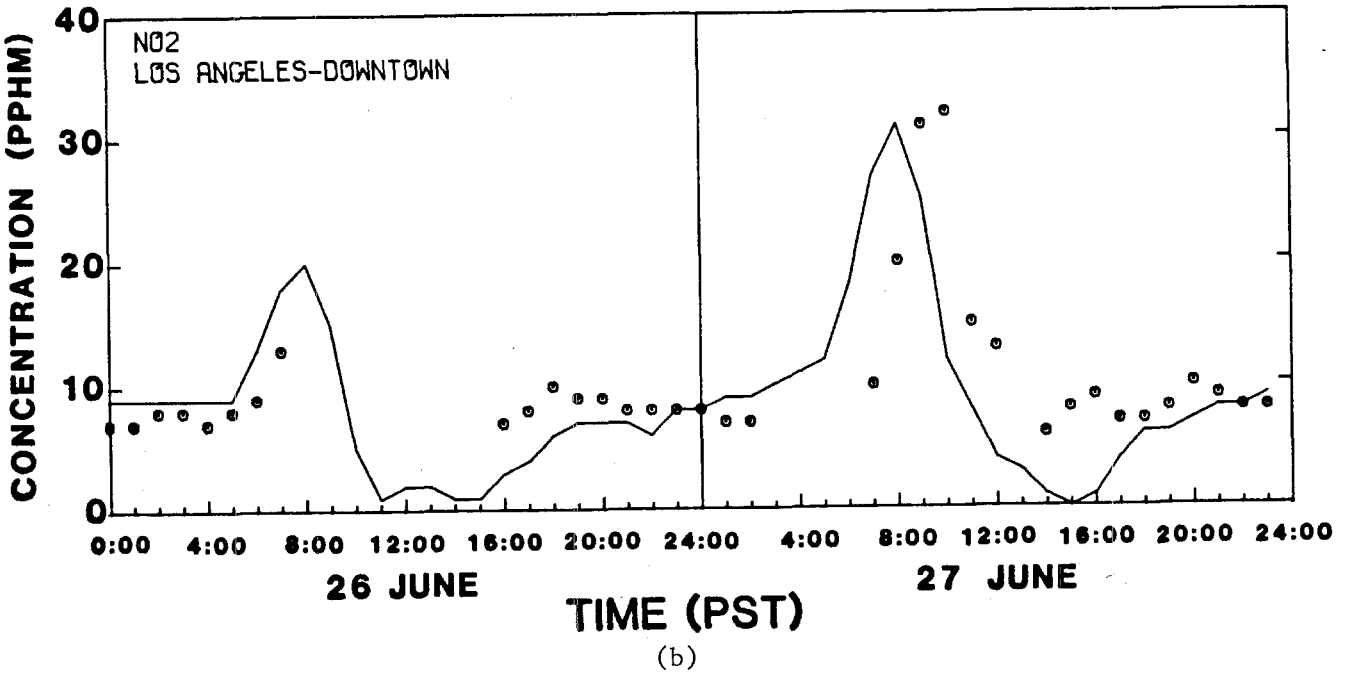

(b)

FIGURE 11.13

Predicted and Observed Concentrations of:
(a) Ozone and (b) Nitrogen Dioxide at Downtown Los Angeles
(- predicted, o observed)

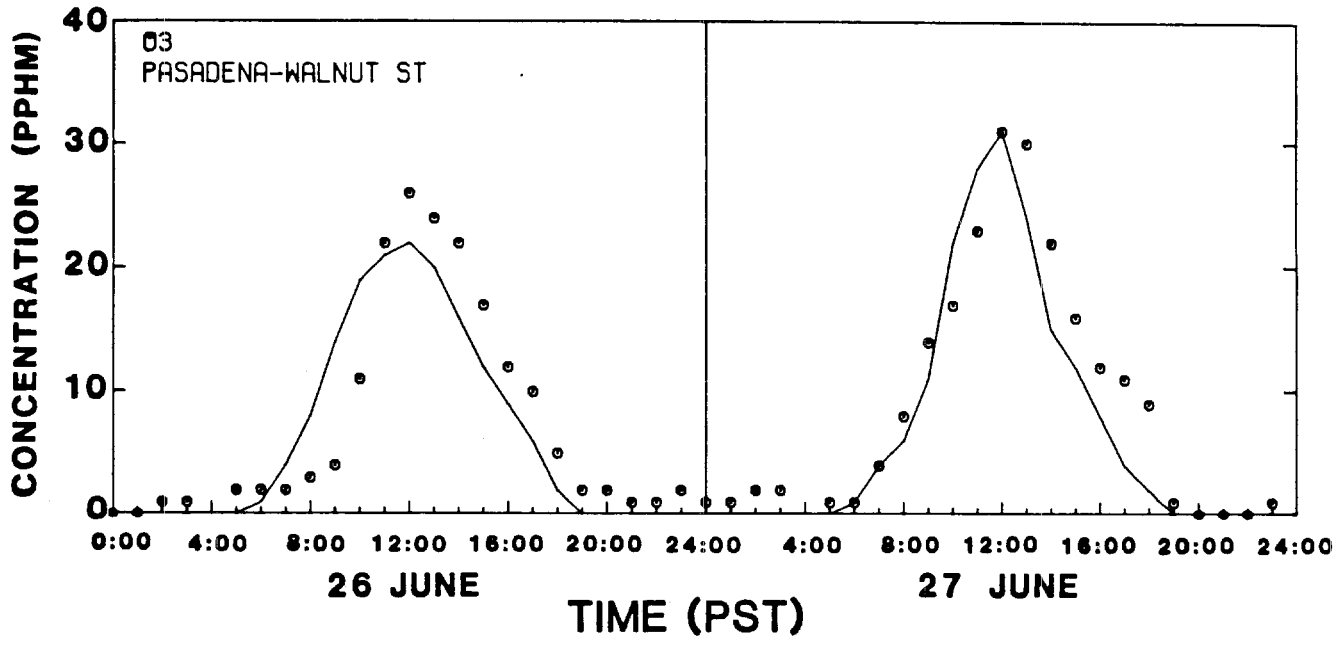

(a)

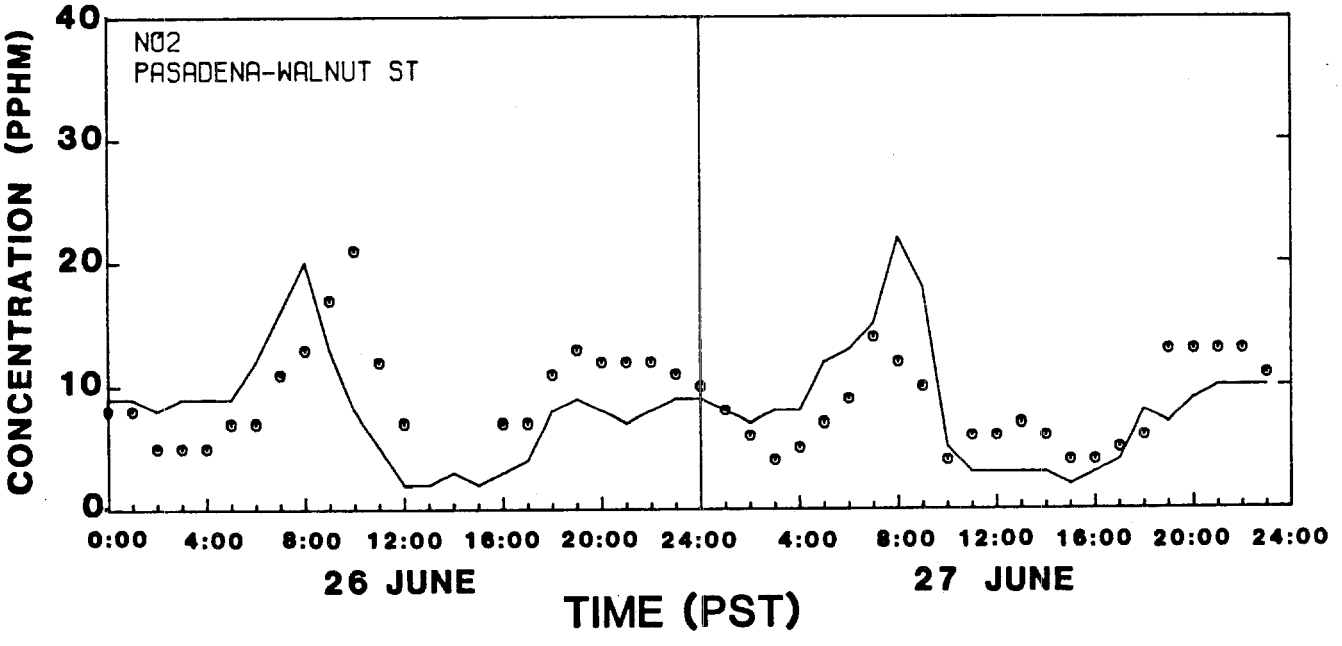

(b)

FIGURE 11.14

Predicted and Observed Concentrations of:
(a) Ozone and (b) Nitrogen Dioxide at Pasadena
(- predicted, o observed)

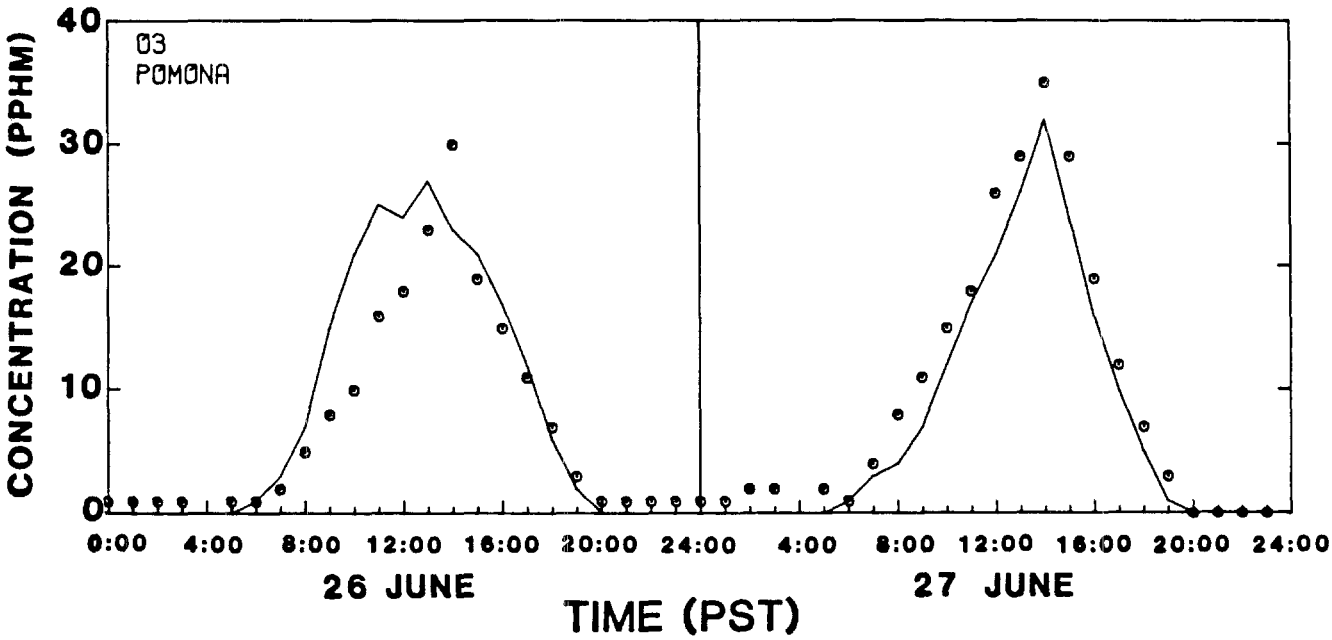

(a)

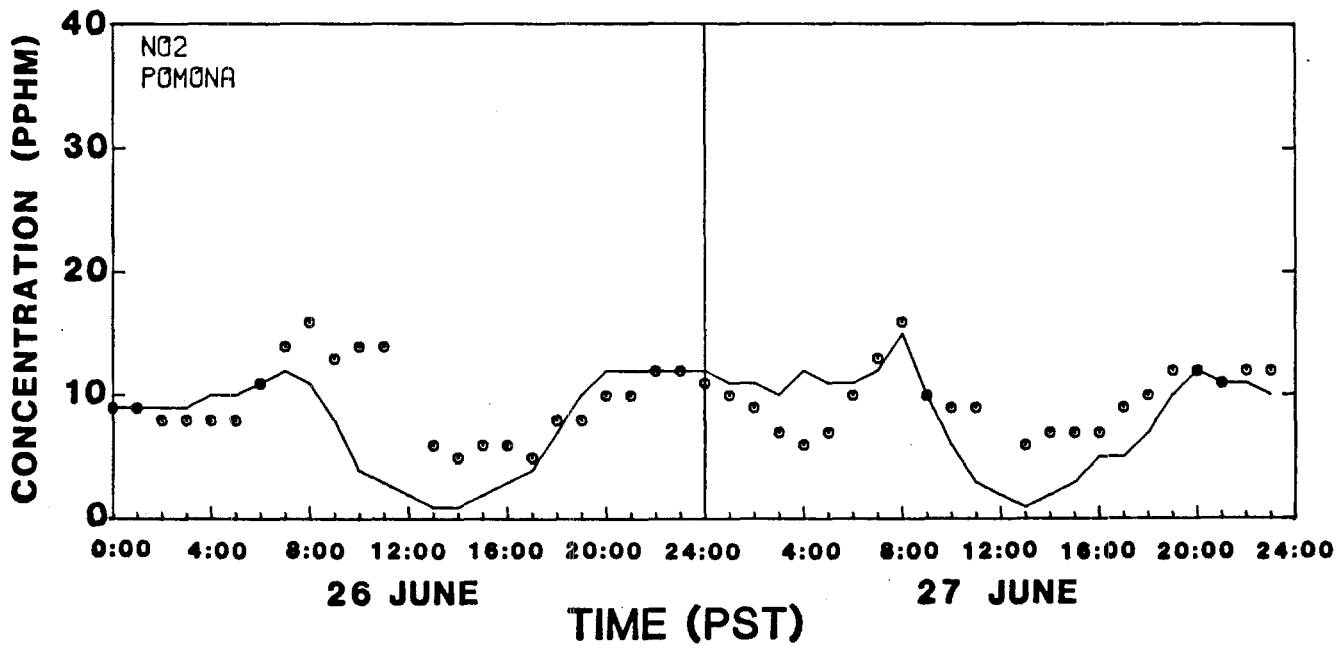

(b)

FIGURE 11.15

Predicted and Observed Concentrations of:
(a) Ozone and (b) Nitrogen Dioxide at Pomona
(- predicted, o observed)

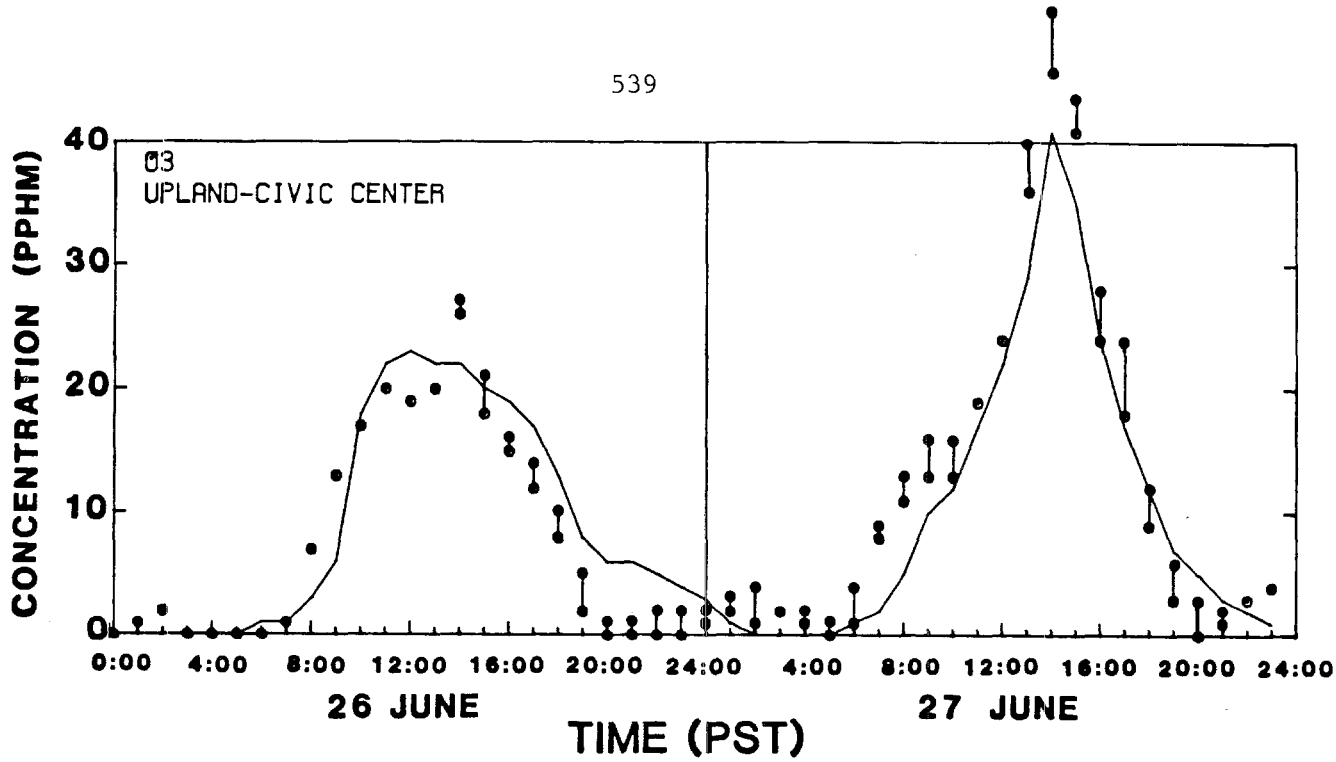

(a)

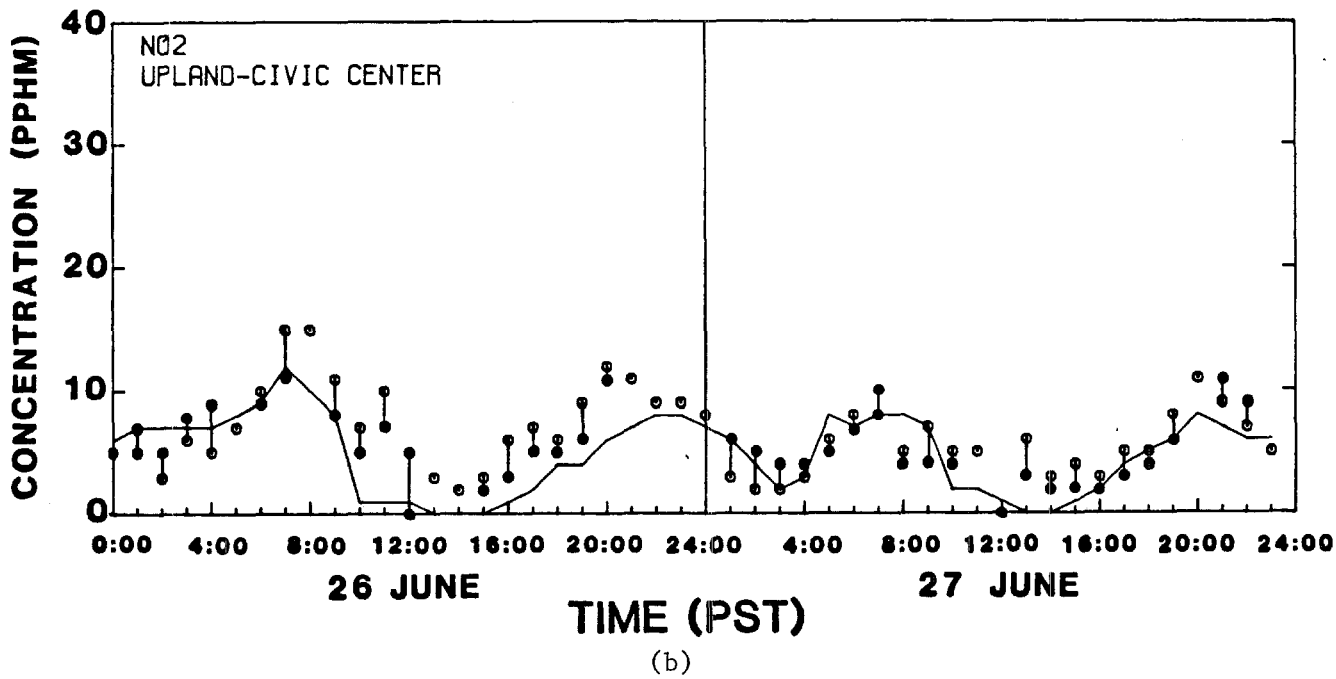

(b)

FIGURE 11.16

Predicted and Observed Concentrations of:
(a) Ozone and (b) Nitrogen Dioxide at Upland
(- predicted, o observed at CARB station,
• observed at APCD monitoring site located 400 meters away).

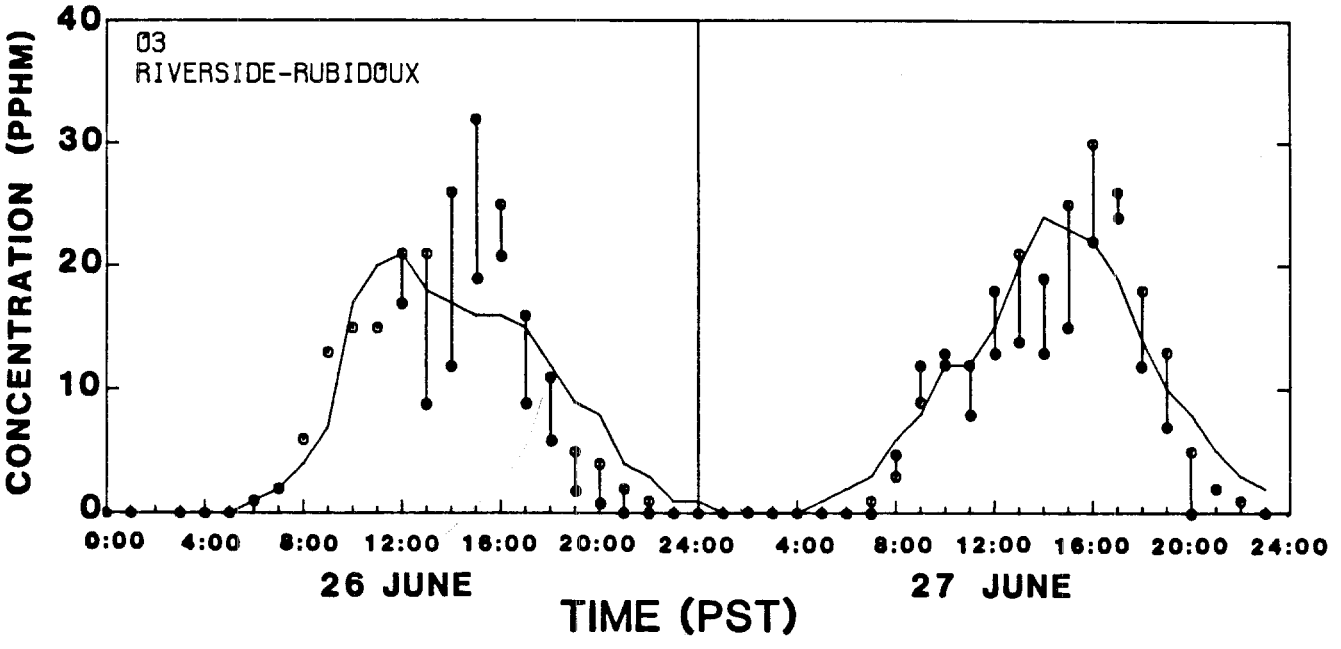

(a)

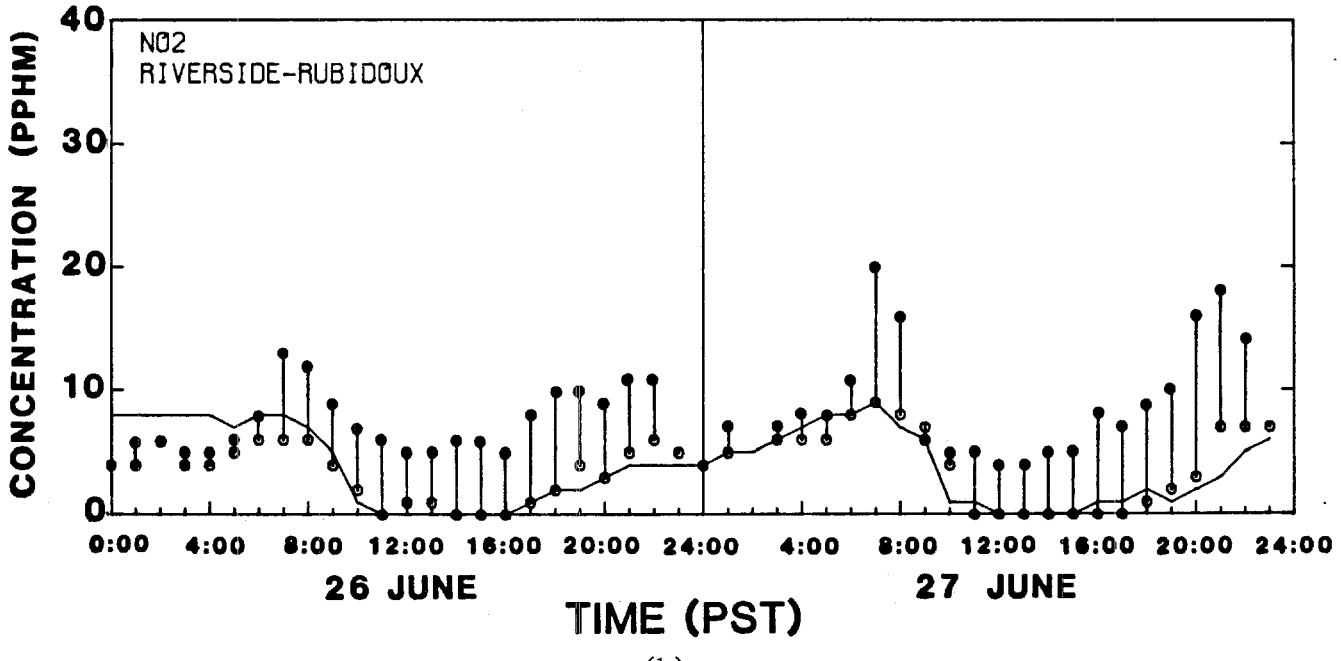

(b)

FIGURE 11.17

Predicted and Observed Concentrations of:
(a) Ozone and Nitrogen Dioxide at Riverside
(- predicted, o observed at APCD station,
• observed at ARB monitoring site located 1200 meters away).

predicted concentration which usually occurs between 1300 and 1400 PST. As air moves onshore and approaches the San Gabriel mountain range, bifuration of the flow occurs. Some of the pollutants emitted in the western and downtown portions of the Basin are carried northward into the San Fernando Valley; other material is transported east to Azusa, Upland and Riverside. In most cases the model accurately reproduced both the magnitude and timing of the peak ozone concentration. Similar behavior was also noted for nitrogen dioxide except that the model tended to predict the peak values one to two hours earlier. The fact that the model satisfactorily described the observed concentration trends on the second day is particularly encouraging for control strategy calculations. The reason for this is that by running the model for a period longer than the characteristic ventilation of the airshed it is possible to minimize the influence of uncertainties in specifying the initial conditions. This capability is important for those situations where it is not possible to derive starting conditions from ambient monitoring data.

In summary, because the essential trends of the predictions and observations are in agreement and because the model components represent state-of-the-art knowledge of each aspect, we assume that the basic model framework is a valid representation of atmospheric concentration dynamics.

11.12 Statistical Analysis of Results

In many respects a statistical analysis of the deviations between predictions and observations is the heart of model performance evaluation. Although raw statistical comparison of observed and predicted values may not reveal the cause of discrepancies, it can tell much about the nature of the mismatch. Considerable attention has been given to statistical measures for comparing predicted and observed air pollutant concentrations. (Brier, 1975; Bowne, 1980; Fox, 1981; Bencala and Seinfeld, 1979 and Rao and Visailli, 1981). Fox (1981) in discussing the results of an American Meteorological Society workshop identified three basic classes of performance measures.

1. Analyses based on observed and predicted concentration field values paired for particular locations and times.
2. Examinations of the ability of the model to predict the peak concentrations.
3. Frequency distributions of the updated (in time) observed and predicted concentration values.

Bencala and Seinfeld (1979), for example, have discussed many of these measures and have developed a general computer program for evaluating them given a set of predicted and observed concentrations. In the present section this program has been applied to analyze the simulation of 26-27 June 1974. The results of these calculations are summarized in Table 11.11. While ideally an assessment of a model's performance, in reproducing observed concentration distributions, should be based on a comparison against recognized criteria no formal standards have as yet been established. The results reported below are offered in the

TABLE 11.11

Summary Statistics Determined Over All Times and Locations for 26-27 June 1974[a]

PERFORMANCE MEASURE	DEFINITION[b]	INTERPRETATION OF STATISTICAL TEST	RESULTS OF TEST: OZONE (O_3)	RESULTS OF TEST: NITROGEN DIOXIDE (NO_2)	EVALUATION OF MODEL PERFORMANCE
Mean of Residuals	$\mu_i = \frac{1}{nm} \sum_{j=1}^{n} \sum_{k=1}^{m} w_i(x_j,t_k)$	A measure of the average bias in the predictions can be inferred from this test. The criterion indicates whether the model predominantly over-or-under-predicts the observed concentration.	0.0019 ppm [3%][c]	0.0078 ppm [11%][c]	While the model exhibits a slight tendency towards underprediction, the bias is of the order of typical monitoring instrument errors.
Root Mean Square Error (RMSE) Centered about the Mean	$\sigma_i = \sqrt{\frac{1}{nm} \sum_{j=1}^{n} \sum_{k=1}^{m} [w_i(x_j,t_k) - \mu_i]^2}$	This test measures the average spread of the residuals and, more importantly, it is insensitive to any bias in the predictions.	0.0382 ppm	0.0348 ppm	These results provide a formal measure of the spread of the residual histograms presented in Figure 10.
Correlation Coefficient	$r_i = \frac{\frac{1}{nm} \sum_{j=1}^{n} \sum_{k=1}^{m} \nu_i(x_j,t_k)\eta_i(x_j,t_k)}{\sqrt{\frac{1}{(nm)^2} (\sum_{j=1}^{n} \sum_{k=1}^{m} \nu_i^2)(\sum_{j=1}^{n} \sum_{k=1}^{m} \eta_i^2)}}$ where $\nu_i(x_j,t_k) = c_i^p(x_j,t_k) - \bar{c}_i^p$, $\eta_i(x_j,t_k) = c_i^o(x_j,t_k) - \bar{c}_i^o$ and $\bar{c}_i = \frac{1}{nm} \sum_{j=1}^{n} \sum_{k=1}^{m} c_i(x_j,t_k)$	The correlation coefficient measures the degree to which the magnitude of the predictions increase linearly with the magnitude of the observations. From a practical point of view it is important to note that the coefficient is insensitive to the extent of the increase. For example, if the predictions increase linearly at 1/10th of the rate of the observations then r will still be one.	0.89	0.67	For ozone (O_3) the predicted performance is excellent. In the case of nitrogen dioxide (NO_2) it is not possible to ascertain whether the low value of r is due to the model performance or interference from $HONO_2$ and PAN in the measurement of NO_2 (Adema, 1979; Higuchi et al., 1976).
Linear Least Squares Curve Fit	$c_i^p = \beta_i c_i^o + \alpha_i$ where the slope β_i is given by $\beta_i = \frac{\frac{1}{nm} \sum_{j=1}^{n} \sum_{k=1}^{m} \nu_i(x_j,t_k)\eta_i(x_j,t_k)}{\frac{1}{nm} \sum_{j=1}^{n} \sum_{k=1}^{m} \nu_i^2(x_j,t_k)}$ and intercept α_i by $\alpha_i = \bar{c}_i^o - \beta_i \bar{c}_i^p$	This performance measure can be used to assess the average increase in the predictions as the observations are increased. The slope parameter of the linear least squares curve fit is this measure. If the slope is nearly equal to one then the intercept is an indication of the bias.	slopes 0.851 intercepts 0.0115 ppm	0.709 0.0262 ppm	Both the slopes and intercepts for ozone (O_3) and nitrogen dioxide (NO_2) indicate that the model satisfactorily reproduces the observed concentration distributions.
Accuracy of Peak Prediction	$\frac{\max c_i^p(x_j,t_k)}{\max c_i^o(x_j,t_k)}$	Ratio of the maximum predicted peak concentration to the highest measured value.	$\frac{0.41}{0.51} = 0.80$	$\frac{0.31}{0.36} = 0.80$	For both ozone (O_3) and nitrogen dioxide (NO_2) the predicted highest concentrations are within 20% of the observations.
Timing of Peak Concentration Predictions	$\Delta t_i = t^o(x_j) - t^p(x_j)$	Difference in timing of predicted and observed peaks at the monitoring site with the highest observed concentration.	0 hrs[d]	-2 hrs[d]	As seen in Table 9 the predicted and observed ozone (O_3) concentration peaks were coincident at most monitoring sites. Differences of up to three hours were noted in the predicted times of the NO_2 peaks.
Error Bands	% of residuals over all j,k that satisfy $\lvert w_i(x_j,t_k) \rvert \leq$ bound	This measure gives the percentage of predictions that fall within a particular concentration bound.	83.8%[e]	88.9%[e]	Most of the residuals were within the $\pm$ 0.05 ppm concentration band.

Footnotes:

(a) In the statistical evaluation of model performance 1336 pairs of predictions and observations were used in the analysis of ozone (O_3) and 973 for nitrogen dioxide (NO_2).

(b) The residual for species i at locations j=1,2,...m and times k=1,2,...,m are defined as $w_i(x_j,t_k) = c_i^o(x_j,t_k) - c_i^p(x_j,t_k)$ where c_i^o and c_i^p are respectively the observed and predicted concentrations of species i.

(c) The values in brackets express the residuals as a percentage of the observed mean concentration. For ozone (O_3) the observed and predicted means were 0.0661 and 0.0641 ppm and for nitrogen dioxide (NO_2) 0.0709 and 0.0630 ppm respectively.

(d) The peak observed value of ozone (O_3) = 0.51 ppm occurred at Upland at 14:00 PST and the highest nitrogen dioxide (NO_2) = 0.36 ppm at downtown Los Angeles at 10:00 PST.

(e) Concentration bound set to $\pm$ 0.05 ppm .

spirit of providing a reference level for performance evaluation of photochemical air pollution models.

11.13 Distribution of Residuals

Figure 11.18 shows the frequency distributions of the residuals, i.e. observed minus predicted concentrations, for NO_2 and O_3 for all monitoring stations over the two day simulation. The distribution of residuals as a function of observed concentration is shown in Figure 11.19 and, as a function of time, in Figure 11.20. The mean residuals over all times and locations were 0.0078 ppm for NO_2 and 0.0020 for O_3 indicating a slight trend towards under-prediction. The standard deviation of the distributions shown in Figures 11.18-11.20 are within the error bounds associated with the routine air quality measurements. As noted by Fox (1981) analysis of paired data sets is one of the most stringent tests of a model. For pollutants that have a pronounced diurnal variation even a one hour difference in timing of the predicted maximum concentration can significantly change the results of some statistical tests. Figure 11.21, for example, shows the effect on a correlation plot of a one hour phase shift in the predicted concentration profile.

11.14 Predicted and Observed Concentration Maxima

An important criterion in evaluating an air pollution model is its ability to predict the observed concentration maxima. Table 11.12 shows a comparison of the magnitudes of the predicted and observed O_3 maxima for 27 June at those stations where the observed maxima exceeded

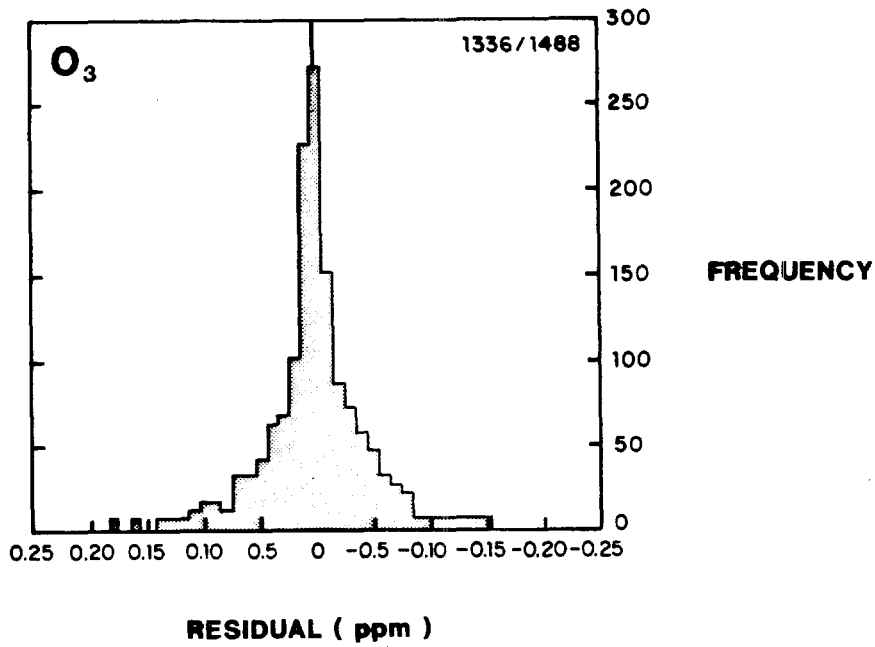

(a)

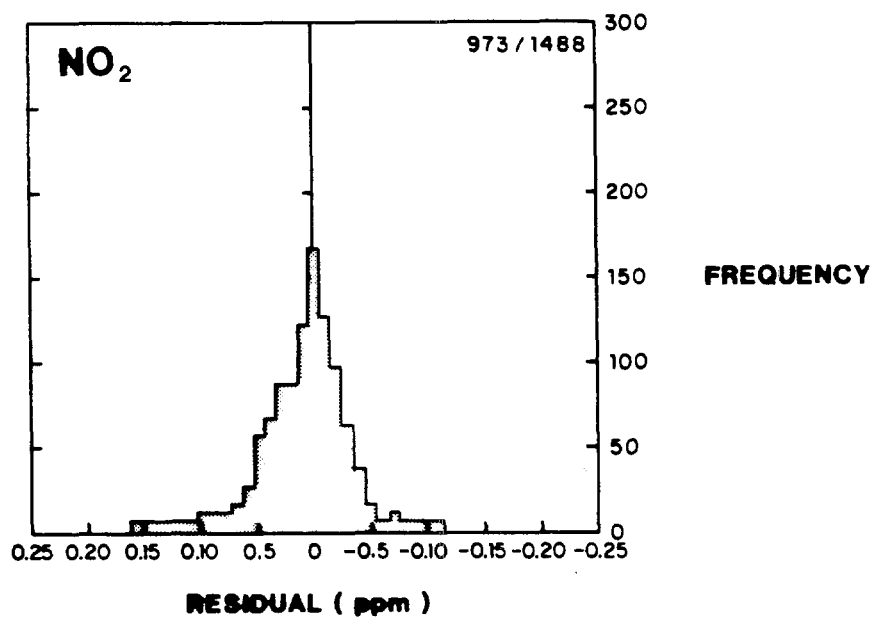

(b)

FIGURE 11.18

Histograms of Concentrations Residuals (Observed-Predicted) Determined Over All Times and Locations for the Two Day Period 26-27 June 1974: (a) Ozone (b) Nitrogen Dioxide

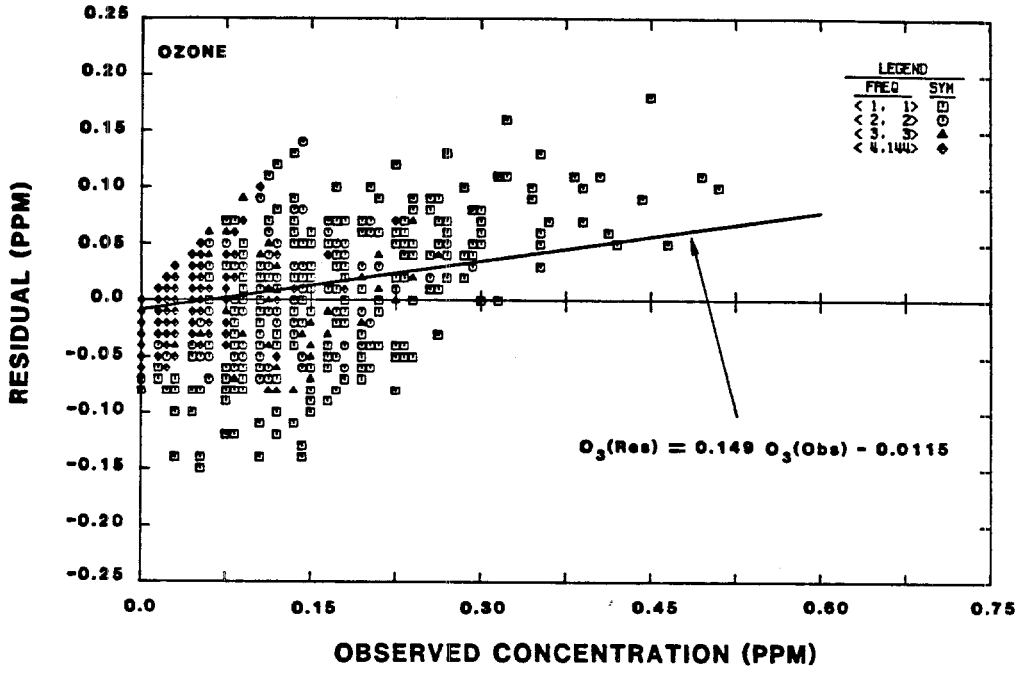

(a)

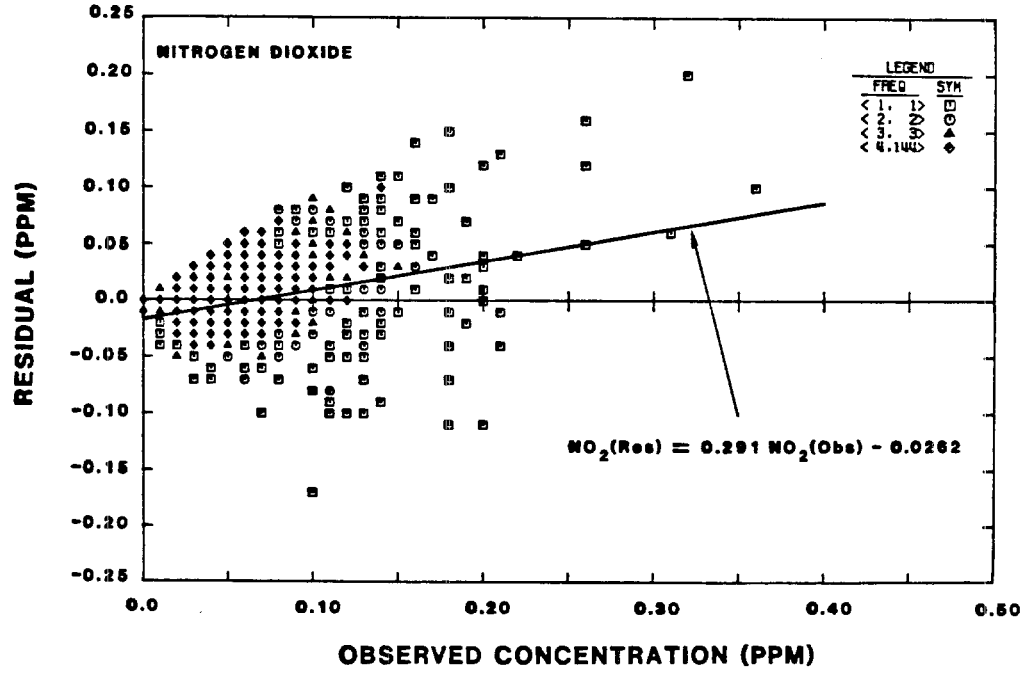

(b)

FIGURE 11.19

Distribution of Concentration Residuals (Observed-Predicted) as a Function of Observed Values Determined Over All Times and Locations for the Two Day Period 26-27 June 1974: (a) ozone (b) nitrogen dioxide

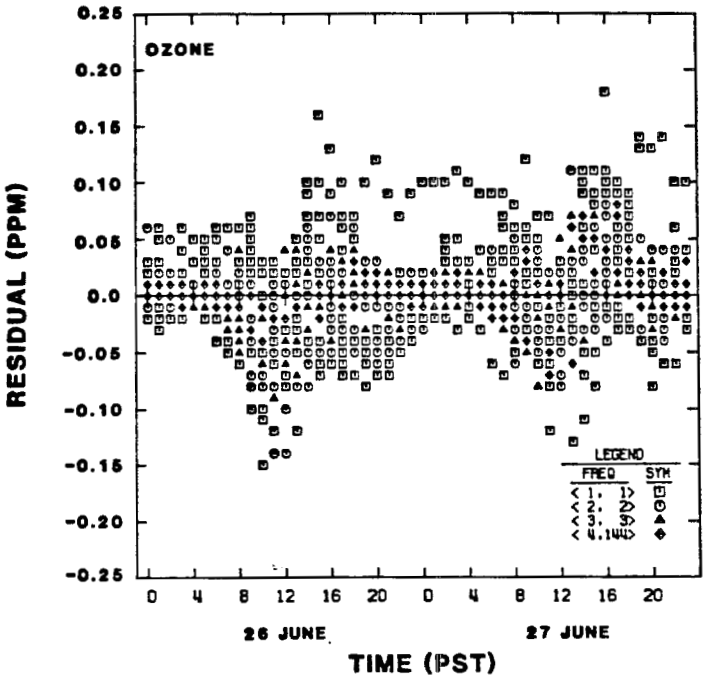

(a)

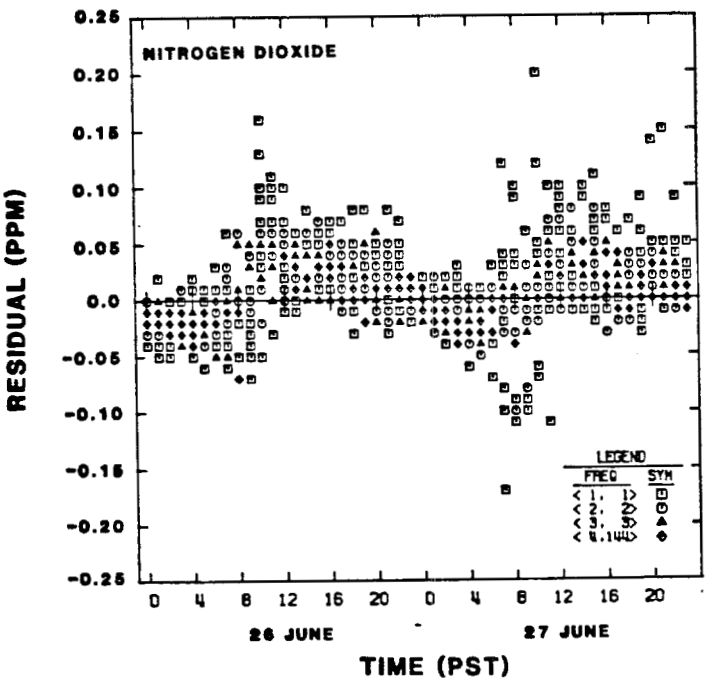

(b)

FIGURE 11.20

Distribution of Concentration Residuals (Observed-Predicted) as a Function of Time Determined Over All Locations for the Two Day Period 26-27 June 1974: (a) Ozone (b) Nitrogen Dioxide

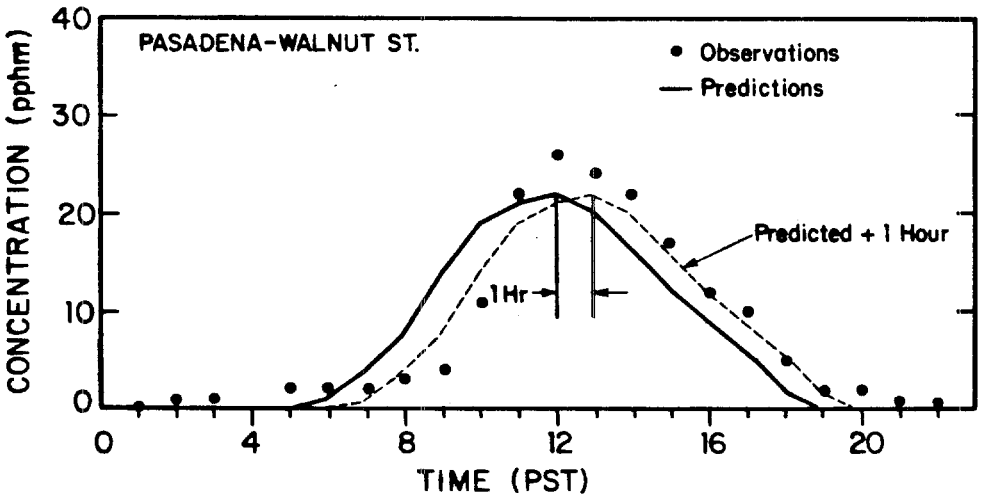

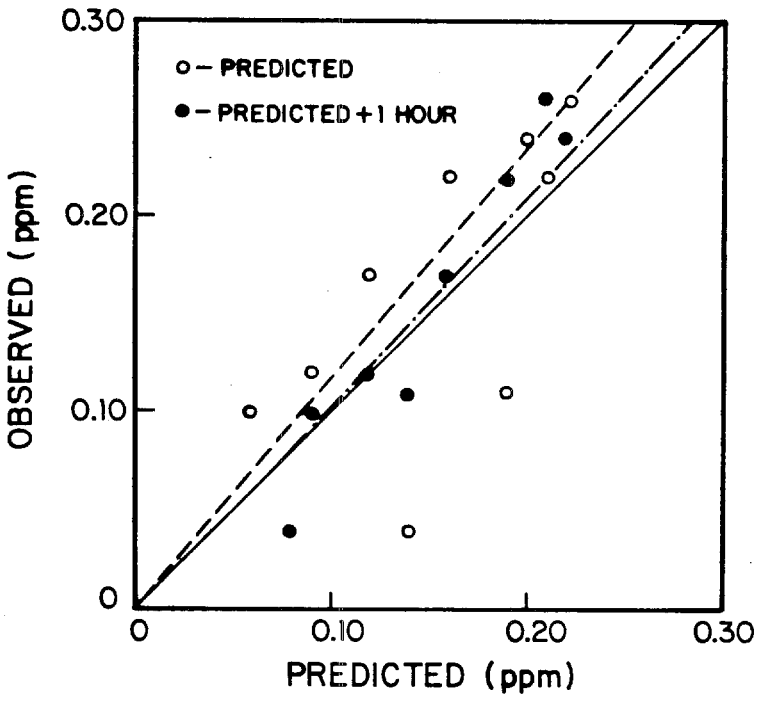

FIGURE 11.21

Effect on a Correlation Plot of a One Hour Phase Shift in the Predicted Concentration Time Profile. (26 June, 1974)

TABLE 11.12

Observed and Predicted Maximum 1-hr Ozone Concentrations at SCAB Stations Where $[O_3] > 0.20$ ppm and Timing of Ozone Maxima, 27 June 1974

	$[O_3]$, ppm		Time of maximum	
Station	Observed	Predicted	Observed	Predicted
Anaheim	0.23	0.21	1600	1600
La Habra	0.31	0.27	1500	1500
Los Alamitos	0.24	0.22	1700	1600
Norco-Prado Park	0.24	0.21	1600	1600
Riverside-Rubidoux	0.30	0.24	1500	1500
Riverside-Magnolia Avenue	0.24	0.24	1500	1500
San Bernardino	0.32	0.23	1500	1500
Chino	0.27	0.25	1400	1400
Upland-Civic Center	0.51	0.41	1600	1500
Upland-ARB	0.46	0.41	1500	1500
Fontana	0.49	0.38	1300	1400
Azusa	0.35	0.29	1200	1200
Burbank	0.30	0.30	1400	1300
Pomona	0.35	0.32	1100	1200
Whittier	0.38	0.30	1300	1200
Pasadena	0.31	0.31	1200	1200

0.20 ppm and a comparison of the predicted and observed hour of the O_3 maximum at the same stations. The tendency toward under-prediction of O_3 concentrations at high O_3 levels is summarized in Figure 11.19, in which the residual O_3 (observed minus predicted) concentrations are shown as a function of observed O_3 concentration for all monitoring stations over the two days. This tendency toward underprediction at high O_3 levels was also exhibited by the Systems Applications, Inc. model in simulations of the same two day period (Seigneur et al., 1981). The predicted times of occurrence of the O_3 maxima agree exactly or are at most hour hour removed from those observed. Because the phasing of predicted O_3 concentrations depends on virtually all the physical and chemical processes involved, the close agreement between observed and predicted temporal behavior suggests that these processes are accurately portrayed relative to their temporal dynamics.

Figures 11.13-11.17 show what might be termed "point comparisons." The observed values represent one-hour average concentrations measured at a fixed monitoring site. The predictions, on the other hand, represent averages over a computational grid volume 5 km by 5 km on a side and typically 10 to 20 m high. If a particular monitoring site is dominated by a local source, concentration measurements may not be representative of the grid-cell average concentration. In so-called grid models of air pollution there are, therefore, two inherent problems in comparing observed and predicted concentrations. On one hand, due to computational costs, there is effectively a minimum grid cell size that may be employed for a certain region. (There also exist

inherent limitations on the spatial and temporal resolution of the atmospheric diffusion equation (Lamb and Seinfeld, 1973).) On the other hand, the spatial representativeness of the measurements at a monitoring site is limited and may be influenced by local sources and flow patterns. An indication of the effects of subgrid scale concentration fluctuations can be seen in Figures 11.16 and 11.17.

11.15 Frequency Distributions

Figures 11.22a and 11.22b show the observed and predicted frequency distributions of hourly-averaged O_3 concentrations at Azusa and Upland-ARB, respectively. Aside from the tendency toward underprediction at the highest concentrations, the agreement is good at both stations. (Similar results, not shown, were obtained at other monitoring sites.)

11.16 Observation Accuracy

Although we have indicated all observed concentrations by data points, suggesting exact values, the observed data have an associated level of accuracy that should be indicated by error bounds on each data point. Using the reported accuracy of the measuring instruments employed in 1974 as a function of concentration level (Higuchi et al., 1976; Higuchi, 1981), we replotted the observed and predicted O_3 concentration at Pasadena including the $\pm 2\sigma$ estimated error bounds on the data. These results, shown in Figure 11.23, again indicate that the model satisfactorily reproduces the ambient concentration dynamics. The model performance as indicated by the magnitude of the

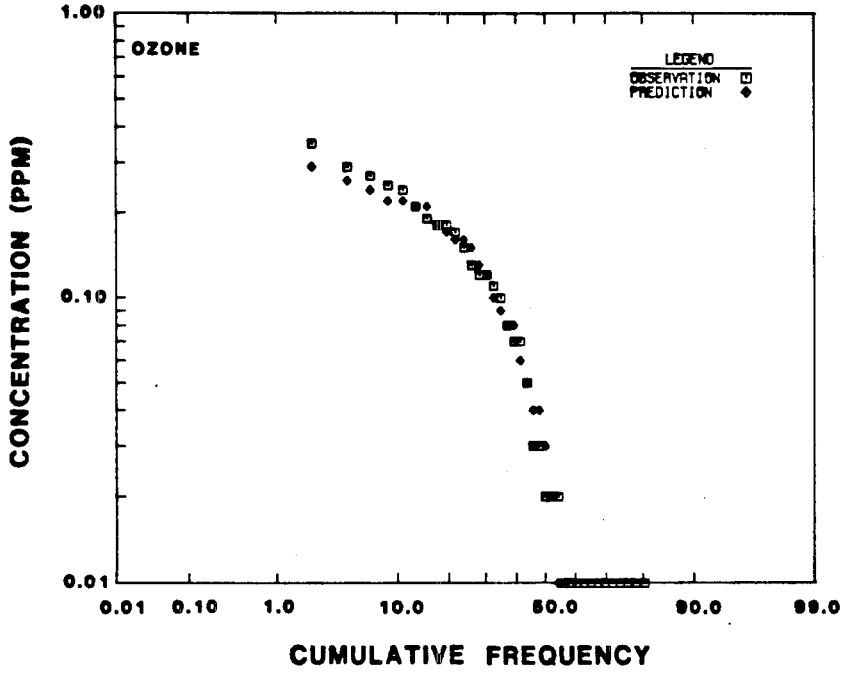

(a)

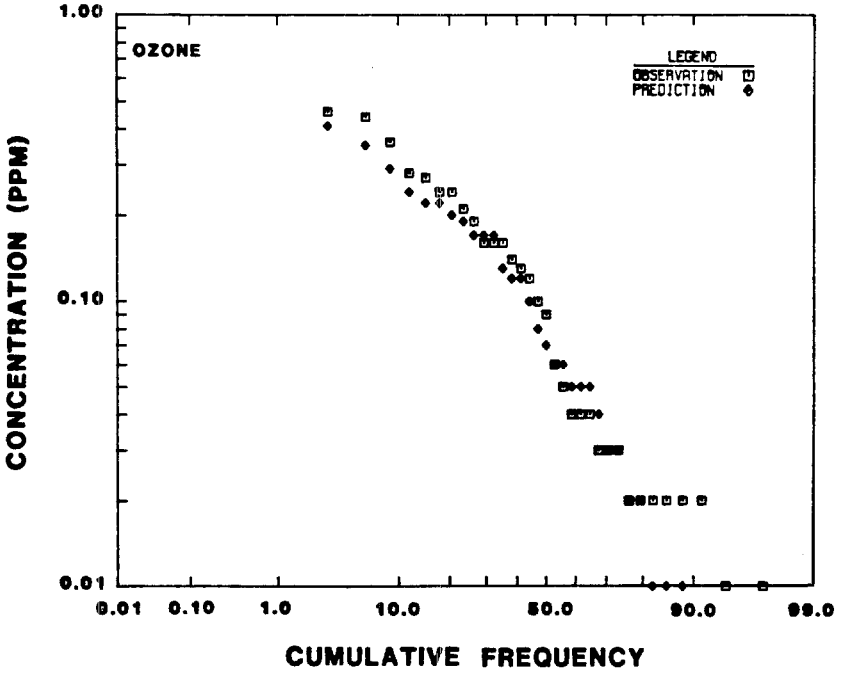

(b)

FIGURE 11.22

Frequency Distributions of Predicted and Observed Concentrations at (a) Azusa and (b) Upland

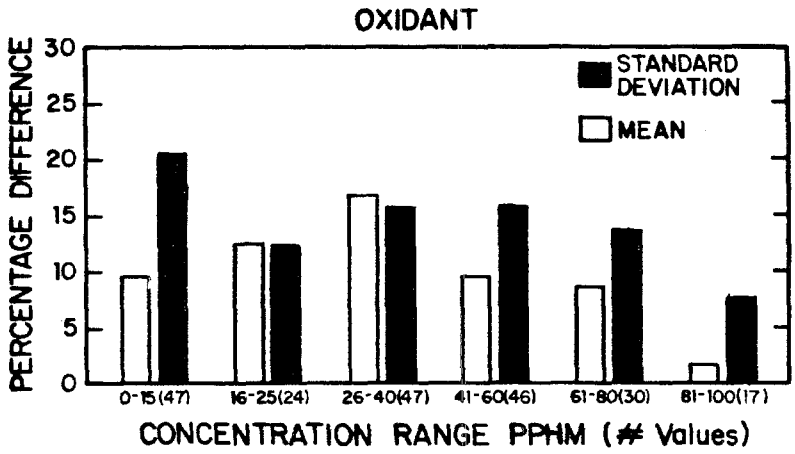

(a)

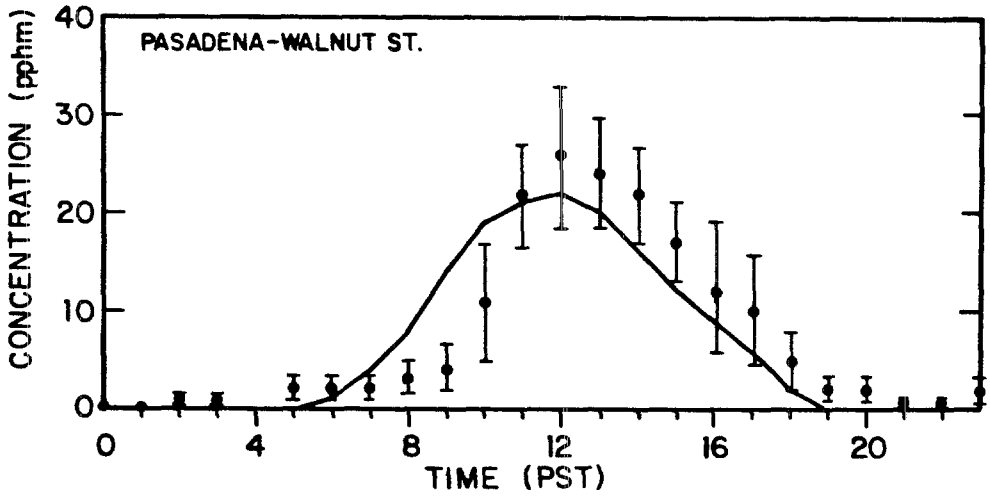

(b)

FIGURE 11.23

(a) Histogram of the Difference Between the Calibration Standards and Observed Concentrations for Oxidant Monitoring Instruments During the Period 1968-1975 (Source: Higuchi, 1981; Higuchi et al., 1976)
(b) Ozone Predictions at Pasadena Together with the $\pm 2\sigma$ Calibration Error Bounds on the Measured Air Quality. (26 June, 1974).

concentration residuals compares quite well with the errors associated with the measurements.

11.17 Conclusions

The major contribution of this research project has been the development of a mathematical model that can be used to describe urban-scale photochemical air pollution. Based on the species continuity equation the model incorporates the combined influences of advective transport, turbulent diffusion, chemical reaction, source emissions and surface removal processes. Satisfactory performance of the model has been demonstrated by comparing predicted and observed air quality over the South Coast Air Basin for the two-day period 26-27 June 1974. The calculated spatial and temporal trends of nitrogen dioxide (NO_2) and ozone (O_3) agree quite closely with routine monitoring measurements. These results and other tests indicate that the model can accurately reproduce the important features of photochemical air pollution over a major metropolitan region. While much of the testing has been performed using data available in the South Coast Air Basin, there is no reason why the model cannot be applied to evaluate air quality impacts of control strategies in other locations.

CHAPTER 12

DIRECTION FOR FUTURE RESEARCH

12.1 Introduction

Inevitably in the course of any research project, topics for future investigation become apparent. The areas identified during this project can be broadly classified into three categories: applications of the modeling methodology, further basic research and additional experimental measurements. This chapter presents a discussion of each of these topics and develops some specific recommendations for further work. Even though there is some scope for additional study this should not be interpreted as a case for forestalling applications of the present modeling system. The verification results for both the individual components as well as the system as a whole indicate that the models can satisfactorily predict the ambient concentration dynamics.

12.2 Model Applications

A major focus of this work has been the development of mathematical models that can predict the air quality impacts of changes in source emissions. Given this capability perhaps the most important question to be addressed is: how can this analysis methodology be best utilized in the design of control strategies that will achieve desired air quality objectives in a cost effective and equitable manner? There are three aspects of this question that need to be considered: the

control strategy design, its economic optimization and the relationship of the model predictions to the air quality standards.

Since the basic goal of most control programs is to achieve emissions reductions from many different sources it is important to distinguish between tactics applied to particular sources and the overall emission reduction strategy. An individual tactic T_i, is a control measure directed at a particular source or source class with the intent of reducing the amount, location or timing of emissions. Some typical control tactics might be the use of low excess air during combustion to reduce emissions of nitrogen oxides, vapor recovery during the handling of liquid hydrocarbons or catalytic reduction of vehicle exhaust gases. A control strategy S_j, on the other hand represents a composite set of tactics that, when applied to the region as a whole, produces a large reduction in emissions from many source classes. The distinction between these two aspects is illustrated in Figure 12.1 where it can easily seen that a particular control strategy is composed of many individual tactics, each of which, are responsible for a small reduction in emissions. At present the most common utilization of air quality models is to simply test the air quality impact of different strategies. One area of research that has the potential for substantially reducing the cost of air pollution control is to identify solutions that are both feasible and optimal.

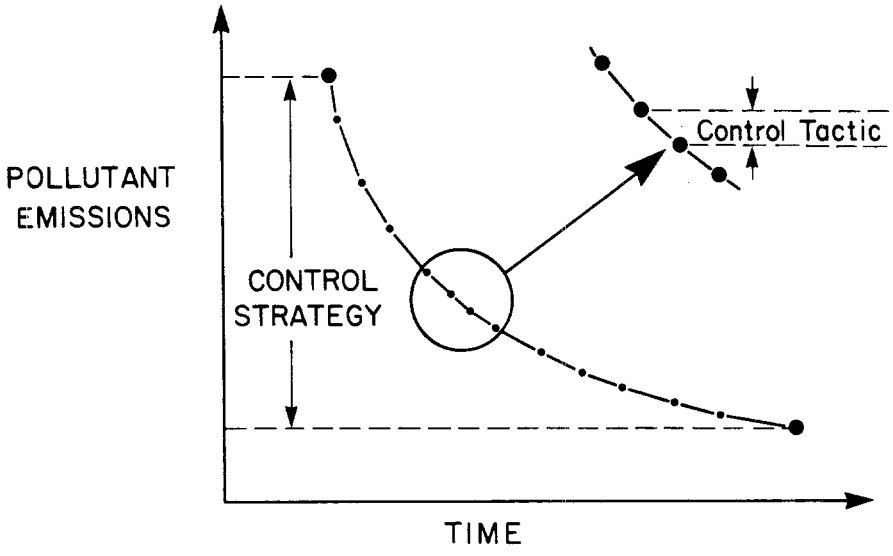

(a)

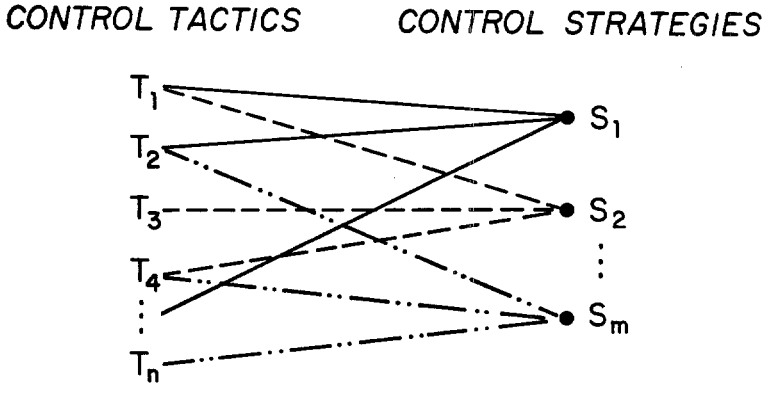

(b)

FIGURE 12.1

(a) Emission Control Strategy Composed of Particular Tactics
(b) Control Strategy Definition in Terms of Individual Tactics

The control strategy design problem can be compactly formulated as a mathematical programming problem

$$\text{select} \qquad S(\underline{T}) \tag{12.1}$$

$$\text{that minimizes} \qquad \underline{C}[S(\underline{T})] \tag{12.2}$$

$$\text{subject to} \qquad \underline{Q}\,[\underline{E}(\underline{x},t),\underline{r}(\underline{x},t),M(\underline{x},t),P] \leq \underline{Q}^S \tag{12.3}$$

This formulation is designed to select a control strategy S, composed of tactics $\underline{T} = (T_1,T_2,\ldots)$, that when applied to an emission pattern $\underline{E}(\underline{x},t)$ minimizes the objective function $\underline{C}$, subject to air quality $\underline{Q}$ at all receptor points $\underline{r}(\underline{x},t)$ within the airshed domain remaining below the desired air quality goal $\underline{Q}^S$. In most applications the objective function $\underline{C}$, represents the total cost of control, however there is no reason why a number of different objectives cannot be addressed simultaneously. Both $\underline{E} = (E_1,E_2,\ldots,E_m)$ and $\underline{Q} = (Q_1,Q_2,\ldots,Q_p)$ have been defined as vector quantities to encompass cases where there are m emission species and p different pollutants. The problem is complicated by the fact that the air quality outcome $\underline{Q}$ is a function not only of emissions but also of the meteorology M, and chemical reaction parameters, P. Other constraints, such as availability of clean fuels or technological limitations of different control techniques may also be incorporated into the formulation.

When there is a linear relation between emissions and air quality the system (12.1-12.3) can usually be stated as a set of linear equations and solved using standard linear or integer programming

techniques. Most of the applicable mathematical programming approaches are summarized in Franklin (1980), Shapiro (1979) and Wismer and Chattergy (1978). The inherently non-linear nature of oxidant formation does complicate the solution of the optimization problem. In fact most of the reported applications of photochemical models have been restricted to simply testing different emission patterns. Some procedures for estimating overall control requirements for oxidant abatement have been demonstrated using smog chamber data (Dimitriades, 1977), aerometric data analysis (Trijonis, 1974; Bilger, 1978; Post, 1979) and mathematical box models that incorporate an explicit photochemical mechanism (Whitten and Hogo, 1978; Derwent and Hov, 1980). The Trijonis study and its extension by Kyan and Seinfeld (1974) provide the only economically optimized control strategy design procedures for photochemical smog demonstrated to date. Dynamic optimization techniques that minimize the cost of attaining emission control objectives over time also have been explored. Seinfeld and Kyan (1972) and Kyan and Seinfeld (1974) have addressed the problem of attaining and maintaining compliance with air quality standards over periods of successive years. The latter study employed dynamic programming together with the empirical photochemical air quality model of Trijonis (1974). A more detailed review of these studies is presented in Cass and McRae (1981). At present there are no studies that combine the use of both advanced air quality models and economic optimization.

While air quality models are an integral element of the control strategy design process there are other aspects that must be considered. Figure 12.2 presents in a highly simplified manner the steps that need to be undertaken if an economically optimized set of emission controls are to be identified. From an inspection of this diagram it is clear that many different types of data are required. What is not apparent, and frequently ignored in practice, is that the air quality model serves as a focus for much of the data used in control strategy analyses. From a practical point of view there is a critical need for developing formal procedures and quality control checks that can be used to collate the needed information at a consistent level of detail. For example, simply assembling emissions data without giving any consideration to the economics of the associated control technologies virtually precludes identifying least cost strategies.

Most of the above discussion has focused on the use of models to design control strategies that will achieve particular air quality goals. Currently the planning efforts of regulatory agencies are directed at satisfying statuatory requirements mandated by the Clean Air Act. Most air quality standards are stated in the form of a particular air quality levels that are not to be exceeded, on an hourly basis, more than once per year. At present the resources required to use photochemical models are such that it is not feasible to model every day of the year. A critical area for future research is to determine if the current worst day design philosophy leads to strategies that will meet air quality objectives on all other days.

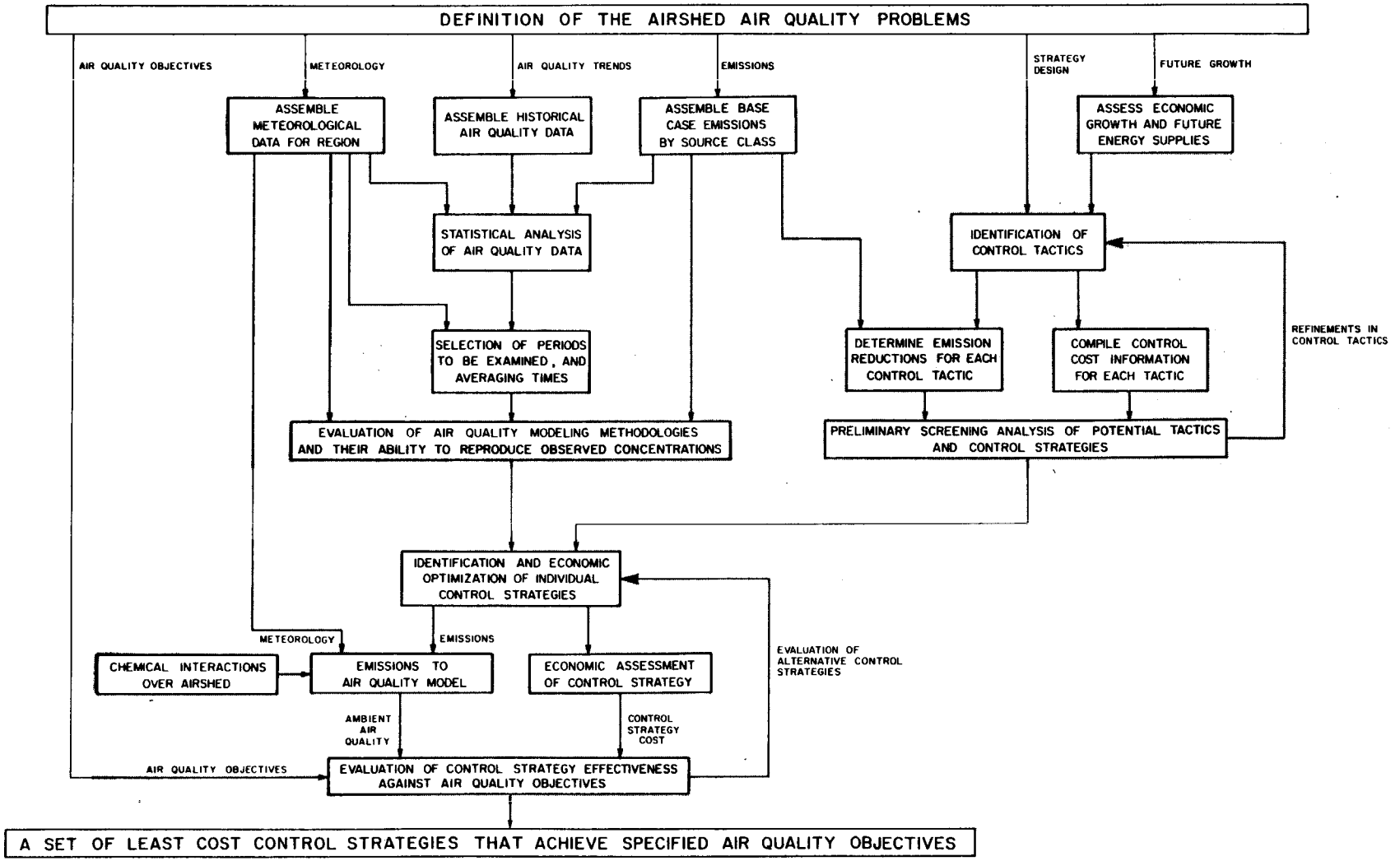

FIGURE 12.2

Detailed Elements of an Integrated Approach to Least Cost Control Strategy Design

12.3 Basic Research

During the course of this study many different research topics were identified. Since most of the potential refinements to the present modeling system have been discussed in previous chapters they will not be repeated here. (A summary of some of the more important issues is contained in Table 12.1.) Most of the current control programs are directed at reducing the concentration of those gas phase species for which there are ambient air quality standards. Two additional topics that offer considerable scope for future research are the incorporation of particulate formation processes into the model and a study of currently unregulated pollutants. Technically the most challenging is the implementation of the aerosol mechanics. The capability to predict the formation and growth of fine particulates will be an integral element of any strategy directed at improving the visibility in urban areas.

In addition to the species of regulatory interest the airshed model also predicts the concentration of many other pollutants that have known or anticipated effects on health and welfare. For example, gas phase nitric acid can react with ammonia to form particulate ammonium nitrate that in turn can have a major influence on visibility degradation. One area that deserves special attention is the feasibility of preferentially abating some of these pollutants as part of ongoing oxidant and particulate control programs.

TABLE 12.1

Summary of Areas and Questions for Additional Research

Turbulence	Chapters 2,4,5,7
Entrainment Process at Inversion Base	
Diffusive Transport Under Stable Conditions	
Cost Effective Closure Models	
Objective Analysis Procedures	3
Wind Field Generation in Remote Areas	
Applications of Remote Sensing	
A priori Generation of Mixing Heights	
Surface Removal Processes	6
Characterization of Deposition for Different Stabilities	
Surface Affinity Characterization	
Point Source Treatment	7
Dispersion Coefficients	
Procedures for Imbedding Plumes in Grid Model	
Plume Rise Calculations in Arbitarily Stratified Environments	
Chemistry	8
More Detailed Lumping Mechanism for Aromatics	
Temperature Effects on Ozone Formation	
Reactions Involving Natural Hydrocarbon Emissions	
Numerical Analysis	9,10,11
Application of Higher Derivative Methods for Chemistry	
Formulation of Filtering Schemes into Advection Algorithms	
Theoretical Treatment of Boundary Conditions	

12.4 Field and Experimental Measurements

In many areas further model development is hampered more by the paucity of measurements than by the understanding of the basic physics and chemistry. Data deficiences occur in three areas: field measurements needed to verify a chemically resolved model, source test information required for construction of emissions inventories, and experimental determination of basic chemical data. These requirements are detailed in Tables 12.2 - 12.3. While not strictly a part of a measurement program one aspect that is often ignored is a thorough assessment of the accuracy of the basic data. This consideration is particularly relevant to the emissions information. Unless the emissions data have been prepared at a level consistent with the desired accuracy of the model predictions there is little point in using air quality models. Consistency checks need to be applied to individual sources, source classes, the region as a whole and should include fuel usage patterns, operating conditions, pollutant ratios, exhaust composition and control efficiencies. One useful approach is to compare the results from top-down and bottom-up estimating procedures. These methods can provide bounds on the accuracy of emissions inventories. A formal methodology using weighted sensitivity analysis techniques is described in Ditto et al. (1976)

TABLE 12.2

SUMMARY OF METEOROLOGICAL MEASUREMENTS NEEDED FOR MODEL EVALUATION

Wind Measurements
Vertical Shear Distributions
Flow Patterns Close to Mountains (Upslope Flows)
Magnitudes of Nocturnal Drainage Flows
Quantitative Evaluation of Monitoring Site Exposure
Characterization of the Effects of Surface Roughness
Mixing Height Distribution
Increased Spatial and Temporal Resolution of Mixing Height
Effect Mixing Height Distributions Close to Mountains
Solar Radiation
Detailed Spatial and Temporal Measurements of uv Flux

TABLE 12.3

SUMMARY OF NEEDED CHEMICAL MEASUREMENTS

Concentration Measurements - General Aspects

Quantitative Evaluation of Interference Effects
Detailed Characterization of Monitoring Site Exposure
Establishment of Bounds on Measurements due to Errors and Averaging
Improved Resolution of Vertical Concentration Distributions
Routine Measurements of Certain Non Criteria Pollutants

Hydrocarbon Measurements

Spatial and Temporal Variations of Hydrocarbon Reactivities
Characterization of Aldehydes and Natural Hydrocarbons
Need for Increased Species Resolution Beyond THC-RHC-CH_4

Background Air Quality

Values Away From Urban Region
Vertical Profiles of Ozone
Hydrocarbon Concentration and Composition
Concentration of NO, NO_2 and O_3

Source Profiles and Emission Factors

Detailed Emissions Distributions From Mobile Sources
Chemical Composition and Solvent Utilization by Industries
Extent and Magnitude of Emissions from Gasoline Evaporation
Industrial Fuel Usage Patterns
Improved Characterization of Emissions from Area Sources

12.5 Conclusions

In this chapter many suggestions have been made for future refinements and the need for additional experimental measurements. Given the present state of model development, perhaps the greatest need is not for basic research, but rather for the application of these new tools to the design of cost-effective and equitable control strategies.

CHAPTER 13

SUMMARY AND CONCLUSIONS

The major contribution of this work has been the formulation and computational implementation of a mathematical description of urban scale photochemical air pollution. Based on the species continuity equation, the modeling system incorporates the combined influences of advective transport, turbulent diffusion, chemical reactions, source emissions and surface removal processes. Given the potential for widespread utilization of these models careful attention has been given to delineating the assumptions underlying the valid applications of: three-dimensional, Lagrangian trajectory, vertically integrated and single cell air quality models.

While the mathematical formulation of the modeling system contains no regional or area specific information performance, evaluation studies were carried out using data measured in the South Coast Air Basin of Southern California. Detailed emissions and meteorological information were assembled for the period 26-28 June 1974. A comparison between calculated and observed air quality indicates that the models can satisfactorily describe urban scale atmospheric concentration dynamics. The results of these and other tests indicate that the models are now in a form that they can be used to predict the air quality impacts of alternative control measures.

APPENDIX A

KINETIC RATE EQUATIONS AND STEADY STATE APPROXIMATIONS

This appendix documents the differential and algebraic forms of the equations used to describe the kinetics of the chemical mechanism presented in Chapter 8. The notation has been chosen to simplify the implementation of the computational solution procedures. The forward reaction rates $\underset{\sim}{r}_i$; i=1,2,...,m for the interactions between the c_i; i=1,...,p species shown in Table 8.1 - 8.2 are given by

```
R1  = K( 1)*NO2              R27 = K(27)*C2H4*O
R2  = K( 2)*O*O2*M           R28 = K(28)*OLE*OH
R3  = K( 3)*NO*O3            R29 = K(29)*OLE*O
R4  = K( 4)*NO2*O            R30 = K(30)*O3*OLE
R5  = K( 5)*NO*O             R31 = K(31)*ALK*OH
R6  = K( 6)*NO2*O            R32 = K(32)*ALK*O
R7  = K( 7)*NO2*O3           R33 = K(33)*ARO*OH
R8  = K( 8)*NO*NO3           R34 = K(34)*RO
R9  = K( 9)*NO*OH            R35 = K(35)*RONO
R10 = K(10)*HNO2             R36 = K(36)*NO*RO
R11 = K(11)*NO2*HO2          R37 = K(37)*NO2*RO
R12 = K(12)*HNO2*OH          R38 = K(38)*NO2*RO
R13 = K(13)*NO2*HO2          R39 = K(39)*NO2*RO2          (A.1)
R14 = K(14)*HNO4             R40 = K(40)*NO2*RO2
R15 = K(15)*NO*HO2           R41 = K(41)*RNO4
R16 = K(16)*NO*RO2           R42 = K(42)*NO2*RCO3
R17 = K(17)*NO*RCO3          R43 = K(43)*PAN
R18 = K(18)*NO2*OH           R44 = K(44)*NO2*NO3
R19 = K(19)*OH*CO            R45 = K(45)*N2O5
R20 = K(20)*O3               R46 = K(46)*N2O5*H2O
R21 = K(21)*HCHO             R47 = K(47)*O3*OH
R22 = K(22)*HCHO             R48 = K(48)*O3*HO2
R23 = K(23)*HCHO*OH          R49 = K(49)*O3
R24 = K(24)*RCHO             R50 = K(50)*HO2**2
R25 = K(25)*RCHO*OH          R51 = K(51)*H2O2
R26 = K(26)*C2H4*OH          R52 = K(52)*RO2**2
```

where K(i);i=1,...,m are the reaction rate constants.

Using the procedures presented in Chapter 11 it is possible to partition the concentration vector $\underset{\sim}{c}$ into two components $(\underset{\sim}{c}_d | \underset{\sim}{c}_s)$ where the species $\underset{\sim}{c}_d$ are described by differential forms and $\underset{\sim}{c}_s$ by algebraic equations. Given (A.1) the reaction set kinetics are of the form

$$\frac{d\,\underset{\sim}{c}_d}{dt} = \underset{\sim}{F}(\underset{\sim}{c}_d, \underset{\sim}{c}_s) \tag{A.2}$$

The differential equations for the individual species are given by

```
F(NO)   = +R1-R3+R4-R5-R8-R9+R10-R15-R16-R17+R35-R36                    (A.3)

F(NO2)  = -R1+R3-R4+R5-R6-R7+2*R8-R11+R12-R13+R14+R15+R16               (A.4)
          +R17-R18-R37-R38-R39-R40+R41-R42+R43-R44+R45

F(O3)   = +R2-R3-R7-R20-R30-R47-R48-R49                                 (A.5)

F(HCHO) = -R21-R22-R23+A2*R30+B2*R34                                    (A.6)

F(RCHO) = -R24-R25+A1*R30+R33+A3*R34+R38+R40                            (A.7)

F(OLE)  = -R28-R29-R30                                                  (A.8)

F(ALK)  = -R31-R32                                                      (A.9)

F(ARO)  = -R33                                                          (A.10)

F(C2H4) = -R26-R27                                                      (A.11)

F(CO)   = -R19+R21+R22+R23+R24                                          (A.12)

F(H2O2) = +R50-R51                                                      (A.13)

F(PAN)  = +R42-R43                                                      (A.14)

F(HNO2) = +R9-R10+R11-R12+R38                                           (A.15)

F(RONO) = -R35+R36                                                      (A.16)

F(RNO4) = +R39-R41                                                      (A.17)
```

The coefficients A1-A6, B1-B3 are defined in Chapter 8.

Some species react sufficiently fast enough that their production and decay rates are approximately equal. Under these conditions it is possible to replace the differential equations by non-linear, implicit algebraic expressions of the general form

$$\underset{\sim}{F}(\underset{\sim}{c}_d, \underset{\sim}{c}_s) = 0 \tag{A.18}$$

The equations which arise for each species are given by

$$F(O) = 0 = +R1-R2-R4-R5-R6+R20-R27-R29-R32 \tag{A.19}$$

$$F(RO) = 0 = +R16+A6*R30-R34+R35-R36-R37-R38+2*R52 \tag{A.20}$$

$$F(OH) = 0 = -R9+R10-R12+R15-R18-R19-R23-R25-R26-R28 +A5*R30-R31+R32-R33-R47+R48+2*R51 \tag{A.21}$$

$$F(NO3) = 0 = +R6+R7-R8-R44+R45 \tag{A.22}$$

$$F(RO2) = 0 = -R16+R17+R24+R26+R27+R28+R29+A4*R30+R31 +R32+R33+(1-B1)*M*R34-R39-R40+R41-2*R52 \tag{A.23}$$

$$F(HO2) = 0 = -R11-R13+R14-R15+R19+2*R21+R23+R24 +R27+A3*R30+B1*R34+R47-R48-2*R50 \tag{A.24}$$

$$F(RCO3) = 0 = -R17+R25+R29-R42+R43 \tag{A.25}$$

$$F(N2O5) = 0 = +R44-R45-R46 \tag{A.26}$$

$$F(HNO4) = 0 = +R13-R14 \tag{A.27}$$

From a computational point of view it is desirable to avoid situations which involve solutions of implicit non-linear systems. Under some conditions it is possible to replace (A.18) by the explicit form

$$\underset{\sim}{c}_s = \underline{G}(\underset{\sim}{c}_d) \tag{A.28}$$

For the system (A.19 - A.27) a solution can be obtained from a series of successive eliminations.

Atomic oxygen can be determined directly from (A.19) as

$$O = (K(1)*NO2+K(20)*O3)/(K(2)*O2*M+K(4)*NO2+K(5)*NO +K(6)*NO2+K(27)*C2H4+K(29)*OLE+K(32)*ALK) \quad (A.29)$$

NO3 and N2O5 can be found from a simultaneous solution of the system defined by (A.22) and (A.26) i.e.

$$Y1(NO3) + Y2(N2O5) = Y3 \quad (A.30)$$

$$Y4(NO3) + Y5(N2O5) = 0 \quad (A.31)$$

where

$$Y1 = -(K(8)*NO+K(44)*NO2) \quad (A.32)$$

$$Y2 = K(45) \quad (A.33)$$

$$Y3 = -(K(6)*NO2*O+K(7)*NO2*O3) \quad (A.34)$$

$$Y4 = K(44)*NO2 \quad (A.35)$$

$$Y5 = -(K(45)+K(46)*H2O) \quad (A.36)$$

Given these coefficients the solutions for NO3 and N2O5 are

$$NO3 = Y3*Y5/(Y1*Y5-Y2*Y4) \quad (A.37)$$

$$N2O5 = -Y4*NO3/Y5 \quad (A.38)$$

For the other species the algebraic expressions can be written as

$$0 = X1 + X2(OH) + X3(RCO3) \quad (A.39)$$

$$0 = X4 + [X5 + X6(RO2)](RO2) + X7(RO) \quad (A.40)$$

$$0 = X8 + X9(OH) + X10(RO) + [X11 + X12(HO2)](HO2) \quad (A.41)$$

$$0 = X13 + X14(HO2) + X15(OH) \quad (A.42)$$

$$0 = X16 + X17(RCO3) + X18(OH) + [X19 + X20(RO2)](RO2) + X21(RO) \quad (A.43)$$

The coefficients X1 - X21 in (A.39 - A.41) are given by

RCO3

$$X1 = K(29)*OLE*O+K(43)*PAN \quad (A.44)$$

$$X2 = K(25)*RCHO \quad (A.45)$$

$$X3 = -(K(17)*NO+K(42)*NO2) \quad (A.46)$$

RO

$$X4 = A6*K(30)*O3*OLE+K(35)*RONO \quad (A.47)$$

$$X5 = K(16)*NO \quad (A.48)$$

$$X6 = 2*K(52) \quad (A.49)$$

$$X7 = -(K(34)+K(36)*NO+K(37)*NO2+K(38)*NO2) \quad (A.50)$$

HO2

$$X8 = 2*K(21)*HCHO+K(24)*RCHO+K(27)*C2H4*O+ A3*K(30)*O3*OLE \quad (A.51)$$

$$X9 = K(19)*CO+K(23)*HCHO+K(47)*O3 \quad (A.52)$$

$$X10 = B1*K(34) \quad (A.53)$$

$$X11 = -(K(11)*NO2+K(13)*NO2+K(15)*NO+K(48)*O3) + K(13)*NO2 \quad (A.54)$$

$$X12 = -2.0*K(50) \quad (A.55)$$

OH

$$X13 = K(10)*HNO2+A5*K(30)*O3*OLE+K(32)*ALK*O+2*K(51)*H2O2 \quad (A.56)$$

$$X14 = K(15)*NO+K(48)*O3 \quad (A.57)$$

$$X15 = -(K(9)*NO+K(12)*HNO2+K(18)*NO2+K(19)*CO+ K(23)*HCHO+K(25)*RCHO+K(26)*C2H4+K(28)*OLE+ K(31)*ALK+K(33)*ARO+K(47)*O3) \quad (A.58)$$

RO2

$$X16 = K(24)*RCHO+K(27)*C2H4*O+K(29)*OLE*O+ A4*K(30)*O3*OLE+K(32)*ALK*O+K(41)*RNO4 \quad (A.59)$$

$$X17 = K(17)*NO \quad (A.60)$$

```
X18 =  K(26)*C2H4+K(28)*OLE+K(31)*ALK+K(33)*ARO          (A.61)

X19 = -(K(16)*NO+K(39)*NO2+K(40)*NO2)                    (A.62)

X20 = -2.0*K(52)                                         (A.63)

X21 =  (1-B1)*M*K(34)                                    (A.64)
```

After considerable algebraic manipulation it is possible to develop a quadratic expression for HO2 of the form

```
D1*HO2**2 + D2*HO2 + D3 = 0                              (A.65)
```

where the coefficients D1-D3 are given by

```
D3 =  X8+GG*X10-X9*X13/X15                               (A.66)

D2 =  X11+EE*X10*X14/X15-X9*X14/X15                      (A.67)

D1 =  X12                                                (A.68)
```

and the intermediate terms by

```
DD =  1.0/(X7*X19-X5*X21)                                (A.69)

FF =  DD*(X5*X16-X4*X19-X1*X5*X17/X3)                    (A.70)

EE =  DD*(X2*X5*X17/X3-X5*X18)                           (A.71)

GG =  FF + EE*X13/X15                                    (A.72)
```

The solution of the quadratic is given by

```
HO2  =  (-D2-SQRT(D2*D2-4*D1*D3))/(2*D1)                 (A.73)
```

Once HO2 is available then the other steady state species are given by

```
OH   = -(X13+X14*HO2)/X15                                (A.74)

RCO3 = -(X1+X2*OH)/X3                                    (A.75)

RO   = -(X8+X9*OH+(X11+X12*HO2)*HO2)/X10                 (A.76)

RO2  = -(X4+X7*RO)/X5                                    (A.77)
```

$$HNO4 = K(13)*NO2*HO2/K(14) \quad (A.78)$$

In some case there may be no NO_x present in the system, when this occurs the following reduced set of steady state expressions can be applied

$$OH = -X13/X15 \quad (A.79)$$

$$RO2 = SQRT(-(X16+X18*OH)/X20) \quad (A.80)$$

$$RO = -(X4+X6*RO2*RO2)/X7 \quad (A.81)$$

$$HO2 = SQRT(-(X8+X9*OH+X10*RO)/X12) \quad (A.82)$$

$$NO3 = N2O5 = RCO3 = HNO4 = 0 \quad (A.83)$$

Considerable care must be exercised during the computational implementation of the above expressions because various terms involve small differences between large quantities. The remaining species {O2,H2O,M} are treated as being constant during a time step and are supplied externally.

APPENDIX B

A LINEAR FINITE ELEMENT SOLUTION OF THE CONSERVATIVE FORM OF THE ADVECTION EQUATION

B.1 Introduction

Finite element methods, as a class, are an increasingly popular approach for numerical solution of fluid flow problems. They are particularly attractive because of their high accuracy and, more importantly, the ease with which boundary conditions can be handled. This appendix is devoted to a detailed derivation of the finite element algorithm employed in Chapter 10 where, as part of the splitting sequence, it was necessary to solve the first order hyperbolic problem (B.1).

$$\frac{\partial u}{\partial t} + Lu = 0 \tag{B.1}$$

Specifically in atmospheric flows (B.1) is associated with the scalar advection equation which is given by

$$\frac{\partial c}{\partial t} + \frac{\partial uc}{\partial x} = 0 \tag{B.2}$$

In (B.2) $c(x,t)$ is the non-negative concentration field and $u(x,t)$ the advective velocity. This appendix extends the recent work of Pepper et al. (1979) which presents a finite element model for the more restrictive nonconservative form of (B.2).

B.2 Galerkin Formulation

A common approach to solve the hyperbolic problem (B.1) is to form the Galerkin equation using finite elements in space (Strang and Fix, 1973; Finlayson, 1972). With this technique approximations to the concentration and velocity fields C(x,t), U(x,t) are expressed in terms of time varying coefficients $\alpha_i(t)$, $\beta_j(t)$ and piecewise continuous basis function $\phi_i(x)$, i.e.

$$c(x,t) \simeq C(x,t) = \sum_{i=1}^{n} \alpha_i(t)\, \phi_i(x) \tag{B.3}$$

$$u(x,t) \simeq U(x,t) = \sum_{i=1}^{n} \beta_i(t)\, \phi_i(x) \tag{B.4}$$

where

$$\phi_i(x) = \begin{cases} \dfrac{x-x_{i-1}}{x_i-x_{i-1}} & ; \quad x_{i-1} \leq x \leq x_i \\ \dfrac{x_{i+1}-x}{x_{i+1}-x_i} & ; \quad x_i \leq x \leq x_{i+1} \\ 0 & ; \quad x < x_{i-1} \text{ or } x > x_{i+1} \end{cases} \tag{B.5}$$

Equation (B.5) describes a set of linear basis function which are sometimes called Chapeau functions because of their similarity to hatlike shapes. The form of these functions is illustrated in Figure B.1. Other basis functions which vanish outside the interval $[x_{i-1}, x_{x+1}]$ are described in Strang and Fix (1973), Connor and Brebbia (1977).

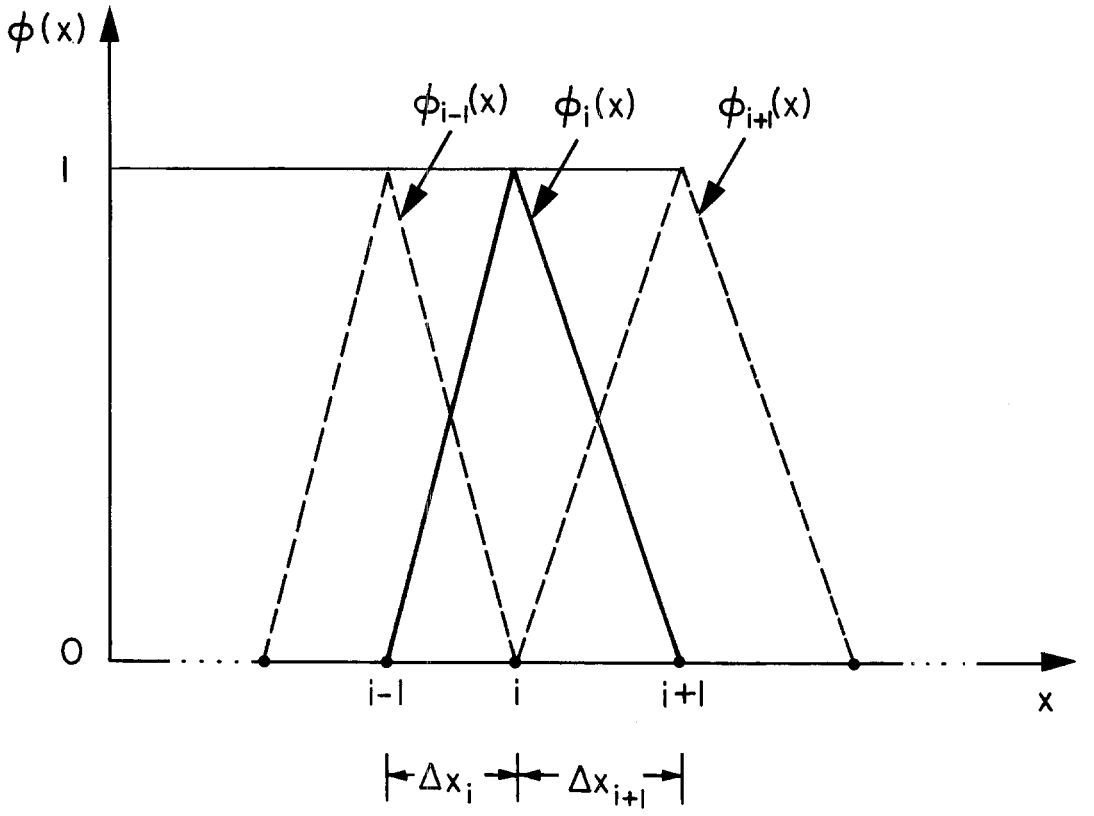

Figure B.1

Linear Basis Functions for Galerkin
Finite Element Model

Using the functions described by (B.3) and (B.4) the Galerkin method requires that for all ϕ_i

$$\left\langle \phi_i, \left\{ \frac{\partial \alpha_j \phi_j}{\partial t} + \frac{\partial}{\partial x} (\beta_k \phi_k \alpha_j \phi_j) \right\} \right\rangle = 0 \qquad \text{(B.6)}$$

Galerkins's method is a particular weighted residual scheme in which the weighting functions are the same as the trial functions (Finlayson, 1972). By expanding the inner product (B.6) the following set of ordinary differential equations in the dependent variable $\alpha_j(t)$ can be derived

$$M_{ij} \frac{d\,\alpha_j(t)}{dt} + \beta_k(t) N_{ijk}\, \alpha_j(t) = 0 \qquad \text{(B.7)}$$

where

$$M_{ij} = \int \phi_i(x)\phi_j(x)dx \qquad \text{(B.8)}$$

$$N_{ijk} = \int \left[\phi_i(x)\phi_j(x) \frac{\partial \phi_k(x)}{\partial x} + \phi_i(x)\, \phi_k(x) \frac{\partial \phi_j(x)}{\partial x} \right] dx \qquad \text{(B.9)}$$

Since $\phi_i(x)$ vanishes outside the interval $[x_{i-1}, x_{i+1}]$ there will be three integrals associated with M_{ij} and nine with N_{ijk} for a typical set of points i-1, i and i+1, i.e.

$$M_{i,i-1} \qquad M_{i,i} \qquad M_{i,i+1}$$

$$N_{i,i-1,i-1} \qquad N_{i,i-1,i} \qquad N_{i,i-1,i+1}$$

$$N_{i,i,i-1} \qquad N_{i,i,i} \qquad N_{i,i,i+1}$$

$$N_{i,i+1,i-1} \qquad N_{i,i+1} \qquad N_{i,i+1,i+1}$$

The integrations are quite straightforward and to illustrate the process consider some typical terms, for example $M_{i,i+1}$

$$M_{i,i+1} = \int_{x_{i-1}}^{x_{i+1}} \phi_i(x)\ \phi_{i+1}(x)\,dx \tag{B.10}$$

$$= \int_{x_{i-1}}^{x_i} \phi_i\phi_{i+1}\,dx + \int_{x_i}^{x_{i+1}} \phi_i\phi_{i+1}\,dx \tag{B.11}$$

Since $\phi_{i+1}(x) = 0$ for $x < x_i$ (B.11) can be written in the form

$$M_{i,i+1} = \int_{x_i}^{x_{i+1}} \left[\frac{x-x_i}{x_{i+1}-x_i}\right]\left[\frac{x_{i+1}-x}{x_{i+1}-x_i}\right] dx = \frac{x_{i+1} - x_i}{6} \tag{B.12}$$

Similarly $N_{i,i,i}$ is given by

$$N_{i,i,i} = \int_{x_{i-1}}^{x_{i+1}} 2\phi_i^{\,2}(x)\ \frac{\partial\phi_i(x)}{\partial x}\ dx = 0 \tag{B.13}$$

After all the terms have been evaluated the governing set of ordinary differential equations is given by

$$\frac{d}{dt}\left[(x_{i+1}-x_i)\,\alpha_{i+1} + 2(x_{i+1}-x_{i-1})\alpha_i + (x_i-x_{i-1})\alpha_{i-1}\right]$$

$$+ (2\beta_{i+1} + \beta_i)\alpha_{i+1} + (\beta_{i+1}-\beta_{i-1})\alpha_i - (2\beta_{i-1}+\beta_i)\alpha_{i-1} = 0 \quad \text{(B.14)}$$

Various simplifications are possible; consider for example the case of constant grid spacing in which $\Delta x = x_{i+1} - x_i = x_i - x_{i-1}$. For this situation (B.14) reduces to

$$\frac{d}{dt}\left[\alpha_{i+1} + 4\alpha_i + \alpha_{i-1}\right] + \frac{1}{\Delta x}\left[(2\beta_{i+1} + \beta_i)\alpha_{i+1} + (\beta_{i+1}-\beta_{i-1})\alpha_i\right. \quad \text{(B.15)}$$

$$\left. - (2\beta_{i-1} + \beta_i)\alpha_{i-1}\right] = 0$$

If the velocity $u(x,t)$ is uniform, then (B.15) simplifies still further to

$$\frac{d}{dt}\left[\alpha_{i+1} + 4\alpha_i + \alpha_{i-1}\right] + \frac{3u}{\Delta x}\left[\alpha_{i+1} - \alpha_{i-1}\right] = 0 \quad \text{(B.16)}$$

Time integration of the difference - differential equations can be accomplished by standard methods. For example, the classic Crank-Nicholson $O(\Delta t^2)$ scheme when applied to (B.15) gives

$$\frac{1}{\Delta t}\left[(\alpha_{i+1}^{k+1} - \alpha_{i+1}^{k}) + 4(\alpha_i^{k+1} - \alpha_i^{k}) + (\alpha_{i-1}^{k+1} - \alpha_{i-1}^{k})\right] = \quad \text{(B.17)}$$

$$\frac{1}{2\Delta x}\left[(\beta_i + 2\beta_{i+1})(\alpha_{i+1}^{k+1} + \alpha_{i+1}^{k}) + (\beta_{i+1} - \beta_{i-1})(\alpha_i^{k+1} + \alpha_i^{k}) - (\beta_i + 2\beta_{i-1})\right.$$

$$\left.(\alpha_{i-1}^{k+1} + \alpha_{i-1}^{k})\right]$$

This system of tridiagonal equations can be readily solved using the Thomas algorithm (Roache, 1976). A discussion of the stability and convergence of the finite element approximation is contained in Chapter 10 and for this reason will not be repeated here.

APPENDIX C

GRAPHICAL DISPLAY OF OBSERVED AND PREDICTED AIR QUALITY FOR THE TWO-DAY PERIOD 26-27 JUNE 1974

This appendix presents the calculated and observed levels of ozone (O_3) and nitrogen dioxide (NO_2) at monitoring sites within the South Coast Air Basin. The spatial distribution of measurement stations is shown in Figure C.1. Within the computational region defined by Figure C.2 each station can be located by using the coordinates presented in Table C.1. The station names, codes and locations correspond to those used by local air pollution agencies in June 1974.

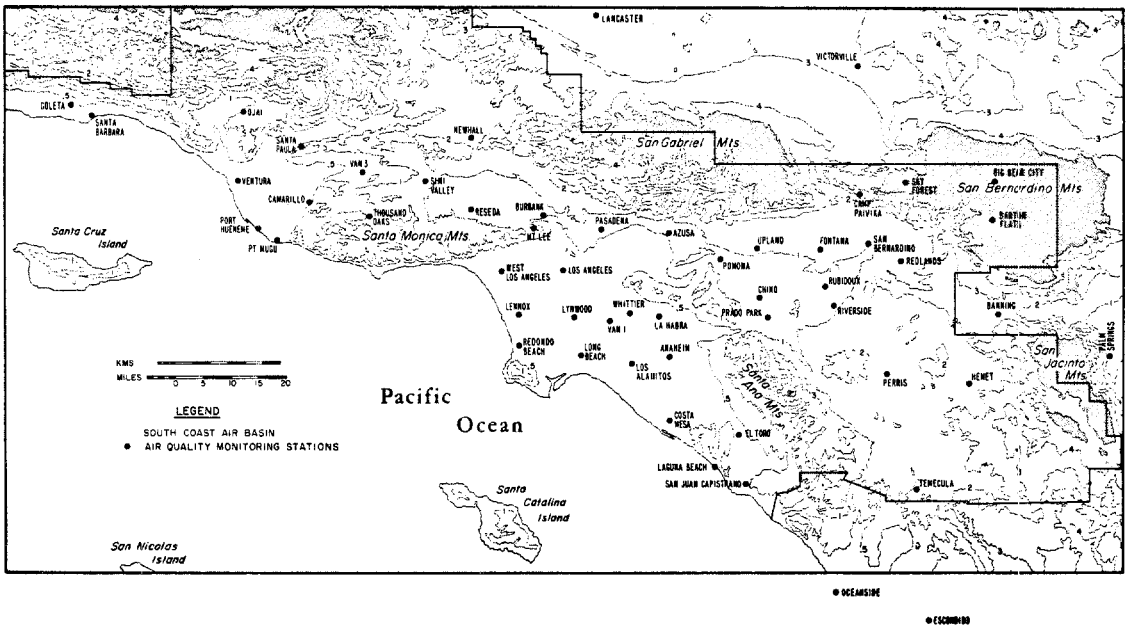

FIGURE C.1

Location of Air Quality Monitoring Sites
within the South Coast Air Basin

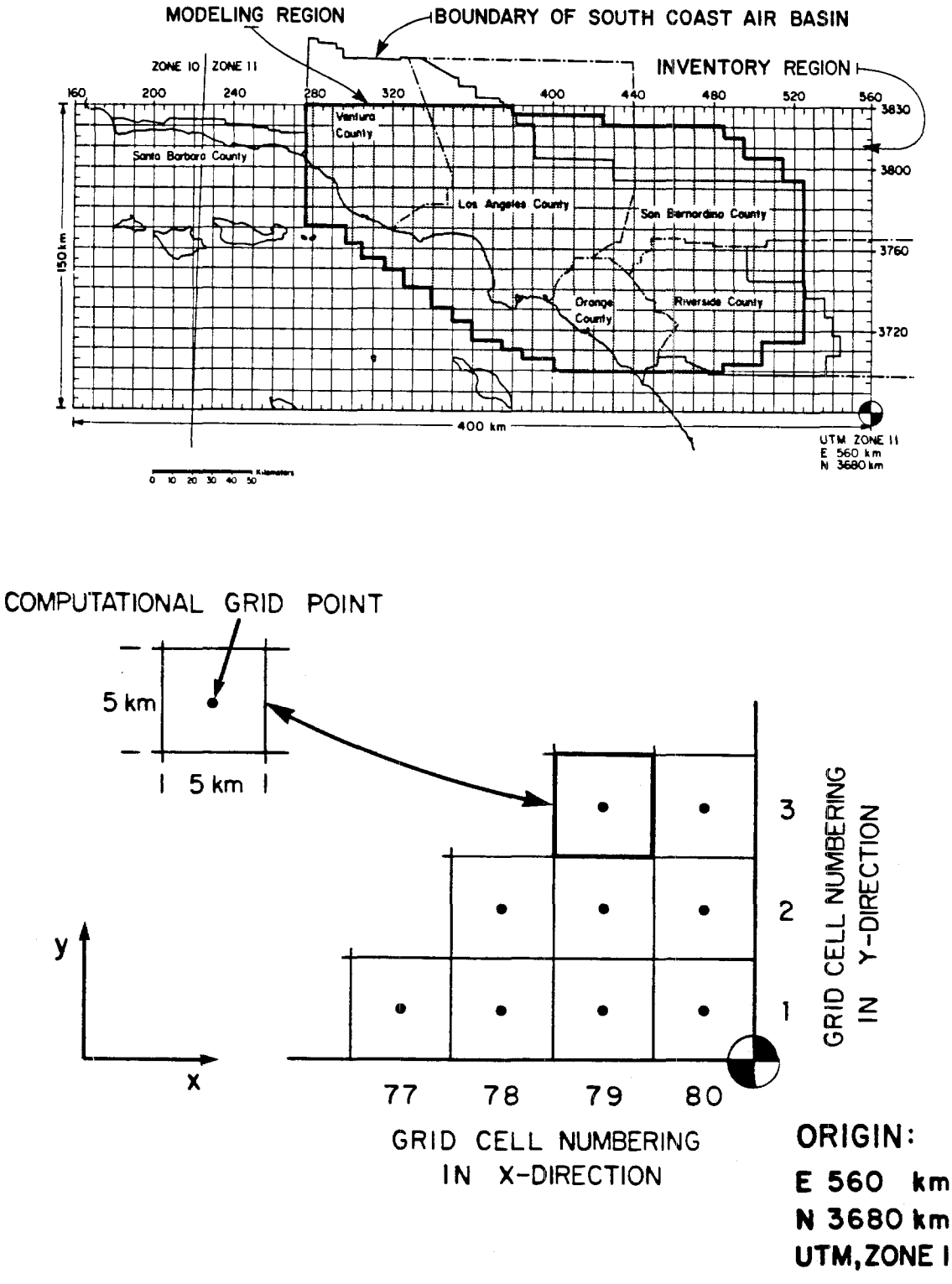

FIGURE C.2

Definition of the Origin of the Computational Grid System

TABLE C.1

Air Quality Monitoring Sites Used in Statistical Analysis of Model Results for 26-27 June 1974

STATION[(a)] CODE	MONITORING STATION	GRID COORDINATES (x,y)	
30176	Anaheim	51.0	12.5
30177	La Habra	50.4	14.8
30190	Los Alamitos-Orangewood Ave	48.8	12.1
33140	Norco-Prado Park	56.8	14.7
33144	Riverside-Rubidoux	60.1	16.5
33146	Riverside-Magnolia Ave	60.4	15.3
36151	San Bernardino	62.6	18.8
36173	Chino-Riverside Ave	56.3	15.8
36174	Upland-Civic Center	56.1	18.7
36175	Upland ARB	56.5	18.8
36176	Fontana-Foothill Blvd	59.8	18.5
36191	Camp Paivika-USFS	62.5	21.9
56408	Camarillo-Palm	30.6	21.6
56409	Point Mugu	28.7	19.6
56412	Port Hueneme	27.6	20.1
56413	Simi Valley	37.2	22.6
56414	Ventura-Telegraph Rd	26.6	22.8
56415	Thousand Oaks-Windsor Dr	34.0	20.7
70001	Los Angeles-Downtown	45.0	17.4
70060	Azusa	51.4	19.6
70069	Burbank	43.9	20.6
70071	West Los Angeles	41.5	17.5
70072	Long Beach	46.0	12.6
70075	Pomona	54.0	18.0
70076	Lennox	42.6	15.0
70078	Redondo Beach	42.4	13.2
70080	Whittier	48.7	15.0
70083	Pasadena-Walnut St	47.2	19.7
70084	Lynwood	45.6	14.8
70406	Mt Lee Dr-Mobile Van	43.3	19.5
70585	Van1-105 Frwy (Prop)	47.6	14.6

Notes:

(a) California Air Resources Board Code Number

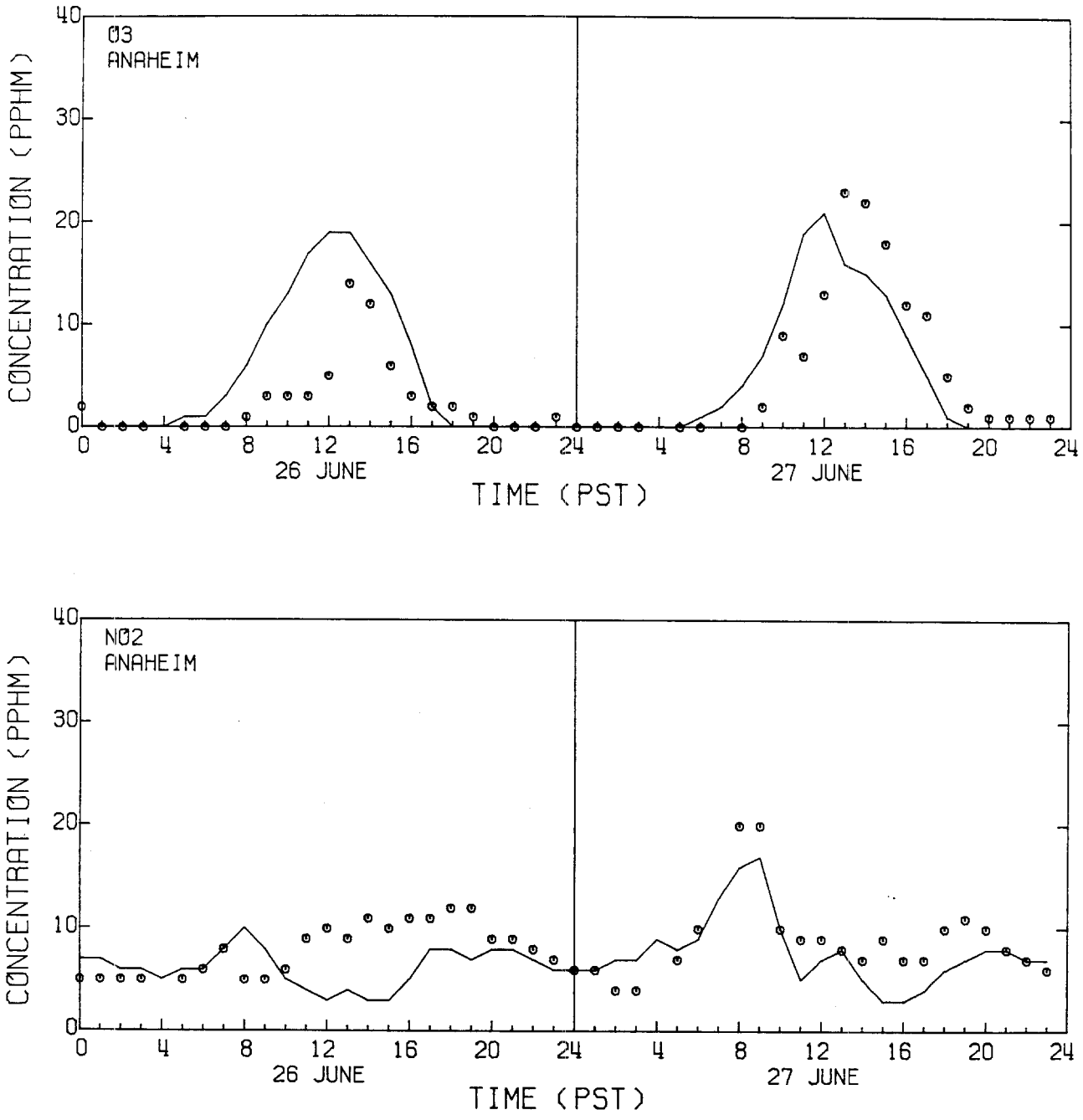

FIGURE C.4

Measured (o) and Predicted (-) Ozone and Nitrogen Dioxide Air Quality at Anaheim

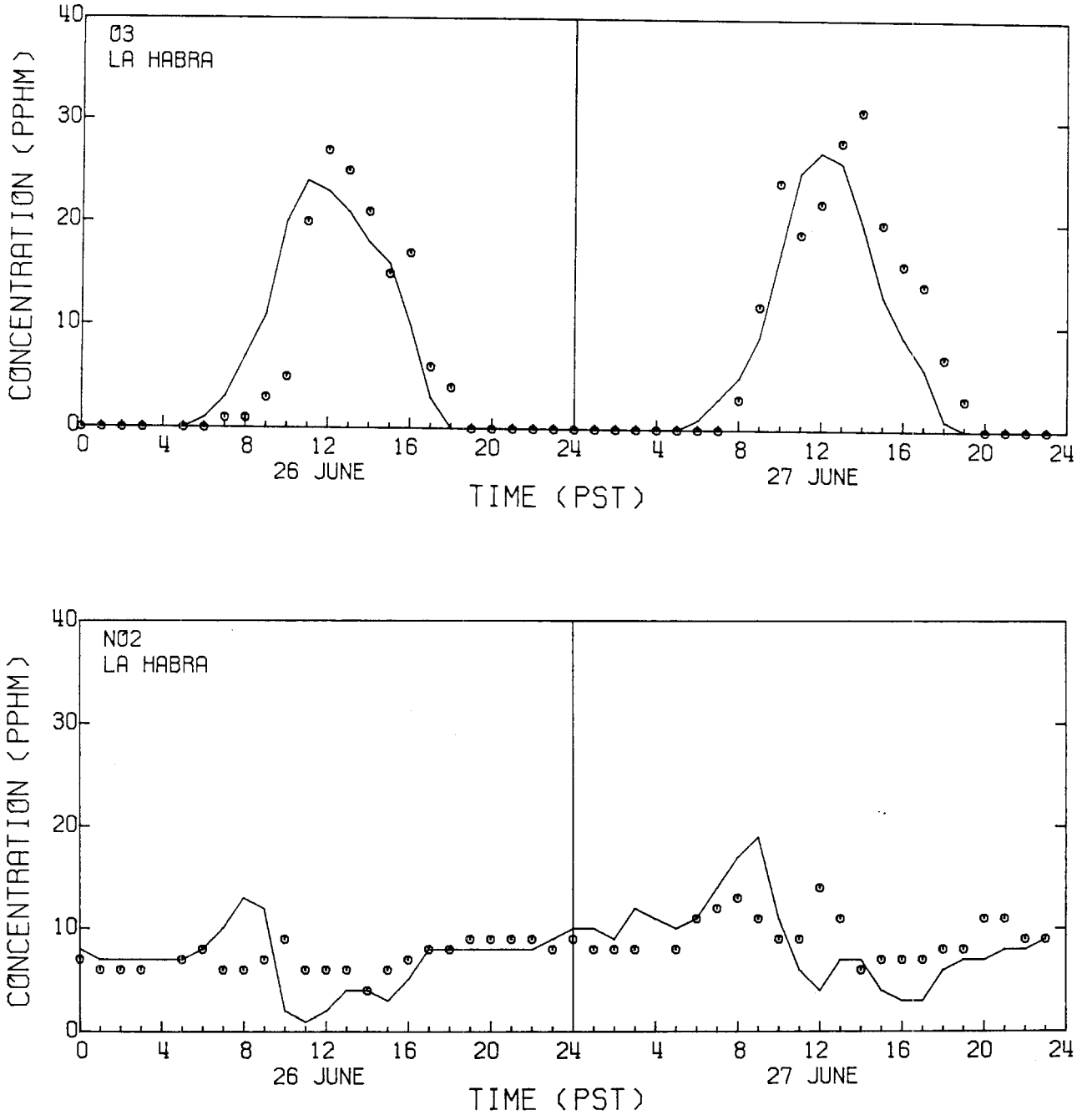

FIGURE C.5

Measured (o) and Predicted (-) Ozone and Nitrogen Dioxide
Air Quality at La Habra

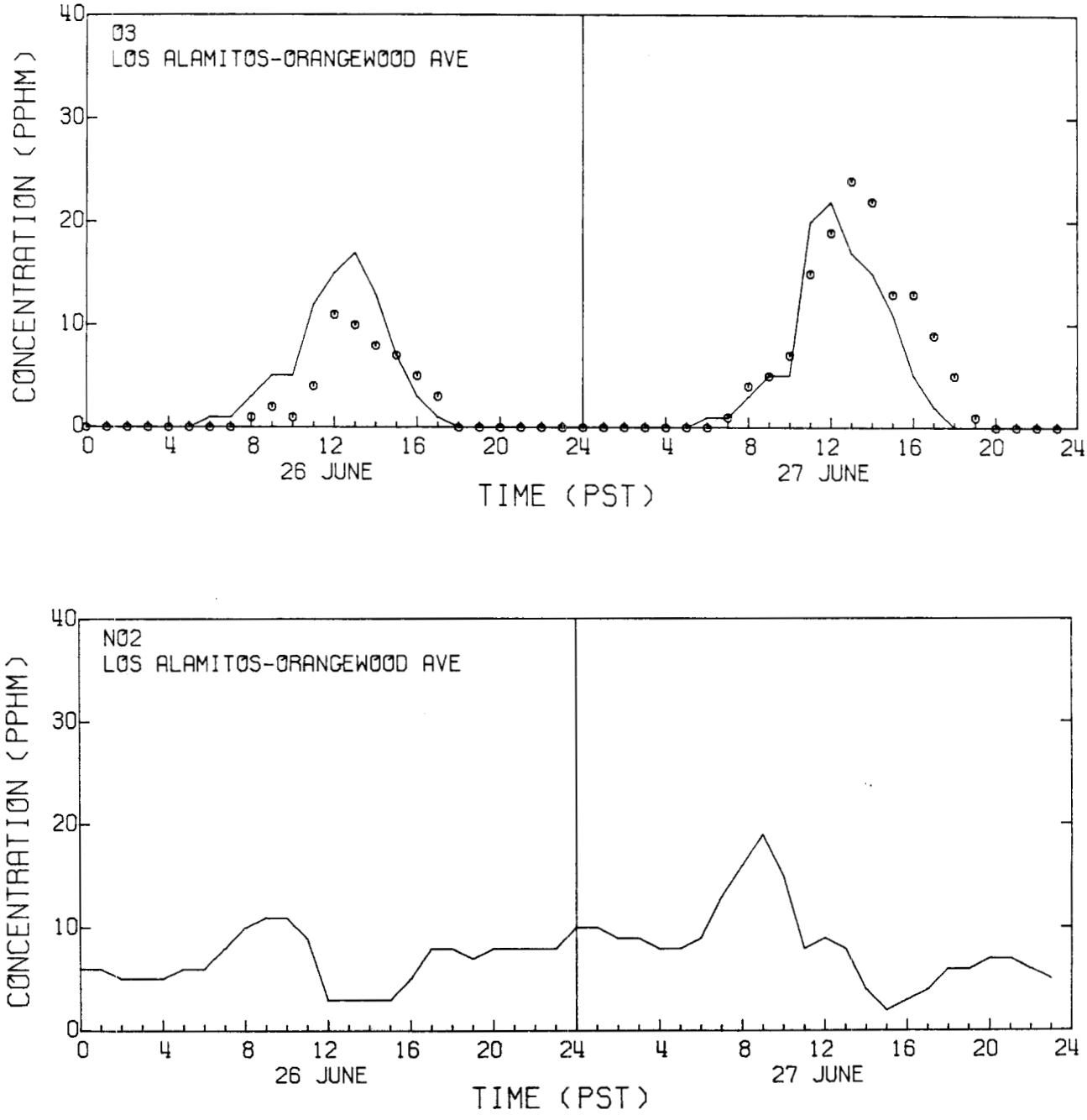

FIGURE C.6

Measured (o) and Predicted (-) Ozone and Nitrogen Dioxide
Air Quality at Los Alamitos-Orangewood Avenue

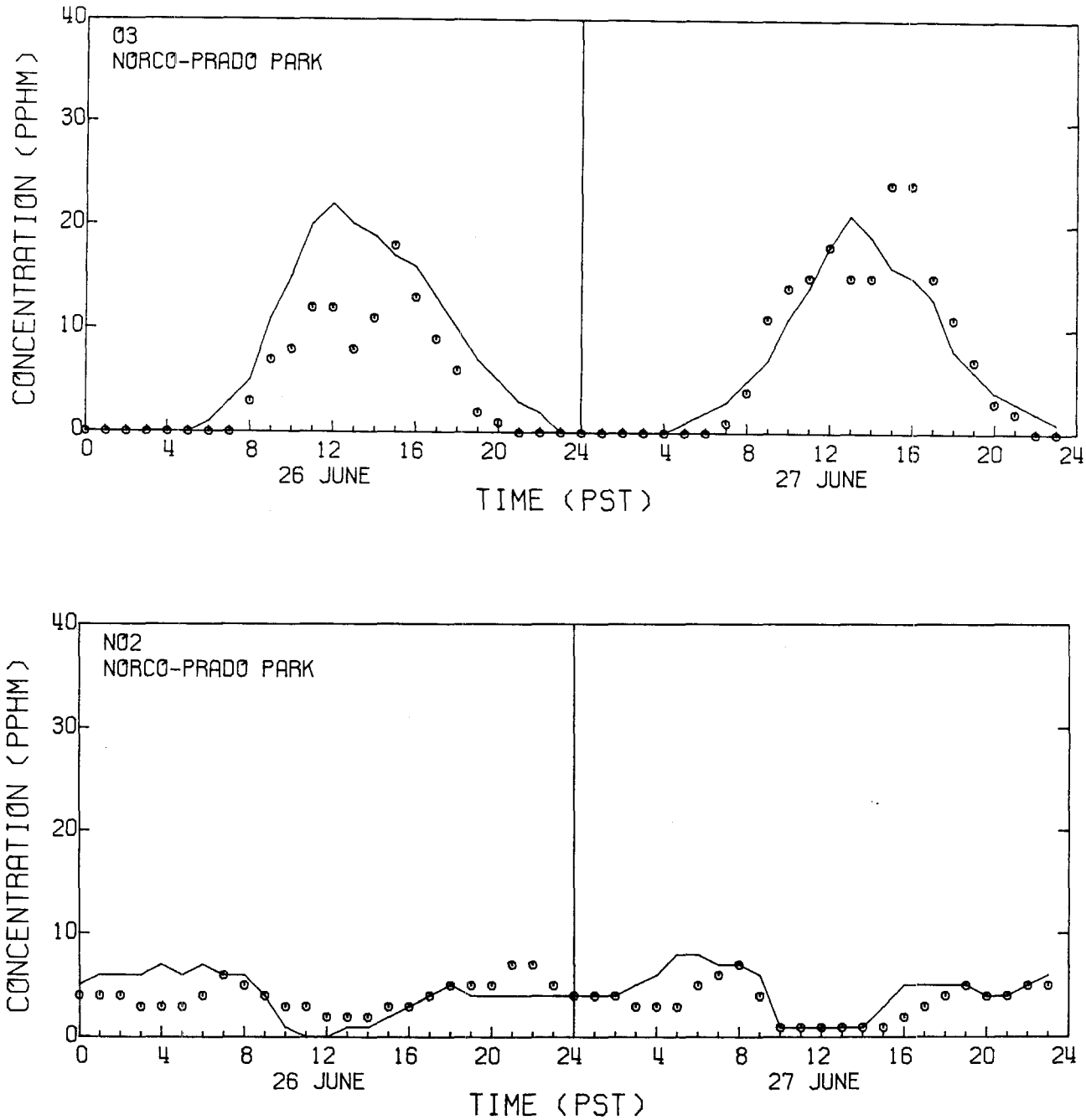

FIGURE C.7

Measured (o) and Predicted (-) Ozone and Nitrogen Dioxide Air Quality at Norco-Prado Park

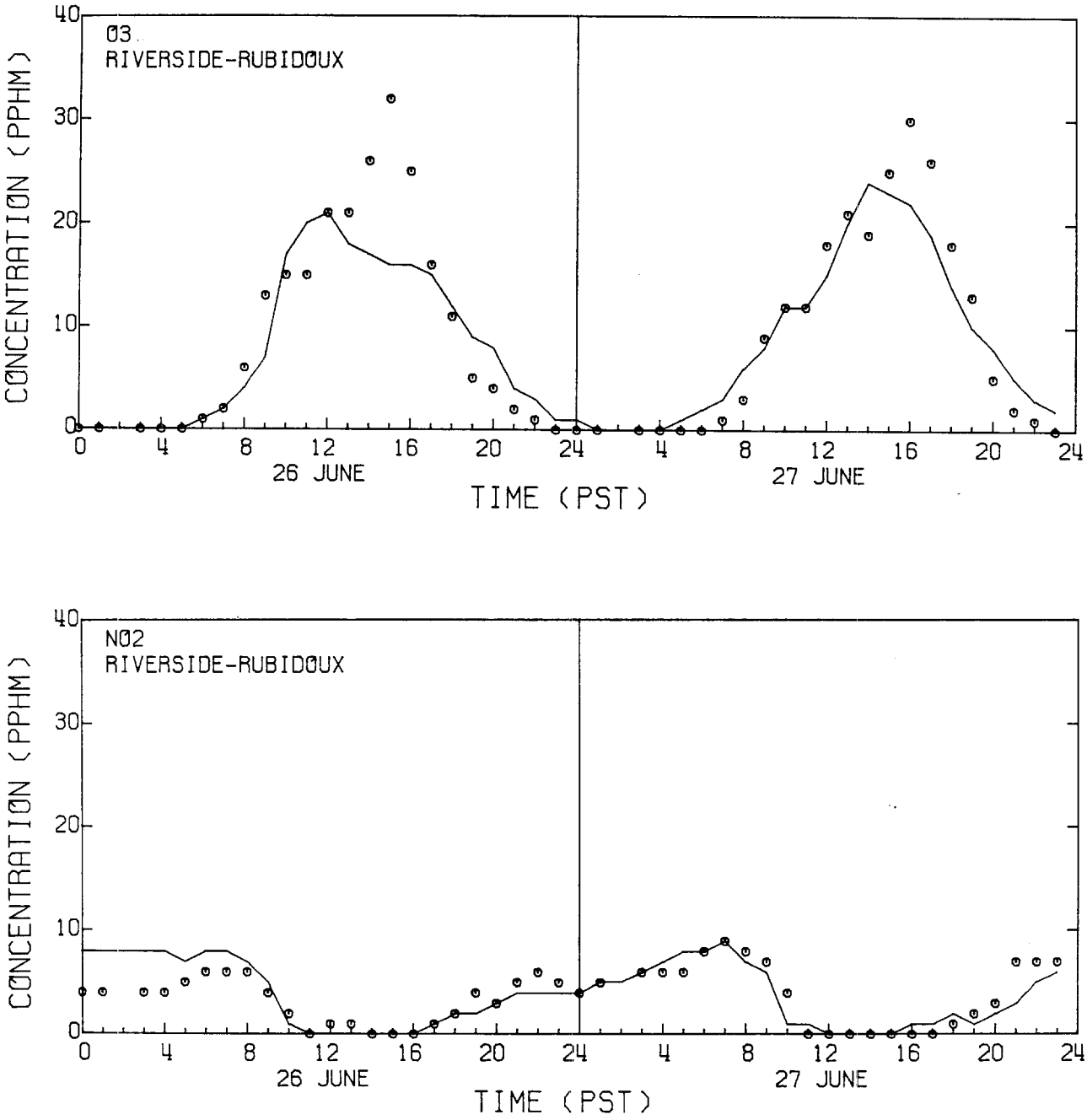

FIGURE C.8

Measured (o) and Predicted (-) Ozone and Nitrogen Dioxide Air Quality at Riverside-Rubidoux

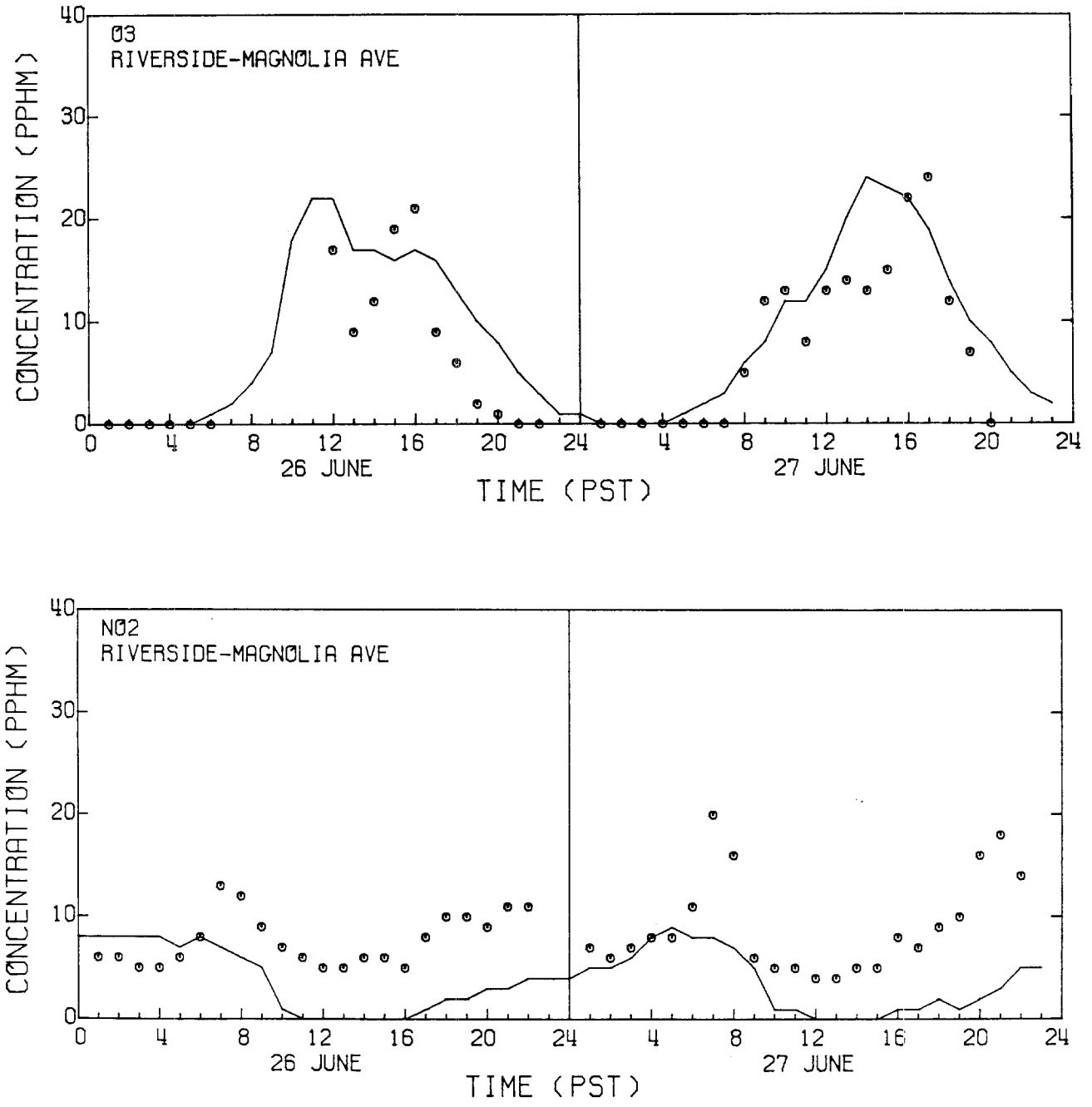

FIGURE C.9

Measured (o) and Predicted (-) Ozone and Nitrogen Dioxide
Air Quality at Riverside-Magnolia Avenue

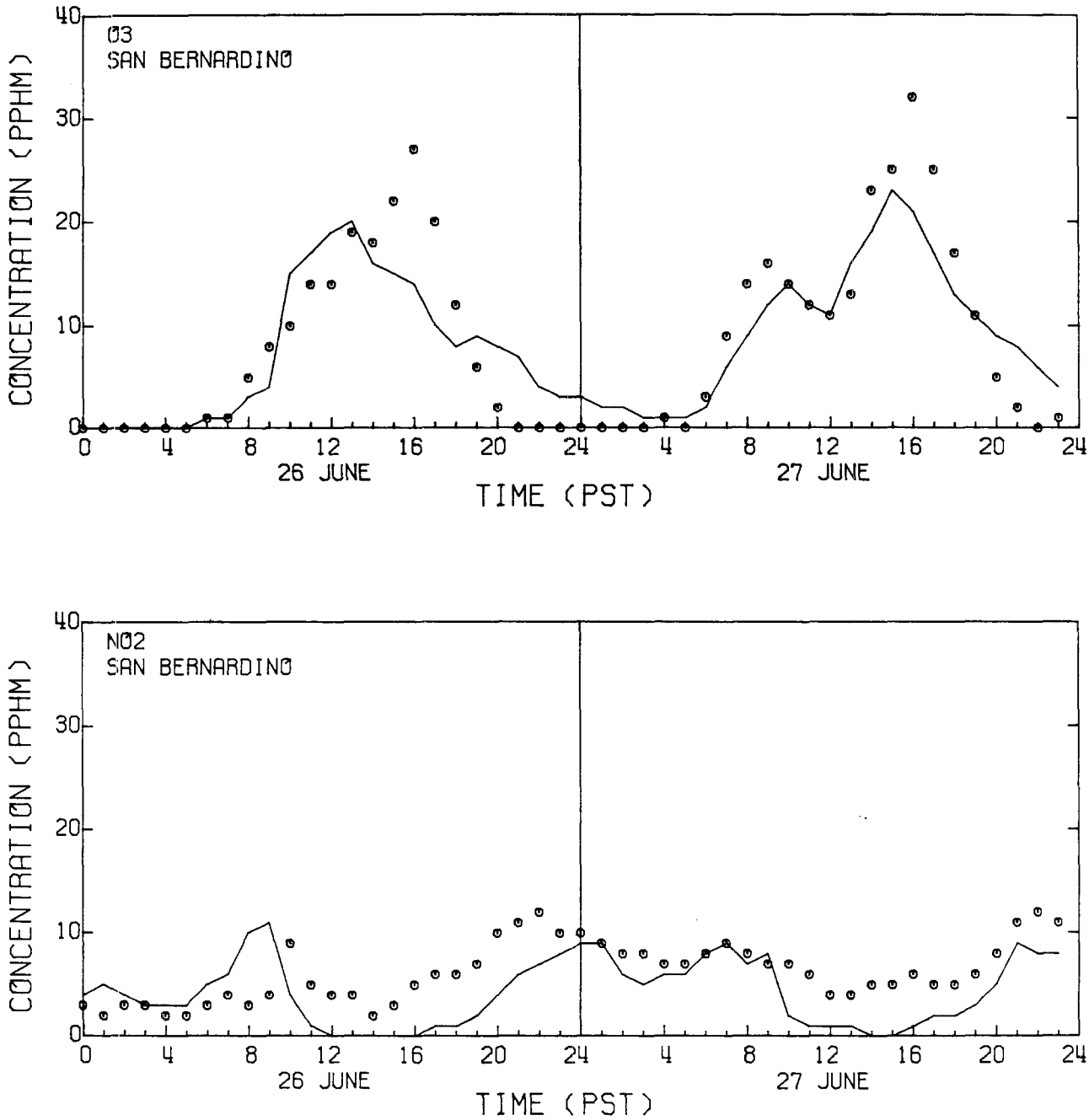

FIGURE C.10

Measured (o) and Predicted (-) Ozone and Nitrogen Dioxide
Air Quality at San Bernardino

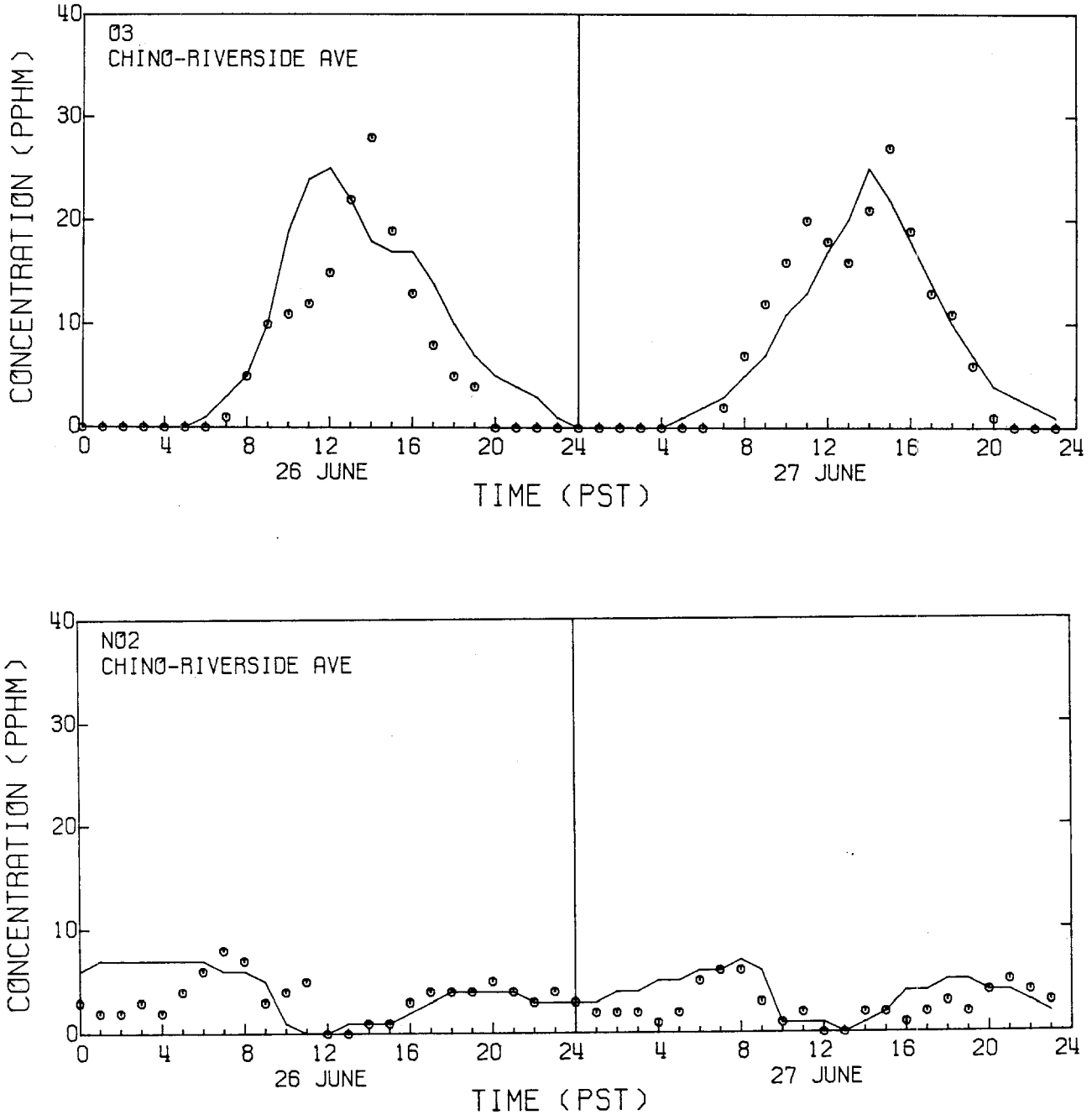

FIGURE C.11

Measured (o) and Predicted (-) Ozone and Nitrogen Dioxide
Air Quality at Chino-Riverside Avenue

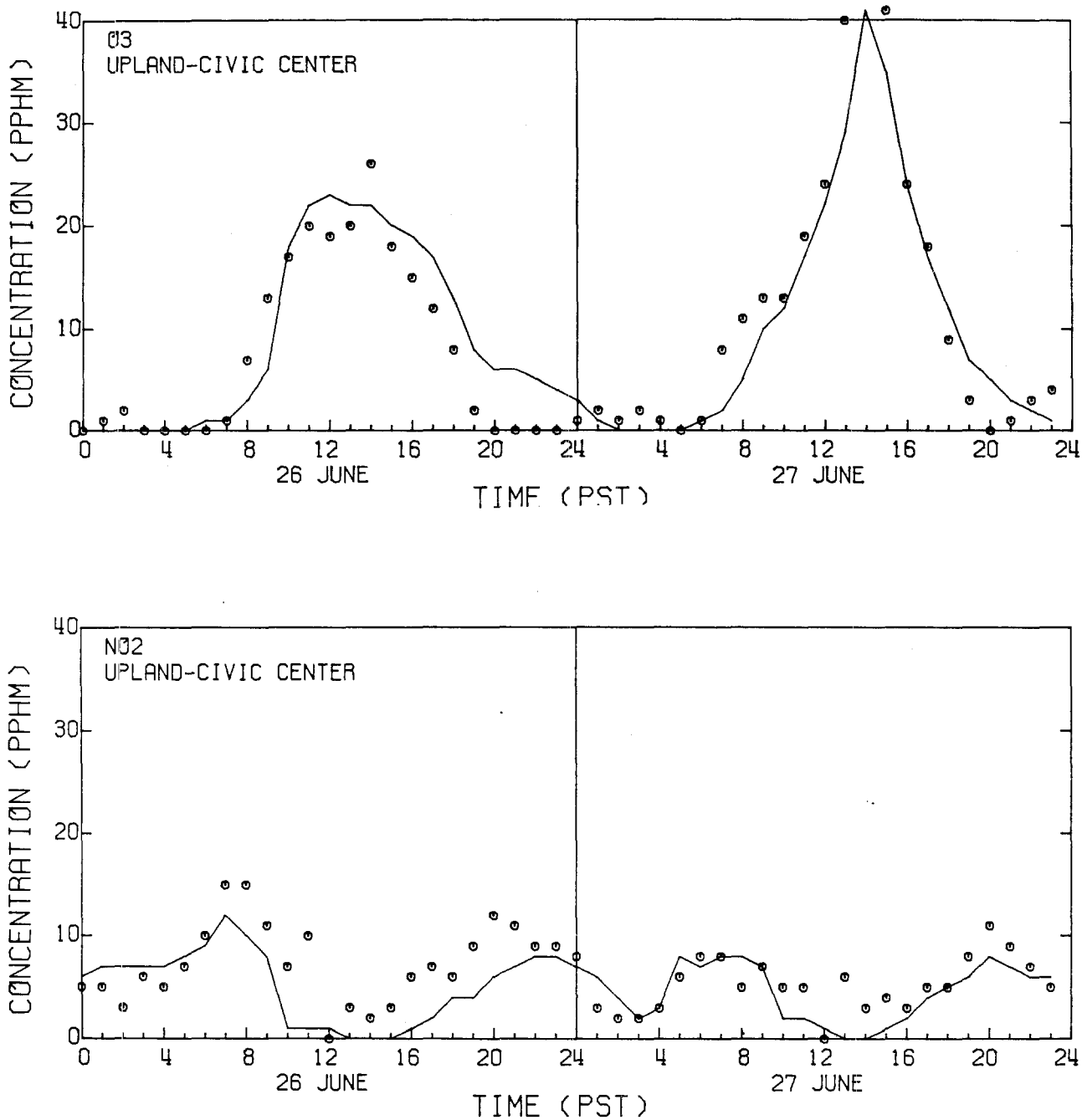

FIGURE C.12

Measured (o) and Predicted (-) Ozone and Nitrogen Dioxide
Air Quality at Upland-Civic Center

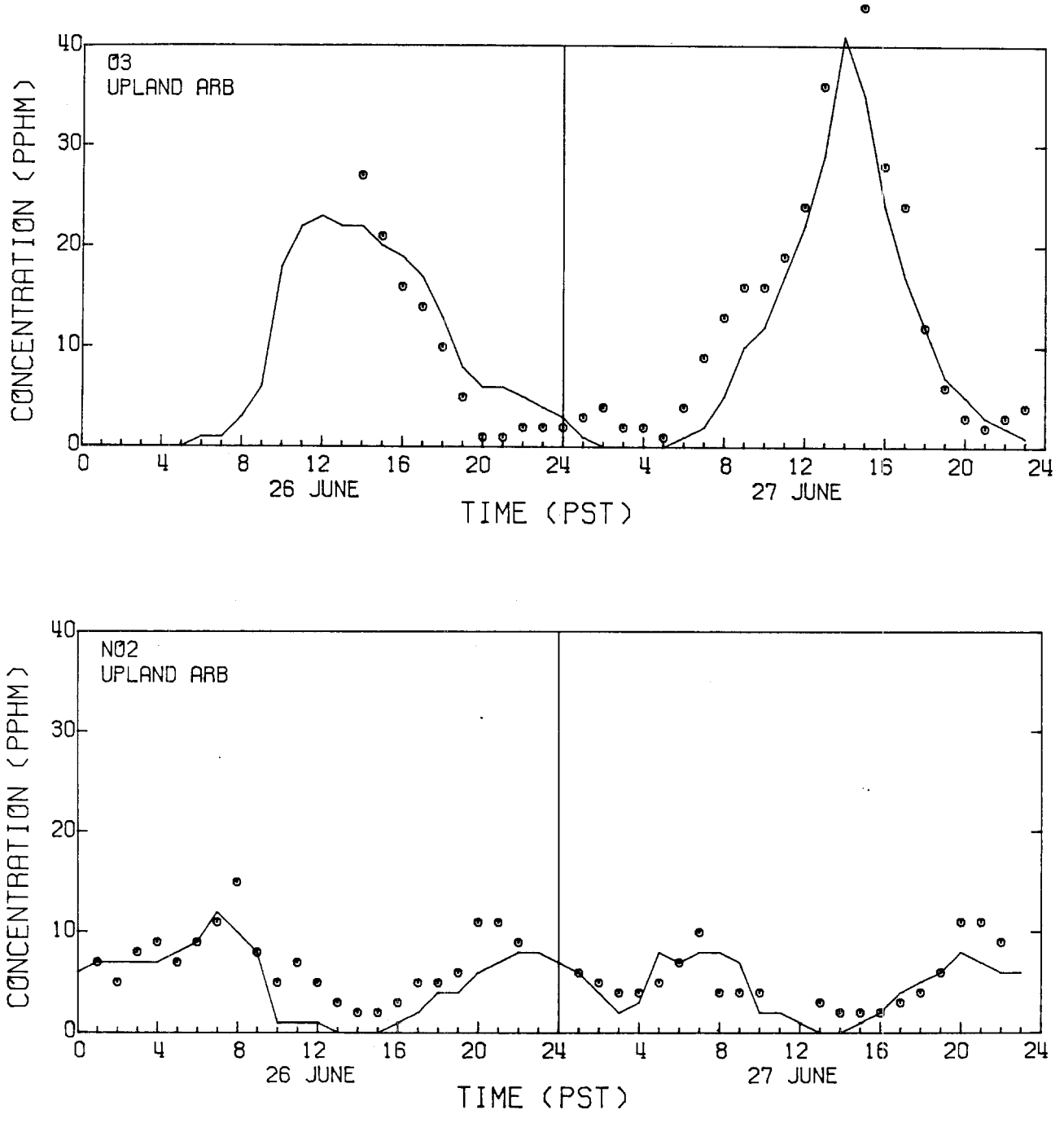

FIGURE C.13

Measured (o) and Predicted (-) Ozone and Nitrogen Dioxide Air Quality at Upland ARB

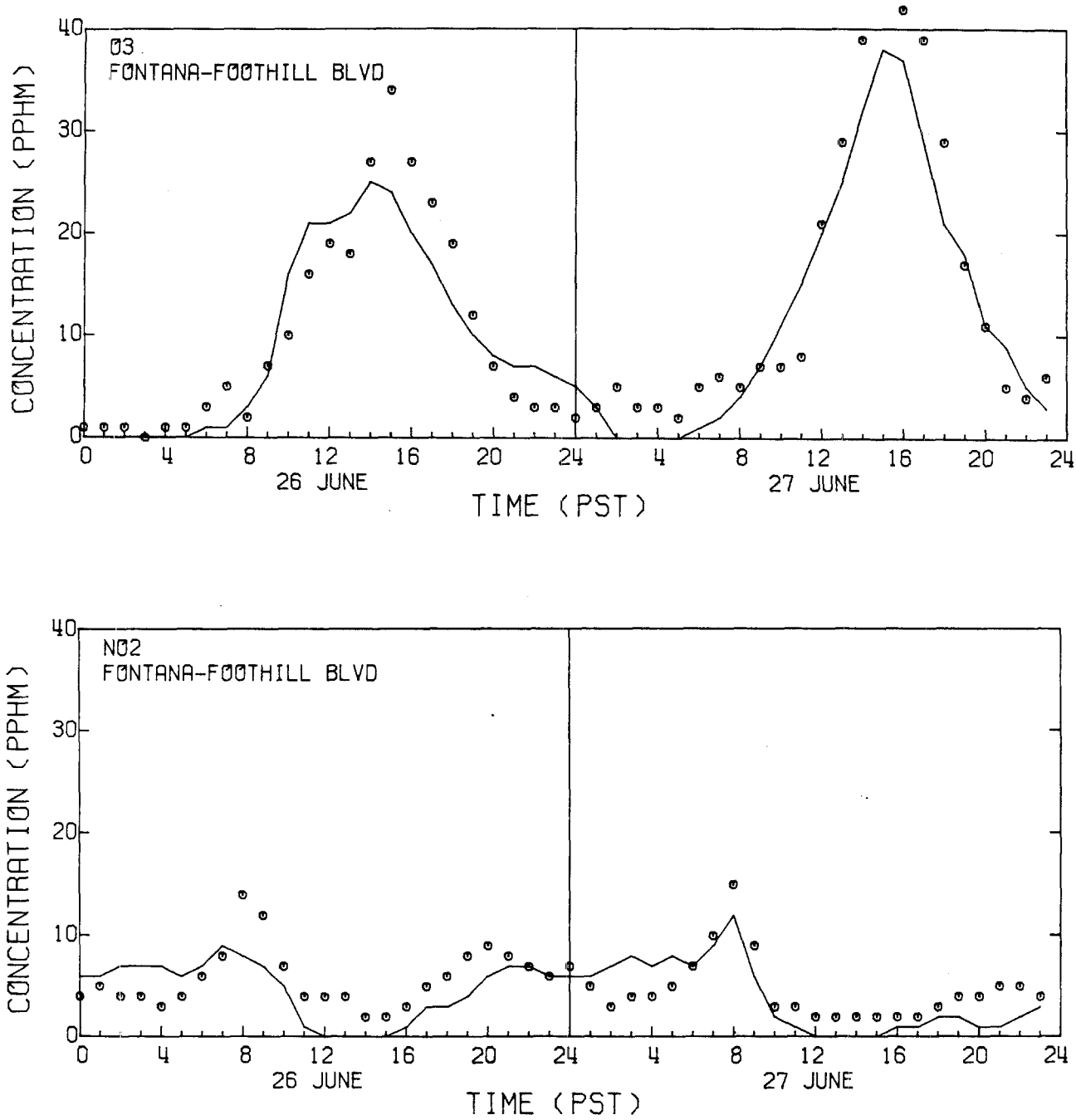

FIGURE C.14

Measured (o) and Predicted (-) Ozone and Nitrogen Dioxide
Air Quality at Fontana-Foothill Blvd

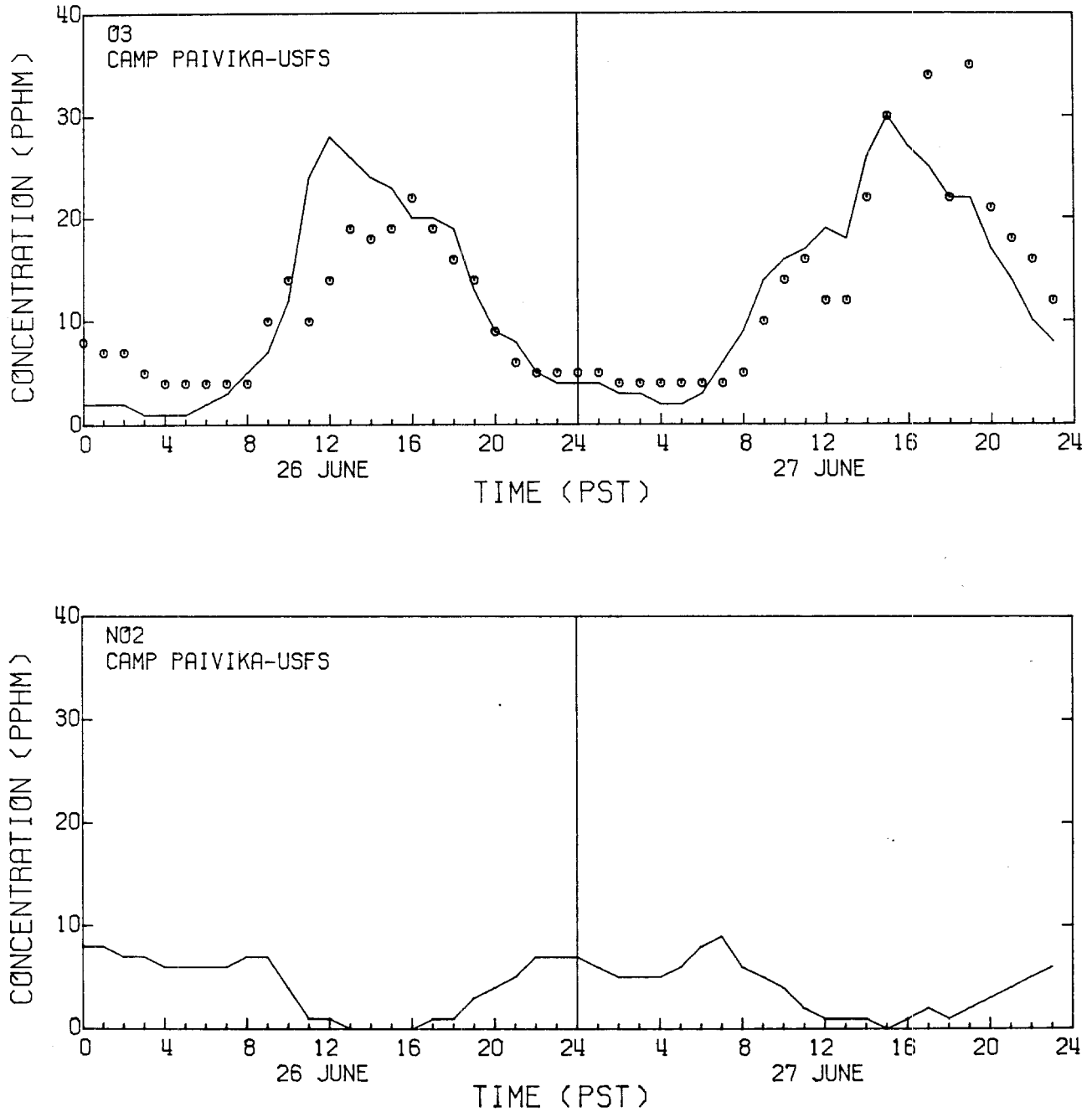

FIGURE C.15

Measured (o) and Predicted (-) Ozone and Nitrogen Dioxide Air Quality at Camp Paivika-USFS

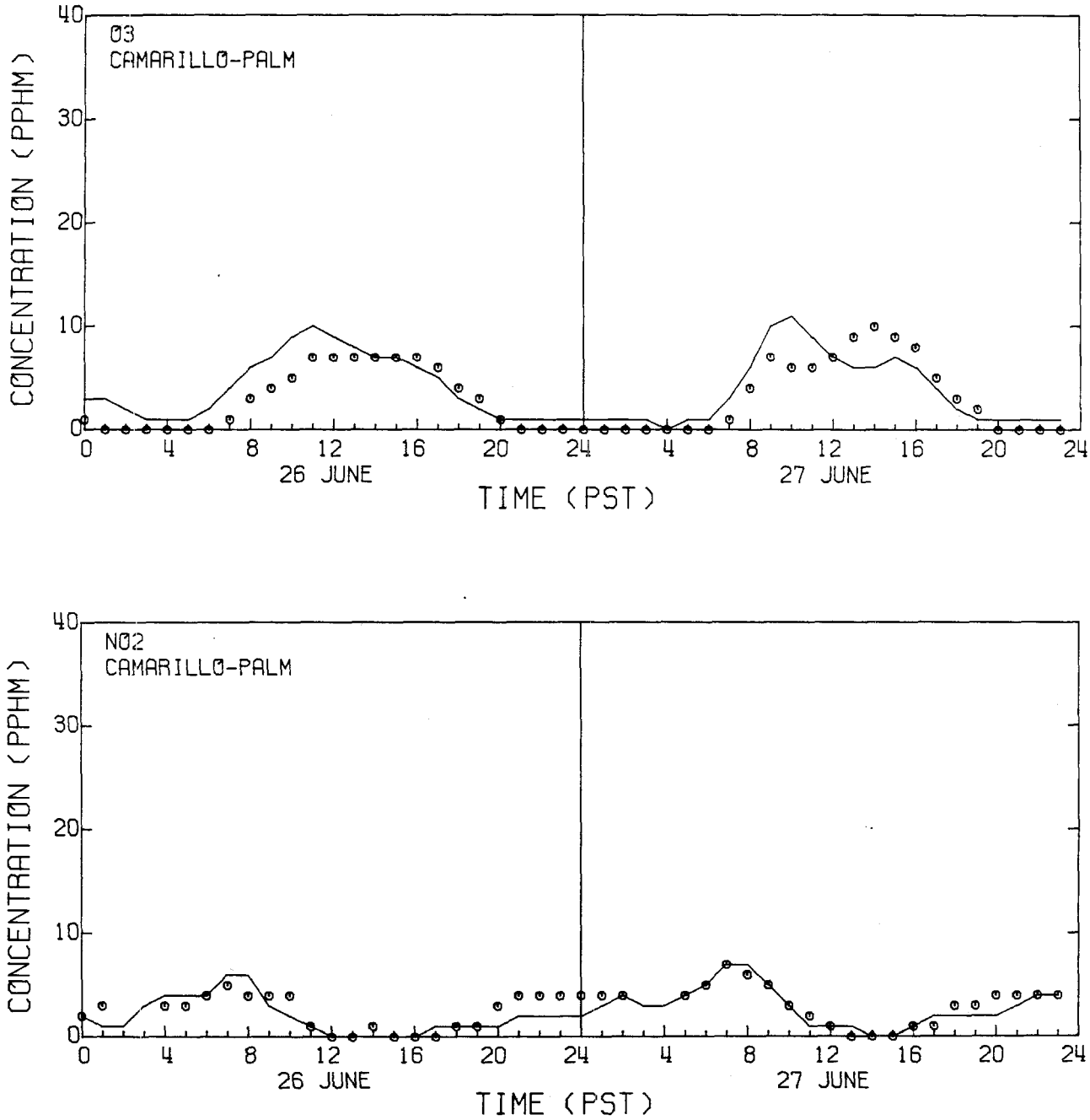

FIGURE C.16

Measured (o) and Predicted (-) Ozone and Nitrogen Dioxide
Air Quality at Camarillo-Palm

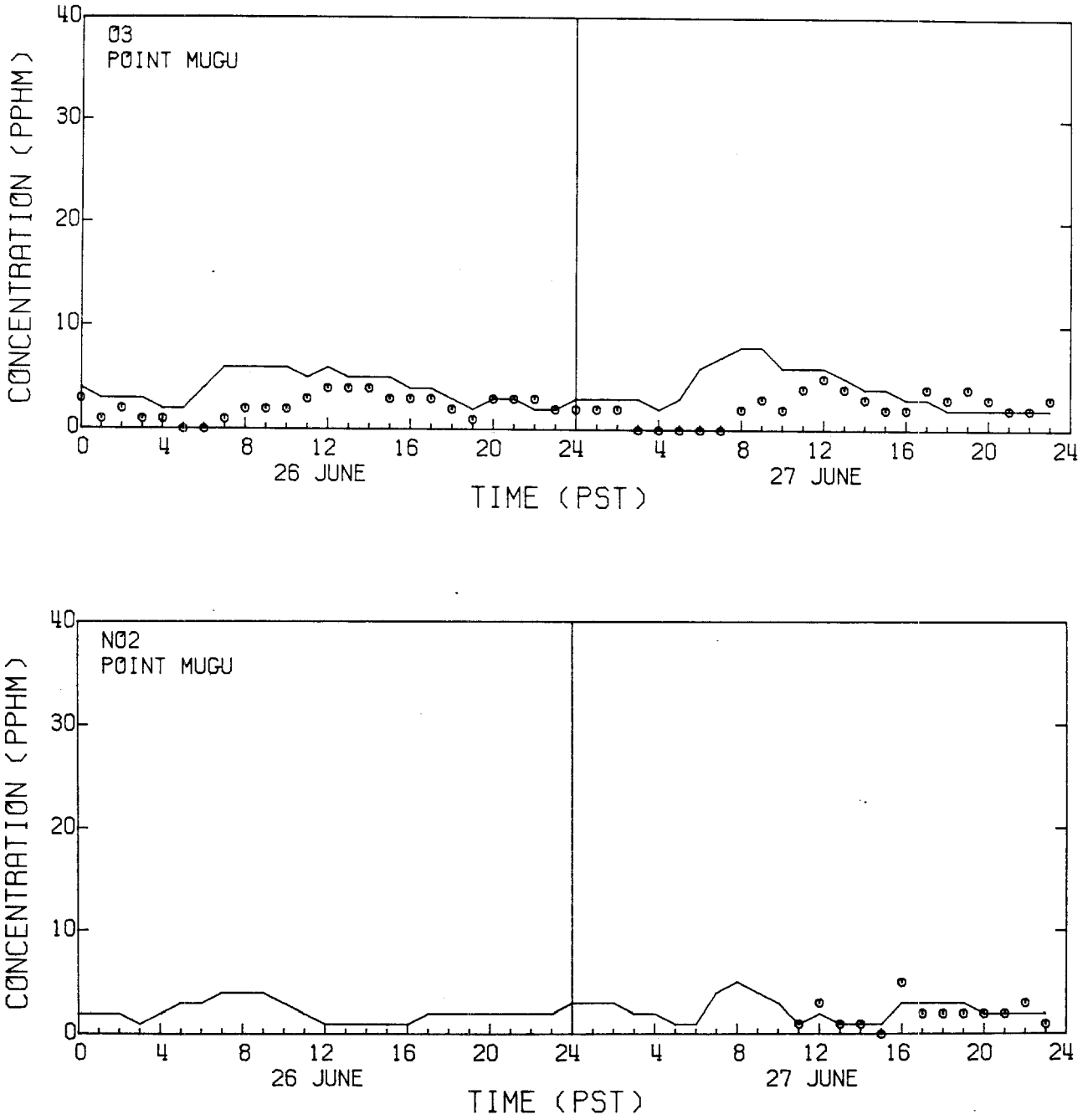

FIGURE C.17

Measured (o) and Predicted (-) Ozone and Nitrogen Dioxide
Air Quality at Point Mugu

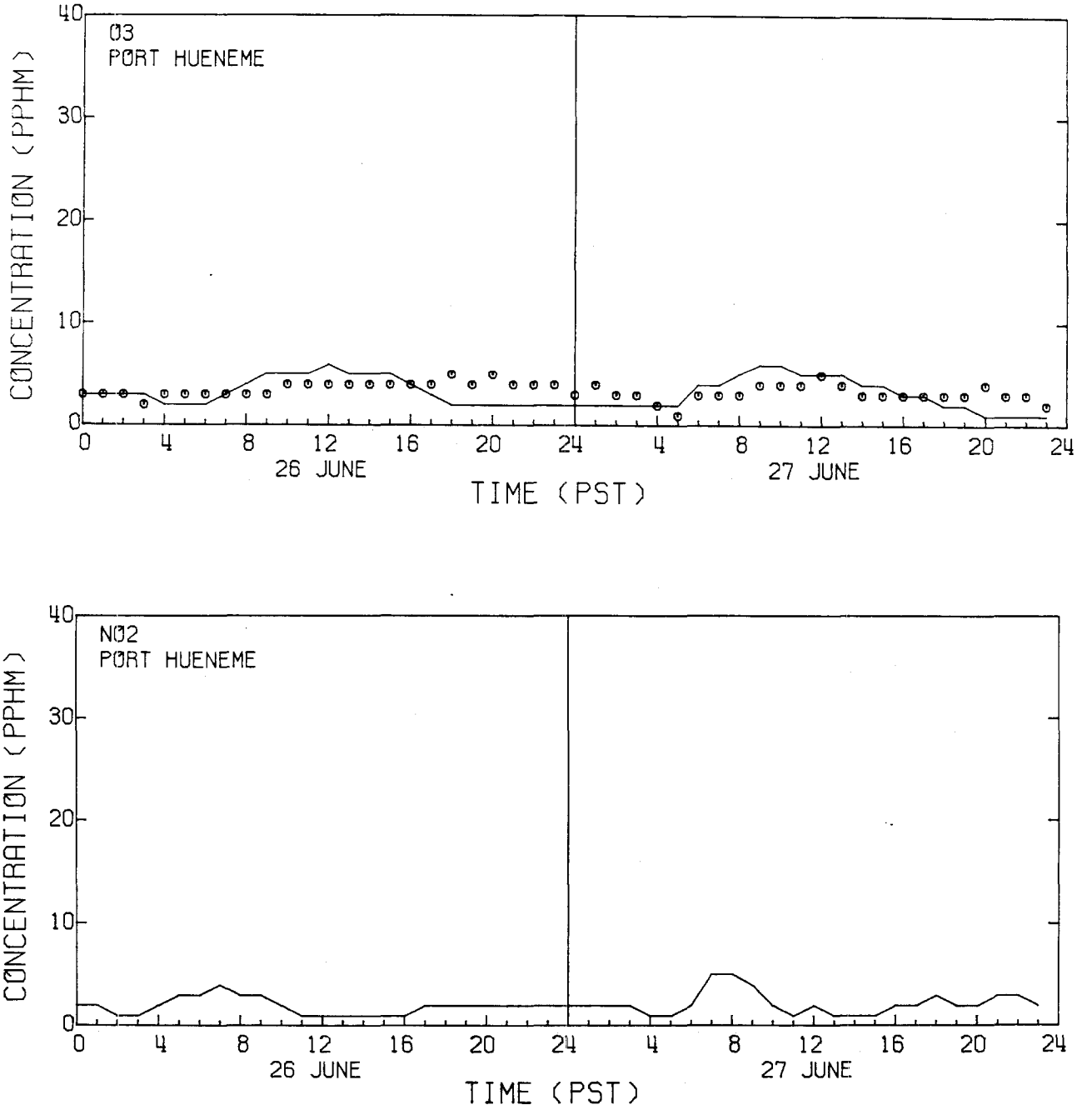

FIGURE C.18

Measured (o) and Predicted (-) Ozone and Nitrogen Dioxide
Air Quality at Port Hueneme

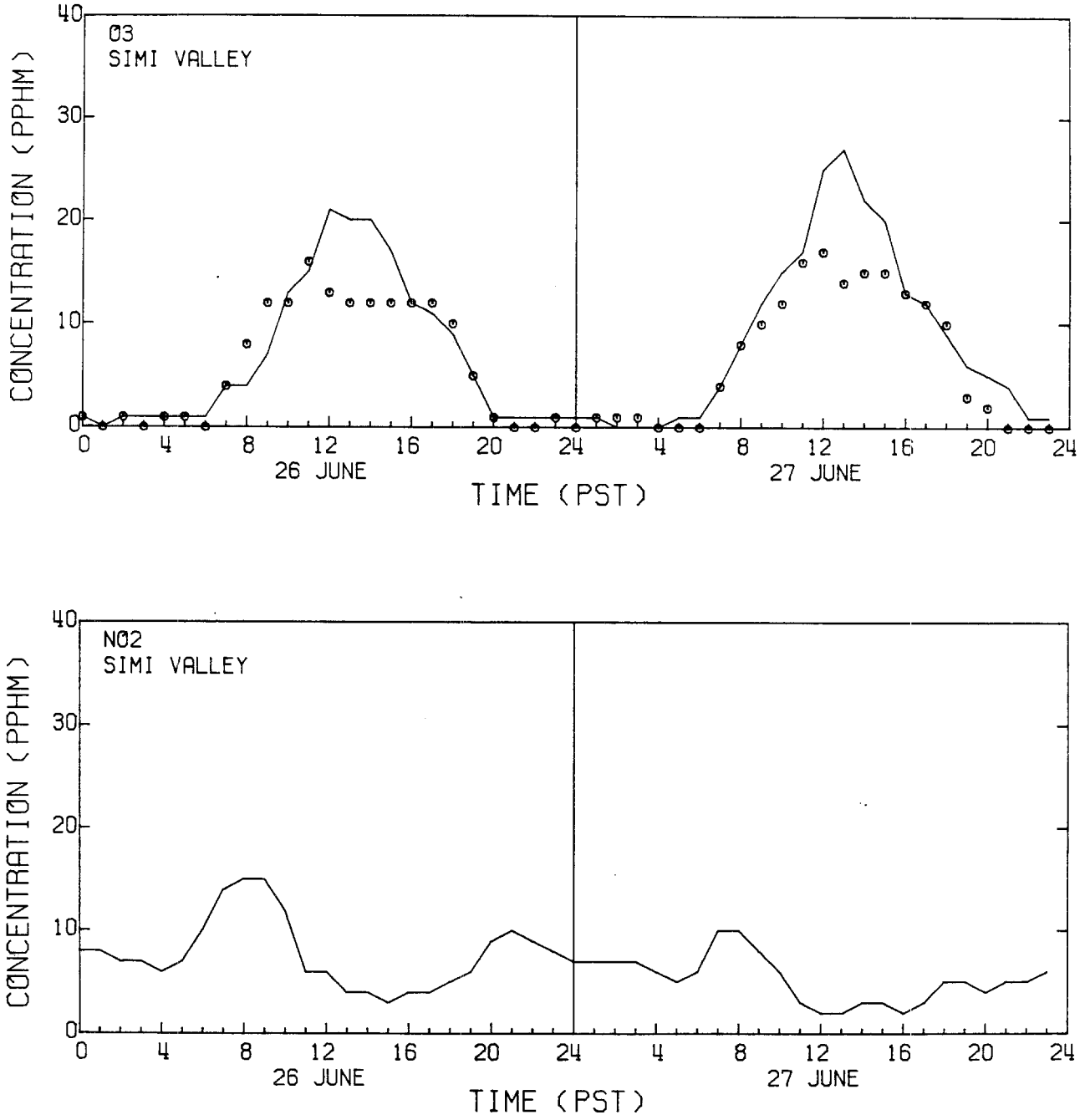

FIGURE C.19

Measured (o) and Predicted (-) Ozone and Nitrogen Dioxide
Air Quality at Simi Valley

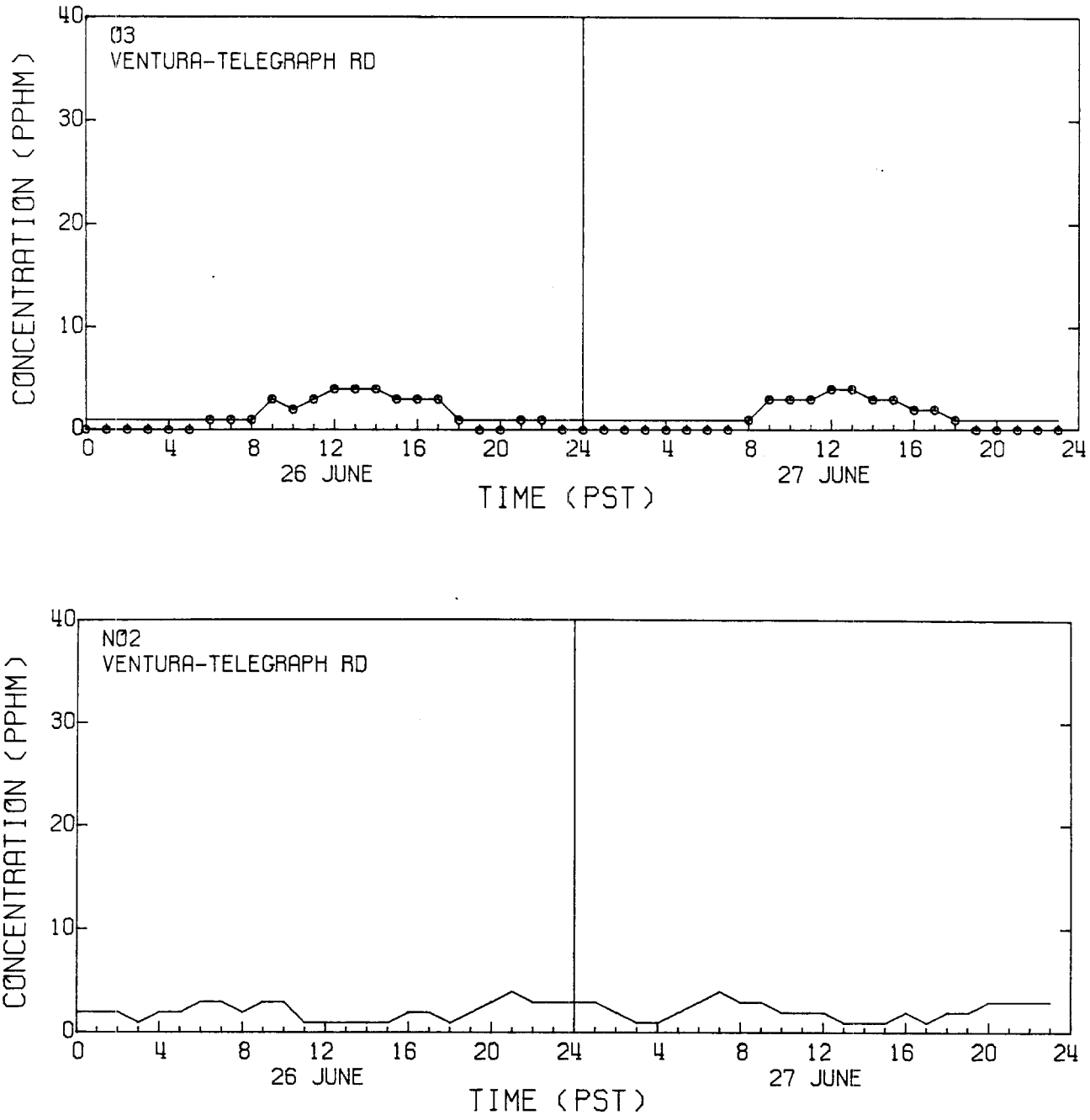

FIGURE C.20

Measured (o) and Predicted (-) Ozone and Nitrogen Dioxide
Air Quality at Ventura-Telegraph Rd

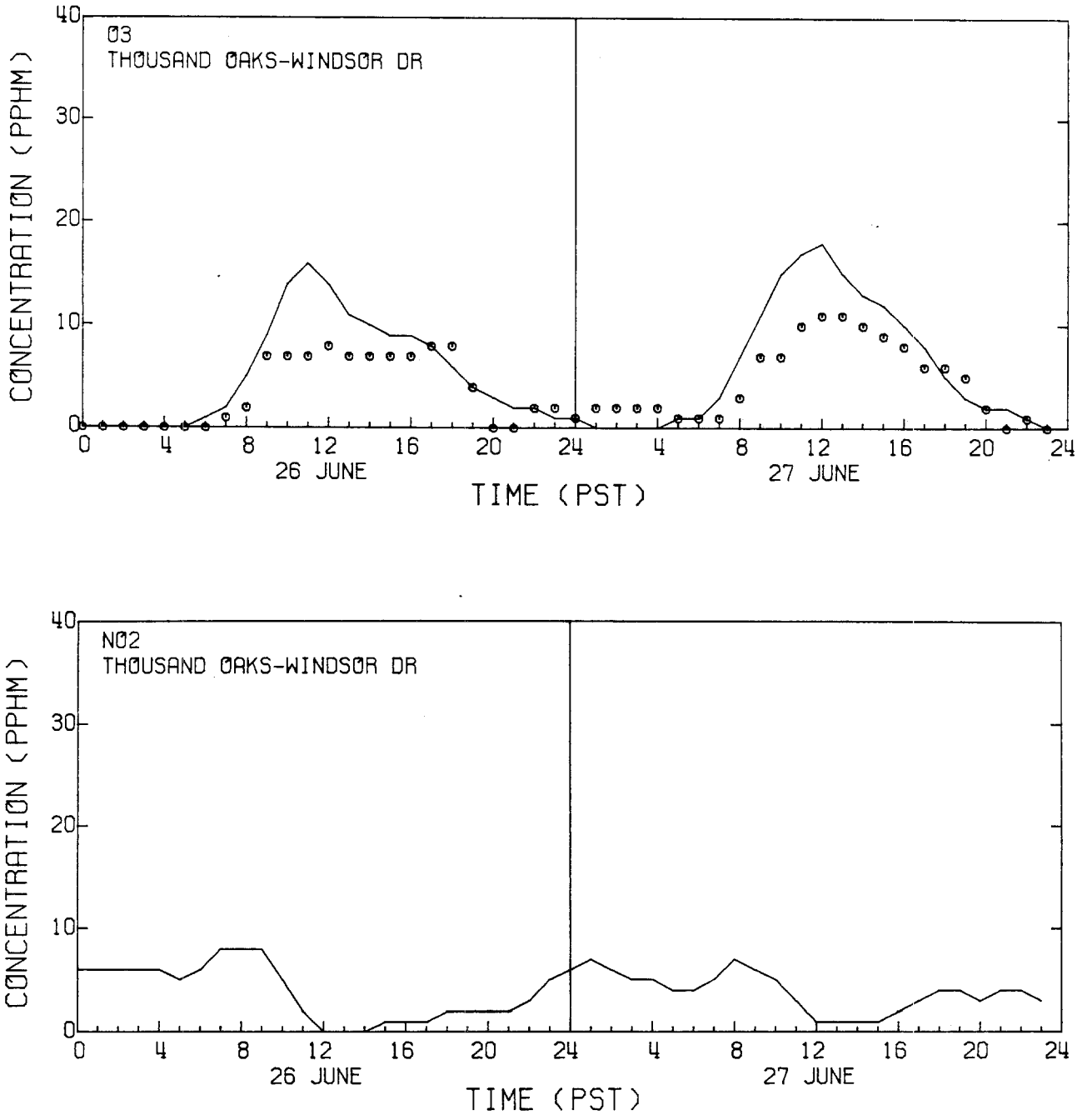

FIGURE C.21

Measured (o) and Predicted (-) Ozone and Nitrogen Dioxide
Air Quality at Thousand Oaks-Windsor Dr

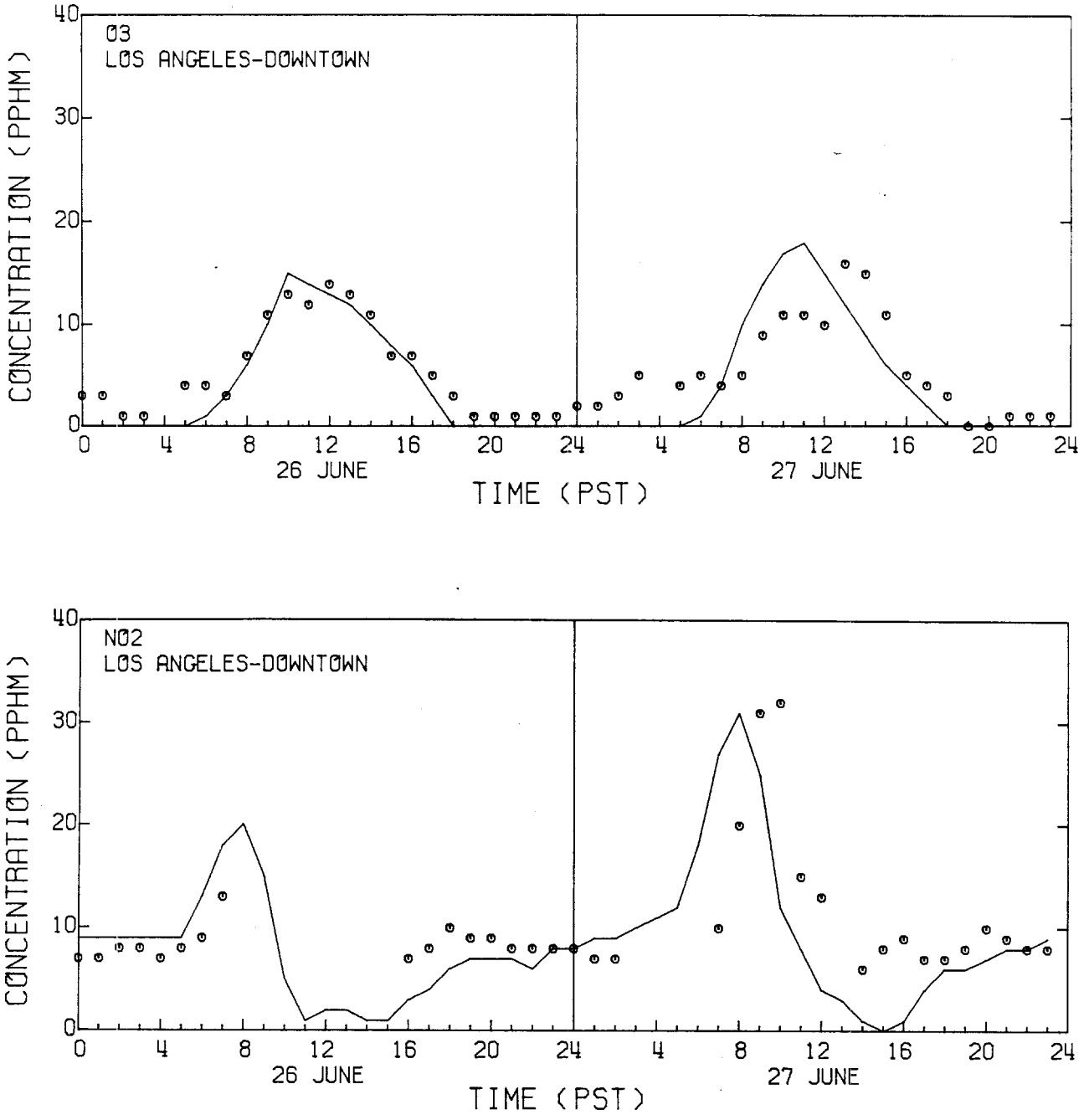

FIGURE C.22

Measured (o) and Predicted (-) Ozone and Nitrogen Dioxide
Air Quality at Los Angeles-Downtown

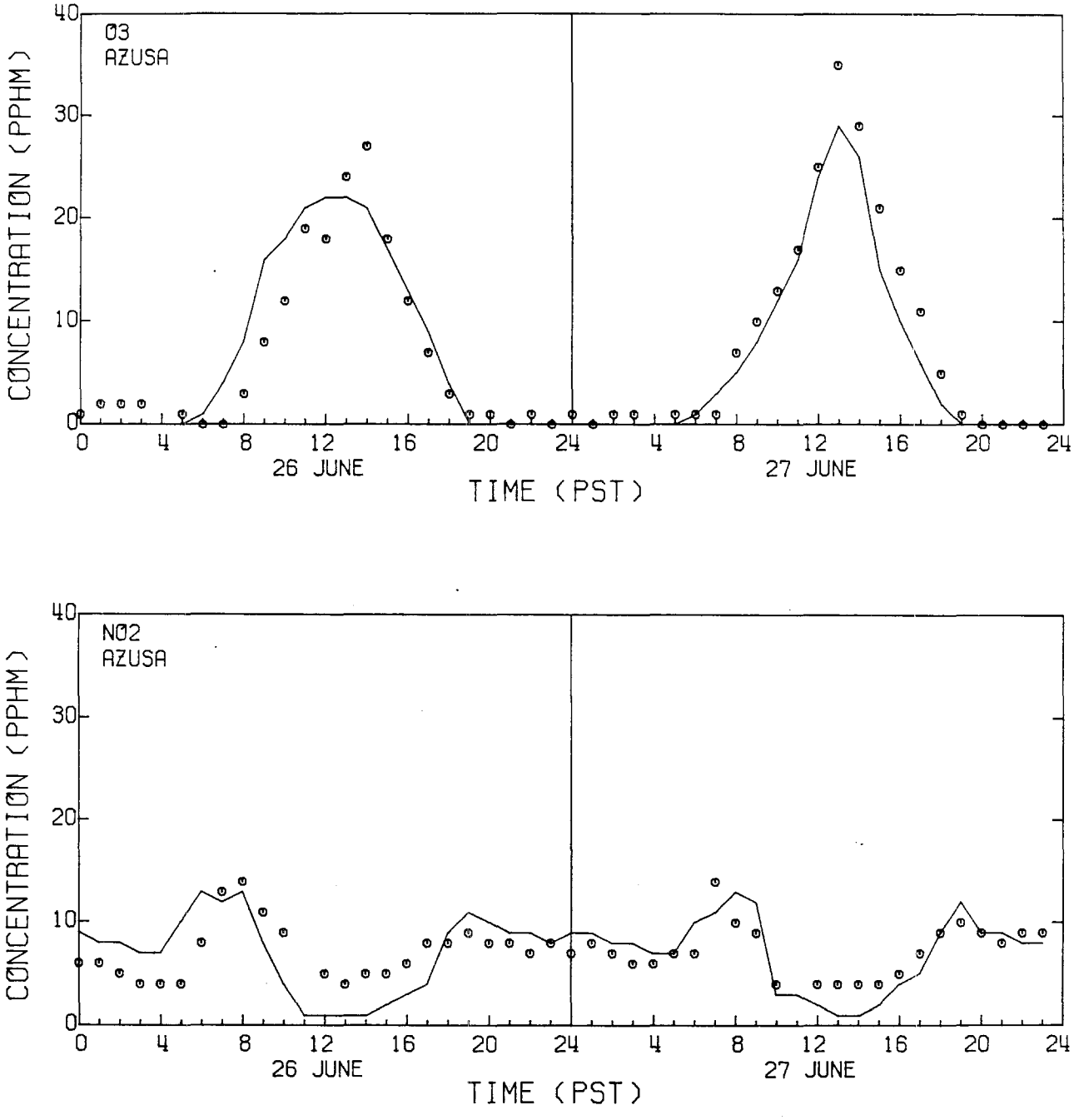

FIGURE C.23

Measured (o) and Predicted (-) Ozone and Nitrogen Dioxide Air Quality at Azusa

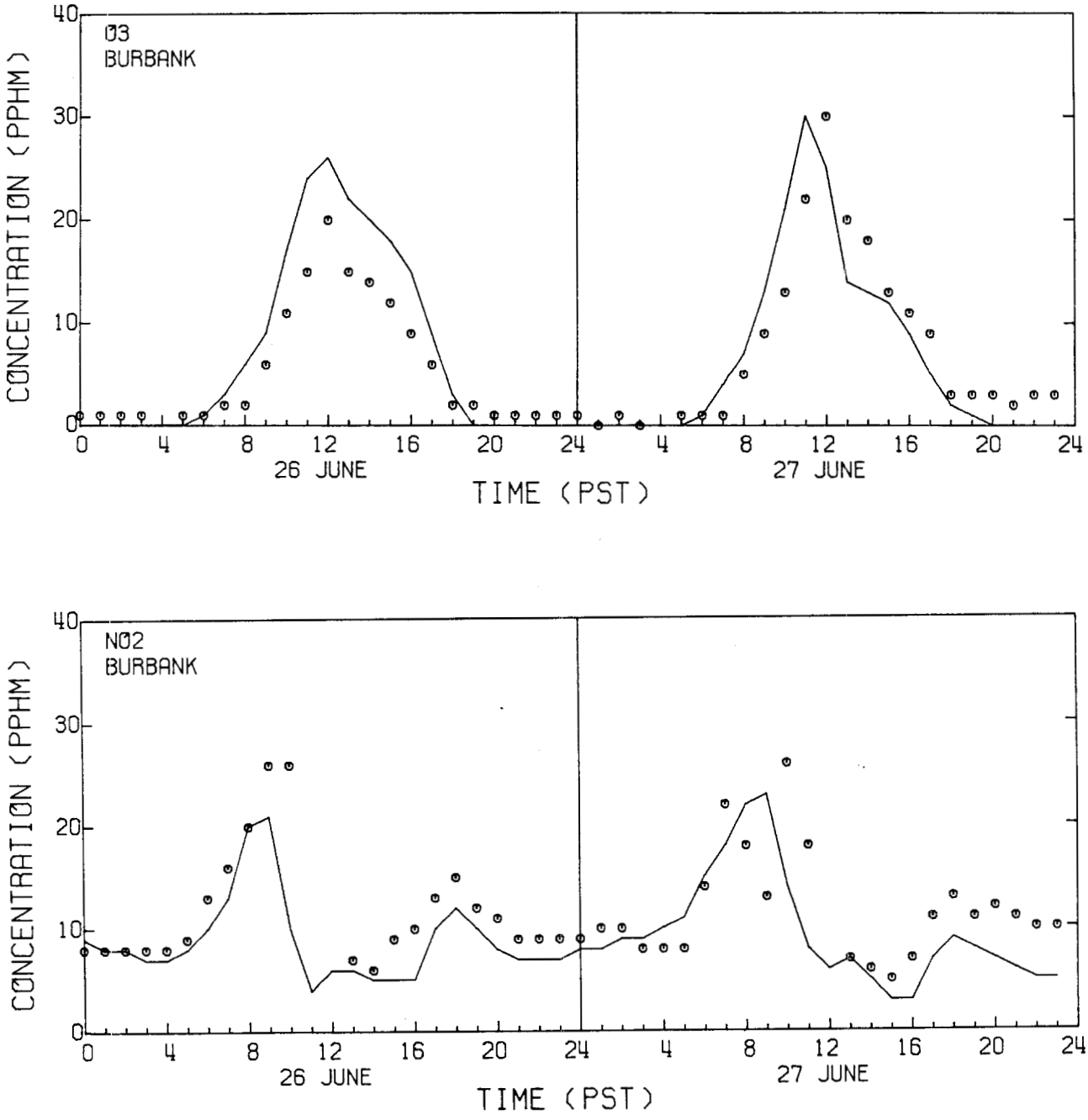

FIGURE C.24

Measured (o) and Predicted (-) Ozone and Nitrogen Dioxide Air Quality at Burbank

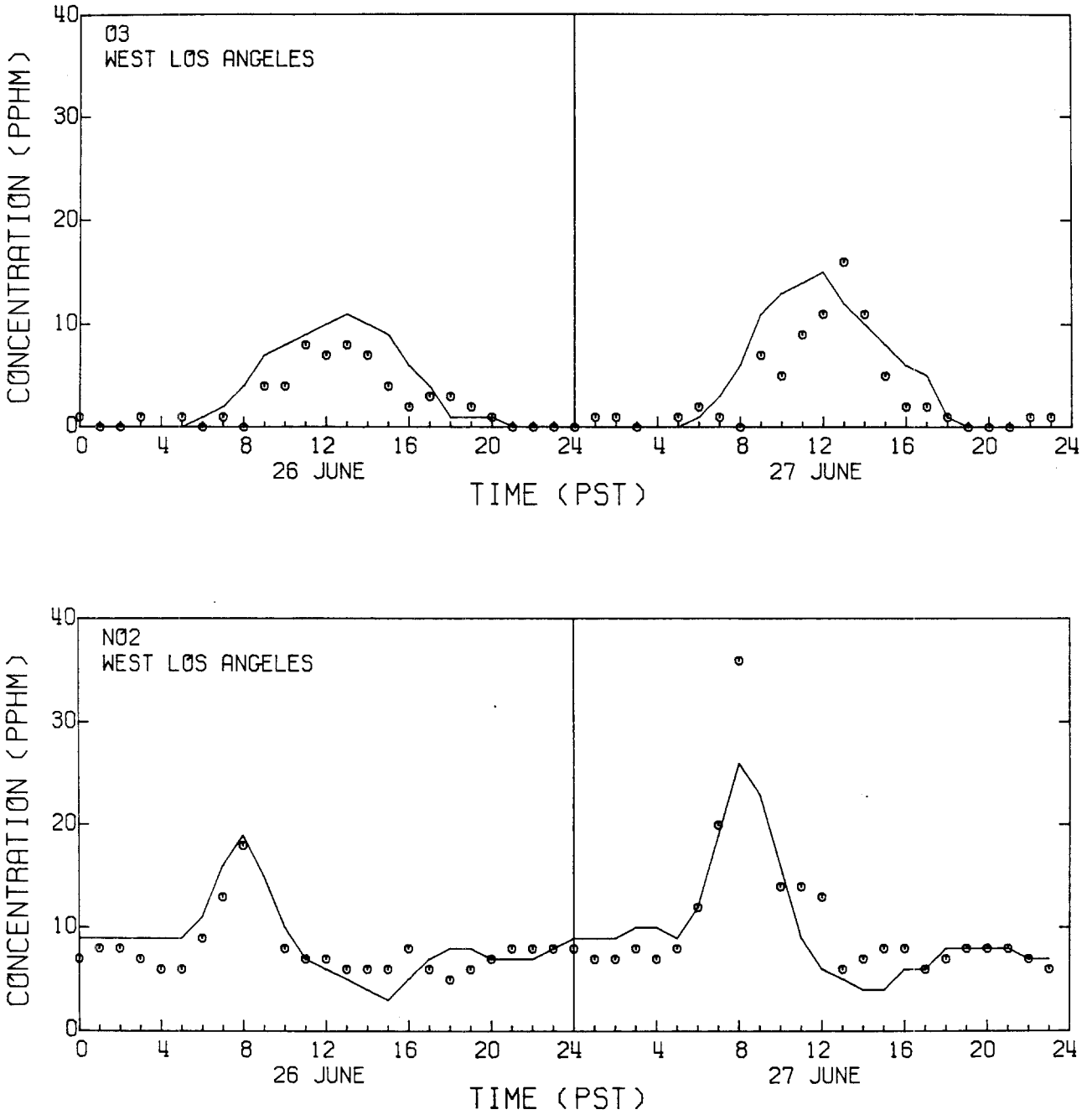

FIGURE C.25

Measured (o) and Predicted (-) Ozone and Nitrogen Dioxide
Air Quality at West Los Angeles

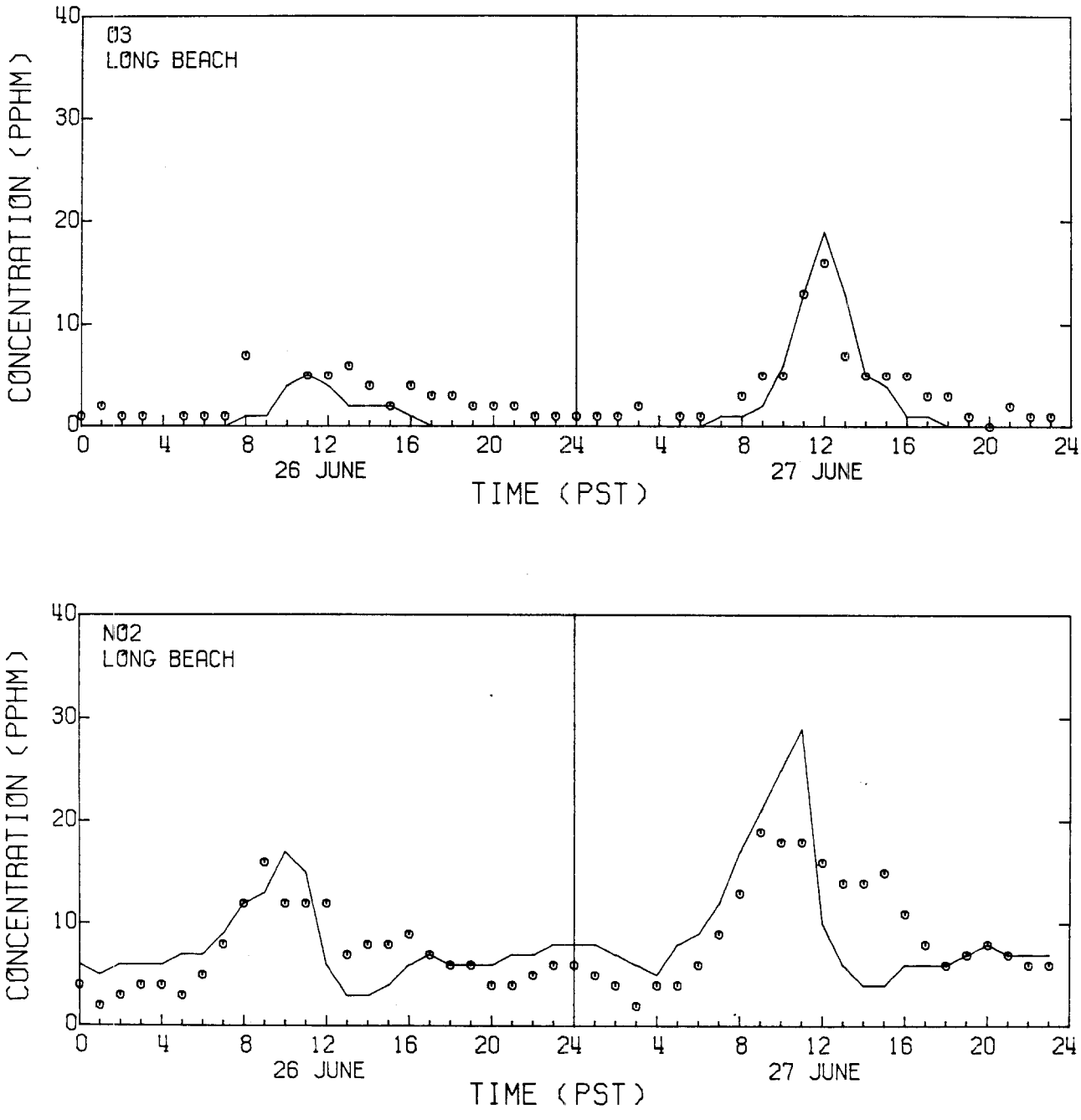

FIGURE C.26

Measured (o) and Predicted (-) Ozone and Nitrogen Dioxide
Air Quality at Long Beach

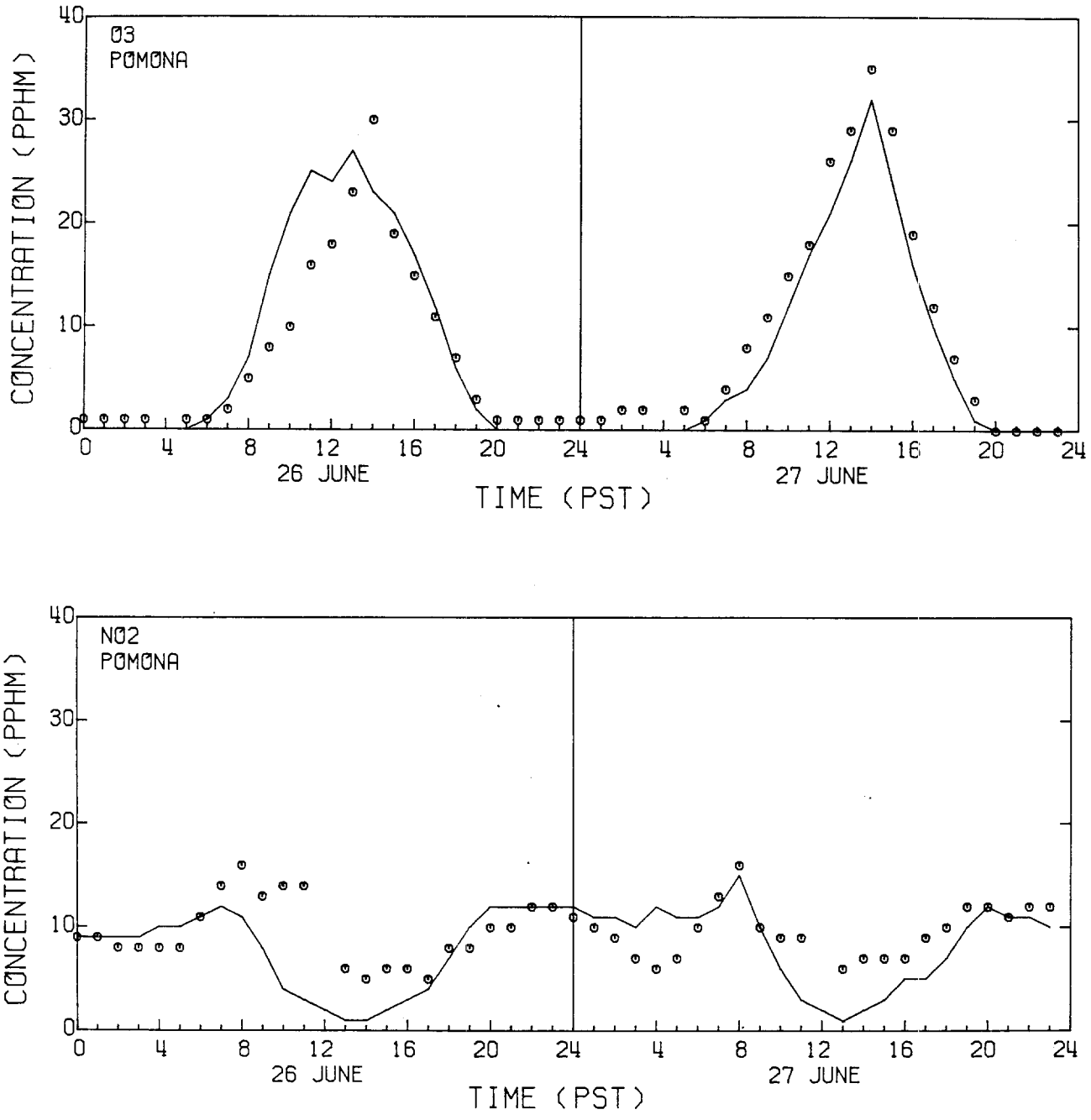

FIGURE C.27

Measured (o) and Predicted (-) Ozone and Nitrogen Dioxide
Air Quality at Pomona

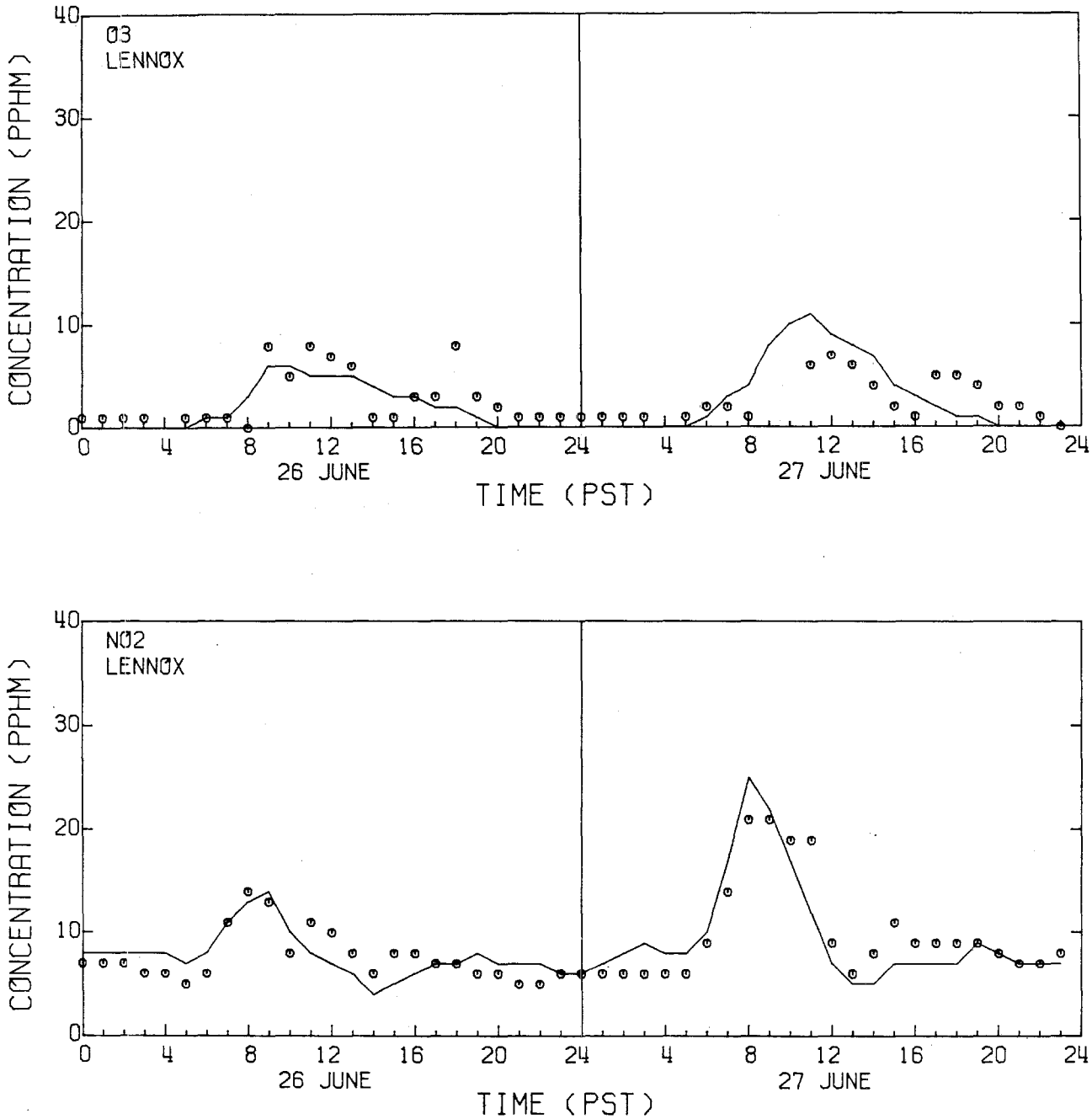

FIGURE C.28

Measured (o) and Predicted (-) Ozone and Nitrogen Dioxide Air Quality at Lennox

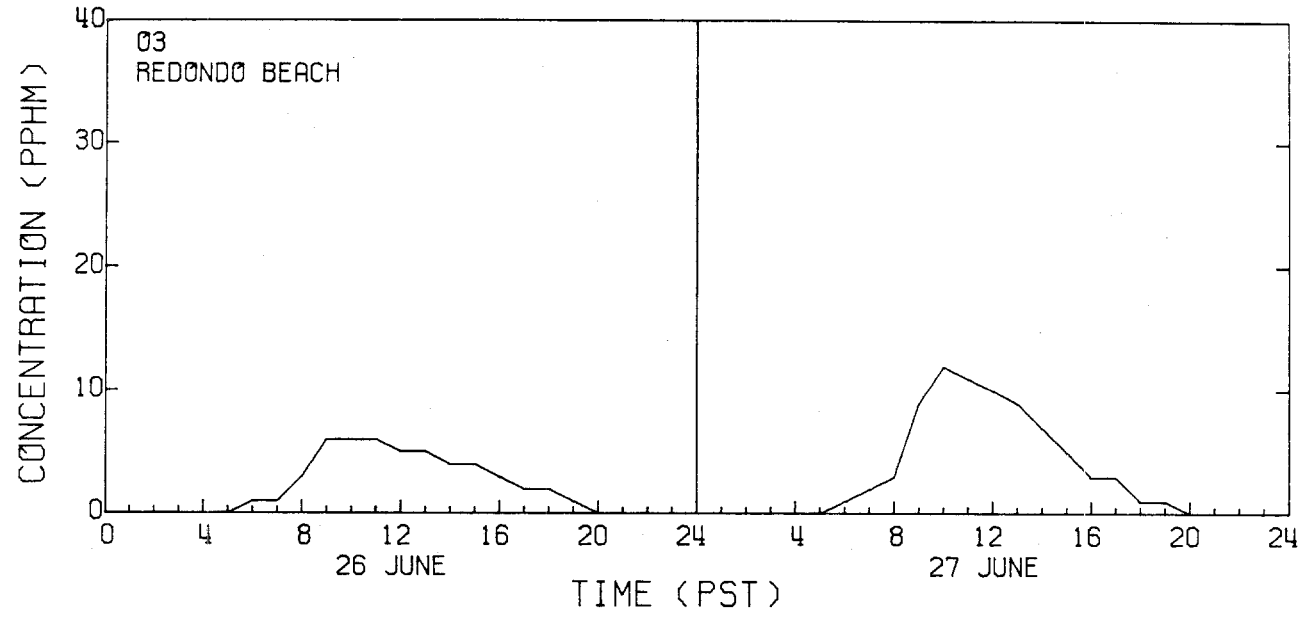
03
REDONDO BEACH
CONCENTRATION (PPHM)
40
30
20
10
0
0
4
8
12
16
20
24
4
8
12
16
20
24
26 JUNE
27 JUNE
TIME (PST)

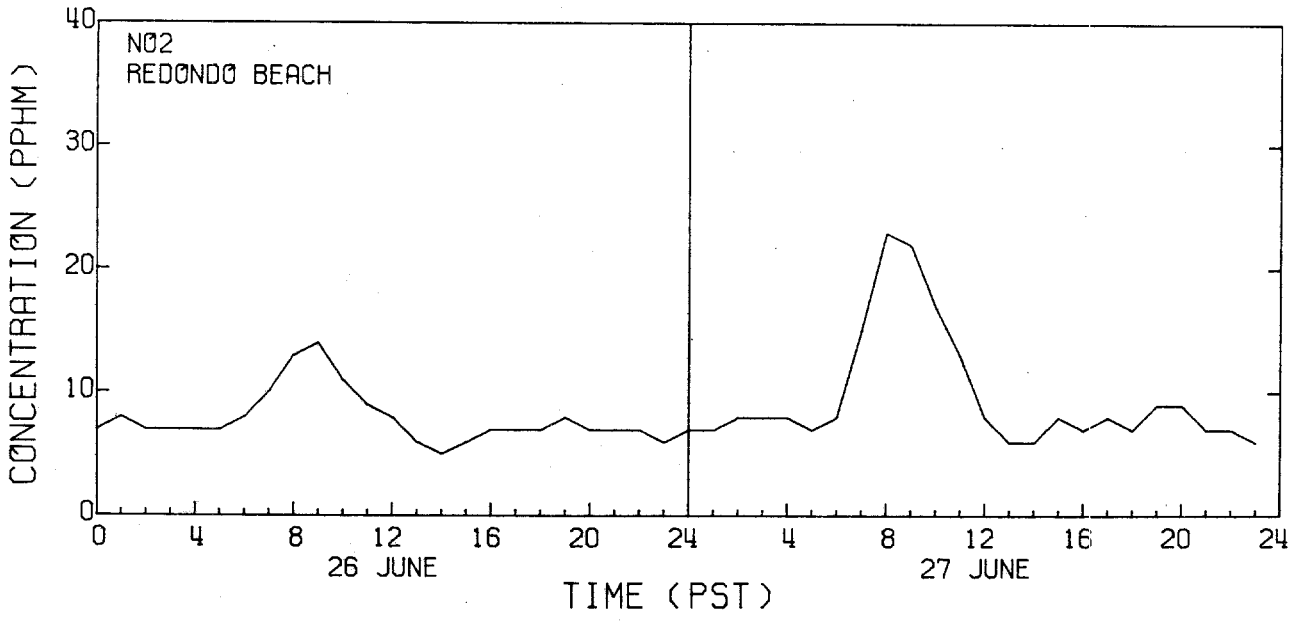
NO2
REDONDO BEACH
CONCENTRATION (PPHM)
40
30
20
10
0
0
4
8
12
16
20
24
4
8
12
16
20
24
26 JUNE
27 JUNE
TIME (PST)

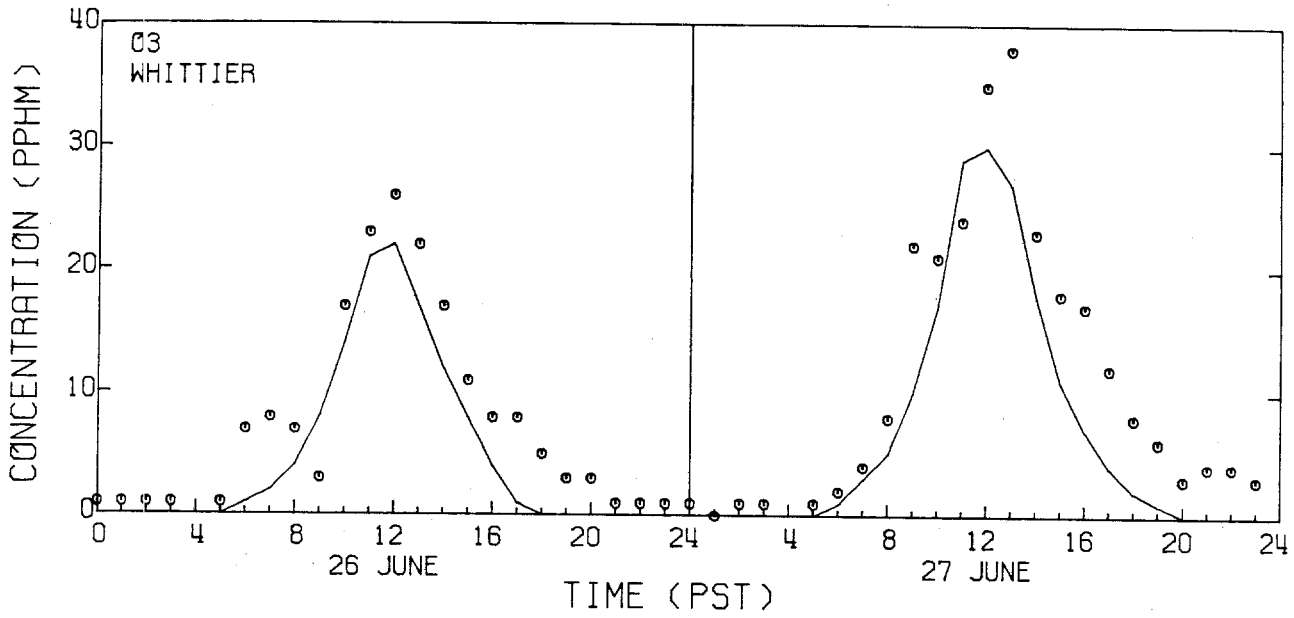
O3
WHITTIER
CONCENTRATION (PPHM)
40
30
20
10
0
0
4
8
12
16
20
24
4
8
12
16
20
24
26 JUNE
27 JUNE
TIME (PST)

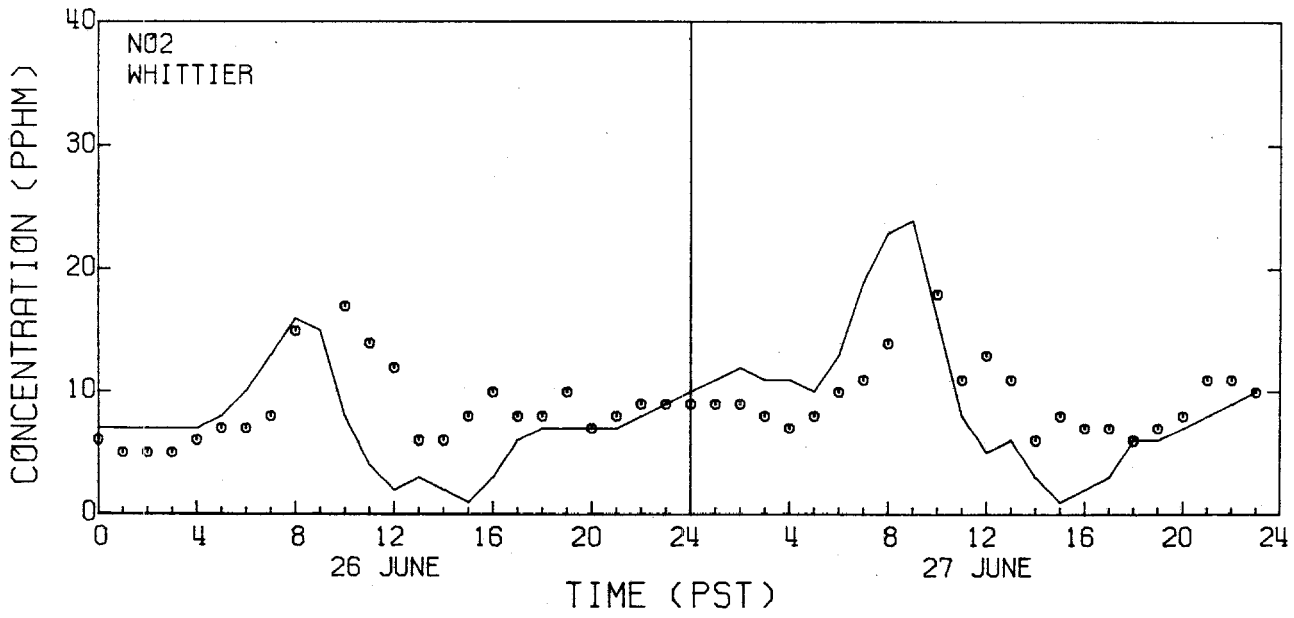
NO2
WHITTIER
CONCENTRATION (PPHM)
40
30
20
10
0
0
4
8
12
16
20
24
4
8
12
16
20
24
26 JUNE
27 JUNE
TIME (PST)

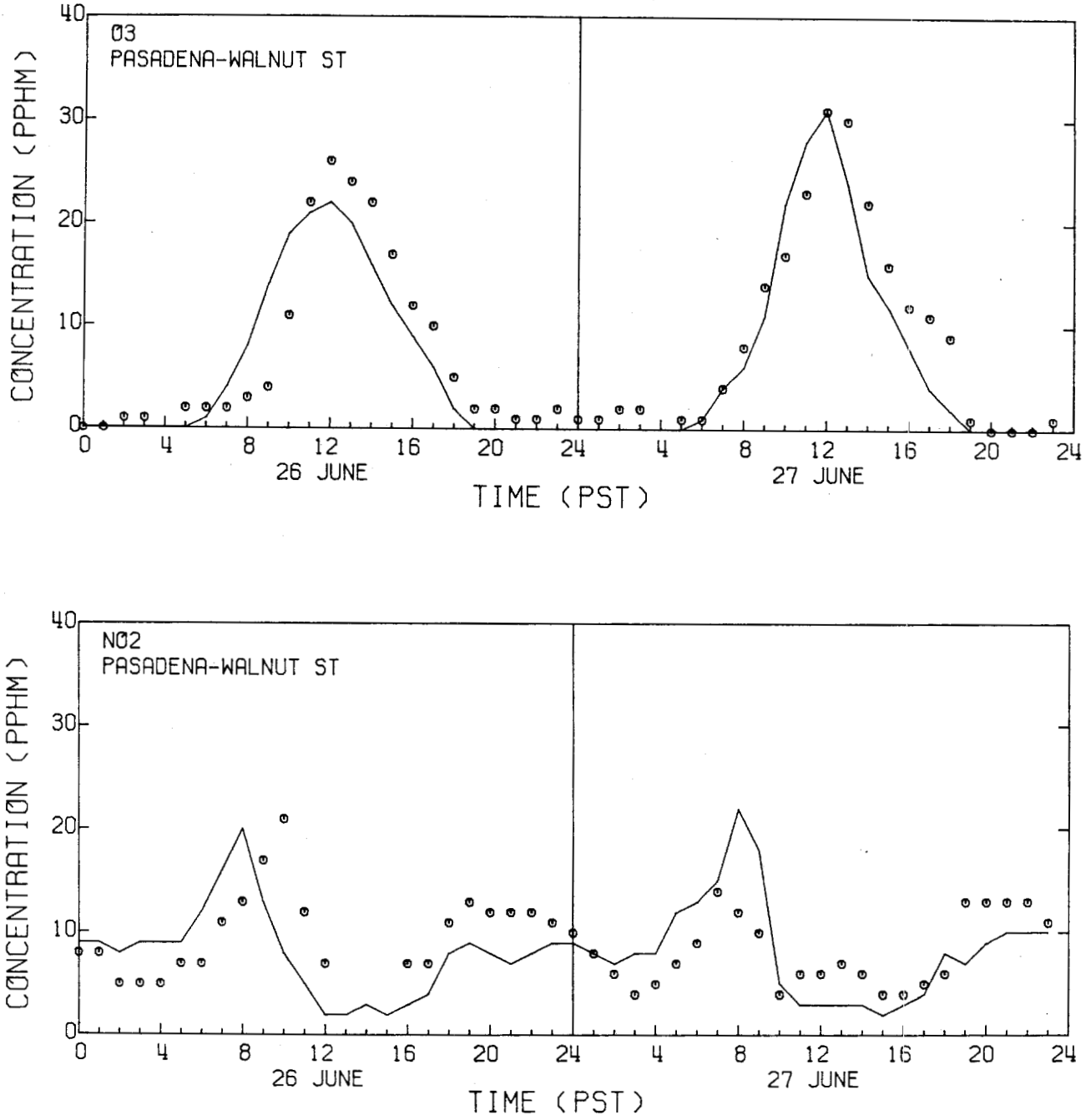

FIGURE C.31

Measured (o) and Predicted (-) Ozone and Nitrogen Dioxide
Air Quality at Pasadena-Walnut St

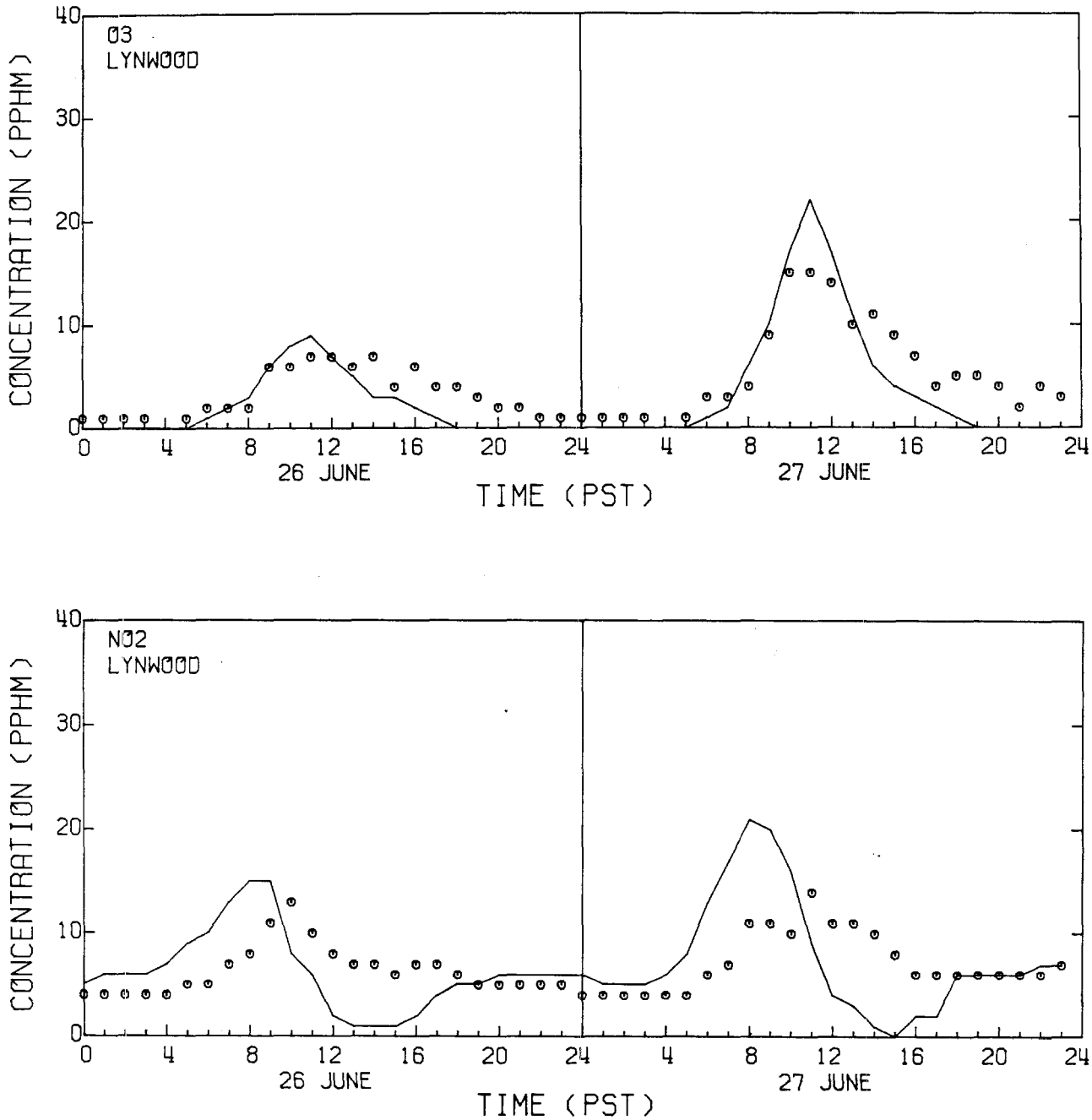

FIGURE C.32

Measured (o) and Predicted (-) Ozone and Nitrogen Dioxide Air Quality at Lynwood

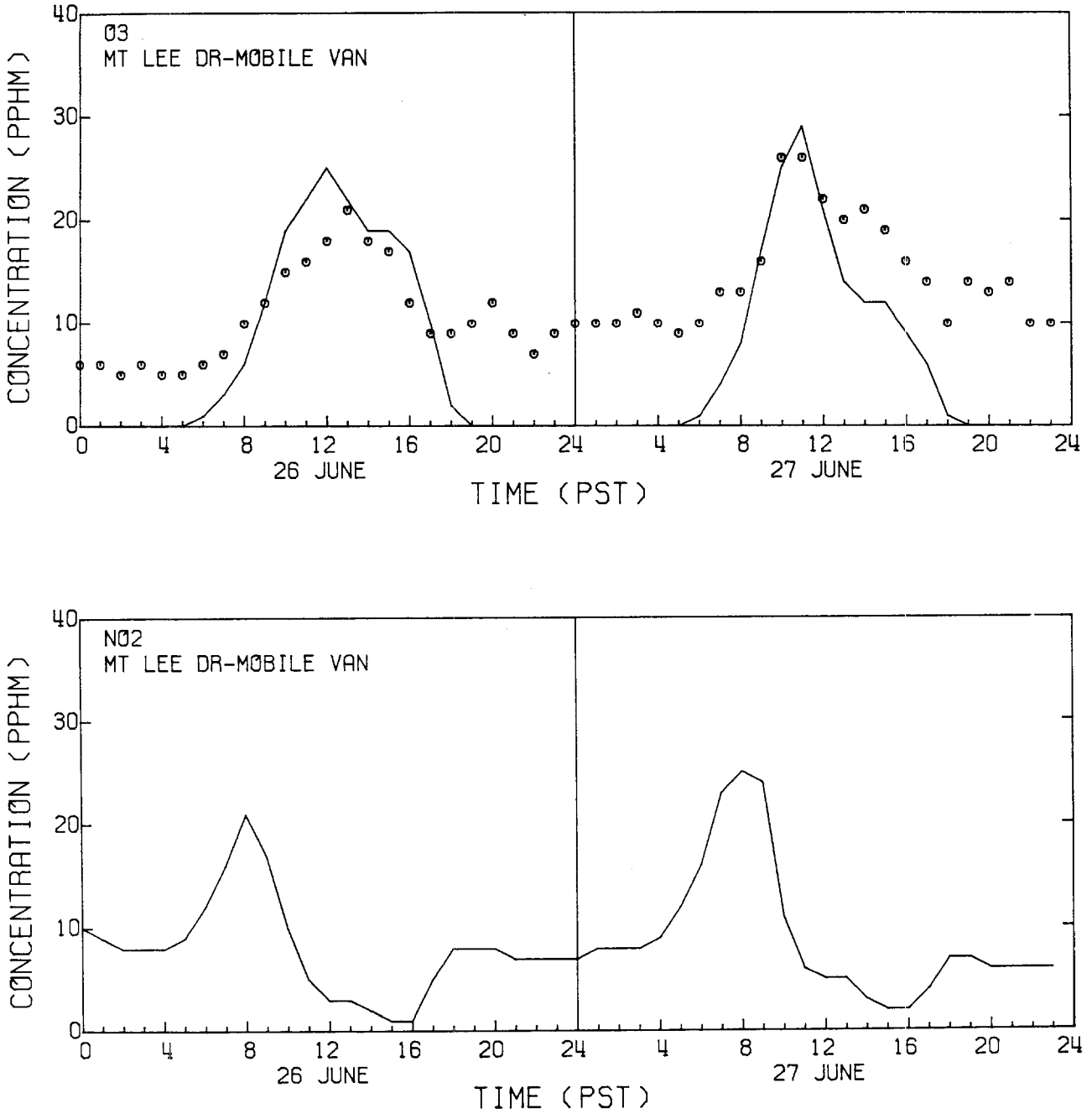

FIGURE C.33

Measured (o) and Predicted (-) Ozone and Nitrogen Dioxide
Air Quality at Mt Lee Dr-Mobile Van

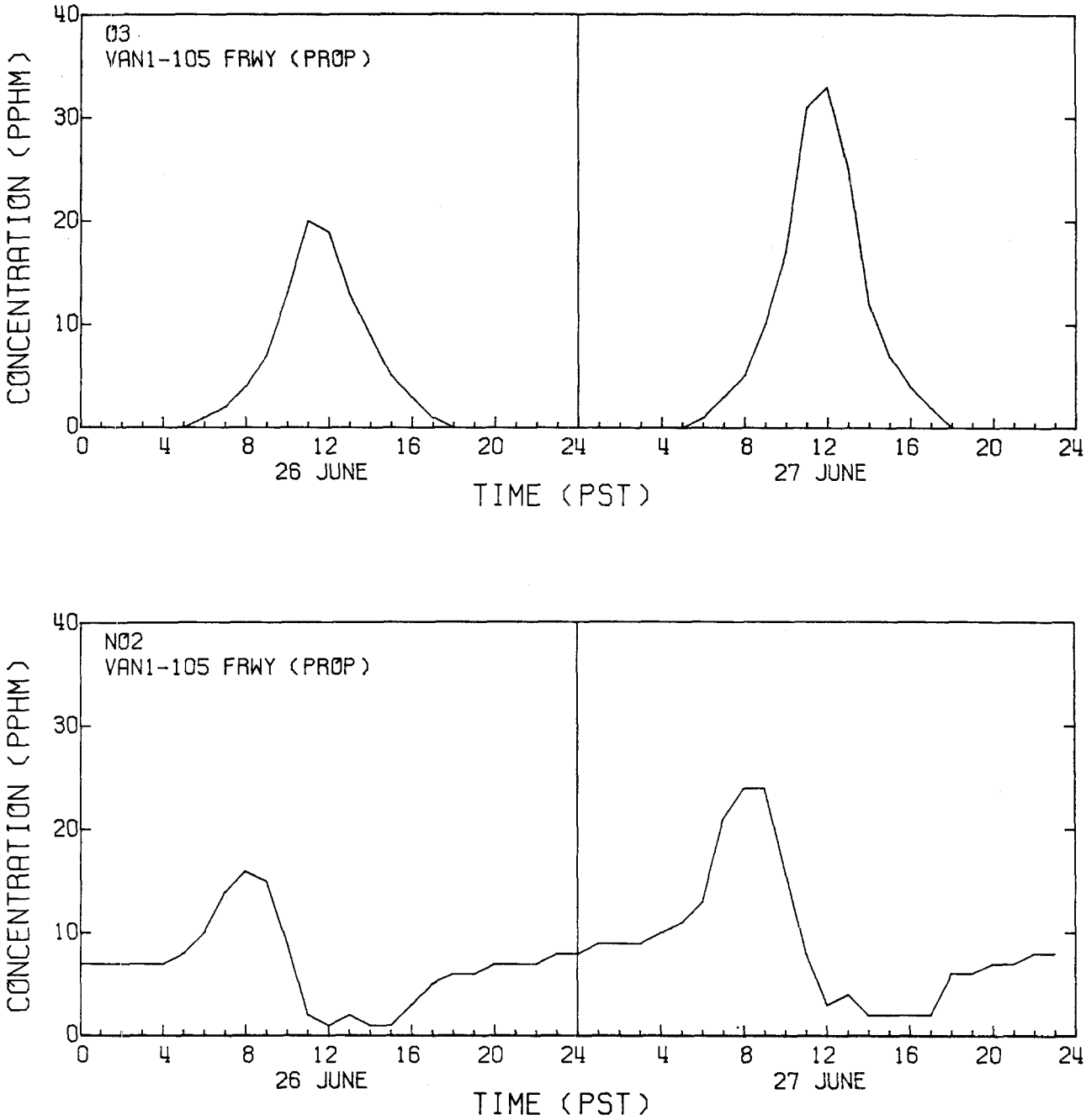

FIGURE C.34

Measured (o) and Predicted (-) Ozone and Nitrogen Dioxide
Air Quality at Vanl-105 Frwy (Prop)

References for Chapter 1

Bailey, B.S. (1975), "Oxidant-HC-NO_x Relationships from Aerometric Data--L.A. Studies," Scientific Seminar on Automotive Pollutants, U.S. Environmental Protection Agency Report, EPA-600/9-75-003, 10-12 February, Washington D.C.

Demerjian, K.L. and Schere K.L. (1979), "Development of Atmospheric Models and Modeling Capability," Internal Report U.S. Environmental Protection Agency, Environmental Sciences Laboratory, Research Triangle Park, North Carolina.

Dimitriades, B. (1972), "Effects of Hydrocarbon and Nitrogen Oxides on Photochemical Smog Formation," Environmental Science Technology, 6,, 253-260.

Dimitriades, B. (1976), "Photochemical Oxidants in the Ambient Air of the United States," U.S. Environmental Protection Agency Report, EPPA-600/3-76-017, 183 pp.

Dimitriades, B. ed. (1977), "International Conference on Photochemical Oxidant Pollution and Its Control: Proceedings Volumes I and II," U.S. Environmental Protection Agency Report, EPA-600/3-77-001a,b, 1171 pp.

Dodge, M.C. (1977), "Combined Use of Modeling Techniques and Smog Chamber Data to Derive Ozone-Precursor Relationships," U.S. Environmental Protection Agency Report, EPA-600/3-77-001a, 881-889.

Duewer, W.H., MacCracken, M.C. and Walton, J.J. (1978), "The Livermore Regional Air Quality Model: II Verification and Sample Application in the Bay Area," Journal of Applied Meteorology, 17, 273-311.

Eschenroeder, A.Q. and Martinez, J.R. (1972), "Concept and Applications of Photochemical Smog Models," Advances in Chemistry Series, 113, 101-168.

Falls, A.H. and Seinfeld, J.H. (1978), "Continued Development of a Kinetic Mechanism for for Photochemical Smog," Environmental Science and Technology, 12,(13), 1389-1406.

Graedel, T.E., Farrow, L.A. and Weber, T.A. (1976), "Kinetic Studies of the Photochemistry of the Urban Troposphere," Atmospheric Environment, 10, 1095-1116.

Graedel, T.E., Farrow, L.A. and Weber, T.A. (1978), "Urban Kinetic Chemical Calculations with Altered Source Conditions," Atmospheric Environment, 12, 1403-1412.

Hamming, W.J., Chass, R.L., Dickinson, J.E. and MacBeth, W.G. (1973), "Motor Vehicle Control and Air Quality: The Path to Clean Air for Los Angeles," Paper 73-73 presented at 66th Annual Meeting of the Air Pollution Control Association, Chicago, Illinois, June 24-28, 19 pp.

Hecht, T.A., Seinfeld, J.H. and Dodge, M.C. (1974), "Further Development of a Generalized Mechanism for Photochemical Smog," Environmental Science and Technology, 8, 327-339.

Horie, Y., Marians, M., Trijonis, J., Hurt, P. and Chang, N. (1979), "Ozone Precursor Emissions/Air Quality Relationships for Use with the Empirical Kinetic Modeling Approach," Technology Service Corporation Report TSC-PD-A196-6, Santa Monica, California.

Lloyd, A.C., Lurmann, F.W., Godden, D.K., Hutchins, J.F., Eschenroeder, A.Q. and Nordsieck, R.A. (1979), "Development of the ELSTAR Photochemical Air Quality Simulation Model and its Evaluation Relative to the LARPP Data Base," Environmental Research and Technology Report P-5287-500, Westlake Village, California, 392 pp.

MacCracken, M.C. and Sauter, G.D., eds, (1975), "Development of an Air Pollution Model for the San Francisco Bay Area-Final Report to the National Science Foundation Volumes I and II, Lawrence Livermore Laboratory Report UCRL-51920, 1169 pp.

MacCracken, M.C., Walton, J.J., Duewer, W.H. and Grant, K.E. (1978), "The Livermore Regional Air Quality Model: I Concept and Development," Journal of Applied Meteorology, 17, 254-272.

McRae, G.J., Goodin, W.R. and Seinfeld, J.H. (1979), "A Second Generation Mathematical Model of Photochemical Air Pollution," Proceedings American Meteorological Society Fourth Symposium on Atmospheric Turbulence, Diffusion and Air Quality, January 15-18, Reno, Nevada, 389-396.

McRae, G.J., Goodin, W.R. and Seinfeld, J.H. (1981), Development of a Comprehensive Mathematical Model of Photochemical Air Pollution, Final Report to California Air Resources Board under Contract A5-046-87, 800 pp.

Merz, P.H., Painter, L.J. and Ryason, P.R. (1972), "Aerometric Data Analysis, Time Series Analysis and Forecast, and an Atmospheric Smog Diagram," Atmospheric Environment, 6, 319-342.

Myrabo, L.N., Wilson, K.R. and Trijonis, J.C. (1977), "Survey of Statistical Models for Oxidant Air Quality Prediction," Advances in Environmental Science and Technology, 7, 391-422.

National Academy of Sciences (1977), Ozone and Other Photochemical Oxidants, National Academy of Sciences, Washington, D.C., 719 pp.

Paskind, J.J. and Kinosian, J.R. (1974), "Hydrocarbons, Oxides of Nitrogen and Oxidant Pollutant Relationships in the Atmosphere over California Cities," 67th Annual Meeting, Air Pollution Control Association, 9-13 June 1974, Denver, Colorado.

Post, K. and Bilger, R.W. (1978), "Ozone-Precursor Relationships in the Sydney Airshed," Atmospheric Environment, 12, 1857-1865.

Reynolds, S.C., Liu, M.K., Hecht, T.A., Roth, P.M. and Seinfeld, J.H. (1974), "Mathematical Modeling of Photochemical Air Pollution - III. Evaluation of the Model," Atmospheric Environment, 8, 563-596.

Reynolds, S.D., Roth, P.M. and Seinfeld, J.H. (1973), "Mathematical Modeling of Photochemical Air Pollution - I. Formulation of the Model," Atmospheric Environment, 7, 1033-1061.

Roth, P.M., Roberts, P.J.W., Liu, M.K., Reynolds, S.D. and Seinfeld, J.H. (1974), "Mathematical Modeling of Photochemical Air Pollution - II. A Model and Inventory of Pollutant Emissions,"Atmospheric Environment, 8, 97-130.

Roth, P.M., Reynolds, S.D., Anderson, G.E., Pollack, R.I., Yocke, M.A. and Killus, J.P. (1976), "An Evaluation of Methodologies for Assessing the Impact of Oxidant Control Strategies," Systems Applications, Inc. Report EF76-112R, San Rafael, California, 221 pp.

Schuck, E.A. and Papetti, R.A. (1973), "Examination of the Photochemical Air Pollution Problem in the Southern California Area," Appendix D of Technical Support Document for the Metropolitan Los Angeles Intrastate Air Quality Control Region Transportation Control Plan Final Promulgation, EPA Region IX, Environmental Protection Agency, San Francisco, California, 19 pp.

Tiao, G.D., Phadke, M.S. and Box, G.E.P. (1975), "Some Empirical Models for the Los Angeles Photochemical Smog Data," 68th Annual Meeting, Air Pollution Control Association, 15-20 June 1975, Boston, Massachusetts.

Trijonis, J.C. (1972), "An Economic Air Pollution Control Model Application: Photochemical Smog in Los Angeles County in 1975," PhD. thesis, California Institute of Technology, Pasadena, California, 376 pp.

Trijonis, J.C. (1974), "Economic Air Pollution Control Model for Los Angeles County in 1975," Environmental Science and Technology, 8, 811-826.

Trijonis, J.C., Peng, T., McRae, G.J. and Lees, L. (1978), "Oxidant and Precursor Trends in the Metropolitan Los Angeles Region," Atmospheric Environment, 12, 1413-1420.

Trijonis, J.C. and Hunsaker, D. (1978), "Verification of the Isopleth Method for Relating Photochemical Oxidant to Precursors," U.S. Environmental Protection Agency Report, EPA-600/3-78-019, 112 pp.

Turner, D.B. (1979), "Atmospheric Dispersion Modeling--A Critical Review," Journal of the Air Pollution Control Association, 29, 502-515.

U.S. Environmental Protection Agency (1971), "Title 42-Public Health, Part 420, Requirements for the Preparation, Adoption, and Submittal of Implementation Plans," Federal Register, 36, 15486-15506.

U.S. Environmental Protection Agency (1974), "Applying Atmospheric Simulation Models to Air Quality Maintenance Regions," in Guidelines for Air Quality Maintenance Planning and Analysis, U.S. Environmental Protection Report, EPA-450/4-74-013.

U.S. Environmental Protection Agency (1978), "Guideline on Air Quality Models," Office of Air Quality Planning and Standards Report OAQPS/1.2-080, U.S. Environmental Protection Agency, Research Triangle Park, North Carolina.

Wayne, L.G., Kokin, A. and Wiesburd, M.I. (1973), "Controlled Evaluation of the Reactive Environmental Simulation Model (REM)," U.S. Environmental Protection Agency Report, EPA R4-73-013a, 176 pp.

Whitten, G.Z. and Hogo, H. (1978), "User's Manual for Kinetics Model and Ozone Isopleth Plotting Package," U.S. Environmental Protection Agency Report, EPA-600/8-78-014a, 239 pp.

Whitten, G.Z., Hogo, H., Meldgin, M.J., Killus, J.P. and Bekowies, P.J. (1979), "Modeling of Simulated Photochemical Smog with Kinetic Mechanisms, Volumes I and II, U.S. Environmental Protection Agency Report, EPA-600/3-79-001a, 718 pp.

References for Chapter 2

Ackerman, T.P. (1977), "A Model of the Effects of Aerosols on Urban Climates with Particular Applications to the Los Angeles Basin," J. Atmospheric Sciences, 34 531-547.

Ackerman, T.P., Liou, K.N., and Leovy, C.B. (1976), "Infrared Radiative Transfer in Polluted Atmospheres," J. Applied Meteorology, 15, 28-35.

Aris, R. (1956), "On the Dispersion of a Solute in Fluid Flowing Through a Tube," Proceedings Royal Society London, Series A, 235, 67-77.

Aris. R. (1962), Vectors, Tensors, and the Basic Equations of Fluid Mechanics, Prentice-Hall, Englewood Cliffs, 286 pp.

Atwater, M.A. (1977), "Urbanization and Pollutant Effects on the Thermal Structure in Four Climatic Regimes," J. Applied Meteorology, 16, 888-895.

Bergstrom, R. and Viskanta, R. (1973a), "Prediction of the Spectral Absorption and Extinction Coefficients of an Urban air Pollution Aerosol Model," Tellus, 12, 468-498.

Bergstrom, R. and Viskanta, R. (1973b), "Modeling of the Effects of Gaseous and Particulate Pollutants in the Urban Atmosphere. Part I: Thermal Structure," J. Applied Meteorology, 12, 901-912.

Bergstrom, R. and Viskanta, R. (1973c), "Modeling of the Effects of Gaseous and Particulate Pollutants in the Urban Atmosphere. Part II: Pollutant Dispersion," J. Applied Meteorology, 12, 913-918.

Binkowski, F.S. (1979), "A Simple Semi-Empirical Theory for Turbulence in the Atmospheric Surface Layer," Atmospheric Environment, 13, 247-253.

Blumenthal, D.L., White, W.H., Smith, T.B. (1978), "Anatomy of a Los Angeles Smog Episode: Pollutant Transport in the Daytime Sea Breeze Regime," Atmospheric Environment, 12, 893-907.

Boussinesq, J. (1877), "Essai sur la Theori des Eaux Courtantes," Mem. Pres. par Aiv. Savants ã l'Acad. Sci., Paris, 23 (1), 1-680.

Bowen, R. (1976), "Theory of Mixures," Continuum Physics, 3, A. Cemal Eringen, ed. Academic Press, New York, 1-127.

Busch, N.E. (1973),"On the Mechanics of Atmospheric Turbulence," in Workshop on Micrometeorology, D.A. Haugen ed., American Meteorology Society, Boston, Massachusetts, 1-66.

Businger, J.A. (1973), Turbulent Transfer in the Atmospheric Surface Layer," Workshop on Micrometeorology, D.A. Haugen ed., American Meteorological Society, Boston, Massachusetts, 67-100.

Clarke, R.H. and Hess, G.D. (1973), "On the Appropriate Scaling for Velocity and Temperature in the Planetary Boundary Layer," J. Atmospheric Sciences, 30, 1346-1353.

Corrsin, S. (1958), Statistical Behavior of a Reacting Mixture in Isotropic Turbulence," Physics of Fluids, 1, 42.

Corrsin, S. (1974), Limitations of Gradient Transport Models in Random Walks and in Turbulence, Advances in Geophysics, 18A, Academic Press, New York, 25-59.

Crane, G., Panofsky, H., and Zeman, O. (1977), "A Model for Dispersion from Area Sources in Convective Turbulence," Atmospheric Environment, 11, 893-900.

Deardorff, J.W. (1966), The Counter-Gradient Heat Flux in the Lower Atmosphere and in the Laboratory," J. Atmospheric Sciences, 23, 503-506.

Deardorff, J.W. (1970), "A Three-Dimensional Numerical Investigation of the Idealized Planetary Boundary Layer," Geophysical Fluid Dynamics, 1, 377-410.

Deardorff, J.W. (1972), "Numerical Investigation of Neutral and Unstable Boundary Layers," J. Atmospheric Sciences, 29, 91-115.

Deardorff, J.W. and Willis, G.E. (1974), "Computer and Laboratory Modeling of the Vertical Diffusion of Nonbuoyant Particles in the Mixed Layer," Advances in Geophysics, 18B, Academic Press, New York, 187-200.

Depazo, C. (1977), "On Conditioned Averages for Intermittent Turbulent Flows," J. Fluid Mechanics, 81, 433-438.

Donaldson, C. du P. (1973), "Construction of a Dynamic Model of the Production of Atmospheric Turbulence and the Dispersal of Atmospheric Pollutants," Workshop on Micrometeorology, D.A. Haugen ed., American Meteorological Society, Boston, Massachusetts, 313-392.

Donaldson, C. du P. (1975), "On the Modelling of the Scalar Correlation Necessary to Construct a Second-Order Closure Description of Turbulent Reacting Flows," A Review in Turbulent Mixing in Non-Reactive and Reactive Flows, ed. S.N.B. Murthy, Plenum Press, New York.

Duewer, W.H., MacCracken, M.C. and Walton, J.J. (1978), "The Livermore Regional Air Quality Model: II Verification and Sample Application in the Bay Area," J. Applied Meteorology, 17, 273-311.

Dutton, J.A. and Fichtl, G.H. (1969), "Approximate Equations of Motion for Gases and Liquids," J. Atmospheric Sciences, 2, 241-254.

Edinger, J.G. (1973), "Vertical Distribution of Photochemical Smog in Los Angeles Basin," Environmental Science and Technology, 7, 247-252.

Eschenroeder, A.Q. and Martinez, J.R. (1972), "Concepts and Applications of Photochemical Smog Models," Advances in Chemistry Series, 113, American Chemical Society, Washington, D.C., 101-168.

Freeman, B.E. (1977), "Tensor Diffusivity of a Trace Constituent in a Stratified Boundary Layer," J. Atmospheric Sciences, 34, 124-136.

Galloway, F.M. (1976), "Criteria for the Use of Vertical Averaging in Environmental Dispersion Models," Water Resources Research, 12(5), 933-940.

Graedel, T.E., Farrow, L.A., and Weber, T.A. (1976), "Kinetic Studies of the Photochemistry of the Urban Troposphere," Atmospheric Environment, 10, 1095-1116.

Hampson, R.F. and Garvin, D. eds. (1977), Reaction Rate and Photochemical Data for Atmospheric Chemistry-1977, NBS Special Publication No. 513, U.S. Department of Commerce, 106 pp.

Hegg, D., Hobbs, P.V., Radke, L.F. and Harrison, H. (1977), "Reaction of Ozone and Nitrogen Oxides in Power Plant Plumes," Atmospheric Environment, 11, 521-526.

Hill, J.C. (1976), "Homogeneous Turbulent Mixing with Chemical Reaction, Annual Review of Fluid Mechanics, 8, 135-161.

Lamb, R.G. (1971), "Numerical Modeling of Urban Air Pollution," Ph.D. Thesis, Department of Meteorology, University of California at Los Angeles, 289 pp.

Lamb, R.G. (1975), "Modeling of Microscale Phenomena," Final Report to Environmental Protection Agency under contract 68-02-1237, Systems Application, Inc., San Rafael, California.

Lamb, R.G., Chen, W.H. and Seinfeld, J.H. (1975), "Numerical-Empirical Analyses of Atmospheric Diffusion Theories," J. Atmospheric Sciences, 32, 1794-1807.

Lamb, R.G. and Durran, D.R. (1977), "Eddy Diffusivities Derived from a Numerical Model of the Convective Boundary Layer," Il Nuova Ciento, 1C(1), 1-17.

Lamb, R.G. and Seinfeld, J.H. (1973), "Mathematical Modeling of Urban Air Pollution--General Theory," Environmental Science and Technology, 7, 253-261.

Lamb, R.G. and Shu, W.R. (1978), "A Model of Second-Order Chemical Reactions in Turbulent Fluid - Part I. Formulation and Validation," Atmospheric Environment, 12, 1685-1694.

Lewellen, W.S., Teske, M. and Donaldson, C. du P. (1974), "Turbulence Model of Diurnal Variations in the Planetary Boundary Layer," Proc. of the 1974 Heat Transfer and Fluid Mechanics Institute, ed. L.R. Davis and E.R. Wilson, Stanford University Press, 301-319.

Liu, M.K. and Seinfeld, J.H. (1975), "On the Validity of Grid and Trajectory Models of Urban Air Pollution," Atmospheric Environment, 9, 553-574.

Liu, M.K., Whitney, D.C. and Roth, P.M. (1976), "Effects of Atmospheric Parameters on the Concentration of Photochemical Air Pollutants," J. Applied Meteorology, 15, 829-835.

Lloyd, A.C., Lurmann, F.W., Godden, D.K., Hutchins, J.F., Eschenroeder, A.Q. and Nordseick, R.A. (1979), "Development of the ELSTAR Photochemical Air Quality Simulation Model and its Evaluation Relative to the LARPP Data Base," Environmental Research and Technology Report No. P-5287-500, Westlake Village, California, 292 pp.

Lumley, J.L. and Khajeh-Nouri, B. (1974), "Computational Modeling of Turbulent Transport," Advances in Geophysics, 18A, Academic Press, New York, 169-192.

MacCracken, M.C., Wuebbles, D.J., Walton, J.J., Duewer, W.H. and Grant, K.E. (1978), "The Livermore Regional Air Quality Model: I. Concept and Development," J. Applied Meteorology, 17, 254-272.

Manins, P.C. (1977), "Fumigation and a Laboratory Experiment," Weather, June, 221-228.

Manton, M.J. (1979), "On the Disperson of Particles in the Atmosphere," Boundary Layer Meteorology, 17, 145-165.

Mellor, G.L. and Yamada, T. (1974), "A Hierarchy of Turbulence Closure Models for Planetary Boundary Layers," J. Atmospheric Sciences, 31, 1791-1806.

Monin, A.S. and Yaglom, A.M. (1971), Statistical Fluid Mechanics: Mechanics of Turbulence, The MIT Press, Cambridge, Massachusetts, 769 pp.

Murthy, S.N.B. (1975), "Turbulent Mixing in Non-Reactive and Reactive Flows," A Review in Turbulent Mixing in Non-Reactive and Reactive Flows, S.N.B. Murthy, ed., Plenum Press, New York, 1-84.

O'Brien, E.E. (1974), "Turbulent Diffusion of Rapidly Reacting Chemical Species," Advances in Geophysics, 18B, Academic Press, New York, 341-348.

Reynolds, S.D., Roth, P.M., and Seinfeld, J.H. (1973), "Mathematical Modeling of Photochemical Air Pollution--I Formulation of the Model," Atmospheric Environment, 7, 1033-1061.

Saffman, P.G. (1962), "The Effect of Wind Shear on Horizontal Spread from an Instantaneous Ground Source," Quarterly J. Royal Meteorological Society, 88, 382-393.

Sheih, C.M. (1980), "On Lateral Dispersion Coefficients as Functions of Averaging Time," J. Applied Meteorology, 19, 557-561.

Shu, W.R. (1976), "Turbulent Chemical Reactions: Application to Atmospheric Chemistry," Ph.D Thesis, Department of Chemical Engineering, California Institute of Technology, Pasadena, 194 pp.

Shu, W.R., Lamb, R.G. and Seinfeld, J.H. (1978), "A Model of Second-Order Chemical Reactions in a Turbulent Fluid, II. Application to Atmospheric Plumes," Atmospheric Environment, 12, 1699-1705.

Smith, T.B., Marsh, S.L., White, W.H., et al. (1976), "Analysis of the Data from the Three-Dimensional Gradient Study, Final Report submitted to the California Air Resources Board under contracts ARB-4-051 and ARB-4-250, Meteorology Research, Inc., Pasadena, California, and System Applications,

Sokolnikoff, I.S. and Redheffer, R.M. (1958), Mathematics of Physics and Modern Engineering, McGraw-Hill Book Company, Inc., New York, 812 pp.

Spalding, D.B. (1975), "Turbulence Modelling: Solved and Unsolved Problems," A Review in Turbulent Mixing In Non Reactive and Reactive Flows, ed. S.N.B. Murthy, Plenum Press, New York, 85-130.

Spiegel, E.A. and Veronis, G. (1960),"On the Boussinesq Approximation for a Compresible Fluid," Astrophysics Journal, 131, 442-447.

Taylor, G.I. (1954), "The Dispersion of Matter in Turbulent Flow Through a Pipe," Proceedings Royal Society London, Series A, 223, 446-468.

Tennekes, H. (1970), "Free Convection in the Turbulent Eckman Layer of the Atmosphere," J. Atmospheric Sciences, 27, 1027-1034.

Viskanta, R., Bergstrom, R.W. and Johnson, R.O. (1977), "Radiative Transfer in a Polluted Planetary Boundary Layer," J. Atmospheric Sciences, 33, 2170-2184.

Viskanta, R. and Daniel, R.A. (1980), "Radiative Effects of Elevated Pollutant Layers on Temperature Structure and Dispersion in an Urban Atmosphere," J. of Applied Meteorology, 19, 53-70.

Welch, R.M., Paegle, J. and Zdunkowski, G. (1978), "Two-Dimensional Numerical Simulation of the Effects of Air Pollution upon the Urban-Rural Complex," Tellus, 30, 136-150.

Whitten, G.Z. and Hogo, H. (1976), "Mathematical Modeling of Simulated Photochemical Smog," Final Report for EPA Contract 68-02-0580, Systems Application, Inc., San Rafael, California.

Wyngaard, J.C. (1973), "On Surface-Layer Turbulence," in Workshop on Micrometeorology, D.A. Haugen ed., American Meteorological Society, Boston, Massachusetts, 101-149.

Wyngaard, J.C. and Cote, O.R. (1974), "The Evolution of a Convective Planetary Boundary Layer--A Higher Order Closure Model Study, Boundary Layer Meteorology, 7, 289-308.

Yamada, T. (1977), "A Numerical Experiment on Pollutant Dispersion in a Horizontally-Homogeneous Atmospheric Boundary Layer," Atmospheric Environment, 11, 1015-1024.

Yamada, T. and Mellor, G.L. (1975), "A Simulation of the Wangara Atmospheric Boundary Layer Data," J. Atmospheric Sciences, 32, 2309-2329.

Yotsukura, N. (1977), "Derivation of Solute-Transport Equations for a Turbulent Natural-Channel Flow," J. Research U.S. Geological Survey, 5(3), 277-284.

Zdunkowski, W.G. and McQuage, N.D. (1972), "Short-Term Effects of Aerosols on the Air Layer Near the Ground," Tellus, 24, 237-254.

Zdunkowski, W.G., Welch, R.M. and Paegle, J. (1976), "One-Dimensional Numerical Simulation of the Effects of Air Pollution on the Planetary Boundary Layer," J. Atmospheric Sciences, 33, 2399-2414.

Zeman, O. and Lumley, J.L. (1976), "Modeling Buoyancy Driven Mixed Layers," J. Atmospheric Sciences, 33, 1974-1988.

Zeman, O. and Tennekes, H. (1977), "Parameterization of the Turbulent Energy Budget at the Top of the Daytime Atmospheric Boundary Layer," J. Atmospheric Sciences, 34, 111-123

Zilitinkevich, S.S. (1972), "On the Determination of the Height of the Eckman Boundary Layer," Boundary Layer Meteorology, 3, 141-145.

References for Chapter 3

Akima, H. (1975), "A Method of Bivariate Interpolation and Smooth Surface Fitting for Values Given at Irregularly Distributed Points," Department of Commerce Report 75-70, 51 pp.

Barnhill. R.E. (1977), "Representation and Approximation of Surfaces," Mathematical Software, III, J.R. Rice ed., Academic Press, New York, 68-119.

Brostow, W., Dussault, J.P. and Fox, B.L. (1978), "Construction of Voronoi Polyhedra," J. of Computational Physics, 29, 81-92.

Bradely, E.F. (1968), "A Micrometeorological Study of Velocity Profiles and Surface Drag in the Region Modified By a Change in Surface Roughness," Quarterly J. Royal Meteorological Society, 94, 361-379.

Busch, N.E. (1973), "On Mechanics of Atmospheric Turbulence," in Workshop in Micrometeorology, ed. D.A. Haugen, American Meteorological Society, Boston, Massachusetts, 1-65.

Buzbee, B.L., Golub, G.H. and Nielson, C.W. (1970), "On Direct Methods for Solving Poisson's Equation," SIAM J. Numerical Analysis, 7, 627-656.

Davenport, A.G. (1960), "Rationale for Determining Design Wind Velocities," Proc. ASCE J. Structural Division, 86, 39-68.

Deacon, E.L. (1949), "Vertical Diffusion in the Lowest Layers of the Atmosphere," Quarterly J. Royal Meteorological Society, 75, 89-103.

Donaldson, C. du P. (1973), "Construction of a Dynamic Model of the Production of Atmospheric Turbulence and the Dispersal of Atmospheric Pollutants," in Workshop in Micrometeorology, ed. D.A. Haugen, American Meteorological Society, Boston, Massachusetts, 1-65.

Dorr, F.W. (1970), "The Direct Solution of the Discrete Poisson Equation on a Rectangle," SIAM Review, 12, 248-263.

Doss, S. and Miller, K. (1979), "Dynamic ADI Methods for Elliptic Equations," SIAM J. Numerical Analysis, 16, 837-856.

Dutton, J.A. and Fichtl G.H. (1969), "Approximate Equations of Motion for Gases and Liquids," J. of Atmospheric Sciences, 26, 241-254.

Finney, J.L. (1979), "A Procedure for the Construction of Voronoi Polyhedra," J. of Computational Physics, 32, 137-143.

Franke, R. (1977), "Locally Determined Smooth Interpolation at Irregularly Spaced Points in Several Variables," J. Institute of Mathematics and its Applications, 19, 471-482.

Frankel, S.P. (1950), "Convergence Rates of Iterative Treatments of Partial Differential Equations," Math Tables and Other Aids to Computation, 4, 66-75.

Glahn, H.R. (1981), Comments on "A Comparison of Interpolation Methods for Sparse Data: Application to Wind and Concentration Fields," J. Applied Meteorology, 20, 89-91.

Goodin, W.R., McRae, G.J. and Seinfeld, J.H. (1979), "A Comparison of Interpolation Methods for Sparse Data: Application to Wind and Concentration Fields," J. Applied Meteorology, 18, 761-771.

Goodin, W.R. and McRae, G.J. (1980), "A Procedure for Wind Field Construction from Measured Data Which Utilizes Local Surface Roughness," Proc. Second Conference on Coastal Meteorology," January 30,- February 1, Los Angeles, California, American Meteorological Society, Boston, Massachusetts, 233-239.

Goodin, W.R., McRae, G.J. and Seinfeld, J.H. (1981), "A Reply," J. Applied Meteorology, 20, 92-94.

Gordon, W.J. and Wixom, J.A. (1978), "Shepard's Method of "Metric Interpolation" to Bivariate and Multivariate Interpolation," Mathematics of Computation, 32, 253-264.

Graham, R.L. (1972), "An Efficient Algorithm for Determining the Convex Hull of a Finite Planar Set," Information Processing Letters, 1, 132-133.

Green, P.J. and Sibson, R. (1978), "Computing Dirichlet Tesselations in the Plane," The Computer Journal, 21, 168-173.

Green, P.J. and Silverman, B.W. (1979), "Constructing the Convex Hull of a Set of Points in the Plane," The Computer Journal, 22, 262-266.

Irwin, J.S. (1979), "A Theoretical Variation of the Wind Profile Power-Law Exponent as a Function of Surface Roughness and Stability," Atmospheric Environment, 13, 191-194

Jarvis, R.A. (1973), "On the Identification of the Convex Hull of a Finite Set of Points in the Plane," Information Processing Letters, 2, 18-21.

Lamb, B.K. and Shair, F.H. (1977), "Atmospheric Tracer Studies to Characterize the Transport and Dispersion of Pollutants in the California Delta Region." Report to California Air Resources Board under Contract No. ARB-A5-065-87.

Lawson, C.L. (1977), "Software for C^1 Surface Interpolation," Mathematical Software III, Academic Press, New York, 161-193.

Maher, Y. and Pielke, R.A. (1977), "A Numerical Study of the Airflow Over Irregular Terrain," Beiträge Zur Physik der Atmosphäre, 50, 98-113.

McLain, D.H. (1974), "Drawing Contours from Arbitrary Data Points," The Computer Journal, 17, 318-324.

McLain, D.H. (1976a), "Two Dimensional Interpolation from Random Data," The Computer Journal, 19, 178-181.

McLain, D.H. (1976b), Errata, The Computer Journal, 19 384.

Mulhearn, P.J. (1977), "Relations Between Surface Fluxes and Mean Profiles of Velocity, Temperature and Concentration, Downwind of a Change in Surface Roughness," Quarterly J. Royal Meteorological Society, 103, 785-802.

Nelson, J.M. (1978), "A Triangulation Algorithm for Arbitrary Planar Domains," Applied Mathematical Modelling, 2, 151-159.

Nielson, G. (1980), "Minimum Norm Interpolation in Triangles," SIAM J. Numerical Analysis, 17, 44-62.

Nickerson, E.C. (1979), "On the Numerical Simulation of Airflow and Clouds Over Mountainous Terrain," Contrib. to Atmos. Phys., 4, 161-175.

Panofsky, H.A. (1973), "Tower Micrometeorology," in Workshop on Micrometeorology, D.A. Haugen ed., American Meteorological Society, Boston, Massachusetts, 151-176.

Peaceman, D.W. and Rachford, H.H., Jr. (1955), "The Numerical Solution of Parabolic and Elliptic Differential Equations," J. SIAM, 3, 28-41.

Powell, M.J.D. and Sabin, M.A. (1977), "Piecewise Quadratic Approximation on Triangles," ACM Transactions on Mathematical Software, 3, 316-325.

Roache, P.J. (1976), Computational Fluid Dynamics, Hermosa Publishers, Albuquerque, New Mexico, 446 pp.

Rodgers, C.A. (1964), Packing and Covering, Cambridge University Press, Cambridge, 111 pp.

Schumaker, L.L. (1976), "Fitting Surfaces to Scattered Data," Approximation Theory II, G.G. Lorentz, C.K. Chui and L.L. Schumaker eds., Academic Press, New York, 203-268.

Shepard, D. (1968), "A Two-Dimensional Interpolation Function for Irregularly-Spaced Data," Proc. 23rd ACM National Conference, Las Vegas, Nevada, 517-524.

Swarztrauber, P.N. (1977), "The Methods of Cyclic Reduction, Fourier Analysis and the FACR Algorithm for the Discrete Solution of Poisson's Equation on a Rectangle," SIAM Review, 19, 490-501.

Sykes, R.I. and Hatton, L. (1976), "Computation of Horizontal Trajectories Based on the Surface Geostrophic Wind," Atmospheric Environment, 10, 925-934.

Temperton, C. (1979), "Direct Methods for the Solution of the Discrete Poisson Equation: Some Comparisons," J. Computational Physics, 31, 1-20.

Thacker, W.C. (1979), "An Improved Triangulation Algorithm," Applied Mathematical Modelling, 3, 471-472.

Thiessen, A.H. (1911), "Precipitation Averages for Large Areas," Monthly Weather Review, 39, 1082-1084.

Thuillier, R.H. and Lappe, U.O. (1964), "Wind and Temperature Profile Characteristics from Observations on a 1400 foot Tower," J. Applied Meteorology, 3, 299-306.

Touma, J.S. (1977), "Dependence of the Wind Profile Power Law on Stability for Various Locations," J. Air Pollution Control Association, 27, 863-866.

Wahba, G. and Wendelberger, J. (1979), "Some New Mathematical Methods for Variational Analysis Using Splines and Cross-Validation," Monthly Weather Review, 108, 1122-1143.

Webb, E.K. (1970), "Profile Relationships: The Loglinear Range, and Extensions to Strong Stability," Quarterly J. Royal Meteorological Society, 96, 67-90.

Wurtele, M.G. and Clark, C. (1965), "The Relative Efficiency of Certain Schema in the Solution of a Poisson Equation," J. Atmospheric Sciences, 22, 436-439.

Young, D. (1954), "Iterative Methods for Solving Partial Difference Equations of Elliptic Type," Transactions of the American Mathematical Society, 76, 92-111.

References for Chapter 4

Arya, S.P.S. (1977), "Suggested Revision to Certain Boundary Layer Parameterization Schemes used in Atmospheric Circulation Models." Monthly Weather Review, 105, 215-227.

Batchelor, G.K. (1950), "The Application of the Similarity Theory of Turbulence to Atmospheric Diffusion." Quarterly J. Royal Meteorological Society, 76, 133-146.

Briggs, G.A. (1974), "Diffusion Estimation for Small Emissions", in Environmental Research Laboratories, Air Resources Atmosphere Turbulence and Diffusion Laboratory 1973 Annual Report, USAEC Report ATDL-106, National Oceanic and Atmospheric Administration, December.

Businger, J.A., Wyngaard, J.C., Izumi, Y. and Bradley, E.F. (1971), "Flux-Profile Relationship in the Atmospheric Surface Layer," J. Atmospheric Sciences, 28, 181-189.

Businger, J.A. and Ayra, S.P.S. (1974), "Height of the Mixed Layer in the Stably Stratified Planetary Boundary Layer," Advances in Geophysics, 18A, 73-92.

Carl, D.M., Tarbell, T.C. and Panofsky, H.A. (1973), "Profiles of Wind and Temperature from Towers Over Homogeneous Terrain," J. Atmospheric Sciences, 30, 788-794.

Counihan, J. (1975), "Adiabatic Atmospheric Boundary Layers: A Review and Analysis of Data from the Period 1880-1972," Atmospheric Environment, 9, 871-905

Crane, G., Panofsky, H.A. and Zeman, O. (1977), "A Model for Dispersion from Area Sources in Convective Turbulence," Atmospheric Environment, 11, 893-900.

Csanady, G.T. (1973), Turbulent Diffusion in the Environment, Geophysics and Astrophysics Monographs, D. Reidel Publishing Company, Boston, Massachusetts, 248 pp.

Deacon, E.L. (1949), "Vertical Diffusion in the Lowest Layers of the Atmosphere," Quarterly J. Royal Meteorological Society, 75, 89-103.

Deardorff, J.W. (1970), "A Three-Dimensional Numerical Investigation of the Idealized Planetary Boundary Layer," Geophysical Fluid Dynamics, 1, 377-410.

Fichtl, G.H. and McVehil, G.E. (1970), "Longitudinal and Lateral Spectra of Turbulence in the Atmospheric Boundary Layer at the Kennedy Space Center," J. Applied Meteorology, 9, 51-63.

Galbally, I.E. (1971), "Ozone Profiles and Ozone Fluxes in the Atmospheric Surface Layer," Quarterly J. Royal Meteorological Society, 97, 18-29.

Gent, P.R. (1977), "A Numerical Model of the Air Flow Above Water Waves Part II," J. Fluid Mechanics, 82, 349-369.

Golder, D. (1972), "Relations Among Stability Parameters in the Surface Layer, Boundary-Layer Meteorology, 3, 47-58.

Haugen, D.A. ed. (1973), Workshop on Micro-Meteorology, American Meteorological Society, Boston, Massachusetts, 392 pp.

Hodgin, C. R. (1980), "Logarithmic Wind Profile Parameters Applied to Air Quality Assessment Studies," Proc. Second Joint Conference on Applications of Air Pollution Meteorology, March 24-27, New Orleans, Louisiana, American Meteorological Society, Boston, Massachusetts, 770-775.

Hsu, S.A. (1974), "A Dynamic Roughness Equation and Its Application to Wind Stress Determination at the Air-Sea Interface," J. Physical Oceanography, 4, 116-120.

Kaimal, J.C., Wyngaard, J.C. Hugen, D.A., Izumi, Y., Cote, O.R. and Caughey, S.J. (1976), "Turbulent Structure in the Convective Boundary Layer," J. Atmospheric Sciences, 33, 2152-2169.

Kitaigorodskii, S.A. (1970), The Physics of Air-Sea Interaction, Translated from Russian by Israel Program for Scientific Translation, TT72-50062, Jerusalem, 237 pp.

Lamb, R.G. and Neiburger, M. (1971), "An Interim Version of a Generalized Air Pollution Model," Atmospheric Environment, 5, 239-264.

Lamb, R.G., Chen, W.H. and Seinfeld, J.H. (1975), "Numerico-Empirical Analyses of Atmospheric Diffusion Theories," J. Atmospheric Sciences, 32, 1974-1807.

Lamb, R.G. and Durran, D.R. (1978), "Eddy Diffusivities Derived From the Numerical Model of the Convective Planetary Boundary Layer," Il Nuovo Cimento, 1C, 1-17.

Lamb, R.G. (1977) Personal communication.

Liu, M.K., Whitney, D.C. and Roth, P.M. (1976), "Effects of Atmospheric Parameters on the Concentration of Photochemical Air Pollutants," J. Applied Meteorology, 15, 829-835.

Lumley, J.L. and Panofsky, H.A. (1964), The Structure of Atmospheric Turbulence, Interscience Publishers, New York, 239 pp.

MacCracken, M.C., Walton, J.J., Duewer, W.H. and Grant, K.E. (1978), "The Livermore Regional Air Quality Model: I Concept and Development," Journal of Applied Meteorology, 17, 254-272.

McElroy, J.L. and Pooler, F. (1968), "St. Louis Dispersion Study," Arlington, Virginia, U.S. Public Health Service, National Air Pollution Control Administration Publication No. AP-53.

Monin, A.S. and Yaglom, A.M. (1971), Statistical Fluid Mechanics: Mechanics of Turbulence Volume 1. The MIT Press, Cambridge, Massachusetts, 769 pp.

Mulhearn, P.J. (1977), "Relations Between Surface Fluxes and Mean Profiles of Velocity, Temperature and Concentration, Downwind of a Change in Surface Roughness," Quarterly J. Royal Meteorological Society, 103, 785-802.

Myrup, L.O. and Ranzieri, A.J. (1976), "A Consistent Scheme for Estimating Diffusivities to be Used in Air Quality Models," California Department of Transportation Report CA-DOT-TL-7169-3-76-32, 69 pp.

O'Brien, J. (1970), "On the Vertical Structure of the Eddy Exchange Coefficient in the Planetary Boundary Layer," J. Atmospheric Sciences, 27, 1213-1215.

Plate, E.J. (1971), Aerodynamic Characteristics of Atmospheric Boundary Layers, AEC Critical Review Series NTIS TID-25465, 190 pp.

Pruitt, W.O., Morgan, D.L. and Lawrence, F.J. (1973), "Momentum and Mass Transfers in the Surface Boundary Layer," Quarterly J. of the Royal Meteorological Society, 99, 370-386.

Reynolds, S.D., Roth, P.M. and Seinfeld, J.H. (1973), "Mathematical Modeling of Photochemical Air Pollution - I. Formulation of the Model," Atmospheric Environment, 7, 1033-1061.

Richardson, L.F. (1920), "The Supply of Energy From and To Atmospheric Eddies," Proceedings Royal Society, A97, (686), 354-373.

Shair, F.H. (1977) Personal communication.

Shir, C.C. (1973), "A Preliminary Numerical Study of Atmospheric Turbulent Flows in the Idealized Planetary Boundary Layer," J. Atmospheric Sciences, 30, 1327-1339.

Slade, D.H. (1969), "Wind Measurements on a Tall Tower in Rough and Inhomogeneous Terrain," J. Applied Meteorology, 8, 293-297.

Stewart, R.W. (1974), "The Air-Sea Mass Momentum Exchange," Boundary Layer Meteorology, 6, 151-167.

Stull, R.B. (1973), "Inversion Rise Model Based on Penatrative Convection," J. Atmosphere Sciences, 30, 1092-1099.

Taylor, G.I. (1938), "The Spectrum of Turbulence," Proceedings Royal Society, A164, 476-490.

Tennekes, H. (1970), "Free Convection in the Turbulent Eckman Layer of the Atmosphere." J. Atmospheric Sciences, 27, 1027-1034.

Tennekes, H. (1973), "Similarity Laws and Scale Relations in Planetary Boundary Layer," in Workshop on Micrometeorology, D.A. Haugen ed., American Meteorological Society, Boston, Massachusetts, 177-216.

Touma, J.S. (1977), "Dependence of the Wind Profile Power Law on Stability for Various Locations," J. Air Pollution Control Association, 27, 863-866.

Turner, D.B. (1969), "Workbook of Atmospheric Dispersion Estimates," Public Health Service Publication No. 999-AP-26, U.S. Department of Health, Education, and Welfare, Cincinnati, Ohio, 84 pp.

Walton, J.J. (1973), "Scale-Dependent Diffusion," Journal of Applied Meteorology, 12, 547-549.

Weber, A.H., Irwin, J.S., Kahler, J.P. and Peterson, W.B. (1975), "Atmospheric Turbulence in the Lowest 300 Meters," U.S. Environmental Protection Agency Report 600/4-75-004, 152 pp.

Willis, G.E. and Deardorff, J.W. (1976a), "On the Use of Taylor's Hypothesis for Diffusion in the Mixed Layer." Quarterly J. Royal Meteorological Society, 102, 817-822.

Willis, G.E. and Deardorff, J.W. (1976b), "A Laboratory Model of Diffusion into the Convective Planetary Boundary Layer," Quarterly J. Royal Meteorological Society, 102, 427-445.

Wipperman, F. (1972), "A Note on Parameterization of Large Scale Wind Stress at the Sea-Surface," Beiträge Physik Atmosphäre, 45, 260-266.

Wyngaard, J.C. (1973), "On Surface-Layer Turbulence," in Workshop on Micrometeorology, D.A. Haugen ed., American Meteorological Society, Boston, Massachusetts, 101-149.

Wyngaard, J.C. (1975), "Modeling the Planetary Boundary Layer-Extension to the Stable Case," Boundary-Layer Meteorology, 9, 441-460.

Yamada, T. (1977), "A Numerical Experiment on Pollutant Dispersion in a Horizontally-Homogeneous Atmospheric Boundary Layer," Atmospheric Environment, 11, 1015-1024.

Yu, T.W. (1977), "A Comparative Study on Parameterization of Vertical Turbulent Exchange Processes." Monthly Weather Review, 105, (1), 57-66.

Zeman, O. and Lumley, J.L. (1976), "Modeling Buoyancy Driven Mixed Layers," J. Atmospheric Sciences, 33, 1974-1988.

Zilitinkevich, S.S. (1972), "On the Determination of the Height of the Ekman Boundary Layer," Boundary-Layer Meteorology, 3, 141-145.

References for Chapter 6

Badgley, F.I.C., Paulson, C.A. and Miyake, M. (1972), Profiles of Wind, Temperature, and Humidity over the Arabian Sea. The University Press of Hawaii, 62 pp.

Busch, N.E. (1973), "On the Mechanics of Atmospheric Turbulence," in Workshop on Micrometeorology, D.A. Haugen ed. American Meteorological Society, Boston, Massachusetts, 1-66.

Businger, J.A., Wyngaard, J.C., Izumi, Y. and Bradley, E.F. (1971), "Flux Profile Relationships in the Atmospheric Surface Layer," J. Atmospheric Sciences, 28, 181-189.

Brutsaert, W. (1975), "The Roughness Length for Water Vapor, Sensible Heat, and other Scalars," J. Atmospheric Sciences, 32, 2028-2031.

Chamberlain, A.C. (1966), "Transport of Gases to and from Grass and Grass-like Surfaces," Proceedings Royal Society Series A, 290, 236-265.

Davidson, C.I. (1977), Deposition of Trace Metal-Containing Aerosols on Smooth, Flat Surfaces and on Wild Oat Grass (Avena Fatua), Ph.D. Thesis, California Institute of Technology, Pasadena, California.

Droppo, J.G. and Hales, J.M. (1974), "Profile Methods of Dry Deposition Measurements," in Atmosphere - Surface Exchange of Particulate and Gaseous Pollutants, ERDA Publication NTIS No. CONF. - 740921, (1976), 192-209.

Droppo, J.G. (1976), "Summary of Field Data on Dry Removal Rates of Gases and Particles from the Atmosphere," in Pacific Northwest Laboratory Annual Report for 1976 to ERDA Assistant Administrator for Environment and Safety: Part 3 Atmospheric Sciences, Battelle Pacific Northwest Laboratories, Richland, Washington, 45-49.

Dyer, A.J. and Hicks, B.B. (1970), "Flux-Gradient Relationships in the Constant Flux Layer," Quarterly J. Royal Meteorological Society, 96, 715-721.

Galbally, I.E. (1971), "Ozone Profiles and Ozone Fluxes in the Atmospheric Surface Layer," Quarterly J. Royal Meteorological Society, 97, 18-29.

Garland, J.A. (1974),"Dry Deposition of SO_2 and Other Gases," in Atmosphere-Surface Exchange of Particulate and Gaseous Pollutants, ERDA Publication, NTIS No. CONF. - 740921, (1976), 212-227.

Garland, J.A. and Penkett, S.A. (1976), "Absorption of Peroxy Acetyl Nitrate and Ozone by Natural Surfaces," Atmospheric Environment, 10, 1127-1131.

Hill, A.C. and Chamberlain, E.M. (1974), "The Removal of Water Soluble Gases from the Atmosphere by Vegetation," in Atmosphere - Surface Exchange of Particulate and Gaseous Pollutants, ERDA Publication, NTIS No. CONF. - 740921, (1976), 153-169.

Kneen, T. and Strauss, W. (1969), "Deposition of Dust from Turbulent Gas Streams," Atmospheric Environment, 3, 55-67.

Liu, T.Y.H. and Ilori, T.A. (1974), "Aerosol Deposition in Turbulent Pipe Flow," Environmental Science and Technology, 8, 351-356.

McMahon, T.A. and Denison, P.J. (1979), "Empirical Atmospheric Deposition Parameters--A Survey," Atmospheric Environment, 13, 571-585.

Monin, A.S. and Yaglom, A.M. (1971), Statistical Fluid Mechanics: Mechanics of Turbulence, Vol. 1, The MIT Press, Cambridge, Massachusetts, 769 pp.

National Academy of Sciences (1978), "Wet and Dry Removal Processes," Chapter 4 in The Tropospheric Transport of Pollutants and Other Substances in the Oceans, prepared by the Workshop on Tropospheric Transport of Pollutants to the Ocean, National Academy of Sciences, Washington, D.C., 53-123.

Owers, M.J. and Powell, A.W. (1974), "Deposition Velocity of Sulfur Dioxide on Land and Water Surfaces using a ^{35}S Tracer Method," Atmospheric Environment, 8, 63-68.

Paulson, C.A. (1970), "The Mathematical Representation of Wind Speed and Temperature Profiles in the Unstable Atmospheric Surface Layer," J. Applied Meteorology, 9, 857-861.

Roberts, P.T. (1975), Gas to Particle Conversion: Sulfur Dioxide in a Photochemically Reactive System, Ph.D. Thesis, California Institute of Technology, Pasadena, California.

Sehmel, G.A. and Hodgson, W.H. (1974), "Predicted Dry Deposition Velocities," in Atmosphere - Surface Exchange of Particulate and Gaseous Pollutants, ERDA Publication, NTIS No. CONF. - 740921, (1976), 399-419.

Sehmel, G.A. (1980), "Particle and Gas Dry Deposition: A Review," Atmospheric Environment, 14, 983-1011.

Slinn, W.G.N. (1974), "Dry Deposition and Resuspension of Aerosol Particles-A New Look at Some Old Problems," in Atmosphere - Surface Exchange of Particulate and Gaseous Pollutants, ERDA Publication, NTIS No. CONF. - 740921, (1976), 1-40.

Slinn, W.G.N., Hasse, L., Hicks, B.B., Hogan, A.W., Lal, D., Liss, P.S., Munnich, K.O., Sehmel, G.A. and Vittori, O. (1978), "Some Aspects of the Transfer of Atmospheric Trace Constituents Past the Air-Sea Interface," Atmospheric Environment, 12, 2055-2087.

Webb, E.K. (1970), "Profile Relationships: The Log Linear Range, and Extension to Strong Stability," Quarterly J. Royal Meteorological Society, 96, 67-90.

Wesely, M.L. and Hicks, B.B. (1977), "Some Factors that Affect the Deposition Rates of Sulfur Dioxide and Similar Gases on Vegetation," J. Air Pollution Control Association, 27, (11), 1110-1116.

Wesely, M.L., Hicks, B.B., Dannevik, W.P., Frisella, S. and Husar, R.B. (1977), "An Eddy-Correlation Measurement of Particulate Deposition from the Atmosphere," Atmospheric Environment, 11, 561-563.

Wesely, M.L., Eastman, J.A., Cook, D.R. and Hicks, D.B. (1978) "Daytime Variations of Ozone Eddy Fluxes to Maize," Boundary Layer Meteorology, 15, 361-373.

Whelpdale, D.M. and Shaw, R.W. (1974), "Sulfur Dioxide Removal by Turbulent Transfer over Grass, Snow and Water Surfaces," Tellus, 26, 196-205.

References for Chapter 7

Baulch, D.L., Drysdale, D.D. and Horne, D.G. (1978), "Evaluated Kinetic Data for High Temperature Reaction: Volume 2 Homogeneous Gas Phase Reactions of the H_2-N_2-O_2 Systems," The CRC Press, Cleveland, Ohio, 285-300.

Binkowski, F.S. (1979), "A Simple Semi-Empirical Theory for Turbulence in the Atmospheric Surface Layer," Atmospheric Environment, 13, 247-253.

Briggs, G.A. (1969), Plume Rise, Atomic Energy Commission Review Series, NTIS TID-25075, 81 pp.

Briggs, G.A. (1975), "Plume Rise Predictions," in Lectures on Air Pollution and Environmental Impact Analysis, D.A. Haugen, ed., American Meteorological Society ,Boston, Massachusetts, 59-111.

Busch, N.E. (1973),"On the Mechanics of Atmospheric Turbulence," in Workshop on Micrometeorology, D.A. Haugen ed., American Meteorology Society, Boston, Massachusetts, 1-66.

Cole, H.S. and Summerhays, J.E. (1979), "A Review of Techniques Available for Estimating Short-Term NO_2 Concentration," J. of the Air Pollution Control Association, 29, 812-817.

CRSTER (1977), Users Manual for Single-Source (CRSTER) Model, U.S. Environmental Protection Agency, Report No. EPA-450/2-77-013, 294 pp.

Csanady, G.T. (1973), Turbulent Diffusion in the Environment, Geophysics and Astrophysics Monograph, 3, D. Riedel Publishing Company, Boston, 248 pp.

Deardorff, J.W. and Willis, G.E. (1975), "A Parameterization of Diffusion into the Mixed Layer," J. Applied Meteorology, 14, 1451-1458.

Draxler, R.R. (1976), "Determination of Atmospheric Diffusion Parameters," Atmospheric Environment, 10, 99-105.

Fabrick, A., Sklarew, R. and Wilson, J. (1977), Point Source Model Evaluation and Development Study, Science Applications, Inc., Final Report to California Air Resources Board under Contract A5-058-87, 197 pp.

Fischer, H.B., List, E.J., Koh, R.C.Y., Imberger, J. and Brooks, N.H. (1979), Mixing in Inland and Coastal Waters, Academic Press, New York, 483 pp.

Gifford, F.A. (1976), "Turbulent Diffusion-Typing Schemes: A Review," Nuclear Safety, 17, 68-86.

Hampson, R.F. and Garvin, D. eds. (1977), Reaction Rate and Photochemical Data for Atmospheric Chemistry-1977, NBS Special Publication No. 513, U.S. Department of Commerce, 106 pp.

Hanna, S.R., Briggs, G.A., Deardorff, J.W., Egan, B.A., and Pasquill, F. (1977), "American Meteorology Society - Workshop on Stability Classification Schemes and Sigma Curves - Summary of Recommendations," Bulletin of American Meteorological Society, 58, 1305-1309.

Hegg, D., Hobbs, P.V., Radke, L.F. and Harrison, H. (1977), "Reaction of Ozone and Nitrogen Oxides in Power Plant Plumes," Atmospheric Environment, 11, 521-526.

Hirst, E.A. (1972), "Buoyant Jets with Three-Dimensional Trajectories," J. Hydraulics Division, American Society of Civil Engineers, 98, 1999-2014.

Hoult, D.P., Fay, F.A. and Forney, L.J. (1969), "A Theory of Plume Rise Compared with Field Observations," Journal of the Air Pollution Control Association, 19, 585-590.

Irwin, J.S. (1979), Scheme for Estimating Dispersion Parameters as a Function of Release Height, U.S. Environmental Protection Agency, Report No. EPA-600/4-79-062, 56 pp.

Kewley, D.J. (1978), "Atmospheric Dispersion of a Chemically Reacting Plume," Atmospheric Environment, 12, 1895-1900.

Koh, R.C.Y. and Brooks, N.H. (1975), "Fluid Mechanics of Wastewater Disposal in the Ocean," Annual Review of Fluid Mechanics, 7, 187-211.

Lamb, R.G. (1978), "A Numerical Simulation of Dispersion from an Elevated Point Source in the Convective Planetary Boundary Layer," Atmospheric Environment, 12, 1297-1304.

Lamb, R.G. (1979), "The Effect of Release Height on Material Dispersion in the Convective Boundary Layer," Proc. Fourth Symposium on Turbulence, Diffusion and Air Pollution, Reno, Nevada, American Meteorological Society, Boston, Massachusetts, 27-33.

Lewellen, W.S. and Teske, M (1975), Turbulence Modeling and its Application to Atmospheric Diffusion Part I: Recent Program Development, Verification, and Application, U.S. Environmental Protection Agency, Report No. EPA-600/4-75-016a, 79 pp.

MacCracken, M.C., Wuebbles, D.J., Walton, J.J., Duewer, W.H. and Grant, K.E. (1978), "The Livermore Regional Air Quality Model: I. Concept and Development," J. Applied Meteorology, 17, 254-272.

Manins, P.C. (1979), "Partial Penetration of An Elevated Inversion Layer by Chimney Plumes," Atmospheric Environment, 13, 733-741.

Morton, B.R., Taylor, G.I. and Turner, J.S. (1956), "Turbulent Gravitational Convection from Maintained and Instantaneous Sources," Proc. Royal Society, London, Series A, 234, 1-23.

Nieuwstadt, F.T.M. (1980), "Application of Mixed-Layer Similiarity to the Observed Dispersion from a Ground-Level Source," J. Applied Meteorology, 19, 157-162.

Nieuwstadt, F.T.M. and van Duuren, H. (1979), "Dispersion Experiments with SF_6 from the 213 m High Meteorological Mast at Cabauw in the Netherlands," Proc. Fourth Symposium on Turbulence, Diffusion and Air Pollution, Reno, Nevada, American Meteorological Society, Boston, Massachusetts, 34-40.

Omms, G. (1972), "A New Method for the Calculation of the Plume Path of Gases Emitted by a Stack," Atmospheric Environment, 6, 899-909.

Panofsky, H.A., Tennekes, H., Lenschow, D.H. and Wyngaard, J.C. (1977), "The Characteristics of Turbulent Velocity Components in the Surface Layer under Convective Conditions," Boundary-Layer Meteorology, 11, 355-361.

Pasquill, F. (1971), "Atmospheric Diffusion of Pollution," Quarterly J. Royal Meteorological Society, 97, 369-395.

Pasquill, F. (1975), "The Dispersion of Material in the Atmospheric Boundary Layer - The Basis for Generalization," in Lectures on Air Pollution and Environmental Impact Analysis, D.A. Haugen, ed., American Meteorological Society, Boston, Massachusetts, 1-34.

Pasquill, F. (1976), Atmospheric Dispersion Parameters in Gaussian Plume Modeling: Part II. Possible Requirements for Change in the Turner Workbook Values, U.S. Environmental Protection Agency Report No. EPA-600/4-76-030b, 53 pp.

Peters, L.K. and Richards, L.W. (1977), "Extension of Atmospheric Dispersion Models to Incorporate Fast Reversible Reactions," Atmospheric Environment, 11, 101-108.

Reynolds, S.D., Roth, P.M. and Seinfeld, J.H. (1973), "Mathematical Modeling of Photochemical Air Pollution --I Formulation of the Model," Atmospheric Environment, 7, 1033-1061.

Schatzmann, M. (1979), "An Integral Model of Plume Rise," Atmospheric Environment, 13, 721-731.

Sheih, C.M. (1980), "On Lateral Dispersion Coefficients as Functions of Averaging Time," J. Applied Meteorology, 19, 557-561.

Shu, W.R., Lamb, R.G. and Seinfeld, J.H. (1978), "A Model of Second-Order Chemical Reactions in a Turbulent Fluid, II. Application to Atmospheric Plumes," Atmospheric Environment, 12, 1699-1705.

Taylor, G.I. (1921), "Diffusion by Continuous Movements," Proc. London Mathematical Society, 20, 196-212.

Tesche, T.W., Whitten, G.Z., Yocke, M.A. and Liu, M-K. (1976), "Theoretical, Numerical, and Physical Techniques for Characterizing Power Plant Plumes," Electric Power Research Institute Topical Report No. RP-572-2 (NTIS PB-253-099), Prepared by Systems Applications Inc., San Rafael, California, 228 pp.

Turner, D.B. (1970), Workbook of Atmospheric Dispersion Estimates, U.S. Environmental Protection Agency, Air Programs Publication No. AP-26, 84 pp.

White, W.H. (1977), "NO_x-O_3 Photochemistry in Power Plant Plumes: Comparison of Theory With Observation," Environmental Science and Technology, 11, 995-1000.

White, W.H. (1979), "The Theoretical Effect of a Second-Order Reaction on the Crosswind Geometry of a Dispersion Plume," Atmospheric Environment, 13, 1501-1503.

Willis, G.E. and Deardorff, J.W. (1976), "A Laboratory Study of Dispersion Into the Convective Planetary Boundary Layer," Quarterly J. Royal Meteorological Society, 102, 427-445.

Willis, G.E. and Deardorff, J.W. (1978), "A Laboratory Study of Dispersion From an Elevated Source in a Convective Mixed Layer," Atmospheric Environment, 12, 1305-1313.

Wright, S.J. (1977), Effects of Ambient Crossflows and Density Stratification on the Characteristic Behavior of Round Turbulent Buoyant Jets, W.M. Keck Laboratory of Hydraulics and Water Resources Report KH-R-36, California Institute of Technology, Pasadena, California, 254 pp.

References for Chapter 8

Aris, R. (1965), Introduction to the Analysis of Chemical Reactors, Prentice Hall, Inc., New Jersey, 536 pp.

Atkinson, R., Darnall, K.R. and Pitts, J.N. (1978), "Rate Constants for the Reaction of the OH Radical with Selected Alkanes at 300°K," J. Physical Chemistry, 82, 1581-1584.

Baldwin, A.C., Barker, J.R., Golden, D.M. and Hendry, D.G. (1977), "Photochemical Smog Rate Parameter Estimates and Computer Simulation," J. Physical Chemistry, 81, 2483-2492.

Barker, J.R., Benson, S.W. and Golden, D.M. (1977), "The Decomposition of Dimethyl Peroxide and the Rate Constant for $CH_3O + O_2 \rightarrow CH_2O + HO_2$," International J. Chemical Kinetics, 9, 31-53.

Batt, L., McCulloch, R.D. and Milne, R.T. (1975), "Thermochemical and Kinetic Studies of Alkyl Nitrates (RONO)-D(RO-NO), The Reaction Between RO and NO, and the Decomposition of RO," International J. Chemical Kinetics Symposium, 1, ed. Sidney W. Benson, (Held at Warrenton, Virginia, September 15-18, 1974).

Baulch, D.L., Cox, R.A., Hampson, R.F., Kerr, J.A., Troe, J. and Watson, R.T. (1980), "Evaluated Kinetic and Photochemical Data for Atmospheric Chemistry," J. Physical and Chemical Reference Data, 9, 295-471.

Bilger, R.W. (1977), "The Effects of Admixing Fresh Emissions on the Photostationary State Relationships in Photochemical Smog," Atmospheric Environment, 12, 1109-1118.

Bowen, R.M. (1976), "Theory of Mixtures," in Continum Physics, 3, ed. A. Cemal Eringen, Academic Press, New York.

Braslau, N. and Dave, J.V. (1973a), "Effect of Aerosols on the Transfer of Solar Energy through Realistic Model Atmospheres, Part I: Non-Absorbing Aerosols," J. Applied Meteorology, 12, 601-615.

Braslau, N. and Dave, J.V. (1973b), "Effect of Aerosols on the Transfer of Solar Energy through Model Atmospheres, Part II: Partly-Absorbing Aerosols," J. Applied Meteorology, 12, 616-619.

Calvert, J.G. (1976), "Test of the Theory of Ozone Generation in Los Angeles Atmosphere," Environmental Science and Technology, 10, 248-256.

Chan, W.H., Nordstrom, R.J., Calvert, J.G. and Shaw, J.H. (1976), "Kinetic Study of HONO Formation and Decay Reactions in Gaseous Mixtures of HONO, NO, NO_2, H_2, and N_2," Environmental Science and Technology, 10, 674-682.

Coulson, J.L. (1975), "Solar and Terrestrial Radiation: Methods and Measurements," Academic Press, New York, 322 pp.

Cox, R.A. and Roffey, M.J. (1977), Thermal Decomposition of Peroxyacetylnitrate in the Presence of Nitric Oxide," Environmental Science and Technology, 11, 900-906.

Demerjian, K.L. (1977), Personal communication.

Demerjian, K.L., Schere, K.L. and Peterson, J.T. (1980), "Theoretical Estimates of Actinic (Spherically Integrated) Flux and Photolytic Rate Constants of Atmospheric Species in the Lower Troposphere," Advances in Environmental Science and Technology, 10, 369-459.

Dodge, M.C. (1977), "Combined Use of Modeling Techniques and Smog Chamber Data to Derive Ozone--Precursor Relationships," U.S. Environmental Protection Agency Report, EPA-600/3-77-001a, 881-889.

Dodge, M.C. (1978), "Proceedings Workshop on Chemical Kinetic Data Needs for Modeling the Lower Troposphere," Conference Held at Reston, Virginia, May 15-17. U.S. Department of Commerce National Bureau of Standards Special Publication 557, ed. J.T. Herron, August 1979, 21-22.

Duewer, W.H., MacCracken, M.C. and Walton, J.J. (1978), "The Livermore Regional Air Quality Model: II Verification and Sample Application in the Bay Area," Journal of Applied Meteorology, 17, 273-311.

Eschenroeder, A.Q. and Martinez, J.R. (1972), "Concepts and Applications of Photochemical Smog Models," Advances Chemistry Series, 113, American Chemical Society, Washington, D.C., 101-168.

Eschenroeder, A.Q., Martinez, J.R. and Nordsieck, R.A. (1972), "Evaluation of a Diffusion Model for Photochemical Smog Simulation," Final Report to U.S. Environmental Protection Agency under Contract No. 68-02-0336, General Research Corporation, Santa Barbara, California.

Falls, A.H. and Seinfeld, J.H. (1978), "Continued Development of a Kinetic Mechanism for Photochemical Smog," Environmental Science and Technology, 12, 1398-1406.

Flowers, E.C., McCormick, R.A. and Kurfis, K.R. (1969), "Atmospheric Turbidity Over the United States, 1961-1966," J. Applied Meteorology, 8, 955-962.

Gavalas, G.R. (1968), Nonlinear Differential Equation of Chemically Reacting Systems, Springer-Verlag, Berlin, 106 pp.

Gelinas, R.J. and Skewes-Cox, P.D. (1975), "Tropospheric-Photochemical Mechanisms," J. Physical Chemistry, 81, 2468-2479.

Goff, J.A. and Gratch, S. (1945), "Thermodynamic Properties of Moist Air," Transactions American Society of Heating and Ventilation Engineers, 51, 125-164.

Graedel, T.E., Farrow, L.A. and Weber T.A. (1976), "Kinetic Studies of the Photochemistry of the Urban Troposphere," Atmospheric Environment, 10, 1095-1116.

Graham, R.A. and Johnston, H.S. (1978), "The Photochemistry of NO_3 and the Kinetics of the N_2O_5-O_3 System," J. Physical Chemistry, 82, 254-268.

Graham, R.A., Winer, A.M. and Pitts, J.N. (1977), "Temperature Dependence of the Unimolecular Decomposition of Pernitric Acid and its Atmospheric Implication," Chemical Physics Letters, 51, 215-220.

Graham, R.A., Winer, A.M. and Pitts, J.N. (1978), "Pressure and Temperature Dependence of the Unimolecular Decomposition of HO_2NO_2," J. Chemical Physics, 68, 4505-4510.

Hampson, R.F. and Garvin, D. (1978), "Reaction Rate and Photochemical Data for Atmospheric Chemistry - 1977," U.S. Department of Commerce National Bureau of Standards Special Publication 513, 111 pp.

Hecht, T.A. and Seinfeld J.H. (1972), "Development and Validation of a Generalized Mechanism for Photochemical Smog," Environmental Science and Technology, 6, 47.

Hecht, T.A., Seinfeld J.H. and Dodge M.C. (1974), "Further Development of Generalized Kinetic Mechanism for Photochemical Smog," Environmental Science and Technology, 8, 327-339.

Herron, J.T. and Huie, R.E. (1977), "Stopped-Flow Studies of the Mechanisms of Ozone-Alkene Reactions in the Gas Phase Ethylene," J. American Chemical Society, 99, 5430-5435.

Hindmarsh, A.C. and Byrne, G.D. (1975), "EPISODE: An Experimental Program for the Integration of Systems of Ordinary Differential Equation Systems," Lawrence Livermore Laboratory Report UCID-30112.

Horn, F. and Jackson, R. (1972), "General Mass Action Kinetics," Archive for Rational Mechanics and Analysis, 47, 81-116.

Iribarne, J.V. and Godson, W.L. (1973), Atmospheric Thermodynamics, Geophysics and Astrophysics Monographs, 6, D. Reidell, Dordrecht, Holland, 222 pp.

Krambeck, F.J. (1970), "The Mathematical Structure of Chemical Kinetics in Homogeneous Single-Phase Systems," Archive for Rational Mechanics and Analysis, 38, 317-347.

Leighton, P.A. (1961), Photochemistry of Air Pollution, Academic Press, New York, 300 pp.

Lettau, H.H. (1970), "Physical and Meteorological Basis for Mathematical Models of Urban Diffusion Processes," Proc. Symposium on Multiple-Source Urban Diffusion Models, ed. A.C. Stern, U.S. Environmental Protection Agency, Publication AP-86, 2.1-2.26.

Lloyd, A.C., Darnall, K.R., Winer, A.M. and Pitts, J.N. (1976), "Relative Rate Constants for Reaction of the Hydroxyl Radical with a Series of Alkanes, Alkenes, and Aromatic Hydrocarbons," J. Physical Chemistry, 80, 789-794.

Luther, F.M. and Gelinas, R.J. (1976), "Effects of Molecular Multiple Scattering and Surface Albedo on Atmospheric Photodissociation Rates," J. Geophysical Research, 81, 1125-1132.

MacCracken, M.C. and Sauter, G.C. eds. (1975), "Development of an Air Pollution Model for the San Francisco Bay Area," Final Report to the National Science Foundation, Lawrence Livermore Report UCRL-51920, 1169 pp.

McRae, G.J. (1980), "A Simple Procedure for Calculating Atmospheric Water Vapor Concentration," J. Air Pollution Control Association, 30, 384.

NASA (1981), "Chemical Kinetics and Photochemical Data for Use in Stratospheric Modeling--Evaluation Number 4," NASA Panel for Data Evaluation, Jet Propulsion Laboratory Report No. 81-3.

Peterson, J.T. (1976), "Calculated Actinic Fluxes (290-700 nm) for Air Pollution Photochemistry Application," U.S. Environmental Protection Agency Report EPA-600/4-76-025, 63 pp.

Peterson, J.T., Demerjian, K.L. and Schere, K.L. (1977), "Actinic Solar Flux and Photolytic Rate Constants in the Troposphere," Proc. International Conference on Photochemical Oxidant and its Control, Vol II, Raleigh, North Carolina, Sept. 12-17, 1976, NTIS PB-264 233, 753-762.

Pitts, J.N., Winer, A.M., Darnell, K.R., Doyle, G.J. and McAfee, J.M. (1976), "Chemical Consequences of Air Quality Standards and of Control Implementation Programs: Roles of Hydrocarbons, Oxides of Nitrogen and Aged Smog in the Production of Photochemical Oxidant," Final Report to the California Air Resources Board Under Contract No. 4-214 by Statewide Air Pollution Research Center, University of California Riverside, 444 pp.

Pitts, J.N. and Winer, A.M. (1978), "Transmittal of Data from Photochemical Runs in Evacuable Chamber: A Report for the Period October 1 through November 11, 1977," Statewide Air Pollution Research Center, University of California, Riverside, Report No. 16, under EPA Grant 800649, Chamber Program, 35 pp.

Platt, U., Perner, D., Harris, G.W., Winer, A.M. and Pitts, J.N. (1980), "Observation of HONO in an Urban Atmosphere by Differential Optical Absorption," Nature, 285, 312-314.

Pratt, G.L. (1969), Gas Kinetics, John Wiley and Sons, London, 246 pp.

Richards, J.M. (1971), "A Simple Expression for the Saturation Vapour Pressure of Water in the Range -50 to 140°C," British J. Applied Physics D, 4, L15-L18.

Rosenbaum, J.S. (1977), "Conservation Properties for Numerical Integration Methods for Systems of Differential Equations," The Journal of Physical Chemistry, Symposium on Reaction Mechanisms, Models and Computers, March 20-25, 1977, 81, 2362-2365.

Sander, S.P. (1979), Personal Communication.

Sander, S.P. and Watson, R.J. (1981), "The Temperature Dependence of the Self-Reaction of CH_3O_2 Radicals," J. Physical Chemistry, 85, 2960.

Schere, K.L. and Demerjian, K.L. (1977), "Calculation of Selected Photolytic Rate Constants Over A Diurnal Range," U.S. Environmental Protection Agency, Report EPA-600/4-77-015, 71 pp.

Seinfeld, J.H. (1977), "Test of the Theory of Ozone Generation in Los Angeles Atmosphere (Letter to Editor)," Environmental Science and Technology, 11, 1218-1219.

Sellers, W.D. (1969), Physical Climatology, The University of Chicago Press, Chicago, 272 pp.

Simonaitis, R. and Heicklen, J.I. (1974), "Reactions of HO_2 with NO and NO_2," J. Physical Chemistry, 78, 653-657.

Stedman, D.H. and Jackson, J.O. (1975), "The Photostationary State in Photochemical Smog," International J. Chemical Kinetics Symposium, 1, ed. Sidney W. Benson, (Held at Warrenton, Virginia, September 15-18, 1974), 493-500.

Stedman, D.H., Harvey, R.B., and Dickerson, R.R. (1977), "Measurement of Photons Involved Involved in Photochemical Oxidant Formation," Proc. Int. Conf. on Photochemical Oxidant and its Control, Vol. II, Rayleigh, North Carolina, September 12-17, 1976, NTIS PB-264-233, 753-762.

Threlkeld, J.L. (1970), Thermal Environmental Engineering, Prentice-Hall, Inc. New Jersey, 495 pp.

Weibe, H.A., Villa, A., Hellman, T.M. and Heicklen, J. (1975), "Photolysis of Methyl Nitrate in the Presence of Nitric Oxide, Nitrogen Dioxide, and Oxygen," J. American Chemical Society, 95, 7-13.

Whitten, G.Z. and Hogo, H. (1976), "Mathematical Modeling of Simulated Photochemical Smog," Final Report to U.S. Environmental Protection Agency Under Contract No. 68-02-0580, Systems Application, Incorporated, San Rafael, California.

Whitten, G.Z., Hogo, H., Meldgin, M.J., Killus, J.P. and Bekowies, P.J. (1979), "Modeling of Simulated Photochemical Smog with Kinetic Mechanisms," Volumes I and II, U.S. Environmental Protection Agency Report, EPA-600/3-79-001a, 718 pp.

Winer, A.M., Graham, R.A., Doyle, G.J., Bekowies, P.J., McAfee, J.M. and Pitts, J.N. (1980), "An Evacuable Environmental Chamber and Solar Simulator Facility for the Study of Atmospheric Photochemistry," Advances in Environmental Science and Technology, 10, 461-511.

Woolf, H.M. (1967), "On the Computation of Solar Elevation Angles and the Determination of Sunrise and Sunset Times," NASA Technical Memorandum 1646, 12 pp.

Zafonte, L. (1977), Personal communication.

Zafonte, L., Rieger, P.L. and Holmes, J.R., (1977), "Nitrogen Dioxide Photolysis in the Los Angeles Atmosphere," Environmental Science and Technology, II, 483-487.

References for Chapter 10

Aird, T.J. and Rice, J.R. (1977), "Systematic Search in High Dimensional Sets," SIAM J. of Numerical Analysis, 14(2), 296-312.

Atherton, R.W., Schainker, R.B. and Ducot, E.R. (1975), "On the Statistical Sensitivity Analysis of Models for Chemical Kinetics," AIChE Journal, 21(3), 441-448.

Beauchamp, K.G. and Yuen, C.K. (1979), Digital Methods for Signal Analysis, George Allen and Unwin, London, 316 pp.

Boni, A.A. and Penner, R.C. (1976), "Sensitivity Analysis of a Mechanism for Methane Oxidation Kinetics," Combustion Science and Technology, 15, 99-105.

Cruz, J.B. (1973), System Sensitivity Analysis, Dowden Hutchinson and Ross, Stroudsburg, Pennsylvania, 428 pp.

Cukier, R.I., Fortuin, C.M., Shuler, K.E., Petschek, A.G. and Schaibly, J.H. (1973), "Study of the Sensitivity of Coupled Reaction Systems to Uncertainties in Rate Coefficients: I. Theory," J. of Chemical Physics, 59(8), 3873-3878.

Cukier, R.I., Schaibly, J.H. and Shuler, K.E. (1975), "Study of the Sensitivity of Coupled Reaction Systems to Uncertainties in Rate Coefficients: III. Analysis of the Approximations," J. of Chemical Physics, 63(3), 1140-1149.

Cukier, R.I., Levine, H.B. and Shuler, K.E. (1978), "Nonlinear Sensitivity Analysis of Multi-Parameter Model Systems," J. of Computational Physics, 26(1), 1-42.

Dickinson, R.P. and Gelinas, R.J. (1976), "Sensitivity Analysis of Ordinary Differential Equation Systems," J. Computational Physics, 21(2), 123-143.

Dieudonne', J. (1960) Foundations of Modern Analysis, Academic Press, New York, 361 pp.

Dodge, M.C. and Hecht, T.A. (1975), "Rate Constant Measurements Needed to Improve a General Kinetic Mechanism for Photochemical Smog," International J. of Chemical Kinetics, 1, 155-163.

Dougherty, E.P., Hwang, J-T, and Rabitz, H. (1979), "Further Developments and Applications of the Green's Function Method of Sensitivity Analysis in Chemical Kinetics," J. of Chemical Physics, 71(4), 1794-1808.

Dunker, A.M. (1980), "The Response of An Atmospheric Reaction-Transport Model to Changes in Input Functions," Atmospheric Environment, 14, 671-679.

Eno, L. and Rabitz, H. (1979), "Generalized Sensitivity Analysis in Quantum Collision Theory," J. of Chemical Physics, 71(12), 4824-4831.

Falls, A.H., McRae, G.J. and Seinfeld, J.H. (1979), "Sensitivity and Uncertainty of Reaction Mechanisms for Photochemical Air Pollution," International J. of Chemical Kinetics, 11, 1137-1162.

Frank, P.M. (1978), Introduction to System Sensitivity Theory, Academic Press, New York, 386 pp.

Freeze, R.A. (1975), "A Stochastic-Conceptual Analysis of One-Dimensional Groundwater Flow in Non-Uniform Homogeneous Media," Water Resources Research, 11(5), 725-741.

Gelinas, R.J. and Vajk, J.P. (1978), Systematic Sensitivity Analysis of Air Quality Simulation Models, Final Report to U.S. Environmental Protection Agency under Contract No. 68-02-2942, Science Applications Inc., Pleasanton, California, 96 pp.

Gifford, F.A. (1961), "Use of Routine Meteorological Observations for Estimating Atmospheric Dispersion," Nuclear Safety,2(4), 47-57.

Gifford, F.A. (1976), "Turbulent Diffusion-Typing Schemes: A Review," Nuclear Safety, 17(1), 68-86.

Hwang, J-T, Dougherty, E.P., Rabitz, S. and Rabitz, H. (1978), "The Green's Function Method of Sensitivity Analysis in Chemical Kinetics," J. of Chemical Physics,69(11), 5180-5191.

Hwang, J-T and Rabitz, H. (1979), "The Green's Function Method of Sensitivity Analysis in Quantum Dynamics," J. of Chemical Physics, 70(10), 4609-4621.

Keller, J.B. (1964), "Stochastic Equations and Wave Propagation in Random Media," Proceedings Symposium in Applied Mathematics of the American Mathematical Society, American Mathematical Society, Providence, Rhode Island, 145-170.

Koda, M., Dogru, A.H. and Seinfeld, J.H. (1979a), "Sensitivity Analysis of Partial Differential Equation with Application to Reaction and Diffusion Processes," J. of Computational Physics,30(2), 259-282.

Koda, M., McRae, G.J. and Seinfeld, J.H. (1979b), "Automatic Sensitivity Analysis of Kinetic Mechanisms," International J. of Chemical Kinetics, 11, 427-444.

Lamb, R.G. (1979), "The Effects of Release Height on Material Dispersion in the Convective Planetary Boundary Layer," Proc. Fourth Symposium on Turbulence, Diffusion and Air Pollution, American Meteorological Society, January 15-18, Reno, Nevada, 27-33.

Leith, C.E. (1975), "Climate Response and Fluctuation Dissipation," J. of Atmospheric Sciences, 32(10), 2022-2026.

Levine, H.B. (1975), Sensitivity Analysis of a Chemical Laser System, Final Report to Advanced Research Projects Agency under Contract No. N00014-75-C-0981, Systems, Science and Software, La Jolla, California, 61 pp.

McRae, G.J. and Tilden, J.W. (1980), "A Sensitivity and Uncertainty Analysis of Urban Scale Air Pollution Models--Preliminary Steps," Proceedings AMS/APCA Second Joint Conference on Application of Air Pollution Meteorology, American Meteorological Society, March 24-27, New Orleans.

Miller, C.W., Little, C.A. and Hoffman, F.O. (1979), "Validation of Turner Workbook Normalized Air Exposure Predictions for Surface Level Releases Using Hanford Dispersion Data," Proc. Fourth Symposium on Turbulence, Diffusion and Air Pollution, American Meteorological Society, January 15-18, Reno, Nevada, 95-102.

Nashed, M.Z. (1971), "Differentiability and Related Properties of Nonlinear Operators: Some Aspects of the Role of Differentials in Nonlinear Functional Analysis," in Nonlinear Functional Analysis and Application, ed. L.B. Rall, Academic Press, New York, 103-309.

Papoulis, A. (1965), Probability, Random Variables, and Stochastic Processes, McGraw-Hill, Inc. New York, 583 pp.

Pasquill, F. (1961), "The Estimation of the Dispersion of Windblown Material," Meteorological Magazine, 90, 33-49.

Pasquill, F. (1976), "Atmospheric Dispersion Parameters in Gaussian Plume Modeling--Part II. Possible Requirements for Changes in Turner Workbook Values," U.S. Environmental Protection Agency, Report EPA-600/4-76-0306, 43 pp.

Rundel, R.D., Butler, D.M. and Stolarski, R.S. (1978), "Uncertainty Propagation in Stratospheric Model, I. Development of a Concise Stratospheric Model," J. of Geophysical Research, 83(C6), 3063-3073.

Schaibly, J.H. and Shuler, K.E. (1973), "Study of the Sensitivity of Coupled Reaction Systems to Uncertainties in Rate Coefficients, II. Applications," J. of Chemical Physics, 59(8), 3879-3888.

Sobol, I.M. (1979), "On the Systematic Search in a Hypercube," SIAM J. of Numerical Analysis, 16(5), 790-793.

Stolarski, R.S., Butler, D.M. and Rundel, R.D. (1978), "Uncertainty Propagation in a Stratospheric Model, II. Monte Carlo Analysis of Imprecision due to Reaction Rates," J. of Geophysical Research, 83(C6), 3074-3078.

Stroud, A.H. (1971), Approximate Calculation of Multiple Integrals, Prentice-Hall, Inc., Englewood Cliffs, New Jersey, 431 pp.

Tang, D.H. and Pinder, G.F. (1977),"Simulation of Groundwater Flow and Mass Transport under Uncertainty," Advances in Water Resources, 1 (1), 25-30.

Tang, D.H. and Pinder, G.F. (1979), "Analysis of Mass Transport with Uncertain Physical Parameters," Water Resources Research,15(5), 1147-1155.

Tapia, R.A. (1971), "The Differentiation and Integration of Nonlinear Operators," in Nonlinear Functional Analysis and Applications, ed., L.B. Rall, Academic Press, New York, 45-101.

Tomovic, R. (1963), Sensitivity Analysis of Dynamic Systems, McGraw-Hill, New York, 142 pp.

Tomovic, R. and Vucobratovic, M. (1972), General Sensitivity Theory, American Elsevier, New York, 258 pp.

Turner, D.B. (1970), "Workbook of Atmospheric Dispersion Estimates," U.S. Environmental Protection Agency, Report AP-26, 84 pp.

Weber, A.H. (1976), "Atmospheric Dispersion Parameters in Gaussian Plume Modeling - Part I. Review of Current and Possible Future Developments," U.S. Environmental Protection Agency, Report EPA-600/4-76-030a, 58 pp.

Weyl, H. (1938), "Mean Motion," American J. Mathematics, 60, 889-896.

References for Chapter 11

Adema, E.H. (1979), "Ozone Inference in the Determination of Nitrogen Dioxide by a Modified Manual Saltzman Method," Analytical Chemistry, 51, 1002-1006.

APCD (1974), Air Quality and Meteorology, XIX, Air Pollution Control District, Los Angeles County, June.

Altshuller, A.P., Lonneman, W.A., Sutterfield, F.D. and Kopczynski, S.L. (1971), "Hydrocarbon Composition of the Atmosphere of the the Los Angeles Basin-1967," Environmental Science and Technology, 5, 1009-1016.

AQMP (1978), "Base Year Emissions Inventory SCAG/SCAQMD - Working Paper 2B," South Coast Air Quality Management District, 60 pp.

Baldwin, A.C., Barker, J.R., Golden, D.M. and Hendry, D.G. (1977), "Photochemical Smog Rate Parameter Estimates and Computer Simulation," J. Physical Chemistry, 81, 2483-2492.

Bartz, D.R., Arledge, K.W., Gabrielson, J.E., Hayes, L.G. and Hunter, S.C. (1974) "Control of Oxides of Nitrogen from Stationary Sources in the South Coast Air Basin of California," Report Number KVB-5800-179, KVB Inc., Tustin, California. (Report is available as NTIS-PB-237-688.)

Baulch, D.L., Cox, R.A., Hampson, R.F., Kerr, J.A., Troe, J. and Watson, R.T. (1980), "Evaluated Kinetic and Photochemical Data for Atmospheric Chemistry," J. Physical and Chemical Reference Data, 9, 295-471.

Baumgardner, R.E., Clark, T.A., Hodgeson, J.A. and Stevens, R.K. (1975), "Determination of an Ozone Interference in the Continuous Saltzman Nitrogen Dioxide Procedure," Analytical Chemistry, 47, 515-521.

Bencala, K.E. and Seinfeld, J.H. (1979), "An Air Quality Model Performance Assessment Package," Atmospheric Environment, 13, 1181-1185.

Blumenthal, D.L., White, W.H., and Smith, T.B. (1978), "Anatomy of a Los Angeles Smog Episode: Pollutant Transport in the Daytime Sea Breeze Regime," Atmospheric Environment, 12, 893-907.

Bowne, N.E. (1980), "Validation and Performance Criteria Air Quality Models," Proceedings Second Joint Conference on Applications of Air Pollution Meteorology, March 24-27, New Orleans, Louisiana, American Meteorological Society, Boston, Massachusetts, 614-626.

Bradley, R. (1981), "Personal Communication."

Brier, G.W. (1975), "Statistical Questions Relating to the Validation of Air Quality Simulation Models," U.S. Environmental Protection Agency Report No. EPA-650/4-75-010.

Bufalini, J.J., Walter, T.A. and Bufalini, M. (1976), "Ozone Formation Potential of Organic Compounds," Environmental Science and Technology, 10, 908-912.

Burton, C.S., Bekowies, P.J., Pollack, R.I. and Connell, P. (1976), "Oxidant/Ozone Ambient Measurement Methods: An Assessment and Evaluation," Report No. EF76-111R, Systems Applications, Inc., San Rafael, California.

CARB (1974a), "Oxidant Episode in the South Coast Air Basin-June 27-28," California Air Quality Data, VII, April, May, June.

CARB (1974b), "Historical Occurrence of Temperatures Aloft Some 5000 Feet Above Sea Level," California Air Quality Data, VII, October, November, December.

CARB (1976), "Adoption of a System for the Classification of Organic Compounds According to Photochemical Reactivity," California Air Resources Board Staff Report No. 76-3-4, February 19.

Cavanagh, L.A., Schodt, C.F. and Robinson, E. (1969), "Atmospheric Hydrocarbon and Carbon Monoxide Measurements at Point Barrow, Alaska," Environmental Science and Technology, 3, 251-257.

Darnall, K.R., Lloyd, A.C., Winer, A.M. and Pitts, J.N. (1976), "Reactivity Scale for Atmospheric Hydrocarbons Based on Reaction with Hydroxyl Radical," Environmental Science and Technology, 10, 692-696.

Dimitriades, B. (1974), "The Concept of Reactivity and its Possible Application in Control," in Proceedings of the Solvent Reactivity Conference. U.S. Environmental Protection Agency Report No. EPA-6503-74-010.

Ditto, F.H., Guitierrez, L.T. and Bosch, J.C. (1976), "Weighted Sensitivity Analysis of Emissions Inventory Data," J. Air Pollution Control Association, 26, 875-880.

Dunker, A.M. (1980), "The Response of an Atmospheric Reaction-Transport Model to Changes in Input Functions," Atmospheric Environment, 14, 671-679.

Dunker, A.M. (1981), "Efficient Calculation of Sensitivity Coefficients for Complex Atmospheric Models," Atmospheric Environment, 15, 1155-1161.

Eldon, J.A. and Trijonis, J.C. (1977), Statistical Oxidant/Precursor Relationships for the Los Angeles Region Part I: Data Quality Review and Evaluation," Report prepared by Technology Service Corporation, Santa Monica, California for California Air Resources Board under Contract Number A5-020-87.

Falls, A.H., McRae, G.J. and Seinfeld, J.H. (1979), "Sensitivity and Uncertainty of Reaction Mechanisms for Photochemical Air Pollution," Int. J. Chemical Kinetics, 11, 1137-1162.

Feller, W. (1968), An Introduction to Probability Theory and its Application, Volume I, John Wiley and Sons, Inc., New York, 509 pp.

Fox, D. (1981), "Judging Air Quality Model Performance," Bulletin of American Meteorological Society, 62 599-609.

Goklany, I.M. (1980), "Emissions Inventory Errors for Point Sources and Some Quality Assurance Aspects," J. Air Pollution Control Association, 30, 362-365.

Goodin, W.R., McRae, G.J. and Seinfeld, J.H. (1979a), "A Comparison of Interpolation Methods for Sparse Data: Application to Wind and Concentration Fields," J. Applied Meteorology, 18, 761-771.

Goodin, W.R., McRae, G.J. and Seinfeld, J.H. (1979b), "An Objective Analysis Technique for Constructing Three-Dimensional, Urban-Scale Wind Fields," J. Applied Meteorology, 19, 98-108.

Goodin, W.R., McRae, G.J. and Seinfeld, J.H. (1981), "Reply to Comments on `A Comparison of Interpolation Methods for Sparse Data: Application to Wind and Concentration Fields,'" J. Applied Meteorology, 20, 92-94.

Graham, R.A. and Johnston, H.S. (1978), "The Photochemistry of NO_3 and the Kinetics of the N_2O_5-O_3 System," J. Physical Chemistry, 82, 254-268.

Grisinger, J. (1981) "Personal Communication."

Higuchi, J.E., Hsu, A. and MacPhee, R.C. (1976), "Dynamic Calibrations of Saltzman Type Analyzers Using NO_2 in Air Mixtures," J. Air Pollution Control Association, 26, 136-138.

Higuchi, J.E. (1981), "Personal Communication."

Hodgeson, J.A. (1972), "Review of Analytical Methods for Atmospheric Oxidants Measurements," Int. J. Environmental and Analytical Chemistry, 2, 113-132.

Kopczynski, S.L., Lonneman, W.A., Sutterfield, F.D. and Darley, P.E. (1972), "Photochemistry of Atmospheric Samples in Los Angeles," Environmental Science and Technology, 6, 342-347.

Lamb, S.I., Petrowski, C., Kaplan, I.R. and Simoneit, B.R.T. (1980), "Organic Compounds in Urban Atmospheres: A Review of Distribution, Collection and Analysis, J. Air Pollution Control Association, 30, 1098-1115.

Lamb, R.G. and Seinfeld, J.H. (1973), "Mathematical Modeling of Urban Air Pollution--General Theory," Environmental Science and Technology, 7, 253-261.

Mayrsohn, H. and Crabtree, J. (1976), "Source Reconciliation of Atmospheric Hydrocarbons," Atmospheric Environment, 10, 137-143.

McRae, G.J. (1981), "Mathematical Modeling of Photochemical Air Pollution," Ph.D. Thesis, California Institute of Technology, Pasadena, California.

McRae, G.J., Goodin, W.R. and Seinfeld, J.H. (1982a), "Development of a Second Generation Mathematical Model for Urban Air Pollution: I Model Formulation," Atmospheric Environment, 16, 679-696.

McRae, G.J., Goodin, W.R. and Seinfeld, J.H. (1982b), "Numerical Solution of the Atmospheric Diffusion Equation for Chemically Reacting Flows," J. Computational Physics, 45, 1-42.

McRae, G.J., Goodin, W.R. and Seinfeld, J.H. (1982c), "Mathematical Modeling of Photochemical Air Pollution," Final Report to the California Air Resources Board under contracts A5-046-87 and A7-187-30, Environmental Quality Laboratory, Report No. 18, California Institute of Technology, Pasadena, California, 800 pp.

McRae, G.J., Shair, F.H. and Seinfeld, J.H. (1981), "Convective Downmixing of Plumes in a Coastal Environment," J. Applied Meteorology, 20, 1312-1324.

Rao, S.T. and Visalli, J.R. (1981), "On the Comparative Assessment of the Performance of Air Quality Models," J. Air Pollution Control Association, 31, 851-860.

Rasmussen, K.H., Taheri, M. and Kabel, R.L. (1974), "Sources and Natural Removal Processes for Some Atmospheric Pollutants," EPA-650/4-74-032, Center for Air Environment Studies, Pennsylvania State University, University Park, Penn.

RTI (1975), "Investigation of Rural Oxidant Levels as Related to Urban Hydrocarbon Control Strategies," EPA-650/4-74-036, Research Triangle Institute, Research Triangle Park, North Carolina.

Seigneur, C., Tesche, T.W., Roth, P.M. and Reid, L.E. (1981), "Sensitivity of a Complex Urban Air Quality Model to Input Data," J. Applied Meteorology, 20, 50-70.

Spicer, C.W. (1975), "The Transport of Oxidant Beyond Urban Areas," Batelle Columbus Laboratory, Columbus, Ohio.

Stephens, E.R. and Burleson, F.R. (1969), "Distribution of Light Hydrocarbons in Ambient Air," J. Air Pollution Control Association, 19, 929-936.

Tilden, J.W. and Seinfeld, J.H. (1982), "Sensitivity Analysis of a Mathematical Model for Photochemical Air Pollution," Atmospheric Environment, 16, 1357-1364.

Trijonis, J.C. and Arledge, K.W. (1975), "Utility of Reactivity Criteria in Organic Emission Control Strategies for Los Angeles," Prepared for U.S. Environmental Protection Agency under contract No. 68-02-1735 by TRW Environmental Services, Redondo Beach, California.

References for Chapter 12

Bilger, R.W. (1978), "Optimum Control Strategy for Photochemical Oxidants," Environmental Science and Technology, 12, 937-940.

Cass, G.R. and McRae, G.J. (1981) "Minimizing the Cost of Air Pollution Control," Environmental Science and Technology, Environmental Science and Technology, 15, 748-757.

Derwent, R.G. and Hov, O. (1980), "Computer Modelling Studies of the Impact of Vehicle Exhaust Emission Controls on Photochemical Air Pollution Formation in the United Kingdom," Environmental Science and Technology, 11, 1360-1366.

Dimitriades, B. (1977), "Oxidant Control Strategies. Part I. Urban Oxidant Control Strategy Derived from Existing Smog Chamber Data," Environmental Science and Technology, 11, 80-88.

Ditto, F.H., Gutierrez, L.T. and Bosch, T.C. (1976), Weighted Sensitivity Analysis of Emission Inventory Data, J. Air Pollution Control Association, 26, 875-880.

Franklin, J. (1980), Methods of Mathematical Economics, Springer-Verlag, New York, 297 pp.

Kyan, C.P. and Seinfeld, J.H. (1972), "Determination of Optimal Multi-Year Air Pollution Control Policies," J. Dynamic Systems, Measurement and Control, 94, 266-273.

Kyan, C.P. and Seinfeld, J.H. (1974), "On Meeting the Provisions of the Clean Air Act," AIChE Journal, 20, 118-127.

Post, K. (1979), "Precursor Distributions, Ozone Formation and Control Strategy Options for Sydney," Atmospheric Environment, 13, 783-790.

Shapiro, J.E. (1979), Mathematical Programming: Structures and Algorithms, John Wiley & Sons, New York, 388 pp.

Trijonis, J.C. (1974), "Economic Air Pollution Control Model for Los Angeles County in 1975," Environmental Science and Technology, 8, 811-826.

Whitten, G.Z. and Hogo, H. (1978), "User's Manual for Kinetics Model and Ozone Isopleth Plotting Package," U.S. Environmental Protection Agency Report, EPA-600/8-78-014a, 239 pp.

Wismer, D.A. and Chattergy, R. (1978), Introduction to Nonlinear Optimization, North Holland, New York, 395 pp.

References for Appendix B

Connor, J.J. and Brebbia, C.A. (1977) Finite Element Techniques for Fluid Flow, Newnes-Butterworths, London, 310 pp.

Finlayson, B.A. (1972) The Method of Weighted Residuals and Variational Principles, Academic Press, New York, 412 pp.

Pepper, D.W., Kern, C.D. and Long, P.E. (1979) "Modeling the Dispersion of Atmospheric Pollution using Cubic Splines and Chapeau Functions," Atmospheric Environment, 13, 223-237.

Roache, P.J. (1976) Computational Fluid Dynamics, Hermosa Publishers, Albuquerque, New Mexico.

Strang, G. and Fix, G.J. (1973) An Analysis of the Finite Element Method, Prentice-Hall, Inc., Englewood Cliffs, New Jersey, 306 pp.